U.S.NRC
United States Nuclear Regulatory Commission
Protecting People and the Environment

NUREG/CR-7113
PNNL-19353

An Assessment of Ultrasonic Techniques for Far-Side Examinations of Austenitic Stainless Steel Piping Welds

Office of Nuclear Regulatory Research

AVAILABILITY OF REFERENCE MATERIALS IN NRC PUBLICATIONS

NRC Reference Material

As of November 1999, you may electronically access NUREG-series publications and other NRC records at NRC's Public Electronic Reading Room at http://www.nrc.gov/reading-rm.html. Publicly released records include, to name a few, NUREG-series publications; *Federal Register* notices; applicant, licensee, and vendor documents and correspondence; NRC correspondence and internal memoranda; bulletins and information notices; inspection and investigative reports; licensee event reports; and Commission papers and their attachments.

NRC publications in the NUREG series, NRC regulations, and *Title 10, Energy*, in the Code of *Federal Regulations* may also be purchased from one of these two sources.

1. The Superintendent of Documents
   U.S. Government Printing Office
   Mail Stop SSOP
   Washington, DC 20402–0001
   Internet: bookstore.gpo.gov
   Telephone: 202-512-1800
   Fax: 202-512-2250
2. The National Technical Information Service
   Springfield, VA 22161–0002
   www.ntis.gov
   1–800–553–6847 or, locally, 703–605–6000

A single copy of each NRC draft report for comment is available free, to the extent of supply, upon written request as follows:

Address: U.S. Nuclear Regulatory Commission
Office of Administration
Publications Branch
Washington, DC 20555-0001
E-mail: DISTRIBUTION.RESOURCE@NRC.GOV
Facsimile: 301–415–2289

Some publications in the NUREG series that are posted at NRC's Web site address http://www.nrc.gov/reading-rm/doc-collections/nuregs are updated periodically and may differ from the last printed version. Although references to material found on a Web site bear the date the material was accessed, the material available on the date cited may subsequently be removed from the site.

Non-NRC Reference Material

Documents available from public and special technical libraries include all open literature items, such as books, journal articles, and transactions, *Federal Register* notices, Federal and State legislation, and congressional reports. Such documents as theses, dissertations, foreign reports and translations, and non-NRC conference proceedings may be purchased from their sponsoring organization.

Copies of industry codes and standards used in a substantive manner in the NRC regulatory process are maintained at—

The NRC Technical Library
Two White Flint North
11545 Rockville Pike
Rockville, MD 20852–2738

These standards are available in the library for reference use by the public. Codes and standards are usually copyrighted and may be purchased from the originating organization or, if they are American National Standards, from—

American National Standards Institute
11 West 42nd Street
New York, NY 10036–8002
www.ansi.org
212–642–4900

Legally binding regulatory requirements are stated only in laws; NRC regulations; licenses, including technical specifications; or orders, not in NUREG-series publications. The views expressed in contractor-prepared publications in this series are not necessarily those of the NRC.

The NUREG series comprises (1) technical and administrative reports and books prepared by the staff (NUREG–XXXX) or agency contractors (NUREG/CR–XXXX), (2) proceedings of conferences (NUREG/CP–XXXX), (3) reports resulting from international agreements (NUREG/IA–XXXX), (4) brochures (NUREG/BR–XXXX), and (5) compilations of legal decisions and orders of the Commission and Atomic and Safety Licensing Boards and of Directors' decisions under Section 2.206 of NRC's regulations (NUREG–0750).

U.S.NRC
United States Nuclear Regulatory Commission
Protecting People and the Environment

NUREG/CR-7113
PNNL-19353

An Assessment of Ultrasonic Techniques for Far-Side Examinations of Austenitic Stainless Steel Piping Welds

Manuscript Completed: October 2011
Date Published: November 2011

Prepared by
M. T. Anderson, A. A. Diaz, A. D. Cinson, S. L. Crawford,
S. E. Cumblidge, S. R. Doctor, K. M. Denslow, and S. Ahmed

Pacific Northwest National Laboratory
P.O. Box 999
Richland, WA 99352

W. E. Norris, NRC Program Manager

NRC Job Code N6398

Office of Nuclear Regulatory Research

Abstract

Austenitic stainless steels are used in operating nuclear power plants primary loop piping because of their resistance to corrosion, or in locations where high strength and creep resistance are required because of elevated temperatures. Austenitic stainless steel piping welds are susceptible to stress corrosion cracking so it is essential to perform effective and reliable inspections. However, their anisotropic and large-grained structure strongly affects the propagation of ultrasound making it difficult to inspect. Another impediment to performing satisfactory inspections is that a significant number of weld locations exist where component geometry or permanent obstructions only provide suitable access to one side of the weld. These "far-side inspections" of piping welds currently are performed on a "best-effort" basis and with the exception of single-side dissimilar metal welds, do not conform to ASME Code Section XI, Appendix VIII, performance demonstration requirements. The industry, through the Electric Power Research Institute (EPRI), is actively involved in improving far-side inspections through the use of phased-array probes.

As a result, confirmatory research is being conducted for the U.S. Nuclear Regulatory Commission at the Pacific Northwest National Laboratory to assess the capabilities of ultrasonic testing (UT) for the examination of austenitic stainless steel piping welds from the far side. Specifically, studies were conducted to assess the ability of advanced UT techniques to detect and determine the size of flaws from the far-side of wrought austenitic piping welds. Far-side inspections of nuclear system piping welds are currently performed on a "best-effort" basis and do not conform to ASME Code Section XI Appendix VIII performance demonstration requirements. To ensure safety in the case of less than 100% examination coverage of a particular weld, the staff requires that the licensee demonstrate in its relief request that other welds of the same examination category have had 100% coverage with no flaws, and that the subject weld has no active degradation mechanism based on operating experience. The staff may also require the licensee to improve its examination coverage by improving its examination technique (e.g., using certain transducers). The staff approves these less-than-100% examination coverage relief requests based on rigorous evaluation to ensure that structural integrity of the piping is maintained in accordance with the ASME Code, Section XI. For the laboratory work in this study, four circumferential welds in 610-mm-diameter, 36-mm-thick ASTM A-358, Grade 304 vintage austenitic stainless steel pipe were examined. The welds were fabricated with varied welding parameters; both horizontal and vertical pipe orientations were used, with air and water backing, to simulate field welding conditions. A series of saws, electro-discharge machined notches, and implanted fatigue cracks were placed into the heat-affected zones of the welds. The saws and notches ranged in depth from 7.5% to 28.4% through-wall. The implanted cracks ranged in depth from 5% through-wall to 64% through-wall. The welds were examined with phased-array technology operating at 1.5 MHz, and with low-frequency/Synthetic Aperture Focusing Technique (SAFT) methods in the 250–400 kHz regime. These results were compared to encoded conventional (monolithic transducer element) ultrasonic techniques as a baseline at 2.0 MHz, a frequency typical for examinations of piping welds in the field. The examinations showed that while phased-array and low-frequency/ SAFT were each able to detect and accurately length-size, but not depth-size, the notches and flaws through the welds, phased-array ultrasonic inspection provided the best results, detecting nearly

all of the flaws from the far side. The ultrasonic results were insensitive to the different welding techniques used in each weld.

Based on the laboratory work conducted in this study, phased-array ultrasonic inspection provided the best results, detecting nearly all of the flaws from the far side. These results were presented at the *Fifth International Conference on NDE in Relation to Structural Integrity for Nuclear and Pressurised Components* in 2006. To better understand acoustic propagation through austenitic welds to determine whether the phased-array inspections currently being conducted are effective and reliable, sound-field mapping was conducted. At the invitation of EPRI, PNNL examined field-removed specimens containing service-induced intergranular stress corrosion cracks at the EPRI Nondestructive Evaluation Center, in Charlotte, North Carolina, to compare results. Collective results from the activities described above are presented here.

Foreword

Article IWB-2500, “Examination and Pressure Test Requirements,” of Section XI, “Rules for Inservice Inspection of Nuclear Power Plant Components,” of the American Society of Mechanical Engineers (ASME) Boiler and Pressure Vessel Code (BPV Code), provides that certain nuclear power plant components be inspected in accordance with Table IWB-2500-1, “Examination Categories.” In most cases, the table states that essentially 100% of any given weld be inspected. The ASME BPV Code is incorporated by reference into Title 10, Part 50, of the *Code of Federal Regulations*, “Domestic Licensing of Production and Utilization Facilities.” Thus, licensees are required by law to adhere to the provisions of the ASME BPV Code.

Conventional transducers operate at fixed frequencies. The location at which a transducer focuses sound is determined by the transducer area and shape, the ultrasound frequency, and the sound velocity of the propagation medium. Conventional transducers require access to both sides of a weld to properly insonify the weld volume and thus detect any defects that may be present. There are a significant percentage of weld locations where component geometry or permanent obstructions only provide suitable access to one side of the weld. Multiple inspection techniques are sometimes required to adequately inspect certain welds which results in additional occupational dose. Various investigations have been performed to determine the potential for inspecting welds from one side using phased-array probes, and the work described herein helped the NRC evaluate the acceptability of these techniques.

Phased-array probes consist of many small ultrasonic elements, each of which can be pulsed individually. By varying the pulsing of the elements one-by-one in sequence, a beam at a known angle can be initiated. This beam can be steered electronically thus sweeping through a weld like a searchlight. Software allows the data from multiple sweeps to be collected into an image showing internal sound reflectors such as counterbores or weld defects. Many studies have demonstrated the superiority of phased-array probes over conventional probes.

Nuclear power plant austenitic stainless steel piping welds are susceptible to stress corrosion cracking. The U.S. Nuclear Regulatory Commission conducted this confirmatory research at the Pacific Northwest National Laboratory (PNNL) to assess the effectiveness and reliability of ultrasonic testing for examining austenitic stainless steel piping welds. The assessment by PNNL shows that the use of phased arrays provides the best overall results with the highest number of far-side flaws being detected. The capability to length-size is well within ASME Code-established acceptance criteria. Flaw-tip signals were not observed from the far-side, so no estimate of flaw depth was possible. Far-side inspections are performed on a best-effort basis. While the ASME Code requires essentially 100 percent inspection of welds, the structure of austenitic stainless steel welds in combination with limitations due to geometry results in some cases of inspection coverage of less than 50 percent. Accordingly, while the use of phased arrays has been shown to be a significant step forward relative to the capability to inspect austenitic stainless steel piping welds, further enhancements by the industry will be required to improve weld coverage.

Contents

Figures

Tables

Executive Summary

Research is being conducted for the U.S. Nuclear Regulatory Commission (NRC) at the Pacific Northwest National Laboratory (PNNL) to assess the effectiveness and reliability of advanced nondestructive examination (NDE) methods for the inspection of light-water reactor components. The scope of this research encompasses many primary system pressure boundary materials including cast austenitic stainless steels (CASS); dissimilar metal welds; piping with corrosion-resistant cladding; weld overlays, inlays and onlays; and examinations of wrought austenitic piping welds. One objective of this work is to evaluate various ultrasonic testing (UT) methods to assess their ability to detect, localize, and size cracks through coarse-grained materials.

This report summarizes an assessment of the capabilities and limitations of various ultrasonic techniques for far-side examinations of austenitic stainless steel welds. Periodic inservice inspection of nuclear power plants is intended to detect service-related degradation that may adversely impact structural integrity, or impair a component's ability to function as designed. Section XI of the American Society of Mechanical Engineers (ASME) Boiler and Pressure Vessel Code, entitled *Rules for Inservice Inspection of Nuclear Power Plant Components*, requires that volumetric examinations be performed for many safety-related components, including those that comprise the primary coolant pressure boundary. The volumetric examination most often applied is ultrasonic testing. Because of the anisotropic microstructural features found in austenitic coarse-grained materials, UT of stainless steel components continues to be a challenge to the industry. This is especially true for detection and characterization of service-induced flaws, including stress corrosion cracking (SCC), that may initiate on the far side of welds where access for examination may be limited to the near side of the weld.

PNNL conducted ultrasonic studies in a three-phased approach, to assess far-side inspection in specimens containing implanted thermal fatigue cracks and machined notches. From the first two phases of work, results were favorable in that nearly all of the flaws were detected. Reported here are the results of this initial work, including conventional, phased-array, and low-frequency/Synthetic Aperture Focusing Technique (SAFT) ultrasonic techniques. The data show that with the use of precise acquisition techniques and rigorous analytical methods, far-side detection and length-sizing for surface-breaking circumferential flaws is quite possible in austenitic piping welds. However, no flaw-tip diffracted signals could be observed from the far side of the weld; therefore, time-of-flight through-wall depth sizing may not be feasible.

Efforts in Phases 1 and 2 show that, while variation in peak amplitudes occur randomly along the length of shop and field welds, no regional effects in acoustic responses from flaws on the far side of welds were observed. In other words, no relationship between circumferential weld microstructures (due to varied welding positions) and acoustic transmission quality of the weld could be ascertained. These results are shown to be valid for implanted thermal fatigue cracks and machined reflectors, with both exhibiting moderately planer shapes. No other service-induced flaws, for example, inter-granular or primary water stress corrosion cracking, were available during Phase 1 and Phase 2 laboratory trials.

Of the UT technologies tested through Phase 2, the ultrasonic phased-array method provided the best overall results with the highest number of far-side flaws being detected, and length-sizing capability well within ASME Code-established acceptance criteria. The conventional UT method also showed good detection and sizing effectiveness, but this is primarily due to the automated data acquisition and extensive analyses performed; it is not expected that manual UT examinations with real-time interpretation would perform at this level. The low-frequency/ SAFT method explored the aspects of using very long wavelengths over a range of frequencies from 250–400 kHz (for insensitivity to coarse-grained weld structures) and their impact on flaw detection performance and sizing accuracy. Reduced performance was noted for this application. The results indicate that one must determine the highest frequency that can effectively penetrate the coarse-grained microstructure with minimal distortion and use this frequency for the inspection, coupled with signal processing such as SAFT.

To better understand acoustic propagation through austenitic welds using phased-array ultrasonic methods, sound-field mapping was conducted, and results were used to guide improved designs for more effective phased-array probes to address this inspection problem. The longitudinal (compressional) wave modality showed little degradation as the sound field propagated through the weld material from the far side. The sound-field maps provided in this report clearly show that the longitudinal wave mode provides suitable penetration and the sound field maintains ample coherence and signal strength as it propagates through the austenitic weld. Only at the highest angles of insonification (70°) coupled with a shallow focal depth (15 mm) do the longitudinal waves start to exhibit slight degradation to the field shape, coherence, and structure. Beam partitioning and scattering of the compressional-wave energy is not evident as the L-wave sound fields appear to be relatively insensitive to the effects of the austenitic weld material at the frequency evaluated. The results from this evaluation show that use of longitudinal waves, coupled with the appropriate frequency (wavelength) relative to the size of the grain boundaries and weld structure, can provide the foundation for an effective inspection.

The initial activities were followed by a Phase 3 effort to employ ultrasonic phased-array inspection on specimens containing service-induced inter-granular stress corrosion cracking (IGSCC) at the Electric Power Research Institute (EPRI) NDE Center, in Charlotte, North Carolina. For the EPRI exercise, phased-array data were acquired on a series of specimens containing service-induced IGSCCs. True-state location information for all flaws was provided during the data analysis phase. The crack lengths were variable and PNNL only examined the specimens for circumferentially oriented cracks (cracks that are parallel to the weld). Flaw depth information was not provided and, once again, flaw-tip signals were not detected, so no estimate of flaw depth was possible.

The investigation was focused on assessing current phased-array ultrasonic techniques for austenitic welds. Detection results should be considered as a best-effort, given equipment and inspection conditions; that is, the arrays were not specifically optimized for the weld conditions and the weld crowns were not removed, which would have provided greater access for each of the phased-array modalities and probes applied. However, as a result of the sound-field mapping activities that occurred at the end of Phase 2, a 1.5-MHz transmit-receive longitudinal probe was designed for application to far-side examinations, in an attempt to obtain a balance between effective penetration through the austenitic weld and suitable resolution for flaw detection.

Because the true-state location data were known for the flaws under examination, the results described here should not be considered representative of a blind test, only an assessment of state-of-art phased-array capabilities to detect actual service-induced IGSCC. Data were acquired with two refracted longitudinal wave phased-array probes, 1.5 MHz and 2 MHz, and one shear-wave probe at 2 MHz from both the near and far side of the weld center relative to the flaw. The far-side detection rate for longitudinal mode inspections was nearly 70% while the detection rate for shear mode inspections was 52%. Signal-to-noise values for the detected flaws were good. Shear wave sound fields are significantly partitioned and attenuated (primarily by scattering) as they propagate through the austenitic weld material, while the longitudinal wave sound fields generally maintain coherence with reduced scattering. Both shear and longitudinal data tended to be cluttered with geometrical and material reflections making signal discrimination the primary challenge in flaw detection. Flaw detection would be improved if the weld crowns were removed because it would provide better access to the far-side region of interest and enable the use of probes with larger footprints; thus allowing large acoustic apertures for better sound field generation. The use of lower frequencies (longer wavelengths) may provide better penetration and reduce scattering effects, while more effective approaches for peaking signals may improve signal discrimination. The improvements cited above coupled with more accurate profiling of the complex part geometry in the critical area of examination, could collectively enhance the detection results from what is reported here.

Several insights were gained from the subject study that could be used by industry as it moves forward to improve far-side inspections, such as further modeling of the inspection process (weld microstructures, acoustics, etc.) to facilitate the design of improved search units, additional laboratory measurements on IGSCC and axial-oriented flaws, and metallographic studies to help interpret and correlate weld microstructures with the findings of the modeling and measurement activities. These activities would strengthen the technical basis for performance-demonstration requirements.

Acknowledgments

The work reported here spans activities conducted over several years and was sponsored by the U.S. Nuclear Regulatory Commission (NRC). This work was conducted under two NRC Job Code Numbers, initially starting under Y6604 and transitioning to N6398. Deborah Jackson was the NRC project manager for the Y6604 work and Wallace Norris is the current NRC project manager for work conducted under N6398. The Pacific Northwest National Laboratory (PNNL) would like to thank Ms. Jackson and Mr. Norris for their involvement and guidance, technical direction, and attention to detail throughout the course of this effort. PNNL also thanks Mr. Jeff Hixon (NRC intern that rotated to PNNL) for his participation and technical support throughout the initial phase of the study. The work reported here was conducted at PNNL in Richland, Washington, and PNNL staff appreciated the opportunity to work side-by-side with NRC personnel. We also thank Mr. Jim Davis (NRC) for his guidance and support of this work.

In addition, the authors express their sincere gratitude to Guy Maes and Patrick Tremblay at ZETEC, Inc. for their willingness and ongoing engineering support with phased-array system functional and operational issues, as well as their guidance and input regarding phased-array probe design and manufacture.

PNNL would like to thank several personnel at the Electric Power Research Institute (EPRI) NDE Center for enabling the work reported here. We appreciate Greg Selby's original invitation to collect and review IGSCC data on the practice specimens, and for making his staff available to PNNL during this activity. During the data collection and analyses, Carl Latiolais, Doug Kull, John Langevin, and Lief Esp provided their support to assist PNNL with set up and true-state review. Mark Dennis facilitated the final contract to allow PNNL to review secure data. We also appreciate the comments provided by EPRI staff on the previous draft sections of this report.

At PNNL, the authors wish to express their gratitude to Mr. Stan Owsley for designing the laboratory platform and peripheral mechanics for effective configuration of the piping segments for laboratory examination. The authors would like to thank Marino Morra for providing initial support to this effort in coordinating the cutting and machining of pipe segments for specimen fabrication. Appreciation is given Mr. Jake Tucker, Mr. Eric S. Andersen, and Mr. George Schuster for their technical support, advice, and assistance on this project. The authors are also grateful to Lori Bisping, Angie Dickson, and Earlene Prickett for their efforts in supporting program procurements, contractual issues, financial tracking, and various other administrative duties pertinent to this effort. Finally, the PNNL technical team would like to extend their thanks to Kay Hass for her ongoing support, attention to detail, and technical editing expertise in preparing and finalizing this document.

PNNL is operated by Battelle for the U.S. Department of Energy under Contract DE-AC05-76RL01830.

Acronyms and Abbreviations

A/D	analog-to-digital
ASME	American Society of Mechanical Engineers
ASTM	American Society for Testing Materials
BWR	boiling water reactor
CASS	cast austenitic stainless steel
CD	compact disc
CSS	cast stainless steel
dB	decibels
DMW	dissimilar metal weld
DVD	digital video disc
EDM	electro-discharge machined
EPRI	Electric Power Research Institute
FSH	full screen height
HAZ	heat affected zone
ID	inner diameter
IGSCC	intergranular stress corrosion crack
ISI	inservice inspection
LF/SAFT	low-frequency/Synthetic Aperture Focusing Technique
LOS	loss of signal
LWR	light water reactor
NDE	nondestructive examination
NPP	nuclear power plant
NRC	U.S. Nuclear Regulatory Commission
NRR	Nuclear Reactor Regulation (Office of)
OD	outer diameter
PA	phased array
PA-UT	phased array ultrasonic testing
PC	personal computer
PD	performance demonstration
PDI	performance demonstration initiative
PNNL	Pacific Northwest National Laboratory
PWSCC	pressurized water stress corrosion crack
RF	radio frequency
RMSE	root mean square error
SAA	signal amplitude anomaly
SAFT	synthetic aperture focusing technique

SNR	signal-to-noise ratio
SS	stainless steel
TFC	thermal fatigue crack
TRL	transmit-receive longitudinal
TRS	transmit-receive shear
UT	ultrasonic testing
WSS	wrought stainless steel
W_{CL}	weld centerline

1 Introduction

The overall objective of the work at PNNL is to determine the effectiveness and reliability of ultrasonic inspection techniques on light water reactor (LWR) components containing cast stainless steel material and other coarse-grained components with dissimilar metal welds, piping with corrosion-resistant cladding, and examinations of austenitic piping welds. This report summarizes the technical evaluations performed to address a limited portion of the objective, specifically aimed at assessing the capabilities and limitations of ultrasonic techniques for examining flaws from the far side of austenitic stainless steel (SS) welds.

Throughout many industrial sectors, efforts are underway to evaluate the potential for new nondestructive examination (NDE) methods to reliably detect structural degradation in aging components while controlling costs and limiting inspection times. In particular, the nuclear industry, through the Electric Power Research Institute (EPRI), is actively involved in determining the feasibility of applying new NDE methods for challenging inspections at operating nuclear power plants. The purpose of this report is to provide the results of laboratory investigations at the Pacific Northwest National Laboratory (PNNL) to determine capabilities of ultrasonic phased-array (PA), low-frequency (LF)/Synthetic Aperture Focusing Technique (SAFT), and conventional technologies as applied to the far-side inspection of wrought austenitic piping welds.

Austenitic stainless steels are generally used for applications where resistance to corrosion, or high strength and creep resistance, are required at elevated temperatures, such as in the primary piping of a light water reactor (LWR). Ultrasonic techniques have routinely been used in various industrial applications for over 50 years and yet, cast or welded austenitic components remain difficult to reliably and effectively examine. Over the past 20 or so years, significant progress has been made towards improving ultrasonic inspection techniques. Typically, conventional ultrasonic Testing (UT) methods are used for inservice inspection (ISI), but these methods are often times hampered by the anisotropic, large-grained texture of the austenitic weld metal.

ISI requirements dictate that piping welds in the pressure boundaries of LWRs are subject to volumetric examination based on the requirements of Section XI of the American Society of Mechanical Engineers (ASME) Boiler and Pressure Vessel Code. The volumetric examination may be either radiographic or ultrasonic. For inservice examinations at operating reactors, background radiation and access limitations may preclude the use of radiography. Hence, volumetric examination of austenitic welds in selected LWR components are generally performed using ultrasonic examination. The purpose of ultrasonic testing/inservice inspection (UT/ISI) of piping and pressure vessels is to reliably detect and characterize material degradation that may develop during operation. The detection of potential degradation typically results from analyzing ultrasonic echo waveforms scattered from inherent material artifacts. Austenitic weld material exhibits a macro-crystalline structure that is established during the solidification process. Typically, the austenite phase forms long columnar grains based on the weld bead size and direction of maximum heat loss during solidification and cooling processes (Moysan et al. 2003). Due to the physical properties of these grains, many inspection problems

can arise, and ultrasonic flaw responses are often obscured by noise and scattered energy from the material structure.

Austenitic welds exist in many LWR piping systems. A large number of welds are the terminal ends of piping systems and consist of pipe-to-component welds. Access to each side of the weld may be limited, so a need exists to develop effective and reliable far-side inspection techniques for these components. Far-side austenitic weld inspection procedures continue to perform unsatisfactorily due to the coarse microstructure that characterizes these materials. The large size and orientation of the anisotropic grains, relative to the acoustic pulse wavelength, strongly affects the propagation of ultrasound by causing severe attenuation, beam skewing, changes in velocity, and scattering of ultrasonic energy (Macdonald et al. 2000). Refraction and reflection of the sound beam occur at the grain boundaries, from root conditions, counterbore, and at the weld fusion lines, resulting in defects being incorrectly characterized, specific volumes of material not being examined, or both. When coherent reflection and scattering of the sound beam occur at grain boundaries or from weld geometry, ultrasonic indications occur that are difficult to distinguish from signals originating from flaws. Conducting far-side inspections of austenitic welds, where signal-to-noise ratios are relatively low, can be confusing, unpredictable, and unreliable during conventional ultrasonic examinations.

PNNL conducted ultrasonic studies in a 3-phased approach. In Phases 1 and 2, technical assessments were conducted for far-side inspection in specimens containing implanted thermal fatigue cracks and machined notches in welds fabricated under variable conditions. In Phase 3, the focus of the technical evaluation was aimed at examining field-removed piping welds containing service-induced inter-granular stress corrosion cracking (IGSCC). Initially, PNNL chose to evaluate two advanced ultrasonic inspection approaches, and compare the performance of these techniques against conventional UT methods. The phased-array approach was selected because industry is evaluating this technology for several applications and anecdotal information indicates that there appear to be “windows” where effective inspections can be made through coarse-grained microstructures. It is not known if these “windows” are related to inspection frequency, inspection angle, or some other microstructural feature. The use of phased-array technology provides the capability to rapidly assess the effect of multiple inspection angles. The LF/SAFT approach was also chosen because of previous success on cast stainless steel (CSS) and the fact that 400-kHz wavelengths are much larger than the austenitic weld microstructure, which should minimize the impact of the microstructure on the sound field. At the same time, PNNL also documented the performance of a conventional, or monolithic element, pulse-echo inspection method as employed to pass the austenitic weld performance demonstration administered at the EPRI NDE Center and developed for ISI, in order to baseline the standard inspection for comparison with these advanced techniques.

The focus of this NUREG report targets far-side examination assessments conducted at PNNL over several years, in support of, and sponsored by, the United States Nuclear Regulatory Commission (NRC). Much information was gathered from lessons learned in detection and characterization of flaws during Phases 1 and 2 (Anderson et al. 2003; Anderson et al. 2006; Anderson et al. 2008). From these assessments, efforts were conducted to better understand sound-field propagation through austenitic welds. These activities focused on modeling and simulation efforts coupled with sound-field mapping exercises to determine austenitic weld

effects (coherence/distortion, shape, etc.) on sound fields as a function of frequency. These laboratory studies were followed by a Phase 3 evaluation aimed at employing optimized phased array-UT methods for examination of IGSCC in field-removed specimens. This NUREG provides a summary of a multi-phased laboratory effort, and in Section 2, the historical background of these efforts is provided, with specific technical objectives of these assessments being defined. Section 3 describes the scope of these evaluations, and Section 4 provides a summary of the inspection challenges encountered in examining wrought stainless steel (WSS) components from the far-side, and through austenitic welds. Section 5 provides all of the technical details associated with the specimens evaluated in this study, while Section 6 describes the ultrasonic probes used to employ conventional, LF/SAFT and phased-array UT techniques. Sections 7 and 8 summarize the data and results of Phase 1 and Phase 2 evaluations, respectively, for all three ultrasonic inspection techniques. Section 9 provides a technical discussion of the results obtained from the work in Phases 1 and 2. Section 10 describes the longitudinal-wave sound field assessments and simulations work. Section 11 provides a summary of the data and results from the Phase 3 evaluation at the EPRI NDE Center, while Section 12 provides the summary and conclusions from all work performed at PNNL on far-side examination effectiveness. Section 13 provides a listing of references cited in this report.

2 Background and Objectives

The United States Nuclear Regulatory Commission has sponsored PNNL to conduct a project titled “Reliability of Nondestructive Examination for Nuclear Power Plant Inservice Inspection.” The objectives of the project are to (1) evaluate the accuracy and reliability of nondestructive examination methods used for the inservice inspection of nuclear power plant (NPP) systems and components; (2) provide information for the Office of Nuclear Reactor Regulation (NRR) to assess the adequacy of proposed industry changes to ISI programs; (3) provide recommendations to the staff of the NRC to improve the effectiveness and adequacy of ISI programs; (4) evaluate the effectiveness of ISI techniques in detecting cracks in reactor coolant system components (e.g., dissimilar metal welds [DMWs], Alloy 52 weld overlays); and (5) provide technical assistance on NDE and related issues to the NRC program offices on an as-needed basis.

The results obtained from this project will assist the NRC by supporting their technical reviews and will serve as confirmatory results for determining the effectiveness and adequacy of NDE and ISI methods and programs presently used in operating nuclear power plants. Recent experience with cracking in reactor vessel penetrations and piping welds has increased reliance on the ability of NDE methods to detect and characterize service-induced flaws over a range of materials, geometries, and configurations. The ability to detect and characterize flaws varies with the selected NDE method. With the industry trend toward reducing inspection time, radiation exposure, and the number of examinations, the effectiveness and reliability of NDE methods becomes more important.

The research described in this report has been organized into three phases. The goal of Phase 1 was to test the capabilities of advanced ultrasonic technology on a limited set of welded specimens, and evaluate the ability of these UT techniques to characterize machined reflectors and fabricated cracks, while establishing a baseline for comparison against the results of conventional UT methods. The pipe samples were examined from several directions, both with the weld crown in place and with the weld crown machined off. In Phase 2, the information gained in Phase 1 was used to evaluate more challenging conditions and assess any affects presented by variations in welding position or procedure. Finally, in Phase 3, lessons learned from the first two phases were incorporated to provide an improved ultrasonic inspection protocol for examination of service-induced IGSCC using the most promising technique(s) evaluated in earlier phases.

Phase 1 and 2 evaluation efforts were conducted at PNNL and involved the application of conventional transducers, and use of LF/SAFT and ultrasonic phased-array methods on specimens containing implanted thermal fatigue cracks and machined reflectors. From these studies, it was concluded that PA inspection provided the best results, detecting nearly all of the flaws from the far side of the welds. These results were presented at the *Fifth International Conference on NDE in Relation to Structural Integrity for Nuclear and Pressurised Components* in 2006. This led to an invitation to examine field-removed specimens containing service-induced IGSCC at the EPRI NDE Center, in Charlotte, North Carolina.

3 Scope of Ultrasonic NDE Assessments

The scope of the work reported here was defined by NRC guidance and is focused toward evaluating UT inspection capabilities in wrought stainless steel (WSS) components with austenitic welds, as examined from the far-side. PNNL was tasked with acquisition and procurement of materials, fabrication of flawed specimens, design and procurement of specialized ultrasonic probes, and conducting data acquisition and analyses on these specimens. The scope of these activities was maintained over the course of evaluating the flawed specimens, with a focus on replicating materials used in the primary coolant headers in boiling water reactor (BWR) recirculation systems. In the first two phases of the work, vintage material was used in the fabrication of specimens; in particular, Schedule 80, American Society for Testing Materials (ASTM) 358 Grade 304 WSS, with nominal 610-mm (24.0-in.) outer diameter, and a wall thickness of approximately 36 mm (1.4 in.). Also, Phase 1 and 2 specimens were welded together using single-Vee girth welds and filler materials typical to nuclear applications such as ASME SA-240, Type 304 and E308-L. In Phase 3 of the assessment, the specimens examined at the EPRI NDE Center were field-removed piping segments removed from several BWR primary recirculation systems containing service-induced IGSCC.

The technical evaluation reported here included results and analyses of data acquired using three primary ultrasonic techniques:

- Conventional Ultrasonic Inspection
- Low-frequency/SAFT-UT
- Phased-Array Ultrasonic Inspection

These examination approaches were used to evaluate inspection performance on a set of implanted/fabricated thermal fatigue cracks (TFCs), machined reflectors, and service-induced IGSCC, to evaluate detection, localization, and sizing performance as a function of frequency and other critical inspection parameters. The work consisted of design and acquisition of sound-field simulations and mapping assessments for various LF/SAFT and phased-array probes, probe configurations, and wedges; development of specific PA focal laws; and use of the latest phased-array UT (PA-UT) data acquisition system (Tomoscan III) for implementing examinations. The experimental parameters of the work reported here include:

- Varied inspection frequencies
  - 1.5 MHz to 2.25 MHz (Conventional UT)
  - 250 kHz to 400 kHz (LF/SAFT UT)
  - 1.5 MHz to 2.0 MHz (Phased-Array UT)
- Varied inspection angles
  - 60° and 70° (Conventional UT)
  - 30° to 70° in 5° increments (LF/SAFT UT)
  - 30° to 70° in 1° increments (Phased-Array UT)

- Varied inspection modalities
  - Longitudinal and shear-wave modes (LF/SAFT and PA-UT)
  - Shear-wave mode only for Conventional-UT
- Varied orientations to the weld
  - Examinations were documented from both near- and far-sides of the welds

During data analysis of the piping specimens evaluated here, ultrasonic flaw detection and sizing performance were quantified against the true state, and assessments of the UT capabilities for flaw localization/positioning versus true state were conducted. In addition, an assessment of sound-field continuity and signal strength (baseline material noise analysis) through the austenitic weld and WSS parent material was performed. Metrics used for the analyses included signal-to-noise ratio (SNR); root-mean-square error (RMSE); and true-state values for flaw length, depth, and axial and circumferential locations relative to the full-penetration piping welds.

Finally, the scope of this effort also entailed modeling, simulation, and laboratory measurements for sound-field mapping, to better understand acoustic propagation through the austenitic welds, and to quantify spatial sound-field characteristics through the weld. These activities focused on such variables as incident angle, position from the weld centerline, and frequency, using the longitudinal (compressional) wave modality.

4 The Far-Side, Austenitic Weld Inspection Challenge

Austenitic steels are generally used for applications where resistance to corrosion, or high strength and creep resistance, are required at elevated temperatures, such as in the primary piping of an LWR. ASME Code Section XI requires volumetric examinations of these welds in the pressure boundary of LWRs. These examinations are either radiographic or ultrasonic. Often, background radiation and access limitations prevent the use of radiography, thus ultrasonic inspection must be employed. Conventional ultrasonic approaches are typically used for ISI; however, many austenitic welds are pipe-to-component welds where outer-diameter (OD) access to either side of the weld may be limited. In many cases, these access limitations often preclude near-side access, thereby requiring a far-side inspection.

Ultrasonic techniques have been routinely used in industry for over 50 years and, yet, cast or welded austenitic components can be difficult to reliably and effectively examine using ultrasound. Over the past 20+ years, significant progress has been made to improve inspection techniques. Assuring the structural integrity of reactor components requires nondestructive examinations during fabrication, and appropriate inservice examinations, to detect the presence of potentially significant fabrication defects or service-related degradation. Successful volumetric examination for selected components is predicated upon the use of satisfactory austenitic welding procedures; however, some of the most common arc-welding processes often exacerbate the inspection problem. Typically, conventional ultrasonic methods are often hampered by the anisotropic, textured structure of the austenitic weld. Figure 4.1 illustrates a typical austenitic weld microstructure.

Far-side austenitic weld inspection procedures continue to perform unsatisfactorily due to the coarse microstructure that characterizes these materials (Macdonald et al. 2000). These weld inspections continue to yield poor results due to the large size of the dendrites and the orientation of the anisotropic grains (relative to the acoustic pulse wavelength). Austenitic weld material exhibits a macro-crystalline structure that establishes itself during the solidification process. Typically, the austenitic phase forms long columnar grains that grow along the directions of maximum heat loss during the cooling process (Moysan et al. 2003). Due to the physical properties of these grains, many inspection problems can arise, and ultrasonic flaw responses are often obscured by noise and scattered energy from the material structure. At the frequencies required to resolve reflections (i.e., detect) from fatigue cracking and IGSCC on the far side of a weld, these conditions lead to severe attenuation (primarily scattering), sound beam re-direction and/or partitioning, changes in acoustic velocity as a function of spatial position on the component, and refraction/reflection of sound energy at grain boundaries, root conditions, counterbore, and weld fusion lines. The complexity inherent to this challenging inspection scenario translates into a lower signal-to-noise ratio (SNR), difficulties in signal (echo) discrimination, and the potential for incomplete insonification of the component.

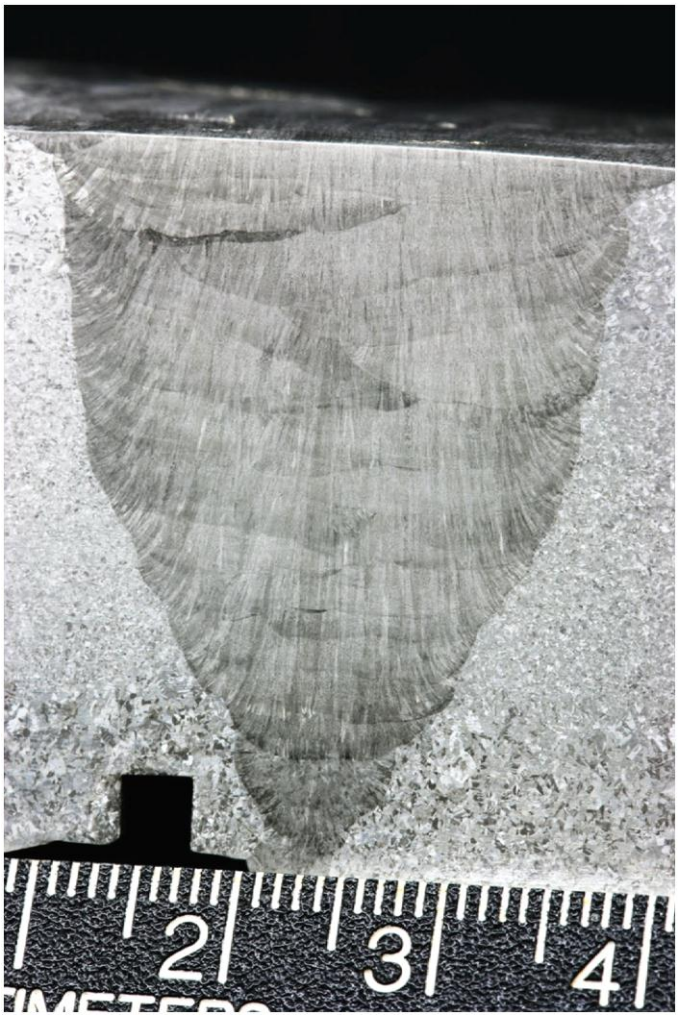

Figure 4.1 Polished and Chemically Etched Side View of an Austenitic Weld Microstructure in Wrought Stainless Steel

Because austenitic welds are used in many nuclear reactor piping systems and access may be limited, there exists a need to develop effective and reliable far-side inspection techniques for varied components.

5 Specimens Evaluated in this Study

5.1 Phase 1: Austenitic Piping Specimen No. 02-24-15

The specimens used in Phase 1 were made with ASTM A-358, Grade 304 vintage austenitic SS piping segments having nominal 610-mm (24.0-in.) outside diameter and approximately 36-mm (1.4-in.) wall thickness. This type and size of piping is typical of that used during original fabrication of primary coolant headers in BWR recirculation systems. The specimen was made by joining two cylinders of this material with a single-Vee girth weld, using procedures and filler material (ASME SA-240, Type 304) typical of those used in nuclear applications. The pipe was shop-welded with air backing in the horizontal position. The pipe was rotated during the welding process to allow the welder to always remain in the most advantageous position above the weld, in the 1G “down-hand” orientation.

During the welding process several thermal fatigue cracks were implanted into the heat-affected zone (HAZ) of the girth weld. The TFCs were generated by thermal cycling of a tension specimen to produce fatigue cracks of a specific size, removing the crack coupon from the tension bar, then in-situ fusing these coupons during the girth-welding process. This technique allows the crack face to be characterized via precise mechanical measurements and photographed prior to implantation, and has been shown to produce cracks in the as-welded condition within ± 1.0 mm (0.04 in.) of the specified length and height in the piping material. Also, this technique enables the vendor (FlawTech) to produce various geometrical and welding conditions that simulate those found during field welding; for example, counterbore, inner-diameter miss-match, weld root, fusion anomalies, and weld crown configurations. Vendor-supplied photographs of the piping material, welding and flaw implantation processes, and implanted flaw configurations are included for review in Appendix A. The implanted TFCs have crack opening dimensions ranging from 25–250 µm (1–10 mils). Figure 5.1 shows where the flaws (TFCs and additional sawcuts) were placed and how the pipe was sectioned. Figures 5.2 and 5.3 depict idealized cross sections of the specimens, and give reference dimensions for implanted crack characteristics. The TFC dimensions and locations for those used in this study are shown in Table 5.1.

It has been experimentally determined (Schuster et al. 2010) that cracks implanted into a sample in this way have an ultrasonic response that is typically 5–6 decibels (dB) lower than a notch of the same depth using 45° shear waves. These cracks most closely resemble low-cycle, high-stress mechanical fatigue cracks. The cracks are straight, with no branching, have mid-sized to large crack opening dimensions, and have a high degree of surface roughness. This is in contrast to high-cycle, low-load mechanical fatigue cracks that are much tighter and have less surface roughness. Service-induced thermal fatigue cracks are usually tighter than the cracks used in this study, possibly nonlinear in shape, occasionally branched, and thus more difficult to detect using ultrasound than the implanted cracks. IGSCC, which is a likely failure mechanism for austenitic SS, are highly variable in nature, but are often highly branched and tight, resulting in an increased level of difficulty for detection and more challenging with regard to acquiring detectable tip responses. Depending on the crack morphology, an IGSCC

can be more difficult (Lemaitre 1994; Gruber et al. 1995) or comparable (Heasler and Doctor 1996) to detect using ultrasound than a thermal fatigue crack of the same size.

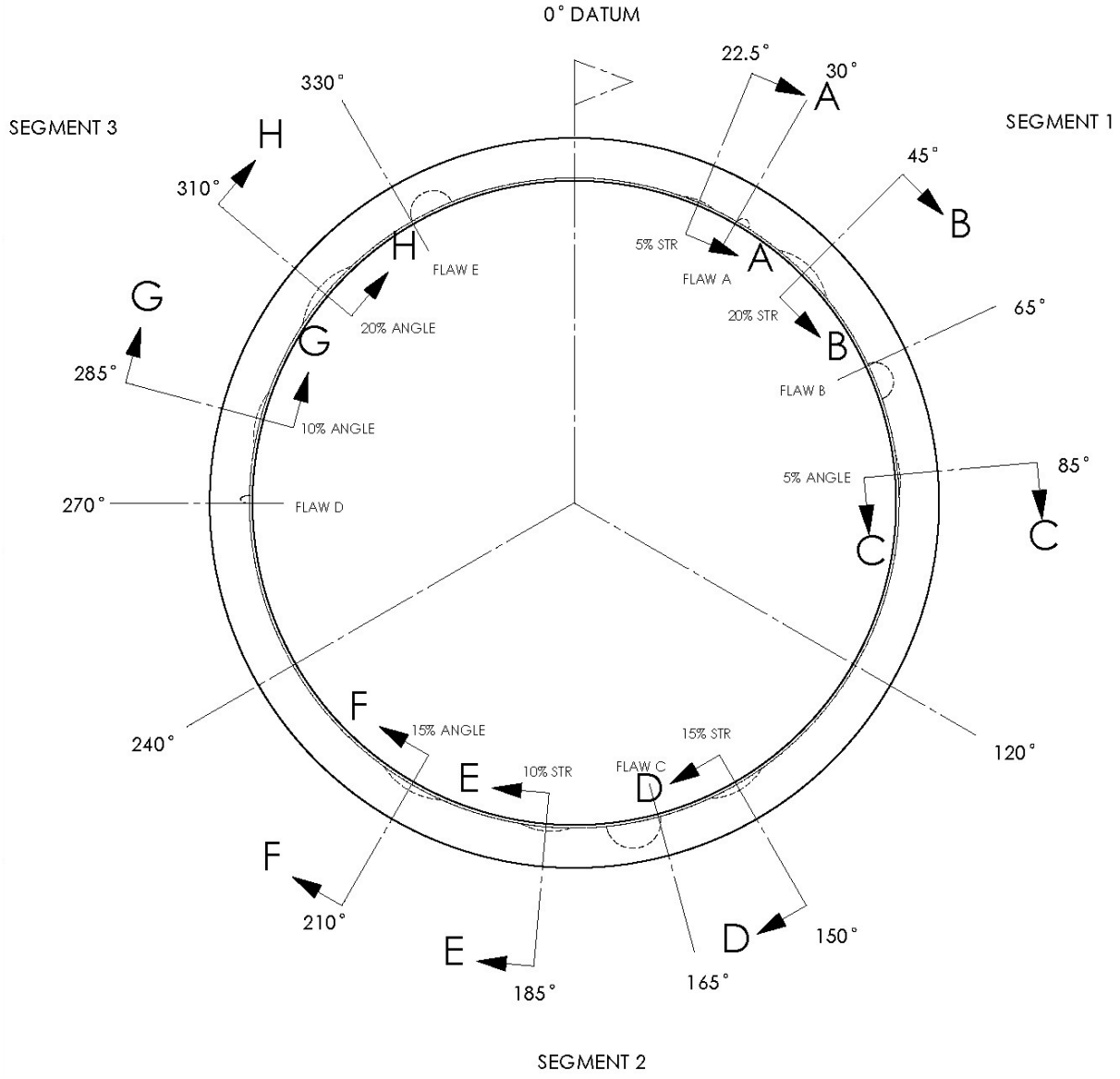

Figure 5.1 Sectioning and Flaw Locations for Pipe Specimen 02-24-15

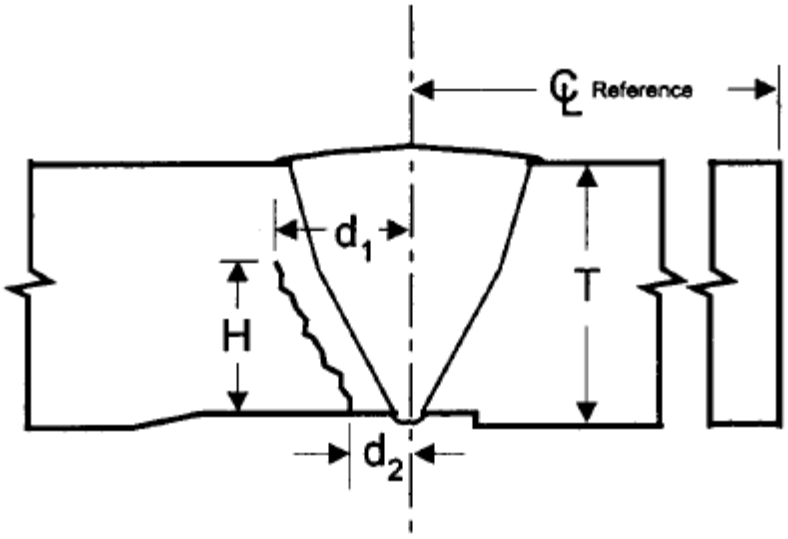

Figure 5.2 Cross-Sectional Schematic (circumferential orientation) Showing Typical Weld Geometry and Implanted Crack in HAZ

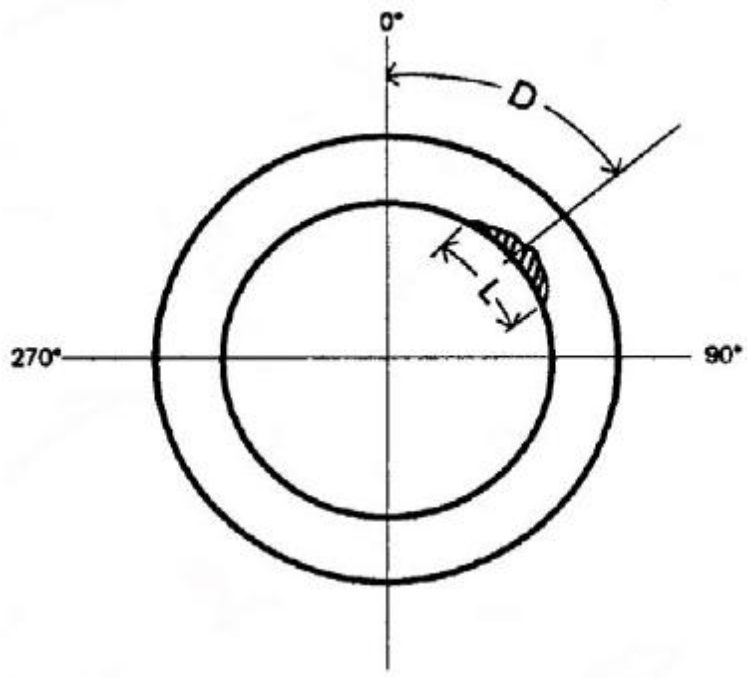

Figure 5.3 Cross-Sectional Schematic (axially oriented) Showing Typical Crack Location

Table 5.1 Implanted Thermal Fatigue Cracks in Austenitic Piping Specimen 02-24-15

Crack Designation	A	B	C	D	E
Crack Orientation	Circ.	Circ.	Circ.	Axial	Circ.
Crack Length - L	10.7 mm	30.5 mm	43.6 mm	13.3 mm	33.8 mm
[± 1.0 mm (0.040 in.)]	(0.42 in.)	(1.2 in.)	(1.715 in.)	(0.525 in.)	(1.33 in.)
Through-wall Depth - H	5.0 mm	14.9 mm	21.5 mm	6.6 mm	16.5 mm
[± 1.0 mm (0.040 in.)]	(0.195 in.)	(0.585 in.)	(0.845 in.)	(0.26 in.)	(0.65 in.)
% Wall Thickness	15	43	64	19	48
Aspect Ratio	2.3	2.1	2.1	2.1	2.1
Circumferential Location - D (from 0°)	30°	65°	165°	270°	330°

The piping specimen was labeled 02-24-15, a 0° reference datum point was inscribed, and each crack arbitrarily assigned an alphabetical designation. Welding and crack implantation were performed with the piping material in the as-formed (cylindrical) shape, then the specimen was axially sectioned into three, 120° segments for ease of handling during the experimental work. The weld crown was machined off to allow improved access for ultrasonic transducer placement during scans from the outside surface of the pipe.

In addition to the implanted TFCs, eight sawcuts were introduced into the heat-affected zone of the girth weld to provide standard ultrasonic reflectors. The sawcuts were made using a 4-in.-diameter radial saw blade and range from 2.5 mm (0.1 in.) deep to 10.2 mm (0.4 in.) deep. Four of the sawcuts are at right angles to the inner surface of the pipe and four follow the 35° angle of the weld HAZ. The exact lengths and depths of the sawcuts were determined by applying EXAMIX (a commercially available vinyl polysiloxane molding material), allowing the material to harden, removing the molds, and then measuring them. This process was repeated three times for each sawcut to better quantify experimental error. The sawcut dimensions and locations are given in Figure 5.4 and Table 5.2. A photograph of the EXAMIX positives is shown in Figure 5.5.

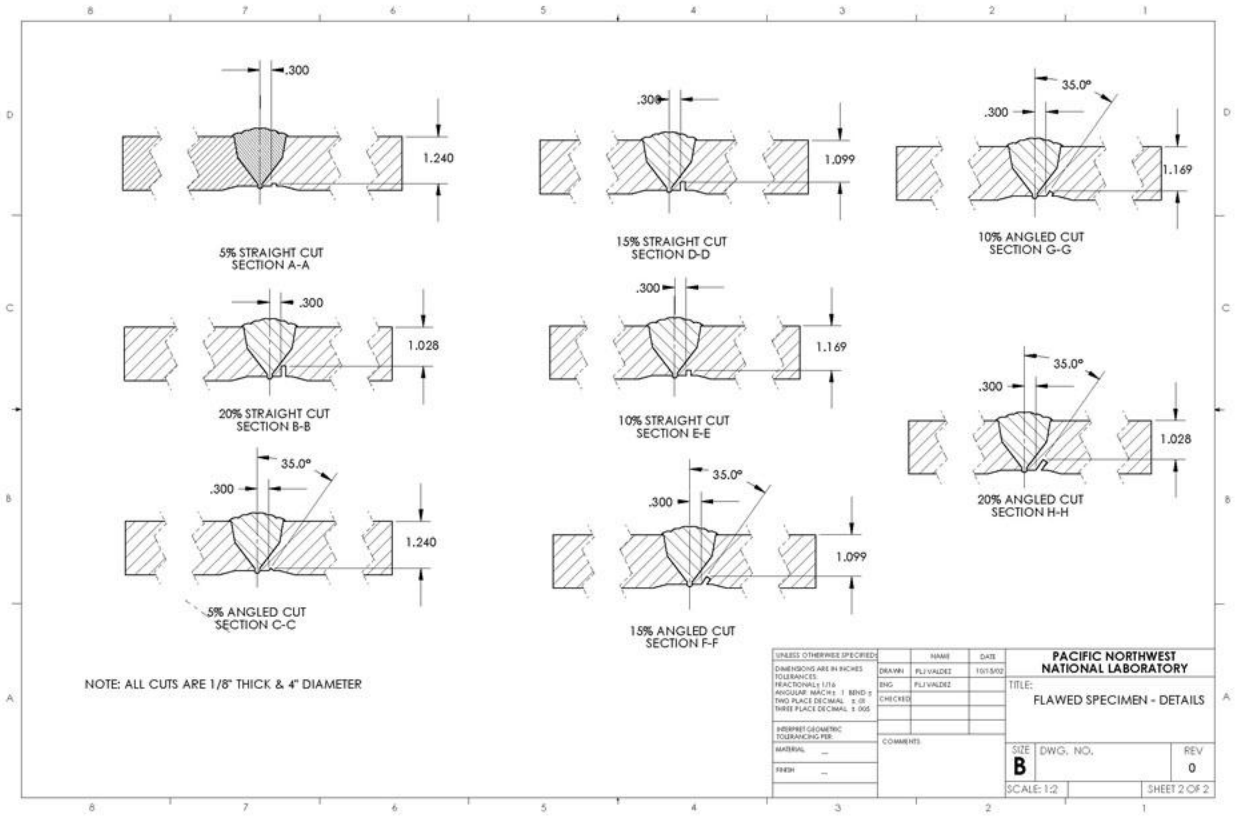

Figure 5.4 Positions and Angles for the Sawcuts in Pipe Specimen 02-24-15

Table 5.2 Sawcuts in Austenitic Piping Specimen 02-24-15

Sawcut Designation	**A**	**B**	**C**	**D**
Sawcut Orientation	Straight Cut	Straight Cut	35° Angle	Straight Cut
Length – L [± 0.4 mm (0.016 in.)]	32.8 mm (1.29 in.)	65.2 mm (2.57 in.)	36.2 mm (1.43 in.)	54.1 mm (2.13 in.)
Through-wall Depth – H [± 0.4 mm (0.016 in.)]	2.7 mm (0.11 in.)	10.2 mm (0.40 in.)	2.5 mm (0.10 in.)	6.8 mm (0.27 in.)
% Wall Thickness	7.5	28.4	7.1	18.8
Aspect Ratio	12	6	15	8
Circumferential Location – D (from 0°)	22.5°	45°	85°	150°

Sawcut Designation	**E**	**F**	**G**	**H**
Sawcut Orientation	Straight Cut	35° Angle	35° Angle	35° Angle
Length – L [± 0.4 mm (0.016 in.)]	43.7 mm (1.72 in.)	59.7 mm (2.35 in.)	57.3 mm (2.25 in.)	68.4 mm (2.69 in.)
Through-wall Depth – H [± 0.4 mm (0.016 in.)]	4.3 mm (0.17 in.)	7.0 mm (0.28 in.)	6.3 mm (0.25 in.)	9.3 mm (0.37 in.)
% Wall Thickness	12	19	18	26
Aspect Ratio	10.2	8.5	9.1	7.4
Circumferential Location – D (from 0°)	185°	210°	285°	310°

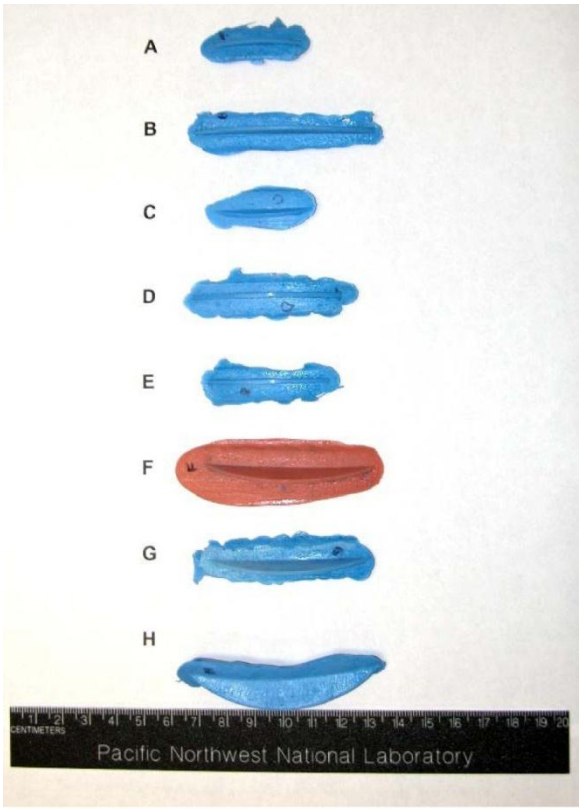

Figure 5.5 EXAMIX Molds Used to Measure the Length and Depth of the Sawcuts in Pipe Specimen 02-24-15

The three axial pipe segments were placed end-to-end on a wheeled cart to facilitate access to both LF/SAFT and PA-UT data acquisition stations. Mechanical scanning was performed by modifying the scanner to accommodate conventional transducers, LF/SAFT transducers or PA probes, with water being used as a coupling medium (see Figures 5.6 and 5.7 showing a typical experimental configuration).

Figure 5.6 Experimental Set-up Showing Piping Specimens and Scanner

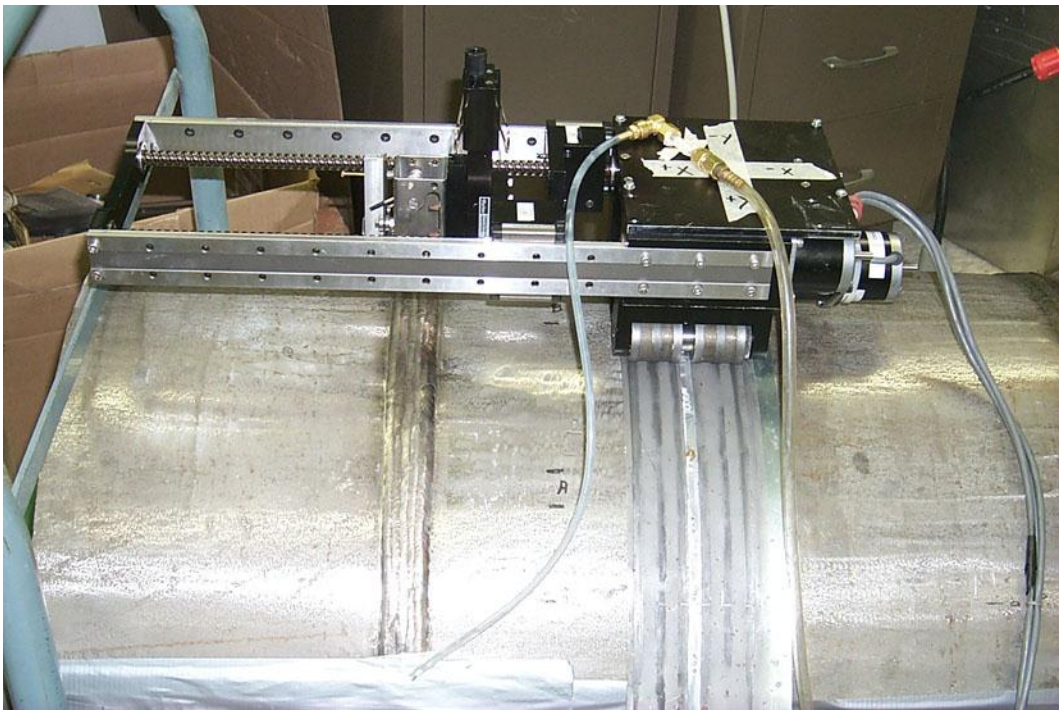

Figure 5.7 Close-up of Scanner on Pipe Specimen

5.2 Phase 2: Austenitic Piping Specimen No. 3C-022

The specimen used in Phase 2 was made using the same vintage material used in the Phase 1 work—Schedule 80, ASTM 358 Grade 304 WSS having a nominal 610-mm (24.0-in.) outer diameter and a wall thickness of approximately 36 mm (1.4 in.). The specimen was made by joining four cylinders of this material with three single-Vee girth welds, using procedures and filler material (E308 L) typical of those used in nuclear applications.

The piping specimen was labeled 3C-022, and a 0° reference datum point was inscribed. The weld crown was machined off to allow improved access for ultrasonic transducer placement during scans from the outside surface of the pipe. The pipe specimen was placed vertically in a water bath to recycle couplant for conventional UT, LF/SAFT, and PA-UT data acquisition systems. Again, mechanical scanning was performed by modifying the scanner to accommodate conventional-UT transducers, LF/SAFT transducers, or PA probes, with water being used as a coupling medium (see Figure 5.8 showing typical experimental configuration). Reference marks were indented 75 mm (3 in.) to the right of the 0° reference point to designate the starting point of scans.

Girth welds number one and number three were made with the pipe held horizontally in a fixed position. The cylinders were welded in a field-like fashion, with the welder starting at the top of the weld and working his way down to the bottom on each side of the pipe. This process is shown in Figure 5.9. Girth weld number one was welded with air backing, and girth weld number three was welded with water backing. After the welding process was completed, a 10% through-wall, 3.6-mm (0.14-in.) deep notch was machined 360° around one side of the weld on the inner diameter in the heat affected zone. This notch provided a full-circumferential, uniform ultrasonic reflector.

Girth weld number two was made with the pipe held vertically with air backing. During the welding process for weld number two, three cracks were implanted into the HAZ of the girth weld. These cracks were implanted by the same vendor and in the same way as the cracks in specimen 02-24-15. After the welding process, three electro-discharge machined (EDM) notches were implanted into one side of the weld on the inner diameter in the HAZ. The three EDM notches are all 10% though-wall, 3.6-mm (0.14-in,) deep, and begin and end 25 mm (1.0 in.) from each implanted crack. The EDM notches are designated flaws 1, 2, and 3 and the cracks are designated cracks 4, 5, and 6. The flaw dimensions and locations for cracks 4, 5, and 6 are shown in Table 5.3.

Figure 5.8 Experimental Set-up Showing Piping Specimen and Scanner

Figure 5.9 Field-like Welding on Horizontally Oriented Pipe Segments (photo courtesy of FlawTech Inc.)

Table 5.3 Thermal Fatigue Cracks in Austenitic Piping Specimen 3C-022

Crack Designation	4	5	6
Crack Orientation	Circ.	Circ.	Circ.
Crack Length – L [± 1.0 mm (0.040 in.)]	3.6 mm (0.14 in.)	7.1 mm (0.28 in.)	10.7 mm (0.42 in.)
Through-wall Depth – H [± 1.0 mm (0.040 in.)]	1.8 mm (0.07 in.)	3.6 mm (0.14 in.)	5.3 mm (0.21 in.)
% Wall Thickness	5	10	15
Aspect Ratio	2.0	2.0	2.0
Circumferential Location – D (from 0°)	45°	165°	285°

5.3 Phase 3: IGSCC - EPRI Practice and Secure Set Specimens

In Phase 3 of this study, a number of specimens from the EPRI performance demonstration set were made available to PNNL for ultrasonic examination. These specimens were field-removed piping segments taken from several U.S. boiling water reactor primary re-circulation systems and contain service-induced IGSCC. Some of the specimens were part of a practice set and some were part of a secure set used for blind performance demonstration tests. PA data were acquired on both sets using identical techniques during multiple visits to the EPRI NDE Center in Charlotte, North Carolina. The practice data were taken back to PNNL for development of an analysis approach and the secure data set was held at EPRI for subsequent data analyses.

5.3.1 EPRI Performance Demonstration Practice Specimens

A number of welded specimens containing service-induced intergranular stress corrosion cracks were available for examination at the EPRI NDE Center. These specimens varied in configuration with different weld crown geometries, counterbore, weld root conditions, etc. Figures 5.10 and 5.11 show some of the variation in specimens as viewed from the outside and inside of the pipe segments. The red arrows painted on two of the specimens show the flow direction so that upstream and downstream sides of the welds are identifiable. Specimens had a nominal 71.0-cm (28.0-in.) diameter and 2.0–4.1 cm (0.8–1.6 in.) wall thickness. A mapping of the flaws was provided, showing flaw location in the circumferential direction and axial position as upstream or downstream from a weld center line (W_{CL}). However, a W_{CL} was not marked on the specimen so axial position for acquired data was referenced relative to the center of the weld crown. True-state location and length-sizing information was given, but no true-state depth information was available. The examinations for this activity focused on detection of inner-diameter (ID)-connected cracks, oriented circumferentially (parallel to the weld).

Figure 5.10 Examples of Specimens as Viewed from the Outer Surface

Figure 5.11 Examples of Specimens as Viewed from the Inner Surface

5.3.2 EPRI Performance Demonstration Secure Specimens

The secure specimens were similar to the practice specimens but access was limited to the outer surface only. These specimens are used by EPRI in administering performance demonstration evaluations so the specimen number and flaw information are purposefully not revealed to maintain the integrity of the test set. The flaw true-state was provided to PNNL personnel during proctored data analysis activities at the EPRI NDE Center and the secure true-state information and data acquired were not allowed to leave the testing room.

6 Ultrasonic Probes and Inspection Protocols

In Phases 1 and 2 of the work reported here, the far-side examination assessment included evaluations of all three ultrasonic inspection techniques—conventional-UT, LF/SAFT and PA-UT. In Phases 1 and 2, the PA-UT technique focused on the use of 2.0-MHz probes, but employed both longitudinal- and shear-wave modalities. In Phase 3 of the evaluation, only the PA-UT approach was assessed, and the focus of the data acquisition included a 1.5-MHz transmit-receive longitudinal (TRL) probe in addition to the 2.0-MHz probes used in the earlier phases.

6.1 Conventional–UT

As a benchmark for comparison, it is useful to understand the common industry practice for the far-side inspection of austenitic welds. The ASME Section XI Code, Appendix VIII, and 10CFR50.55a require successful demonstration of the far-side inspection of austenitic welds. The test administered by EPRI may be biased in that flaws are selected based on the fact that conventional techniques can successfully detect them. This test is still very challenging because, even when the flaws have been selected in this manner, the far-side inspection is very difficult due to the geometry and metallurgical signals that must be correctly classified. EPRI NDE Center staff indicated that they recommend (and this is what many inspectors employ) the following approach for a candidate to pass the performance demonstration test:

- The first probe to use is a dual shear-wave transducer having two 10 mm by 18 mm (0.4 in. by 0.7 in.) piezo-composite elements, operating at 1.5 MHz and focused for 80% of the wall thickness with an inspection angle of 60° to 70°.
- After indications are found, evaluate with a 60° dual longitudinal probe operating in the 1- to 2-MHz range with a 2-MHz most commonly used.

The images of the raw data from the 60° longitudinal LF/SAFT inspections shown in Appendix B are similar to detection results that are expected for a conventional, dual-element inspection. It should be noted that these results are not exactly the same as the results that would be obtained when using the EPRI NDE Center recommendations; however, they are similar and illustrate the challenge the inspector must deal with regarding the detection of far-side austenitic weld flaws. The high-angle, shear-wave modality is effective because most of the piping welds are of a single "V" design and, thus, only a small amount of weldment must be traversed by the sound field near the inner diameter (ID) of the component, there are no mode-converted signals, and one may be able to obtain a corner trap from the flaw. However, one of the major problems with the inspection is the access limitation produced by the weld crown. Because, for most welds, the probe cannot be scanned on top of the weld, it is very difficult to get the full echo dynamic response for far-side flaws. Acoustic signals are reflected from existing flaws but only a limited portion of the echo dynamic curve is obtained and at the same time there can be many signals of geometric and metallurgical origin. The crown also provides limits on the ability to skew the transducer to assess the angular dependence of flaw signals from those produced by the geometry and metallurgical conditions. Refracted longitudinal probes are used for the assessment of indications. However, with refracted longitudinal waves, there is a problem of

mode conversion at the inner surface producing many more signals that may overlap in time with signals coming from the indication or from the metallurgical and geometrical conditions, which can create problems in classification of the signals. Also, tip-diffracted signals may not be reliably detected, so time-of-flight depth sizing is improbable.

Automated, single-element, conventional shear-wave ultrasonic techniques were employed on the wrought-austenitic SS specimens 02-24-15 and 3C-022, for comparison with the PA-UT and LF/SAFT techniques. The conventional ultrasonic system at PNNL consisted of the SAFT data acquisition software, a PNNL pipe scanner, a Ritec SP-801A square-wave pulser, and a Ritec BR-640A receiver. The four Krautkramer probes that were used in this study were chosen based on discussions with EPRI staff to identify probes that were most commonly used by inspectors during manual austenitic stainless steel performance demonstrations. The probes include two 1.5-MHz transducers, one with a diameter of 9.5 mm (0.375 in.) and one with a diameter of 12.7 mm (0.5 in.), and two 2.25-MHz transducers with the aforementioned diameters. The transducers were mounted on wedges to provide 60° and 70° shear waves in the material. The scans were completed from both sides of the weld to examine the effects of the weld microstructure on the UT response from implanted cracks and notches. The laboratory scans differ from standard manual ultrasonic examinations of pipes in that the scans were taken using an automated scanner and the data were stored digitally. This method was chosen to provide images for a more direct comparison with the PA-UT and LF/SAFT data.

In Phase 1 of the study, the specimen was cut into three segments to allow easier handling and scanning. The first section of specimen 02-24-15 was scanned with all four probes at both 60° and 70° incident shear waves, and the weld was examined from both the near- and far-side, for a total of 16 scans. The raster scan path length in the x-direction (axial direction, perpendicular to the weld) was 152 mm (6.0 in.) allowing the probe to traverse over the machined weld crown while digitizing the radio frequency (RF) data at a sampling rate of 20 MHz. The scanner would then index (step) 1.3 mm (0.05 in.) in the y-direction (circumferential direction, parallel to the weld) and then translate the ultrasonic probe a distance of 152 mm (6.0 in.) parallel and adjacent to the preceding stroke. A total of 508 mm (20.0 in.) of travel in the y-direction was completed for each scan on these pipe welds, and required about 40 minutes per search unit to scan (total scan time for all probes was approximately 10 hours, 40 minutes).

Preliminary screening of these initial data sets was performed immediately after the scanning process to determine which transducer(s) provided the best signals and highest SNR performance. After examining the 16 scans of pipe section one, it was determined that the 1.5-MHz probes performed marginally better than the 2.25-MHz probes, and the larger 12.7-mm (0.5-in.) diameter transducers performed much better than the 9.5-mm (0.375-in.) transducers. Figure 6.1 provides views of the conventional-UT probe configuration with associated gimbaling and couplant connections, with the 1.5-MHz, 12.7-mm (0.5-in.) diameter probe.

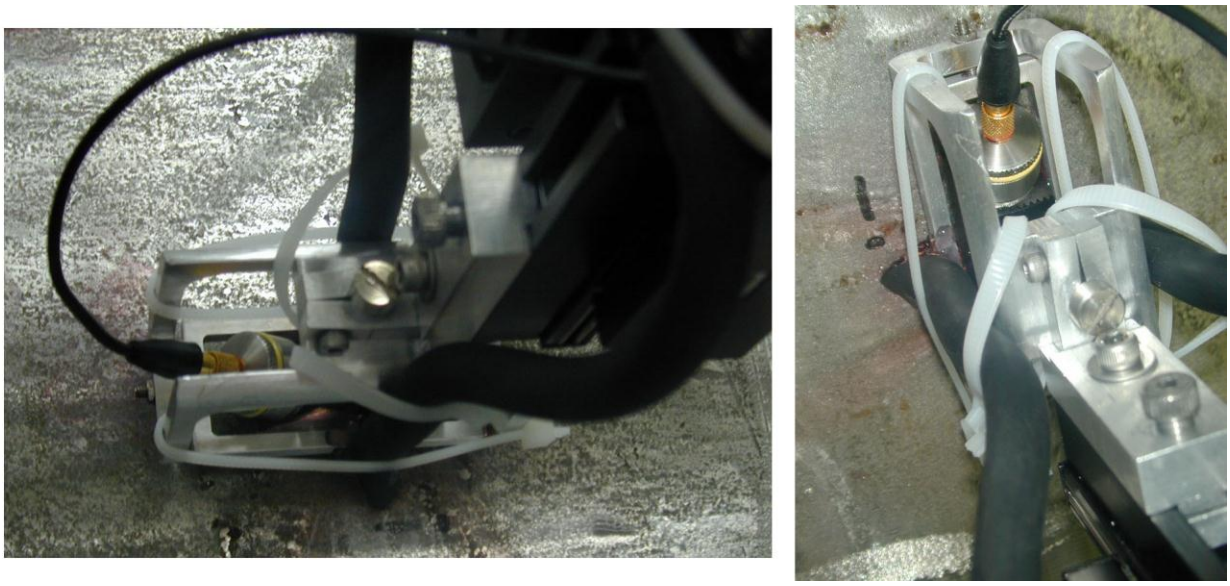

Figure 6.1 Side and Top Views of the 1.5-MHz, Conventional-UT, Shear-Wave Probe and Gimbal/Couplant-Delivery Configuration for Translation of the Ultrasonic Transducer Across the Specimens

After this analysis was conducted, the total number of scans was reduced to four scans per weld. The 1.5-MHz, 12.7-mm (0.5-in.) diameter 60° and 70° shear wave scans were completed on the near and far sides for pipe sections two and three, and for all of Phase 2. Therefore, only the 1.5-MHz results will be discussed in subsequent sections of this report.

In Phase 2 of the study, conventional-UT methods were applied using much longer raster scan patterns for volumetric coverage of the three circumferential welds provided by specimen 3C-022. Each of the three welds was scanned using 60° and 70°, 1.5-MHz shear waves. The data were stored electronically and analyzed using the SAFT 2002 software package. For weld number one (as described in Section 5), the 10% notch was scanned using 1.5-MHz, 60° and 70° shear waves from the far side of the weld. The probes were raster-scanned over the pipe specimen, with 152-mm (6.0-in.) scan-strokes in the x-direction (axial direction, perpendicular to the weld) and indexed (stepped) in 1.3-mm (0.05-in.) increments for a total of 1966 mm (77.4 in.) around the outside circumference of the pipe specimen (parallel to the weld), which produced a total of 1548 lines (strokes) per data set. Each scan was started at a distance of 76 mm (3.0 in.) after the centerline of the longitudinal seam weld and indexed 360° around the pipe. The scan duration was approximately 4 hours per scan, for a total of 16 hours of scanning for weld number one.

Weld number two was scanned from the near side with the 1.5-MHz, 60° shear-wave probe and from the far side with the 60° and 70° shear-wave probes. The probes were raster-scanned over the pipe specimen, with 152-mm (6.0-in.) scan-strokes in the x-direction (axial direction, perpendicular to the weld) and indexed (stepped) 2118-mm (83.4-in.) around the outside circumference of the pipe specimen (in the y-direction, parallel to the weld). The probes were indexed in 1.3-mm (0.05-in.) increments, for a total of 1668 lines per data set. Again, each scan

was initiated at a distance of 76 mm (3.0 in.) before the centerline of the longitudinal seam weld, indexed 360° around the pipe, and then continued indexing an additional 152 mm (6.0 in.) to 76 mm (3.0 in.) beyond the longitudinal weld centerline. The 152 mm (6.0 in.) of overlap in each scan provides two built-in fiduciaries in the scans as the longitudinal seam appears as a "dead zone" in the scans. These scans took approximately 4 hours each to complete, for a total of 16 hours of scanning.

Finally, weld number three was raster-scanned using identical x-direction scan-strokes as in the previous welds, but were indexed in the y-direction (circumferential direction, parallel to the weld) 2118 mm (83.4 in.) around the outside circumference of the pipe specimen. The probes were indexed in 1.3-mm (0.05-in.) increments, for a total of 1668 scan lines per data set. Once again, these scans were initiated at the same position as the other two welds, starting at a distance of 76 mm (3.0 in.) before the centerline of the longitudinal seam weld, indexed 360° around the pipe, and then continued indexing an additional 152 mm (6.0 in.) to 76 mm (3.0 in.) beyond the longitudinal weld centerline. The scans took approximately 4 hours per scan, for a total of 16 hours of scanning.

6.2 Low-Frequency/SAFT–UT

The low-frequency/SAFT inspection technique uses a zone-focused, high-bandwidth, low-frequency (400-kHz) inspection protocol coupled with the SAFT technique (Doctor et al. 1996). The examination protocol is based on the premise that there exist sufficient differences between the characteristics of coherently scattered ultrasonic energy from grain boundaries and geometrical reflectors from that of the scattered ultrasonic energy from surface-breaking fatigue and stress corrosion cracks in wrought austenitic piping welds. PNNL's empirical approach relies on the notion that acoustic impedance variations at the grain boundaries (and in the HAZ along the weld fusion lines) can be minimized by using lower frequencies (longer wavelengths), and the degree of coherent energy scattered from these boundaries should be inconsistent as a function of frequency, insonification angle, scan direction, and the amplitude of returning signals. The LF/SAFT approach is directed toward detecting the corner-trap response from the surface-breaking crack as a function of time and spatial position. If the frequency is low enough, the examination is less sensitive to geometry and the effects of the microstructure and the probability of detection increases for surface-breaking cracks. The tradeoff is resolution. However, with the addition of SAFT signal processing, the examination can be performed at lower frequencies while maintaining sufficient resolution and sensitivity to effectively detect cracks. Therefore, by using multiple examination frequencies and incident angles, and inspecting from both sides of a weld, the LF/SAFT technique invokes a composite approach for detection, localization, and sizing of cracks in these types of materials.

The examination process is further enhanced by the addition of low-frequency, piezo-composite, high-bandwidth search units that enable the inspector to use a wide range of examination frequencies centered around 250 kHz and 400 kHz. The zone-focal characteristics of the Krautkramer-AGFA dual-element search units provide optimal insonification of the inner surface (ID) over an incremental range of incident angles for pipe wall thicknesses of approximately 3.56 cm (1.4 in.).

PNNL staff conducted a preliminary ultrasonic evaluation of the LF/SAFT inspection method on a set of three sectioned segments (specimen 02-24-15) of a wrought 304 SS pipe with an austenitic weldment and a limited array of cracks and notches. From this work, a more extensive study was proposed, and the LF/SAFT approach was evaluated in more detail as a result of recommendations derived from earlier work. Extensive laboratory work using this novel approach has been performed at PNNL and other sites in the field prior to the study described here. This inspection technique has evolved to focus on inspection problems associated with thick-section, reactor-coolant piping that exhibit coarse-grained microstructures or multi-layered boundary conditions such as centrifugally and statically cast pipe, elbows, and dissimilar metal welds. Due to the difficulties encountered in far-side examinations through austenitic welds, this technique was identified as having potential for improved inspection performance due to the utility of longer wavelengths, thereby reducing the attenuative effects of the weld material. This study is an extension of previous evaluations and focuses on applying the inspection methodology to far-side examinations in wrought piping with austenitic welds, where a suite of fabricated flaws and cracks have been introduced for performance evaluation and comparison to other inspection methods.

"Synthetic aperture focusing" refers to a process in which the focal properties of a large-aperture focused transducer are synthetically generated from data collected over a large area using a small transducer with a divergent sound field. The processing required to focus this collection of data has been called beam-forming, coherent summation, or synthetic aperture processing. The resultant image is a full-volume focused characterization of the inspected area (Doctor et al. 1996).

SAFT-UT technology is able to provide significant enhancements to the inspection of austenitic welds and other anisotropic, coarse-grained materials. The resolution of an imaging system is limited by the effective aperture area; that is, the area over which data can be generated, collected, and processed. SAFT is an imaging method that was developed to overcome some of the limitations imposed by large physical apertures, and has been successfully applied in the field of ultrasonic testing. Relying on the physics of ultrasonic wave propagation, SAFT is a very robust technique (Doctor et al. 1996).

Using a pitch-catch configuration for typical data collection throughout these activities, the transducer was positioned on the surface of the specimens, and RF ultrasonic data were collected. As the transducer was scanned over the surface of the specimens, the A-scan record (RF waveform) was amplified, filtered, and digitized for each position of the transducer. Each introduced flaw produced a collection of echoes in the A-scan records. The unprocessed or RF data sets were then post-processed using the SAFT algorithm, invoking a variety of full beam-processing angles (between 6° and 24°) to evaluate and optimize the temporal/spatial averaging enhancement. If the reflector is an elementary single-point reflector, then the collection of echoes will form a hyperbolic surface within the data-set volume. The shape of the hyperboloid is determined by the depth of the introduced flaws in the specimens and the velocity of sound in the specimens. This relationship between echo location in the series of A-scans and the actual location of the introduced flaws within the specimens makes it possible to reconstruct a high-resolution, high signal-to-noise ratio image from the acquired raw data.

If the scanning and surface geometries are well known, it is possible to accurately predict the shape of the locus of echoes for each point within the test object. The process of coherent summation for each image point involves shifting a locus of A-scans, within a regional aperture, by predicted time delays and summing the shifted A-scans. This process may also be viewed as performing a temporal/spatial matched filter operation for each point within the volume to be imaged. Each element is then averaged by the number of points that were summed to produce the final processed value. If the particular location correlates with the elementary point response hyperboloid, then the values summed will be in phase and produce a high-amplitude result. If the location does not correlate with the predicted response, then destructive interference will take place and the spatial average will result in a low-amplitude value; thus, reducing the noise level to a very small value. SAFT processing is also effective at removing constant-time signals that are not near the front surface, and sub-volume selection during data analysis readily removes any residual near-surface signals (Doctor et al. 1996).

The LF/SAFT-UT inspection system is an automated, computerized UT imaging system designed and developed by PNNL, and evolved from a system originally employed by NRC Region 1 inspectors as a mobile SAFT-UT inspection system. The LF/SAFT-UT system is a field-tested system, consisting of several subsystems and components. The Panametrics pulser used for this study is a high-voltage model 5058 pulser-receiver unit that produces high-voltage spike pulses for broadband excitation of the transducer. This unit provides damping control, step attenuation and gain control, high-pass and low-pass filtering options, and a variable pulse voltage control of up to 900 volts. This unit provides the capability to exploit the high bandwidth of the piezo-composite transducers and allow utility of both 250-kHz and 400-kHz examination frequencies. This unit also includes an embedded dual-stage receiver that consists of a low-frequency, low-noise pre-amplifier in series with a high performance, 60-dB low-noise amplifier for conditioning and amplification of the received UT signal responses. A stand-alone 866-MHz personal computer (PC) contained in this subsystem fulfills the role of data acquisition control, where the operator invokes the LF/SAFT scanning software menus and adjusts the scanning parameters prior to initiating a scan. The analog-to-digital (A/D) converter resides on this PC, which also controls the motor drivers and pipe scanner. This computer is directly connected to the data analysis PC. Unprocessed ultrasonic data streams from the data acquisition PC to the data analysis PC where it resides for SAFT post-processing, analysis, and archival. The data processing and storage subsystem performs SAFT processing of the raw (unprocessed) UT data using a Dell Precision 650 high-performance PC with dual high-speed processors (2.4 GHz each). This PC platform contains both read/write compact disc (CD) and digital video disc (DVD) drives for storage of digital data. This PC also contains two flat-panel 19-in. monitors for displaying the SAFT-UT processed data (A-scans, B-scans, C-scans, and D-scans). The photographs in Figure 6.2 illustrate the LF/SAFT inspection system in its configuration as used in this study.

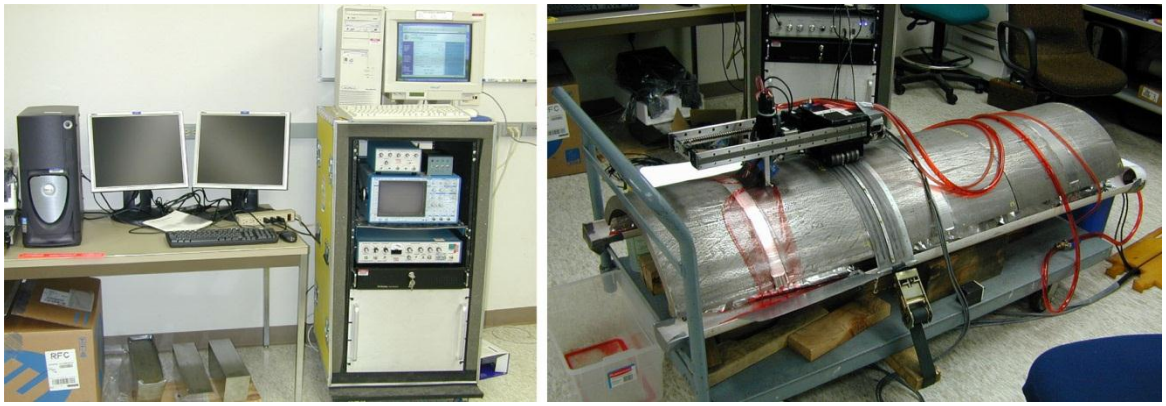

Figure 6.2 The Low-Frequency/SAFT-UT Ultrasonic Data Acquisition System

The low-frequency ultrasonic data acquisition system used in this study allowed ultrasonic data to be efficiently acquired under rapid, low-noise conditions, for a number of sectioned pipe segments and weld conditions using a field-ready automated pipe scanner. The LF/SAFT automated pipe scanner shown in Figure 6.2 was used for accurate and smooth scanning of the search unit through a specified number of points in the X-Y plane, while maintaining low-noise conditions and a constant coupling of the transducer to the surface. The pipe scanner was configured with tailored gimbals for transducer attachment and translation over the surface of the specimens. A network of specially fabricated drip lines attached to a couplant reservoir with a peristaltic pump was used to provide a constant stream of water on the specimen surface for improved coupling and transducer motion. Figure 6.3 shows photographs of the pipe scanner's front-end configuration.

Figure 6.3 Front-end Transducer Configuration, Including Gimbal and Coupling Lines. Colored water was used as couplant to facilitate assessing the presence of air bubbles at the transducer wedge-to-component interface.

The LF/SAFT system's 866-MHz control PC contains the A/D converter used to sample (digitize) the data. The motor controller electronics initialize a trigger output to the A/D and pulser-receiver unit which, in turn, was used to sync the remaining instrumentation. The received signal responses (echoes) were initially amplified by a low-noise, low-frequency, ultrasonic preamplifier, and then bandpass filtered using the Panametrics 5058 to allow suitable amplification while reducing extraneous low-frequency noise components under 100 kHz and higher-frequency noise components over 500 kHz.

The preamplified and conditioned signal responses were then amplified by the second stage wideband Panametrics 5058 amplifier and sent to the control PC's A/D converter for digitizing. All signals (excitation pulses and received signal responses) were monitored using a LeCroy 9450 digital oscilloscope, providing the capability to view the trigger and sync pulses, the excitation pulse before and after amplification, and the received signal response just prior to digitization, simultaneously. The LeCroy oscilloscope also provided linear averaging, and the capability to analyze the frequency characteristics of the A-scan data. A linear averaging scheme was implemented with the RF ultrasonic A-scan data being averaged eight times per repetition, to minimize the effects of motor noise and random electronic noise, and to increase the unprocessed SNR. The data acquisition system was capable of acquiring low-frequency, low-noise, ultrasonic data within a region of 0 dB to 100 dB total system gain.

After storage of the RF ultrasonic data sets to CD media (with the option for DVD archival), the data was signal processed using SAFT. The raw data sets were post-processed using a variety of beam processing angles, ranging from 6° to 24°. The SAFT software provides the user the capability to view the entire ultrasonic data set (three-dimensional array of points) in two-dimensional slices, by viewing color-enhanced composite images that depict slices of the three-dimensional array in the X-Y plane (C-scan view), the Y-Z plane (B-scan end-view or D-scan view), and X-Z plane (B-scan side view). The X-axis defines the axis of motion for translation of the transducer, perpendicular to the circumferential weld axis. The Y-axis defines the translation of the transducer in the circumferential direction, parallel to the centerline of the weld. The Z-axis defines the depth into the specimen from the contacting top surface of the specimen, and is correlated to the time-of-flight data.

In 2002, preliminary assessments with the LF/SAFT inspection system on wrought piping with austenitic welds resulted in a number of recommendations. These lessons learned were accommodated in subsequent efforts. Of primary significance was a re-design of the transducers used for the inspection of these components. The originally designed low-frequency, variable-angle transducer used for thicker-section cast piping components did not provide a suitable sound field for the thinner-section 304 WSS piping. PNNL staff worked with Krautkramer-AGFA staff in developing the necessary specifications for fabricating high-bandwidth, piezo-composite, low-frequency transducers and a set of associated wedges for application to this component geometry. A set of 10 dual-angled wedges providing inspection angles of 30°, 45°, 50°, 55°, 60°, 65°, 70° (L-wave in 304 SS) and 45°, 60°, 70° (shear-wave in 304 SS) were acquired for the initial data acquisition activities.

The transducers were fabricated to operate as dual (pitch-catch), isolated (to reduce cross-talk), high-bandwidth (at the −6 dB, half-power point), low-frequency, piezo-composite transducers. The nominal and peak operating frequencies were to be approximately 350 kHz and the −6-dB

bandwidth for both transducers were greater than 90%. This provided a suitable operational frequency range for employing both 250 kHz and 400 kHz as the two primary examination frequencies for this study. To reduce the acoustic "footprint" on the specimen surface and minimize the transducer size, the housings were specified to be no larger than 2.54 cm (1.0 in.) × 3.81 cm (1.5 in.) rectangular housings. In addition, the wedge sets were to be configured with an appropriate roof angle to provide a zone-focus (cross-over point where receive and transmit sound-field zones coincide) in the range of approximately 4.45–7.62 cm (1.75–3.0 in.) along the sound field propagation path (i.e., 4.98 cm at 45° in 304 SS). The photographs in Figures 6.3 and 6.4 show the dual-element, pitch-catch transducer configuration employed.

Figure 6.4 Transducer-Wedge Configuration for Dual-Element, Pitch-Catch Scanning

Because the inspection technique takes advantage of two frequencies and two wave-modes, the wavelength (and effectively the system's resolution capability) will vary as a function of frequency and wave-mode. The longitudinal-wave acoustic velocity in 304 SS is 5.790 mm/µs (0.228 in./µs), while the shear-wave acoustic velocity is 3.180 mm/µs (0.125 in./µs). The equation for calculating wavelength is given by

$$\lambda = C / f \qquad (6.1)$$

where λ is the wavelength, C is the appropriate acoustic velocity for the specific wave-mode employed, and f is the frequency. Typically the calculation is made using velocity units of cm/sec or mm/sec and frequency units of Hz or cycles/sec. In this manner, the wavelength calculation results in a familiar unit length. For 250-kHz longitudinal (L)-wave inspection, the wavelength is 2.32 cm (0.91 in.), and for shear-wave inspection the wavelength is 1.27 cm (0.50 in.). For 400-kHz L-wave inspection, the wavelength is 1.45 cm (0.57 in.), and for shear-wave inspection the wavelength is 0.79 cm (0.31 in.). Near the weld root, the typical thickness of the specimens ranged from 3.53–3.61 cm (1.39–1.42 in.). A 10% through-wall notch would have a depth of approximately 0.36 cm (0.14 in.). Thus, the smallest wavelength employed (at 400 kHz in the shear-wave mode) is still over two times larger than a 10% through-wall crack or notch.

Another key element in understanding the resolution capability of the LF/SAFT inspection technique is to know the characteristic zone focal dimensions of the transducers. The intersection (or cross-over point) in the component of the transmit and receive transducers is where the sound-field energy is quasi-focused and the "zone" where the two transducers interact. The dimensions of the zone-focal area are functions of the frequency, the size of the transducer element, the spacing and roof-angle (geometric configuration and alignment of the side-by-side pair of transducers), the incident angle, and the acoustic velocity of both the wedge and the material being examined. A number of calculations were conducted at the −6 dB points to better understand the lateral and depth dimensions (Y axis and Z-axis relative to the coordinate plane of inspection) of the zone-focused sound field.

- For 250-kHz 45° L-wave configuration, the sound field overlap in the Y-axis is approximately 4.1 cm (1.6 in.) and the overlap in the X and Z-axes is approximately 3.0 cm (1.2 in.).
- For 250-kHz 70° L-wave configuration, the sound field overlap in the Y-axis is approximately 3.3 cm (1.3 in.) and the overlap in the X and Z-axes is approximately 2.0 cm (0.8 in.).
- For 400-kHz 45° L-wave configuration, the sound field overlap in the Y-axis is approximately 3.0 cm (1.2 in.) and the overlap in the X and Z-axes is approximately 2.5 cm (1.0 in.).
- For 400-kHz 70° L-wave configuration, the sound field overlap in the Y-axis is approximately 2.8 cm (1.1 in.) and the overlap in the X and Z-axes is approximately 1.5 cm (0.6 in.).

This illustrates the slight convergence and "zone-focusing" effect inherent in the design of the transducer configuration. These dimensions are generally much larger than the depth size of the introduced flaws in the piping segments examined for this study, and much larger than the length of its cracks or sawcuts, with the exception of the 360° notches.

A general scanning procedure was developed to provide consistent and repeatable data acquisition and to provide technical support staff with routine guidelines for conducting data acquisition and data processing/analytical tasks. It is recognized that this is not an ASME Code qualified procedure, and no calibration on machined reflectors was conducted, but follows the general approach of such a procedure. The following process was used:

- Invoke scanning setup menu on control PC.
- Configure proper transducer/wedge into spring-loaded gimbal and adjust for optimal translation.
- Calculate required two-way time-of-flight for adjustment of sampled time-window.
- Modify header files and parameters for transducer, material, sampling, and scan pattern.
- Examine A-scan trace on computer monitor.
- Verify proper coupling and flow rate for drip lines.
- Slowly scan transducer over largest indication (flaw or crack) and verify proper gain settings on instrumentation, setting the total system gain just below saturation of the highest amplitude signal to be found.
- When all parameters have been set, outline scan aperture.

- Print out header file.
- Initiate scanning.
- Complete documentation of instrument settings.
- When file is completed, verify proper data acquisition by a quick analysis of the raw UT data file and store to hard drive and to CD media.
- Initiate SAFT processing on separate PC platform for analysis and data storage.
- Repeat step 1 until data acquisition activity is completed.

Initially, it was thought that all scan-angle-frequency combinations could be acquired, SAFT-processed using various beam processing angles, and analyzed individually by wave modality to compare and contrast the results to the true state of the specimens. However, the large volume of scans, the time for data acquisition, and required time for post-processing and analysis of the entire set of scan combinations could not be achieved given the schedule and resources available for this portion of the study. To address detection performance issues and provide the best possible conditions for evaluating the LF/SAFT technique, the full complement of scans were conducted on one of the sectioned pieces and an initial analysis was performed to determine which combination of modalities, angles, and frequencies would provide the most meaningful and useful data. Using the results as guidance from these initial tests on piping segment number two, it was determined that the combination of inspection parameters depicted in Table 6.1 would be implemented for each pipe segment over the remainder of the study.

Table 6.1 Final Combination of Scan-Angle-Frequency-Modality for Phase 1 Evaluation Using the LF/SAFT Inspection Technique

Piping Segment ID #	Inspection Frequency (kHz)	Orientation of Scan	Examination Incident Angle	Wave Mode
All	250	Far-side	45°, 70°	Longitudinal
All	250	Near-side	45°	Shear
#2	250	Near-side	60°, 70°	Shear
#2	250	Far-side	45°, 60°, 70°	Shear
All	400	Near-side	45°, 60°, 70°	Longitudinal and Shear
All	400	Far-side	45°, 60°, 70°	Longitudinal and Shear

In Phase 2, where the focus was on assessing specimen 3C-022, each of the three welds was scanned using 400-kHz and 250-kHz probes. The welds were examined using 45° shear and longitudinal waves, 60° longitudinal waves, and 70° longitudinal waves at both frequencies. The probes were raster-scanned over the pipe specimen, with 152.4-mm (6.0-in.) scan strokes in the x-direction (axial direction, perpendicular to the weld) and indexed 2118 mm (83.4 in.) around the outside circumference of the pipe specimen in the y-direction (parallel to the weld). The 400-kHz probes were indexed or stepped in 1.3-mm (0.05-in.) increments and the 250-kHz probes were indexed or stepped in 2.5-mm (0.10-in.) increments. Thus the index increments represented approximately $1/10^{th}$ of a wave length and an over-sampling in the lateral plane but these small steps produced a more detailed data image for analysis. Again, as described for

the conventional-UT scans, each scan was initiated at a distance of 76.2 mm (3.0 in.) before the centerline of the longitudinal seam weld, indexed 360° around the pipe, and then continued indexing to 76.2 mm (3.0 in.) beyond the longitudinal weld centerline. The 152.4 mm (6.0 in.) of overlap in each scan provides two built-in fiduciaries in the scans as the longitudinal seam appears as a “dead zone” in the scans. The data were stored electronically and analyzed using SAFT post-signal processing software.

The SAFT procedure used on the vertical pipe section (3C-022) was the same as used for processing the Phase 1 pipe specimens. The SAFT beam-angle used for the processing was 12° and the beam entry diameter was 12.7 mm (0.5 in.). No skipping was used so all of the data was processed independent of threshold level.

6.3 Phased Array–UT

Recent advances in electronics miniaturization, computer processing capabilities, and fabrication methods for ultrasonic transducers have enabled phased-array technology to become a viable approach for many field applications. The geometrical design of a PA transducer is typically a function of specific implementation variables; that is, geometries such as linear, annular, circular, or matrix designs are developed to address a particular ultrasonic application need (Poguet et al. 2001). However, the basic premise for all PA transducers involves a set of small, individual piezoelectric elements that are independently driven. Although these elements may be pulsed individually, or in groups, to simulate conventional transducer excitation, the real strength of this technique lies in the capability of the system to electronically delay each of these elements during both generation and reception of ultrasonic sound fields. The wave-fronts produced by subsets of elements interfere within the inspected component to produce a resultant, phase-integrated ultrasonic wave. This is commonly referred to as *beam forming*. The PA system can, therefore, steer and focus the integrated ultrasonic beam within the component.

Generally, all PA ultrasonic systems are computer-controlled enabling software to define the groups and sequences of elements being electronically delayed. Parameters such as the number of individual elements in a virtual element, the delay sequence for firing of the virtual elements, element amplitudes, and the delays in reception are programmed into the system operating software. The setting of these generation and reception parameters for a particular response is called a focal law. Because practically all aspects of the sound beam are being controlled electronically, many iterations, or sequences of iterations, can be run in nearly real time. This allows a single array to inspect a component with variable inspection angles and focusing depths almost simultaneously. For instance, depending on the array design and the component thickness, a one-dimensional linear array, with major axis oriented normal to a pipe weld, may interrogate close to an entire planar cross section of the weld by sweeping through a series of inspection angles without having to mechanically move the transducer toward and away from the weld. Theoretically, an entire pipe weld can then be examined with a single circumferential scan motion. Most PA systems capture, digitize, and store the ultrasonic data, which enhances repeatability and permits off-line analysis and imaging. Specialized computer software and hardware (including upgraded RAM and hard disc memory) are needed to support analyses of PA data. Also, because of the variations of images that can be produced, a

systematic method should be employed when performing these analyses by using a standardized procedure.

The PA system at PNNL consists of a Tomoscan III 32-channel instrument, produced off-the-shelf by R/D Tech, Inc. (now ZETEC). This is a standard piece of commercial NDE equipment used for PA applications in several industrial sectors. This type of system is used by General Electric to inspect reactor internals and at the EPRI NDE Center for a variety of applications including far-side procedure development and initial true-state characterization of Performance Demonstration Initiative (PDI) specimens. The instrument can be programmed (by development of focal laws) to control up to 32 channels for transmission and 64 channels for reception of ultrasonic signals. It has 12-bit logic and operates through a local Ethernet connection to a standard desktop computer. Figure 6.5 shows the Tomoscan III and associated data acquisition computer used during the trials.

Figure 6.5 Phased Array Data Acquisition System

Two PA probes were used in the initial work, a transmit-receive longitudinal wave probe and a transmit-receive shear-wave probe. The TRL wave array was specially designed for near- and far-side applications in austenitic material ranging from about 13 to 38 mm (0.5 to 1.5-in.) in thickness. It consists of two pairs of 2D arrays, each array having 14 × 2 elements. One array pair is used for transmitting, the other for reception of ultrasonic signals. There exists a slight angular pitch, or roof angle, between the planes of the transmit and receive pairs. This provides mechanical focusing by setting the nominal cross-over point between transmit and receive rays at a certain depth in the material. Also, by using a pair of arrays for each transmit and receive

segment, electronic lateral beam skewing is also possible so that the cross-over point may be slightly adjusted for a specific application, within the thickness range in this probe design. Both the transmit and receive arrays are inclined so that a nominal 50° longitudinal beam will be produced, if no focal law delays are introduced.

The array is integrally mounted on a wedge within the probe housing to produce the sound-field orientations described above. The overall contact cross section on the surface of the specimen, or footprint, of the probe has been made as small as possible to facilitate placement adjacent to the weld crown. This is approximately 25-mm (1.0-in.) square. A “skirt” is fixed to the housing with tubes for applying a coupling medium (water was used for these trials). The TRL array probe has a nominal frequency of 2.0 MHz (1.9 MHz center) and is highly damped exhibiting approximately 70% bandwidth. The TRL array has an average wavelength of 3.1 mm (0.12 in.) in stainless steel. The aperture for each transmit and receive pair is 20 mm (0.79 in.) × 10 mm (0.39 in.). The pitch of elements in each array (distance between element center lines) is 1.4 mm (0.05 in.). See Figure 6.6.

Figure 6.6 The 2.0 MHz TRL Phased-Array Probe

The transmit-receive shear wave (TRS) array consists of two 24-element 2D arrays in a similar arrangement as the TRL array. The TRS array has a roof angle that mechanically focuses the shear-wave beam by setting a cross-over point with a depth of 30 mm (1.18 in.). The TRS array, as with the TRL array, has a “skirt” to allow for efficient coupling. The footprint of the probe is 50 mm (2.0 in.) along the active direction and 30 mm (1.18 in.) in the passive direction. The transmit and receive arrays are inclined to provide a nominal 55° shear wave in stainless steel if no focal laws are used to steer the beam. The system has a nominal frequency of 2.0 MHz (2.14 MHz center) and has a −6 dB bandwidth of 65%. The TRS array has an average wavelength of 1.4 mm (0.06 in.) in stainless steel. The aperture for each transmit and receive pair is 32 mm (1.26 in.) in the active direction and 10 mm (0.39 in.) in the passive. The pitch of elements in each array is 1.33 mm (0.05 in.). See Figure 6.7.

Figure 6.7 The 2.0 MHz TRS Phased-Array Probe

Prior to the trials, focal laws were developed for the TRL and TRS arrays and programmed into the TomoView acquisition software. The focal laws were developed to provide ultrasonic longitudinal beam angles from 30° to 70°, at 1° increments for the TRL array in the piping specimens and from 40° to 70°, at 1° increments for the TRS array. This resulted in the sound field being swept through several discrete beam angles in near real time along the entire length of the linear scan. In other words, for each axially oriented cross section of material, data were acquired from 30° to 70° for the TRL and from 40° to 70° for the TRS, while the linear scans progressed circumferentially.

For Phase 1 scans of the three segments of pipe specimen 02-24-15, each linear scan was approximately 480 mm (19.0 in.) in length to facilitate scanning while avoiding edge effects from the specimens. Large data files on the order of 45–60 megabytes resulted for each linear scan. This results in 50.8 to 76.2 mm (2.0 to 3.0 in.) of weld not available for scanning near the edges of each specimen. The Phase 2 scans on specimen 3C-022 went completely around the pipe specimen circumference, with 100 mm (4.0 in.) of overlap, and were approximately 2060 mm (81.0 in.) in length. These scans resulted in data files of 220–250 megabytes in size.

For both arrays and both specimens (in Phases 1 and 2), data were acquired by positioning the probe with the mechanical scanner adjacent to the weld (illustration shown in Appendix E, on page E.1); the sound beam was directed toward the weld, perpendicular to the weld centerline. Then linear scan motions were performed along the weld from both the near and far sides, with respect to the implanted crack locations. Several linear scans were performed from the far side; the first with the probe positioned as close as possible to the toe of the weld crown. Additional far-side scans farther from the weld centerline were also performed for several flaws.

For Phase 2 assessments on specimen 3C-022, each weld was scanned using both TRL and TRS phased arrays. The welds were scanned with the front edge of the arrays directly against the weld toe and with the front edge of the arrays 6.4 mm (0.25 in.), 12.7 mm (0.5 in.), and 19 mm (0.75 in.) back from the weld toe. The scans were initiated at a distance of 51 mm (2.0 in.) back from the longitudinal seam (L-seam) weld, traveling circumferentially, 360° around the pipe, and continuing until the L-seam was scanned again. By running over the L-seam twice a beginning and end fiduciary was put into the data. This locator worked well, as the L-seam appeared as a "dead" zone in the scan. Welds one and three were scanned using both the TRL and TRS arrays and were only scanned from the far-side. Weld two was scanned from both the near and far side using both arrays.

For the assessments carried out in Phase 3, an additional 1.5-MHz TRL wave PA probe was introduced into the data acquisition protocol. Therefore, in Phase 3, three different PA probes were employed—two TRL probes designed to operate at 1.5 MHz and 2.0 MHz, respectively, and a 2.0-MHz TRS wave probe. All three probes were specially designed for near- and far-side applications in austenitic material ranging from approximately 13 to 38 mm (0.5 to 1.5 in.) in thickness. The 1.5-MHz probe is shown in Figure 6.8. The 2.0-MHz probes have integral wedges that were contoured to fit the appropriate pipe curvature for these specimens. The 1.5-MHz probe was designed specifically for the far-side IGSCC inspection. It contains three elements in the secondary direction, which allows for improved lateral (side-to-side) beam skewing.

Figure 6.8 1.5-MHz TRL Probe, Configured with Gimbal and Couplant Lines

The 2.0-MHz TRL array was designed for near- and far-side applications in thinner pipe sections. This probe allowed for data collection in tight geometrical configurations. This smaller size generally provided insonification of the far side even with a weld crown present. Skew angles of ±10 degrees were possible with this array. Skewing was not possible with the 2.0-MHz TRS probe.

The 1.5-MHz TRL array consists of two, 3-element by 10-element matrix arrays with a 62% bandwidth at −6 dB. This array was designed with a non-integral wedge allowing change out of the wedge for inspecting pipes of varying diameters or flat plates. Its footprint is approximately 50 by 50 mm (2.0 by 2.0 in.). The larger size and increased number of elements in the lateral direction provides improved beam forming and skewing but limits its application in tight geometrical conditions. This TRL array has a wavelength of 3.8 mm (0.15 in.) in stainless steel, at its average center frequency of 1.5 MHz. Skew angles of ±10 and ±20 degrees were possible with the larger number of elements in the secondary axis of this probe.

Focal laws were developed for the TRL and TRS arrays and programmed into the TomoView acquisition software. The focal laws were developed to provide ultrasonic longitudinal beam angles from 30° to 70° at 1° increments for the 2.0-MHz TRL array in the piping specimens, and from 40° to 70° at 1° increments for the 1.5-MHz TRL. Shear-wave focal laws were developed for the 2.0-MHz TRS array to provide beam angles from 40° to 70° at 1° increments. This resulted in the sound field being swept through many discrete beam angles in near real time at each position along the entire length of the linear scan. In other words, for each axially oriented cross section of material, data were acquired from 30° to 70° or from 40° to 70°, while the linear scans progressed circumferentially.

Sound-field modeling results are summarized in Figures 6.9 through 6.11 for the 1.5-MHz TRL, 2.0-MHz TRL, and 2.0-MHz TRS probes in stainless steel. The left portion of each figure shows an idealized sound field as a function of depth, in a side view, for a 45° inspection angle. The designed focal depth is noted in the image by a black crossed circle. A top view of the sound field at the focal depth is shown in the right portion of each figure. Note that the top view color scheme has been normalized to show the full color range, white to red, in the view. Reference lines separated by 2 mm are displayed in Figures 6.9 through 6.11 to show scale. Theoretical spot sizes as measured from these simulations at the red level, approximately 3 dB points, are 3.4 by 2.7 mm (0.13 by 0.11 in.) for the 1.5-MHz TRL probe, 5.0 by 4.3 mm (0.20 by 0.17 in.) for the 2.0-MHz TRL probe, and 2.9 by 1.7 mm (0.11 by 0.07 in.) for the 2.0-MHz TRS probe. The spot sizes at the yellow, approximately 6 dB points, are 9 by 6.9 mm (0.35 by 0.27 in.) for the 1.5-MHz TRL probe, 11.2 by 9.0 mm (0.44 by 0.35 in.) for the 2.0-MHz TRL probe, and 7.2 by 2.6 mm (0.28 by 0.10 in.) for the 2.0-MHz TRS probe.

These beam plot images show that the 1.5-MHz TRL and 2.0-MHz TRS arrays are operating near the center of their focal region at a depth of approximately 30 mm (1.18 in.). At this depth the 2.0-MHz TRL array is performing beyond its ideal focal plane as shown in the side view of the beam plot in Figure 6.10; however, in practice, good signals at the 30-mm depth were detected and recorded. The advantage of this 2.0-MHz TRL probe is its small footprint, which allows better sound field access to the far side of the weld in the presence of a limiting weld crown or other geometrical condition. On at least one of the EPRI pipe specimens, this was the only probe that could effectively collect data on both sides of the weld due to geometrical constraints.

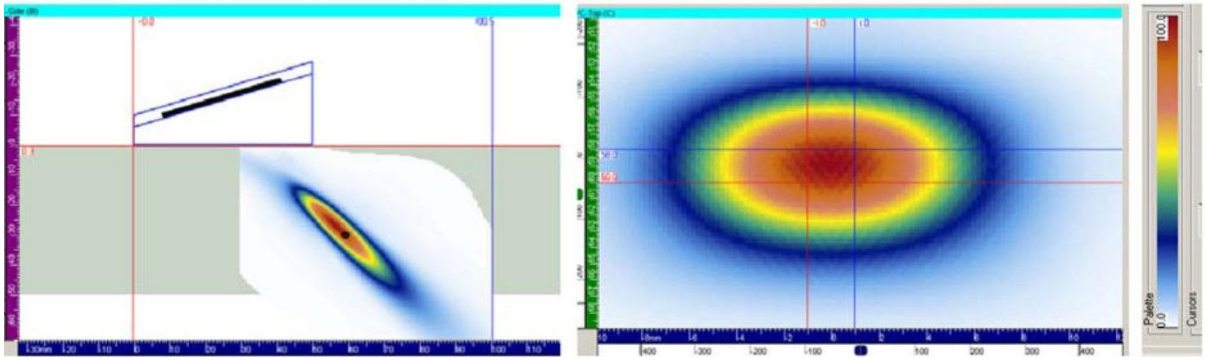

Figure 6.9 TRL 1.5-MHz Beam Model at 45° with the Side View on the Left and Top View on the Right. The top view is at the focal depth of 30 mm. Vertical and horizontal lines with 2-mm separation are shown for reference.

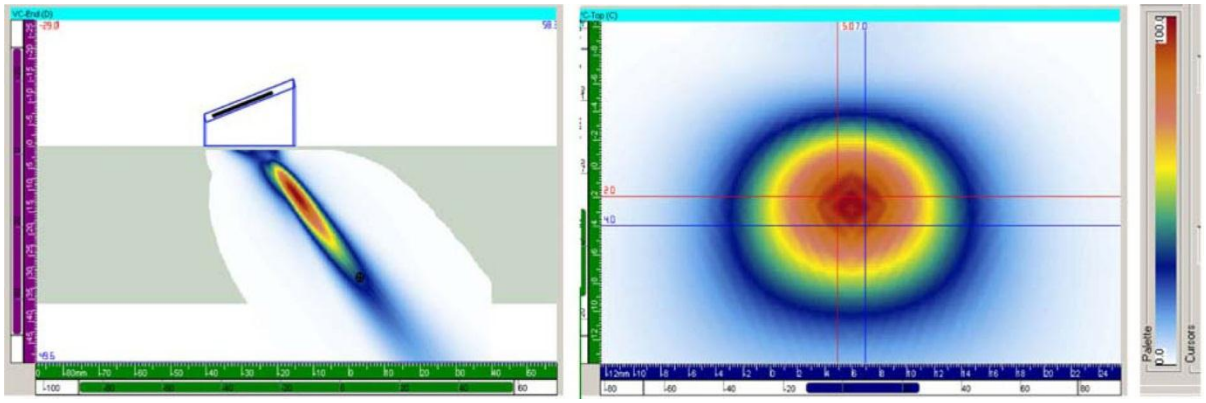

Figure 6.10 TRL 2.0-MHz Beam Model at 45° with the Side View on the Left and Top View on the Right. The top view is at the focal depth of 30 mm. Vertical and horizontal lines with 2-mm separation are shown for reference.

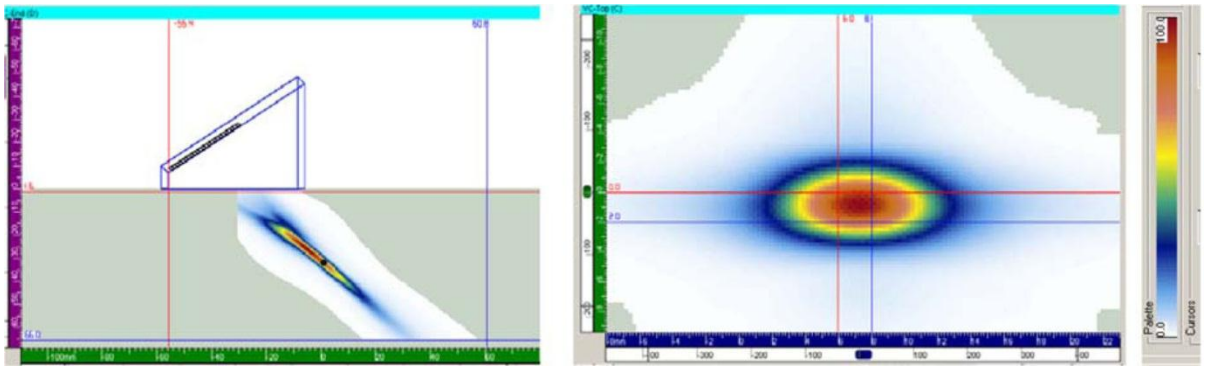

Figure 6.11 TRS 2.0-MHz Beam Model at 45° with the Side View on the Left and Top View on the Right. The top view is at the focal depth of 32 mm. Vertical and horizontal lines with 2-mm separation are shown for reference.

Additional beam-field modeling for the 1.5-MHz TRL array shows the ability of the probe to form a coherent beam at skew angles up to 20°. The modeling results are shown in Figure 6.12. Skewed data can improve detection of IGSCC because it can be more sensitive to cracks branching out of the primary plane of the flaw and also be less sensitive to planar geometrical reflectors such as counterbore.

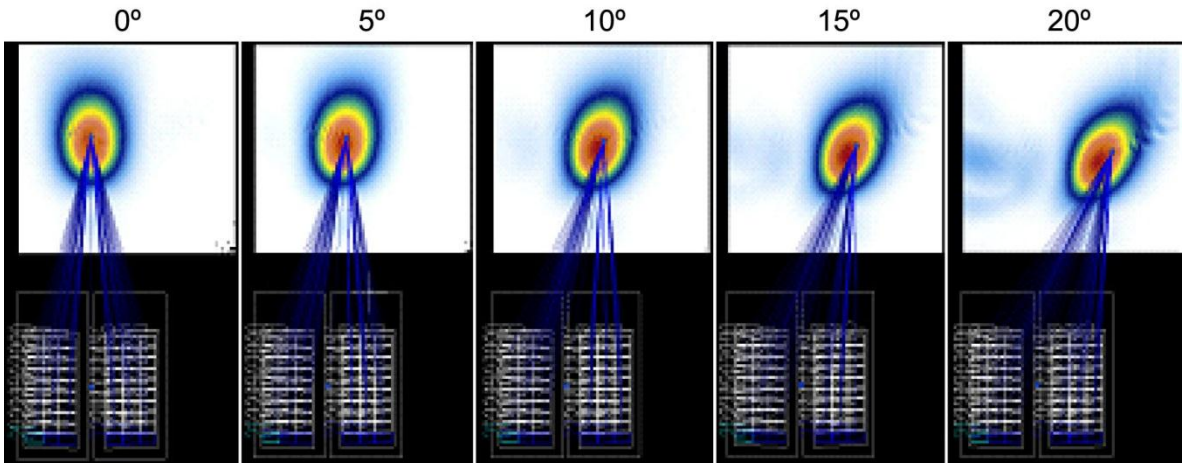

Figure 6.12 Beam Skewing Model for the 1.5-MHz TRL, 10 by 3 Element Probe

For the three probes and all Phase 3 IGSCC specimens, data were acquired with a manual scanner. The scanner was mounted on a curved section or ring positioned adjacent to the specimen. The 1.5-MHz TRL probe and scanner are shown in Figure 6.13. Data were acquired with the sound beam directed perpendicular to and pointing toward the weld, while the manual scanner was moved in the circumferential direction. The scanner encoder was calibrated to the specimen to give circumferential position information. Several linear scans were acquired from both the near side and the far side when specimen configuration allowed. A line scan with the probe positioned as close as possible to the weld crown center was acquired first. Additional scans with added offsets from this close position were then acquired from both sides when possible, typically at offset distances of 0.64 cm (0.25 in.) and/or 1.27 cm. (0.5 in.). The line scans proceeded clockwise with respect to the flow and the flow direction was noted by an arrow on the specimens. Skewed data were also acquired because the flaws were true IGSCCs and typically exhibited branching out of the plane of the flaw parallel or axial to the weld. Data obtained at skewed angles can be sensitive to the crack branching, and when combined with the normal data, may improve the flaw detection. Skew angles of ±10° and ±20° were used with the 1.5-MHz TRL probe. The linear TRS probe was not skewed and the 2.0-MHz TRL probe was skewed at ±10°. Data were acquired such that each file contained only a single skew angle. The default skew was 0°.

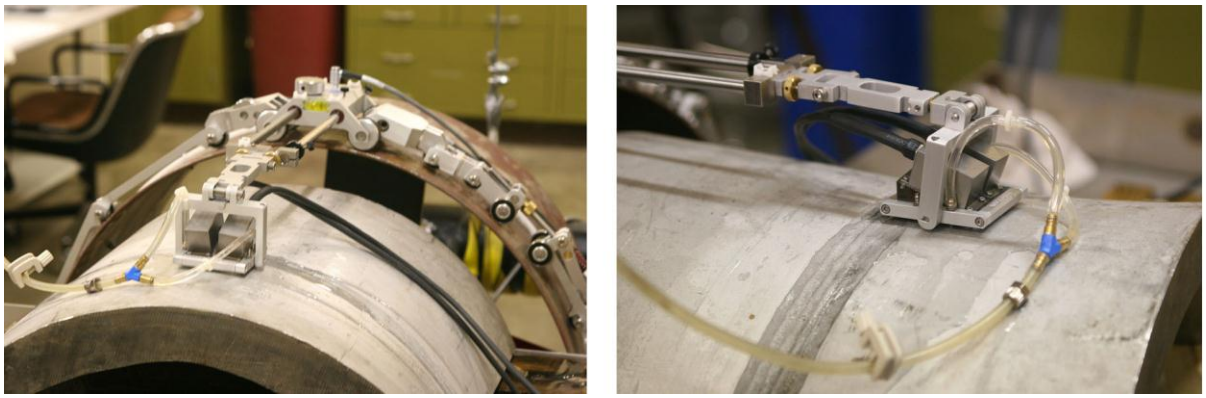

Figure 6.13 Mechanical Scanner Mounted on a Ring Section in the Background with the Scanner Arm and Probe Extending to the Foreground (left) and Side View of the 1.5-MHz TRL Probe Next to a Weld (right)

7 Phase 1 Evaluation

The Phase 1 evaluation was focused on assessing the far-side inspection performance of three ultrasonic NDE techniques—automated conventional-UT, low-frequency/SAFT-UT, and phased-array UT. The focus of the Phase 1 evaluation was aimed at far-side detection and characterization of fabricated thermal fatigue cracks and machined reflectors in the wrought austenitic, SS pipe specimen 02-24-15.

7.1 Conventional-UT: Data Analysis and Results

Automated conventional shear wave ultrasonic techniques were employed on the wrought-austenitic stainless steel specimen 02-24-15 for comparison with the advanced phased-array and low-frequency/SAFT techniques. These scans differ from standard manual ultrasonic examinations of pipes in that the scans were taken using an automated scanner and the data were stored digitally. This method was chosen to provide images for a more direct comparison with the phased-array and LF/SAFT data. As described in Section 5, pipe specimen 02-24-15 consists of two 610-mm (24-in.) diameter, 36-mm (1.4-in.) thick pieces of ASTM A-358, Grade 304 vintage austenitic stainless steel. The specimen was cut into three segments to allow easier handling and scanning. Preliminary screening of data sets was performed immediately after scanning of the first pipe segment to determine which transducer(s) had the best signals and highest SNR performance. The 12.7-mm (0.5-in.), 1.5-MHz probe was identified as the transducer of choice for evaluation of conventional UT, reducing the total number of required scans significantly. Thus, 1.5-MHz, 60° and 70° shear-wave scans were completed on the near and far sides for pipe sections two and three of specimen 02-24-15. All of the B-scan end-views and C-scans are contained in Appendix C. Appendix C also contains the detailed analysis for each crack and saw-cut. Only results from the 1.5-MHz, 12.7-mm (0.5-in.) diameter, 60° and 70° shear-wave scans will be discussed in this section.

Figure 7.1 shows the C-scan images for pipe segment 1 taken using the 1.5-MHz probes and angles described above from the near and far side of the weld. Pipe segment 1 contains thermal fatigue cracks A (15% through-wall) and B (43% through-wall), and sawcuts A (7.5% through-wall straight cut), B (28.4% through-wall straight cut), and C (7.1% through-wall 35° angled cut). To summarize the results, sawcut A was detectable from the far side with both 60° and 70° shear waves. From the far side, with the 60° probe, sawcut A is detected as a 6 dB increase in the response versus the weld root response. Using the 70° probe from the far side, the response from sawcut A is not mixed in with the response from the weld root and is 11 dB above the average local noise. The 60° response from thermal fatigue crack A, which is only 15% through-wall, is difficult to resolve from the weld root response. In contrast, the 70° shear waves are able to clearly detect crack A. Sawcut and crack B are very easily detected with the 60° and 70° shear waves through the weld. Sawcut C gives a weak response and is only detectable from the near-side of the weld using 60° shear waves.

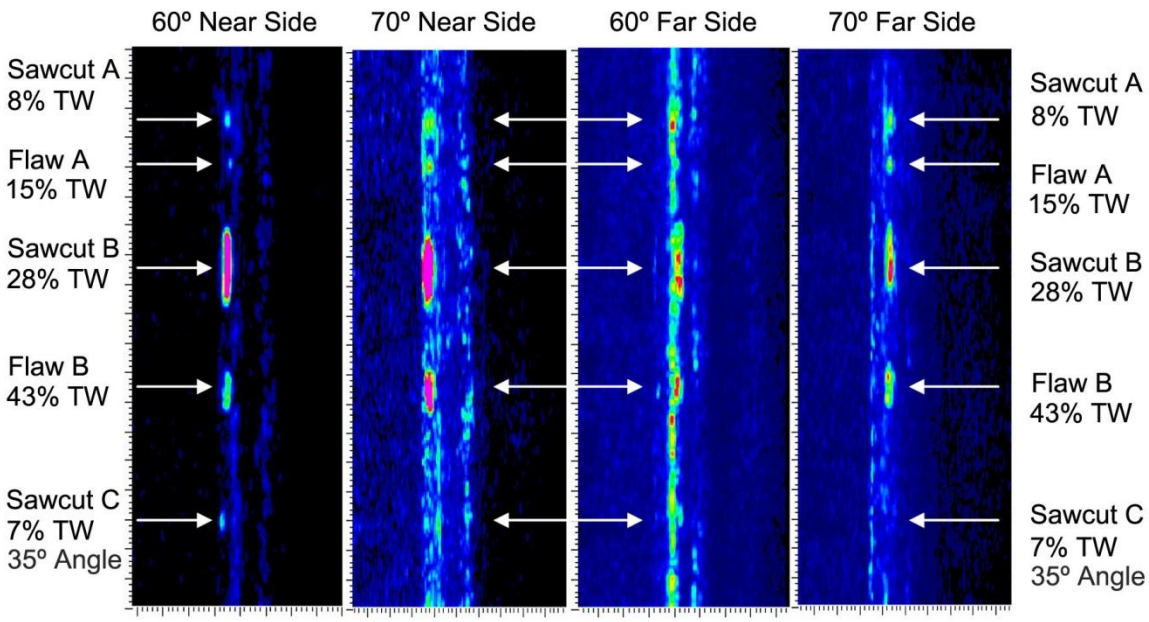

Figure 7.1 C-scan Views for Pipe Segment 1 from the Near and Far Side with the 1.5-MHz, 60° and 70° Conventional Shear-Wave Probes

By comparing the gains used during scanning and the peak responses from the same reflectors when viewed on the near and far sides of the weld, it was determined that the weld metal absorbed or redirected 11 dB of 60° ultrasound (4 dB near-side vs. 15 dB far-side gains to obtain the same amplitude response from sawcut B) and virtually no absorption for the 70° ultrasound (17 dB gain for the same response from sawcut B from both near and far sides).

Figure 7.2 shows the near-side and far-side C-scan images for pipe segment 2 taken using the 12.7-mm (0.5-in.), 1.5-MHz probe mounted on wedges that provide 60° and 70° shear waves in the material from the near and far side. Pipe segment 2 contains crack C (64% through-wall) and sawcuts D (19% through-wall straight cut), E (12% through-wall straight cut), and F (19% through-wall 35° angled cut). The term “straight cuts” refers to sawcuts that were made 90° to the inner surface, and the 35° angled cuts follow the HAZ as shown in Section 5, Figure 5.4. Sawcuts D, E, and F returned strong signals from the near and far side and were easily detected. This is to be expected, as they are all at least 19% through wall. Crack C, which is a 64% through-wall implanted thermal fatigue crack, was also easily detected.

The weld in segment 2 exhibited less sound absorption characteristics than segment 1. Once again, the 60° scan showed more absorption, with the 60° probe seeing a 4 dB drop through the weld and the 70° probe seeing only a 1 dB drop through the weld.

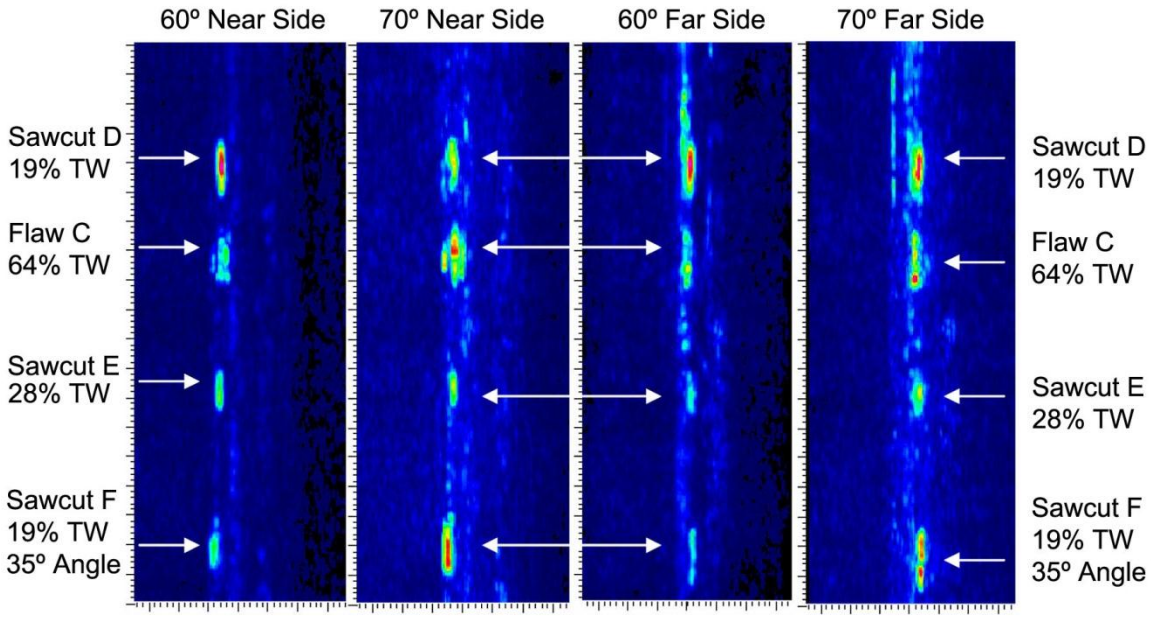

Figure 7.2 C-scan Views for Pipe Segment 2 from the Near and Far Side with the 1.5-MHz, 60° and 70° Conventional Shear-Wave Probes

Figure 7.3 shows the near-side and far-side C-scan images for pipe segment 3 using the 12.7-mm (0.5-in.), 1.5-MHz probe. Pipe segment 3 contains cracks D (19% through-wall axially oriented) and E (48% through-wall), and sawcuts G (18% through-wall 35° angled cut) and H (26% through-wall 35° angled cut). Crack E and sawcut H are easily detected by both probes. Sawcut G appears as a series of closely spaced smaller indications from the far side of the weld for both the 60° and 70° scans. Crack D, which is axially oriented, is not detected with any of the probes from the near or far side.

The sound absorption characteristics for the weld in segment 3 were similar to segments 1 and 2. The 60° scan showed the strongest sound loss through the weld, with the 60° probe seeing a 7 dB drop through the weld and the 70° probe seeing a 4 dB drop through the weld.

Once it was determined which cracks could be detected, the next step was to length- and depth-size the flaws. Each detected flaw and sawcut was length-sized four times, once from each angle (60° and 70°), for the near and far side, and with two techniques, the 6 dB drop and loss of signal (LOS) methods. The length-sizing data is contained in Tables 7.1 through 7.4 and is represented graphically in Figures 7.4 and 7.5. To summarize, the 6 dB drop technique slightly undersizes the sawcuts but is very accurate for the implanted fatigue cracks. The LOS technique is very accurate for the sawcuts and slightly oversizes the implanted TFCs.

The root mean square error (RMSE) values for each column were calculated following these steps:

- Subtracting each empirical value from its corresponding true-state value.
- Squaring each of these differences.

- Calculating the mean of the squared differences.
- Calculating the square root of this mean.

The formula summarizing these steps is

$$\sqrt{\frac{\sum_{1 \to n} (x_1 + x_n)}{n}}$$

where x = (empirical value – true-state value). The RMSE values provide a measure of the magnitude of deviation from true state.

The LOS length measurements have RMSE values ranging from 4 mm (0.16 in.) to 10.8 mm (0.43 in.), which is better than the 19.1-mm (0.75-in.) RMSE value required to satisfy ASME Code Section XI, Appendix VIII, length-sizing accuracy requirements. The 6 dB drop technique has RMSEs ranging from 2.2 mm (0.09 in.) to 19.4 mm (0.76 in.), and, while close, does not always meet ASME Code requirements. Note that the ASME sizing criteria are based on blind test results and the PNNL examinations are non-blind, thus represent more of a "best case" scenario.

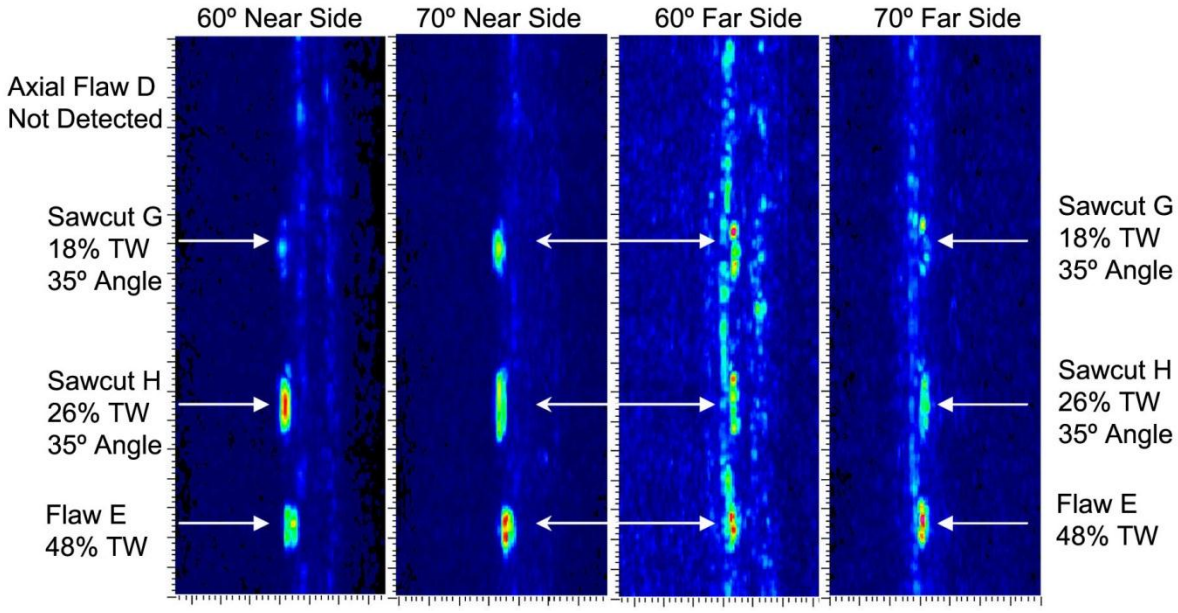

Figure 7.3 C-scan Views for Pipe Segment 3 from the Near and Far Side with the 1.5-MHz, 60° and 70° Conventional Shear-Wave Probes

Table 7.1 Sawcut Lengths in Pipe Specimen 02-24-15 as Measured by the 60° Conventional UT Technique

		Near Side		Far Side	
Sawcut	**Actual Length**	**60° −6 dB**	**60° LOS**	**60° −6 dB**	**60° LOS**
A	32.8 mm (1.29 in.)	17.8 mm (0.70 in.)	40.6 mm (1.60 in.)	29.2 mm (1.15 in.)	34.3 mm (1.35 in.)
B	65.1 mm (2.57 in.)	52.1 mm (2.05 in.)	69.9 mm (2.75 in.)	45.7 mm (1.80 in.)	55.9 mm (2.20 in.)
C	36.3 mm (1.43 in.)	15.2 mm (0.60 in.)	19.1 mm (0.75 in.)	8.9 mm (0.35 in.)	8.9 mm (0.35 in.)
D	54.1 mm (2.13 in.)	36.8 mm (1.45 in.)	52.1 mm (2.05 in.)	41.9 mm (1.65 in.)	57.1 mm (2.25 in.)
E	43.7 mm (1.72 in.)	31.7 mm (1.25 in.)	41.9 mm (1.65 in.)	36.8 mm (1.45 in.)	52.1 mm (2.05 in.)
F	59.7 mm (2.35 in.)	39.4 mm (1.55 in.)	50.8 mm (2.00 in.)	48.3 mm (1.90 in.)	59.7 mm (2.35 in.)
G	57.3 mm (2.25 in.)	52.1 mm (2.05 in.)	57.1 mm (2.25 in.)	43.2 mm (1.70 in.)	54.6 mm (2.15 in.)
H	75.2 mm (2.96 in.)	39.4 mm (1.55 in.)	73.7 mm (2.90 in.)	52.1 mm (2.05 in.)	73.7 mm (2.90 in.)
RMS Error		19.4 mm (0.76 in.)	7.7 mm (0.30 in.)	16.6 mm (0.65 in.)	10.8 mm (0.42 in.)

Table 7.2 Sawcut Lengths in Pipe Specimen 02-24-15 as Measured by the 70° Conventional UT Technique

		Near Side		Far Side	
Sawcut	**Actual Length**	**70° −6 dB**	**70° LOS**	**70° −6 dB**	**70° LOS**
A	32.8 mm (1.29 in.)	40.6 mm (1.60 in.)	40.6 mm (1.60 in.)	29.2 mm (1.15 in.)	30.5 mm (1.20 in.)
B	65.1 mm (2.57 in.)	48.3 mm (1.90 in.)	61.0 mm (2.40 in.)	48.3 mm (1.90 in.)	57.1 mm (2.25 in.)
C	36.3 mm (1.43 in.)	47.0 mm (1.85 in.)	47.0 mm (1.85 in.)	Not detected	Not detected
D	54.1 mm (2.13 in.)	41.9 mm (1.65 in.)	49.5 mm (1.95 in.)	35.6 mm (1.40 in.)	54.6 mm (2.15 in.)
E	43.7 mm (1.72 in.)	29.2 mm (1.15 in.)	39.4 mm (1.55 in.)	24.1 mm (0.95 in.)	44.5 mm (1.75 in.)
F	59.7 mm (2.35 in.)	47.0 mm (1.85 in.)	58.4 mm (2.30 in.)	47.0 mm (1.85 in.)	55.9 mm (2.20 in.)
G	57.3 mm (2.25 in.)	30.5 mm (1.20 in.)	50.8 mm (2.00 in.)	35.6 mm (1.40 in.)	58.4 mm (2.30 in.)
H	75.2 mm (2.96 in.)	57.1 mm (2.25 in.)	67.3 mm (2.65 in.)	62.2 mm (2.45 in.)	69.8 mm (2.75 in.)
RMS Error		15.9 mm (0.63 in.)	6.5 mm (0.26 in.)	16.1 mm (0.64 in.)	4.0 mm (0.16 in.)

Table 7.3 Implanted Thermal Fatigue Crack Lengths in Pipe Specimen 02-24-15 as Measured by the 60° Conventional UT Technique

		Near Side		Far Side	
Crack	**Actual Length**	**60° −6 dB**	**60° LOS**	**60° −6 dB**	**60° LOS**
A	10.7 mm (0.42 in.)	12.7 mm (0.42 in.)	17.78 mm (0.70 in.)	11.43 mm (0.45 in.)	12.7 mm (0.50 in.)
B	30.5 mm (1.20 in.)	31.75 mm (1.25 in.)	41.91 mm (1.65 in.)	26.67 mm (1.05 in.)	30.48 mm (1.20 in.)
C	43.6 mm (1.72 in.)	39.37 mm (1.55 in.)	54.61 mm (2.15 in.)	45.72 mm (1.80 in.)	57.15 mm (2.25 in.)
E	33.8 mm (1.33 in.)	30.48 mm (1.20 in.)	50.8 mm (2.00 in.)	34.29 mm (1.35 in.)	49.53 mm (1.95 in.)
RMS Error		2.94 mm (0.12 in.)	12.15 mm (0.48 in.)	2.23 mm (0.09 in.)	10.43 mm (0.41 in.)

Table 7.4 Implanted Thermal Fatigue Crack Lengths in Pipe Specimen 02-24-15 as Measured by the 70° Conventional UT Technique

		Near Side		Far Side	
Crack	**Actual Length**	**70° −6 dB**	**70° LOS**	**70° −6 dB**	**70° LOS**
A	10.7 mm (0.42 in.)	13.97 mm (0.55 in.)	16.51 mm (0.65 in.)	12.7 mm (0.50 in.)	15.24 mm (0.60 in.)
B	30.5 mm (1.20 in.)	27.94 mm (1.10 in.)	36.83 mm (1.45 in.)	26.67 mm (1.05 in.)	30.48 mm (1.20 in.)
C	43.6 mm (1.72 in.)	41.91 mm (1.65 in.)	55.88 mm (2.20 in.)	44.45 mm (1.75 in.)	52.07 mm (2.05 in.)
E	33.8 mm (1.33 in.)	33.02 mm (1.30 in.)	46.99 mm (1.85 in.)	34.29 mm (1.35 in.)	41.91 mm (1.65 in.)
RMS Error		2.28 mm (0.09 in.)	9.98 mm (0.39 in.)	2.22 mm (0.09 in.)	6.29 mm (0.25 in.)

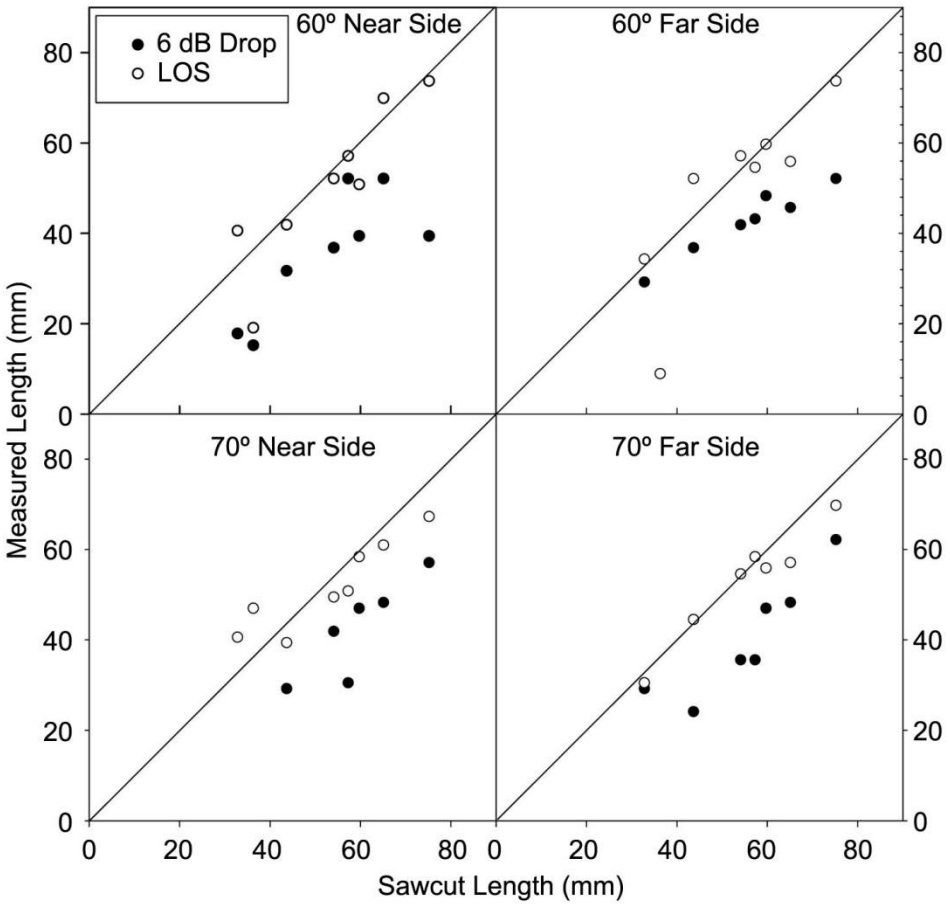

Figure 7.4 Sawcut Lengths Measured Using the 6 dB Drop and Loss of Signal Techniques with the 1.5-MHz 60° and 70° Probes from the Near and Far Side of the Weld Versus the Actual Sawcut Lengths

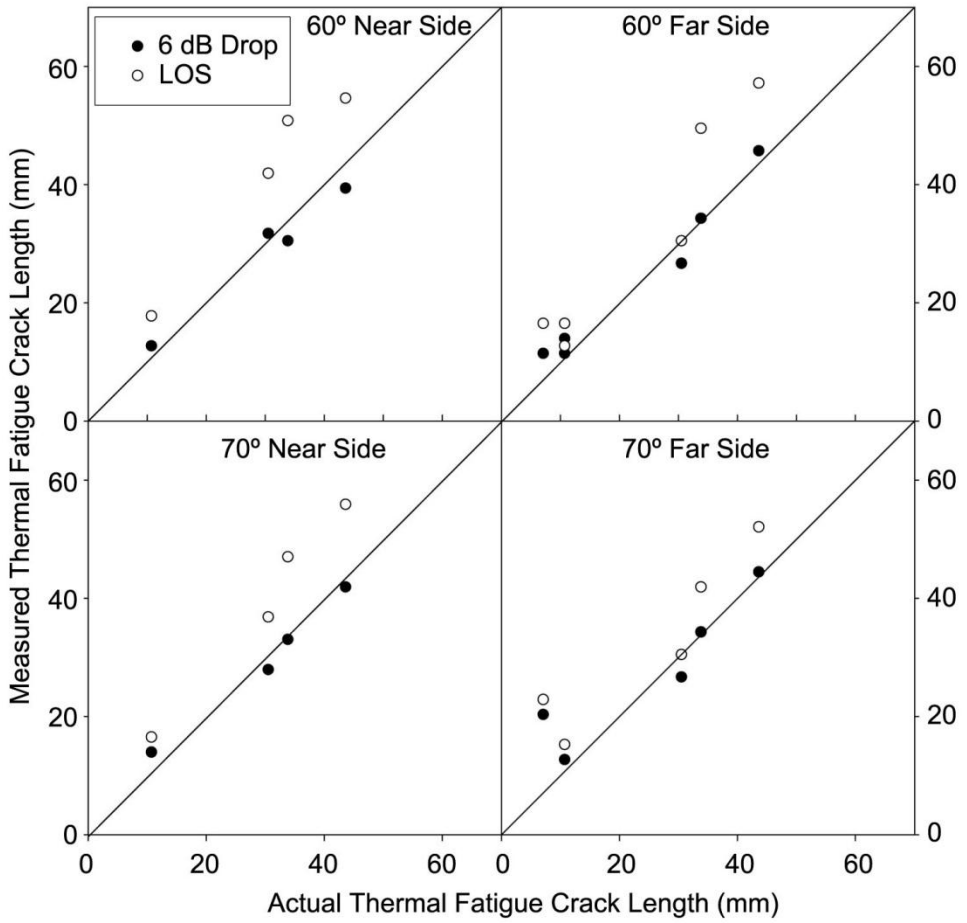

Figure 7.5 Thermal Fatigue Crack Lengths Measured Using the 6 dB Drop and Loss of Signal Techniques with the 1.5-MHz 60° and 70° Probes from the Near and Far Side of the Weld Versus the Actual Crack Lengths

Depth-sizing the flaws proved to be much more difficult than length-sizing. While identifying the corner trap signals in the data was not difficult, no tip signals could be positively identified in any of the scans. When looking at the B-scan end views, no crack tip energy could be discerned. The A-scans associated with each flaw were then analyzed for possible crack tip responses. Some of the A-scan images in Appendix C contain what look like crack tip signals. Standard techniques were applied to each of these crack tip indications to determine the depth of the crack based on these possible tip signals. Many of the potential tip signals did not have the proper echo-dynamic response that is characteristic of crack tips. Therefore, it was determined that no crack tip signals were present in the data. These apparent crack tips are the result of high noise from the coarse-grained weld metal and the weld root response.

It is important to note that it was challenging to know that these apparent crack tips were merely noise. Figure 7.6 shows the depths calculated using the 6 dB drop technique and using the apparent crack tips. Figure 7.6 includes calculated depths for both sawcuts and cracks. The 6 dB drop depths tended to size near 5 mm (0.2 in.), independent of the actual crack depth. The depths calculated from the apparent tip signals have no relation to the actual crack depth, and have an RMSE of 5 mm (0.2 in.).

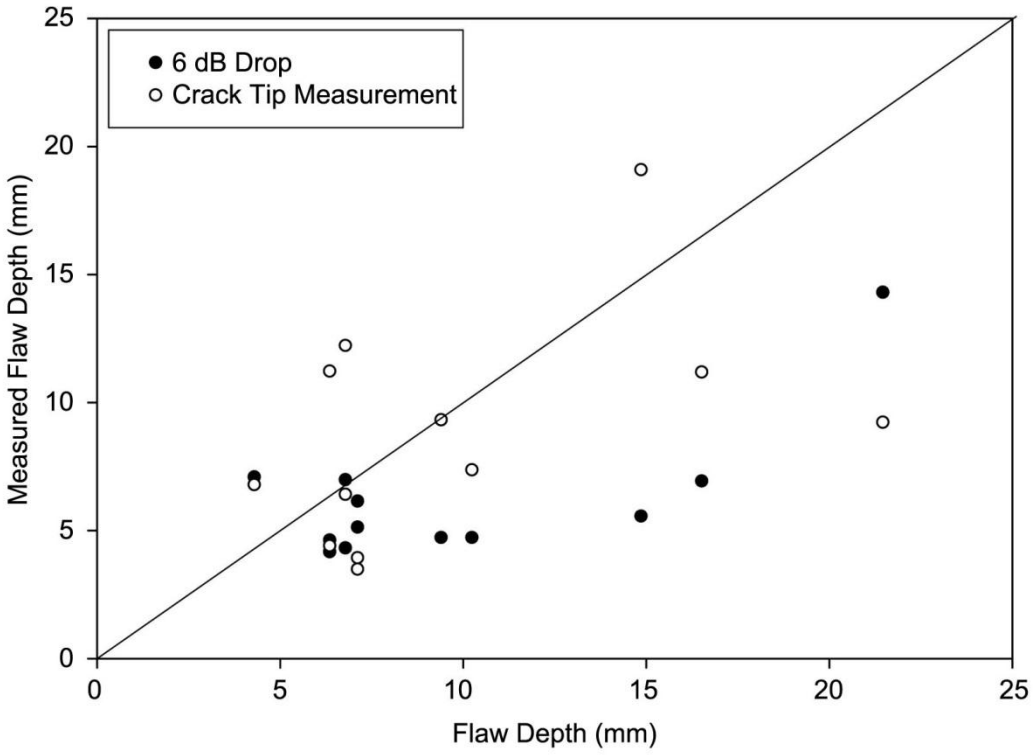

Figure 7.6 Sawcut and Crack Depths Measured Using the 6 dB Drop and Crack Tip Techniques with the 1.5-MHz 60° and 70° Probes from the Near and Far Side of the Weld Versus the Actual Sawcut and Crack Depths

Figure 7.7 shows the corner-trap SNR for the four detected cracks (A, B, C, and E) in Phase 1 and the three cracks (cracks 4, 5, and 6; 5%, 10%, and 15% through-wall, respectively) from Phase 2 plotted versus the crack depths. The corner-trap SNR for the cracks on the far side of the weld ranged from 2–5, with no strong relationship between the crack depth and the SNR.

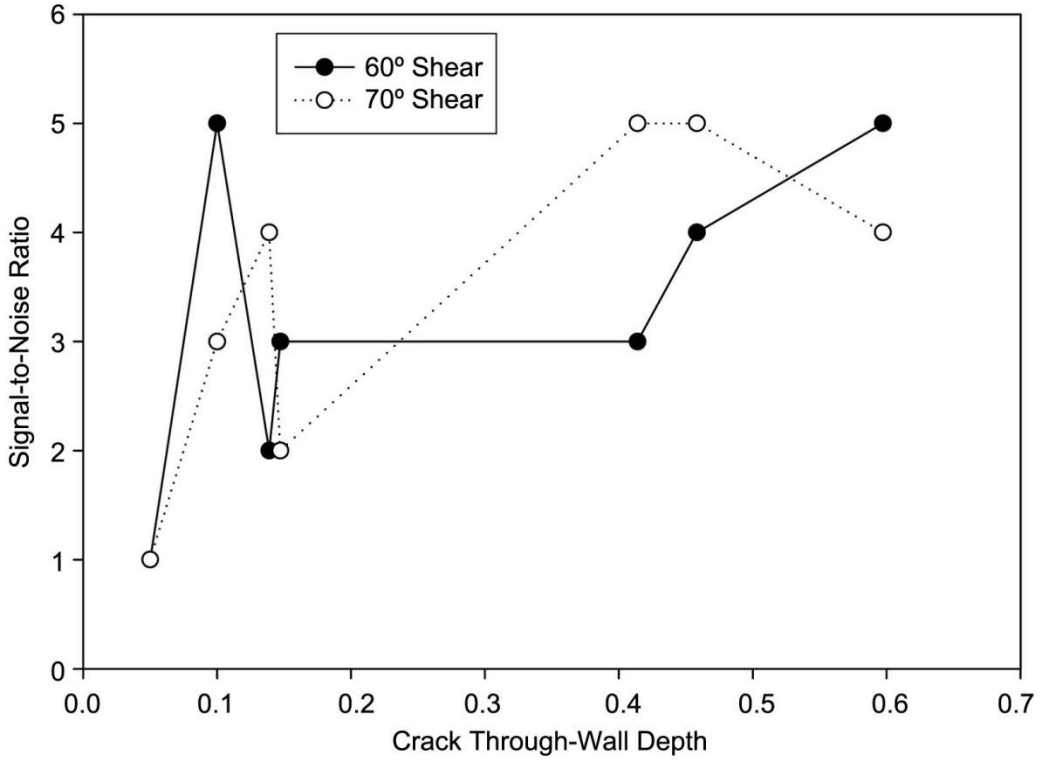

Figure 7.7 Signal-to-Noise Ratio Plotted Against the Crack Depth for the 60° and 70° Far-Side Scans

7.2 Low-Frequency/SAFT: Data Analysis and Results

Data analysis was conducted using an established protocol and referencing specific crack identification and length-sizing criteria. Within any given planar view (B-scan side view, B-scan end view, or C-scan view), the analysis focused on an established criteria for identifying or rejecting regions as cracked in the material, where ultrasonic signal amplitude anomalies occurred. Signal amplitude anomalies (SAAs) were used as the primary ultrasonic markers for determining detection capability. The criteria described here are based upon acquiring SAAs above an established amplitude threshold in the ultrasonic data as a function of spatial position on the image (axial and circumferential position relative to the true-state). SAAs occurring in the volumetric space surrounding the weld root were fully insonified and examined from the far side. SAAs occurring outside of this region were not examined as part of this study.

The following criteria were used in the assessment of SAAs detected in the SAFT-processed images. SAAs may occur above, on, or below the back-surface line appearing on the SAFT-processed images. Differences in position of ±0.51 cm (±0.2 in.) above or below this line are not deemed significant, and SAA position will be measured from the peak amplitude point. When an SAA occurs in this region, its entire shape will be included in the boxed examination region of the image. When the back-surface line is positioned accurately, corner trap signal returns from cracking in the material will result in SAAs that lie just on the back-surface line, with overlap of the SAA above and below the line. The accuracy of the back-surface line is a

function of the material velocity and transducer delay, and the actual position of a SAA relative to this line is a function of incident angle, acoustic velocity, frequency, wavelength, and zone focal dimensions of the transducer. Because material velocity varies with spatial position and incident angle in the material, inaccuracies must be accommodated. The specimen documentation data were used to determine nominal wall thickness values. SAAs should have some degree of characteristic shape (elliptical) to them, with somewhat smooth contours on their edges, as opposed to random, blotchy, scattered amplitude blips that appear with little symmetry and rough contours. Also, SAAs should have reasonable and proper orientation with respect to the examination incident angle of the insonifying beam. A perpendicular orientation is normal for opposite surface-breaking defects. Once again, differences in lateral position of ±0.51 cm (±0.2 in.) or less are not deemed significant.

The 12° beam processing angle was used for analysis purposes here, as processing angles greater than 12° did not significantly improve image enhancements and processing angles lower than 12° did not provide the necessary focusing and SNR enhancements to the imaged data. The higher the angle, the more time-intensive the SAFT process becomes. So the decision to stay with a 12° beam processing angle for all data sets was made early in the study. The SAFT data analysis protocol used for identifying SAAs was initiated by generating projected B-scan side view images and correlating the weld centerline position and back-surface line position to the image based upon component thickness information and scan parameter settings relative to transducer spatial position on the component. In this manner, the analyst uses positional information to accurately employ the SAFT-UT "boxing" feature to magnify SAAs in the area of interest. It should be noted that the SAFT presentation images are defaulted to use dimensions in English units only.

Next, the composite B-scan end view was generated to provide an orthogonal perspective that yields the circumferential perspective, and again the back-surface line position was used for analysis of the image as well. The analyst can then crop and magnify SAAs from both views and analyze characteristics and features as a function of view perspective, position relative to the weld centerline and back-surface line, orientation to the sound field incident angle, characteristic shape, etc. At this point, the various longitudinal- and shear-wave data sets were analyzed and features were identified. SAAs and pertinent commonalities between perspectives for determining root condition and geometrical reflectors were noted. SAAs present in the various views were then further reduced using both 6 dB and 3 dB drop methods (clipping the view’s dynamic range by this value) and length sizing was then recorded using the 6 dB drop and LOS methods. The 3 dB clipping was only used to further reduce background and examine redundancy between modes where only the most prominent high-amplitude responses were evident. Depth sizing was initially attempted, but calculations based upon known depths of sawcuts could not be correlated with any method as tip-diffracted signals were not detected. Amplitude drop methods were ineffective because the sound-beam dimensions were always larger than the flaws being examined. Depth information was not recorded for this inspection technique.

It should be noted that the dynamic range of each scan was configured by translating the transducer over the area containing the introduced flaw that provided the largest amplitude responses and setting system gain and A/D sensitivity values accordingly. This provided a means to use the full dynamic range of the digitizer without saturating the highest amplitude

responses. However, each scan varied regarding system gain, resulting in variable ranges for total system gain between scans. In general, the results are consistent between all SAFT analyses in that the images are always normalized to the signal responses of interest within the data set being evaluated. All signal-to-noise calculations were conservatively made using the highest amplitude background noise levels from nearby zones of the specimen being evaluated.

The summary analysis documentation for each notch, crack, and sawcut as a function of inspection modality, incident angle, and frequency from the far side is provided in Appendix D.

In the first phase of this evaluation, the low-frequency/SAFT inspection technique was employed for examination of a sectioned, Grade 304 WSS pipe (specimen 02-24-15) containing an austenitic weld. This specimen was sectioned into three pieces, with each 120° segment of the full pipe section laid on a platform in horizontal fashion and secured for scanning with the automated pipe scanner using a magnetic scanner track. In Section 6, the photograph on the right hand side in Figure 6.2 illustrates the Phase 1 configuration for data acquisition.

Here in this section, a tutorial is provided for the reader to follow and understand the process used in compiling detection results from the data and interpreting the SAFT-processed images. Because this was an iterative process that was undertaken for each individual SAA occurring in the SAFT-processed images, the reader is directed to Appendix D for the large volume of data, images, and spreadsheets for detailed information on the remaining analyses. A discussion of the results of this study will be described after the tutorial provided here.

7.2.1 Tutorial on SAFT Data Analysis Process

This tutorial uses images, positional data (axial, circumferential, and depth values), and the detection and length-sizing criteria described earlier in the document as the basis for the analysis procedure. The example provided for the tutorial is one of the benchmark data sets that were used for verification of scanning parameters, procedures, and other variables. In this case, the 400-kHz, 45° shear-wave inspection of piping segment 2, from the near side, was used for illustrating the procedures, imaging combinations, and calculations employed for conducting the analysis.

The raw, unprocessed ultrasonic C-scan image is analyzed first. This top-view visual is a composite view of the peak-amplitude signal responses in the X-Y plane. From this, any evidence of transducer de-coupling, electronics failures, or other problems with the data acquisition system can immediately be identified, and the data can be re-taken if necessary. Also, the operator looks for signs of signal amplitude saturation, and when satisfied with the integrity of the ultrasonic data, the data set is then SAFT-processed using a 12° beam processing angle. From an analysis of the SAFT-processed C-scan image, SAAs are then identified and isolated using a boxing feature to segregate and magnify SAAs of interest. This C-scan analysis process is visually illustrated in Figure 7.8. For this tutorial, the focus will be directed at the SAA highlighted in the yellow box.

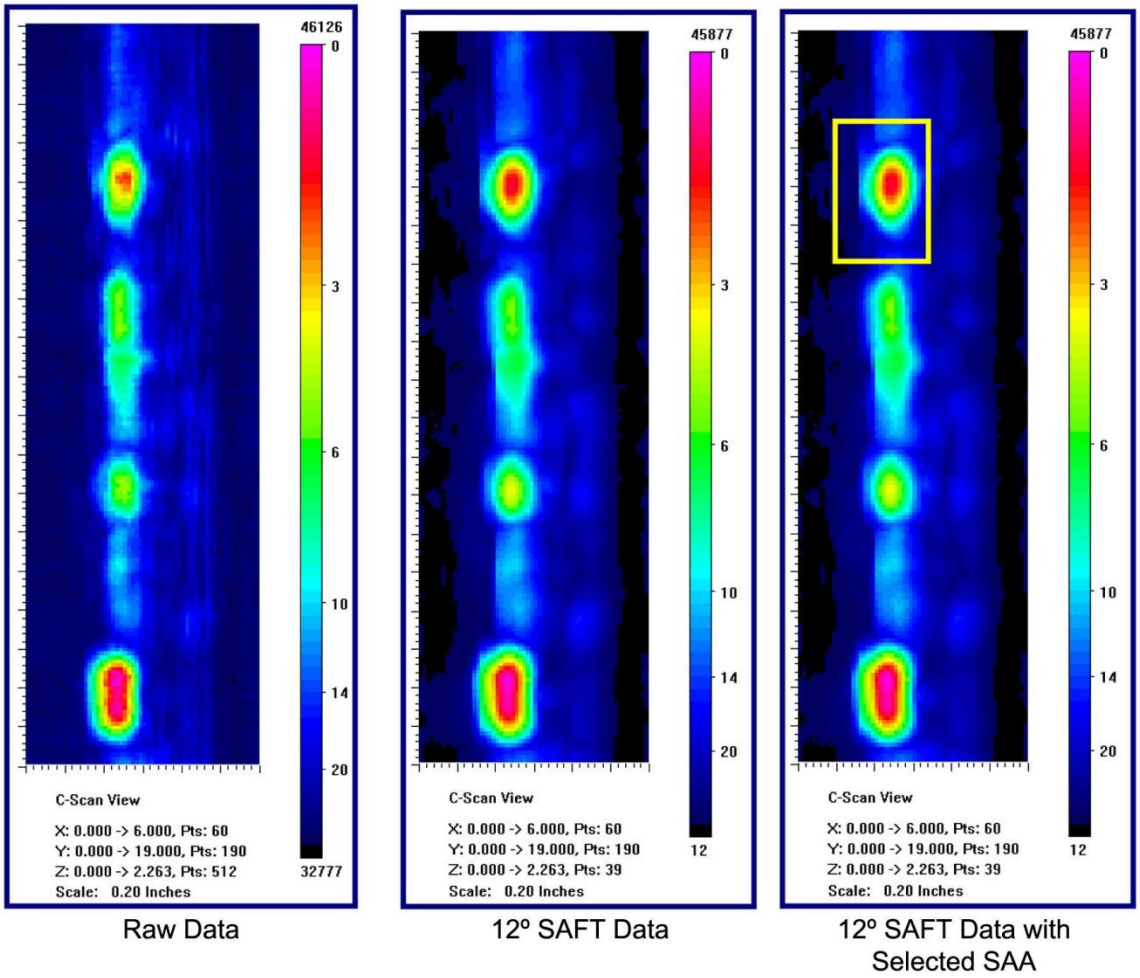

Figure 7.8 C-scan Analysis Process. From left to right, the unprocessed ultrasonic data in C-scan view. Next, the 12° SAFT-processed data in C-scan view. Finally, the processed C-scan view depicting an isolated SAA using the "box" feature embedded in the SAFT analysis menus.

From these initial views, information relative to axial position and length information can be retrieved. Also, application of specific rules defined in the detection and length-sizing criteria can begin to be evaluated.

Next, a similar process using the B-scan end-view (sometimes referred to as a D-scan view) is then employed. The B-scan end-view is an orthogonal planar representation of the B-scan side-view and represents a composite view of the peak-amplitude signal responses in the Y-Z plane. This process allows the analyst the opportunity to view the raw unprocessed data, the 12° SAFT-processed data, and the isolated indications of interest (SAAs) from a perspective that highlights the depth information while maintaining the circumferential aspect of the indications. Quite often these views are examined simultaneously in a side-by-side fashion to better understand the enhancement and reduction of various features between the processed and unprocessed data sets. Using these images, the detection and length-sizing criteria is again

reviewed and applied to the SAAs, and magnification of the isolated indications is performed for a more detailed analysis. Figure 7.9 illustrates the B-scan end-view analysis. Again, the SAA identified by the yellow box (and corresponding to the same SAA discussed in the C-scan analysis and shown in Figure 7.8) is the focus of this discussion.

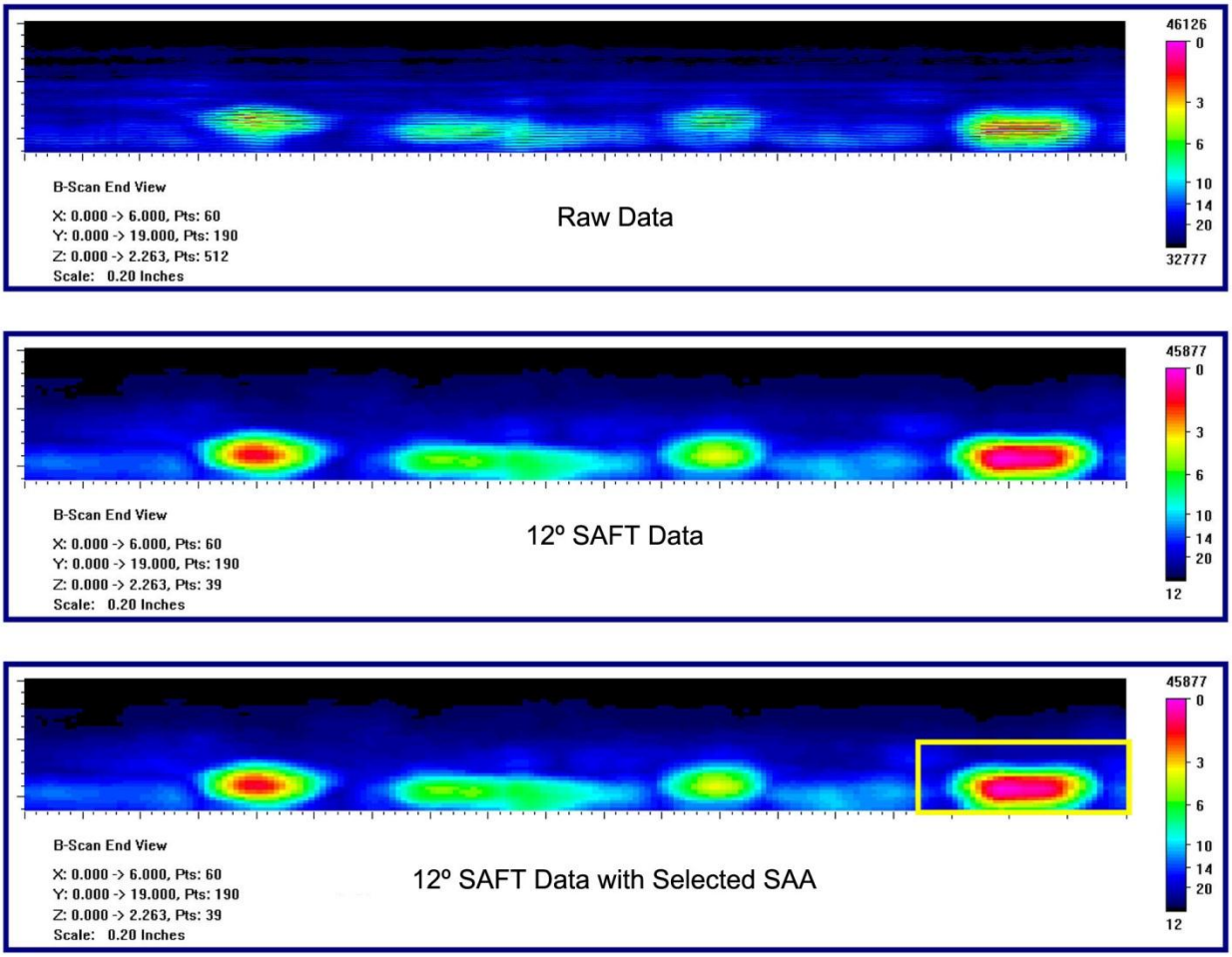

Figure 7.9 B-scan End-View Analysis. From top to bottom, the unprocessed ultrasonic data in B-scan end-view. Next, the 12° SAFT-processed data in B-scan end-view. Finally, the processed B-scan end-view depicting an isolated SAA using the "box" feature embedded in the SAFT analysis menus.

After review and application of pertinent detection and length-sizing criteria (SAA shape, orientation, and position), the magnified B-scan end-view is examined. This view is analyzed against the criteria established for SAA shape, spatial position, and other parameters defined in the detection and length-sizing criteria, and a determination is made as to the status of this SAA. If the SAA is determined to represent a crack (crack, notch, or sawcut in this case), then signal-to-noise measurements are computed, length sizing is conducted using both LOS and a −6 dB drop method, and spatial position is recorded from interactively placing the cursors at

specific locations on the SAA and recording the X, Y, and Z coordinates respectively. The resultant image is cut and pasted into an Excel spreadsheet and length sizing and signal-to-noise calculations are recorded in this fashion. The magnified B-scan end-view embedded on the Excel spreadsheet with the associated calculations is shown in Figure 7.10.

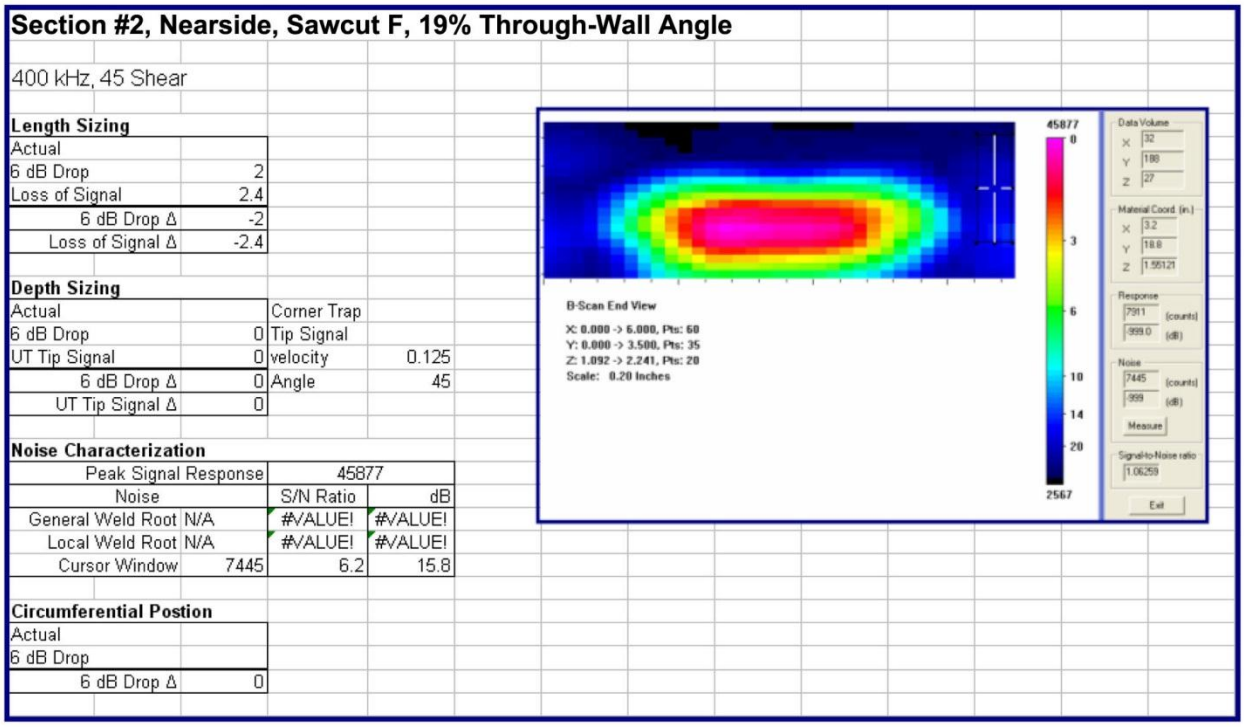

Section #2, Nearside, Sawcut F, 19% Through-Wall Angle

400 kHz, 45 Shear

Length Sizing	
Actual	
6 dB Drop	2
Loss of Signal	2.4
6 dB Drop Δ	-2
Loss of Signal Δ	-2.4

Depth Sizing			
Actual		Corner Trap	
6 dB Drop	0	Tip Signal	
UT Tip Signal	0	velocity	0.125
6 dB Drop Δ	0	Angle	45
UT Tip Signal Δ	0		

Noise Characterization			
Peak Signal Response		45877	
Noise		S/N Ratio	dB
General Weld Root	N/A	#VALUE!	#VALUE!
Local Weld Root	N/A	#VALUE!	#VALUE!
Cursor Window	7445	6.2	15.8

Circumferential Postion	
Actual	
6 dB Drop	
6 dB Drop Δ	0

Figure 7.10 Excel Spreadsheet and Associated Magnified B-scan End-View for S Analysis and Detailed Calculations for Length Sizing and Recording of Positional Data

From the various spreadsheets that contain each SAA and the associated calculations, tables are then created where the resultant detection and length-sizing data can be reviewed and compared to true-state conditions. For a comprehensive review of each Excel datasheet for all SAAs recorded in this study, please refer to Appendix D. As described earlier, the analysis process is an iterative activity, where the analyst must conduct this detailed procedure for each SAA that satisfies the detection and length-sizing criteria, documenting the results as discussed here. The data in the Excel spreadsheet is then translated into tabular format and compared with results from other incident angles, examination frequencies, and wave modalities. For this particular SAA, the measured and actual values for this sawcut were determined as shown in Table 7.5 where the measured length is shown for the −6 dB drop calculation and the LOS calculation.

Table 7.5 Actual Versus Measured Values for Detection Results of Sawcut F from a Tutorial-Based Analysis of the 400-kHz, 45° Shear-Wave Inspection of Piping Segment #2, from the Near Side

Piping Segment ID#	Flaw or Crack ID#	Actual Length	Actual Depth	Measured Length −6 dB/LOS	Measured Depth (%TW)	Signal-to-Noise Ratio
Segment #2	Sawcut F	5.97 cm (2.35 in.)	19%TW Angled @35°	5.08 cm/6.10 cm (2.0 in./2.4 in.)	Not determined	15.8 dB

This section describes the results from the LF/SAFT inspection of austenitic piping specimen 02-24-15, providing the detection and length-sizing data as a function of examination frequency, incident angle, wave modality, and scan orientation relative to the introduced flaw. For a review of the true-state information for all flaws and sawcuts, the reader is referred to Section 5, Tables 5.1 and 5.2 of this report. The following sub-sections will discuss the results by piping segment.

The data acquired were first qualitatively evaluated by determining the "quality" of the data set for each frequency, angle, wave mode, and orientation to the introduced flaw. Each data set was reviewed and labeled as good, marginal, or poor, relative to the specific quality factor of the data. The quality factor was based on SNR, evidence of coupling problems in the images, saturation of signal responses, scattered ultrasonic energy from the austenitic weld structure, and the prevalence of SAAs attributed to geometrical reflectors, weldment structure, and other features other than introduced flaws.

After this initial qualitative assessment, the detailed analysis procedure discussed in the tutorial section was employed and the detection determinations, length-sizing data, and SNR calculations were recorded in an Excel spreadsheet for subsequent comparative analysis. Although near-side data were acquired using both modalities, both frequencies, and all incident angles, this section will only focus on inspection results acquired from the far-side scan orientation. Near-side data were used for benchmarking purposes only, as the objectives of this study are directed at evaluating the detection performance of inspection methodologies for far-side examinations through austenitic welds.

7.2.2 Piping Segment 1

Piping segment 1, defined as the first 120° segment of pipe spanning from the 0° datum to the 120° point, consists of five implanted fatigue cracks and machined sawcuts. In circumferentially ascending order, these are sawcut A, crack A, sawcut B, crack B, and sawcut C. A discussion of the resultant detections and flaw characterization data is best described in tabular format. Table 7.6 depicts the far-side detection calls for piping segment 1 along with a grading for data quality and flaw characterization data as a function of incident angle and wave mode for 250-kHz inspections. Table 7.7 depicts the same information for inspections acquired at 400-kHz. The nomenclature used for deciphering the tables is described here. The split column beneath each incident angle and wave mode describes the measured −6 dB length-sizing value of the flaw in centimeters, the length determined by using LOS in centimeters, and

the measured SNR in decibels (dB). The column labeled with the “Q” designates the pre-assigned quality of the data set defined earlier in the discussion. A “G” represents good quality, an “M” represents marginal quality, and a “P” represents poor quality. Good quality data sets provided the analyst with the best opportunities for detecting the introduced flaws. Marginal data sets contained anomalies in the data and higher background noise levels that introduced a reasonable level of difficulty for interpreting the SAFT-processed data. Poor data sets resulted in SAFT-processed images that could rarely be used to extract useful detection, localization, or sizing information; and these data sets exhibited poor resolution, unusually high incidence of SAAs that were not attributed to introduced flaws, and generally very high background noise levels. Cells containing “--" indicates no data were acquired for that particular combination of scan parameters, and “ND” indicates that the introduced flaw was not detected.

Analysis of the far-side, 250-kHz data using the 70° L-wave modality indicated that the quality of the resultant images were marginal as the SNR was generally lower than anticipated. Good separation of signal responses from counterbore geometry is illustrated from the data, and this modality and frequency combination provided the capability to clearly detect three of the five introduced flaws in this piping segment. Sawcut B, crack B, and sawcut C were detected and sized in the length dimension. The computed SNR for these detectable introduced flaws ranged from approximately 4 dB to nearly 12 dB. From a review of the data in Table 7.6, the measured length-sizing data correlates very well with the true-state values for these introduced flaws. C-scan and B-scan end-view images as well as the individual data sheets for each detected flaw can be found in the Appendix D.

Analysis of the results from the 45° L-wave scans were of marginal quality due to signal response saturation of significant portions of the volume of interest. The total system gain is pre-selected based upon a quick preliminary manual scan of the largest response amplitude in the particular specimen being evaluated. On occasion, this manual scan procedure for detecting the highest amplitude signal response is not accurate, and results in a higher total system gain value; in turn, yielding areas of saturation that were not anticipated. The data in the 45° L-wave scans did not provide suitable information or clarity for detections to be made for any of the five introduced flaws in this piping segment.

Table 7.6 250-kHz, Far-Side Detection Results for Piping Segment 1

Introduced Flaw	70° L		60° L		45° L		70° S		60° S		45° S	
	−6 dB (cm), LOS (cm), SNR (dB)	"Q"	−6 dB (cm), LOS (cm), SNR (dB)	"Q"	−6 dB (cm), LOS (cm), SNR (dB)	"Q"	−6 dB (cm), LOS (cm), SNR (dB)	"Q"	−6 dB (cm), LOS (cm), SNR (dB)	"Q"	−6 dB (cm), LOS (cm), SNR (dB)	"Q"
Sawcut A	ND	M	--	--	ND	M	--	--	--	--	--	--
Flaw A	ND	M	--	--	ND	M	--	--	--	--	--	--
Sawcut B	6.35, 6.60, 11.4	M	--	--	ND	M	--	--	--	--	--	--
Flaw B	3.05, 3.05, 5.1	M	--	--	ND	M	--	--	--	--	--	--
Sawcut C	3.30, 3.81, 3.5	M	--	--	ND	M	--	--	--	--	--	--

Table 7.7 400-kHz, Far-Side Detection Results for Piping Segment 1

Introduced Flaw	70° L		60° L		45° L		70° S		60° S		45° S	
	−6 dB (cm), LOS (cm), SNR (dB)	"Q"	−6 dB (cm), LOS (cm), SNR (dB)	"Q"	−6 dB (cm), LOS (cm), SNR (dB)	"Q"	−6 dB (cm), LOS (cm), SNR (dB)	"Q"	−6 dB (cm), LOS (cm), SNR (dB)	"Q"	−6 dB (cm), LOS (cm), SNR (dB)	"Q"
Sawcut A	ND	G	ND	M	3.56, 4.57, 6.0	G	ND	P	ND	P	4.32, 3.81, 4.1	G
Flaw A	ND	G	ND	M	ND	G	ND	P	ND	P	ND	G
Sawcut B	3.81, 4.32, 8.3	G	3.05, 3.30, 10.4	M	7.87, 8.89, 10.6	G	ND	P	4.32, 5.59, 7.2	P	5.33, 5.84, 16.1	G
Flaw B	2.79, 2.79, 5.6	G	1.52, 2.03, 6.4	M	ND	G	ND	P	2.79, 2.79, 8.6	P	3.30, 3.05, 10.6	G
Sawcut C	ND	G	ND	M	ND	G	ND	P	ND	P	ND	G

Analysis of the 400-kHz data using the 45°, 60°, and 70° L-wave combinations indicates that although the quality of the data were generally good, (marginal for the 60° data set), the SNR was again lower than anticipated. Some images illustrate a higher degree of clarity for detection of crack A and sawcut B in the unprocessed data sets, as the SAFT process at times would smear signal responses from indications or otherwise reduce their relative signal strength in the processed images. This is because the inspection probe does not employ a divergent sound field, but rather is a large zone-focused sound field and the flaws are all smooth specular reflectors. The analysis also illustrates that higher L-wave angle inspections (60° and 70°) result in less attenuation of the sound field and reduced signal responses from counterbore, weld root, and other structure that contributes to the "noise" in the images. The 45° L-wave data resulted in the detection of sawcut A and sawcut B, while the 60° and 70° L-wave inspections resulted in the detection of sawcut B and flaw B. Three of the five introduced flaws went undetected for any given data set using the L-wave mode. The computed SNR for the detected introduced flaws ranged from approximately 6 dB to nearly 11 dB. In reviewing the measured length values for the 45° L-wave data, the −6 dB drop method provided close correlation with the true-state length for sawcut A, while slightly oversizing sawcut B. The 60° L-wave inspection data provided undersized length values for both sawcut B and crack B, while the 70° L-wave data undersized sawcut B but correlated well with the true-state value for crack B. The reader is directed to view any composite C-scan, B-scan end-view, or magnified/isolated views of SAAs in Appendix D.

The data quality for the 400-kHz shear-wave data, specifically the 60° and 70° scans, were poor. The unprocessed images were very grainy and exhibited a generally noisy background where little clarity was provided. In particular, the SAFT-processed 70° data provided no useful information for resolving or detecting SAAs that even remotely met the detection criteria. SAFT processing of the 60° data improved the image quality, enabling separation of SAAs and positional criteria to be used in the detection of sawcut B and crack B. The 45° shear-wave data exhibited good clarity, separation, low background noise levels, and was regarded as a good quality data set. Detection criteria were employed for the detection and sizing of three of the introduced flaws in this piping segment, including sawcut A, sawcut B, and crack B. The computed SNR for the two detected introduced flaws at 60° ranged from 7 dB to nearly 9 dB, while the SNR for the three detected introduced flaws at 45° ranged from 4 dB to approximately 16 dB. A review of the −6 dB measured values for length show that the 60° data resulted in undersizing sawcut B and slightly under-sizing crack B, while the 45° data oversized sawcut A and sawcut B but correlated well with the true-state value for crack B.

From a detection performance standpoint, it is interesting to note the specific introduced flaws that were not detected or those that were only detected at a specific angle. From the far-side, flaw A went undetected throughout the evaluation. Sawcut A was only detected at the 45° incident angle, but was detected by both longitudinal and shear wave modalities. Sawcut C was only detected with the 250-kHz, 70° L-wave inspection. As expected, the two deepest flaws, sawcut B and crack B, were detected most often across the range of angles, modalities, and frequencies employed.

7.2.3 Piping Segment 2

Piping segment 2, defined as the second 120° segment of pipe spanning from the 121° point to the 240° point, consists of four introduced flaws consisting of implanted fatigue cracks and machined sawcuts. In circumferentially ascending order, these introduced flaws are sawcut D, crack C, sawcut E, and sawcut F. The discussion of the resultant detections and flaw characterization data continues here based on the tabular format. Table 7.8 depicts the far-side detection calls for piping segment 2 along with a grading for data quality and flaw characterization data as a function of incident angle and wave-mode for 250-kHz inspections. Table 7.9 depicts the same information for inspections acquired at 400-kHz. The same nomenclature as described previously is used for deciphering the tables discussed here.

Analysis of the far-side, 250-kHz data using the 70° L-wave modality indicated that the quality of the resultant images were marginal as the SNR was again lower than anticipated. At the higher incident angles, particularly 60° and 70°, ultrasonic signal scatter and anomalous amplitude responses from component geometry and weld structure should be reduced. On occasion, resultant images sometimes illustrate unusually high background noise levels, higher than anticipated prevalence of non-flaw–related SAAs, or consistent signal responses that appear to result from weld structure such as counterbore or weld root. Typically, these conditions are not anticipated at the higher angles of inspection and often can only be attributed to the microstructure or attenuative characteristics of the austenitic weld.

Reasonable separation of signal responses from background noise levels can be seen from the data at 70°, and this modality and frequency combination provided the capability to detect and length-size all four of the introduced flaws in this piping segment. The computed SNR for these detectable introduced flaws ranged from approximately 4.5 dB to nearly 10 dB. From a comparative review of the data in Table 7.8 with that of the true-state values for length, it is shown that the −6 dB length-sizing method resulted in slightly oversizing sawcut D and sawcut E, and more significantly undersized crack C and sawcut F. Again, the reader is referenced to the C-scan and B-scan end-view images as well as the individual data sheets for each detected introduced flaw in Appendix D.

Analysis of the results from the 45° L-wave scans at 250 kHz were of poor quality due to higher background noise levels and less clarity and definition for the lower amplitude SAAs that met the detection criteria. This data set did not provide suitable information for detecting sawcut D, crack C, or sawcut E. The only detectable introduced flaw in the processed data was the SAA corresponding with sawcut F. The SNR for this call was approximately 10 dB and the measured length for this SAA undersized the true-state length.

Table 7.8 250-kHz, Far-Side Detection Results for Piping Segment 2

Introduced Flaw	70° L		60° L		45° L		70° S		60° S		45° S	
	−6 dB (cm), LOS (cm), SNR (dB)	"Q"	−6 dB (cm), LOS (cm), SNR (dB)	"Q"	−6 dB (cm), LOS (cm), SNR (dB)	"Q"	−6 dB (cm), LOS (cm), SNR (dB)	"Q"	−6 dB (cm), LOS (cm), SNR (dB)	"Q"	−6 dB (cm), LOS (cm), SNR (dB)	"Q"
Sawcut D	5.84, 9.02, 6.0	M	--	--	ND	P	3.30, 3.30, 4.6	M	2.29, 3.30, 6.0	M	4.06, 4.06, 10.6	G
Flaw C	2.54, 3.43, 6.0	M	--	--	ND	P	ND	M	4.32, 5.08, 5.6	M	5.97, 6.48, 6.9	G
Sawcut E	4.57, 5.21, 4.6	M	--	--	ND	P	ND	M	ND	M	ND	G
Sawcut F	4.19, 5.84, 9.5	M	--	--	4.83, 4.83, 9.8	P	ND	M	ND	M	3.43, 4.70, 13.1	G

Table 7.9 400-kHz, Far-Side Detection Results for Piping Segment 2

Introduced Flaw	70° L		60° L		45° L		70° S		60° S		45° S	
	−6 dB (cm), LOS (cm), SNR (dB)	"Q"	−6 dB (cm), LOS (cm), SNR (dB)	"Q"	−6 dB (cm), LOS (cm), SNR (dB)	"Q"	−6 dB (cm), LOS (cm), SNR (dB)	"Q"	−6 dB (cm), LOS (cm), SNR (dB)	"Q"	−6 dB (cm), LOS (cm), SNR (dB)	"Q"
Sawcut D	ND	P	ND	P	ND	G	ND	P	3.81, 3.56, 6.0	P	5.33, 5.59, 11.1	M
Flaw C	ND	P	ND	P	ND	G	ND	P	4.83, 5.59, 11.8	P	5.08, 4.83, 7.2	M
Sawcut E	ND	P	ND	P	ND	G	ND	P	ND	P	ND	M
Sawcut F	ND	P	ND	P	4.83, 5.33, 17.2	G	ND	P	ND	P	ND	M

Analysis of the far-side, 250-kHz data using the shear-wave modality is discussed here. The 70° incident angle demonstrated marginal data quality due to the high amount of background noise and lack of SAAs meeting the detection criteria. Reasonable separation of only one SAA from background noise levels can be seen from the data, and this modality and frequency combination provided the capability to detect and length-size only sawcut D in this piping segment. The computed SNR for this introduced flaw was approximately 5 dB. Both the −6 dB and LOS length-sizing methods resulted in significantly undersized measured lengths for this flaw from the true-state value. The 60° incident angle also provided marginal data quality due to image graininess, higher than anticipated background noise levels, and a lack of SAAs meeting the detection criteria. However, the 60° shear wave did provide suitable information and separation of SAAs for the detection of both sawcut D and crack C, but did not detect sawcut E or sawcut F. The computed SNR for the two detections was approximately 6 dB. The measured length for sawcut D was significantly undersized, while the measured length for crack C correlated quite well with the true-state length (see Section 5, Tables 5.1 and 5.2). The 45° incident angle provided good quality data where the SAAs were easily separated and the background noise levels were reasonably low relative to the SAA peak amplitudes in the processed data. A good degree of clarity and SAA separation were provided allowing for the detection of all introduced flaws in this piping segment with the exception of sawcut E. The measured SNR values for these SAAs ranged from 7 dB to over 13 dB. Sawcut D and sawcut F were both undersized in length, while both −6 dB and LOS length-sizing methods oversized crack C.

Analysis of the 400-kHz data using the 60° and 70° L-wave combinations indicates that the quality of the data at both incident angles was poor, and the SNR was again lower than anticipated. These data exhibited higher background noise levels and areas of signal saturation from material and/or weldment structure. The 60° data also exhibited a large area where the transducer had lost coupling, either as a result of physical de-coupling of the wedge from the part surface or from a malfunction of the coupling drip lines. From an analysis of these data and by employing the detection criteria, it is shown that neither of these scans provided suitable information for detection of any introduced flaws in this piping segment. The 45° L-wave incident angle provided good quality data and clearly allowed for the detection of one SAA. The background noise levels in the volume of interest were lower than anticipated, and the clarity and continuity of the signal responses from weldment geometry and material structure were not difficult to discriminate from the SAA of the introduced flaw. The computed SNR for this SAA was nearly 18 dB. This data set provided a detection of only one of the introduced flaws in this piping segment, that being sawcut F. In reviewing the measured length values for the 45° L-wave data, both the −6 dB drop and LOS length-sizing methods resulted in undersizing the true-state length for sawcut F.

The data quality for the 400-kHz shear-wave data, specifically the 60° and 70° scans, were poor. The unprocessed images were very grainy and exhibited a generally noisy background where little clarity was provided. In particular, the SAFT-processed 70° data provided no useful information for resolving or detecting SAAs that even remotely met the detection criteria. SAFT processing of the 60° data improved the image quality, enabling separation of SAAs and positional criteria to be used in the detection of sawcut D and crack C. The 45° shear-wave data exhibited marginal quality as the clarity, separation, and lower background noise levels

provided a suitable means for identifying two SAAs and applying the detection criteria for properly detecting and sizing sawcut D and crack C. The computed SNR for the two detected introduced flaws at 60° ranged from 6 dB to nearly 12 dB, while the SNR for the same two detected introduced flaws at 45° ranged from 7 dB to approximately 11 dB. A review of the −6 dB measured values for length show that the 60° data resulted in undersizing sawcut D and slightly undersizing crack C, while the 45° data oversized crack C and correlated quite well with the true-state value for sawcut D.

From a detection performance standpoint, it is again interesting to note the specific introduced flaws that were not detected or those that were only detected at a specific angle. From the far side, no introduced flaw went undetected in this piping segment. Sawcut E was only detected at the 70° incident angle using the lower frequency of 250 kHz. The data from this piping segment showed that the 400-kHz L-wave modality had a very difficult time providing suitable information for detection of any of the introduced flaws in this segment with the exception of sawcut F being detected using 45°.

7.2.4 Piping Segment 3

Piping segment 3, defined as the third 120° segment of pipe spanning from the 241° point to the 0° datum point, consists of the final four introduced flaws consisting of implanted fatigue cracks and machined sawcuts. In circumferentially ascending order, these are crack D, sawcut G, sawcut H, and crack E. The discussion of the resultant detections and flaw characterization data continues here based on the tabular format. Table 7.10 depicts the far-side detection calls for piping segment 3 along with a grading for data quality and flaw characterization data as a function of incident angle and wave-mode for 250-kHz inspections. Table 7.11 depicts the same information for inspections acquired at 400 kHz. Again, the same nomenclature as described previously is used for deciphering the tables discussed here.

Analysis of the far-side, 250-kHz data using the 70° L-wave modality indicated that the quality of the resultant images were marginal as the SNR was generally lower than anticipated. The SAFT-processed data, however, provided good separation of signal responses from back-ground noise levels as illustrated from the data, and this modality and frequency combination provided the capability to clearly detect three of the four introduced flaws in this piping segment. Sawcut G, sawcut H, and crack E were detected and sized in the length dimension. The computed SNR for these detectable introduced flaws ranged from approximately 5 dB to over 9 dB. From a review of the data in Table 7.10, the measured length-sizing data correlates very well with the true-state values for sawcut H and crack E, but significantly oversized sawcut G. C-scan and B-scan end-view images as well as the individual data sheets for each detected introduced flaw can be found in Appendix D.

Table 7.10 250-kHz, Far-Side Detection Results for Piping Segment 3

Introduced Flaw	70° L		60° L		45° L		70° S		60° S		45° S	
	−6 dB (cm), LOS (cm), SNR (dB)	"Q"	−6 dB (cm), LOS (cm), SNR (dB)	"Q"	−6 dB (cm), LOS (cm), SNR (dB)	"Q"	−6 dB (cm), LOS (cm), SNR (dB)	"Q"	−6 dB (cm), LOS (cm), SNR (dB)	"Q"	−6 dB (cm), LOS (cm), SNR (dB)	"Q"
Flaw D	ND	M	--	--	ND	G	--	--	--	--	--	--
Sawcut G	10.92, 11.18, 9.3	M	--	--	7.62, 7.87, 8.0	G	--	--	--	--	--	--
Sawcut H	6.35, 6.10, 8.6	M	--	--	8.13, 8.13, 19.0	G	--	--	--	--	--	--
Flaw E	3.30, 3.30, 4.6	M	--	--	ND	G	--	--	--	--	--	--

Table 7.11 400-kHz, Far-Side Detection Results for Piping Segment 3

Introduced Flaw	70° L		60° L		45° L		70° S		60° S		45° S	
	−6 dB (cm), LOS (cm), SNR (dB)	"Q"	−6 dB (cm), LOS (cm), SNR (dB)	"Q"	−6 dB (cm), LOS (cm), SNR (dB)	"Q"	−6 dB (cm), LOS (cm), SNR (dB)	"Q"	−6 dB (cm), LOS (cm), SNR (dB)	"Q"	−6 dB (cm), LOS (cm), SNR (dB)	"Q"
Flaw D	ND	G	ND	G	ND	G	ND	P	ND	P	ND	G
Sawcut G	6.10, 6.86, 8.9	G	4.32, 3.81, 6.9	G	5.59, 5.33, 12.3	G	ND	P	5.33, 5.33, 8.1	P	1.78, 2.03, 11.6	G
Sawcut H	5.33, 6.35, 11.8	G	4.83, 5.08, 8.1	G	5.84, 7.11, 12.3	G	ND	P	3.05, 3.30, 12.0	P	4.83, 5.33, 15.6	G
Flaw E	2.79, 3.30, 13.6	G	ND	G	ND	G	ND	P	2.03, 4.06, 6.4	P	3.30, 3.30, 9.3	G

Analysis of the results from the 45° L-wave scans at 250 kHz demonstrated good quality data due to lower levels of background noise and good clarity and definition for the SAAs that met the detection criteria. Sufficient separation is evident in the SAFT-processed images for effective detection of two of the four introduced flaws in this piping segment. This data set did not provide suitable information for detecting crack D or crack E; however, application of the detection criteria did result in the detection of both sawcuts (G and H) from these data. The computed SNR for these calls ranged from approximately 8 dB to 19 dB, and the measured lengths for these introduced flaws were significantly oversized in comparison to the true-state lengths.

Analysis of the 400-kHz data using the 45°, 60°, and 70° L-wave combinations shows that the quality of the data were good, as the background noise levels were lower than anticipated. These data sets exhibited good clarity and provided the necessary separation of detected introduced flaws from other SAAs and background noise levels for detection purposes. The SAFT-processed images resulting from these data sets illustrate a high degree of coherence and smoothness for the SAAs that were identified by applying the detection criteria. The 45° and 60° L-wave data resulted in the detection of sawcut G and sawcut H, but did not detect crack D or crack E. The computed SNR for the detected introduced flaws ranged from approximately 7 dB to over 12 dB. In reviewing the measured length values for the 45° L-wave data, the −6 dB drop method provided close correlation with the true-state lengths for the two sawcuts, while the 60° L-wave inspection data provided undersized length values for each of these sawcuts. The 70° L-wave data resulted in the detection of all introduced flaws in this piping segment with the exception of crack D. The computed SNR for the detected introduced flaws ranged from approximately 9 dB to nearly 14 dB. The measured length values for the −6 dB sizing method undersized sawcut H and crack E and oversized sawcut G, while the LOS method correlated well with the true-state values for sawcut H and crack E. The LOS method did however oversize sawcut G. Again, the reader is directed to view any of the specified composite C-scan, B-scan end-view, or magnified/isolated views of SAAs in Appendix D.

The data quality for the 400-kHz shear-wave data, specifically the 60° and 70° scans, were poor. The unprocessed images were again very grainy and exhibited a generally noisy background where little SAA separation or identification could be accomplished. In particular, the SAFT-processed 70° data provided no useful information for resolving or detecting SAAs that even remotely met the detection criteria. SAFT processing of the 60° data improved the image quality, enabling separation of SAAs and positional criteria to be used in the detection of all of the introduced flaws in this piping segment with the exception of crack D. The SNR for the three detected introduced flaws ranged from approximately 6 dB to over 12 dB. Length-sizing measurements using the −6 dB method undersized the introduced flaws relative to the true-state length values, while the LOS method undersized sawcut G and sawcut H and oversized crack E. The 45° shear-wave data exhibited good quality data resulting in clear processed images, good separation of SAAs, and generally low background noise levels. Detection criteria were employed for the detection and sizing of three of the introduced flaws in this piping segment, including sawcut G, sawcut H, and crack E. Once again, flaw D went undetected. The computed SNR for the three detected introduced flaws at 45° ranged from over 9 dB to nearly 16 dB. A review of the −6 dB measured values for length show that the 45° data resulted in significant undersizing both sawcut G and sawcut H, while matching very well with the true-state value for crack E.

From a detection performance standpoint, it is again interesting to note the specific introduced flaws that were not detected, or those that were only detected at a specific angle. From the far side, crack D went undetected throughout the evaluation. The remaining introduced flaws were detected by combinations of both longitudinal- and shear-wave modalities. As expected, sawcut G and sawcut H were detected most often across the range of angles, modalities, and frequencies employed.

7.3 Phased Array UT: Data Analysis and Results

One of the advantages of PA data is that all information is stored digitally during each scan, allowing off-line processing and interpretation to be performed in an environment better suited for analysis than one usually encounters during data acquisition. Several image channels of the data can be displayed, based on the preference of the analyst. The volume-corrected B-, C- and S-scan images, along with supplemental A-scans, were used to assist our understanding of the data.

For the TomoView PA software used during these trials, the B-scan image is a projection of the sound field through the component, oriented as if looking along the direction of sound propagation, displaying a circumferential cross section of the weld (shown in the right pane of the analysis screen). The S-scan (shown in the upper left pane of the analysis screen), or sector view, provides a projection of the sound fields (from initial to final angle being used; i.e., 30° to 70° for the TRL and 40° to 70° for the TRS arrays). The black line in the S-scan shows which angle is currently selected. Finally, the A-scan (lower-left pane of analysis screen) represents the electronic responses for reflectors based on X-Y axes of time and amplitude, respectively. A typical analysis screen showing the scan images described above is included as Figure 7.11.

Each of the B- and S-scan images contains all data in the linear scan. Measurement, gating, and sound field cursors are used to provide “slices” of material to view along the projected sound beam and discrete beam angle responses are shown in the A-scan. By manipulating these cursors, the analyst is able to “walk-through” cross sections of the material along each linear scan. As Figure 7.11 was made using the longitudinal-wave array, a mode-converted shear-wave response is also detected. Images in the A-, B-, and S-scans appearing farther in time (greater than 36-mm [1.4-in.] wall thickness) are the result of mode-converted shear waves produced when longitudinal waves strike the inner surface, or other reflectors, in the component. This echo is not present in the shear-wave data.

One important analysis tool of the phased-array system is the ability to examine each angle individually. This allows the investigator to view the different response images in a given scan and discriminate between the various features in a specimen. In Figure 7.11 the system is displaying the results for 35°, which shows the counterbore of the weld. When the 53° scan is displayed, shown in Figure 7.12, the weld root becomes visible, and when one displays 65°, shown in Figure 7.13, the flaws become visible. This angular discrimination is a very useful tool when coupled with the S-scan and B-scans. Using the location of the weld root, one can distinguish between weld-root response and flaw responses and determine if a flaw is on the near side or far side of a weld. The results of all scans and details of each flaw are given in Appendix E.

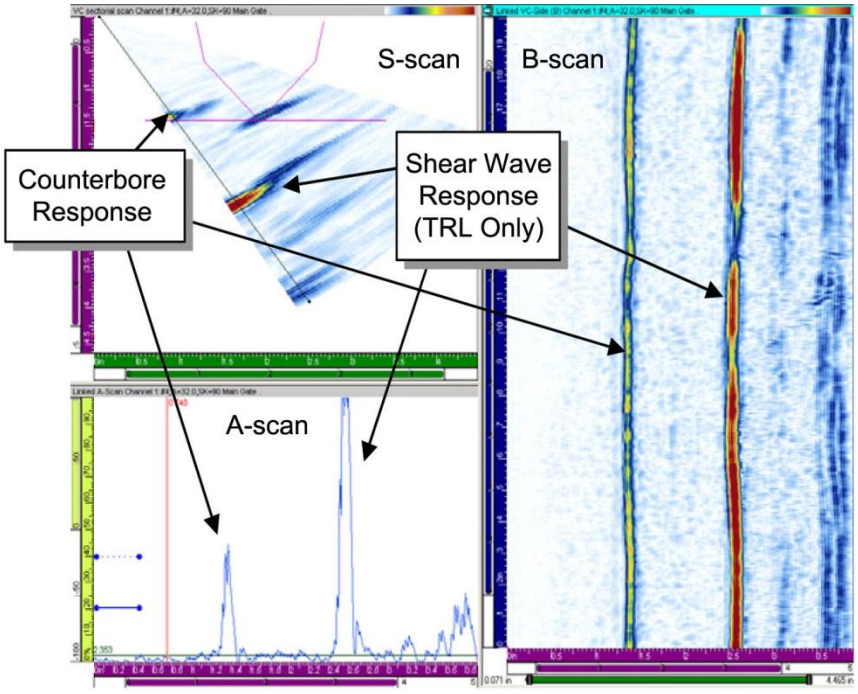

Figure 7.11 Typical Analysis Screen with a Low Angle (35°) Selected, Showing the Weld Counterbore with the TRL Array

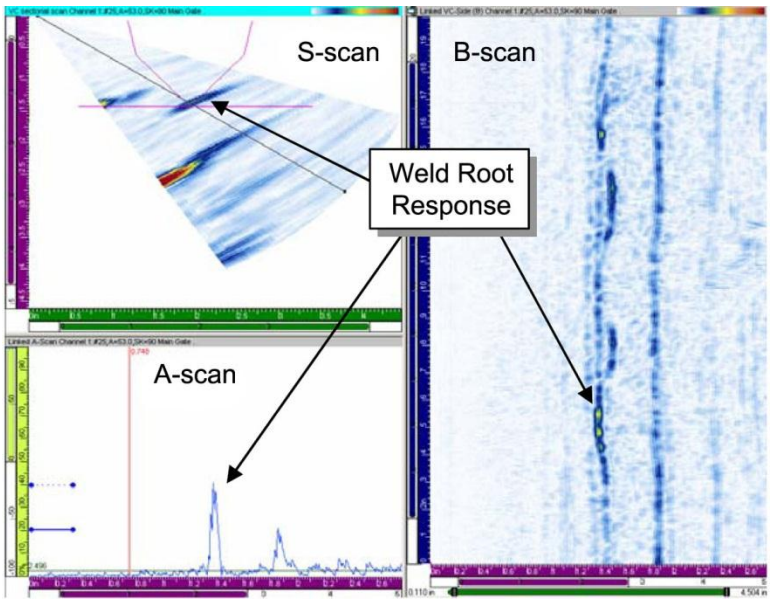

Figure 7.12 Typical Analysis Screen with a Mid-Range Angle (53°) Selected, Showing the Weld Root with the TRL Array

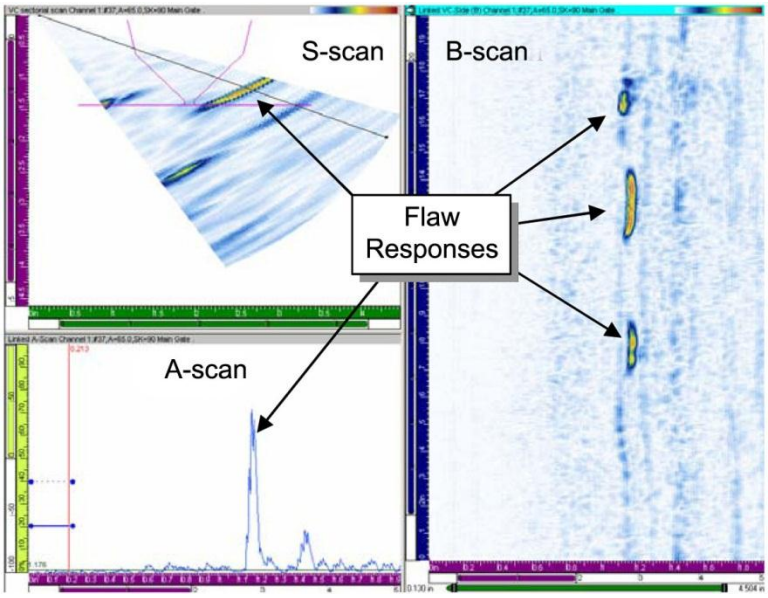

Figure 7.13 Typical Analysis Screen with a High Angle (65°) Selected, Showing the Flaws with the TRL Array

In Phase 1 of this study, a series of implanted cracks and sawcuts were examined from the near and far side of welds using both the longitudinal- and shear-wave arrays. As described in Section 1, the pipe specimen 02-24-15 consists of two 610-mm (24.0-in.) diameter, 36-mm (1.4-in.) thick pieces of ASTM A-358, Grade 304 vintage austenitic stainless steel. The specimen is cut into three segments to allow easier handling and scanning. For the TRL array, which is optimized for lower angles, the segments were scanned with the front of the array situated against the toe of the weld, 12.7 mm (0.5 in.) back from the weld toe, 12.7 mm (0.5 in.) onto the weld, and with the probe centered on the weld crown. For the TRS array, which is optimized for higher angles, the segments were scanned with the probe next to the weld crown, 6 mm (0.25 in.) back, 12.7 mm (0.5 in.) back, and 19 mm (0.75 in.) back from the weld crown.

Figure 7.14 shows the best near-side and far-side B-scan images for pipe segment 1 using both the TRL and TRS arrays. Pipe segment 1 contains cracks A (15% through-wall) and B (43% through-wall), and sawcuts A (8% through-wall, straight cut), B (28% through-wall, straight cut), and C (7% through-wall, 35° angled cut). The term “straight cuts” refers to sawcuts that were made 90° to the inner surface, and the 35° angled cuts follow the heat-affected zone as shown in Section 5, Figure 5.4. The near-side scans (left two images) show all defects very clearly with both arrays. Sawcut A and crack A are both detected and easily resolved as two distinct defects, and sawcut C is also easily detected. Sawcut A appears as two nearby indications in the shear wave scan. The TRL array is able to clearly detect tip signals for the sawcuts and cracks from the near side. The TRS array is not able to detect tip signals from the near-side.

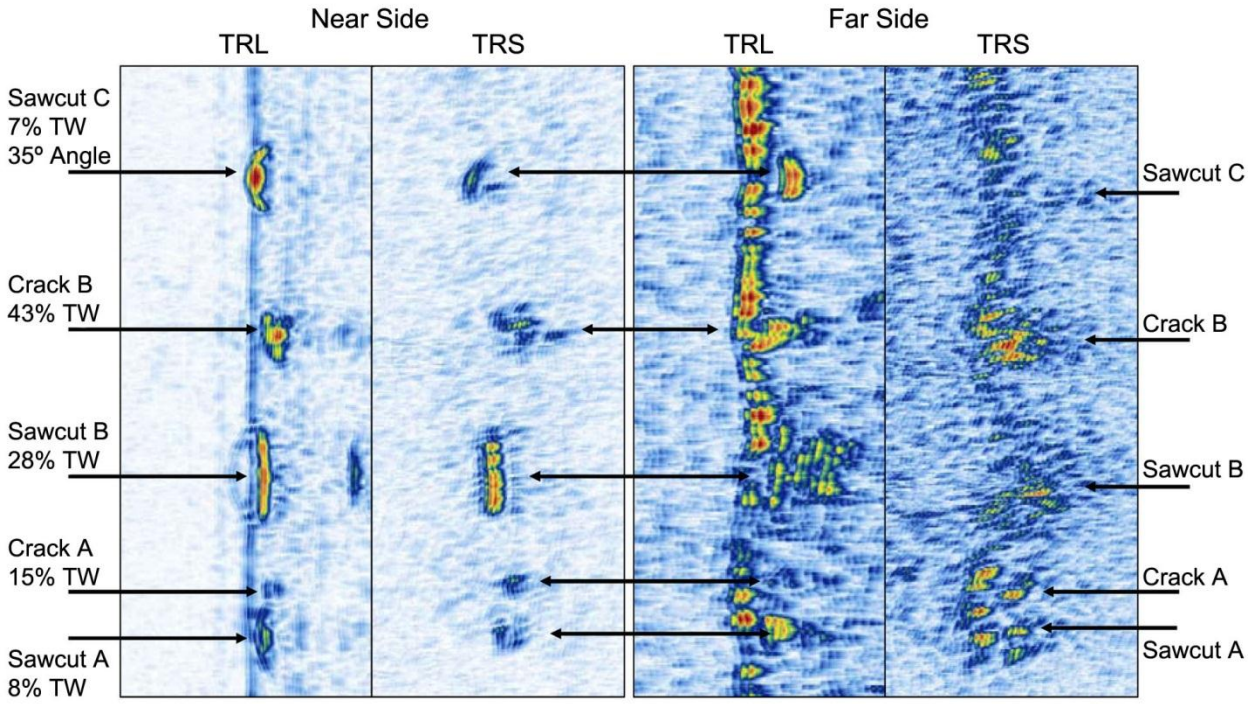

Figure 7.14 B-scan Views for Pipe Segment 1 from the Near (left two images) and Far Side (right two images) with the Longitudinal- and Shear-Wave Arrays

Detecting the flaws from the far side is more challenging. The far-side B-scans in Figure 7.14 (right two images) were taken at an angle that hits the shallow defects, which results in the weld root being visible in these images. The TRL array is able to clearly detect sawcut A but is challenged to detect crack A. The TRS array is able to clearly see both sawcuts and crack A, but the response from the 35° angled sawcut C is weaker for the TRS than for the TRL. The deeper sawcut B and crack B were easily and clearly detected by both arrays.

Figure 7.15 shows the best near-side and far-side B-scan images for pipe segment 2 using both the TRL and TRS arrays. Pipe segment 2 contains crack C (64% through-wall) and sawcuts D (19% through-wall, straight cut), E (12% through-wall, straight cut), and F (19% through-wall, 35° angled cut). Each of these defects is easily detected using both arrays. The TRL array again shows clear tip signals on the near side of the weld, but no tips are detectable from the far side of the weld. The TRS array did not detect clear tip signals from the near side, however. Neither array was able to detect tip signals for any of the defects from the far side of the weld.

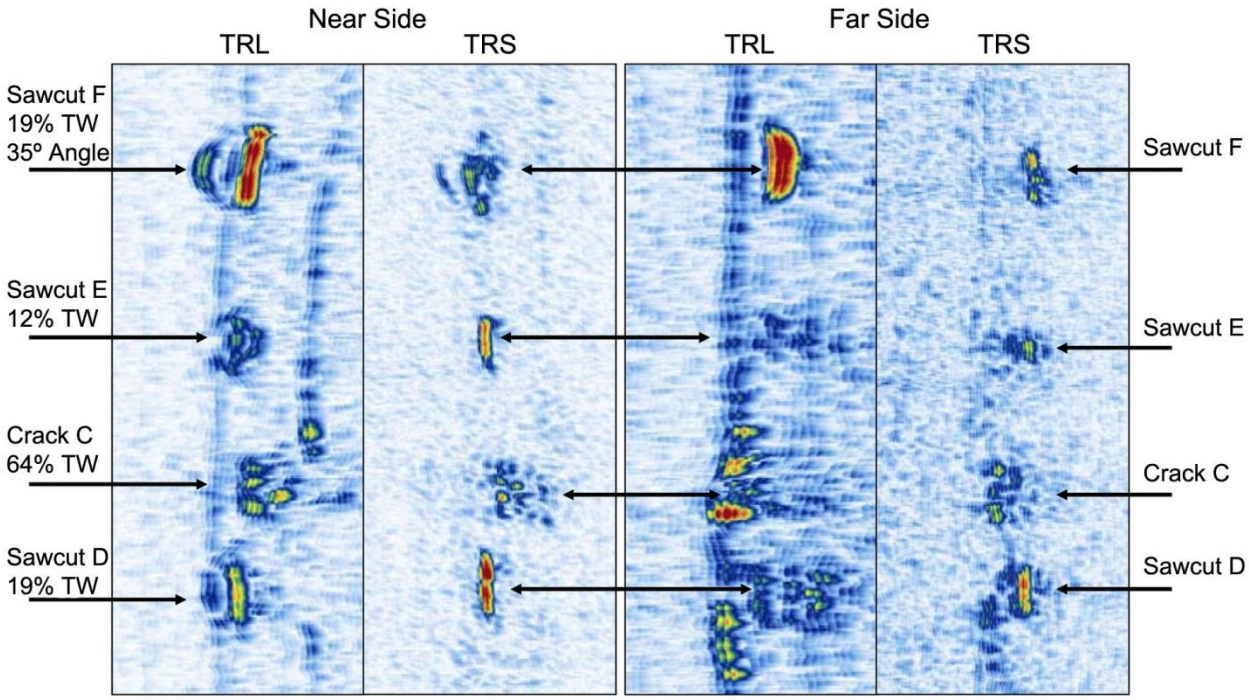

Figure 7.15 B-scan Views for Pipe Segment 2 from the Near and Far Side with the Longitudinal- and Shear-Wave Arrays

Figure 7.16 shows the best near-side and far-side B-scan images for pipe segment 3 using both the TRL and TRS arrays. Pipe segment 3 contains cracks D (19% through-wall, axially-oriented) and E (48% through-wall), and sawcuts G (18% through-wall, 35° angled cut) and H (26% through-wall, 35° angled cut). Once again the TRL array is able to detect strong corner traps and tip signals from the near side of the weld. These deeper flaws are easily detected by both arrays from the far side of the weld. Neither array was able to detect the axially oriented crack D from the near or far side. This is to be expected as the axial crack presents virtually no cross section to the beam in this configuration. To detect the axial flaw, the arrays would have to be oriented so that the sound field would strike the flaw at near 90°. While an array could be designed to detect axially oriented flaws, this was not feasible during these trials.

The results for pipe segments show that while all cracks and sawcuts are visible, the shallower defects are somewhat more difficult to detect than the flaws with features that penetrate farther through-wall. The scans taken from the near side of the weld show all implanted features very clearly. The longitudinal-wave array shows both a strong corner trap and a clear tip signal from the near side. The shear-wave array shows the corner trap and a weak tip signal, if any, from the near side. From the far side of the weld, the longitudinal-wave array does a very good job detecting the 35° angled sawcuts while both arrays are able to detect the straight sawcuts and cracks.

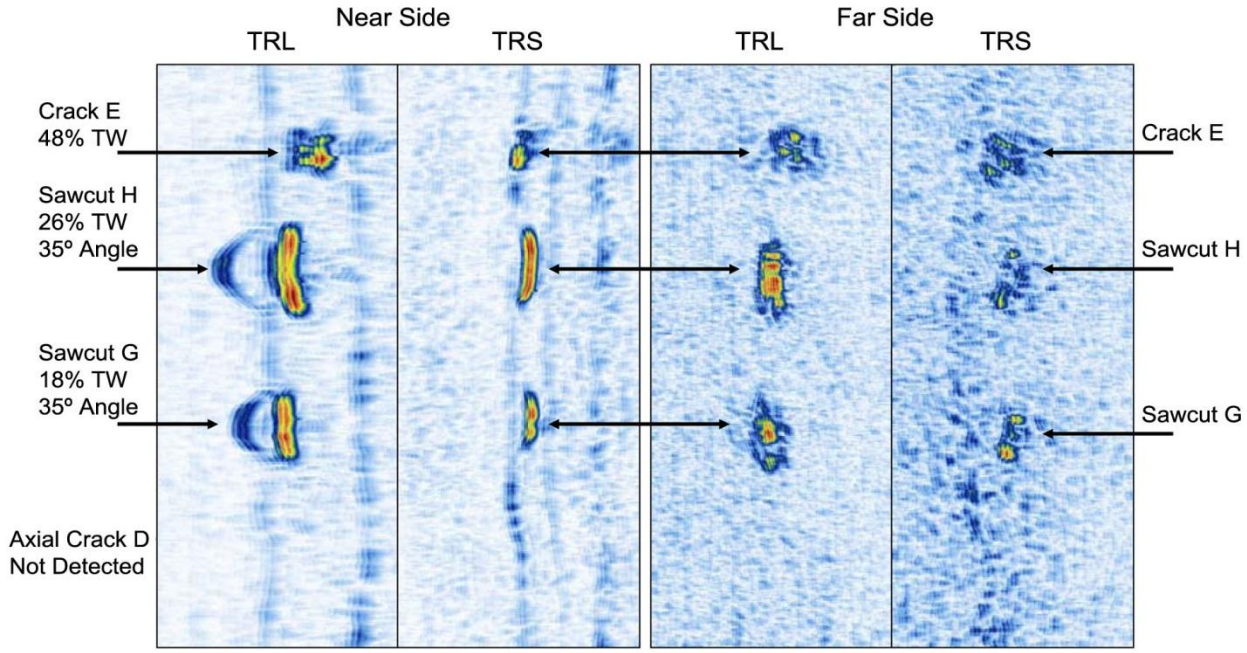

Figure 7.16 B-scan Views for Pipe Segment 3 from the Near and Far Side with the Longitudinal- and Shear-Wave Arrays

The most challenging circumferential flaw for the longitudinal array is crack A. The response from crack A is weak and is difficult to distinguish from the edge of the stronger response from the very nearby sawcut A. The most challenging circumferential flaw for the shear-wave array to detect is sawcut C. This is most likely the result of the shallow depth of sawcut C (7% through-wall) and the 35° angle of the cut which weakens the corner trap response.

Neither array is able to detect tip signals for the defects from the far side of the weld. This presents a significant challenge to depth-sizing for any detected flaws. Length-sizing of flaws from the far side of a weld is quite accurate, however. As the UT signal from a linear defect is often interrupted as it passes through the weld microstructure, the 6 dB drop technique is not as useful as the loss of signal technique. The sawcuts and implanted cracks were length-sized using the 6 dB drop technique and the LOS technique. The length-sizing results for the sawcuts for the TRL probe are given in Table 7.12. The RMSE for far-side length sizing of the sawcuts from the far side of the weld was 6.3 mm (0.25 in.), well within the 19-mm (0.75-in.) acceptance criteria of ASME Section XI Code, Appendix VIII. The results for length sizing of the sawcuts with the TRS probe are given in Table 7.13. The TRS results for the 6 dB drop technique were consistently undersized from both the near and far side of the weld. This is the result of the discontinuous nature of the ultrasonic responses from the sawcuts. While the sawcuts are straight linear features, the ultrasonic response from them can appear as a series of tightly spaced smaller features. The LOS technique did provide reasonably accurate lengths for the sawcuts, although they were also undersized. The RMSE from the far side of the weld was 15.3 mm (0.60 in.), which is lower than the 19-mm (0.75-in.) ASME Section XI, Appendix VIII acceptance criteria, but is not as accurate as the TRL results. Sawcut length-sizing data is plotted in Figure 7.17.

Table 7.12 Sawcut Lengths in Pipe Specimen 02-24-15 as Measured by the TRL Array

		Near Side		Far Side	
Sawcut	**Actual Length**	**TRL −6 dB**	**TRL LOS**	**TRL −6 dB**	**TRL LOS**
A	32.8 mm (1.29 in.)	33.0 mm (1.30 in.)	42.0 mm (1.65 in.)	18.0 mm (0.71 in.)	21.4 mm (0.84 in.)
B	65.1 mm (2.57 in.)	55.9 mm (2.20 in.)	73.7 mm (2.90 in.)	60.0 mm (2.36 in.)	60.0 mm (2.36 in.)
C	36.3 mm (1.43 in.)	19.1 mm (0.75 in.)	49.9 mm (1.96 in.)	30.5 mm (1.20 in.)	42.3 mm (1.67 in.)
D	54.1 mm (2.13 in.)	44.0 mm (1.73 in.)	51.1 mm (2.01 in.)	47.0 mm (1.85 in.)	61.6 mm (2.43 in.)
E	43.7 mm (1.72 in.)	29.0 mm (1.14 in.)	53.5 mm (2.11 in.)	37.1 mm (1.46 in.)	48.7 mm (1.92 in.)
F	59.7 mm (2.35 in.)	57.9 mm (2.28 in.)	64.4 mm (2.54 in.)	45.2 mm (1.78 in.)	65.6 mm (2.58 in.)
G	57.3 mm (2.25 in.)	48.3 mm (1.90 in.)	67.7 mm (2.66 in.)	35.6 mm (1.40 in.)	54.0 mm (2.13 in.)
H	75.2 mm (2.96 in.)	68.6 mm (2.70 in.)	83.8 mm (3.30 in.)	58.4 mm (2.30 in.)	75.6 mm (2.98 in.)
RMS Error		10.2 mm (0.40 in.)	9.0 mm (0.36 in.)	12.9 mm (0.51 in.)	6.3 mm (0.25 in.)

Table 7.13 Sawcut Lengths in Pipe Specimen 02-24-15 as Measured by the TRS Array

		Near Side		Far Side	
Sawcut	**Actual Length**	**TRS −6 dB**	**TRS LOS**	**TRS −6 dB**	**TRS LOS**
A	32.8 mm (1.29 in.)	13.0 mm (0.51 in.)	33.0 mm (1.30 in.)	8.0 mm (0.32 in.)	29.4 mm (1.16 in.)
B	65.1 mm (2.57 in.)	53.0 mm (2.09 in.)	75.5 mm (2.97 in.)	61.0 mm (2.40 in.)	45.1 mm (1.77 in.)
C	36.3 mm (1.43 in.)	24.0 mm (0.95 in.)	40.0 mm (1.58 in.)	N/A	32.1 mm (1.26 in.)
D	54.1 mm (2.13 in.)	(18.0 mm 0.71 in.)	65.1 mm (2.56 in.)	35.0 mm (1.38 in.)	47.1 mm (1.86 in.)
E	43.7 mm (1.72 in.)	(29.0 mm 1.14 in.)	48.4 mm (1.90 in.)	18.0 mm (0.71 in.)	28.1 mm (1.11 in.)
F	59.7 mm (2.35 in.)	30.0 mm (1.18 in.)	74.5 mm (2.93 in.)	25.0 mm (0.98 in.)	42.2 mm (1.66 in.)
G	57.3 mm (2.25 in.)	15.0 mm (0.59 in.)	66.0 mm (2.60 in.)	13.0 mm (0.51 in.)	38.7 mm (1.52 in.)
H	75.2 mm (2.96 in.)	N/A	79.0 mm (3.11 in.)	N/A	53.0 mm (2.09 in.)
RMS Error		26.4 mm (1.04 in.)	8.5 mm (0.33 in.)	28.3 mm (1.12 in.)	15.3 mm (0.60 in.)

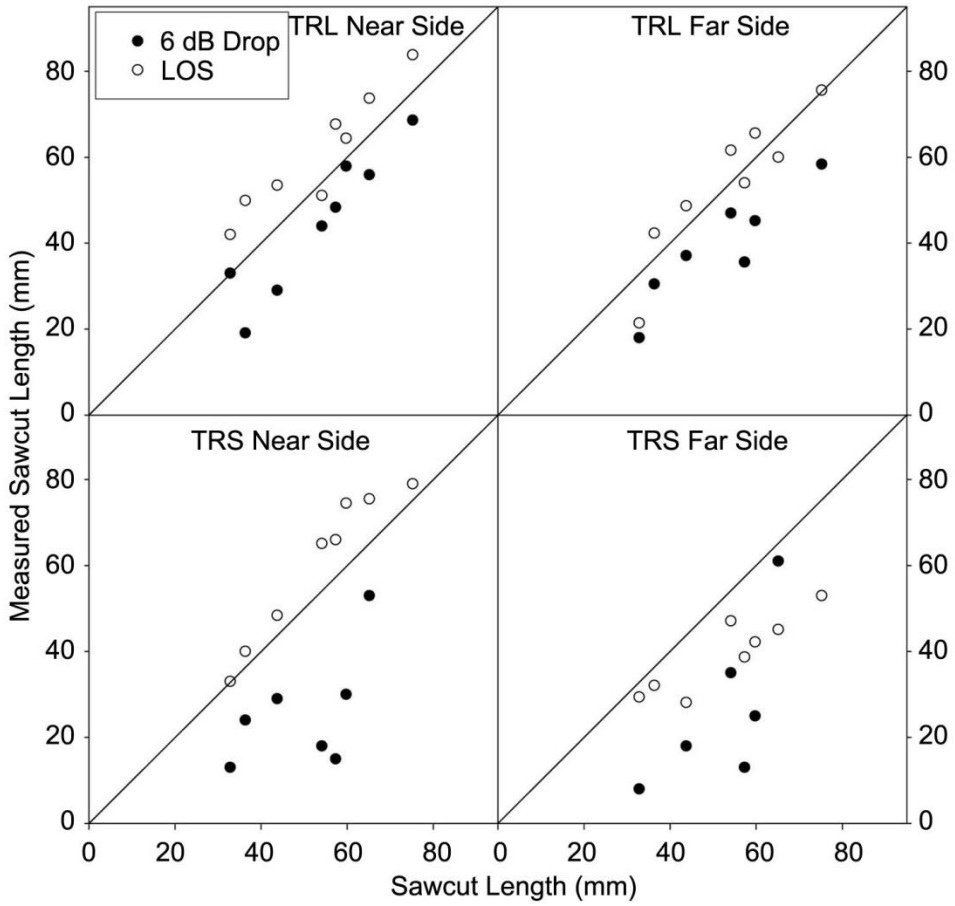

Figure 7.17 Sawcut Lengths Measured Using the 6 dB Drop and Loss of Signal Techniques with the TRL and TRS Probes from the Near and Far Side of the Weld Plotted Versus the Actual Sawcut Lengths

Tables 7.14 and 7.15 show the results for the length sizing of the implanted thermal fatigue cracks for the TRL and TRS probes, respectively. This data is plotted in Figure 7.18. The LOS technique performed much better than the 6 dB drop technique for both probes from the far side of the weld. This is again the result of the uneven amplitude along the scanning direction of the ultrasonic responses from the implanted cracks. Both the TRL and TRS were able to accurately length size the defects from the far side; the TRL had an RMSE of 6.3 mm (0.25 in.) and the TRS array had an RMSE of 8.9 mm (0.35 in.). It should be noted that the best scans were taken with the front of the probe either against the toe of the weld or slightly back from the toe of the weld. These scans could easily be taken with the weld crown left in the as-welded position and do not require the weld crown to be machined off.

Table 7.14 Thermal Fatigue Crack Lengths in Pipe Specimen 02-24-15 as Measured by the TRL Array

		Near Side		Far Side	
TFC	**Actual Length**	**TRL −6 dB**	**TRL LOS**	**TRL −6 dB**	**TRL LOS**
A	10.7 mm (0.42 in.)	12.0 mm (0.47 in.)	16.2 mm (0.64 in.)	16.0 mm (0.63 in.)	17.3 mm (0.68 in.)
B	30.5 mm (1.20 in.)	27.9 mm (1.10 in.)	27.6 mm (1.09 in.)	21.0 mm (0.83 in.)	27.1 mm (1.07 in.)
C	43.6 mm (1.72 in.)	22.1 mm (0.87 in.)	50.1 mm (1.97 in.)	16.0 mm (0.63 in.)	53.1 mm (2.09 in.)
E	33.8 mm (1.33 in.)	17.8 mm (0.70 in.)	43.5 mm (1.71 in.)	17.8 mm (0.70 in.)	37.4 mm (1.47 in.)
RMS Error		13.5 mm (0.53 in.)	6.6 mm (0.26 in.)	16.8 mm (0.66 in.)	6.3 mm (0.25 in.)

Table 7.15 Thermal Fatigue Crack Lengths in Pipe Specimen 02-24-15 as Measured by the TRS Array

		Near Side		Far Side	
TFC	**Actual Length**	**TRS −6 dB**	**TRS LOS**	**TRS −6 dB**	**TRS LOS**
A	10.7 mm (0.42 in.)	12.0 mm (0.47 in.)	20.1 mm (0.79 in.)	6.0 mm (0.24 in.)	20.9 mm (0.82 in.)
B	30.5 mm (1.20 in.)	14.0 mm (0.55 in.)	40.0 mm (1.58 in.)	7.4 mm (0.29 in.)	42.3 mm (1.67 in.)
C	43.6 mm (1.72 in.)	7.0 mm (0.28 in.)	60.1 mm (2.37 in.)	21.0 mm (0.83 in.)	45.0 mm (1.77 in.)
E	33.8 mm (1.33 in.)	30.0 mm (1.18 in.)	74.5 mm (2.93 in.)	25.0 mm (0.98 in.)	42.2 mm (1.66 in.)
RMS Error		20.1 (0.79 in.)	23.0 mm (0.90 in.)	16.9 mm (0.67 in.)	8.9 mm (0.35 in.)

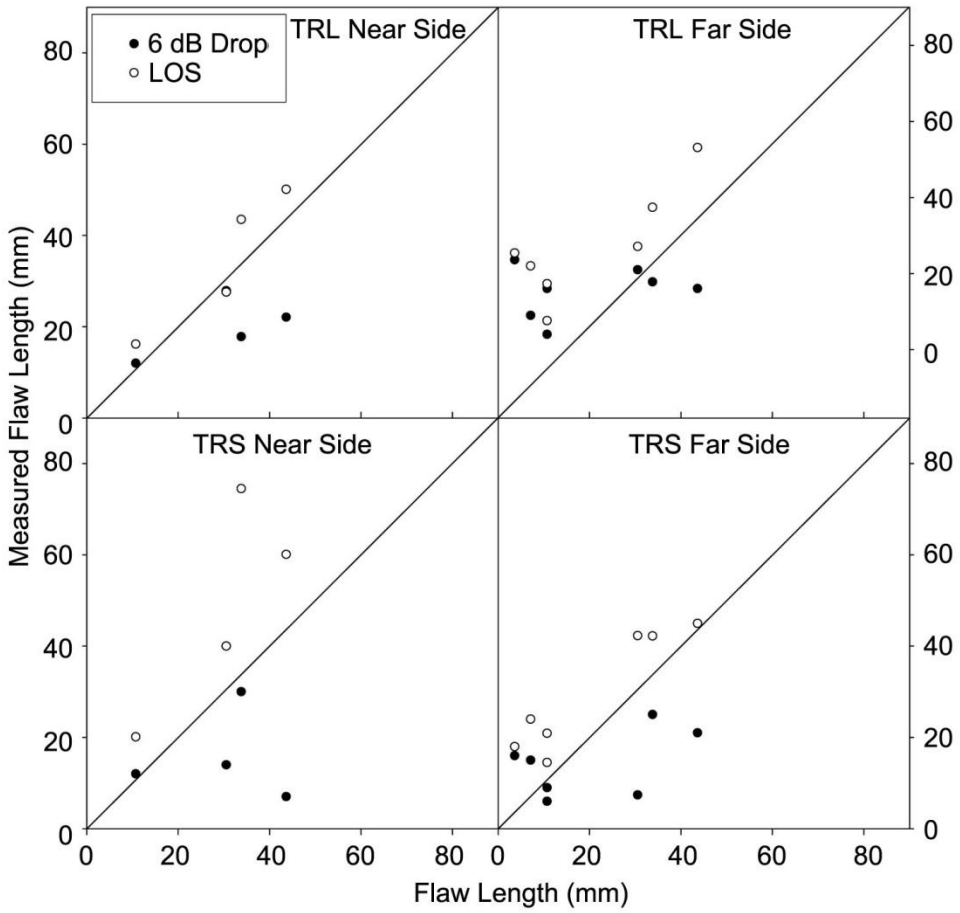

Figure 7.18 Thermal Fatigue Crack Lengths Measured Using the 6 dB Drop and Loss of Signal Techniques with the TRL and TRS Probes from the Near and Far Side of the Weld Plotted Versus the Actual Flaw Lengths

8 Phase 2 Evaluation

The Phase 2 evaluation focused on examination of three full-circumferential welds to determine the effects of weld microstructure on far-side inspections. Austenitic pipe specimen 3C-022 was used for this assessment. Work conducted in Phase 2 again included all three ultrasonic NDE techniques—conventional-UT, low-frequency/SAFT-UT, and phased-array UT. As described in Section 5, pipe specimen 3C-022 is made of Schedule 80 ASTM 358 Grade 304 wrought stainless steel and consists of four 610-mm (24.0-in.) diameter pipe sections joined by three welds: (1) weld horizontally with air backing, (2) welded vertically with air backing, and (3) welded horizontally with water backing. A 10% through-wall, 360° notch is machined into the heat-affected zone of welds one and three to provide a consistent standard reflector. Weld two has three 10% through-wall EDM notches and three implanted cracks of 5%, 10%, and 15% through-wall depth in the HAZ. See Appendix F for all conventional-UT data and images on specimen 3C-022.

8.1 Conventional UT: Data Analysis and Results

8.1.1 Weld One

Weld number one, as described in Section 5, was made in the horizontal position in a field-simulated manner with air backing. The longitudinal seam weld was at the top (12 o'clock position) of the pipe during welding. The 10% notch in weld one was scanned using 1.5-MHz, 60° and 70° shear waves from the far side of the weld. The probes were raster-scanned in the x-direction (perpendicular to the weld) over the pipe specimen over a distance of 152 mm (6.0 in.) and indexed (stepped) at 1.3-mm (0.05-in.) increments for a total of 1966 mm (77.4 in.) around the outside circumference of the pipe specimen, which produced a total of 1548 lines (strokes) per data set. These scans were time-intensive.

Figure 8.1 shows C-scans for the 60° and 70° scans for a representative section of weld one. The 10% notch in weld number one was easily detected by both the 60° and 70° shear waves. The signal-to-noise ratios were very similar—the SNR for the 60° shear waves is 19 dB and the SNR for the 70° shear waves is 20 dB. Responses for the 10% notch varied by approximately $\pm$6 dB in amplitude along the length of the notch at both angles. There was no measurable difference in the amplitude of the response from the 10% through-wall notch related to the overall position on the weld. The amplitude response from near the 12 o'clock position that was welded from above is virtually identical to the amplitude response from the areas near the 3 and 6 o'clock positions on the weld. There is no correlation between the welding orientation and the locations of the high-amplitude responses in the 60° and 70° scans.

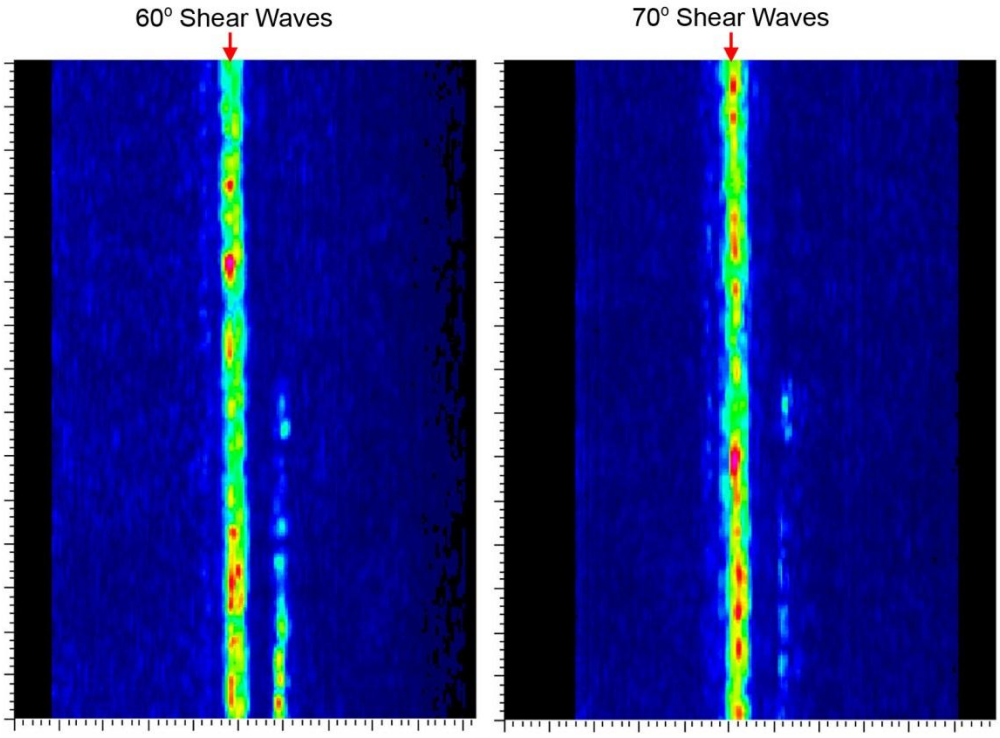

Figure 8.1 C-scan Views for a Representative Area of Weld Number One Acquired with 1.5-MHz 60° and 70° Shear Waves from the Far Side. The 10% notch response is marked by arrows and varies throughout the length of each scan by 6 dB.

8.1.2 Weld Two

Weld two was fabricated in the horizontal position with air backing. Weld number two was scanned from the near side with the 60° shear-wave probe and from the far side with the 60° and 70° shear-wave probes. The probes were raster-scanned over the pipe specimen where the x-direction scan length was 152 mm (6.0 in.) and y-direction increment step was 1.3 mm (0.05 in.). The total circumferential path traveled (with the inclusion of overlapped part path) was 2118 mm (83.4 in.) around the outside circumference of the pipe specimen for a total of 1668 lines per data set. The 152 mm (6.0 in.) of overlap in each scan provides two built-in fiduciaries in the scans as the longitudinal seam appears as a “dead zone” in the scans. Again, these scans were time-intensive.

Figure 8.2 shows C-scan images of a representative section of the 10% though-wall EDM notch in weld two from the 60° near-side scan, the 60° far-side scan, and the 70° far-side scans. The near-side scan provides the sharpest image of the EDM notch and has the best SNR of 27 dB. The 60° and 70° far-side scans both have SNRs of 24 dB. The amplitude along the 60° far-side scan varies by 6 dB, but the amplitude of the response in the 70° scan varies by as much as 10 dB in some sections.

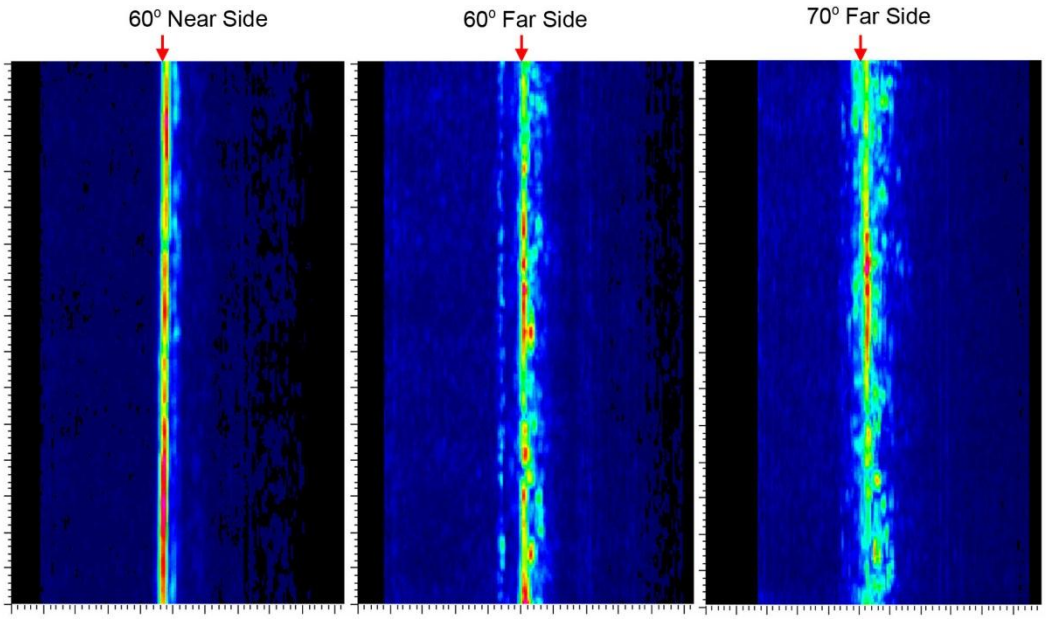

Figure 8.2 C-scan Views for a Representative Area of Weld Number Two Acquired with 1.5-MHz, 60° and 70° Shear Waves. The 10% notch response is marked by arrows in each image and varies by as much as 10 dB in the 70° data.

Figures 8.3 through 8.5 show ultrasonic typical responses using 60° and 70° shear-wave probes from three implanted cracks in weld two. Figure 8.3 shows the response from crack 4 (5% through-wall), Figure 8.4 shows the response from crack 5 (10% though-wall), and Figure 8.5 shows the response from crack 6 (15% though-wall). Crack 4 was only detectable from the near side. Neither the 60° nor 70° shear-wave probes were able to detect the 5% though-wall crack from the far side of the weld. All three scans were able to detect crack 5. The strongest response for crack 5 comes from the near side, and the 60° far-side scan has a better SNR than the 70° far-side scan. As with the phased-array scans, the amplitude of the response from crack 5 is roughly 6 dB smaller than the response from the peak responses of the 10% EDM notch. This is to be expected as the crack is tighter than the EDM notch, the crack is much shorter than the EDM notch, and the crack is at a 35° angle and provides a weaker corner trap than the perpendicular EDM notch. Crack 6 is easily detected by all three scans. No tip responses are visible from any of the cracks, from the near or far side. This makes accurate depth-sizing of the cracks virtually impossible. The cracks were length-sized using the 6 dB drop technique and the loss of signal (LOS) technique. Table 8.1 shows the results for the length-sizing of the three cracks. Both the 6 dB drop and LOS technique oversized each crack in all scans.

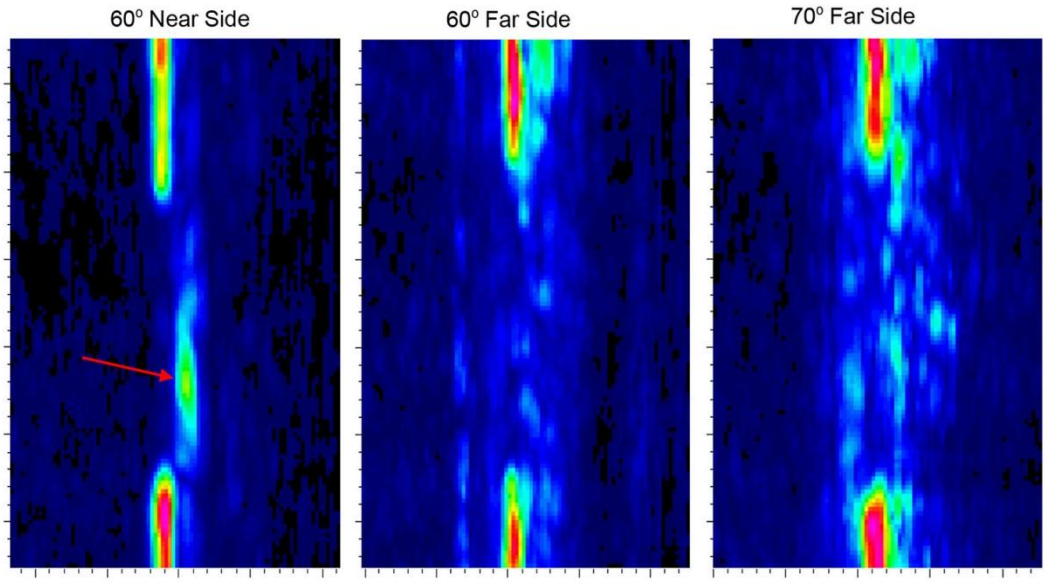

Figure 8.3 C-scan Views of Crack 4 in Weld Number Two Acquired with 1.5-MHz, 60° and 70° Shear Waves. The crack was not detected in the two far side data sets.

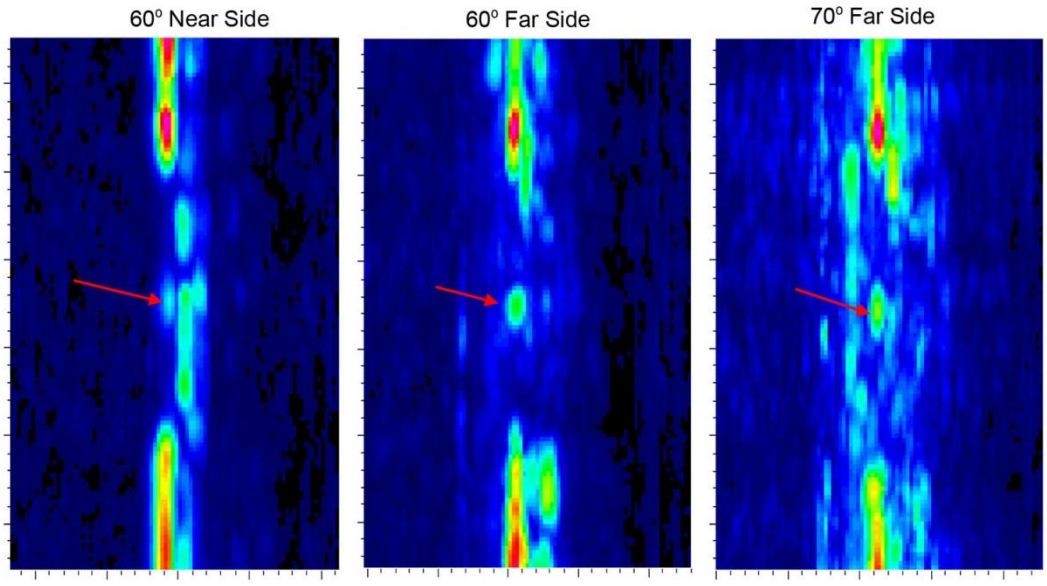

Figure 8.4 C-scan Views of Crack 5 in Weld Number Two Acquired with 1.5-MHz, 60° and 70° Shear Waves

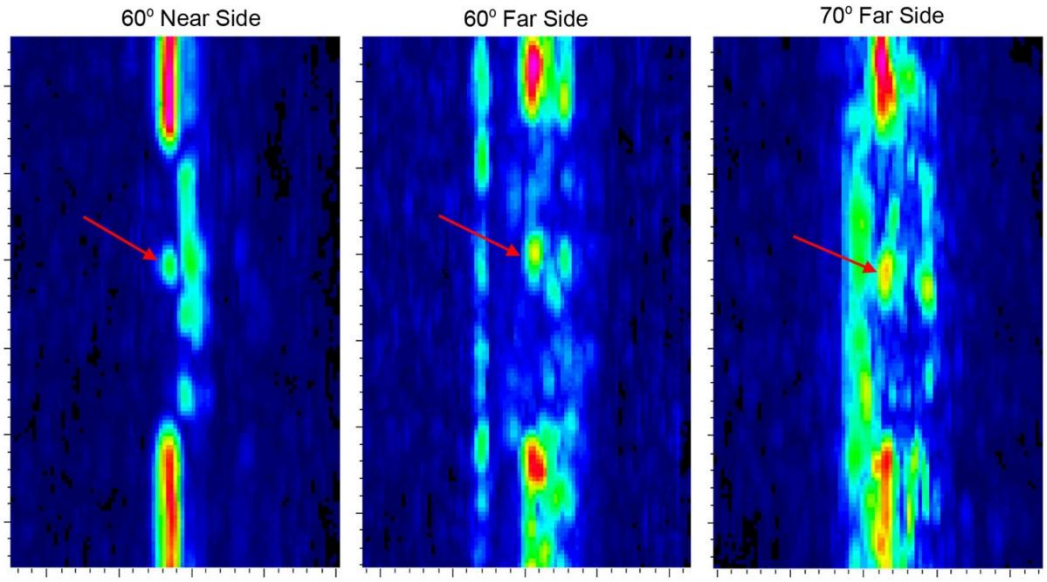

Figure 8.5 C-scan Views of Crack 6 in Weld Number Two Acquired with 1.5-MHz, 60° and 70° Shear Waves

Table 8.1 Thermal Fatigue Crack Lengths in Weld Two of Pipe Specimen 3C-022 as Measured by the 60° and 70° Conventional-UT Probes

		60° Near		60° Far		70° Far	
Crack	**Actual Length**	**6 dB**	**LOS**	**6 dB**	**LOS**	**6 dB**	**LOS**
4	3.6 mm (0.14 in.)	19 mm (0.75 in.)	50.8 mm (2.00 in.)	No detection		No detection	
5	7.1 mm (0.28 in.)	6.4 mm (0.25 in.)	31.8 mm (1.25 in.)	10.2 mm (0.40 in.)	16.5 mm (0.65 in.)	10.2 mm (0.40 in.)	17.8 mm (0.70 in.)
6	10.7 mm (0.42 in.)	11.4 mm (0.45 in.)	15.2 mm (0.60 in.)	12.7 mm (0.50 in.)	20.3 mm (0.80 in.)	11.4 mm (0.45 in.)	20.3 mm (0.80 in.)
RMS Error		8.9 mm (0.35 in.)	30.9 mm (1.22 in.)	2.6 mm (0.10 in.)	9.5 mm (0.37 in.)	2.2 mm (0.09 in.)	10.2 mm (0.40 in.)

8.1.3 Weld Three

Weld number three was made in the horizontal position in a field-like manner with water backing. The longitudinal seam weld was at the top (12 o'clock position) of the pipe during welding. The probes were again raster-scanned over the pipe specimen, with an x-direction scan stroke length of 152 mm (6.0 in.) and a total y-direction (circumferential) indexing length of 2118 mm (83.4 in.) around the outside circumference of the pipe specimen. The probes were indexed in 1.3-mm (0.05-in.) increments, for a total of 1668 lines per data set. As in the previous scans, these scans were also initiated at a distance of 76 mm (3.0 in.) before the centerline of the longitudinal seam weld, indexed 360° around the pipe, and then continued

indexing an additional 152 mm (6.0 in.) to 76 mm (3.0 in.) beyond the longitudinal weld centerline to obtain sufficient overlap. These scans were also quite time-intensive.

Figure 8.6 shows C-scans for the 60° and 70° scans for a representative section of weld three. The 10% notch in weld number three was easily detected by both the 60° and 70° shear waves. The SNRs for the different scans of weld number three were very similar—the SNR for the 60° shear waves is 8 and the SNR for the 70° shear waves is 5. The amplitude of the responses from the 10% notch varied by 6 dB along the length of the notch for both angles. There was no measurable difference in the amplitude of the response related to the overall position on the weld. The amplitude response from near the 12 o'clock position that was welded from above is virtually identical to the amplitude response from the areas near the 3 and 6 o'clock positions on the weld. As with weld one, there was no correlation between the locations of the high-amplitude responses in the 60° and 70° scans.

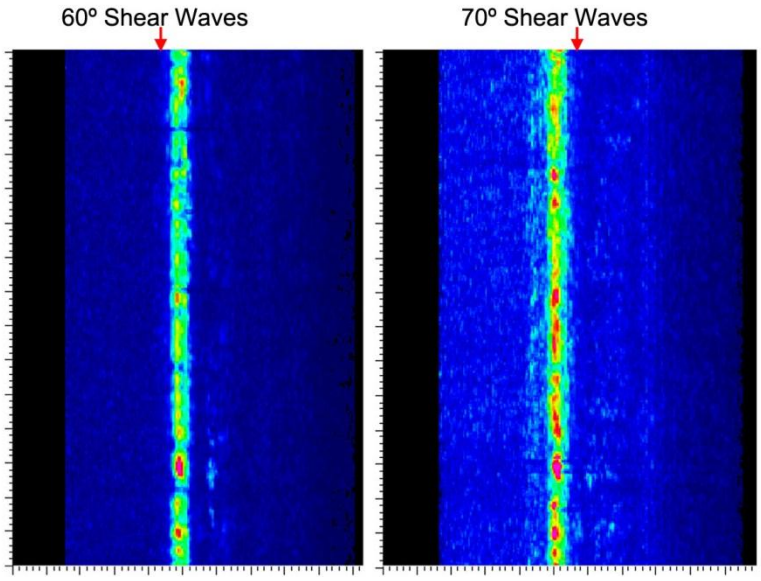

Figure 8.6 C-scan Views for a Representative Area of Weld Number Three Acquired with 1.5-MHz, 60° and 70° Shear Waves from the Far Side. The 10% notch response is marked by an arrow in each image and varies by 6 dB along the length of the notch at both angles

8.2 Low-Frequency/SAFT: Data Analysis and Results

Each of the three welds was scanned using 400-kHz and 250-kHz probes. The welds were examined using 45° shear and longitudinal waves, 60° longitudinal waves, and 70° longitudinal waves at both frequencies. The data were stored electronically and analyzed using SAFT. The SAFT procedure used on the vertical pipe section was the same as used for processing the Phase 1 pipe segments. The SAFT angle used for the processing was 12° and the beam entry diameter was 12.7 mm (0.5 in.). No skipping was used and a dynamic range factor of one was

used. Scans obtained using LF/SAFT proved very time-intensive with regard to both data collection and SAFT post-processing of the data.

8.2.1 Weld One

Weld number one, as described in Section 5, was made in the horizontal position in a field-like manner with air backing. The longitudinal seam weld was at the top of the pipe during welding. The 10% notch in weld one was scanned using 400-kHz 45° shear and longitudinal waves and 60° longitudinal waves.

Each scan angle was able to detect the 10% notch. The 45° shear wave sound field was more suitable at consistently detecting the notch with the lowest variability (between 3 dB and 6 dB) in the reflected amplitude along the circumferential extent of the notch. The 45° longitudinal scan had the poorest response from the notch, with the amplitude of the response dropping 6 dB for several centimeters at a time along the notch. The 45° shear-wave scan provides the best width sizing for the notch, with the 6.35 mm (0.25 in.) wide notch appearing to be 15.2 mm (0.6 in.) in width using the 6 dB drop method. In both of the longitudinal scans, the notch appears to be much wider than it is while the shear-wave response is more tightly defined. The 45° longitudinal scan shows the notch to have a width of 22.9 mm (0.9 in.) to 48.3 mm (1.9 in.). The 60° longitudinal scan shows a width ranging from 45.7 mm (1.8 in.) to 55.9 mm (2.2 in.). Width sizing of the narrow notch really provides an indication of the probe beam size rather than the notch width. As the probe sweeps past the flaw the beam width is mapped out. For this inspection, the data demonstrates that the 45° shear probe has a tighter beam than the 45° longitudinal probe.

Figure 8.7 shows representative C-scans from the three angles used to scan the notch (each taken from the same 38.1-cm [15.0-in.] section of pipe). It is interesting to note that there is weak, if any, correlation between the regions of high and low amplitude in these scans. The weld metal absorbs or redirects the 45° shear and longitudinal and 60° longitudinal waves uniquely. There was no strong correlation with the overall position on the weld with the amplitude of the responses from the different angles and modes for the 400-kHz transducers. The amplitude of the responses from the 10% notch was similar at the region near the 12 o'clock position as the region near the 6 o'clock position.

The 10% notch in weld one was also scanned using 250-kHz probes with 45° and 70° longitudinal waves. The 250-kHz scans had a poorer response from the notch, with the 45° having as much as a 10 dB drop along the scan and showing the 6.4-mm (0.25-in.) wide notch to be over 50.8-mm (2.0-in.) wide in places. The response amplitude using 70° longitudinal waves had a lower variability, with regions dropping as many as 6 dB, and showing the notch to be 25.4–50.8-mm (1.0–2.0-in.) wide. As with the 400-kHz scans, the 250-kHz 45° and 70° scans show no correlation with specific regions of the pipe allowing the sound to penetrate and which regions absorb or redirect sound. The weld metal appears to have a different profile for the two angles. Figure 8.8 shows representative C-scans from the three angles used to scan the notch (each taken from the same 38.1-cm [15.0-in.] section of pipe).

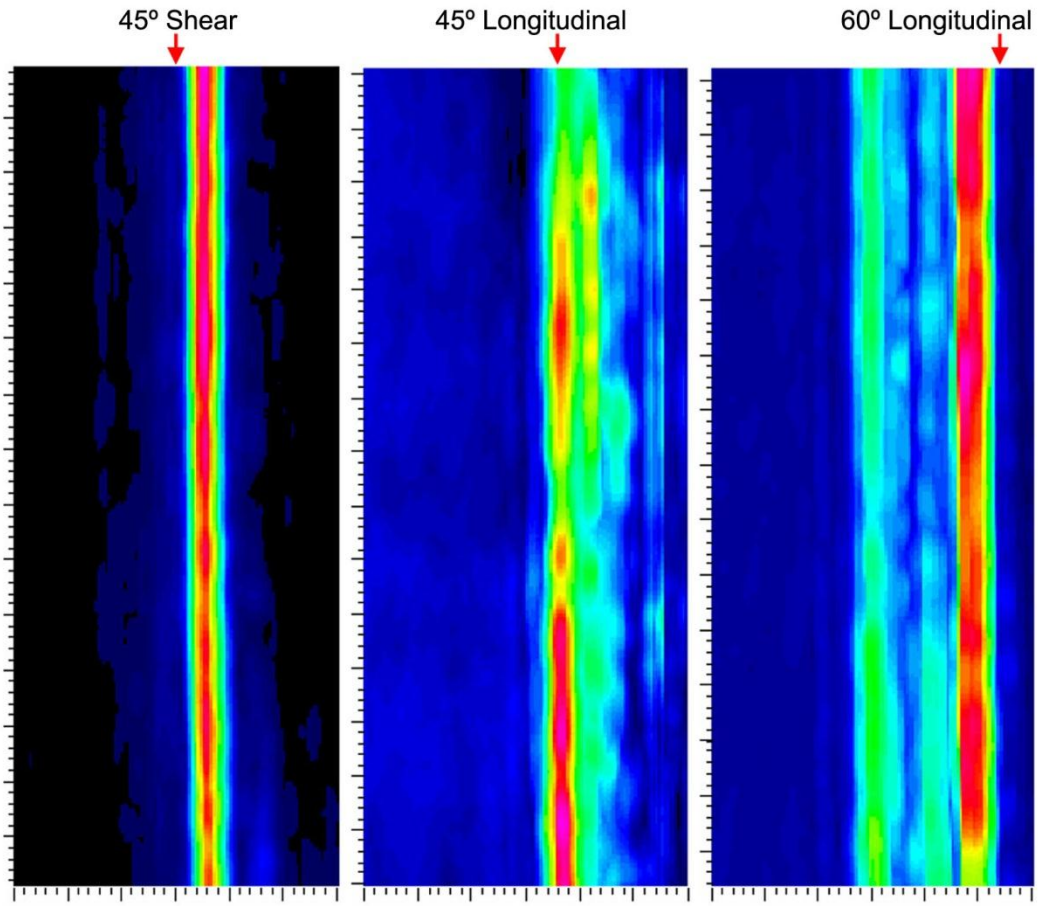

Figure 8.7 C-scan Views for a Representative Area of Weld Number One Acquired with 400-kHz, 45° S-waves, 45° L-waves, and 60° L-waves from the Far Side. The 10% notch response is best at 45° shear with the least amount of signal loss and worst at 45° longitudinal.

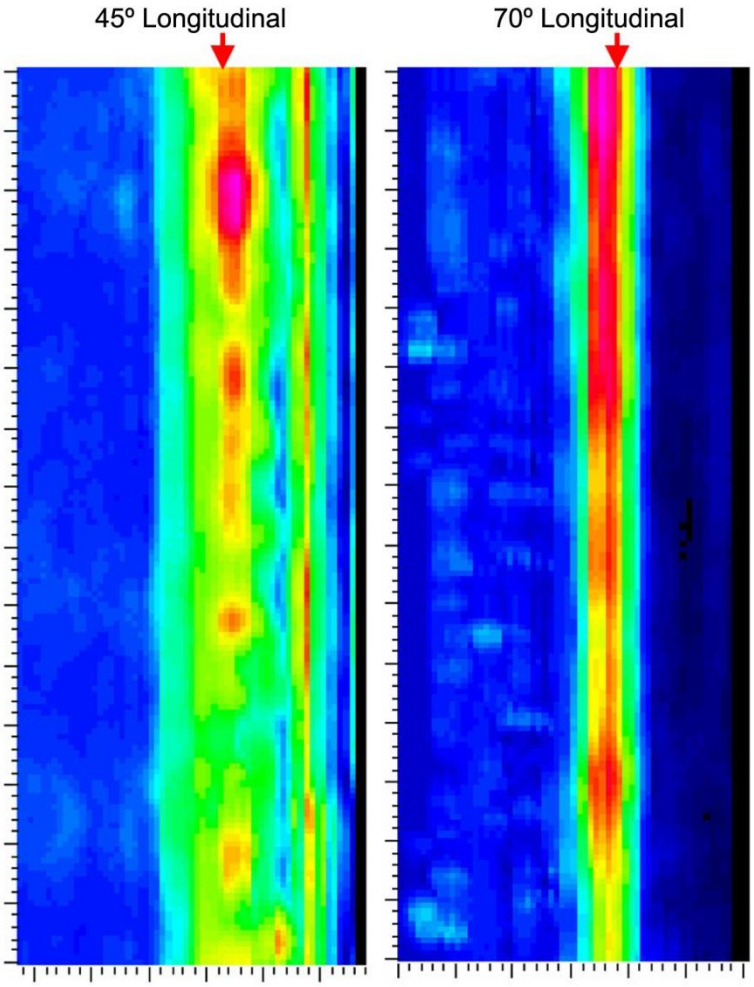

Figure 8.8 C-scan Views for a Representative Area of Weld Number One Acquired with 250-kHz, 45° L-waves and 70° L-waves from the Far Side. The 45 L-wave response has as much as a 10 dB variation along the imaged length of the 10% notch.

As with the 400-kHz transducers, the 250-kHz scans showed no correlation with the overall position on the weld and with the amplitude of the responses from the different angles. The amplitude of the responses from the 10% notch was similar at the 12 o'clock position as at the 6 o'clock position for the 250-kHz scans.

Finally, the weld metal appears to have a different ultrasonic profile depending entirely on the inspection frequency. Weld one was scanned with 45° longitudinal waves at both 400 kHz and 250 kHz, and these two scans show no correlation as to where the weld allows sound to penetrate and where it interferes with the response from the 10% notch. Figure 8.9 shows the two 45° longitudinal-wave scans. This limited correlation between the different scans show that the weld metal microstructure is very complex and the ability of sound to pass through the weld metal is a strong function of the angle and frequency of the sound.

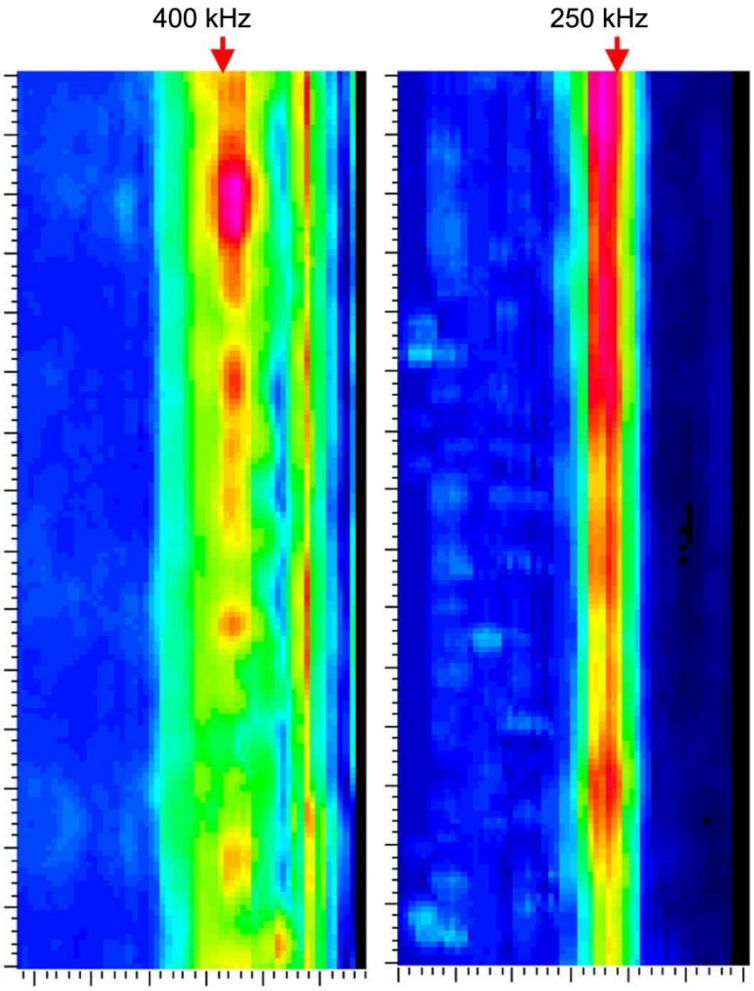

Figure 8.9 Same Section of Weld Number One Scanned Using 45° Longitudinal Waves at Both 400 kHz and 250 kHz from the Far Side. There is limited correlation between the two frequencies in where sound penetrates and where it drops out.

8.2.2 Weld Two

Weld two was welded in the vertical position with air backing. It has three EDM notches with depths of 10% through-wall and three implanted cracks, one with a depth of 5% through-wall, one with a depth of 10% through-wall, and one with a depth of 15% through-wall. The flaws were scanned from the far side of the weld using 400-kHz 45° shear waves, and 45°, 60°, and 70° longitudinal waves. Each of the scans was able to detect the 10% EDM notches easily. The amplitude of the response from the four scans was very similar in sensitivity. All four scans showed a 6 dB variation along the EDM notches and the signal responses from the very thin EDM notches are shown to slightly smear, covering a larger axial extent at lower frequencies. This effect is reduced as the frequency is increased to 400 kHz (see Figure 8.9) and a more representative signal response is shown for axial extent of the notch in the images. Unlike in weld one, there was some correlation in the response amplitude from the EDM notches and the

position along the pipe. The highest amplitude responses for each scan were found at the beginning and end of the EDM notches. None of the scans were able to detect any of the three implanted flaws. As discussed in Section 6, the dimensions of the sound field (in particular the dimensions of the overlap or cross-over point between transmit and receive transducers) and the wavelength play a key role in the resolution capability of the inspection approach. At these low frequencies, resolution of small flaws is limited.

Figure 8.10 shows C-scans for each 400-kHz scan from the same representative region of the pipe. The region chosen shows the end of the second EDM notch, the region with the 15% through-wall crack (two thirds of the way down in each figure), and the beginning of the third EDM notch. In each C-scan the 10% EDM notches are clearly discernable as is the gap between them but the implanted flaw is not detected in the gap.

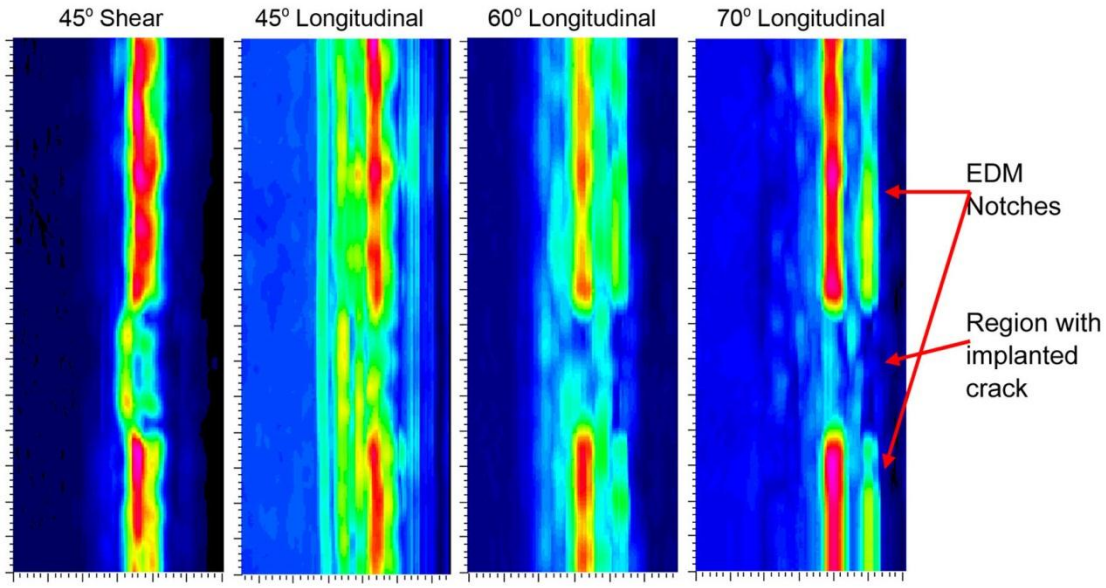

Figure 8.10 C-scan Views for a Representative Area of Weld Number Two Acquired with 400-kHz, 45° S-waves, 45° L-waves, 60° L-waves, and 70° L-waves. The 10% notches are detected but not the 15% implanted crack.

The EDM notches and cracks were also scanned using 250-kHz probes with 45° shear waves and 45° and 70° longitudinal waves. The results for the 250-kHz scans show that the amplitude of the three scans varies by 6 dB along the length of the EDM notches. As with the 400-kHz scans, none of the implanted flaws were detected with the 250-kHz scans. Figure 8.11 shows C-scans for each 400-kHz scan from the same representative region of the pipe. The EDM notches are discernable in all three scans, but the 45° longitudinal method does not resolve the gap between the EDM notches very clearly and the implanted 15% flaw is not detected.

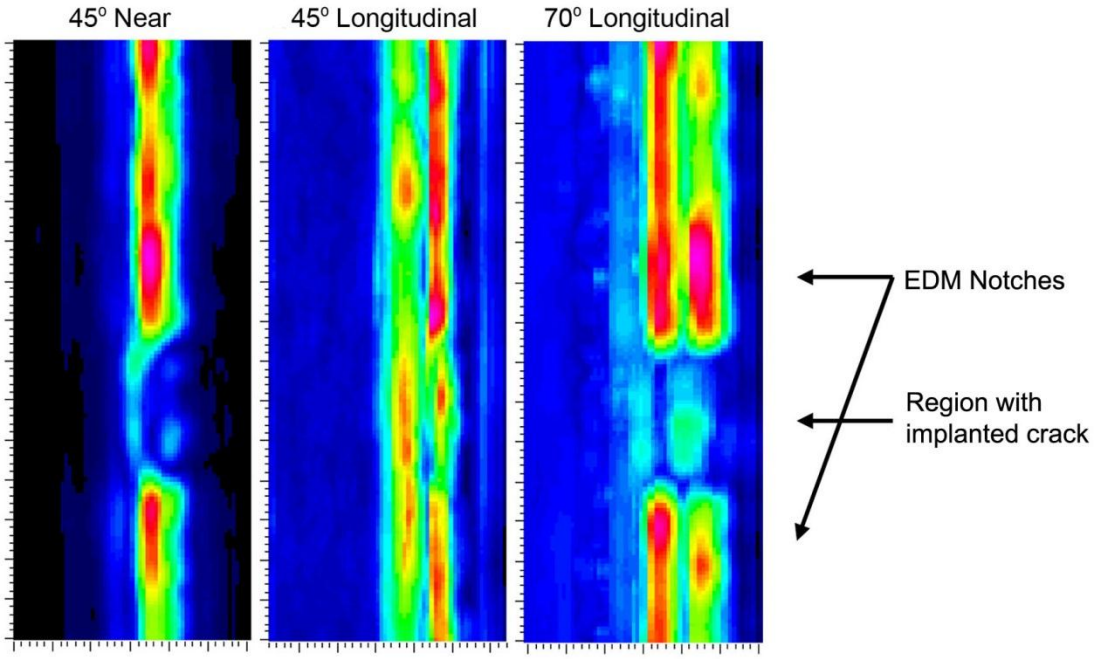

Figure 8.11 C-scan Views for a Representative Area of Weld Number Two Acquired with 250-kHz, 45° S-waves, 45° L-waves, and 70° L-waves. The 10% notches are detected but not the 15% implanted crack.

8.2.3 Weld Three

Weld number three, as described in Section 5, was made in the horizontal position in a field-like manner with water backing. The longitudinal seam weld was at the top of the pipe during welding. As with weld one, there is a 10% through-wall notch machined into the heat-affected zone of the weld. The 10% notch was scanned at 400 kHz from the far side of the weld with 45° shear waves, and 45°, 60°, and 70° longitudinal waves. The 45° shear waves, and 45° and 60° longitudinal waves, were able to clearly and consistently detect the 10% through-wall notch. The amplitude of the signal varies by 6 dB along the length of the notch for these angles. The 70° longitudinal wave scan was very uneven, however, and has regions in which the amplitude drops to the noise level. C-scans from a representative region of the four scans are shown in Figure 8.12.

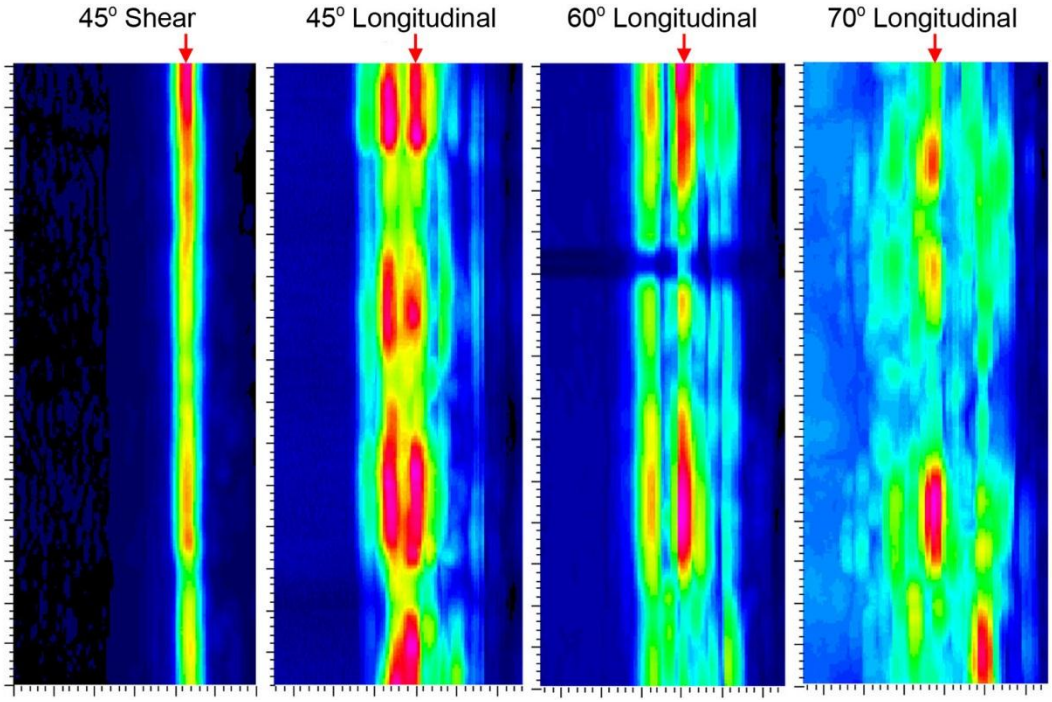

Figure 8.12 C-scan Views for a Representative Area of Weld Number Three Acquired with 400-kHz, 45° S-waves, 45° L-waves, 60° L-waves, and 70° L-waves. The 10% notch responses as viewed from the far side are noted with arrow in each image.

Weld number three was also scanned using 250-kHz transducers. The 10% notch was examined using 45° and 70° longitudinal waves. The 45° scan was very poor. The amplitude of the response from the 10% notch was very uneven and often fell to the level of the noise. The 70° scan was much more consistent. The amplitude of the response from the 10% through-wall notch was always less than −6 dB and was usually less than −4 dB. As with weld number one, the 400-kHz and 250-kHz scans showed no correlation with the overall position on the weld with the amplitude of the responses from the different angles. Figure 8.13 shows C-scans from a representative region of the two scans. The uneven nature of the 45° scan is visible.

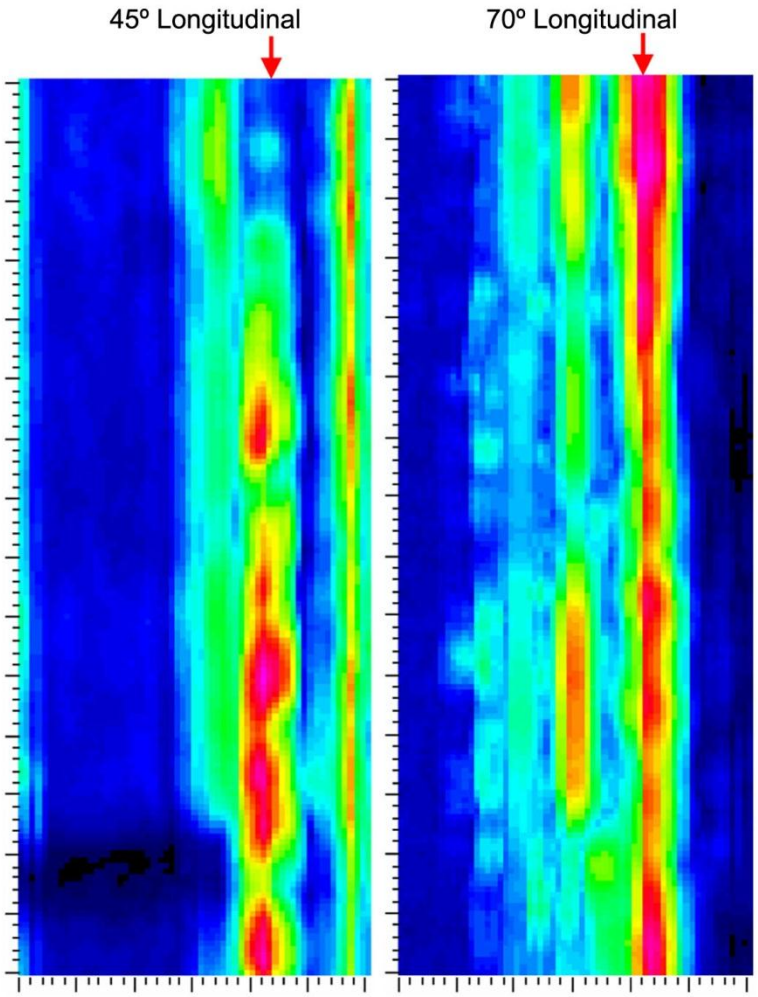

Figure 8.13 C-scan Views for a Representative Area of Weld Number Three Acquired with 250-kHz, 45° L-waves and 70° L-waves. The 10% notch responses as viewed from the far side are noted with arrow in each image.

8.3 Phased Array UT: Data Analysis and Results

For the Phase 2 PA-UT assessments of specimen 3C-022, each weld was scanned using both TRL and TRS phased arrays. Unlike pipe specimen 02-24-15, this pipe specimen was not cut into individual sections. The welds were scanned with the front edge of the arrays directly against the weld toe and with the front edge of the arrays 6.4 mm (0.25 in.), 12.7 mm (0.5 in.), and 19 mm (0.75 in.) back from the weld toe. The scans were initiated at a distance of 51 mm (2.0 in.) back from the longitudinal seam (L-seam) weld, and traveled 360° around the pipe, continuing until the longitudinal seam was scanned again. By running over the L-seam twice, a beginning and ending fiduciary is put into the data. This locator works well, as the L-seam appears as a dead zone in the scan. Welds one and three were scanned using both the TRL and TRS arrays and were only scanned from the far side. Weld two was scanned from both the near and far side using both arrays.

8.3.1 Weld One

The 10% through-wall notch in the HAZ of weld one was examined using the TRL and TRS arrays. A sample region of the ultrasonic response of the 10% notch is shown in Figure 8.14. The dead zone near the top of both scans is caused by the longitudinal seam weld in the pipe. To allow for consistency, both figures are shown with the gain set so that the peak noise level was approximately 20% full screen height (FSH).

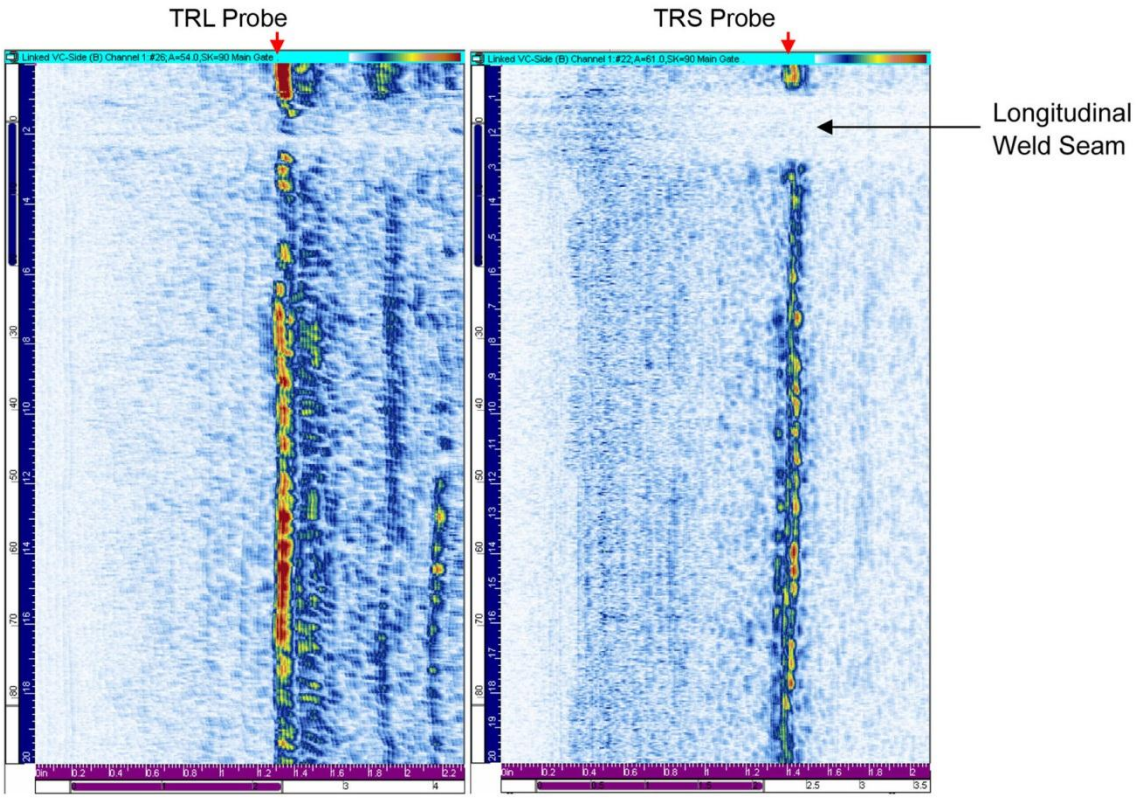

Figure 8.14 B-scan Views for the Ultrasonic Response for the 10% Notch in a Portion of Weld One from the Far Side with the Longitudinal- and Shear-Wave Arrays. Arrows Mark the Notch Response.

The scans showed that while there was strong short-range variability in the strength of the ultrasonic notch response, there was no overall "structure" to the interference. The overall amplitude response for the notch located near the top (at the 12 o'clock position and welded downhand from above) is essentially the same as the notch response from both sides and the bottom (at the 6 o'clock position and welded from underneath). The amount of sound coming back through the weld along its length varies strongly, however. The amplitude of the ultrasonic response from the 10% through-wall notch was not constant and steady, but instead increased and decreased strongly along the scanning direction. Both the TRL and TRS showed "cold spots" in the responses from the 10% notch that were as much as 20 dB lower than the peak response. These cold spots were between 1 and 5 mm (0.04 and 0.20 in.) long. Overall, the TRL array has a better SNR than the TRS array.

8.3.2 Weld Two

Weld number two contains three 10% through-wall EDM notches and three implanted thermal fatigue cracks with depths of 5%, 10%, and 15% through-wall. As described in Section 1, this weld was made in the vertical position with air backing. The EDM notches and cracks provided both standard reflectors and realistic cracks to test the longitudinal- and shear-wave methods to penetrate and detect flaws from the far side of the weld.

Weld number two was examined from both the near and far side. Figure 8.15 shows the response from the 10% EDM notch for the TRL array with the gain in both scans set to 44 dB. Using this gain, the peak signal amplitude in the near-side scan is 100% FSH with a low value of 57% FSH along the notch response. A clear corner response is visible in the scan. The far-side scan shows a similarly intense response, but the ultrasonic response from the notch is less discrete than from the near side. No tip signal responses can be called in either scan. Using a gain of 44 dB, the peak response from the far side is 100% FSH and the lowest signal along the response is 40% FSH. The results show that the 2-MHz longitudinal waves are able to pass through the weld metal without a large loss of amplitude, but with varied levels of sound field redirection. Typical A-scans, shown in Figure 8.16, show the differences in the nature of the signal coming back from the EDM notch. The far side response is much broader than the near side response.

The shear-wave response from the EDM notch was quite different than the longitudinal-wave response. The shear waves were severely attenuated but appear to be less strongly redirected by the weld metal. Figure 8.17 shows a typical response for the EDM notch scanned from the near and far side using the TRS array. In both scans, the gain is set to 23 dB. (Much less gain is needed for the TRS array as it has a larger aperture and there is no mode conversion compared to the TRL array.) From the near side, the maximum response is 100% FSH and the minimum response along the EDM notch is 78% FSH; and from the far side, the maximum response is 30% FSH with a minimum of 5% FSH. This represents an amplitude drop of 10 to 20 dB through the weld. The EDM notch response does, however, look like the response from a linear feature and shows that the shear-wave beam is not redirected as severely as the longitudinal waves. The A-scans, shown in Figure 8.18, show that the largest effect on the beam as it passes through the weld metal is the reduction in amplitude.

The three implanted thermal fatigue cracks are all detectable from the far side using both the TRL and TRS arrays. The 5% through-wall crack has the smallest response, as would be expected. The 15% through-wall crack is the easiest to detect. No tip signals were detected from the far side by either array for any of the flaws. Figures 8.19 and 8.20 show the ultrasonic responses from the far side for the three implanted cracks using the TRL and TRS arrays, respectively. In each figure the crack is in the center and the linear indications above and below the crack result from the 10% through-wall EDM notches. It is interesting to note that crack 5 (10% through-wall crack) returns a response that is 6 dB smaller than the 10% through-wall EDM notch for both the shear and longitudinal probes. Crack 5 is 7.1-mm (0.28-in.) long, which is larger than two wavelengths for the longitudinal-wave probe and more than four wavelengths for the shear-wave probe. Also, the cracks are at a 35° angle while the notch is perpendicular to the pipe wall, so there will be associated differences in the strength of the reflection. The

6 dB difference in the amplitude of the responses from the crack and the EDM notch are consistent with previous PNNL studies (Schuster et al. 2010).

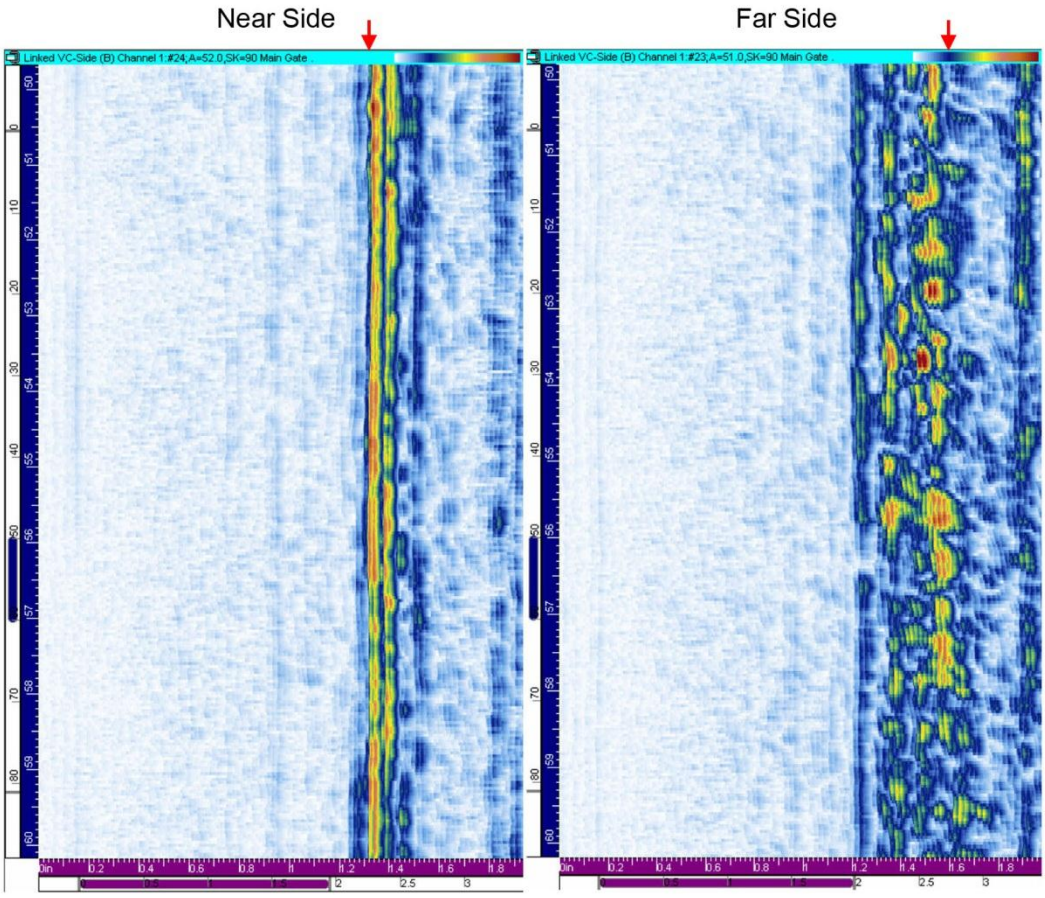

Figure 8.15 B-scan Views for the Ultrasonic Response from the EDM Notch in Weld Two from the Near and Far Side with the Longitudinal-Wave Array. Arrows Mark the Notch Response.

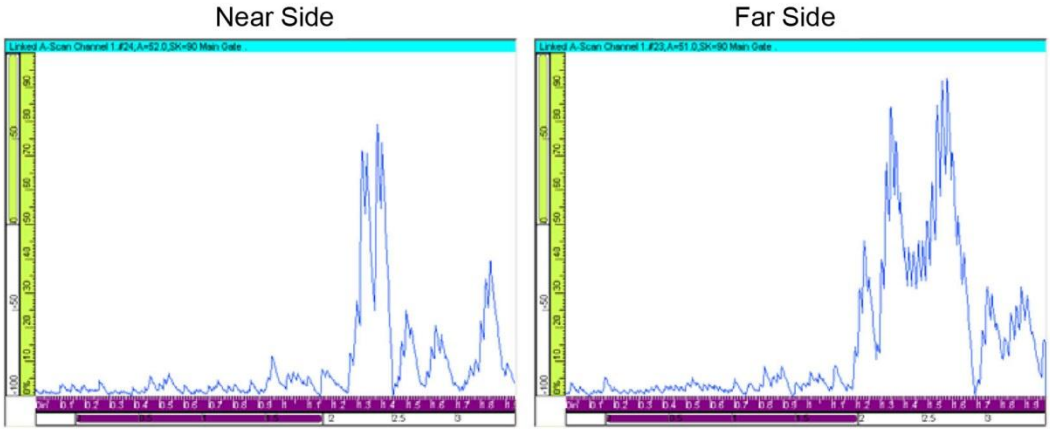

Figure 8.16 A-scan Views for the Ultrasonic Response from the EDM Notch in Weld Two from the Near and Far Side with the Longitudinal-Wave Array

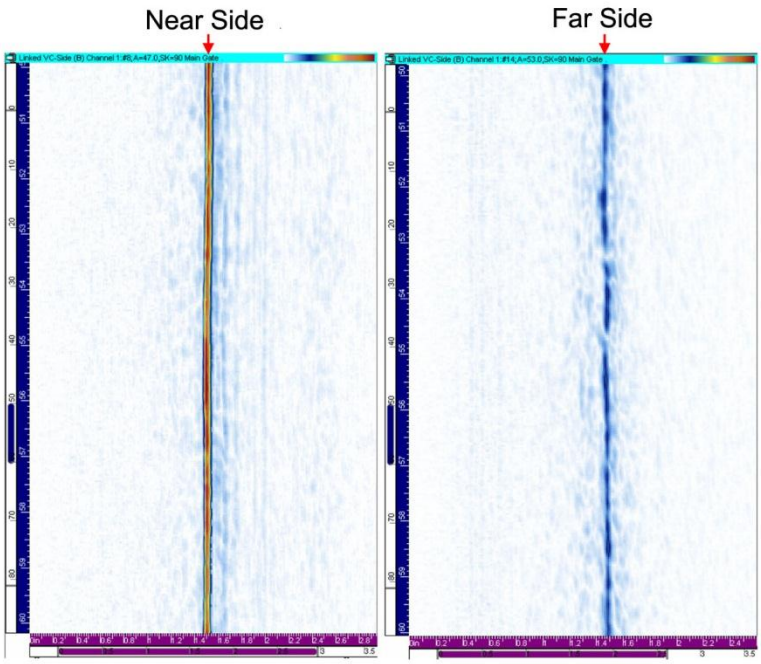

Figure 8.17 B-scan Views for the Ultrasonic Response from the EDM Notch in Weld Two from the Near and Far Side with the Shear-Wave Array. Arrows Mark the Notch Response.

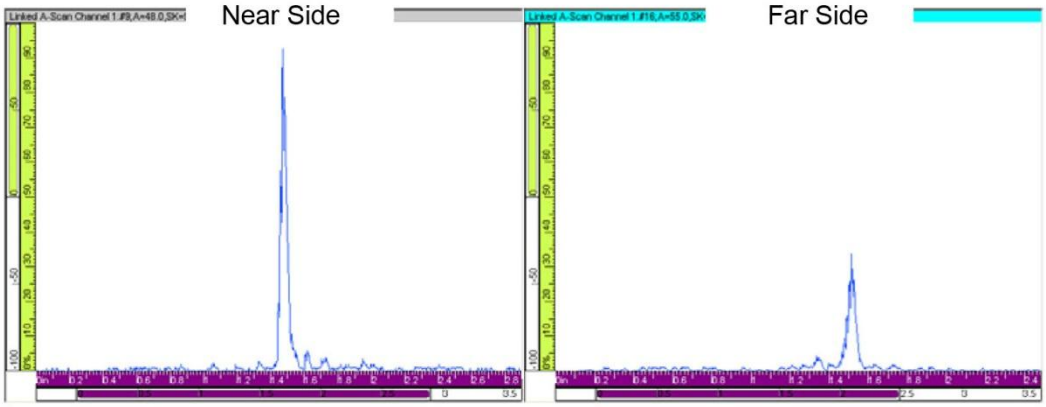

Figure 8.18 A-scan Views for the Ultrasonic Response from the EDM Notch in Weld Two from the Near and Far Side with the Shear-Wave Array

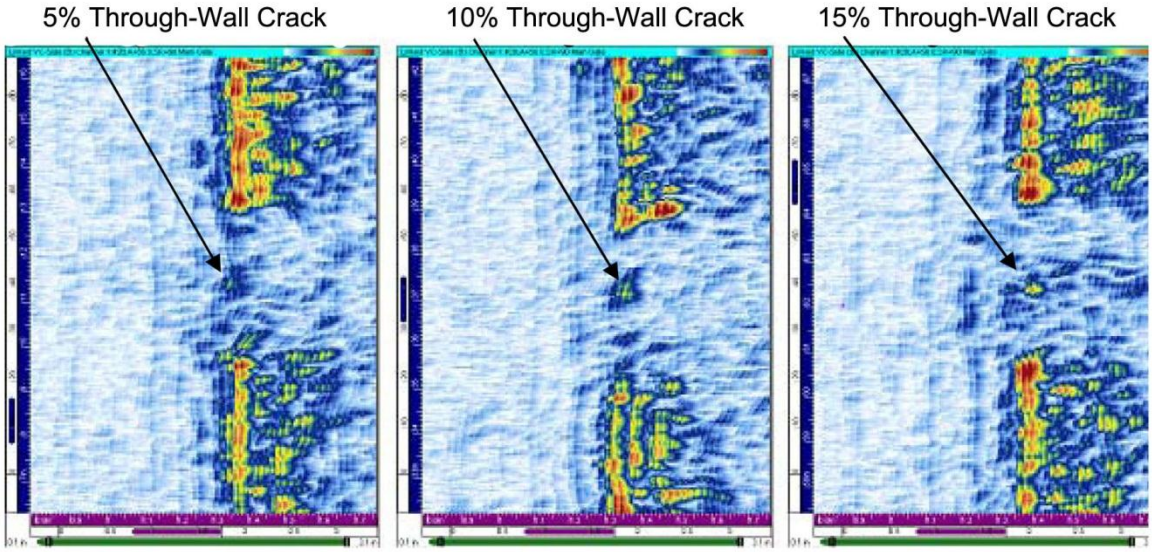

Figure 8.19 B-scan Views for the Ultrasonic Response from the Three Implanted Cracks in Weld Two from the Far Side with the Longitudinal-Wave Array.

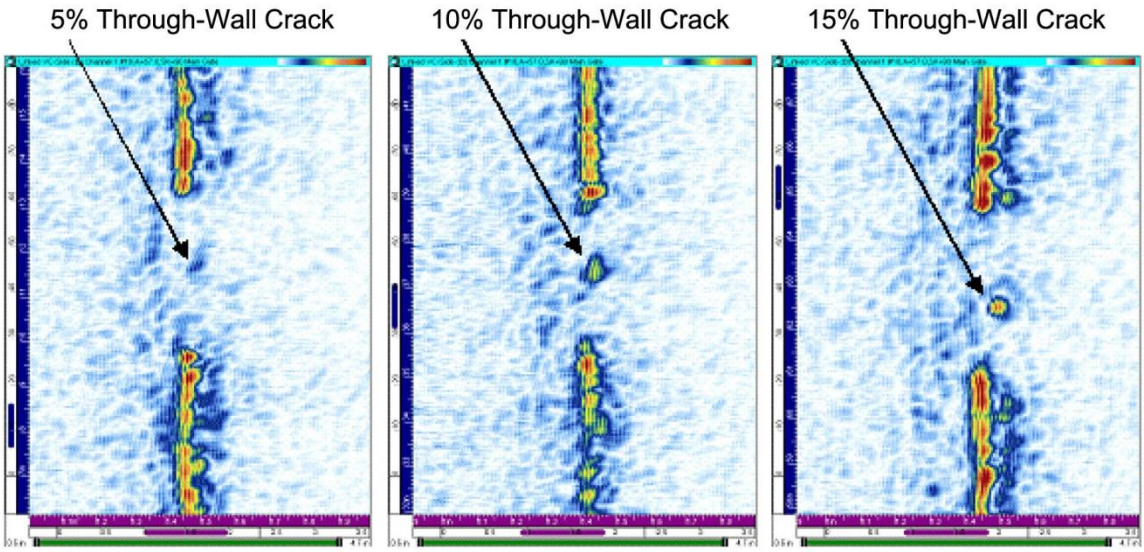

Figure 8.20 B-scan Views for the Ultrasonic Response from the Three Implanted Cracks in Weld Two from the Far Side with the Shear-Wave Array

While the lack of tip signals is a barrier to depth-sizing the cracks, length-sizing is possible. The flaws were consistently oversized by both the TRL and TRS arrays, but the values were well within the ASME Code acceptance criterion of 19-mm (0.75-in.) RMSE. Table 8.2 shows the results of the length sizing using the 6 dB drop and LOS-sizing methods.

Table 8.2 Thermal Fatigue Crack Lengths in Weld Two of Pipe Specimen 3C-022 as Measured by the TRL and TRS Arrays

		Far Side			
		TRL Results		TRS Results	
Crack	Actual Length	TRS −6 dB	TRS LOS	TRS −6 dB	TRS LOS
4	3.6 mm (0.14 in.)	23.6 mm (0.93 in.)	25.4 mm (1.00 in.)	16.0 mm (0.63 in.)	18.0 mm (0.71 in.)
5	7.1 mm (0.28 in.)	9.0 mm (0.35 in.)	22.0 mm (0.87 in.)	15.0 mm (0.59 in.)	24.0 mm (0.95 in.)
6	10.7 mm (0.42 in.)	4.0 mm (0.16 in.)	7.6 mm (0.30 in.)	9.0 mm (0.35 in.)	14.5 mm (0.57 in.)
RMS Error		12.2 mm (0.48 in.)	15.7 mm (0.62 in.)	8.6 mm (0.34 in.)	13.0 mm (0.51 in.)

8.3.3 Weld Three

The 10% through-wall notch in the HAZ of weld three (water-backed) was examined using the TRL and TRS arrays. A sample region of the ultrasonic response of the 10% notch is shown in Figure 8.21. The dead zone near the top of both scans is caused by the L-seam weld in the

pipe. As in weld one, both figures are shown with the gain set so that the maximum noise level was 20% FSH.

As in weld one, there was no correlation with the overall azimuthal position on the quality of the ultrasonic response; that is, the ultrasonic response from the 10% notch at the 12 o'clock position is essentially the same as the ultrasonic response at the 6 o'clock position. Again, as in the air-backed weld one, the ultrasonic response can randomly vary strongly over the weld length, and the response from the 10% notch appears as a string of high-intensity points connected by lower-intensity regions. The TRS array had a higher SNR compared to the TRL array.

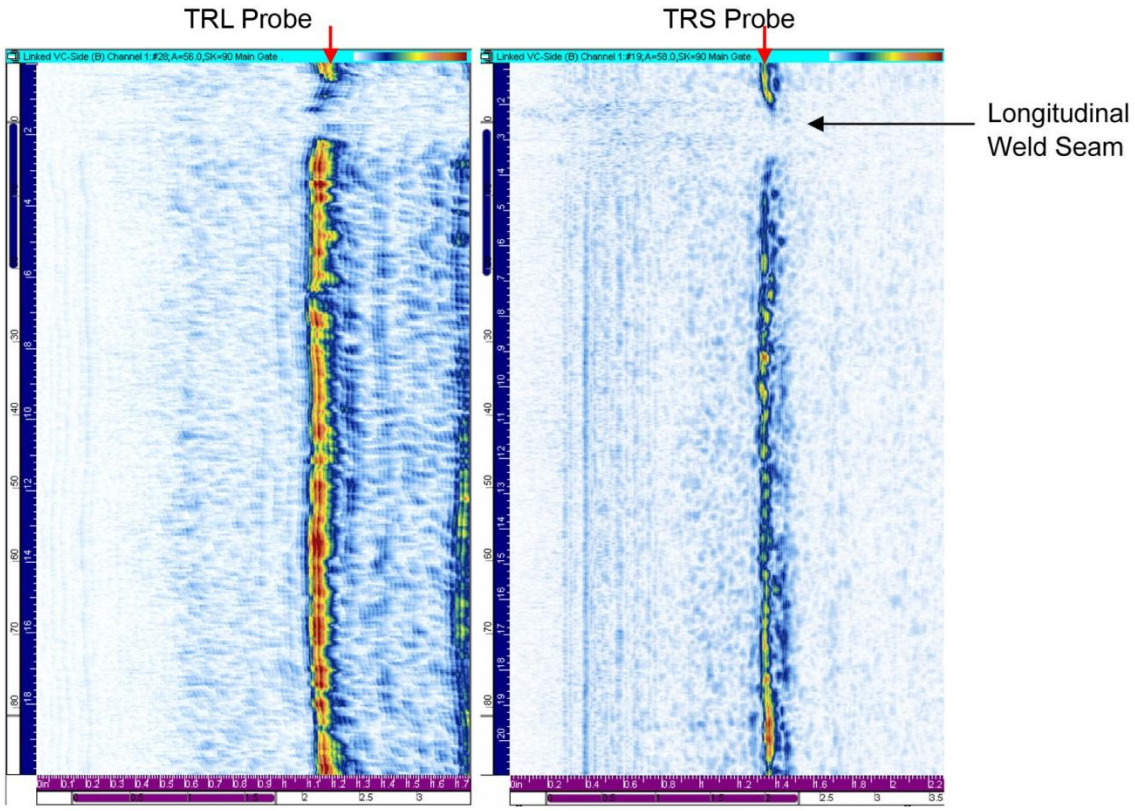

Figure 8.21 B-scan Views for the Ultrasonic Response for the 10% Notch in Weld Three from the Far Side with the Longitudinal- and Shear-Wave Arrays. Arrows Mark the Notch Response.

9 Discussion

The technical discussion presented in this section is focused on efforts conducted for the assessment of Phase 1 and Phase 2 evaluations, where conventional-UT, low-frequency/SAFT-UT and phased array-UT were assessed on specimens 02-24-15 and 3C-022.

9.1 Conventional UT – Phase 1

The Phase 1 results show that the 60° and 70° 1.5-MHz probes used together can detect and length-size flaws through welds in wrought austenitic piping. All of the circumferential flaws were detected, and the subsequent length-sizing was accurate enough to meet the ASME Section XI, Appendix VIII requirements. It was not possible to depth-size the flaws from the far side of the welds, as there were no tip signals detected. Depth-sizing is complicated by the high noise levels associated with through-weld inspections, as the noise can in some circumstances mimic a tip signal and provide false depth information.

The automated scanning, digital data collection, and electronic post-scan analysis provided improved detection and more accurate length-sizing results than the manual ultrasonic tests performed in 2002. In the 2002 manual scans, crack A was considered undetectable and crack E was only detectable with medium confidence. The 70° shear-wave automated scan can clearly detect crack A, and crack E is clearly detectable by both the 60° and 70° automated scans. The automated scans are able to detect implanted cracks as small as 5% through-wall from the near side of the weld and cracks as small as 10% through-wall from the far side. The main drawback of the automated scanning is the very long scan times. Under laboratory conditions, one circumferential scan of a 610-mm (24.0-in.) diameter pipe takes over four hours. If one wants to scan a pipe using multiple angles, this becomes prohibitive for inspections in the field. Also, the 60° probe would not be able to insonify the region of interest on the far side of the weld unless the weld crown has been removed so as to be flush with the pipe.

9.2 Conventional UT – Phase 2

The Phase 2 work showed that the welding process had little effect on the ultrasonic response from a 10% through-wall notch on the far side of the weld. The signal-to-noise ratio for weld one was slightly better than the SNR for weld three. The amplitude of the response from the 10% through-wall notch varies along the scans. There was no effect in the azimuthal position along the weld on the ultrasonic response of the 10% notch through the welds. The amplitude response from the 10% through-wall notch near the 12 o'clock positions is virtually identical to the responses from the 3 and 6 o'clock positions, despite the different positions during welding. These results strongly suggest that the Phase 1 results on a shop-welded pipe specimen are valid for field-welded specimens.

One method for potentially improving the conventional scanning would be the use of longitudinal-wave probes for possible tip-diffracted signals. While the shear waves were very effective at detecting the corner trap responses without any confusing mode-converted signals, the shear-wave probes were not able to provide any tip signals.

9.3 Low-Frequency/SAFT-UT – Phase 1

The low-frequency/SAFT inspection technique uses lower frequencies to employ longer wavelengths and thereby improve penetration and reduce the attenuative effects typically attributed to microstructure and weld geometry. In the case of 304 wrought stainless steel piping components, it is the austenitic weldment that contributes to reducing the inspection effectiveness as the weld structure is attenuative to standard inspection frequencies. Coupled with the requirement to reliably and consistently detect cracks from the far side of the weld, these inspections are often difficult to conduct with standard inspection techniques used in industry. In addition, typical weld crowns quite often preclude the use of inspection angles less than 60°, limiting the inspections that can be conducted and thereby reducing the capability to employ effective inspection protocols from the far side. In this evaluation, the weld crowns were ground smooth and the inspection methodologies were provided opportunities for the use of shallow angles from 30° through 70° in both the longitudinal- and shear-wave modalities. Although the LF/SAFT inspection technique takes advantage of lower frequencies for improved penetration and reduction of microstructural and geometric attenuation, the performance of the technique is also reduced as the wavelength is too long and the sound-field dimensions too large for detection of smaller flaws. By employing advanced signal processing in the form of the SAFT post-processing methodology, some degree of resolution can be maintained while using lower frequencies.

As expected, many of the smaller introduced flaws were not consistently detected, and some introduced flaws were not detected at all with any combination of employed frequency, wave-mode, or incident angle. In large part, this is attributed to the resolution issues described here; however, physical size of the transducers and key sound-field parameters also play a role in the detection system's ability to detect flaws in these materials. The inspection technique has been primarily developed for thicker section, primary loop cast stainless steel components, 5.8-cm (2.3-in.) thick and greater, where the sound path lengths typically range from 8.9 cm to 18.6 cm (3.5 to 7.3 in.). In this study, the transducers and associated wedges were modified and fabricated to conform to the smaller diameter and smaller wall thickness dimensions, 3.6-cm (1.4-in.) thick, of the wrought piping components evaluated here. Typical sound path lengths in this study ranged from 5.0 cm to 10.4 cm (2.0 to 4.1 in.). The "footprint" or contacting surface area of the transducer/wedge configuration against the part surface was still rather large for these components, as coupling, smooth translation of the transducer over the part surface, and overall sound field dimensions limited the effectiveness of the technique for detection of smaller flaws. Table 9.1 shows the detection results for the LF/SAFT inspection technique as a function of wave-mode and incident angle for 250-kHz far-side inspections of each piping segment. "D" represents a detected flaw, "ND" represents not detected, and "--" means that the specific scan combination was not conducted.

Table 9.1 illustrates the detection performance for the inspection technique at 250 kHz, and indicates that the 70° longitudinal-wave scans were generally successful in detecting the vast majority of the introduced flaws in all three piping segments. This particular scan combination demonstrated an optimal balance between penetration capabilities, resolution, and reduction of signal clutter and noise due to the microstructure and austenitic weld material. This frequency-angle-modality combination proved to be the most effective and consistent at detecting the

introduced flaws provided for this study. Table 9.2 shows the detection results for the LF/SAFT inspection technique as a function of wave-mode and incident angle for 400-kHz far-side inspections of each piping segment. Again, the same nomenclature is used for Table 9.2. As the frequency increases to 400 kHz, the data shows a reduction in resolution and detection capabilities. In the longitudinal mode, the 45° 250-kHz scan combination did not provide useful detection data even though the weld crowns were ground smooth. This is primarily due to a large portion of the energy being mode-converted. Because the corner-trap signal responses peak at 45°, the poor detection performance at this angle may also be attributed to the fact that the main lobe of the sound field at 45° must propagate through the thickest portion of the weld volume, thereby encountering more scattering and attenuation from the austenitic weld structure

Table 9.1 Summary of Detection Results for the 250-kHz Low-Frequency/SAFT Inspection Technique

Introduced Flaw	70°L	60°L	45°L	70°S	60°S	45°S
Sawcut A	ND	--	ND	--	--	--
Flaw A	ND	--	ND	--	--	--
Sawcut B	D	--	ND	--	--	--
Flaw B	D	--	ND	--	--	--
Sawcut C	D	--	ND	--	--	--
Sawcut D	D	--	ND	D	D	D
Flaw C	D	--	ND	ND	D	D
Sawcut E	D	--	ND	ND	ND	ND
Sawcut F	D	--	D	ND	ND	D
Flaw D	ND	--	ND	--	--	--
Sawcut G	D	--	D	--	--	--
Sawcut H	D	--	D	--	--	--
Flaw E	D	--	ND	--	--	--

Table 9.2 Summary of Detection Results for the 400-kHz Low-Frequency/SAFT Inspection Technique

Introduced Flaw	70°L	60°L	45°L	70°S	60°S	45°S
Sawcut A	ND	ND	D	ND	ND	D
Flaw A	ND	ND	ND	ND	ND	ND
Sawcut B	D	D	D	ND	D	D
Flaw B	D	D	ND	ND	D	D
Sawcut C	ND	ND	ND	ND	ND	ND
Sawcut D	ND	ND	ND	ND	D	D
Flaw C	ND	ND	ND	ND	D	D
Sawcut E	ND	ND	ND	ND	ND	ND
Sawcut F	ND	ND	D	ND	ND	ND
Flaw D	ND	ND	ND	ND	ND	ND
Sawcut G	D	D	D	ND	D	D
Sawcut H	D	D	D	ND	D	D
Flaw E	D	ND	ND	ND	D	D

than the 70° sound field. The higher angle of incidence directs the sound field toward the lower sections of the weld, where the distance across the austenitic weld material is shorter. This, in turn, means that the sound field encounters less weld material and attenuation effects are reduced when employing larger incident angles.

At 400 kHz, the overall detection performance is less effective than the lower-frequency (250-kHz) inspections, and although both conventional and phased-array technologies should provide strong performance results, the reason for the reduced 400-kHz performance is not well understood. The longitudinal-wave modality is generally not as effective as the shear-wave results especially when compared to the 45° and 60° incident angles. Table 9.2 illustrates the trends in reduced detection performance. The 70° shear-wave inspection mode provided no useful information for detection of any introduced flaws in the piping segments. It is seen from the data provided in Appendix D that the general background noise levels increased at 400 kHz, adding to the reduced capability for resolving SAAs and detecting introduced flaws from the data. The significant decrease in detection performance (and general increase in background noise) associated with a relatively small increase in inspection frequency (from 250 kHz to 400 kHz) is not well understood. As noted in this study, both the conventional method and the phased-array technique are operating at much higher frequencies, and both of these methods are shown to exhibit more effective detection performance using the same wave modality. The 45° and 60° shear-wave results indicate promising detection performance; however, sawcuts C, E, and F were not detected, revealing the inconsistency so prevalent in the 400-kHz data.

It should also be noted that to effectively meet project milestones within the constraints of scope and budget, the number of scan combinations were optimized and reduced from initial plans to conduct the entire range of scan-angle-frequency-mode combinations. In reviewing the 250-kHz data, the acquisition of 45° and 60° shear-wave scans for piping segments 1 and 3 would definitely have provided additional insight into the detection performance results for the lower-frequency inspections.

Regarding length-sizing accuracy, the LF/SAFT inspection technique again is limited by the resolution issues described earlier. The longer wavelengths will not provide the resolution for accurate sizing as only the deepest portions of the introduced flaws will be detected and the size of the wavelength relative to the flaw size tends to smear the actual SAA in the SAFT-processed images, thereby making sizing of small flaws difficult to accurately determine. Table 9.3 summarizes the −6 dB drop length-sizing results for the LF/SAFT inspection technique as a function of incident angle and wave mode for 250-kHz data relative to the true-state values for each introduced flaw. Dimensions are in centimeters. Again, an “ND” represents not detected, and “--" means that the specific scan combination was not conducted.

Table 9.4 summarizes the LOS length-sizing results for the LF/SAFT inspection technique as a function of incident angle and wave mode for 250-kHz data relative to the true-state values for each introduced flaw. Dimensions are in centimeters. The nomenclature used is the same as in Table 9.3.

In general, the data shown in Table 9.3 show well-correlated measured length values for the 70° L-wave inspection mode with the exception of crack C and sawcut G.

Table 9.3 Summary of Length-Sizing Results for the 250-kHz Low-Frequency/SAFT Inspection Technique Using the −6 dB Drop Method

Introduced Flaw	True-State Length (cm)	70°L Measured Length (cm)	60°L Measured Length (cm)	45°L Measured Length (cm)	70°S Measured Length (cm)	60°S Measured Length (cm)	45°S Measured Length (cm)
Sawcut A	3.28	ND	--	ND	--	--	--
Flaw A	1.07	ND	--	ND	--	--	--
Sawcut B	6.52	6.35	--	ND	--	--	--
Flaw B	3.05	3.05	--	ND	--	--	--
Sawcut C	3.63	3.30	--	ND	--	--	--
Sawcut D	5.41	5.84	--	ND	3.30	2.29	4.06
Flaw C	4.36	2.54	--	ND	ND	4.32	5.97
Sawcut E	4.37	4.57	--	ND	ND	ND	ND
Sawcut F	5.97	4.19	--	4.83	ND	ND	3.43
Flaw D	1.33	ND	--	ND	--	--	--
Sawcut G	5.73	10.9	--	7.62	--	--	--
Sawcut H	6.84	6.35	--	8.13	--	--	--
Flaw E	3.38	3.30	--	ND	--	--	--
RMS Error		1.84	N/A	1.48	2.11	2.21	1.90

Table 9.4 Summary of Length-Sizing Results for the 250-kHz Low-Frequency/SAFT Inspection Technique Using the Loss-of-Signal Method

Introduced Flaw	True-State Length (cm)	70°L Measured Length (cm)	60°L Measured Length (cm)	45°L Measured Length (cm)	70°S Measured Length (cm)	60°S Measured Length (cm)	45°S Measured Length (cm)
Sawcut A	3.28	ND	--	ND	--	--	--
Flaw A	1.07	ND	--	ND	--	--	--
Sawcut B	6.52	6.60	--	ND	--	--	--
Flaw B	3.05	3.05	--	ND	--	--	--
Sawcut C	3.63	3.81	--	ND	--	--	--
Sawcut D	5.41	9.02	--	ND	3.30	3.30	4.06
Flaw C	4.36	3.43	--	ND	ND	5.08	6.48
Sawcut E	4.37	5.21	--	ND	ND	ND	ND
Sawcut F	5.97	5.84	--	4.83	ND	ND	4.70
Flaw D	1.33	ND	--	ND	--	--	--
Sawcut G	5.73	11.2	--	7.87	--	--	--
Sawcut H	6.84	6.10	--	8.13	--	--	--
Flaw E	3.38	3.30	--	ND	--	--	--
RMS Error		2.12	n/a	1.59	2.11	1.58	1.63

Table 9.5 summarizes the −6 dB drop length-sizing results for the LF/SAFT inspection technique as a function of incident angle and wave mode for 400-kHz data relative to the true-state values for each introduced flaw. Dimensions are again in centimeters and the nomenclature remains the same as in previous tables.

Table 9.5 Summary of Length-Sizing Results for the 400-kHz Low-Frequency/SAFT Inspection Technique Using the −6 dB Drop Method

Introduced Flaw	True-State Length (cm)	70°L Measured Length (cm)	60°L Measured Length (cm)	45°L Measured Length (cm)	70°S Measured Length (cm)	60°S Measured Length (cm)	45°S Measured Length (cm)
Sawcut A	3.28	ND	ND	3.56	ND	ND	4.32
Flaw A	1.07	ND	ND	ND	ND	ND	ND
Sawcut B	6.52	3.81	3.05	7.87	ND	4.32	5.33
Flaw B	3.05	2.79	1.52	ND	ND	2.79	3.30
Sawcut C	3.63	ND	ND	ND	ND	ND	ND
Sawcut D	5.41	ND	ND	ND	ND	3.81	5.33
Flaw C	4.36	ND	ND	ND	ND	4.83	5.08
Sawcut E	4.37	ND	ND	ND	ND	ND	ND
Sawcut F	5.97	ND	ND	4.83	ND	ND	ND
Flaw D	1.33	ND	ND	ND	ND	ND	ND
Sawcut G	5.73	6.10	4.32	5.59	ND	5.33	1.78
Sawcut H	6.84	5.33	4.83	5.84	ND	3.05	4.83
Flaw E	3.38	2.79	ND	ND	ND	2.03	3.30
RMS Error		1.43	2.26	0.92	n/a	1.85	1.69

Table 9.6 summarizes the LOS length-sizing results for the LF/SAFT inspection technique as a function of incident angle and wave mode for 400-kHz data relative to the true-state values for each introduced flaw. Dimensions are again in centimeters and the nomenclature remains the same as in previous tables.

A review of Table 9.5 shows that no trend is evident, the length-sizing results are less accurate, and vary in both oversizing and undersizing of the true-state lengths in apparently random fashion. From the −6 dB drop length-sizing method, the data indicates that the 45° shear-wave inspection was more accurate (in a relative sense) in determining the introduced flaw lengths than the other modes at 400 kHz. Table 9.6 depicting the LOS measured length values also shows no trends regarding oversizing or undersizing the true-state lengths. In general, the LOS method is less accurate than the −6 dB drop method from a review of the 400-kHz data.

Table 9.6 Summary of Length-Sizing Results for the 400-kHz Low-Frequency/SAFT Inspection Technique Using the Loss-of-Signal Method

Introduced Flaw	True-State Length (cm)	70°L Measured Length (cm)	60°L Measured Length (cm)	45°L Measured Length (cm)	70°S Measured Length (cm)	60°S Measured Length (cm)	45°S Measured Length (cm)
Sawcut A	3.28	ND	ND	4.57	ND	ND	3.81
Flaw A	1.07	ND	ND	ND	ND	ND	ND
Sawcut B	6.52	4.32	3.30	8.89	ND	5.59	5.84
Flaw B	3.05	2.79	2.03	ND	ND	2.79	3.05
Sawcut C	3.63	ND	ND	ND	ND	ND	ND
Sawcut D	5.41	ND	ND	ND	ND	3.56	5.59
Flaw C	4.36	ND	ND	ND	ND	5.59	4.83
Sawcut E	4.37	ND	ND	ND	ND	ND	ND
Sawcut F	5.97	ND	ND	5.33	ND	ND	ND
Flaw D	1.33	ND	ND	ND	ND	ND	ND
Sawcut G	5.73	6.86	3.81	5.33	ND	5.33	2.03
Sawcut H	6.84	6.35	5.08	7.11	ND	3.30	5.33
Flaw E	3.38	3.30	ND	ND	ND	4.06	3.30
RMS Error		1.13	2.13	1.26	n/a	1.65	1.46

In summary, the detection performance results indicate that the 70° longitudinal-wave inspections at 250 kHz provide the most meaningful data and result in the best detection results of any of the scan combinations evaluated here. Crack A and crack D were by far the most difficult introduced flaws to detect, as neither introduced flaw was detected using any of the scan combinations in this study. These two thermal fatigue cracks were the smallest in the depth dimension. Regarding length-sizing, the 400-kHz inspections provided more accurate results (of those introduced flaws that were detected) in comparison to the true-state lengths, in particular for the 45° inspection angle. The LOS length-sizing method provided an RMSE of 3.4 mm (0.13 in.) for the 45° shear-wave inspections of thermal fatigue cracks, and proved to be the most accurate of the scan combinations. The −6 dB length-sizing method provided an RMSE of 9.2 mm (0.36 in.) for the 45° L-wave inspections for sawcuts. From the work reported here, it is shown that lower frequencies generally are not appropriate for the inspection problem in these piping components as the sound field is too large and the wavelength too long for effective detection and sizing of smaller cracks. With a range of longer wavelengths spanning 0.79 cm (0.31 in.) to 2.32 cm (0.91 in.) and the large zone-focal dimensions of the sound field (discussed in Section 6) employed in this study, the resolution is generally too low relative to the size of the introduced flaws. The application of the LF/SAFT inspection technique does, however, shed light on the effectiveness of lower examination frequencies and provides a general lower bound for the use of longer wavelengths for flaw detection from the far side.

9.4 Low-Frequency/SAFT-UT – Phase 2

The Phase 2 results show that the 400-kHz and 250-kHz probes are able to detect the 10% through-wall notch from the far side of the weld using a variety of angles and with both shear and longitudinal waves. The scans along welds one and three show that the amplitude of

the sound returning from the 10% through-wall notch is not strongly affected by the position of the pipe during the welding process.

None of the scans were able to detect the three implanted flaws in weld number two. The long wavelengths, 7.5 mm (0.3 in.) for the shear waves and 15 mm (0.6 in.) for the longitudinal waves, are larger than the 3.5-mm (0.14-in.) depth of the EDM notches, but are able to detect the EDM notches as they are very long and essentially fill the sound field with a continuous reflector. The implanted cracks are much shorter in length, with the 15% crack being only 10.7-mm (0.42-in.) wide. With the shear-wave probe, which has the smaller wavelength, the largest implanted flaw is less than half a wavelength deep and only slightly more than one wavelength long. While this is within the theoretical limit (½ of a wavelength) for resolving a defect, the defects are not detectable from the far side of the weld. The longitudinal waves are at the far limit of being able to detect the 15% through-wall crack, as this crack is much less than ½ of a wavelength deep and just over ½ of a wavelength long.

The different welding techniques did not strongly affect the amount of sound returning from the 10% through-wall notch. Table 9.7 shows the gains used when scanning the pipe specimen. The gains were chosen to provide a near-saturation response from the 10% through-wall notch and represent a rough measure of how well the weld transmits the ultrasound. Analysis of total system gain values indicate that the air-backed weld appears to be the most efficient at transmitting longitudinal waves. The water-backed weld appears to absorb 3–4 dB of the longitudinal waves when compared to the air-backed weld. The opposite was true for the shear waves, in which the water-backed weld absorbed 3 dB less sound than the air-backed weld.

Table 9.7 Gain (in dB) Settings Used for Scanning to Reach Near-Saturation for 10% Notch

	400 kHz		
	Air-Backed	**Middle Weld**	**Water-Backed**
45° Shear	33	35	30
45° Longitudinal	29	31	33
60° Longitudinal	29	30	33
70° Longitudinal	Na	29	30

	250 kHz		
	Air-Backed	**Middle Weld**	**Water-Backed**
45° Longitudinal	17	17	21
70° Longitudinal	17	16	20

The true benefit of using the LF/SAFT inspection technique is the composite approach taken when all incident angles, frequencies, and wave modes can be evaluated together to take a comprehensive approach to the inspection and use SAA redundancy to capture the true value in the detection and discrimination capabilities of this technique. In this study, each scan combination was evaluated on its own merit, and in reviewing the individual detection performance results, the 250-kHz, 70° L-wave scans offered the most reliable and consistent

combination of inspection parameters for effectively inspecting the piping segments from the far side. These results echo the conventional-UT inspection results, and also show that the addition of the 45° incident angle provides a suitable means for accurate length-sizing for using such a low-frequency regime. The LF/SAFT technique as employed in this study does not exploit the advantages of the SAFT signal processing algorithms to the fullest, as the zone-focused, low-frequency transducers provide a spatially wide but non-divergent sound field. For a SAFT-based inspection technique to hold any promise for addressing this inspection problem, a truly divergent beam (using a smaller transducer) and examination frequencies near 1–2 MHz might provide a more effective means for far-side detection and sizing of cracks through austenitic weld material. The SAFT signal processing enhancements are truly realized in three dimensions and the resultant focusing effects might very well provide a reliable and effective means for detection and sizing.

To provide the optimal conditions for employing and evaluating a SAFT-based inspection technique, a modeling and simulation effort is recommended. Modeling plays a key role in providing guidance for optimizing inspection frequencies, incident angles, and other important inspection parameters, and should be an integral part of strategic planning design of future experimental evaluations.

9.5 Phased-Array UT – Phase 1

The Phase 1 results show that the longitudinal-wave and the shear-wave arrays are both capable of detecting and length-sizing defects from the far side of a weld in wrought austenitic stainless steel piping. All circumferential flaws were detected, although crack A (15% through-wall) was difficult to discern from the weld-root response. For the TRL array, this is most likely due to the limited flaw face available for L-wave reflection, and the flaw face proximity (spatially and temporally) with weld-root responses. Because no corner-trap or tip-diffracted responses were evident from far-side flaws, only spectral reflectors can be used for detection. The TRS array was more effective in detecting the corner-trap response for crack A from the far side of the weld than the TRL array. This is the result of the better corner-trap response from shear waves and the larger aperture of the shear-wave array, allowing for a more tightly focused beam at the higher angles. Neither array was able to accurately depth-size the defects from the far side of the weld as crack-tip signals could not be detected. Also, a LOS technique may not be feasible, as many defects have ultrasonic responses that go beyond the highest angles used by the probe and the sound fields produced by the probes are larger than the smaller flaws. For an example of this, see the sector scan in Section 7, Figure 7.13.

The results from Phase 1 show that PA technology provides a viable alternative to conventional ultrasonic techniques for detecting service-induced flaws (cracking) on both the near and far side of austenitic piping welds. While this technology offers essentially the same sound fields as could be obtained with monolithic element (conventional) transducers, the ability to interrogate the weld with varied angular sound fields in near real time drastically reduces acquisition time on the component. During this study, full linear data scans of approximately 508 mm (20.0 in.) of circumferential weld were inspected in less than one minute for each segment of specimen 02-24-15. This included discrete data sets swept through angles of 30° to 70°, at 1° increments for the TRL array and 40° to 70° for the TRS array. If one attempted to

duplicate this volumetric scanning conventionally using raster scanning, multiple set-ups and scans for the same length of piping weld would exceed several hours and did, in fact, exceed several hours for a single transducer in our conventional-UT trials on the same pipe specimens. Also, the phased-array measurements can be made with the weld crowns in the as-welded condition, while the 60° and possibly the 70° conventional raster scanning would require the weld crowns to be machined off to acquire similar far-side weld data.

Another asset of PA technology is evident during data review. Analyses occur off-line, with the analyst having options to simultaneously display varied images of raw, or merged, data sets. Software features such as gating, sound field, and measurement cursors, as well as traditional time and amplitude presentations, enable one to initially screen the data for optimum responses (as related to angles of sound propagation and cross sections of the weld) and to target suspected flaw regions. This iterative operation is performed by moving the respective cursor though the sector scan (S-scan) image(s) based on a given sound-beam angle, then walking through the B- or C-scan image(s) to produce A-scans for that "slice" of material. Once the suspect regions have been identified, the analyst may call up different images and preferred ultrasonic angles to aid interpretation of these regions. Conventional ultrasonic imaging and analysis systems do not generally provide these capabilities for data fusion and manipulation. However, the PA analysis system flexibility and large sets (about 50 megabytes each) for each linear scan performed during the Phase 1 trials indicate that thorough analyses of field data for many welds may require significantly more time than data acquisition.

9.6 Phased Array-UT – Phase 2

The results from Phase 2 show that the ultrasonic response from a continuous feature on the far side of a weld can have variable amplitude along the feature’s length. This effect may cause the feature to appear as a series of shorter responses. While there was a strong centimeter-by-centimeter variability in the strength of the returning signal, the overall nature of the ultrasonic response from the 10% notches did not vary with the general azimuthal position along the field-like welds. In all welds of pipe specimen 3C-022, the ultrasonic response from the 10% through-wall notch was very similar in terms of positional variation. The results also show that the 1.4-mm (0.06-in.) wavelength shear waves are more strongly attenuated as they pass through the weld metal than the longitudinal waves with a 3.1-mm (0.12-in.) wavelength. While the longitudinal waves were redirected significantly as they passed through the weld, they were not strongly attenuated by the weld. The flaws in weld number two were detectable with both longitudinal- and shear-wave arrays from the far side of the weld.

The variation in amplitude response along the 10% notches may help explain the inability of the two arrays to detect tip signals from the far sides of the welds. While the longitudinal waves were better able to penetrate the weld metal, both the TRL and TRS arrays showed large variability in the response from a continuous 10% through-wall notch. This effect can be seen in the Phase 1 results as well.

There was little difference in the ultrasonic responses from standard reflectors with the different welding techniques used on the Phase 2 piping specimen. There was no evidence that suggests that the “down-hand” weld used in the Phase 1 pipe specimen is significantly different

from the field-like welds in the Phase-2 pipe specimen. Therefore, Phase 2 results strongly corroborate Phase 1 findings and show validity for field-welded piping.

There are several ways to improve flaw detectability and sizing from the far side of a weld in wrought austenitic materials. A larger-aperture longitudinal-wave probe should be better able to resolve the far-side defects, as it would have a more strongly focused beam at the higher angles. In addition, a lower-frequency longitudinal-wave probe would be better able to penetrate the weld metal. With the weld crowns removed, such a probe may be able to better depth-size the cracks by the loss-of-signal technique even in the absence of a tip signal. A lower-frequency longitudinal-wave array would also suffer less beam redirection in the material.

10 Longitudinal-Wave Sound-Field Assessments and Simulations

The evaluation of ultrasonic fields emitted from longitudinal-wave phased-array probes provides insights on the behavior of sound one might expect in a material undergoing volumetric examination. Computer simulations of these same sound fields in parallel with the actual characterizations allows one to verify that the focal laws employed for a given phased-array probe will produce adequate beam steering with sufficient field densities and provide focusing at the desired depth within the material.

Beam simulations and sound-field characterizations were performed for a 1.5-MHz, 1.5-D matrix phased-array longitudinal-wave probe on an austenitic stainless steel coupon at several incident angles and focal depths. These simulations were performed along with sound-field characterizations using commercial modeling software to verify and validate the phased-array focal laws. Focal laws were generated using the wrought austenitic piping and Rexolite wedge material properties, and manufacturer-supplied phased-array parameters (e.g., frequency, number of elements, element spacing, etc.) in conjunction with the specified wave mode, focal depth, sample volume, and incident angle(s).

The objective of the beam mapping exercise is to evaluate the effectiveness and coherence of phased-array sound-field propagation through wrought stainless steel (WSS) components with austenitic welds. This evaluation was conducted as a function of discrete incident angle, focal depth in the material, and probe position relative to the weld centerline. The sound fields were imaged through both parent material, WSS, and through parent material plus austenitic weld material, and subsequently analyzed visually for degradation effects (scattering, attenuation, field partitioning, etc.) and by measuring signal-to-noise and sound field dimensions (in both X- and Y-axes) at the −6 dB and −10 dB points. Longitudinal-wave sound fields produced by the PA probe were evaluated through a 36-mm (1.4-in.) thick WSS coupon at several discrete angles. The coupon was extracted from a larger WSS piping component with an austenitic weld (a small coupon from specimen 3C-022 was used). One end of the coupon is comprised of an austenitic weld that was cut along the weld fusion line while the bulk of the coupon is comprised of WSS parent material. Both ends of the coupon were cut at a 60° angle, representative of a single-V counterbore, and then machined to accommodate sound-field characterizations. This provided the capability to obtain sound-field maps of identical inspection parameters through both WSS (alone), and through WSS plus the austenitic weld material. Figure 10.1 illustrates different views of the WSS coupon used in this study.

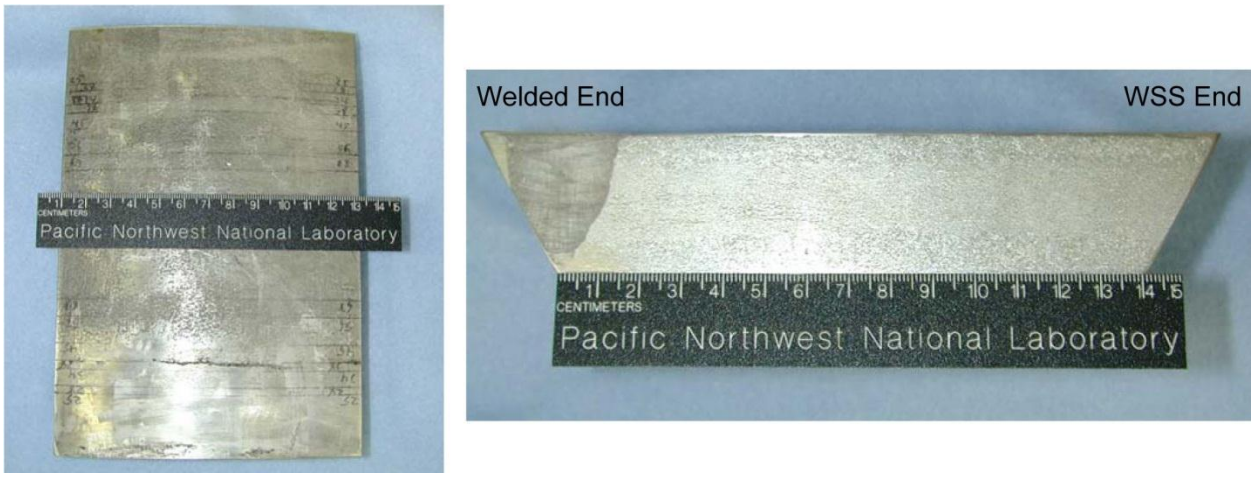

Figure 10.1 WSS Coupon Used for Sound Field Mapping. Left: Top view of WSS coupon with positional markings for probe position of various sound-field scans. Right: Side view of WSS coupon showing the austenitic weld and WSS material.

A hybrid immersion-scanning configuration where the water level in the scanning tank was filled so that the receiver pin-transducer was completely immersed while only the elements of the transmit PA probe were immersed. This was necessary in order to protect the electrical connections in the PA probe, which was not designed for full immersion. Sound fields generated by the transmitting PA probe were mapped at different incident angles and focal depths. The calculated exit point on the PA probe-wedge configuration was positioned at theoretical locations from the inspection ends of the coupon to achieve focusing at the plane of interest at focal depths of 15 mm (0.59 in.) and 25 mm (0.98 in.) for the various incident angles. See Table 10.1 for a matrix of the sound-field evaluations performed. Figure 10.2 shows a schematic setup for incident angle 70° with a focal depth of 15 mm (0.59 in.). For data acquisition, the assembly is rotated to position the 60° cut end in a horizontal plane, parallel to the scanning bridge.

Table 10.1 Sound Field Mapping Parameter Matrix for Data Acquired from Both Ends of the Coupon

Focal Depth	Incident Angle	Distance Back from Coupon Edge
15 mm (0.59 in.)	70°	57 mm (2.24 in.)
25 mm (0.98 in.)	50°	50 mm (1.97 in.)
25 mm (0.98 in.)	60°	64 mm (2.52 in.)

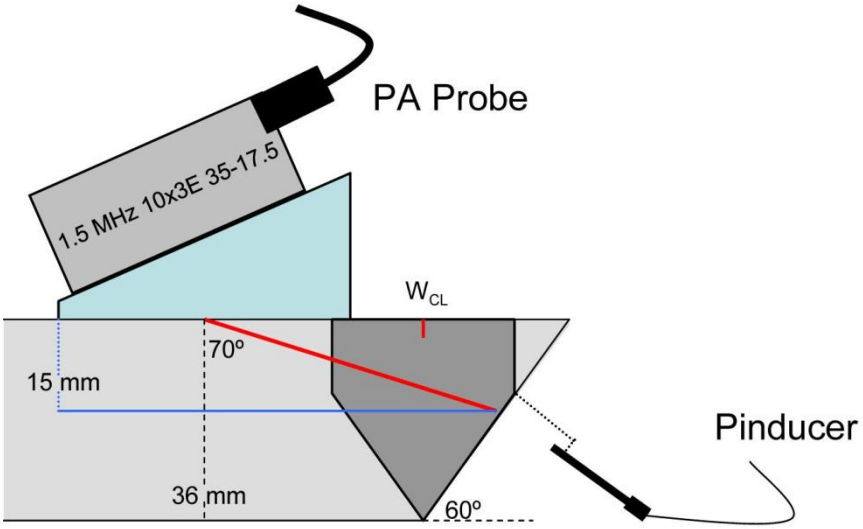

Figure 10.2 Side View Schematic Showing Orientations of PA Probe, Specimen, and Pinducer

Prior to scanning, the WSS coupon was fitted with a PA probe and then mounted in a fixture that allowed free positioning (rotation) of the coupon and the probe assembly (Figure 10.3). The coupon was leveled relative to the X-Y scanning bridge (C-scan plane). The picture on the left in Figure 10.3 shows the transmit/receive longitudinal probe mounted on a Rexolite wedge and secured to the specimen using latex banding. Note that for this mapping study, only the transmit side of the probe was active and was operated in this mode via the ZETEC Tomoscan III phased-array system (Figure 10.4). Using ZETEC's UltraVision 1.2R4 software package to control the Tomoscan III, the probe was pulsed with an 180V, 330-nsec square-wave signal (optimized for 1.5 MHz) with the desired output being a longitudinal-wave signal focused at the coupon face of interest.

A Valpey-Fisher pinducer was chosen to be the receiver in this study. It has a 1.5-mm (0.059-in.) diameter active aperture and a flat bandwidth of DC to 20 MHz in the receive mode. This type of miniature transducer was originally designed for shock-wave applications. More recently, newer applications have been identified where these probes are used as acoustic emission receivers and for sound-field characterization of ultrasonic transducers. Valpey-Fisher has developed these custom pinducers by incorporating standard NDT fabrication techniques, such as quarter-wave matching layers and dense backings, to dramatically increase bandwidth and sensitivity.

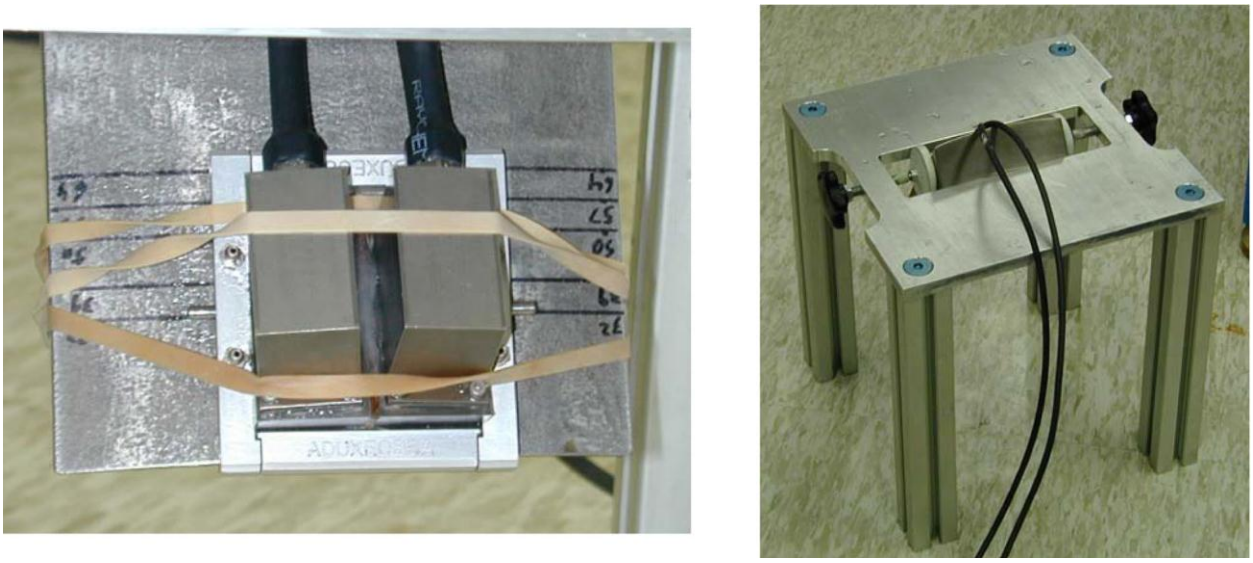

Figure 10.3 Left: Phased Array Probe Mounted and Secured on Austenitic WSS Coupon; Right: Coupon Positioning Fixture for Sound Field Mapping

Figure 10.4 Phased-Array Data Acquisition System

Operating in a through-transmission configuration, the broadband pinducer acted as the receiver and was raster-scanned under the end of the coupon being characterized (Figure 10.5). Raster scanning set up involved using the PNNL-developed SAFT acquisition software to control the XYZR scanning bridge. The pinducer was attached via epoxy and zip

ties to the end of a search tube and positioned normal to and under the face of the coupon to be scanned. The offset distance to the specimen (water path) was approximately 2 mm (0.08 in.). A quick and coarse XY raster scan with resolution of 2.54 mm (0.1 in.) in both axes was acquired so that adjustments could be made if necessary to place the beam response in the center of the C-scan view. Additionally, the maximum response in the image was adjusted to avoid saturation. The final raster scan resolution was set at 0.25 mm (0.01 in.) in the scan direction and 0.25 mm (0.01 in.) in the index direction over a total area of 25.4 mm × 25.4 mm (1.0 in. × 1.0 in.). The selected scanning resolution and area is sufficient to capture and show the resulting sound fields at a high degree of precision because at 1.5 MHz the wavelength in this material is on the order of 4 mm (0.15 in.). At this resolution, the mapping exercise will show minor changes/distortions in the shape and intensity of the sound fields.

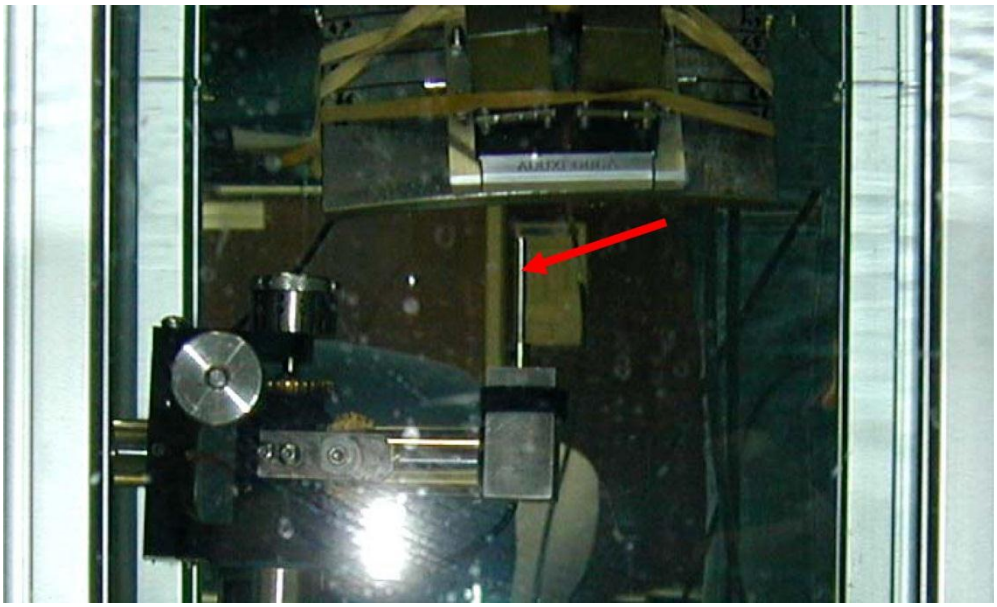

Figure 10.5 Pinducer (highlighted by red arrow) Positioned Just Beneath a Coupon End During Beam Mapping. Side view through Plexiglas wall of automated immersion scanning tank.

The received signals from the pinducer were routed to a Ritec ultrasonic receive amplifier, where the signals were filtered and conditioned prior to digital sampling. Because the frequency to be mapped was 1.5 MHz, the receiver was set to filter out contributions below 100 kHz and above 3 MHz. This filtering reduces unwanted signals thus increasing the SNR of the beam image. The signal output from the Ritec receiver was routed to the SAFT data acquisition system where the analog signals were digitized (8-bit) and C-scan (X-Y axis) sound-field plots were generated and analyzed.

10.1 Results

The computer-generated beam simulations and the empirical sound-field maps resulting from specimen scans can be found in Figures 10.6–10.11. Figures 10.6, 10.8, and 10.10 display beam simulations with the B-scan side views on the left and B-scan end views on the right. An indication of focal length and position of maximum intensity are seen in the side views. The end views indicate the beam shape and size in the lateral – depth (y-z) plane. Figures 10.7, 10.9, and 10.11 display images acquired from scanning the end of the specimen at the 60° slant, as shown in Figure 10.2. The images in the left of these figures are from the WSS side of the specimen while the images on the right side are from the WSS plus weld material, and display sound field distortion in shape and coherence. Note that the data obtained from the actual specimen was along the 60° slant of the end while the beam simulation software is essentially on a 90° slant (vertical). The simulation display software only allows viewing of results along the three orthogonal axes. It should also be noted that the beam simulation only allows isotropic media.

Both the simulated beam images and the specimen data images were analyzed for size in the vertical and horizontal directions. Table 10.2 displays the sizing results from the beam simulations while Tables 10.3 and 10.4 provide measured information from the specimen images. The beams were sized at the −6 dB and −10 dB levels. Tables 10.3 and 10.4 additionally provide signal-to-noise ratios.

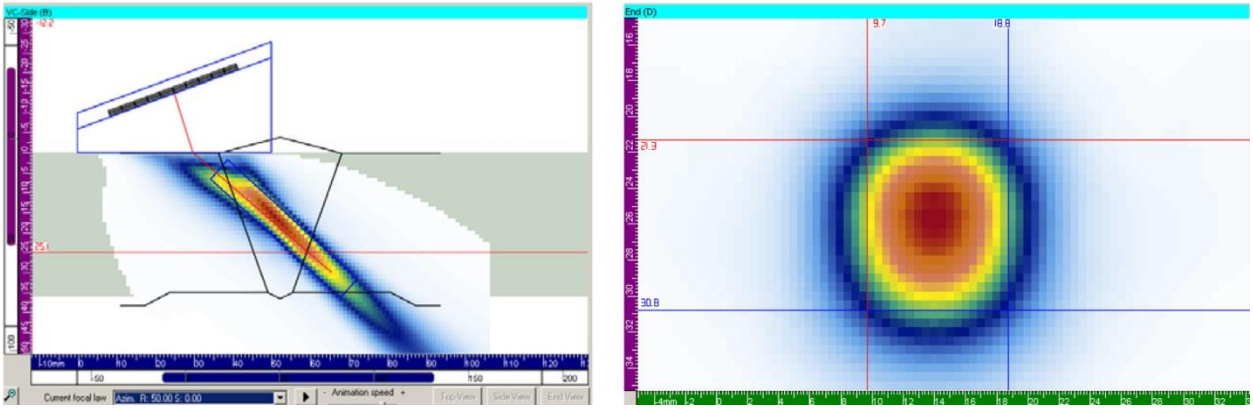

Figure 10.6 L-Wave Sound Beam Simulation at 50°, 25-mm (0.98-in.) Depth Focus; Side View on the Left and End View on the Right

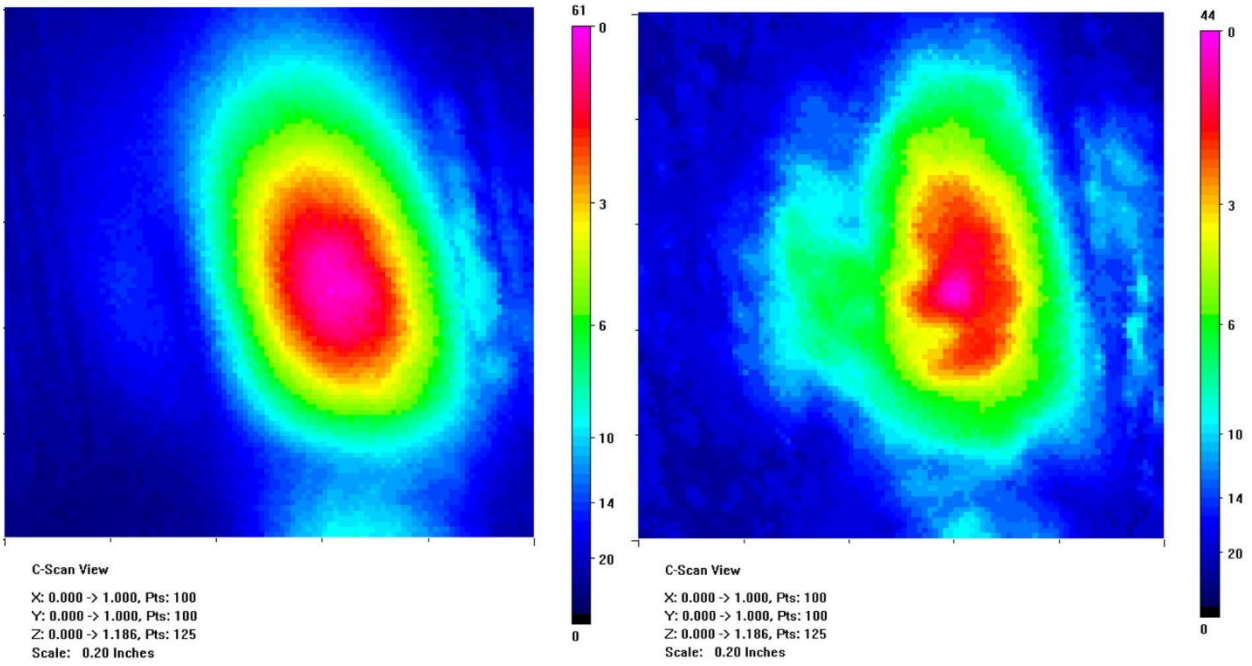

Figure 10.7 Data Images at 50°, 25-mm (0.98-in.) Depth Focus, 19 dB, 50 mm (1.9 in.) Back from WSS Side on the Left and from the Weld Side on the Right

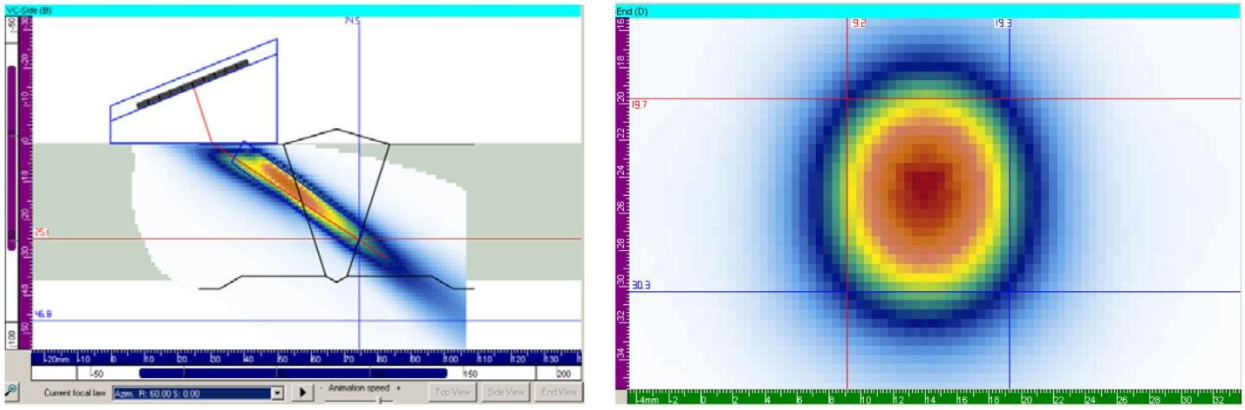

Figure 10.8 L-Wave Sound Beam Simulation at 60°, 25-mm (0.98-in.) Depth Focus; Side View on the Left and End View on the Right

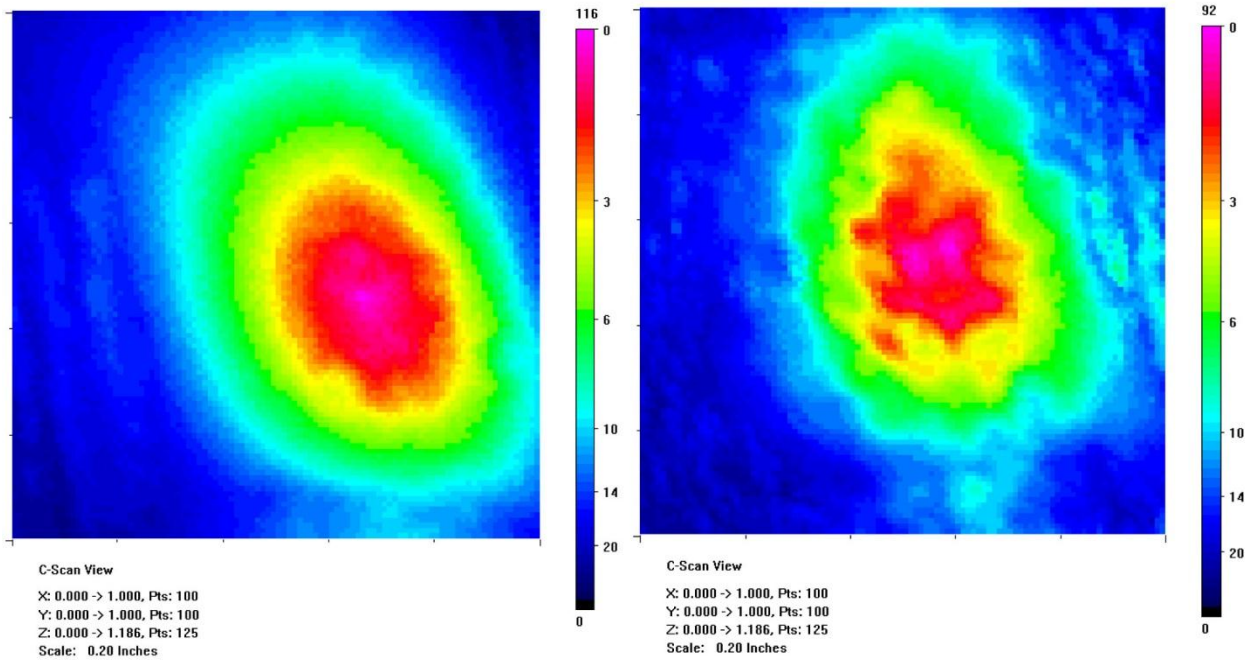

Figure 10.9 Data Images at 60°, 25-mm (0.98-in.) Depth Focus, 27 dB, 64 mm (2.5 in.) Back from WSS Side on the Left and from the Weld Side on the Right

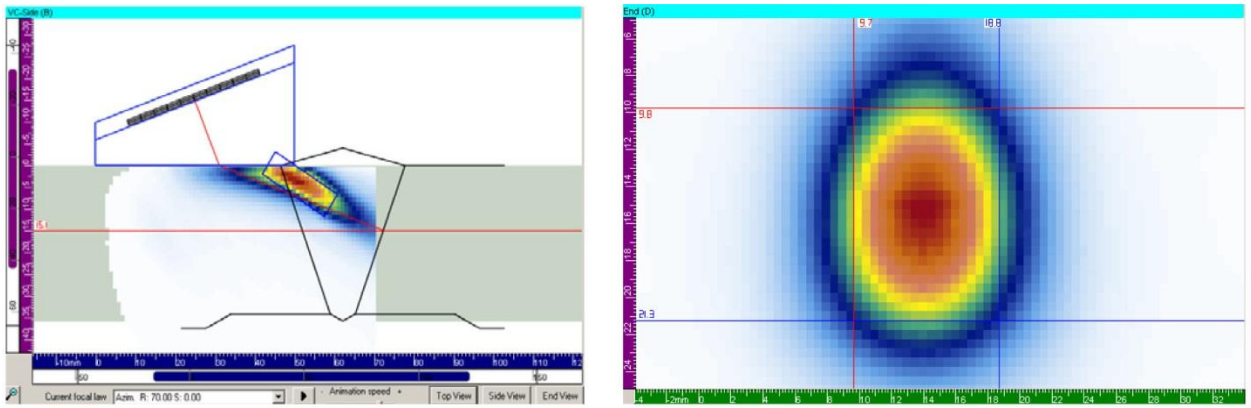

Figure 10.10 L-Wave Sound Beam Simulation at 70°, 15-mm (0.59-in.) Depth Focus; Side View on the Left and End View on the Right

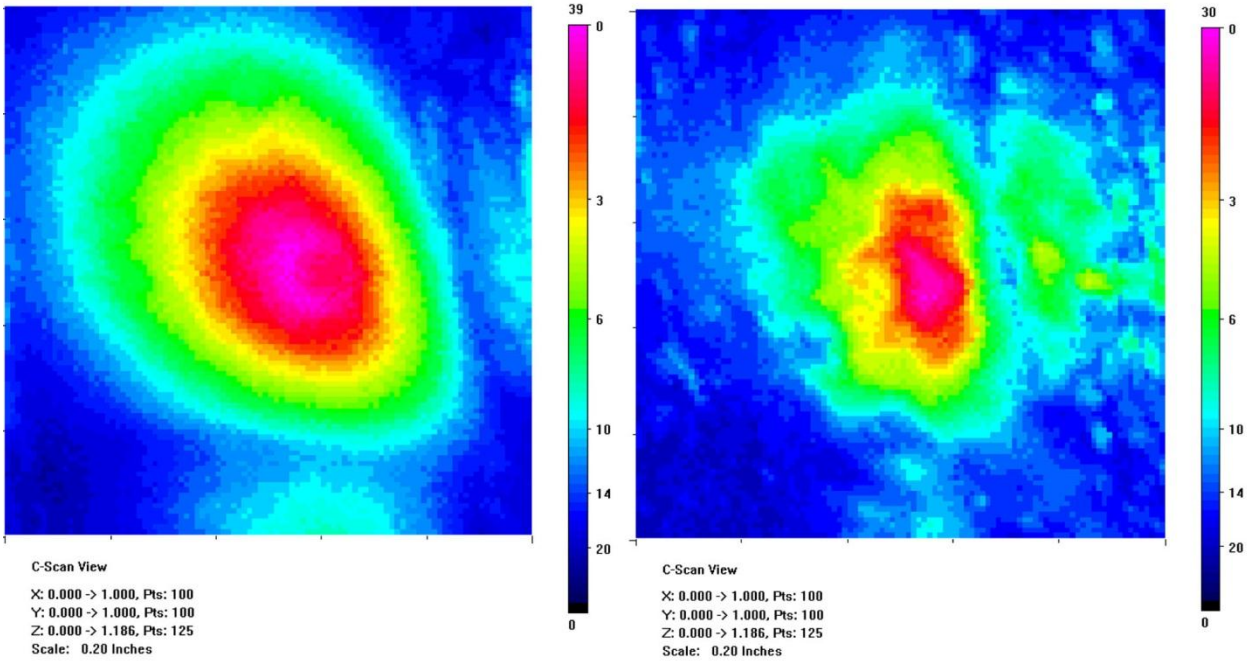

Figure 10.11 Data Images at 70°, 15-mm (0.59-in.) Depth Focus, 19 dB, 57 mm (2.2 in.) Back from WSS Side on the Left and from the Weld Side on the Right

Table 10.2 Simulated Beam Size

			10 dB Size		6 dB Size	
Angle	Focus	Distance Back	X	Y	X	Y
70°	15 mm (0.59 in.)	57 mm (2.24 in.)	11.7 mm (0.46 in.)	14.9 mm (0.59 in.)	9.1 mm (0.36 in.)	11.5 mm (0.45 in.)
50°	25 mm (0.98 in.)	50 mm (1.97 in.)	11.6 mm (0.46 in.)	11.6 mm (0.46 in.)	9.1 mm (0.36 in.)	10.6 mm (0.42 in.)
60°	25 mm (0.98 in.)	64 mm (2.52 in.)	13.0 mm (0.51 in.)	13.6 mm (0.54 in.)	10.1 mm (0.40 in.)	10.6 mm (0.42 in.)

Table 10.3 Wrought Stainless Steel Coupon End, Longitudinal-Wave Data

							10 dB Size		6 dB Size	
Angle	Focus	Distance Back	Gain (dB)	Average Noise (Counts)	Peak Signal (Counts)	Signal to Noise	X	Y	X	Y
70°	15 mm (0.59 in.)	57 mm (2.24 in.)	19	5.92	39	6.59	19.1 mm (0.75 in.)	21.3 mm (0.84 in.)	14.7 mm (0.58 in.)	15.5 mm (0.61 in.)
50°	25 mm (0.98 in.)	50 mm (1.97 in.)	19	3.70	61	16.49	13.5 mm (0.53 in.)	20.1 mm (0.79 in.)	9.1 mm (0.36 in.)	14.5 mm (0.57 in.)
60°	25 mm (0.98 in.)	64 mm (2.52 in.)	27	12.80	116	9.06	17.8 mm (0.70 in.)	22.9 mm (0.90 in.)	12.7 mm (0.50 in.)	16.0 mm (0.63 in.)

Table 10.4 Coarse-Grain (Weld Side) Coupon End, Longitudinal-Wave Data

Angle	Focus	Distance Back	Gain (dB)	Average Noise (Counts)	Peak Signal (Counts)	Signal to Noise	10 dB Size		6 dB Size	
							X	Y	X	Y
70°	15 mm (0.59 in.)	57 mm (2.24 in.)	19	4.84	30	6.20	12.7 mm (0.50 in.)	17.3 mm (0.68 in.)	9.4 mm (0.37 in.)	13.0 mm (0.51 in.)
50°	25 mm (0.98 in.)	50 mm (1.97 in.)	19	4.08	44	10.78	15.2 mm (0.60 in.)	20.3 mm (0.80 in.)	7.9 mm (0.31 in.)	14.5 mm (0.57)
60°	25 mm (0.98 in.)	64 mm (2.52 in.)	27	11.80	92	7.80	16.3 mm (0.64 in.)	20.8 mm (0.82 in.)	11.9 mm (0.47 in.)	16.0 mm (0.63 in.)

The approximate sound-field dimensions based on the X and Y measurements in Tables 10.3 and 10.4 are plotted in Figure 10.12 at the −6 dB sizing level to assist in visualizing the relative change in sound fields as observed from the WSS side and from the WSS-plus-weld side of the specimen. At 50° and 60° the shapes are similar in the Y direction and slightly smaller in the X direction when passing through the WSS and weld material. At 70° there is a greater difference seen. In the X direction, the beam is 36% smaller after passing through the WSS and weld material and in the Y direction the beam is 16% smaller. At the higher angle (70°) the sound path is longer and therefore the beam has more opportunity for distortion which the data show. These are idealized plots because they do not show the image distortion, skewing, and amplitude variation that are evident in the actual specimen images.

Table 10.5 shows the difference in peak-signal response for the longitudinal-wave modality between the base material (WSS) and the weld. For example, at the 50° angle with a 25-mm (0.98-in.) focal depth, the peak weld response is 3 dB lower than the base material response. In all of the longitudinal data, the weld response is lower by 2–3 dB than the base material, which is a reasonable expectation. This reduction in peak response is likely due to the fact that the weld region is comprised of a different material than the base material thus creating boundary conditions that can attenuate or redirect sound from the desired target area.

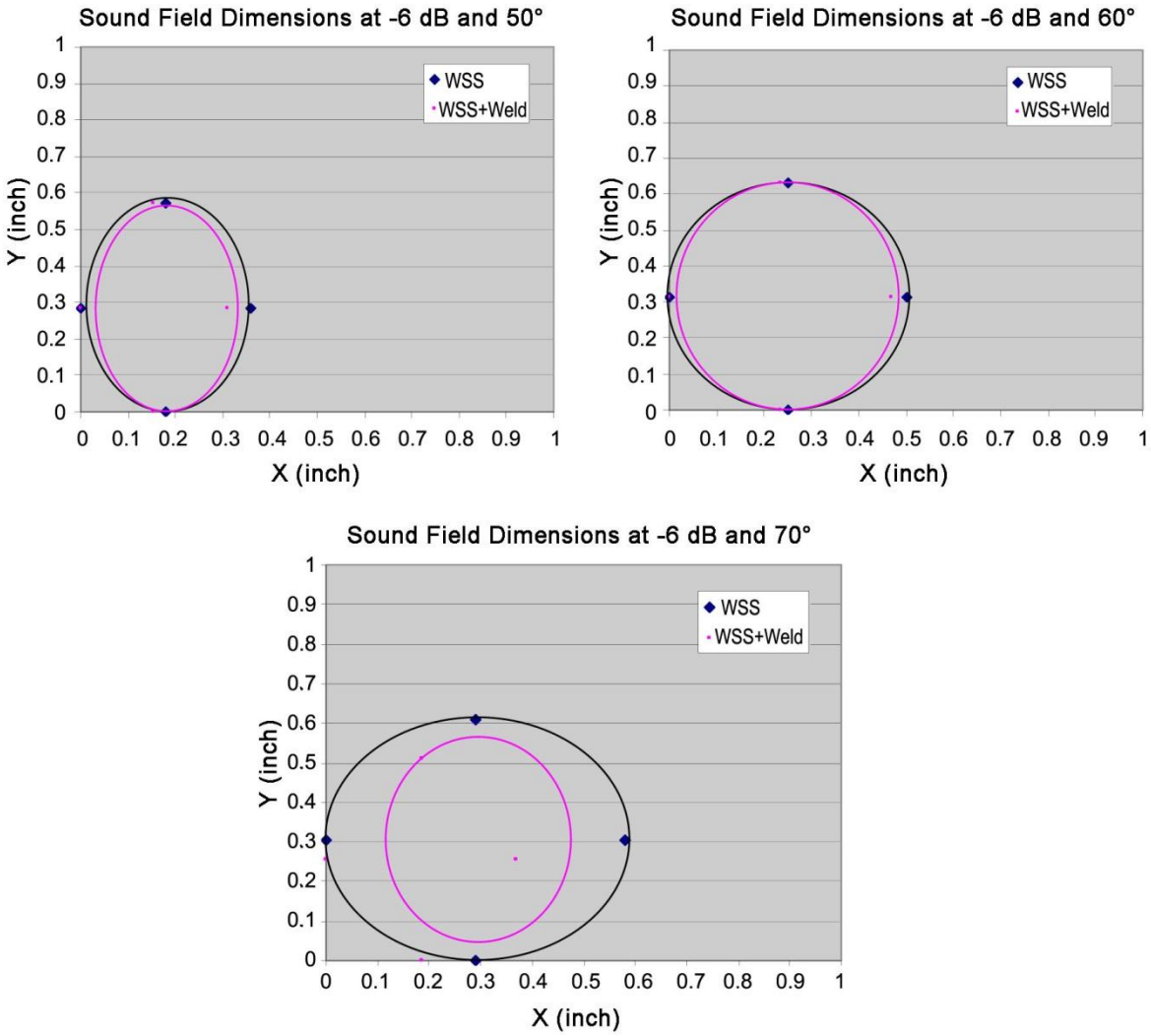

Figure 10.12 Sound-Field Sizing Comparison at a −6 dB Level Showing WSS Results with Black Ovals and WSS + Weld Results with Magenta Ovals. Data are displayed for 50°, 60°, and 70° longitudinal waves

Table 10.5 Comparison of Peak Signal Response from the Weld to the Base Material

Angle	Focus	Weld-to-Base Metal Response (dB)
70°	15 mm (0.59 in.)	−2.4
50°	25 mm (0.98 in.)	−3.0
60°	25 mm (0.98 in.)	−2.1

10.2 Theoretical Analysis of Longitudinal-Wave Propagation through Austenitic Weld

To understand resulting complex wave fields as ultrasonic beams propagate through parent material (WSS) and then through austenitic weld material, a simplified mathematical model has been developed. Figure 10.13 shows a simplified representation of the propagation media under consideration. The austenitic stainless steel weld region is modeled as truncated V-shaped region and illustrated by solid heavy lines. For the sake of additional simplicity, the weld region is divided into a finite number of segments having planar interfaces, each having its own crystallographic axis of rotational symmetry typical of austenitic stainless having columnar grains. The dotted lines appearing in the schematic diagram represents the alignment of these crystallographic directions ([001] axis). More accurate and detailed segmentation of the weld region will be used in future calculations, when ultrasonic beams will also be more correctly approximated by finite Gaussian beams. The origin of the coordinate system (XOZ) is placed at the intersection of phased-array centerline and the surface of the WSS section of the specimen.

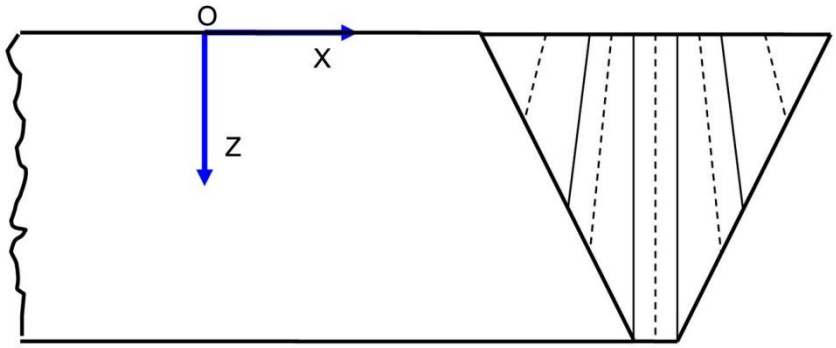

Figure 10.13 Schematic Diagram of Wrought Stainless Steel – Austenitic Stainless Steel Composite Media

In this report, we present a simplistic mathematical model of the ultrasonic beam propagation through the medium in question. Specifically, we begin by replacing the ultrasonic beam by a ray along its axis. At each interface between two generally anisotropic regions, mentioned in the previous paragraph, the beam is reflected and transmitted. Generation of various modes (L-, SV-, SH-waves) at each interface will be duly accounted for, as described below.

The weak-contrast reflection transmission coefficients at interfaces between two generally anisotropic media are given by

$$R^1 = \Delta R^1,\ R^2 = \Delta R^2,\ R^3 = \Delta R^3, R^4 = -\Delta R^4, R^5 = -\Delta R^5, R^6 = 1 - \Delta R^6. \tag{10.1}$$

$$\Delta R^{\alpha} = \frac{\Delta\rho\, e_i^{\alpha} E_i - \Delta c_{ijkl}\, e_i^{\alpha} p_j^{\alpha} E_k P_l}{2\rho_{\alpha}\, v_i^{\alpha}\left(P_i^{\alpha} - p_i^{\alpha}\right)} \tag{10.2}$$

where α = 1,2,3,4,5 for a non-degenerate incident wave and α = 1,2,3,4 for a degenerate incident wave. In the aforementioned equations, c_{ijlk}, and ρ represent elastic moduli and density at the incident side of the plane interface; $c_{ijkl} + \Delta c_{ijkl}, \rho + \Delta\rho$ represent elastic moduli and density at the transmitted side of the plane interface; P_i, n_i, E_i denote the slowness vector, normal to the interface, and unit polarization vector of the incident plane wave; $p_i^\alpha, e_i^\alpha, R^\alpha, \alpha = 1, 2, 3$ denote the slowness vectors and the unit polarization vectors of the reflected waves and the corresponding displacement reflection coefficients; $p_i^\alpha, e_i^\alpha, R^\alpha, \alpha = 4, 5, 6$ denote the slowness vectors and the unit polarization vectors of the transmitted waves and the corresponding displacement transmission coefficients.

The weak-contrast displacement transmission coefficient of the unconverted wave is given by

$R^6 = 1 + \sum_{\alpha=1}^{5} e_i^\alpha E_i \Delta R^\alpha$ for non-degenerate incident wave and $R^5 = 1 + \sum_{\alpha=1}^{4} e_i^\alpha E_i \Delta R^\alpha$.

These expressions for reflection-transmission coefficients also apply to evanescent-generated waves. Snell's law for the generated waves can be expressed as

$$p_i^\alpha = P_i + n_i a^\alpha, \alpha = 1,2,3,4,5,6. \tag{10.3}$$

The normal slowness vector discontinuities can be calculated as the relevant solutions of the sixth-order equations obtained by inserting Snell's law into Christoffel equations.

To carry out the calculations, we have chosen the following physical properties of the base and the weld materials having same crystal elastic constants (Table 10.6). Table 10.7 shows the summary of computational predictions of beam propagation through weld at two different incidence angles. In both cases, beam exits the weld at a different location than the desired/designed focal point. Even though our formalism can track mode-converted beams, we present only the beam path for incident longitudinal wave. However, we do show that at the incident face of the weld, the beam splits into two beams – L-wave and SV-wave. Because of the two-dimensional nature of our model, no conversion to the SH-wave mode occurs.

More detailed calculations will be made in the future where (1) more realistic beam cross sections will be used, (2) scattering attenuation will be included, and (3) macroscopic predictions of forward-scattered grain-induced noise accommodated. The last of these future enhancements of our computational strategy is important to predict signal-to-noise ratio.

Table 10.6 Material Properties of Base and Weld Metal

Material	C_{11} (GPa)	C_{12} (GPa)	C_{44} (GPa)	ρ (kg/m^3)	Orientation
WSS	219.2	136.8	109.2	7860	Random
Weld	219.2	136.8	109.2	7860	[001]

Table 10.7 Summary of Computational Results

Angle	Focus	Point of Exit: L-wave (x, z)	Point of Ideal Exit: L-wave (x, z)	Trans. Coef.: L-wave (Entry Face)	Trans. Coef.: SV-wave (Entry Face)
70°	15 mm (0.59 in.)	(41.35 mm, 17.57 mm) (1.75 in., 0.69 in.)	(41.21 mm, 15.0 mm) (1.62 in., 0.59 in.)	0.9621	0.1103
60°	25 mm (0.98 in.)	(42.11 mm, 27.06 mm) (1.66 in., 1.07 in.)	(43.30 mm, 25.0 mm) (1.70 in., 0.98 in.)	1.1588	-0.1164

10.3 Discussion and Conclusions

From a review of the data provided in Tables 10.3 and 10.4 and the sound-field plots in Figures 10.6–10.11, the effectiveness and coherence of sound-field propagation can be compared in both parent material and austenitic weld material as a function of the various inspection parameters evaluated in this study. Because this comparative evaluation is aimed at a number of inspection parameters, it is important to discuss the relationship between wave speed (acoustic velocity), inspection frequency, and wavelength. The longitudinal wave velocity v_l in wrought stainless steel is 5790 m/s (0.228 in./μs). From the relationship in Eq. (10.4),

$$\lambda = v_l / f \tag{10.4}$$

where f is the inspection frequency (Hz) and λ is the wavelength, the wavelength for a frequency of 1.5 MHz was calculated to be 3.9 mm (0.15 in.) in WSS for longitudinal waves. A review of the phased-array probe beam simulations in Figures 10.6, 10.8, and 10.10 provide some baseline information regarding sound-field shape, contour, directionality, orientation, and intensity; however, the modeling software does not simulate the effects of material inhomogeneities or anisotropy (due to grain boundaries or austenitic weld structure). Thus, these results are what would be expected in an isotropic, fine-grained, homogeneous material structure and were used as baseline information for the sound fields propagating in the WSS parent material.

The phased-array probe used in this evaluation was constructed from 1.5-D arrays of small rectangular elements. The active area (aperture) for the 1.5-MHz TRL probe was 35 mm × 17.5 mm (1.3 in. × 0.69 in.). This essentially results in a 2:1 aperture ratio. The effective aperture defines the focusing capabilities, directional characteristics, and overall shape of the primary sound-field lobe (when using all elements to beam form). In a non-scattering, homogeneous, and isotropic material structure, the primary sound-field lobes of this transducer configuration are expected to yield asymmetric distributions of acoustic energy, which is evident from a review of the dimensional data in Tables 10.2 through 10.4.

With an understanding of what the sound-field distributions should look like, it is quite apparent that the austenitic weld does not significantly contribute to degrading the coherence and structure of the longitudinal-wave sound field. It is observed that the compression-wave modality actually shows little degradation as the sound field propagates through the weld

material from the far side. In this modality, particle oscillations occur in the same direction as the direction of the traveling sound field. The sound-field plots provided in Figures 10.7, 10.9, and 10.11 clearly show that the longitudinal-wave mode provides good penetration and the sound field maintains ample coherence and signal strength as it propagates through the austenitic weld from the far side. Only at the highest angles of insonification (70°) coupled with a shallow focal depth (15 mm [0.59 in.]) do the longitudinal waves start to exhibit slight degradation to the field shape, coherence, and structure, as is evident by a review of Figure 10.11. This is to be expected because for the larger incident angle, the ultrasonic beams strike each columnar zone interface of the weld with smaller incidence angle and thus suffers from larger scattering attenuation and generate greater forward-scattered signals. More detailed analysis of the signal-to-noise ratio at various angles of incidence will be carried out in the future.

The results of this evaluation show that longitudinal (compression-wave) phased array is an effective means for inspection of austenitic welds from the far side. When coupled with the appropriate wavelength relative to the size of the grain boundaries and weld structure, this method can provide a very effective inspection.

11 Phase 3 Evaluation

The Phase 3 evaluation incorporated lessons learned from Phases 1 and 2 of this study, and focused on employing phased-array-UT techniques only for examination of field-removed piping segments with serviced-induced IGSCC. These specimens (discussed in Section 5) were provided by the EPRI NDE Center, Charlotte, North Carolina.

Flaw data from the EPRI specimens were analyzed for detection with the three PA probes described in Section 6. The detection criteria are discussed here. Given the true state of a specimen, if a clear response that was distinct from geometry and possessing a good signal-to-noise ratio (SNR) was found at any of the skew angles in the region noted as flawed, a “Yes” result was recorded for the flaw. If a weak signal that was discernable but not clearly separate from geometry or close to the noise levels was found in the region noted as flawed, a “Marginal” result was recorded. If no signal was found in the region noted as flawed, then a “No” result was recorded.

Figure 11.1 shows data from a region classified as “Yes” in the detection results. Arrows point to the flaw signals in the three views. The top view shows an ID geometrical signal on the left edge that runs nearly the entire length of the scan. The flaw signal is farthest to the right in the top view with other material reflectors in the middle. The signal of interest is gated in the side view using red and blue vertical lines and these gated results are shown in the end view. Arrows in the end view point to the flaw.

Figure 11.2 shows data from a region that was categorized as “Marginal” in detection. There is a signal in the region of interest that is slightly higher than the background but it does not have much length associated with it compared to surrounding area signals. Another signal in the data (end view) with similar amplitude stands out as a possible flaw but this region was not shown to be flawed. This could potentially lead to a false call in this area. False calls were not tracked in this analysis but contributed to the Marginal result as opposed to Yes detected calls.

Figure 11.3 shows data from a region that was classified as “No” in detection. There is no signal in the flaw region that stands out from the surrounding area. A lack of signal might be evident in the region of interest in the end view but this was not used as one of the flaw criteria.

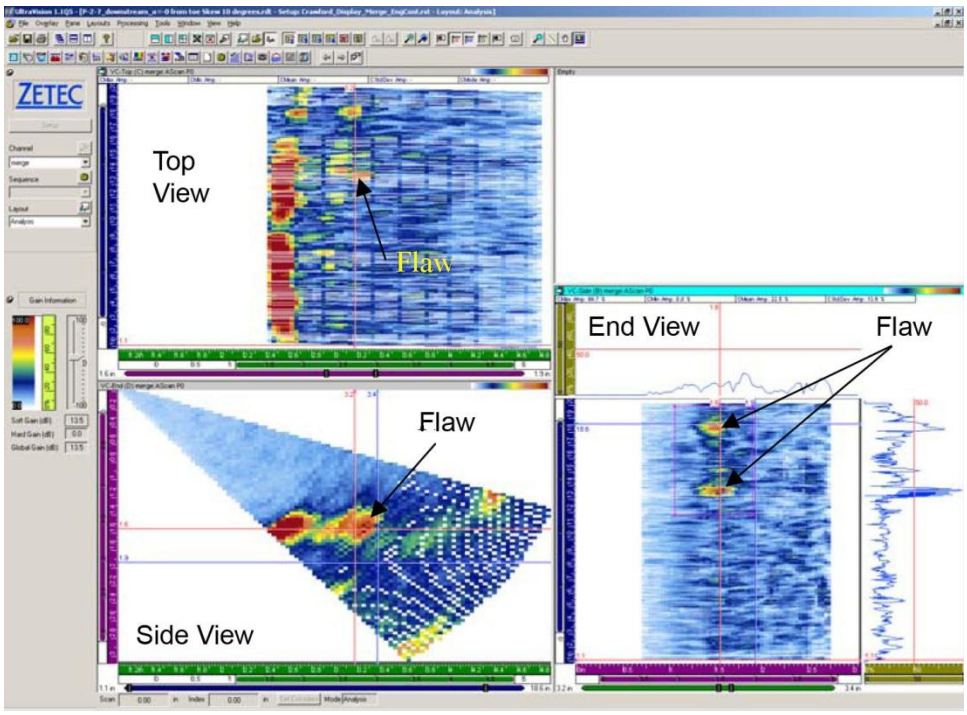

Figure 11.1 Example of a "Yes" Call

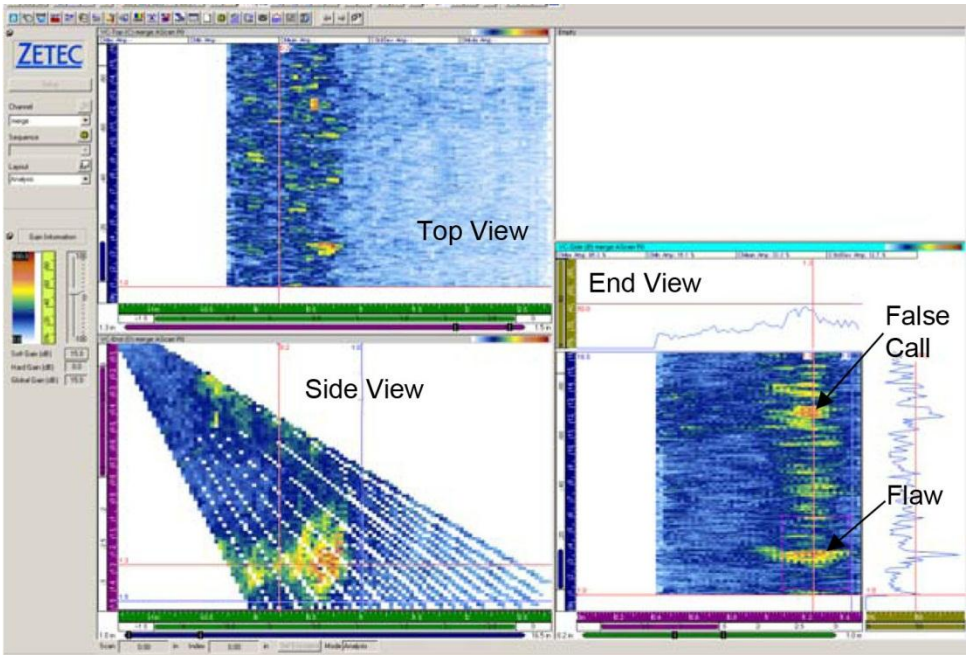

Figure 11.2 Example of a "Marginal" Call

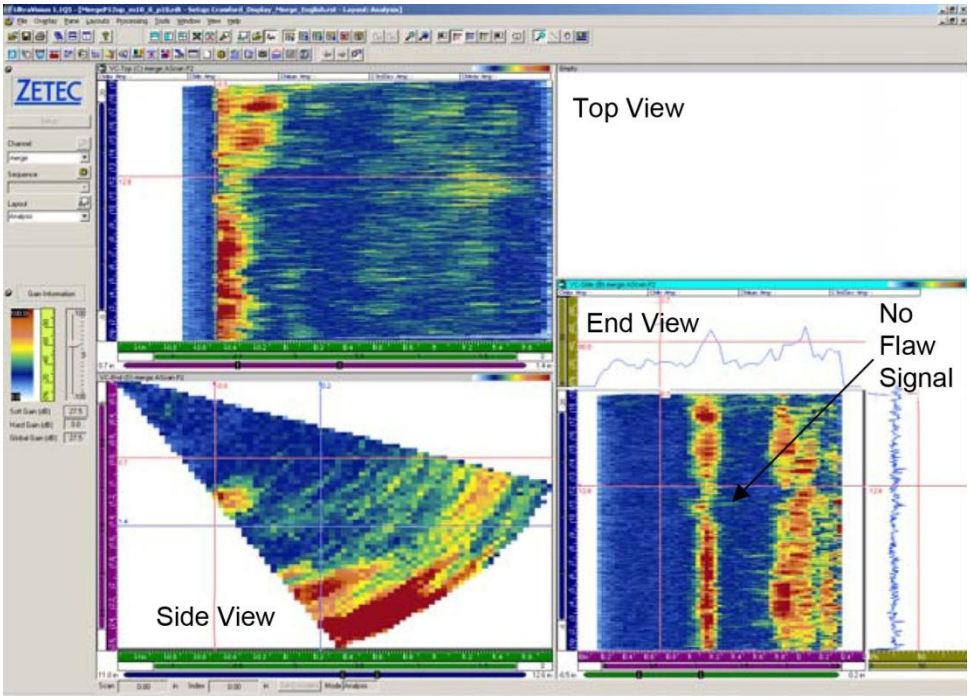

Figure 11.3 Example of a "No" Call

The practice specimen data were taken to PNNL and analyzed shortly after data acquisition. Some of the images and detection calls are shown in Appendix G from both the near and far side. The data are presented from the downstream side first for a given specimen and then from the upstream side for the three PA probes. The secure data were later analyzed at the EPRI site. Data images and information on detection calls relative to particular specimens were not allowed to leave the EPRI testing room. Only approved summary information is included in this report. Results from the aggregate sets of data are summarized in Figure 11.4, with data plotted to show the percent detection (Yes, No, or Marginal) for all flaws with a particular PA probe. The "Yes" calls are represented with blue boxes, the "Marginal" calls with green triangles, and the "No" calls with brown circles. Secure data are shown with dotted line connections and practice specimen data with solid lines. Results for the three probes from the near side and far side are provided. In most of the data sets, the far-side "Yes" call is lower than the near-side "Yes" call, as expected. However, from the secure set at 1.5-MHz TRL, it can be seen that the near-side and far-side "Yes" detected calls are the same at approximately 80%. Another interesting difference is shown for the 1.5-MHz shear wave on the secure data set, with far-side out-performing the near-side detections. Other differences in results from the secure and practice data sets may also be due to experience of the data analysts in interpretation, or in the specimens themselves. In general, the Yes calls fall in the 50% to 80% range for the far-side inspection.

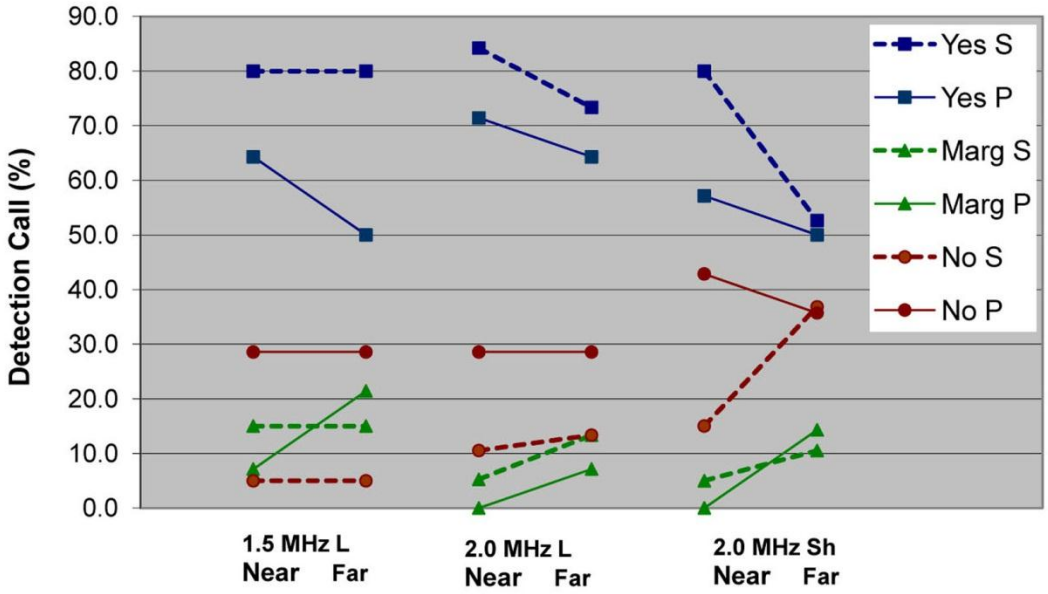

Figure 11.4 Detection Calls on the Secure (S) and Practice (P) Data Sets as a Function of PA Probe and Near- and Far-Side Inspection

The secure and practice data results were combined to give a larger sample population and to protect the integrity of the secure set. A summary of the results are listed in Table 11.1. This combined data set represents a number of service-induced cracks in a variety of pipe and component configurations joined with an austenitic weld. The depth of the cracks were not known nor measured from the data as tip-diffracted signals were not sought out. The lengths of the cracks were variable, as reported by EPRI true-state information. This study focused on flaw detection, so crack lengths were not measured. In general, cracks on the small end of the observed length range could be confused with material noise, and cracks on the long end of the range could be confused with part geometrical reflectors such as counterbore or weld root. Medium to long indications whether from a flaw or geometry could also exhibit signal drop out due to sound-field redirection, scattering, or attenuation. These issues make signal discrimination on service-induced IGSCC more challenging.

Table 11.1 IGSCC Detection Summary

	1.5-MHz TRL			2.0-MHz TRL			2.0-MHz TRS		
Access	**Yes**	**No**	**Marginal**	**Yes**	**No**	**Marginal**	**Yes**	**No**	**Marginal**
Near Side	73.5	14.7	11.8	78.8	18.2	3.0	70.6	26.5	2.9
Far Side	67.6	14.7	17.6	69.0	20.7	10.3	51.5	36.4	12.1

The detection summary shows that near-side inspection using methods similar to those described in this report will be superior with approximately 70% to 80% of the flaws being detected. On a far-side inspection using similar methods, the detection rate drops to approximately 50% for shear waves and is just under 70% for the longitudinal-wave modality.

Flaw detection generally involves two parts. One part of the detection process relates to signal amplitude. How high above the background noise level is the signal of interest? A measurement used for this process is the signal-to-noise ratio (SNR). A SNR of at least 2:1, or 6 dB, is commonly desired, but current analytical techniques allow lower values with most procedures requiring analyses of flaw responses down to the material noise level. The SNR for these data were calculated from the peak signal responses from "Yes" detected flaw responses and the average noise level around the flaws. Noise values were taken at the same part path as the signal responses. SNR values from the different detected cracks were averaged with results shown in Figure 11.5 for each probe and for near- and far-side access. Results indicate that the SNR values are good; all exceeding 10 dB (signal is 3.2 times the noise level). The higher near-side SNR for the TRS probe is possibly due to the lack of mode conversion taking place. From the far side, the SNRs are similar for each of the three probes for a detected flaw. With SNRs being adequate in these data sets, the challenge in flaw detection then becomes one of signal discrimination.

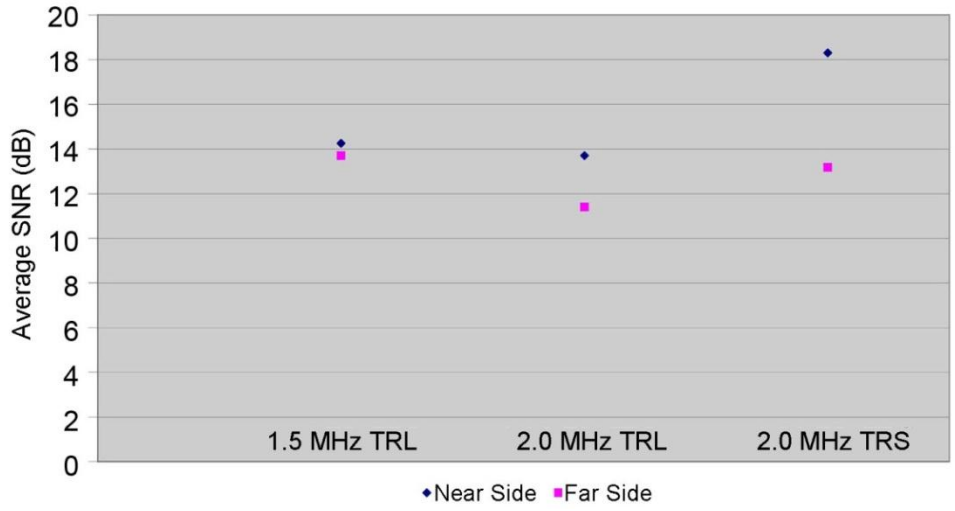

Figure 11.5 Signal-to-Noise Ratios for "Yes" Detected Cracks

The second major variable for flaw detection is signal discrimination—is the ultrasonic response being generated from a geometrical condition, material noise, or a flaw? Ideally, one would determine the weld area profile along the pipe axis using a contour gauge on the OD surface and UT thickness readings to exhibit the approximate ID contour. These contour measurements were not made during this exercise. In fact, the presence of weld crowns on the field-removed specimens prohibited the collection of normal-beam ultrasonic measurements to accurately map the ID surface in the weld region. If the weld area is diagramed, indications from subsequent specimen evaluations can be mapped to the originating location in the specimen profile. Signals mapped to the counter bore, weld root, etc. can be classified as geometrical indications. Often geometrical signals have significant length and amplitude associated with them. A strong counterbore signal provides a reference point for all other signals whether the weld area profile is known or not. As shown in previous sections of this report, an example of a known configuration for an austenitic stainless steel piping specimen

typical of that found in a primary coolant BWR recirculation system, was fabricated with sawcuts and implanted thermal fatigue cracks. The approximate weld cross section is shown in Figure 11.6. PA data of a flaw acquired from the far side of the weld is shown in Figure 11.7. The sector side view on the left of Figure 11.7 shows, from left to right in the image, a geometrical signal from the inner-diameter mismatch step, a geometrical signal from the weld root, and the flaw signal (as if UT data was acquired from the OD surface on the right side of the weld shown schematically in Figure 11.6).

Data from the EPRI specimens were generally not as straightforward and were cluttered with many signals to consider. Figure 11.8 shows near-side data from a practice specimen. The geometrical signal from the far side of the weld is clearly seen and can be used as a reference. The side view shows three main reflectors between the red and blue horizontal lines. This region is gated and shown in the top view. The far-side geometrical signal is identified and all other signals referenced to it. Notice that the far-side geometry produces a strong signal, but with signal dropout evident. The flaw signal is sandwiched between two geometrical signals in the side and top views and the near-side geometry signal does not extend the full length of the image. The vertical red and blue lines in the side view are used to gate out the flaw signal with results shown in the end view. The flaw signal is at the bottom of the end view and is boxed with the magenta lines. Other signals are detected at that same axial position but are lower in amplitude. For this reason, the flaw was considered “Yes” detected. In general, for data analyses, a narrow vertical gate such as that shown in the side view is moved across the image while looking at the end view for signals of interest. In the PNNL analyses, analysts considered whether there was a signal in the area documented as flawed that was separable from other signals and of sufficient amplitude, when making these calls. All images in this report are from merged data, but unmerged data were also reviewed during the flaw detection analyses.

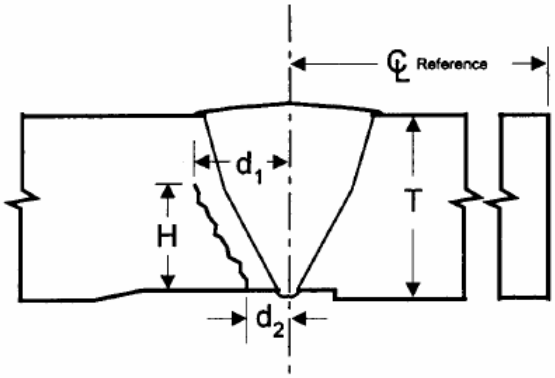

Figure 11.6 Cross-Sectional Schematic Showing the Weld Geometry and Location of an Implanted Crack in the Weld Heat Affected Zone

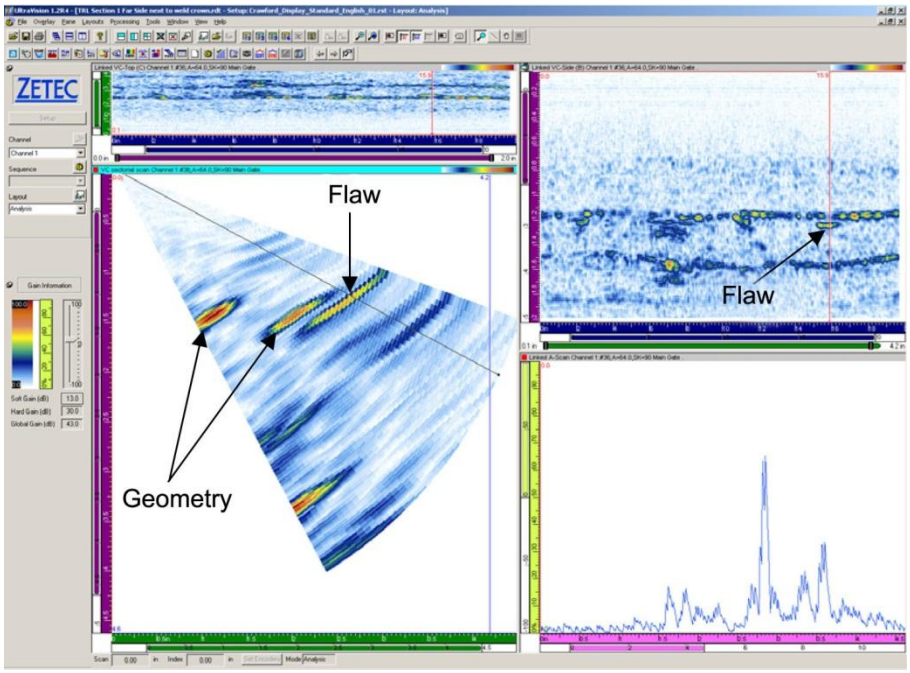

Figure 11.7 Far Side Data from a Specimen with the Cross Section Shown in Figure 11.6. Geometrical signals from the inner-diameter mismatch step and weld root are noted. The flaw signal is also identified.

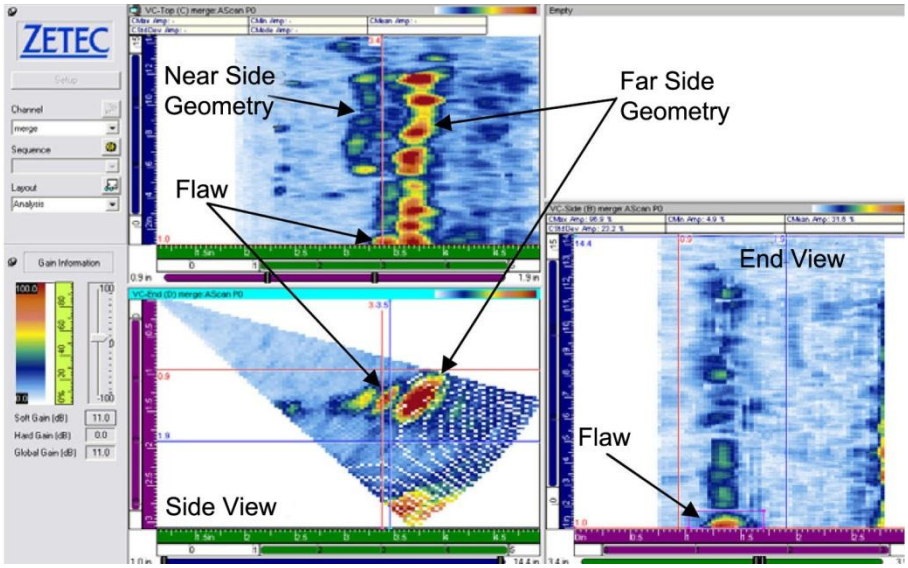

Figure 11.8 Data Images Showing a Flaw Signal Separated from Geometrical Indications

The combined data indicate that near-side detection of IGSCC provides for a 71%–79% detection rate when using the applied phased-array methods and scanning techniques. However, far-side detection rates drop, with shear-wave detection from the far side representing the lower extreme at 52%, as compared to the longitudinal-wave detections at 68% or 69%.

Earlier work (Anderson et al. 2003; Anderson et al. 2006; Anderson et al. 2008), based on machined-notch responses and TFCs, showed that a longitudinal sound field passed through the weld with a minimal amplitude loss but sound-field redirection was observed. The shear-wave sound field (having a shorter wavelength) was severely attenuated (primarily by a scattering mechanism) by the weld material, but showed less redirection and beam skewing. At the frequencies typically applied, shear waves do not transmit through austenitic weld microstructures as efficiently as longitudinal waves, therefore resulting in lower detection rates. Another, albeit undocumented, contribution to the detection rates involves the location of the flaws on the actual pipe segments. If IGSCC flaws were very close to the edges of the specimens, the optimized PA probe footprints may have precluded a proper insonification near these edge areas. This problem would not be an issue in the field, where access to the full circumferential weld length is available.

PNNL was supplied with flaw true-state information, so analyses should not be considered representative of blind tests or field inspections. The investigation was focused on assessing current PA ultrasonic techniques for austenitic welds. In this regard, the detection results are a best-effort, given equipment and inspection conditions; that is, the arrays were not specifically optimized for the weld conditions encountered, and, more importantly, the weld crowns were not removed, which would have provided greater access for each of the PA modalities and probes applied. Typically, the detection process involved first identifying geometrical reflectors based on axial position and circumferential extent. A strong ID-geometrical signal that had a large circumferential extent provided a good reference point. The geometrical reflectors were then removed from further consideration and the remaining signals evaluated based on the true-state knowledge. If an indication was present in the location of a known flaw and the signal was separable from other signals by amplitude or length, for example, the indication was called a detected flaw. The data, whether from the near side or the far side, were generally cluttered with many signals to consider. The smaller footprint of the 2.0-MHz TRL probe provided better access to some flaws, and in a few cases, allowed the only access. Its sound field, however, was not as well focused or coherent as the 1.5-MHz TRL probe. Far-side detection rates were similar with both of these probes, but it is believed that detection improvement would be obtained if the weld crowns were removed. This would ensure full insonification of the far-side area of interest. The results might then be augmented with a 1.0-MHz PA evaluation that would be less effected by attenuation, scattering, and beam skewing. At this lower frequency, the probe footprint (due the required aperture for proper focusing) would be larger, so weld crown removal would be required for a meaningful inspection. The shear-wave inspection did not add value to the longitudinal-wave results of this study. While it is recognized that shear-mode near-side inspections are an acceptable industry practice, this limited study did not show any improvement in the shear-mode results (even on the near side of the welds) as compared to the longitudinal-mode results.

In order to fully understand UT flaw detection capabilities from the far side of austenitic welds, weld crown removal would be required. Signal discrimination could be improved by more effectively peaking of ultrasonic signals where weld crowns presently limit this function. More accurate specimen profiling in the critical weld area, presently not possible with the weld crowns in place, would also improve the data interpretation. It is also possible that flaw-tip signals could be detected in a linear or raster PA scan if closer access to the flaw could be achieved.

12 Summary and Conclusions

The ultrasonic examination of austenitic coarse-grained structures continues to be a challenge to the industry during inservice inspection of nuclear power plant components. This is especially true for detection and characterization of service-induced flaws that may initiate at welds where access for examination may be limited to a single side of the weld. This limited access is generally caused by outside surface geometries encountered; for example, pipe-to-valve, nozzle-to-pipe, or elbow-to-pipe configurations, but examination access may also be affected by rough as-built surface conditions of the weld crown. For these reasons, this study was conducted to begin to ascertain the effectiveness of ultrasonic technologies for reliable examination of austenitic piping welds when flaws are manifested on the far side of these welds.

In the case of wrought stainless steel piping components, it is the austenitic weldment and as-built conditions that adversely impact the inspection effectiveness. Coupled with the need to reliably and consistently detect cracks from the far side of the weld, manual ultrasonic inspection techniques used in industry do not achieve the desired detection reliability. In this study, spatially-encoded data sets using conventional inspection techniques, phased-array techniques, and low-frequency/SAFT inspection techniques were employed to examine a set of introduced flaws in piping specimens containing austenitic welds when inspecting from the far side. The piping specimens developed for the first two phases of research included a 610 mm (24 in.) OD, with a wall thickness of 36 mm (1.4 in.). The phase three specimens were salvaged from piping that had been in service at commercial operating plants, and were nominally 711 mm (28.0 in.) in OD, with thickness ranging from 20–41-mm (0.8–1.6 in.). The frequencies chosen for this work are in the range of those used for examining piping welds in the field. A significant amount of data were acquired for each UT technique and extensive analyses performed on this large database from which the following conclusions and recommendations are made.

It has been shown that the far-side detection of inner-diameter surface-breaking flaws is possible with precise data acquisition and rigorous analysis methods. In addition, acceptable length-sizing of the flaws has also been demonstrated. However, because no diffracted flaw tip signals could be observed with any of the UT methods applied, accurate through-wall depth-sizing may not be feasible. Figure 12.1 provides a graphic representation of the detection capabilities for each of the technologies employed.

The phased-array technology provided the best overall detection performance, followed by conventional UT. Flaws greater than 20% through-wall were detected by at least one technique for each of the methods used; however, very small flaws (<10% through-wall) were only consistently detected by phased array. Note the through-wall range of 11–20% included a 19% axially-oriented flaw that was not detected by any of the methods. This was expected, as the techniques used by all methods were aimed at more structurally significant circumferentially-oriented flaws because only scans perpendicular to the weld were performed. Figure 12.2 compares images from the implanted and machined flaws for the best parameters of each method applied during this study. The capability to length-size flaws on the far side of welds is summarized by the comparison in Table 12.1.

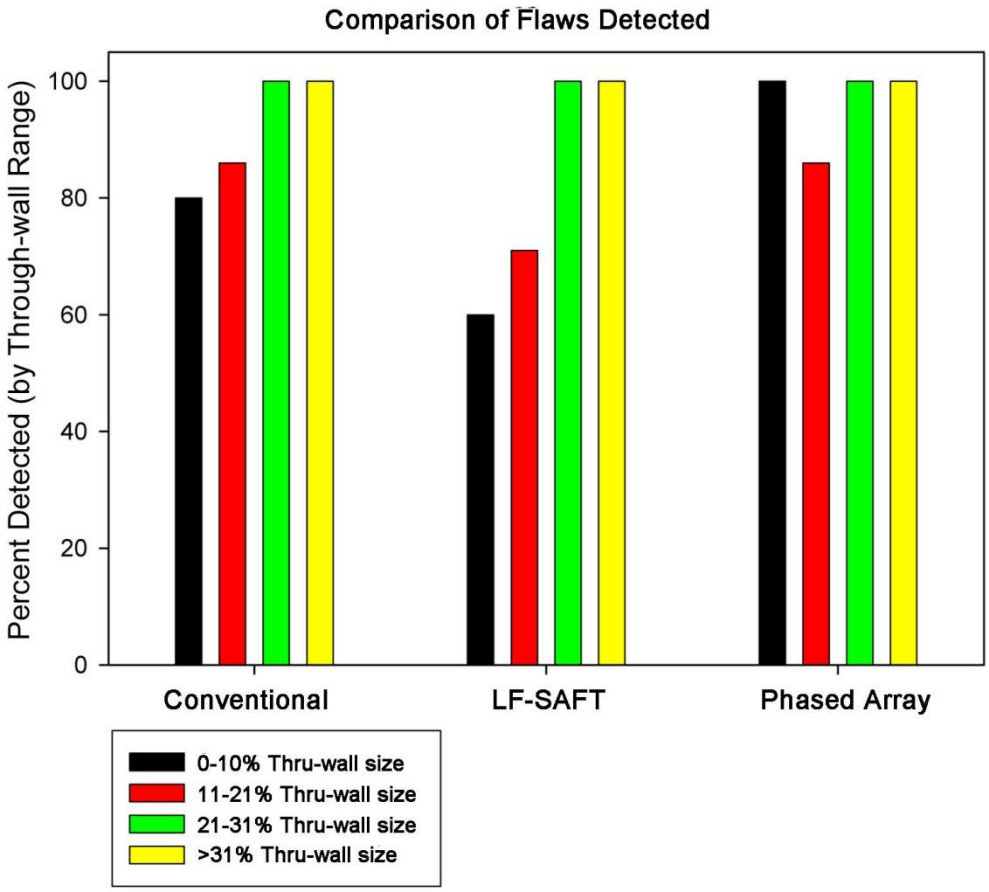

Figure 12.1 Far-Side Detection Results for All Techniques Applied on All Thermal Fatigue Cracks and Machined Sawcuts and Notches as a Function of Through-Wall Flaw Size

Table 12.1 Far-Side Length-Sizing Comparison for All Methods Applied

	Thermal Fatigue (RMSE)	Best Technique	Sawcuts (RMSE)	Best Technique
Conventional	2.2 mm	70° −6 dB	4.0 mm	70° LOS
LF/SAFT	3.4 mm	400 kHz, 45°S - LOS	9.2 mm	400 kHz, 45°L −6 dB
Phased Array	6.3 mm	TRL LOS	6.3 mm	TRL LOS

The conventional-UT method set a high performance benchmark for detection and length-sizing of flaws during these laboratory tests. This is somewhat surprising, based on poorer results obtained during previous round-robin trials (Heasler and Doctor 1996). Only the smallest reflectors could not consistently be detected with conventional transducers, and the best RMSE was obtained by the conventional method. The reader is cautioned that, while the conventional transducers represent those typically used during manual performance demonstrations, all data

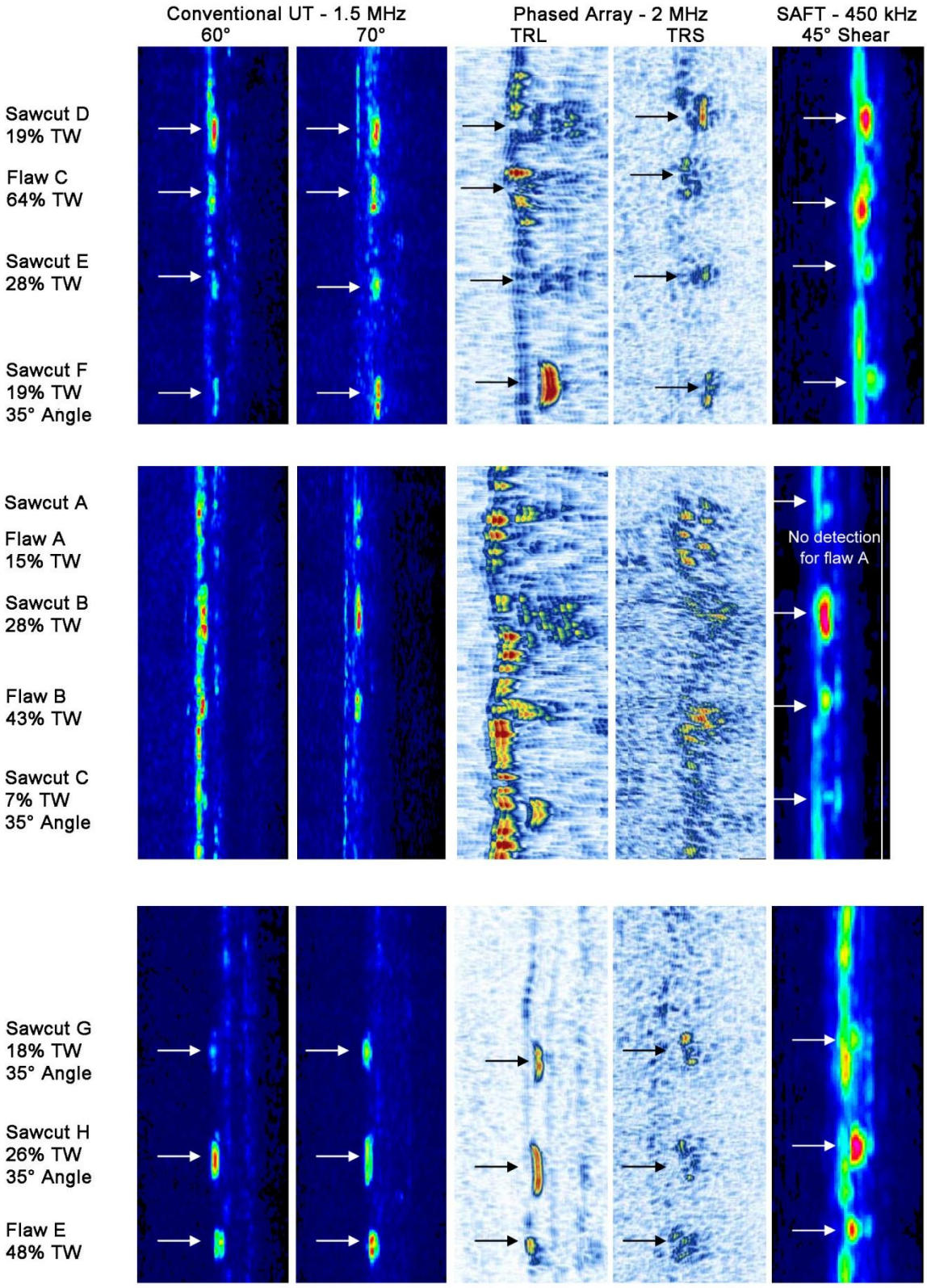

Figure 12.2 Images of Flaws Comparing Results from Conventional-UT, Low-Frequency/ SAFT and Phased Array-UT Methods

were acquired with automated scanners, and digitally stored for off-line image analyses. Therefore, the increased accuracy of scans and ability to thoroughly evaluate the large amount of data acquired during these tests significantly contributed to the success of the conventional UT applied. It is not believed that manual techniques, interpreted in real-time, would perform at this level. The down-side of automated conventional examinations is that weld crown removal may be needed to facilitate raster scans, and these scans can typically require long durations (on the order of hours for large-diameter piping). In addition, multiple scans at various inspection angles and propagation modes are indicated to ensure a high probability of detection.

A summary review of the low-frequency/SAFT inspection results indicate that the detection performance of the 70° longitudinal-wave inspections at 250 kHz provided the most meaningful data and the best detection results of any of the LF/SAFT scan combinations evaluated here. Crack A and crack D were by far the most difficult introduced flaws to detect, as neither introduced flaw was detected using any of the scan combinations for this inspection technique. With regard to length-sizing, the 400-kHz inspections provided more accurate results (of those introduced flaws that were detected) in comparison to the true-state lengths, in particular for the 45° inspection angle. The LOS length-sizing method provided an RMSE of 3.4 mm (0.13 in.) for the 45° shear-wave inspections of thermal fatigue cracks, and proved to be the most accurate of the scan combinations. The −6 dB length-sizing method provided an RMSE of 9.2 mm (0.36 in.) for the 45° L-wave inspections for sawcuts, as shown in Table 12.1. From the work reported here, it is shown that lower frequencies generally are not appropriate for reliable and consistent detection of small-dimension flaws in these piping components as the sound field is too large and the wavelength too long for effective detection and sizing of smaller cracks. With a range of longer wavelengths spanning 7.9 mm (0.31 in.) to 23.2 mm (0.91 in.) and the large zone-focal dimensions of the sound field (discussed in Section 6) employed in this study, the resolution is generally too low relative to the size of the introduced flaws as a 10% flaw is 3.8 mm (0.15 in.) in through-wall size. The zone-focused transducer may not be appropriate in this application, as the non-divergent beam results in a reduction in SAFT focusing in the processed images. The application of the LF/SAFT inspection technique does, however, shed light on the effectiveness of lower examination frequencies and provides a general lower bound for the use of longer wavelengths for flaw detection from the far side.

As reported above, the phased-array method provided the best detection results with the highest number of flaws detected. The capability of phased array to generate a broad range of discrete, incrementally steered beams with both shear and longitudinal waves increases the probability that an optimum incidence angle will occur for all, including small, spectral reflectors. For the austenitic welds and implanted/machined flaws examined in this study, good signal-to-noise ratios were obtained by both longitudinal- and shear-wave arrays, and far-side length-sizing was well within the acceptable range (RMSE of 19 mm or 0.75 in.) required by the ASME Code Section XI, Appendix VIII, Supplement 2. Data sampling and digitization rates during continuous line scans slightly increase the RMSE for length-sizing of circumferential flaws, but this error, as stated above, is well within acceptable tolerances. In addition, acquisition rates on the order of inches per second are easily achievable and off-the-shelf analysis software is available to simplify off-line interpretation. There has been some hesitancy in the industry to use phased-array probes due to the initial costs for instrumentation and the expense of

individual arrays. However, these costs are expected to be outweighed by the savings achieved with shorter scan times and the increased performance level of the method.

It is important to note that, as with any UT technique applied, acoustic physics must be optimized to produce the quality of inspection results observed during these laboratory tests. For this reason, modeling of the sound fields significantly contributed to the selection of appropriate UT parameters. This is especially true when using phased arrays to achieve optimum performance while controlling fabrication costs, as the arrays are much more expensive than conventional transducers.

During Phase 1 of this work, it was shown that far-side detection and length-sizing of planar reflectors, including implanted thermal fatigue cracks and small sawcuts, could be adequately performed. It should be noted that these results may vary for service-induced flaws such as IGSCC or primary water stress corrosion cracking (PWSCC), which tend to exhibit more branching and faceting than the planar flaws used in this study. In general, these planar flaws are expected to produce strong specular reflections that can be more readily detected, whereas branched and faceted flaws may return noncontiguous (or partitioned) sound fields, which can be redirected at multiple angles, thus more difficult to discriminate from other acoustic noise sources. The results were further validated in Phase 2 on piping fabricated to simulate field-weld microstructures. Prior to the laboratory trials, it was believed that the anisotropic nature of field-weld microstructures could vary azimuthally, and subsequently, affect the transmitted acoustic field with respect to circumferential weld position. It was shown that, while small (approximately 6 dB) through-weld variations in acoustic beam intensities were evident along the weld length, this effect was random, and no overall influence based on welding position was seen to affect transmission efficiency. In other words, no relation of welding position to acoustic transmission quality could be ascertained.

After initial studies (Phases 1 and 2) on inspection of machined flaws and implanted thermal fatigue cracks through austenitic stainless steel piping welds showed favorable results, PNNL was invited to examine specimens containing service-induced IGSCC at the EPRI NDE Center. Phased-array ultrasonic data were acquired on a series of specimens with three different probes and two different inspection modalities. The specimens were divided into two groups—a practice set and a secure set. Full access to the specimens was given for the practice set and the data were taken to PNNL for flaw detection analysis. During data analyses, the flaw true state on these practice specimens was known. The secure data were acquired with only OD access to the specimens. Secure data analyses took place at the EPRI NDE Center with a proctor in place to ensure specimen security. True-state information was also provided for the secure data set.

The practice and secure data results were combined to maintain integrity of the secure set and showed that TRL inspection techniques produced a far-side detection rate of approximately 69%. The TRS results were lower at 52% and this data showed much more scattering of the beam in passing through the austenitic weld material. SNRs in both longitudinal- and shear-wave responses were good for detected flaw signals, suggesting that signal discrimination remains the most challenging aspect of flaw detection.

The 2.0-MHz TRL probe, while not producing as well defined a beam as the 1.5-MHz TRL probe, had a smaller footprint and therefore allowed better access to some of the far-side area of interest. This was an advantage in tight geometrical configurations. Lower-frequency probes are less susceptible to beam steering, scattering, and attenuation, but require a larger probe design footprint and therefore make weld crown removal necessary for a far-side inspection. Additional justification for weld crown removal includes enhanced signal discrimination by allowing more effective peaking of the ultrasonic signal and better inner diameter profiling of the specimen in the complex weld region. Access afforded by weld crown removal may also allow tip signals to become evident for enhanced flaw detection and depth-sizing.

This work was systematically conducted to evaluate the basic inspection performance of conventional-UT, low-frequency/SAFT-UT, and phased-array UT methods by iteratively evaluating notches, sawcuts, machined reflectors, fabricated thermal fatigue cracks, and finally, service-induced, field-removed IGSCC. As the industry progresses towards developing an effective and reliable inspection approach for far-side examinations in components with austenitic welds, insights gained from the subject study that may prove useful are: modeling could be employed to determine optimal inspection parameters for improved phased-array UT probe and inspection protocol design; modeling of the inspection process, weld microstructures, physical acoustic propagation phenomena, and other critical aspects of the inspection could also be employed; and metallographic studies could be performed on existing specimens and results would be interpreted and correlated with the findings of the modeling and measurement activities.

13 References

Anderson MT, SL Crawford, SE Cumblidge, AA Diaz and SR Doctor. 2008. "A Comparison of Ultrasonic Flaw Responses as Observed through Austenitic Stainless Steel Piping Welds." In *Proceedings of the Sixth International Conference on NDE in Relation to Structural Integrity for Nuclear and Pressurised Components*, EUR 23356 EN-2008, pp. 798–806. October 8–10, 2007, Budapest, Hungary. eds: M Bieth and J Whittle. European Communities.

Anderson MT, SE Cumblidge and SR Doctor. 2003. "Applying Ultrasonic Phased Array Technology to Examine Austenitic Coarse-Grained Structures for Light Water Reactor Piping." In *Third EPRI Phased Array Inspection Seminar*. June 9–11, 2003, Seattle, Washington.

Anderson MT, AA Diaz, SE Cumblidge and SR Doctor. 2006. "Capabilities of Ultrasonic Techniques for the Far-Side Examination of Austenitic Stainless Steel Piping Welds." In *Fifth International Conference on NDE in Relation to Structural Integrity for Nuclear and Pressurised Components*, May 10–12, 2006, San Diego, California. eds: M Bieth and J Whittle. European Commission Joint Research Centre.

Doctor SR, GJ Schuster, LD Reid and TE Hall. 1996. *Real-Time 3-D SAFT-UT Evaluation and Validation*. NUREG/CR-6344, PNNL-10571, U.S. Nuclear Regulatory Commission, Washington, D.C.

Gruber GJ, RL Edwards and PD Watson. 1995. "Fabrication of Performance Demonstration Initiative Specimens with Controlled Flaws." In *13th International Conference on NDE in the Nuclear and Pressure Vessel Industries*. May 1995, Kyoto, Japan.

Heasler PG and SR Doctor. 1996. *Piping Inspection Round Robin*. NUREG/CR-5068, PNL-10475, U.S. Nuclear Regulatory Commission, Washington, D.C.

Lemaitre P. 1994. *Report on the Evaluation of the Inspection Results of the Wrought-to-Wrought PISC III Assemblies No. 31, 32, 33, 34, 35 and 36*. PISC III Report No. 33, Programme for Inspection of Steel Components, Joint Research Centre, EEC, Petten, The Netherlands.

MacDonald D, M Dennis, J Landrum and GP Selby. 2000. *Phased Array UT Performance on Dissimilar Metal Welds: Interim Report*. TE-1000116, EPRI Nondestructive Evaluation Center, Electric Power Research Institute, Charlotte, North Carolina.

Moysan J, A Apfel, G Corneloup and B Chassignole. 2003. "Modeling the Grain Orientation of Austenitic Stainless Steel Multipass Welds to Improve Ultrasonic Assessment of Structural Integrity." *International Journal of Pressure Vessels and Piping* 80:77–85.

Poguet J, J Marguet, F Pichonnat and L Chupin. 2001. "Phased Array Technology: Concepts, Probes and Applications." In *3rd International Conference of NDE in Relation to Structural Integrity for Nuclear and Pressurized Components*. November 14–16, 2001, Seville, Spain.

Schuster GJ, SL Crawford, AA Diaz, PG Heasler and SR Doctor. 2010. *Reliability of Ultrasonic In-Service Inspection of Welds in Reactor Internals of Boiling Water Reactors*. PNNL-14561, U.S. Nuclear Regulatory Commission, Washington, D.C.

Appendix A

Piping Specimen Fabrication Photographs

Appendix A

Piping Specimen Fabrication Photographs

Figure A.1 Austenitic Pipe Segments Shipped from PNNL for Flaw Implantation

Figure A.2 Liquid Penetrant Inspection of Weld Preparation Surfaces

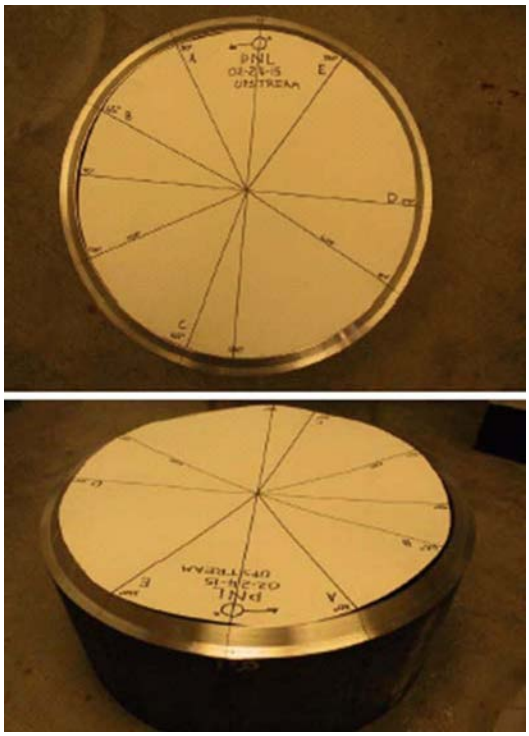

Figure A.3 Implant Locations

Figure A.4 Preparing Weld Bevel Area for Flaw Implantation

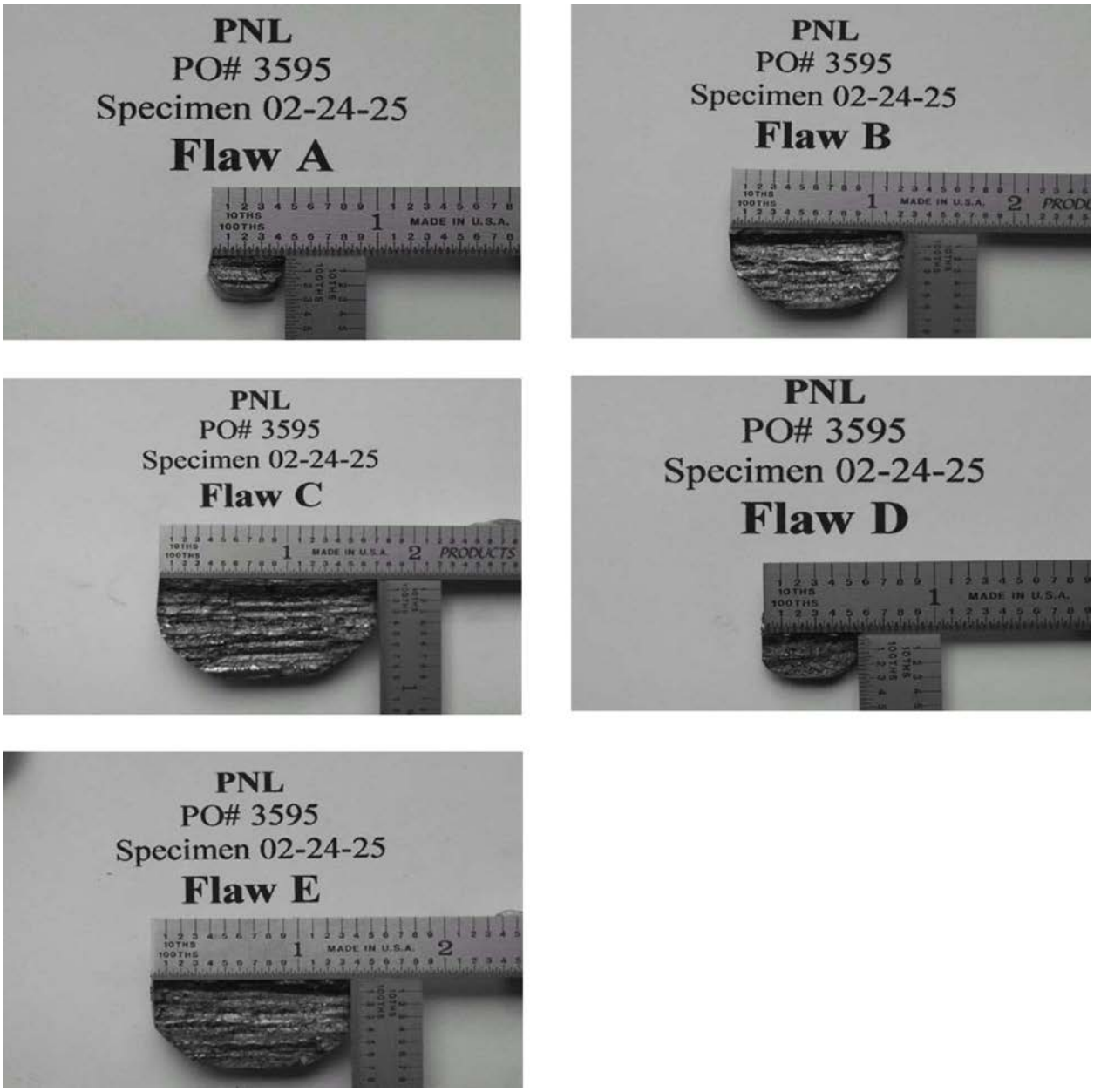

Figure A.5 Flaw Coupons

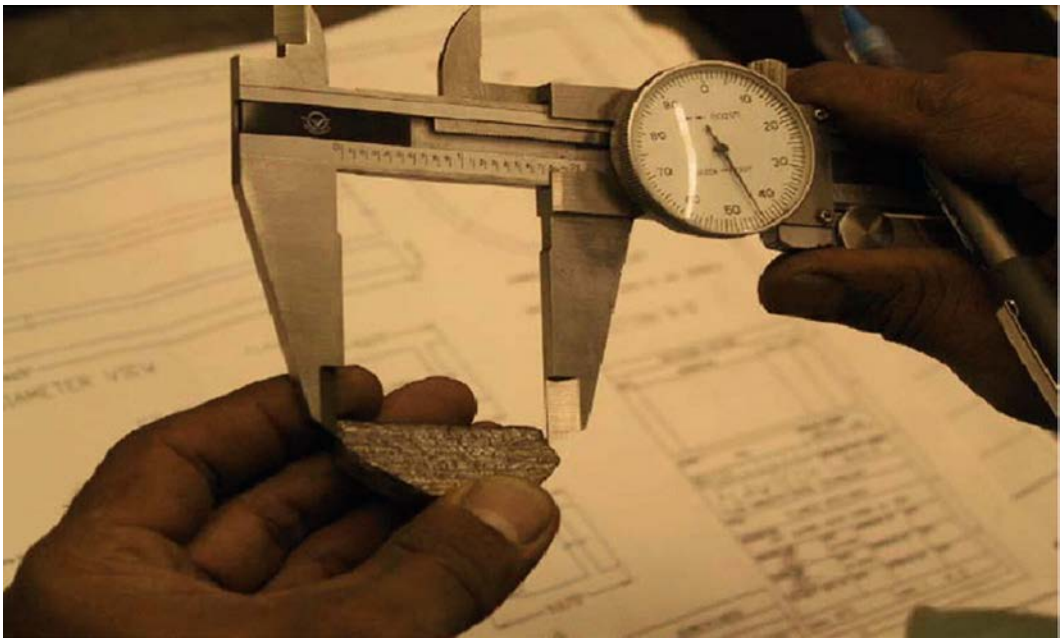

Figure A.6 Quality Assurance of Implantation Coupons

Figure A.7 Welding Set-up During Flaw Implantation

Figure A.8 Upstream Pipe Segment Ready for Joining to Downstream Segment After Flaw Implantation is Completed

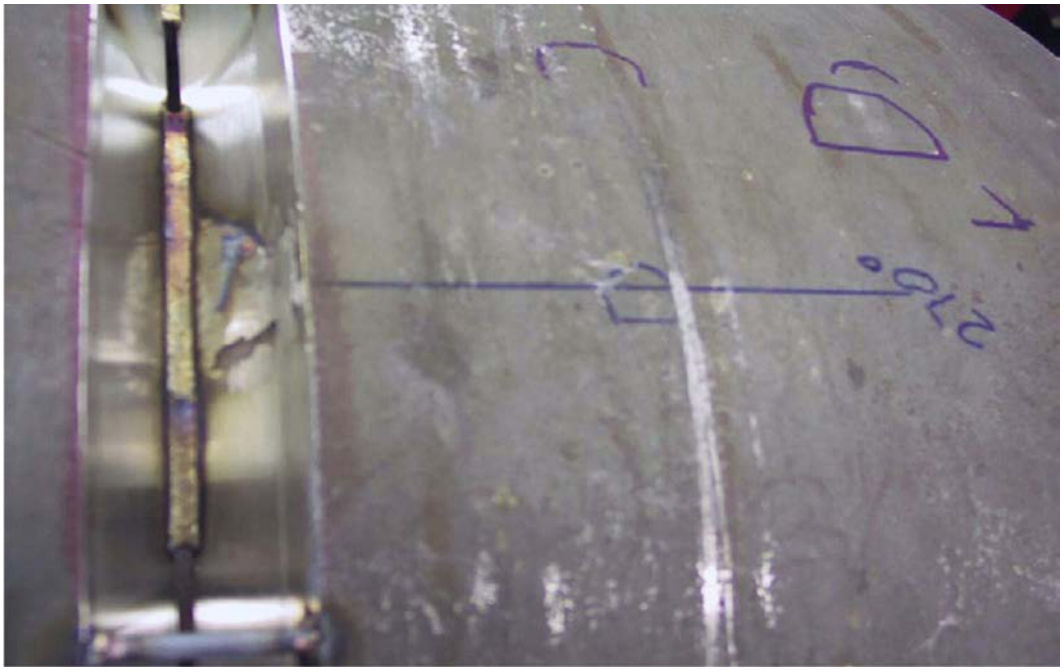

Figure A.9 Root Pass of Full Penetration Weld Near Implanted Flaw

Figure A.10 Welding Root Pass with MIG

Figure A.11 Inter-Pass Filler Welding of Full Penetration Girth Weld

Figure A.12 Completed Girth Weld Prior to Axially Sectioning the Pipe

Appendix B

Enhanced Far-Side Analysis Using a Synthetic Aperture Focusing Technique

Appendix B

Enhanced Far-Side Analysis Using a Synthetic Aperture Focusing Technique

B.1 Introduction

This appendix illustrates the value of using SAFT processing of the raw ultrasonic data and is typical of the improvements for all of the specimens.

B.2 Part Inspected

The raw data was taken on pipe segment 2 from the downstream side of the weldment. This segment included Flaw C, which was on the far side of the weld (upstream side). Due to physical constraints, only the steeper, 60° angles were used for this inspection, and far-side access due to the weld crown limited insonification of the weld region. In this case, the 60° sound path was only adequate to detect a part of the flaw's through-wall extent.

B.3 Data Analysis

Analysis was performed on a typical, industry standard 2.0 GHz dual-processor computer workstation. The processing time varies depending on the size of the data file and the size of the synthetic aperture. The wider the SAFT processing aperture angle, the more summations are required and the longer the processing. Processing of the 60° shear, 190-MB data file from pipe segment 2 with a 12° synthetic aperture angle took approximately 14 hours. A B-scan end view image comparison of the raw data and the processed data are provided as Figures B.1 and B.2.

B.4 Results

The raw data contained a significant amount of "noise" at and above the 6 dB level. This is evident in Figure B.1 as the greens, yellows, and reds indicate signal response in the upper end of the dynamic range. Using a typical 6 dB signal drop for sizing would make this image very difficult to interpret for detection and sizing of defects. Figure B.2 demonstrates how the 12° SAFT processing has removed much of the incoherent noise that would make analysis of the raw data difficult. Additionally, Flaw C has been enhanced by the processing and is indicated in red. The image represents the entire range of data collected, and it has not been envelope detected. The location of the pipe specimen ID is at 34.3 mm (1.35 in.) in these images.

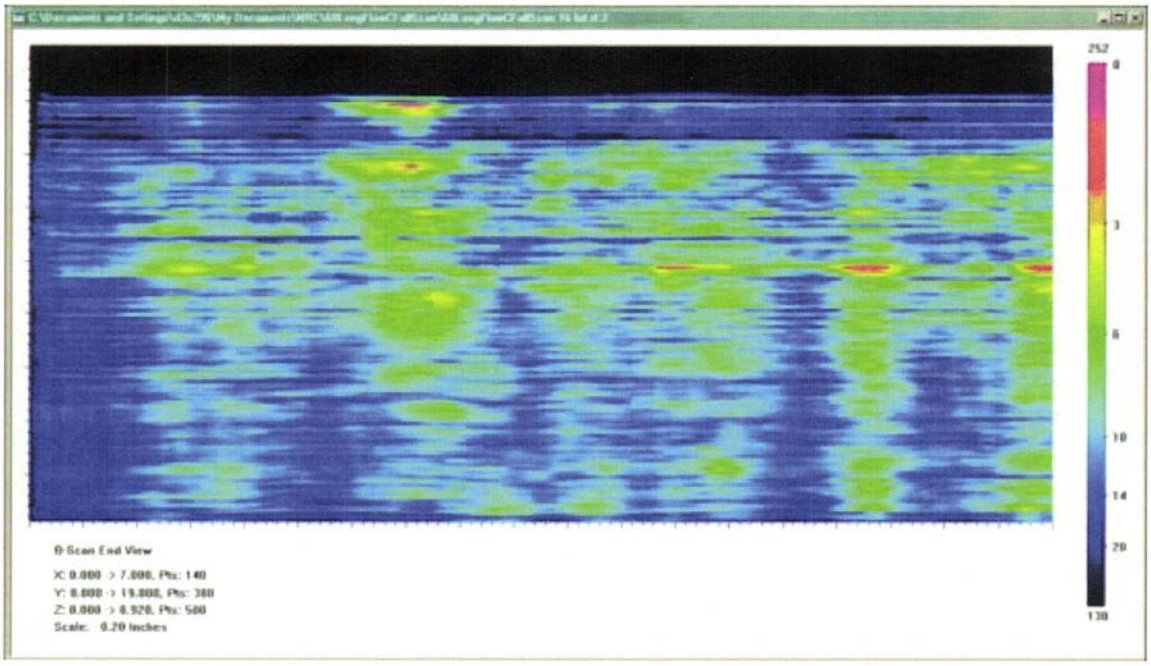

Figure B.1 Pipe Segment 2, B-scan End View, Raw Data

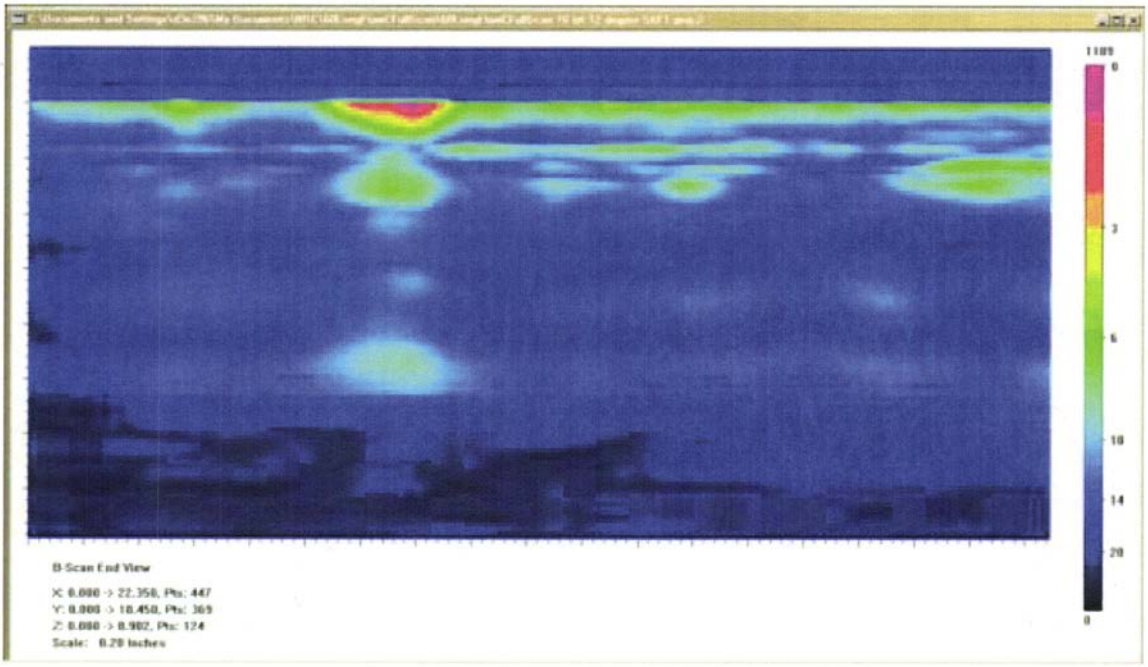

Figure B.2 Pipe Segment 2, Raw Data from Above, After SAFT Processing with a 12° Synthetic Aperture, B-scan End View

Appendix C

Conventional UT Data and Analysis Images

Appendix C

Conventional UT Data and Analysis Images

All scales are in inches

End view images are given in each figure as well as length and depth sizing information and noise characteristics. The data includes the 60 and 70 degree shear modality.

Appendix C Content:

Sawcut A, 8%	1.5 and 2.25 MHz	Near side
Flaw A, 15%	1.5 and 2.25 MHz	Near side
Sawcut B, 28%	1.5 and 2.25 MHz	Near side
Flaw B, 43%	1.5 and 2.25 MHz	Near side
Sawcut C, 7%	1.5 and 2.25 MHz	Near side
Sawcut A, 8%	1.5 and 2.25 MHz	Far side
Flaw A, 15%	1.5 and 2.25 MHz	Far side
Sawcut B, 28%	1.5 and 2.25 MHz	Far side
Flaw B, 43%	1.5 and 2.25 MHz	Far side
Sawcut C, 7%	1.5 and 2.25 MHz	Far side
Sawcut D, 19%	1.5 MHz	Near and Far side
Flaw C, 64%	1.5 MHz	Near and Far side
Sawcut E, 12%	1.5 MHz	Near and Far side
Sawcut F, 19%	1.5 MHz	Near and Far side
Sawcut G, 18%	1.5 MHz	Near and Far side
Sawcut H, 26%	1.5 MHz	Near and Far side
Flaw E, 48%	1.5 MHz	Near and Far side

Section #1, Nearside, Saw Cut A, 8% Through Wall

1.5-MHz, 0.5-in.-diameter, 60° Shear

Length Sizing

Actual	1.292
6 dB Drop	0.7
Loss of Signal	1.6
6 dB Drop Δ	0.592
Loss of Signal Δ	-0.308

Depth Sizing

Actual	0.106	Corner Trap	
6 dB Drop	0.219	Tip Signal	None
UT Tip Signal	None	Velocity	0.125
6 dB Drop Δ	-0.113	Angle	60
UT Tip Signal Δ	None		

Noise Characterization

Peak Signal Response		3304	
Noise		S/N Ratio	dB
General Weld Root	N/A	N/A	N/A
Local Weld Root	N/A	N/A	N/A
Cursor Window	619	5.3	14.5

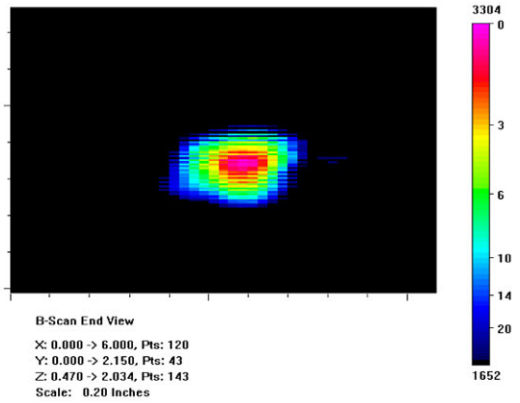

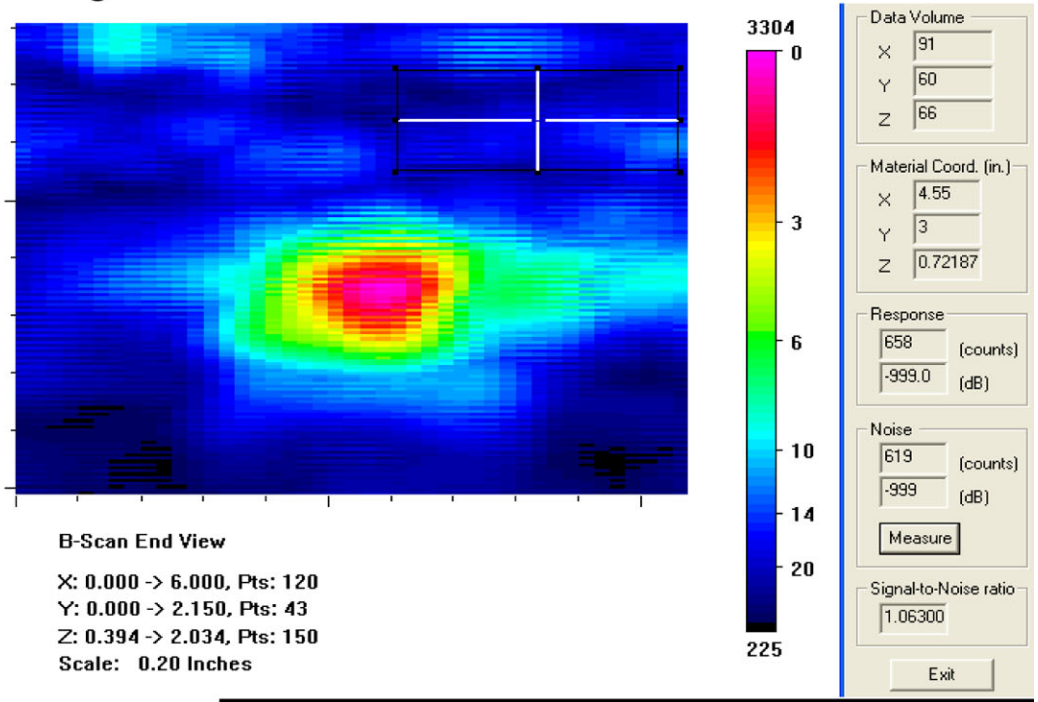

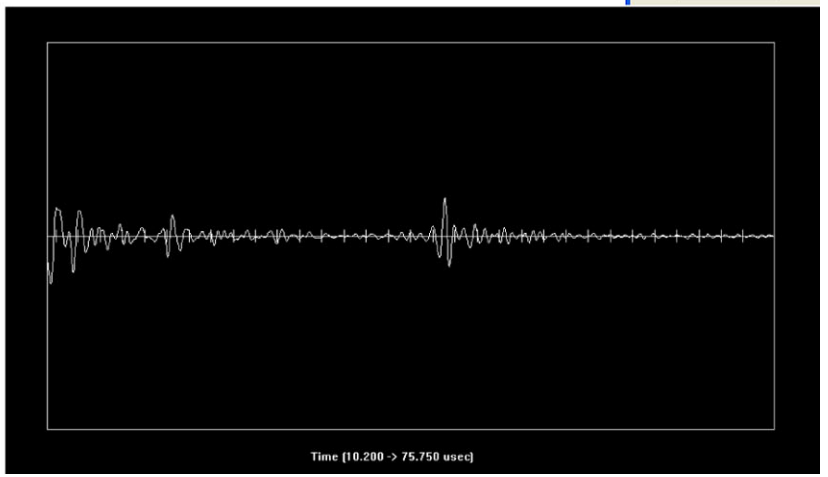

Section #1, Nearside, Saw Cut A, 8% Through Wall

1.5-MHz, 0.5-in.-diameter, 70° Shear

Length Sizing

Actual	1.292
6 dB Drop	1.6
Loss of Signal	1.6
6 dB Drop Δ	-0.308
Loss of Signal Δ	-0.308

Depth Sizing

Actual	0.106	Corner Tra	55.05
6 dB Drop	0.392	Tip Signal	47.3
UT Tip Signal	0.184581	Velocity	0.125
6 dB Drop Δ	-0.286	Angle	67.6
UT Tip Signal Δ	-0.07858		

Noise Characterization

Peak Signal Response		5172	
Noise		S/N Ratio	dB
General Weld Root	N/A	N/A	N/A
Local Weld Root	N/A	N/A	N/A
Cursor Window	1492	3.5	10.8

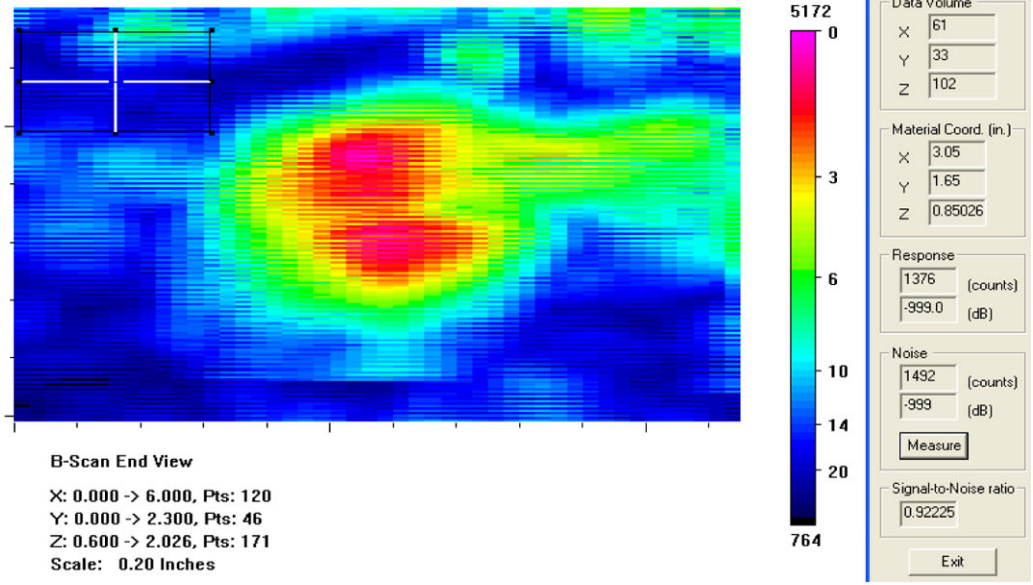

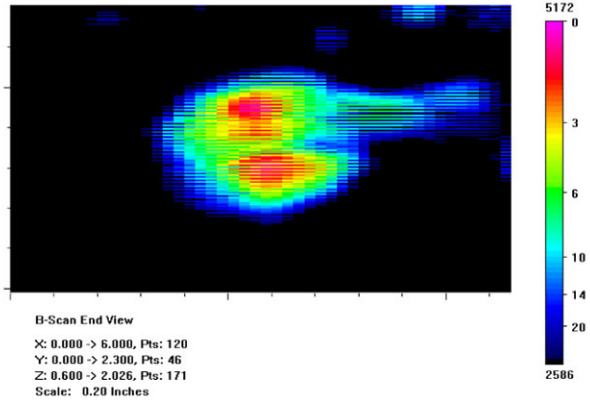

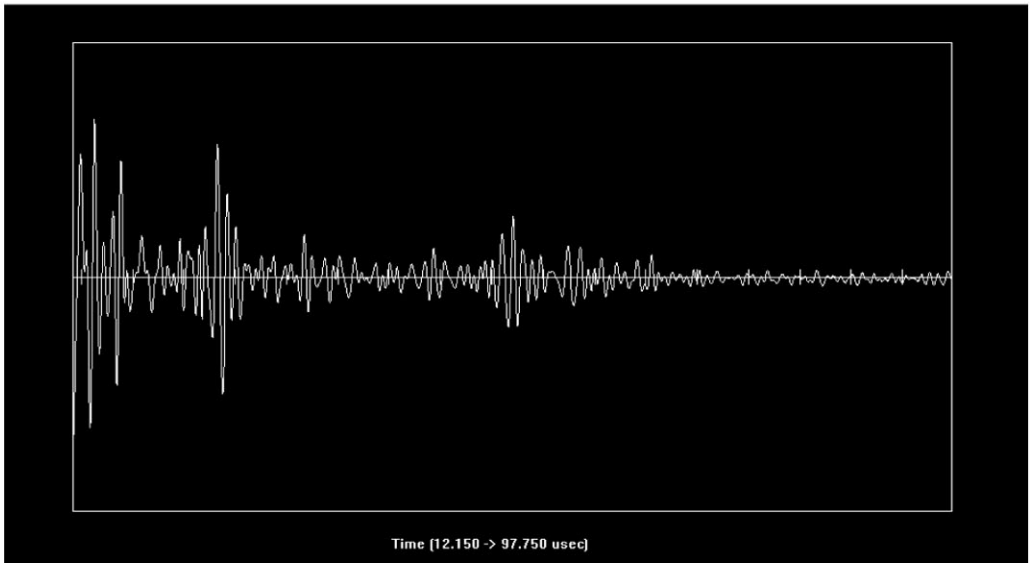

Section #1, Nearside, Saw Cut A, 8% Through Wall

1.5-MHz, 0.375-in.-diameter, 60° Shear

Length Sizing

Actual	1.292
6 dB Drop	0.9
Loss of Signal	1
6 dB Drop Δ	0.392
Loss of Signal Δ	0.292

Depth Sizing

Actual	0.106	Corner Trap	
6 dB Drop	0.247	Tip Signal	None
UT Tip Signal	None	Velocity	0.125
6 dB Drop Δ	-0.141	Angle	59
UT Tip Signal Δ	None		

Noise Characterization

Peak Signal Response		1228	
Noise		S/N Ratio	dB
General Weld Root	N/A	N/A	N/A
Local Weld Root	N/A	N/A	N/A
Cursor Window	432	2.8	9.1

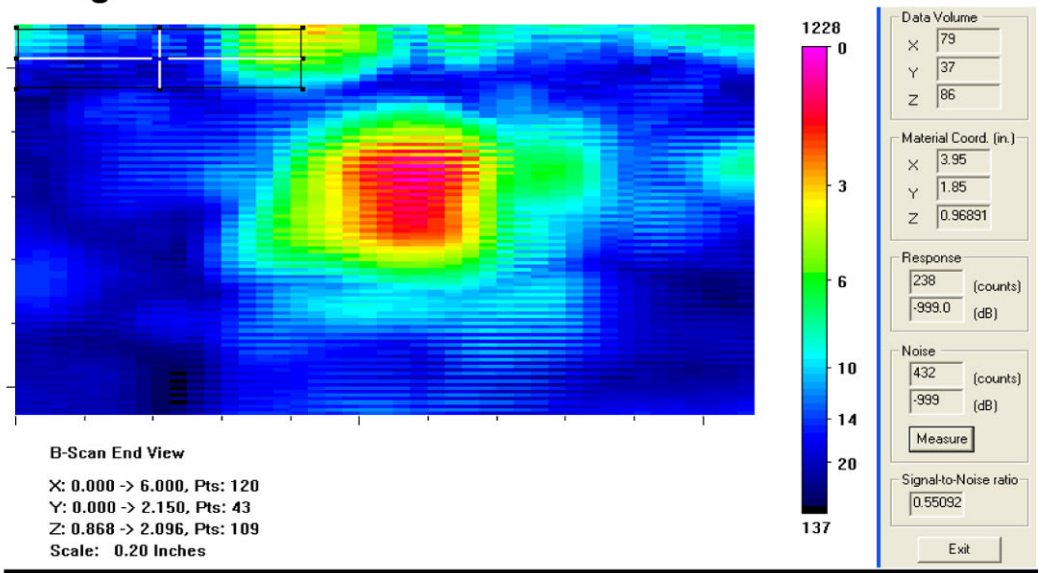

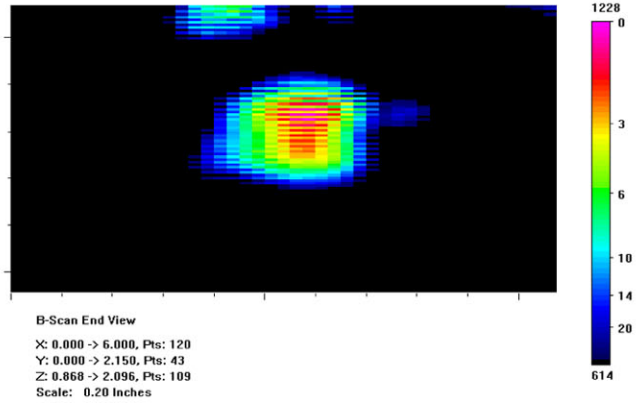

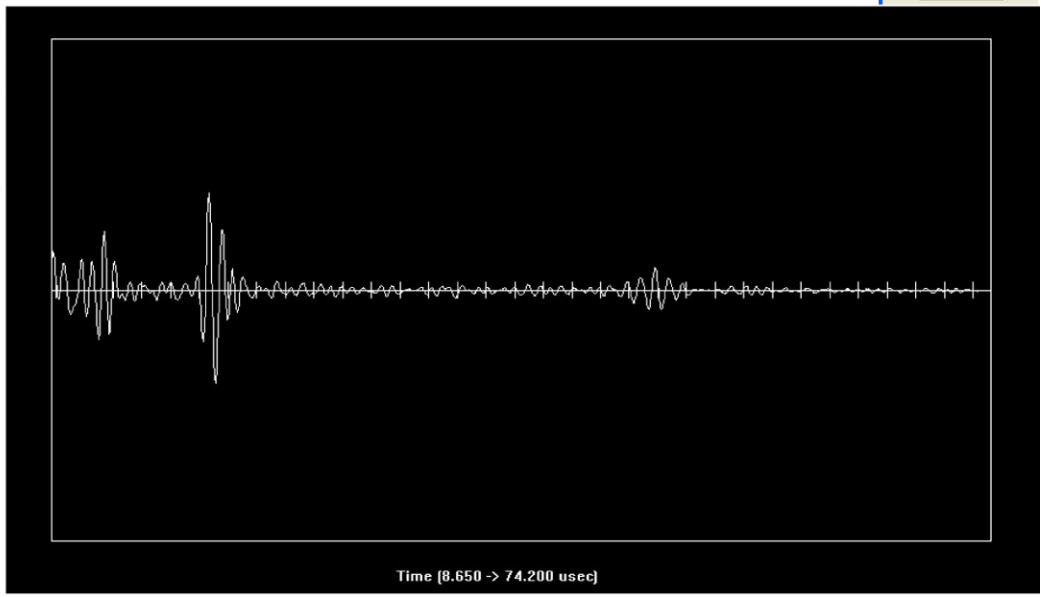

Section #1, Nearside, Saw Cut A, 8% Through Wall

1.5-MHz, 0.375-in.-diameter, 70° Shear

Length Sizing

Actual	1.292
6 dB Drop	1.5
Loss of Signal	1.5
6 dB Drop Δ	-0.208
Loss of Signal Δ	-0.208

Depth Sizing

Actual	0.106	Corner Trap	
6 dB Drop	0.384	Tip Signal	None
UT Tip Signal	None	Velocity	0.125
6 dB Drop Δ	-0.278	Angle	64
UT Tip Signal Δ	None		

Noise Characterization

Peak Signal Response		6616	
Noise		S/N Ratio	dB
General Weld Root	N/A	N/A	N/A
Local Weld Root	N/A	N/A	N/A
Cursor Window	2066	3.2	10.1

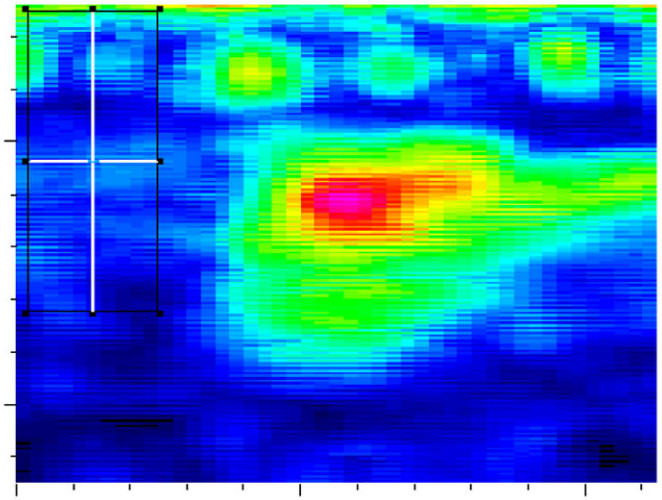

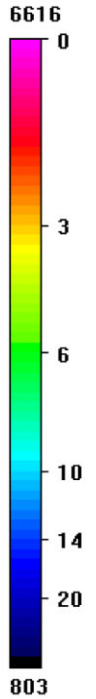

B-Scan End View

X: 0.000 -> 6.000, Pts: 120
Y: 0.000 -> 2.250, Pts: 45
Z: 0.489 -> 2.311, Pts: 190
Scale: 0.20 Inches

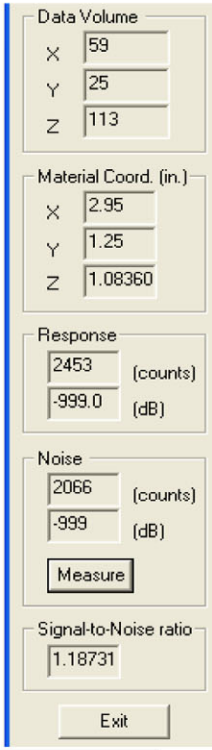

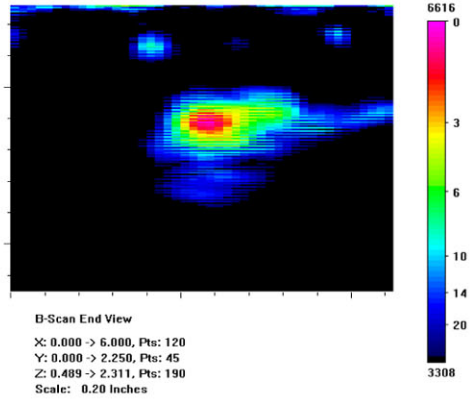

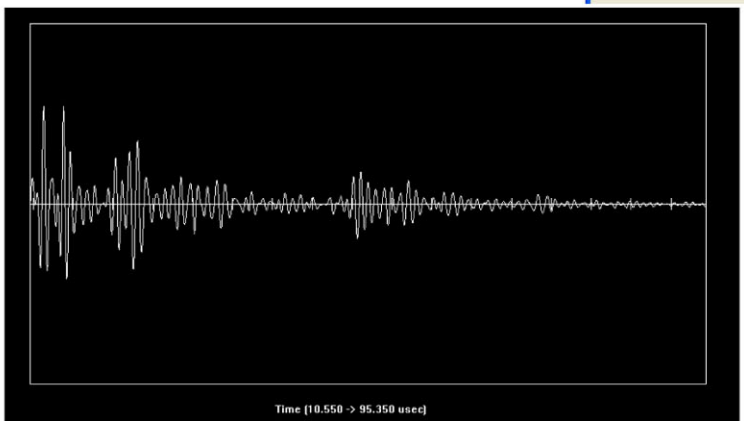

Section #1, Nearside, Saw Cut A, 8% Through Wall

2.25-MHz, 0.5-in.-diameter, 60° Shear

Length Sizing

Actual	1.292
6 dB Drop	0.7
Loss of Signal	1.15
6 dB Drop Δ	0.592
Loss of Signal Δ	0.142

Depth Sizing

Actual	0.106	Corner Tra	49.45
6 dB Drop	0.227	Tip Signal	46.95
UT Tip Signal	0.078125	Velocity	0.125
6 dB Drop Δ	-0.121	Angle	60
UT Tip Signal Δ	0.027875		

Noise Characterization

Peak Signal Response		2869	
Noise		S/N Ratio	dB
General Weld Root	N/A	N/A	N/A
Local Weld Root	N/A	N/A	N/A
Cursor Window	488	5.9	15.4

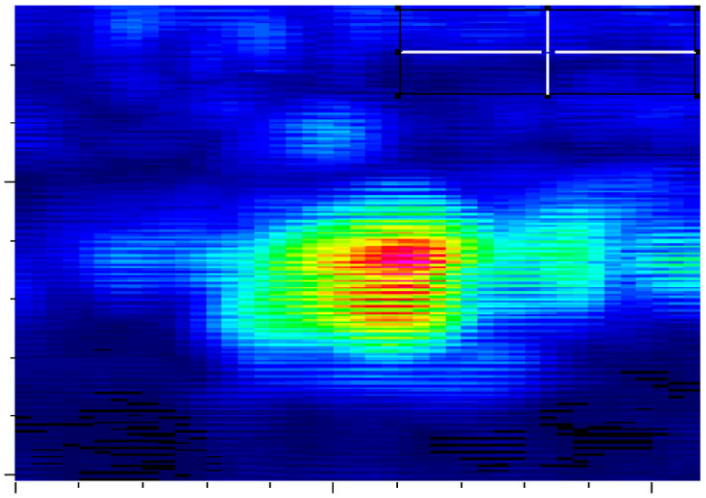

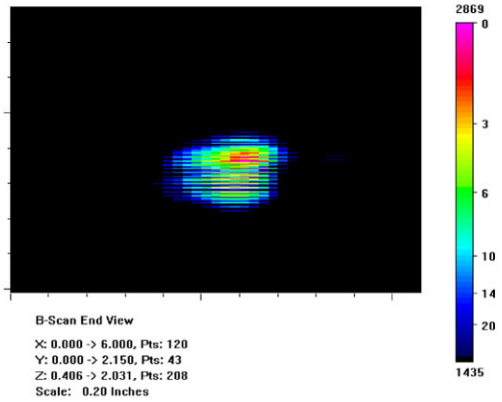

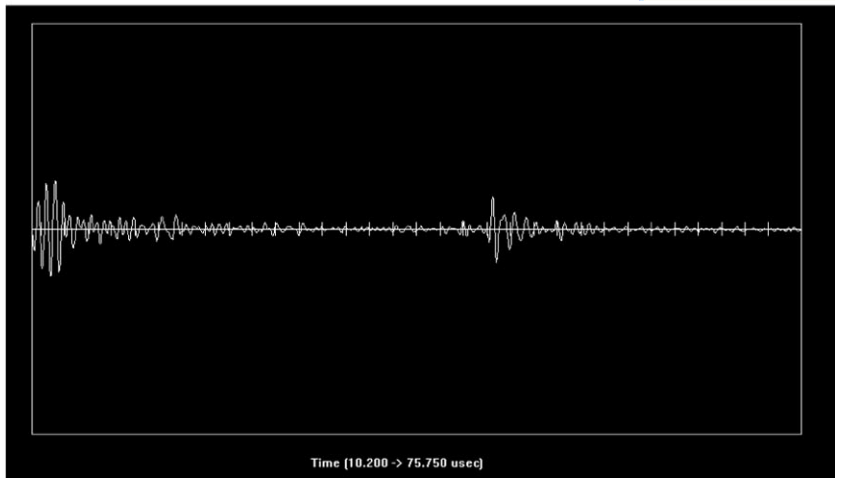

Section #1, Nearside, Saw Cut A, 8% Through Wall

2.25-MHz, 0.5-in.-diameter, 70° Shear

Length Sizing

Actual	1.292
6 dB Drop	1.05
Loss of Signal	1.1
6 dB Drop Δ	0.242
Loss of Signal Δ	0.192

Depth Sizing

Actual	0.106	Corner Tra	61.9
6 dB Drop	0.277	Tip Signal	56.3
UT Tip Signal	0.125429	Velocity	0.125
6 dB Drop Δ	-0.171	Angle	69
UT Tip Signal Δ	-0.01943		

Noise Characterization

Peak Signal Response		3965	
Noise		S/N Ratio	dB
General Weld Root	N/A	N/A	N/A
Local Weld Root	N/A	N/A	N/A
Cursor Window	1253	3.2	10.0

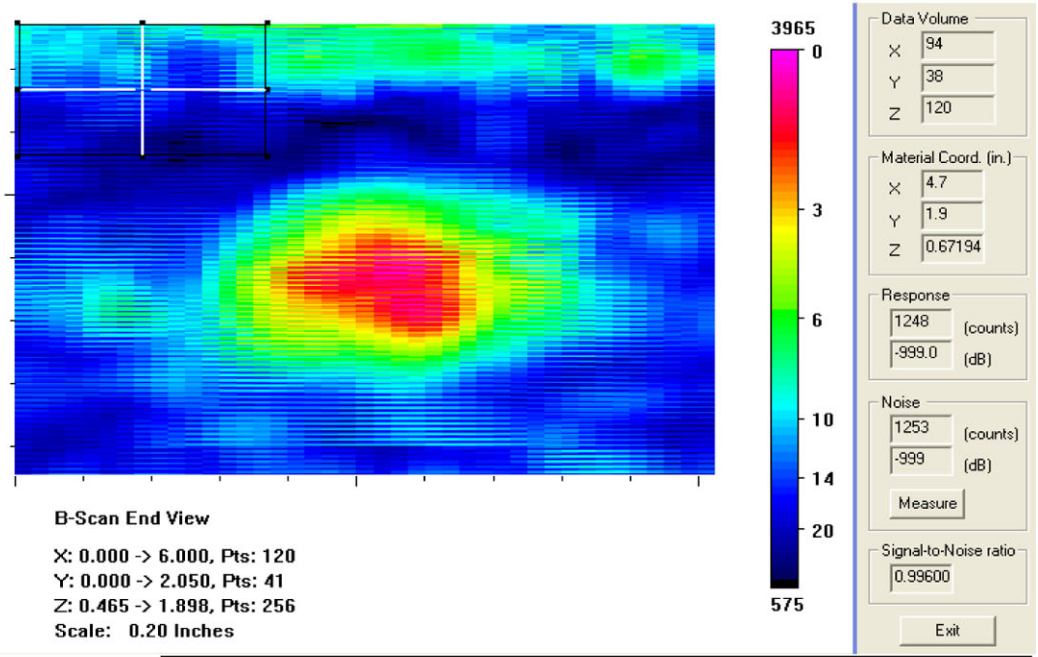

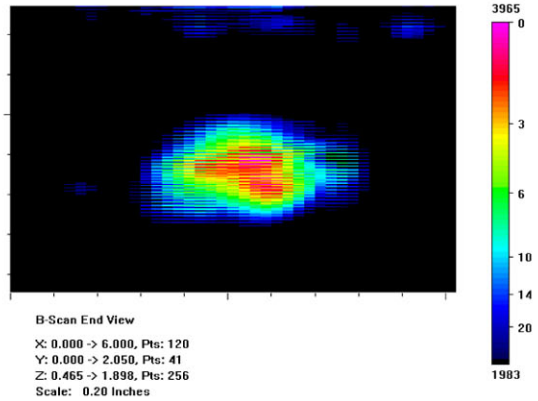

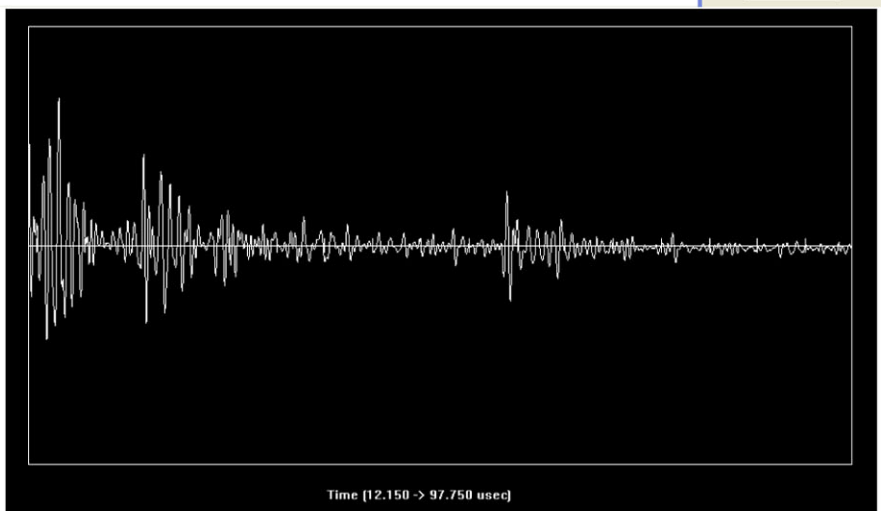

Section #1, Nearside, Saw Cut A, 8% Through Wall

2.25-MHz, 0.375-in.-diameter, 60° Shear

Length Sizing

Actual	1.292
6 dB Drop	0.7
Loss of Signal	1.05
6 dB Drop Δ	0.592
Loss of Signal Δ	0.242

Depth Sizing

Actual	0.106	Corner Trap	
6 dB Drop	0.199	Tip Signal	None
UT Tip Signal	None	Velocity	0.125
6 dB Drop Δ	-0.093	Angle	60
UT Tip Signal Δ	None		

Noise Characterization

Peak Signal Response		2486	
Noise		S/N Ratio	dB
General Weld Root	N/A	N/A	N/A
Local Weld Root	N/A	N/A	N/A
Cursor Window	486	5.1	14.2

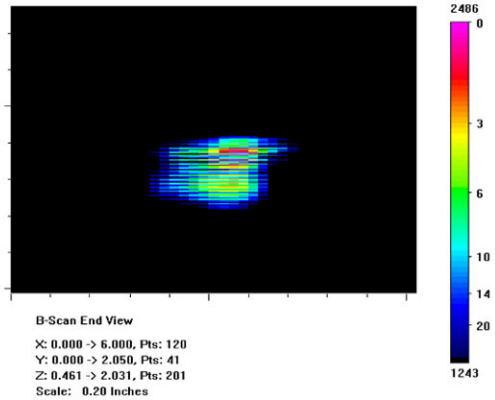

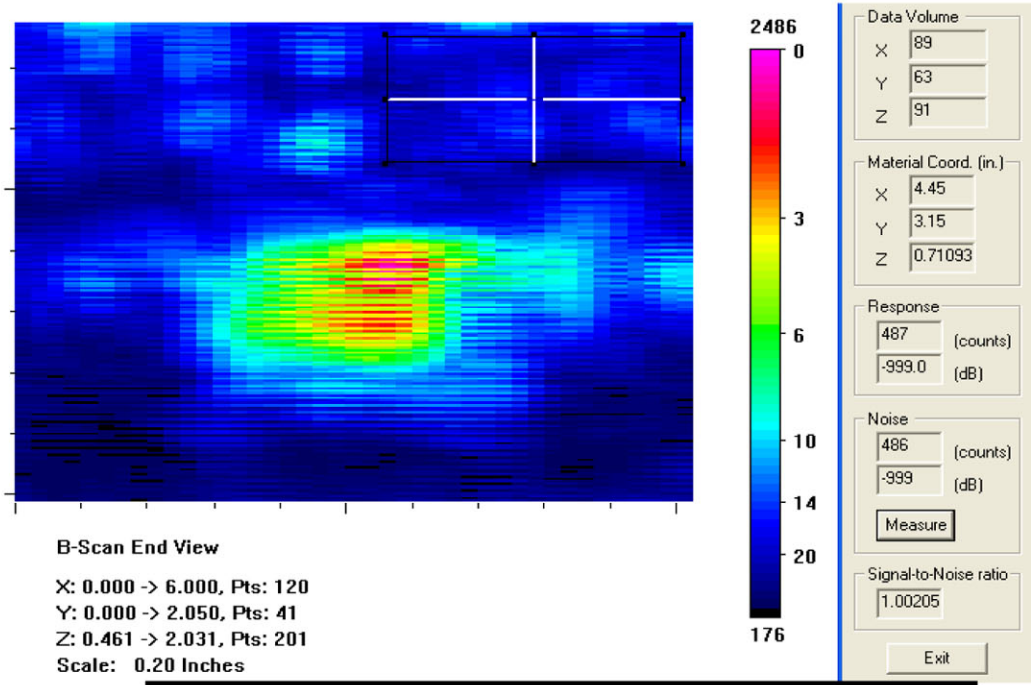

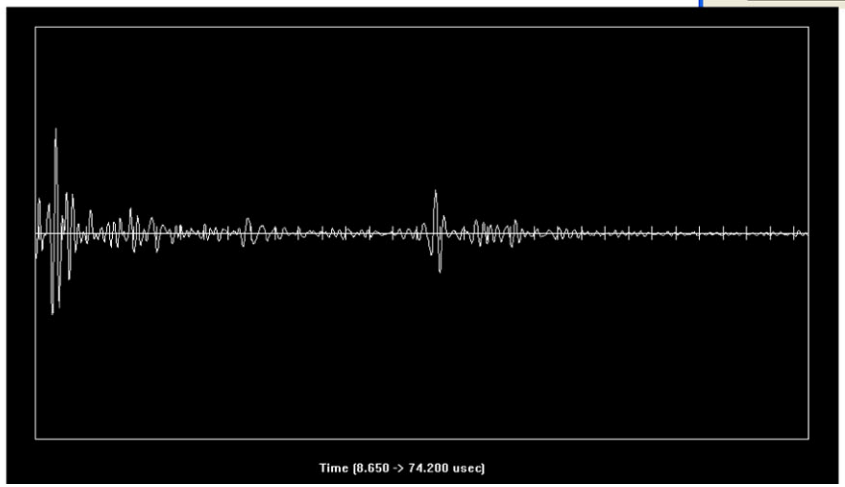

Section #1, Nearside, Saw Cut A, 8% Through Wall

2.25-MHz, 0.375-in.-diameter, 70° Shear

Length Sizing

Actual	1.292
6 dB Drop	0.9
Loss of Signal	1.1
6 dB Drop Δ	0.392
Loss of Signal Δ	0.192

Depth Sizing

Actual	0.106	Corner Trap	
6 dB Drop	0.458	Tip Signal	None
UT Tip Signal	None	Velocity	0.125
6 dB Drop Δ	-0.352	Angle	66
UT Tip Signal Δ	None		

Noise Characterization

Peak Signal Response		4300	
Noise		S/N Ratio	dB
General Weld Root	N/A	N/A	N/A
Local Weld Root	N/A	N/A	N/A
Cursor Window	950	4.5	13.1

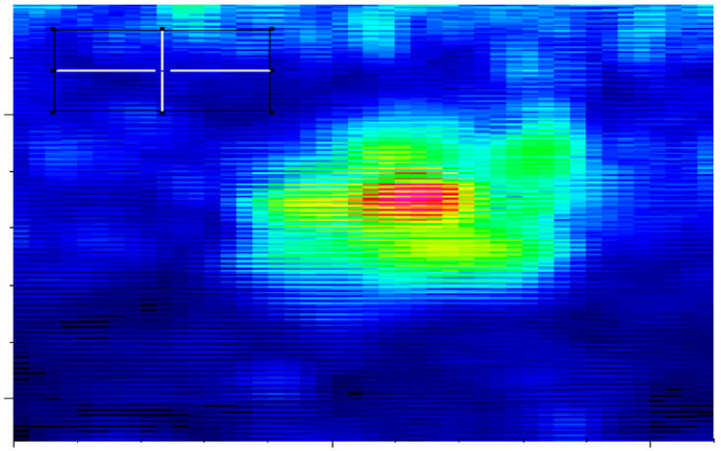

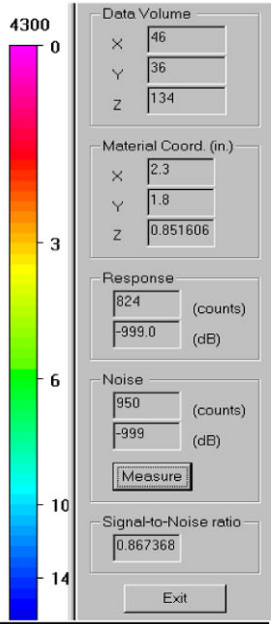

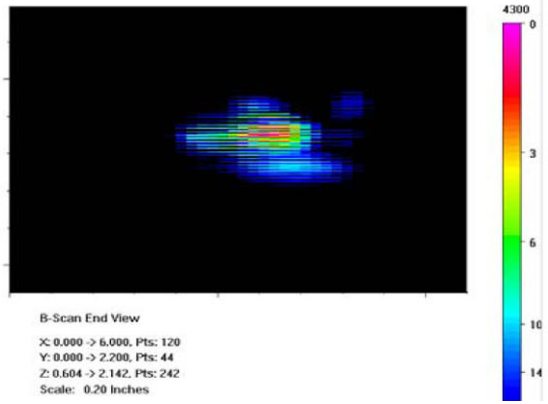

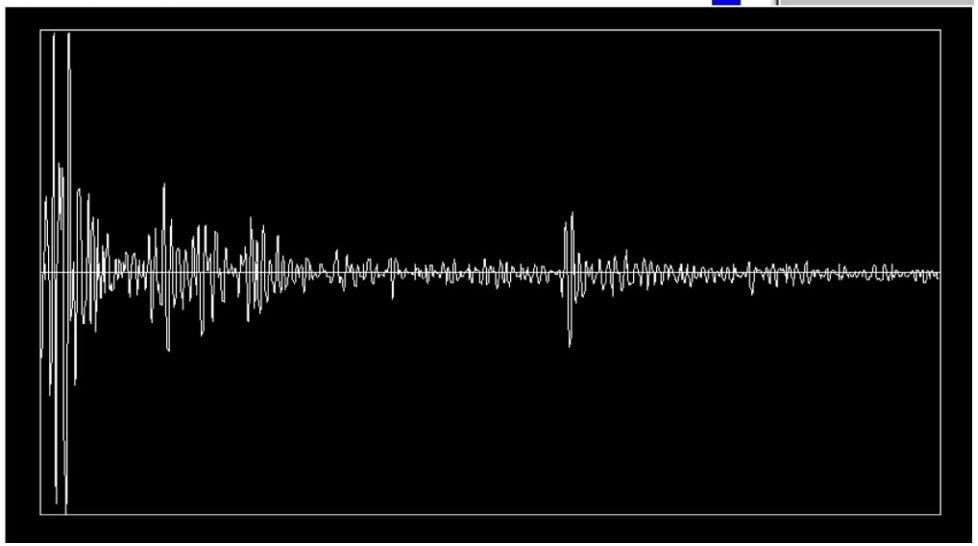

Section #1, Nearside, Flaw A, 15% Through Wall

1.5-MHz, 0.5-in.-diameter, 60° Shear

Length Sizing

Actual	0.42
6 dB Drop	0.5
Loss of Signal	0.7
6 dB Drop Δ	-0.08
Loss of Signal Δ	-0.28

Depth Sizing

Actual	0.195	Corner Trap	
6 dB Drop	0.213	Tip Signal	None
UT Tip Signal	None	Velocity	0.125
6 dB Drop Δ	-0.018	Angle	60
UT Tip Signal Δ	None		

Noise Characterization

Peak Signal Response		2969	
Noise		S/N Ratio	dB
General Weld Root	N/A	N/A	N/A
Local Weld Root	N/A	N/A	N/A
Cursor Window	669	4.4	12.9

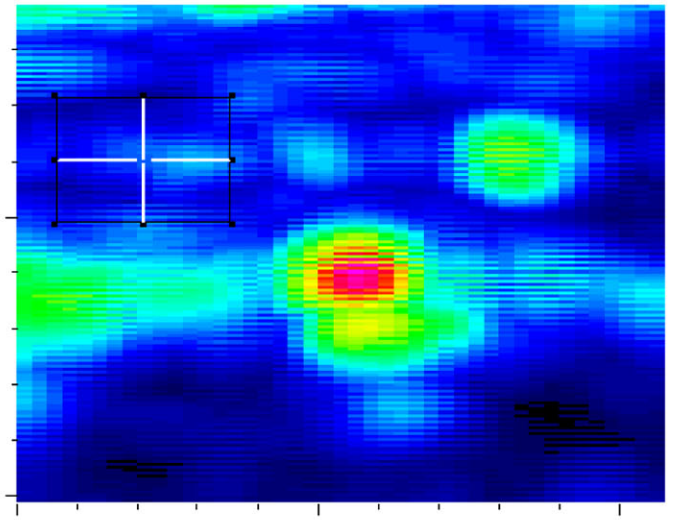

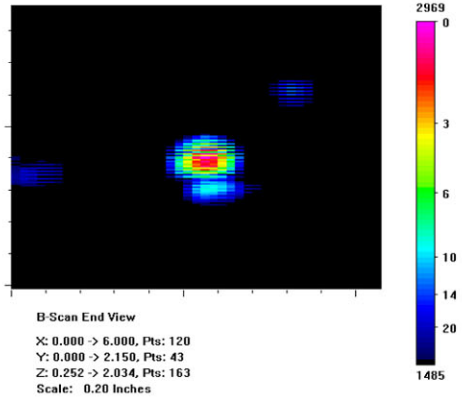

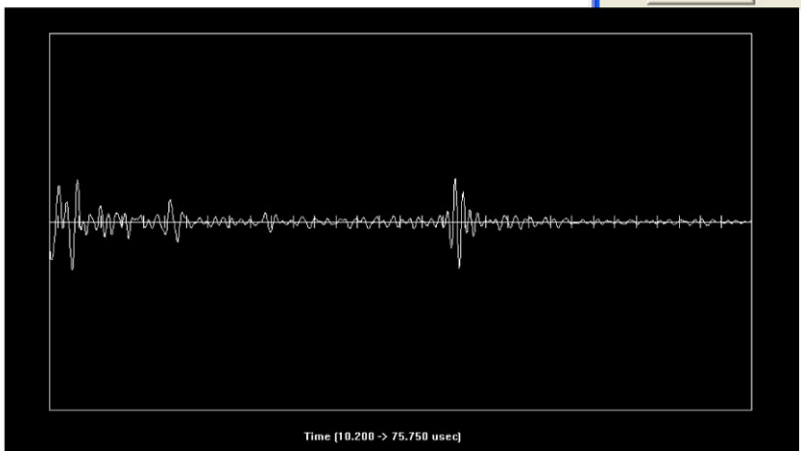

Section #1, Nearside, Flaw A, 15% Through Wall

1.5-MHz, 0.5-in.-diameter, 70° Shear

Length Sizing

Actual	0.42
6 dB Drop	0.55
Loss of Signal	0.65
6 dB Drop Δ	-0.13
Loss of Signal Δ	-0.23

Depth Sizing

Actual	0.195	Corner Tra	70.2
6 dB Drop	0.275	Tip Signal	63.35
UT Tip Signal	0.163146	Velocity	0.125
6 dB Drop Δ	-0.08	Angle	67.6
UT Tip Signal Δ	0.031854		

Noise Characterization

Peak Signal Response		6536	
Noise		S/N Ratio	dB
General Weld Root	N/A	N/A	N/A
Local Weld Root	N/A	N/A	N/A
Cursor Window	1785	3.7	11.3

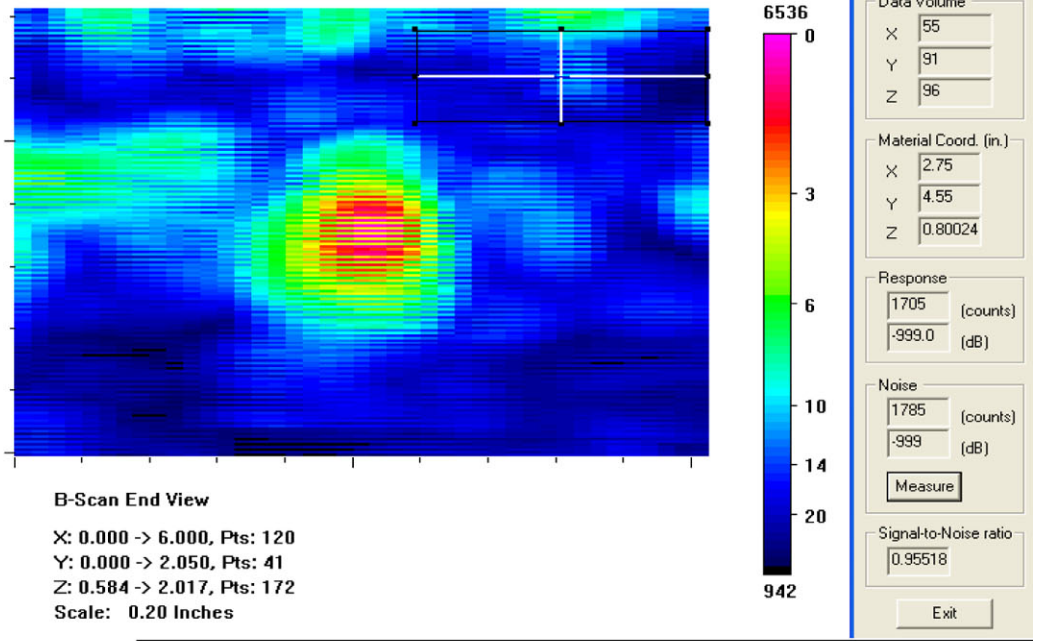

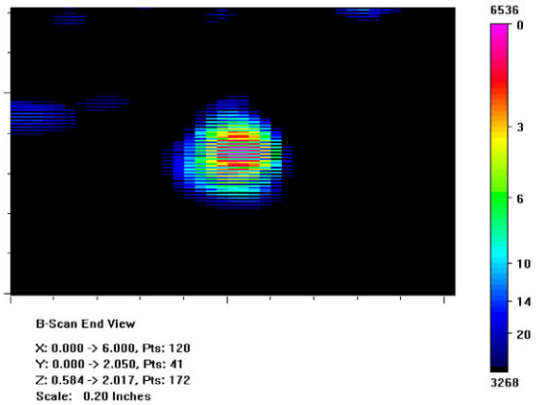

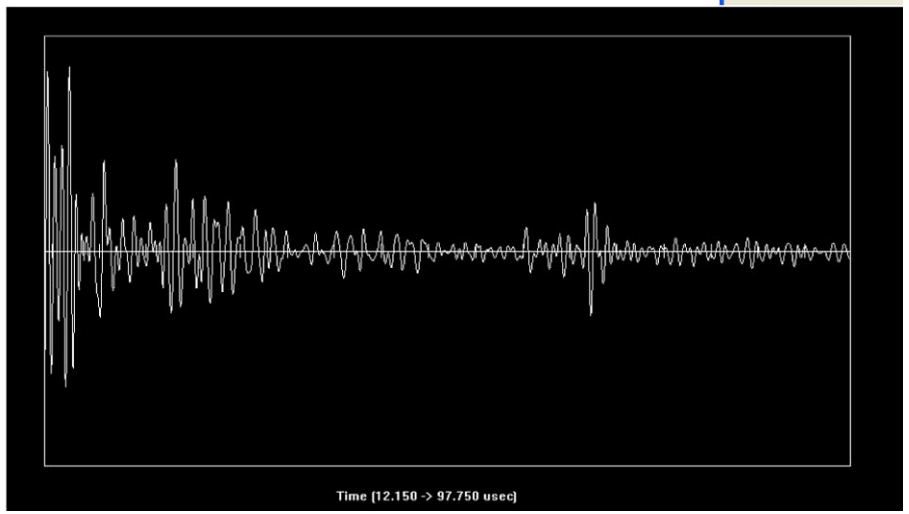

Section #1, Nearside, Flaw A, 15% Through Wall

1.5-MHz, 0.375-in.-diameter, 60° Shear

Length Sizing

Actual	0.42
6 dB Drop	0.6
Loss of Signal	0.5
6 dB Drop Δ	-0.18
Loss of Signal Δ	-0.08

No Call due to low signal to noise ratio and high amplitude noise peaks

Depth Sizing

Actual	0.195	Corner Trap	
6 dB Drop	0.141	Tip Signal	None
UT Tip Signal	None	Velocity	0.125
6 dB Drop Δ	0.054	Angle	59
UT Tip Signal Δ	None		

Noise Characterization

Peak Signal Response		992	
Noise		S/N Ratio	dB
General Weld Root	N/A	N/A	N/A
Local Weld Root	2580	N/A	N/A
Cursor Window	973	1.0	0.2

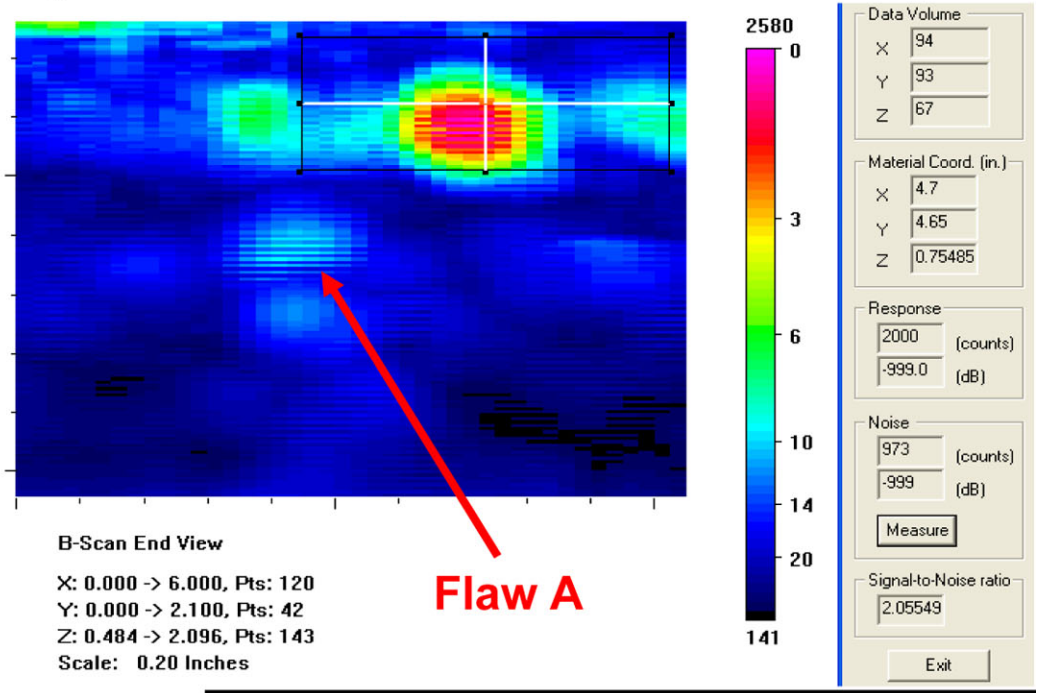

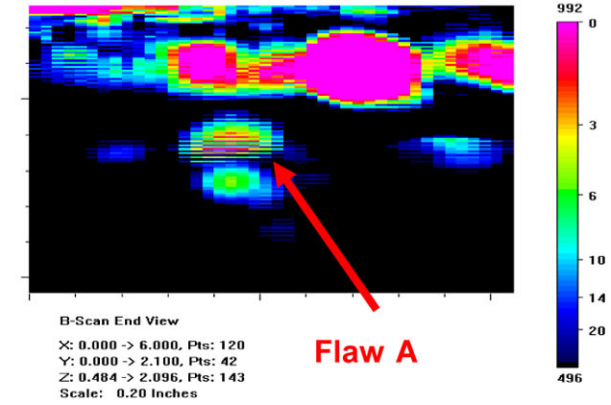

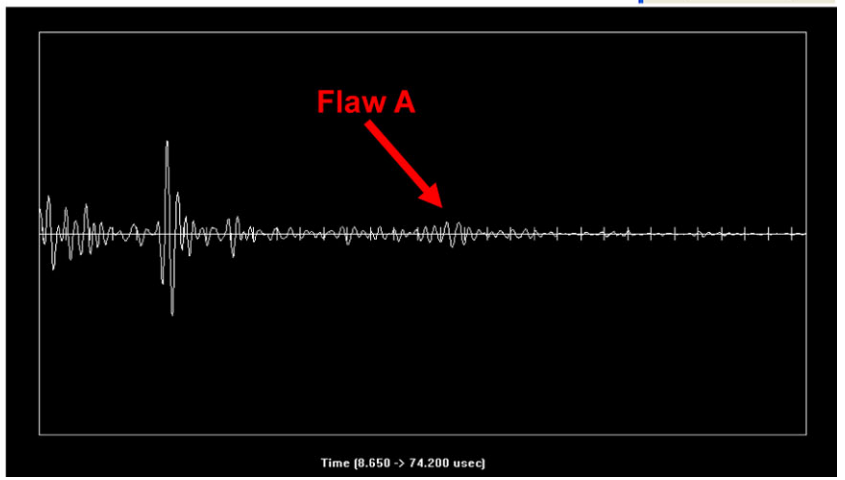

Section #1, Nearside, Flaw A, 15% Through Wall

1.5-MHz, 0.375-in.-diameter, 70° Shear

Length Sizing

Actual	0.42
6 dB Drop	0.55
Loss of Signal	0.65
6 dB Drop Δ	-0.13
Loss of Signal Δ	-0.23

Depth Sizing

Actual	0.195	Corner Trap	
6 dB Drop	0.369	Tip Signal	None
UT Tip Signal	None	Velocity	0.125
6 dB Drop Δ	-0.174	Angle	64
UT Tip Signal Δ	None		

Noise Characterization

Peak Signal Response		6482	
Noise		S/N Ratio	dB
General Weld Root	N/A	N/A	N/A
Local Weld Root	N/A	N/A	N/A
Cursor Window	1798	3.6	11.1

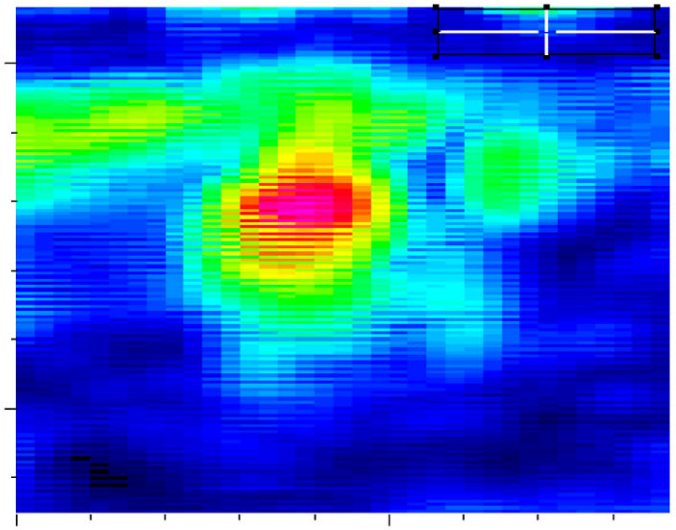

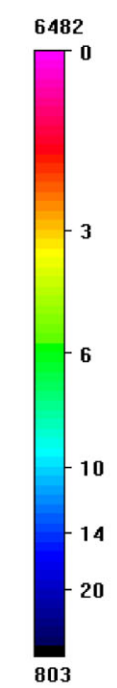

B-Scan End View

X: 0.000 -> 6.000, Pts: 120
Y: 0.000 -> 1.750, Pts: 35
Z: 0.844 -> 2.311, Pts: 153
Scale: 0.20 Inches

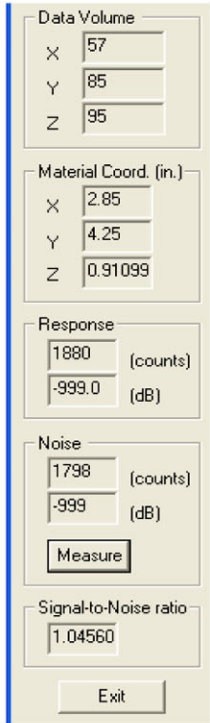

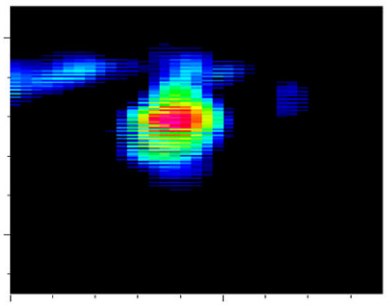

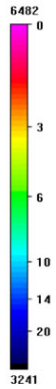

B-Scan End View

X: 0.000 -> 6.000, Pts: 120
Y: 0.000 -> 1.750, Pts: 35
Z: 0.844 -> 2.311, Pts: 153
Scale: 0.20 Inches

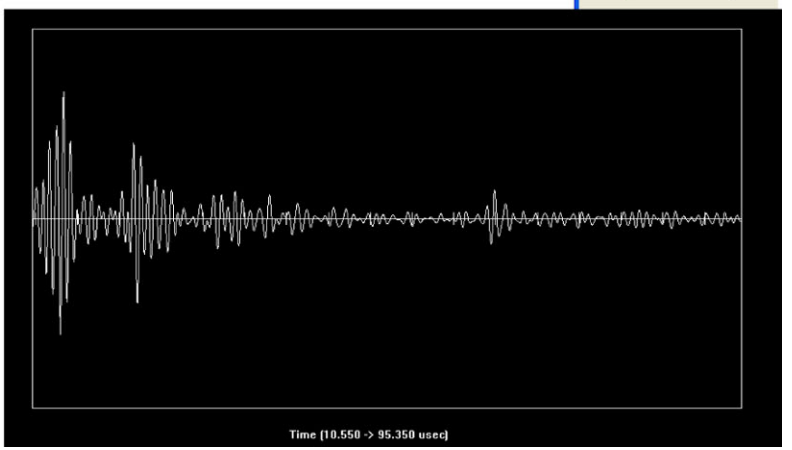

Section #1, Nearside, Flaw A, 15% Through Wall

2.25-MHz, 0.5-in.-diameter, 60° Shear

Length Sizing

Actual	0.42
6 dB Drop	0.55
Loss of Signal	0.65
6 dB Drop Δ	-0.13
Loss of Signal Δ	-0.23

Depth Sizing

Actual	0.195	Corner Trap	
6 dB Drop	0.25	Tip Signal	None
UT Tip Signal	None	Velocity	0.125
6 dB Drop Δ	-0.055	Angle	60
UT Tip Signal Δ	None		

Noise Characterization

Peak Signal Response		2314	
Noise		S/N Ratio	dB
General Weld Root	N/A	N/A	N/A
Local Weld Root	N/A	N/A	N/A
Cursor Window	515	4.5	13.1

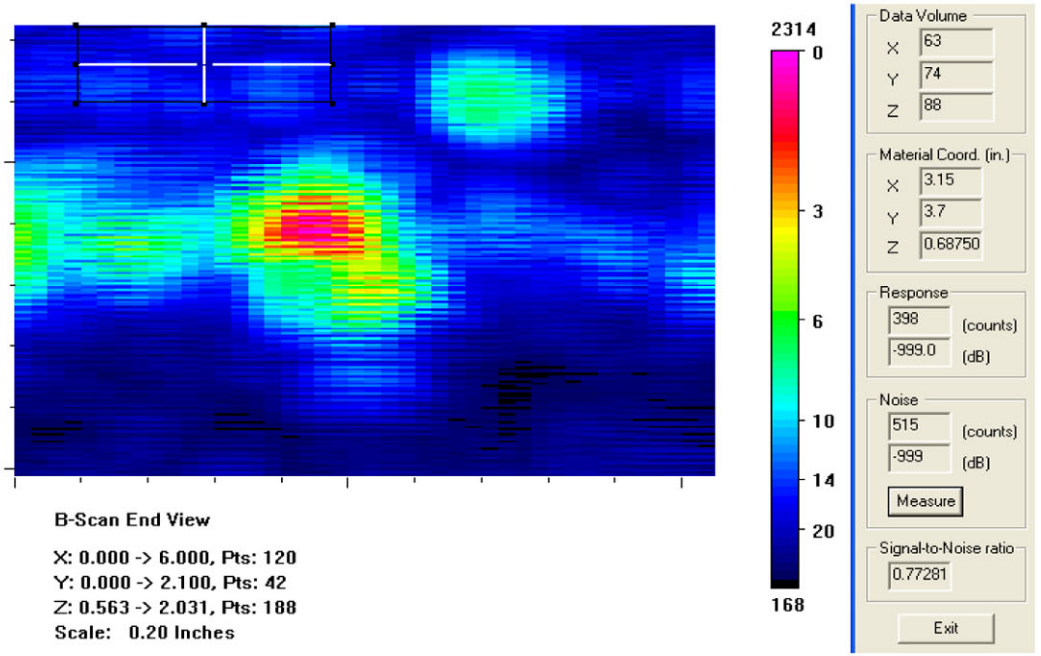

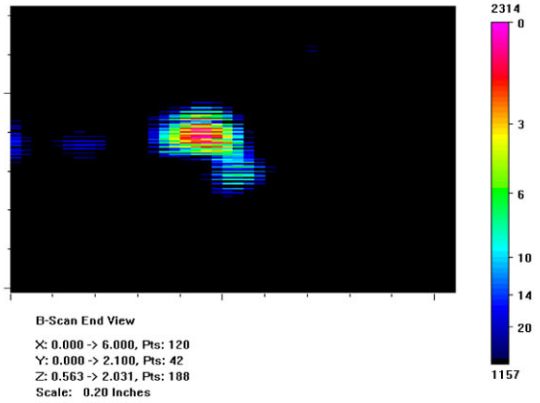

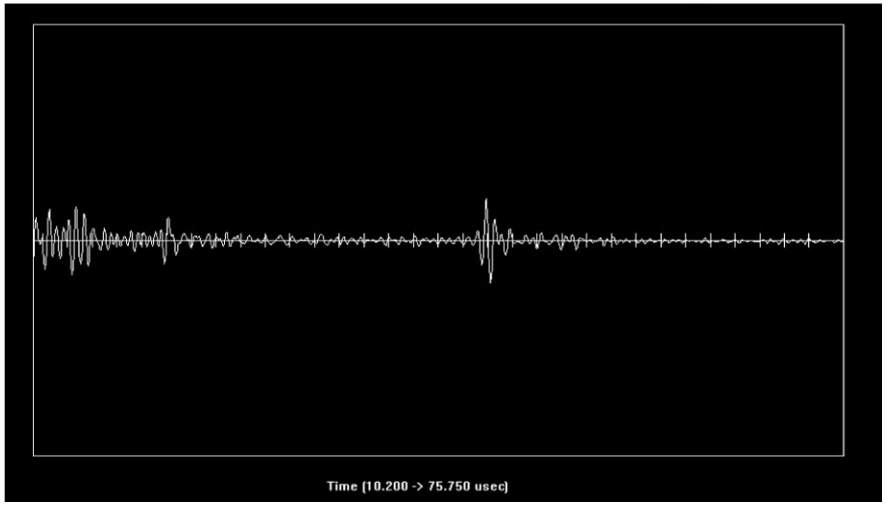

Section #1, Nearside, Flaw A, 15% Through Wall

2.25-MHz, 0.5-in.-diameter, 70° Shear

Length Sizing

Actual	0.42
6 dB Drop	0.55
Loss of Signal	0.75
6 dB Drop Δ	-0.13
Loss of Signal Δ	-0.33

Depth Sizing

Actual	0.195	Corner Tra	70.65
6 dB Drop	0.263	Tip Signal	66.45
UT Tip Signal	0.094072	Velocity	0.125
6 dB Drop Δ	-0.068	Angle	69
UT Tip Signal Δ	0.100928		

Noise Characterization

Peak Signal Response		4758	
Noise		S/N Ratio	dB
General Weld Root	N/A	N/A	N/A
Local Weld Root	N/A	N/A	N/A
Cursor Window	974	4.9	13.8

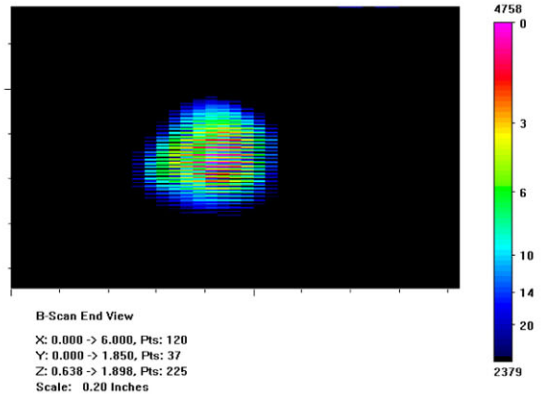

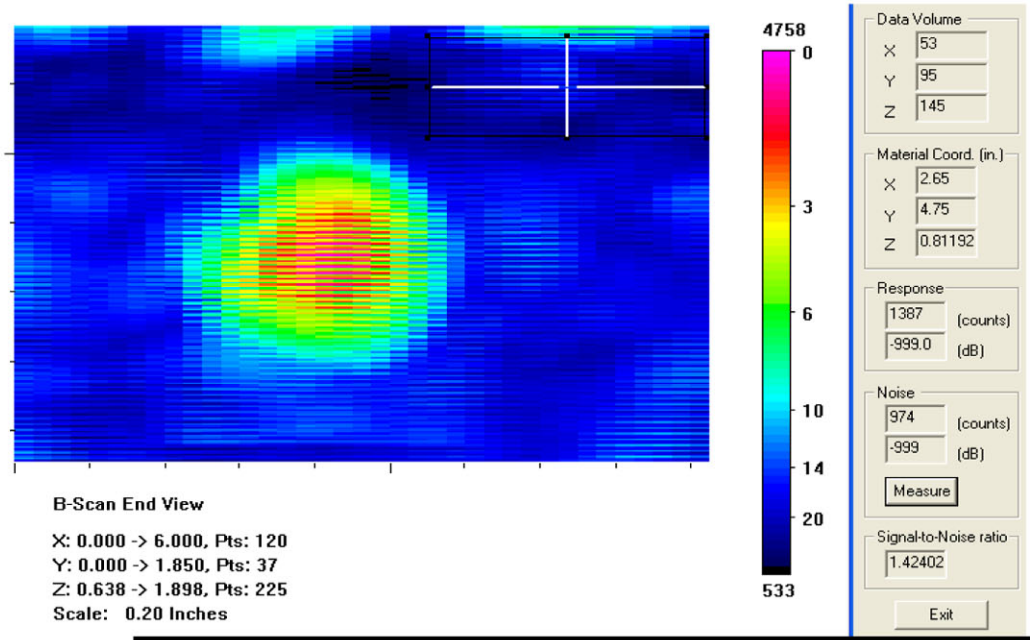

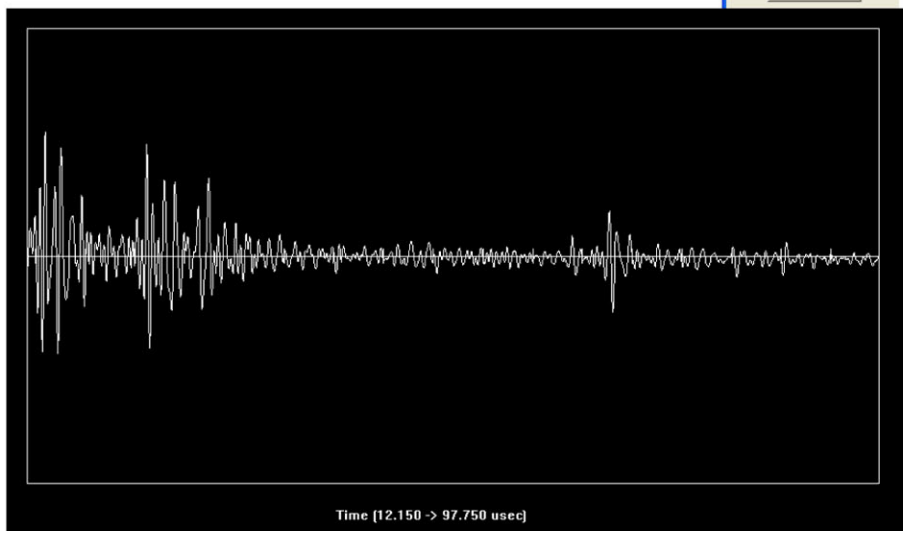

Section #1, Nearside, Flaw A, 15% Through Wall

2.25-MHz, 0.375-in.-diameter, 60° Shear

Length Sizing

Actual	0.42
6 dB Drop	0.5
Loss of Signal	0.65
6 dB Drop Δ	-0.08
Loss of Signal Δ	-0.23

Depth Sizing

Actual	0.195	Corner Trap	
6 dB Drop	0.172	Tip Signal	None
UT Tip Signal	None	Velocity	0.125
6 dB Drop Δ	0.023	Angle	60
UT Tip Signal Δ	None		

Noise Characterization

Peak Signal Response		2515	
Noise		S/N Ratio	dB
General Weld Root	N/A	N/A	N/A
Local Weld Root	N/A	N/A	N/A
Cursor Window	528	4.8	13.6

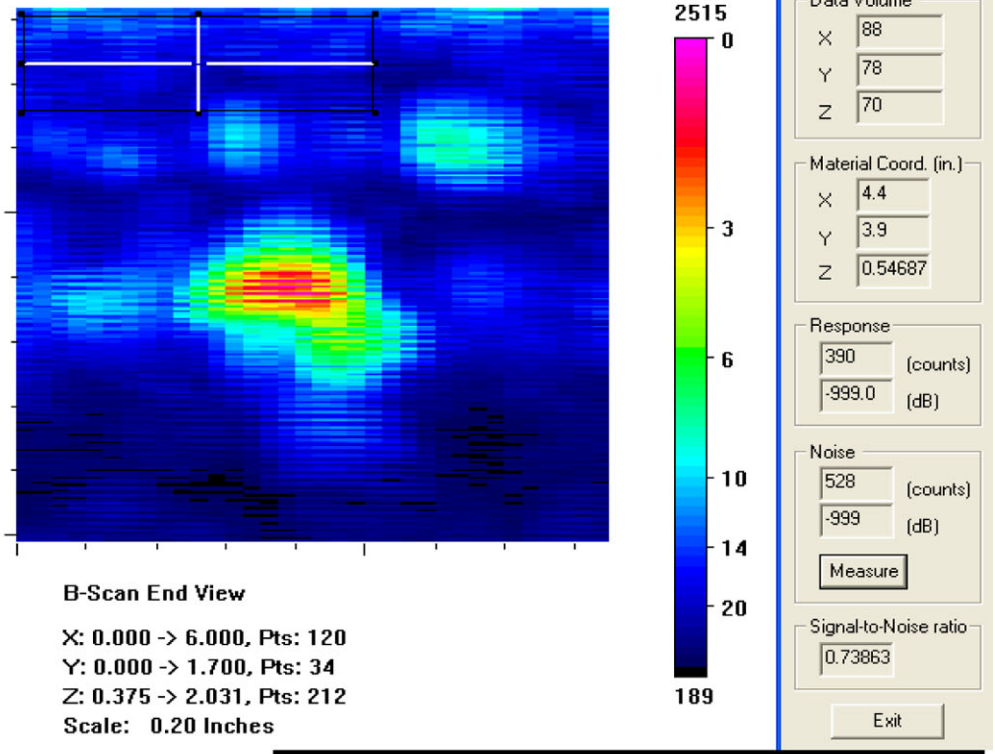

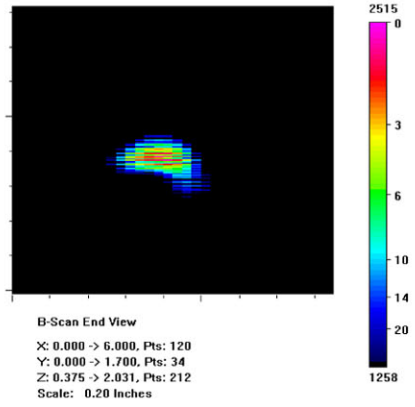

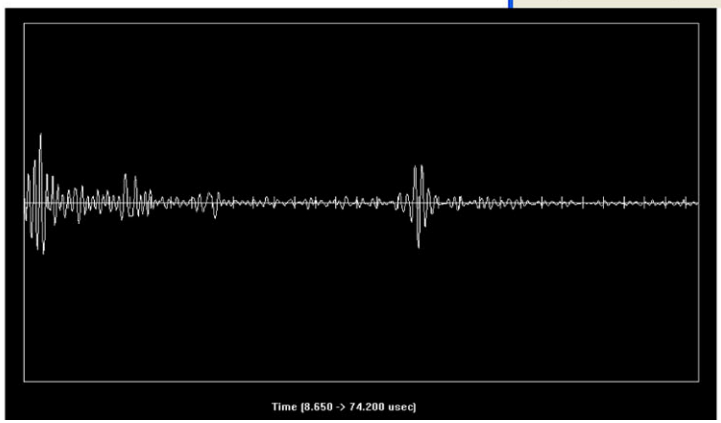

Section #1, Nearside, Flaw A, 15% Through Wall

2.25-MHz, 0.375-in.-diameter, 70° Shear

Length Sizing

Actual	0.42
6 dB Drop	0.65
Loss of Signal	0.85
6 dB Drop Δ	-0.23
Loss of Signal Δ	-0.43

Depth Sizing

Actual	0.195	Corner Trap	
6 dB Drop	0.292	Tip Signal	None
UT Tip Signal	None	Velocity	0.125
6 dB Drop Δ	-0.097	Angle	66
UT Tip Signal Δ	None		

Noise Characterization

Peak Signal Response		3274	
Noise		S/N Ratio	dB
General Weld Root	N/A	N/A	N/A
Local Weld Root	N/A	N/A	N/A
Cursor Window	1231	2.7	8.5

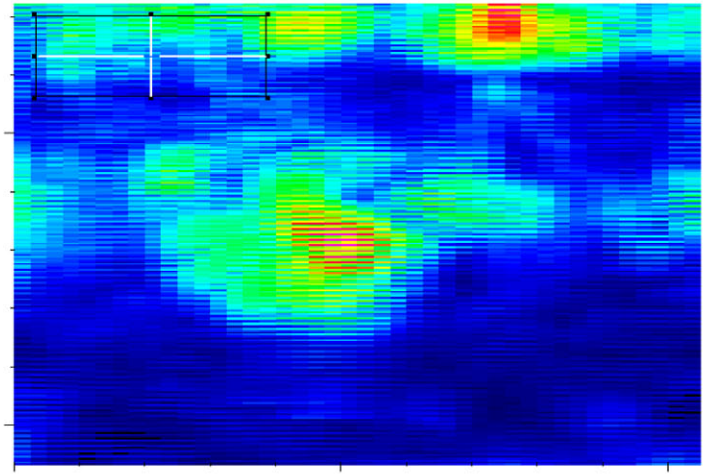

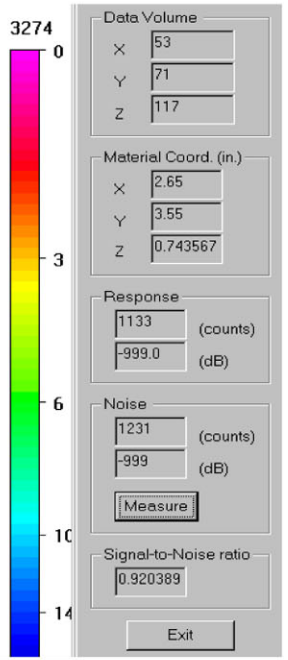

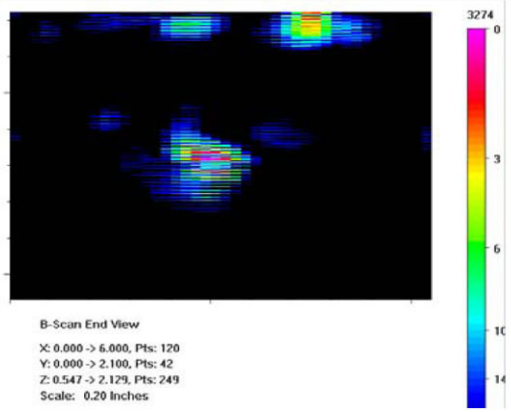

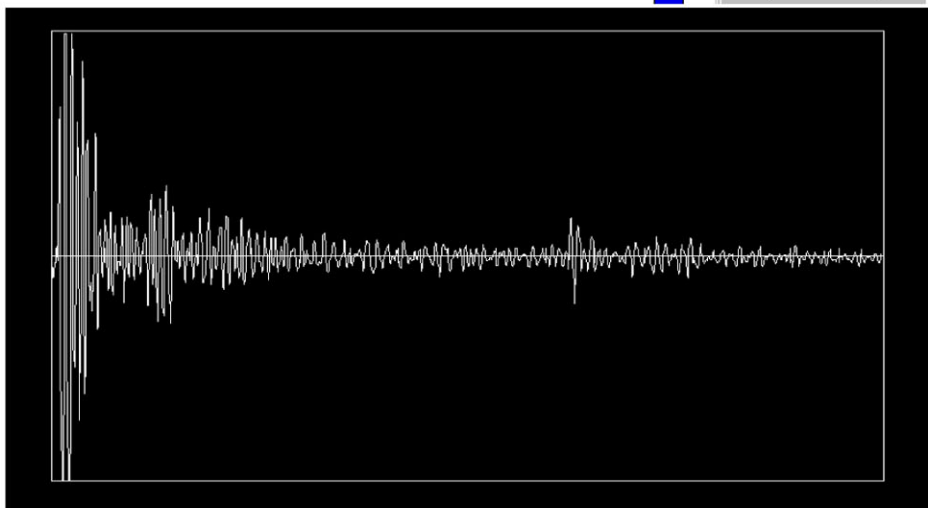

Section #1, Nearside, Saw Cut B, 28% Through Wall

1.5-MHz, 0.5-in.-diameter, 60° Shear

Length Sizing

Actual	2.565
6 dB Drop	2.05
Loss of Signal	2.75
6 dB Drop Δ	0.515
Loss of Signal Δ	-0.185

Depth Sizing

Actual	0.403	Corner Tra	47.5
6 dB Drop	0.159	Tip Signal	39.25
UT Tip Signal	0.257813	Velocity	0.125
6 dB Drop Δ	0.244	Angle	60
UT Tip Signal Δ	0.145188		

Noise Characterization

Peak Signal Response		15316	
Noise		S/N Ratio	dB
General Weld Root	N/A	N/A	N/A
Local Weld Root	N/A	N/A	N/A
Cursor Window	661	23.2	27.3

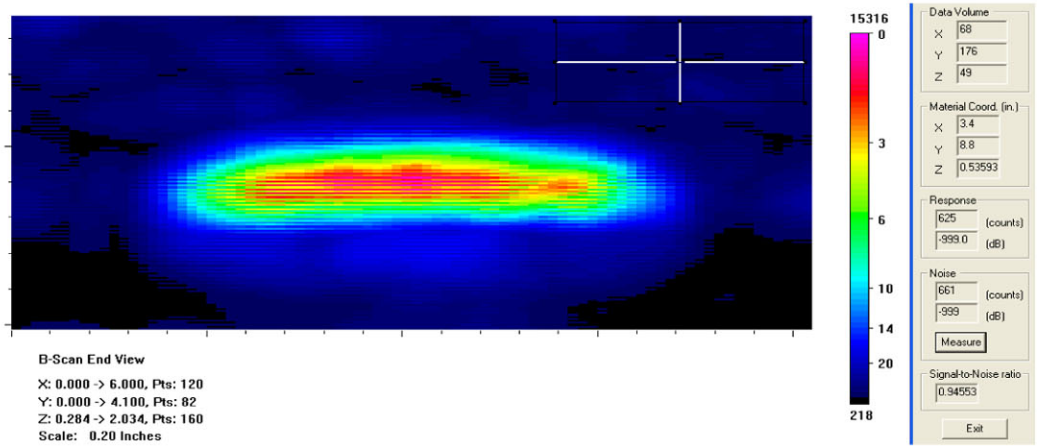

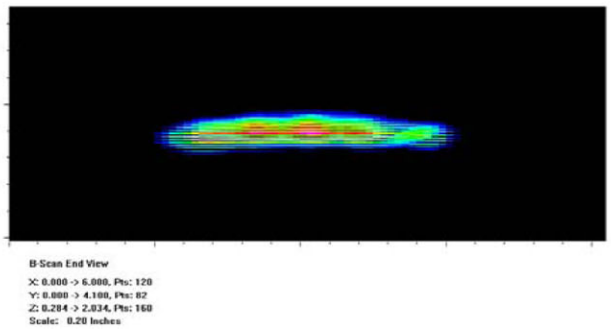

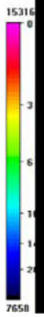

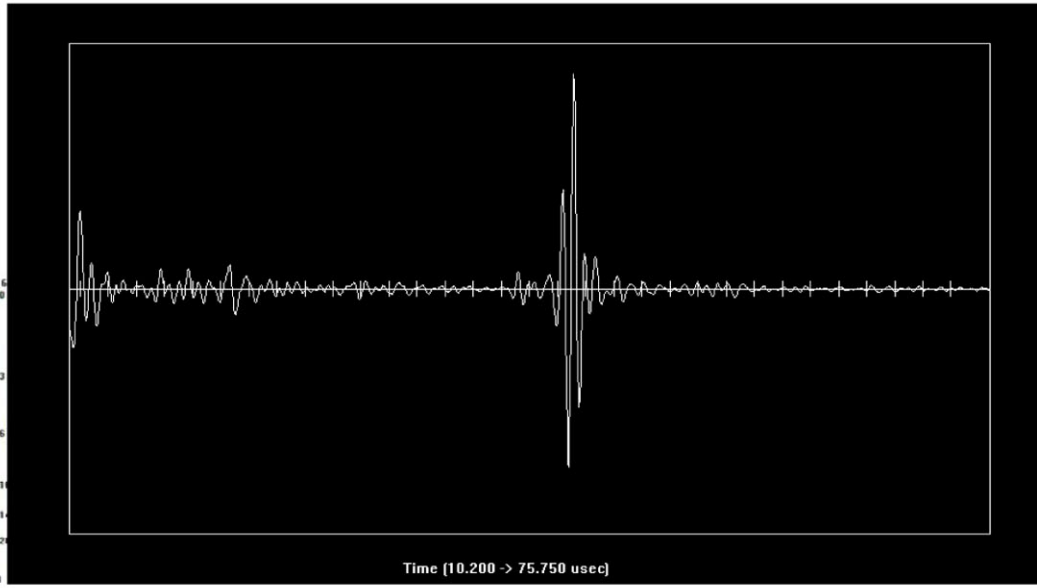

Section #1, Nearside, Saw Cut B, 28% Through Wall

1.5-MHz, 0.5-in.-diameter, 70° Shear

Length Sizing

Actual	2.565
6 dB Drop	1.9
Loss of Signal	2.4
6 dB Drop Δ	0.665
Loss of Signal Δ	0.165

Depth Sizing

Actual	0.403	Corner Tra	52.15
6 dB Drop	0.18339	Tip Signal	44.3
UT Tip Signal	0.186963	Velocity	0.125
6 dB Drop Δ	0.21961	Angle	67.6
UT Tip Signal Δ	0.216037		

Noise Characterization

Peak Signal Response		15279	
Noise		S/N Ratio	dB
General Weld Root	N/A	N/A	N/A
Local Weld Root	N/A	N/A	N/A
Cursor Window	2716	5.6	15.0

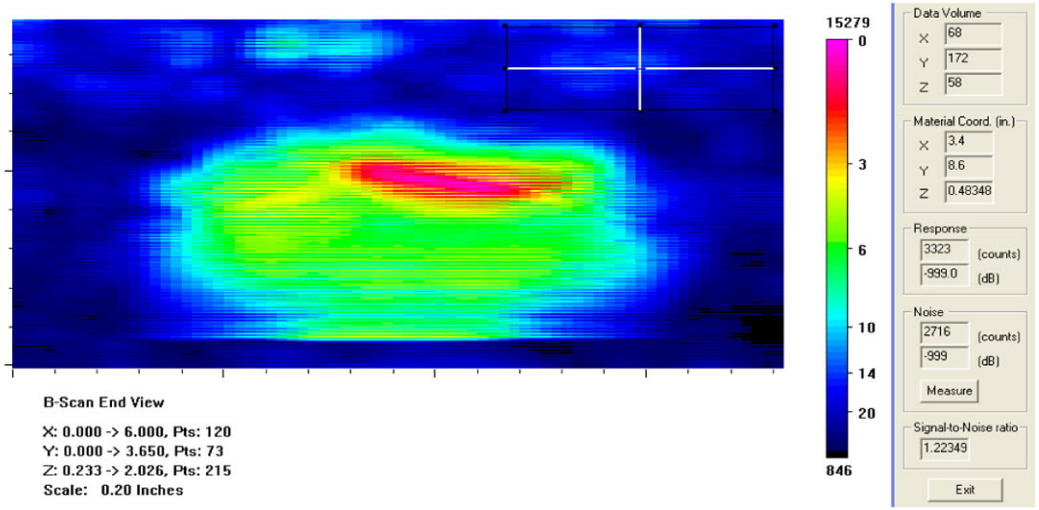

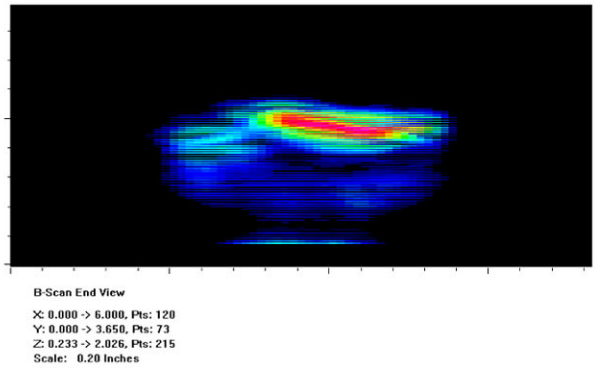

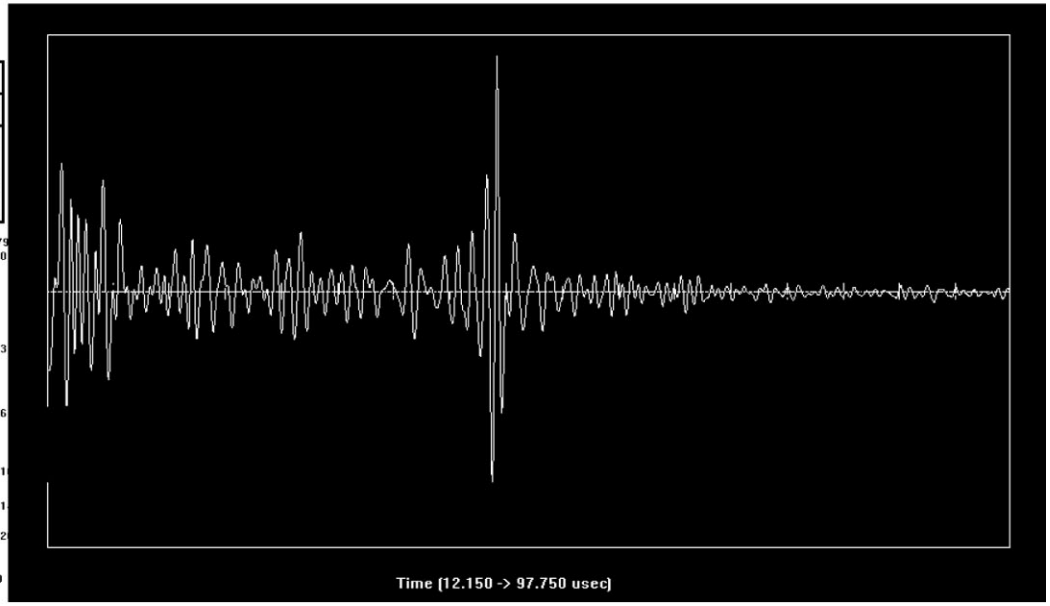

Section #1, Nearside, Saw Cut B, 28% Through Wall

1.5-MHz, 0.375-in.-diameter, 60° Shear

Length Sizing

Actual	2.565
6 dB Drop	1.8
Loss of Signal	2.25
6 dB Drop Δ	0.765
Loss of Signal Δ	0.315

Depth Sizing

Actual	0.403	Corner Tra	45.25
6 dB Drop	0.141	Tip Signal	40.25
UT Tip Signal	0.160949	Velocity	0.125
6 dB Drop Δ	0.262	Angle	59
UT Tip Signal Δ	0.242051		

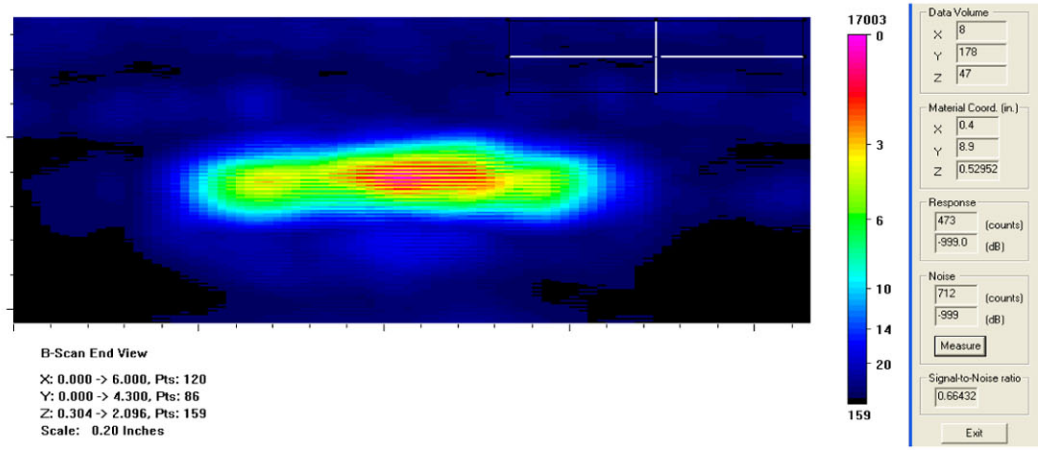

Noise Characterization

Peak Signal Response		17003	
Noise		S/N Ratio	dB
General Weld Root	N/A	N/A	N/A
Local Weld Root	N/A	N/A	N/A
Cursor Window	473	35.9	31.1

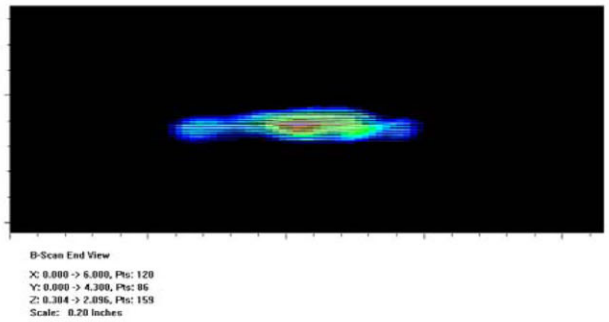

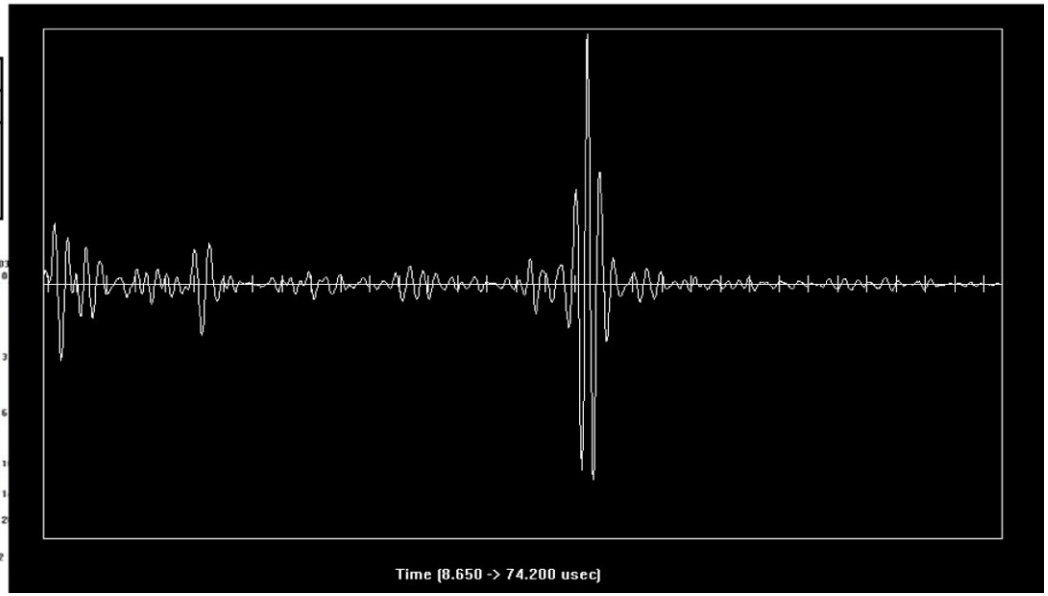

Section #1, Nearside, Saw Cut B, 28% Through Wall

1.5-MHz, 0.375-in.-diameter, 70° Shear

Length Sizing

Actual	2.565
6 dB Drop	1.85
Loss of Signal	2.25
6 dB Drop Δ	0.715
Loss of Signal Δ	0.315

Depth Sizing

Actual	0.403	Corner Tra	58.8
6 dB Drop	0.24453	Tip Signal	54.9
UT Tip Signal	0.106853	Velocity	0.125
6 dB Drop Δ	0.15847	Angle	64
UT Tip Signal Δ	0.296147		

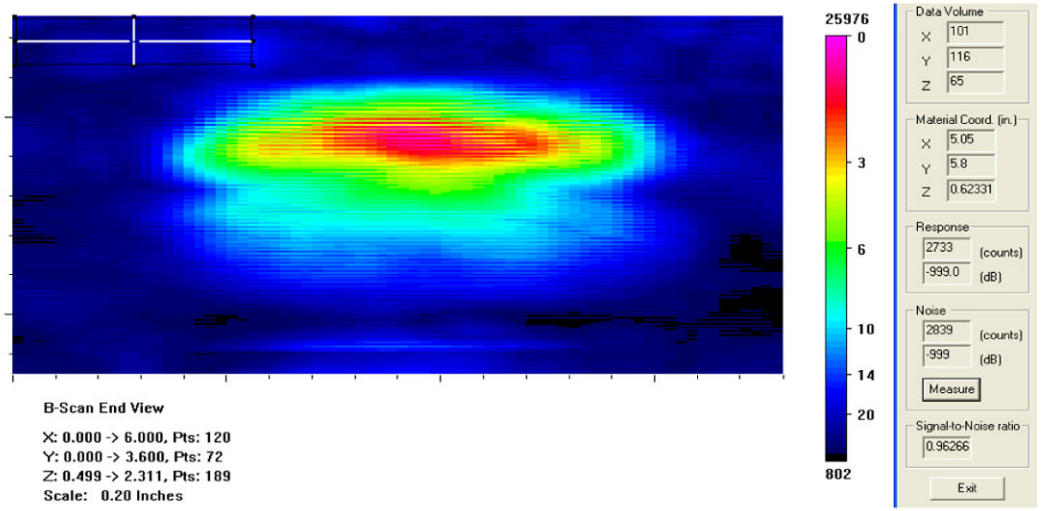

Noise Characterization

Peak Signal Response		25976	
Noise		S/N Ratio	dB
General Weld Root	N/A	N/A	N/A
Local Weld Root	N/A	N/A	N/A
Cursor Window	2839	9.1	19.2

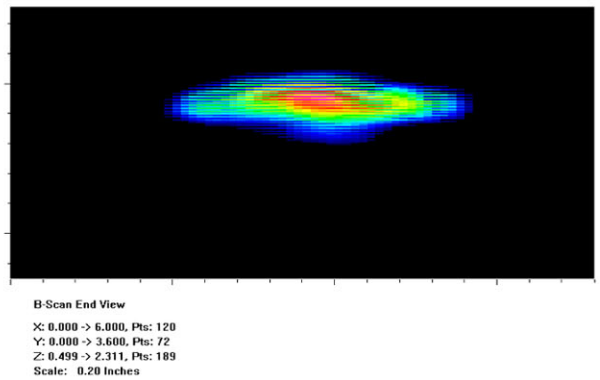

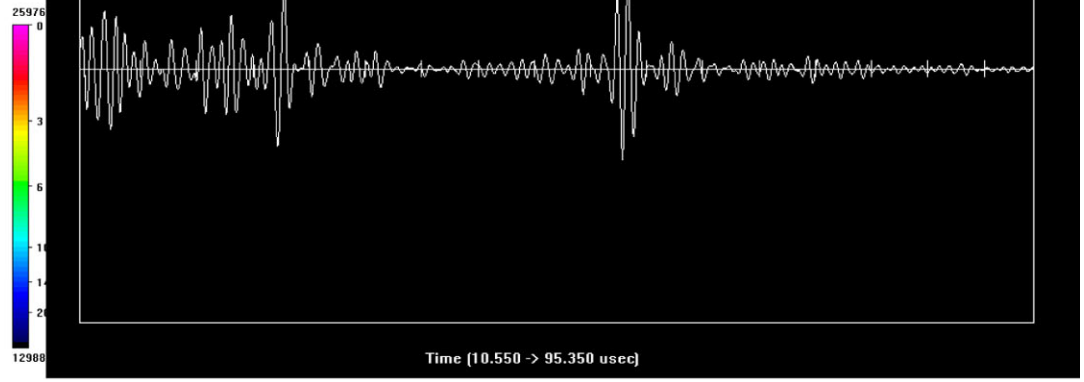

Section #1, Nearside, Saw Cut B, 28% Through Wall

2.25-MHz, 0.5-in.-diameter, 60° Shear

Length Sizing

Actual	2.565
6 dB Drop	2
Loss of Signal	2.35
6 dB Drop Δ	0.565
Loss of Signal Δ	0.215

Depth Sizing

Actual	0.403	Corner Tra	43.8
6 dB Drop	0.164	Tip Signal	41.35
UT Tip Signal	0.076562	Velocity	0.125
6 dB Drop Δ	0.239	Angle	60
UT Tip Signal Δ	0.326438		

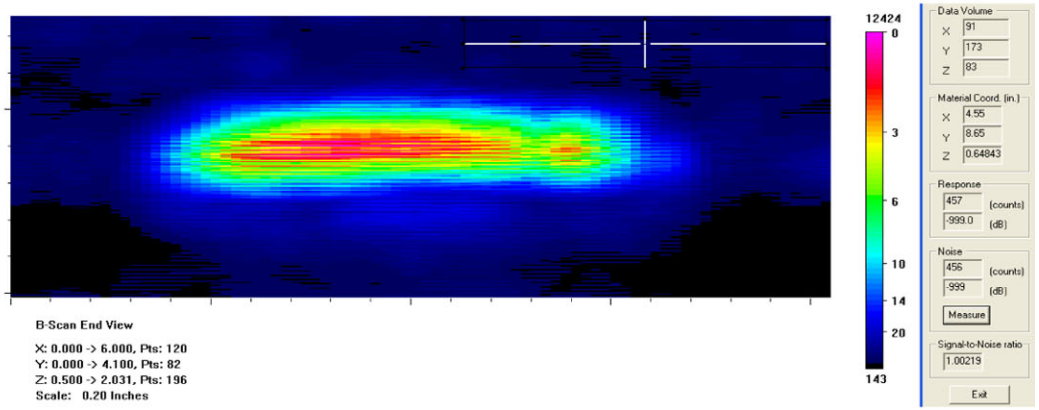

Noise Characterization

Peak Signal Response		12424	
Noise		S/N Ratio	dB
General Weld Root	N/A	N/A	N/A
Local Weld Root	N/A	N/A	N/A
Cursor Window	456	27.2	28.7

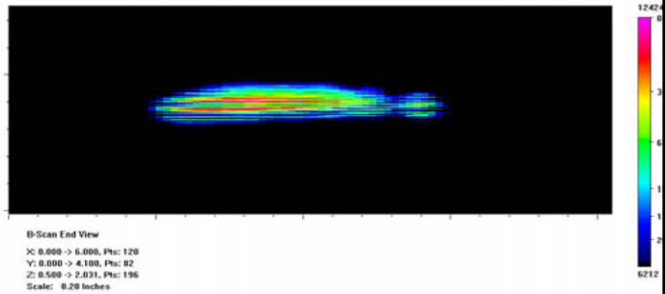

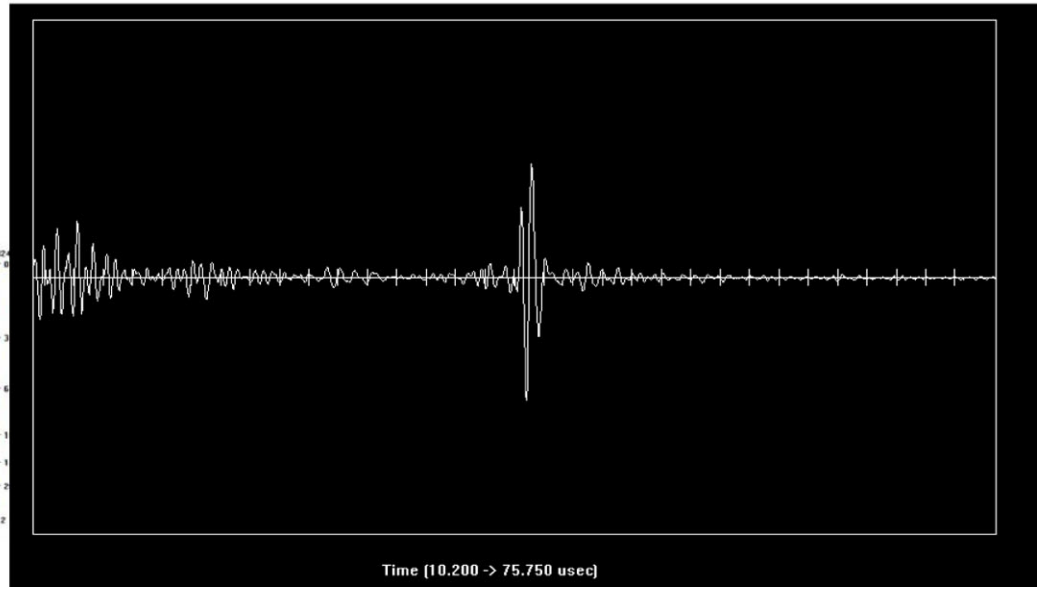

Section #1, Nearside, Saw Cut B, 28% Through Wall

2.25-MHz, 0.5-in.-diameter, 70° Shear

Length Sizing

Actual	2.565
6 dB Drop	1.94
Loss of Signal	2.4
6 dB Drop Δ	0.625
Loss of Signal Δ	0.165

Depth Sizing

Actual	0.403	Corner Tra	75.25
6 dB Drop	0.406	Tip Signal	72.35
UT Tip Signal	0.064954	Velocity	0.125
6 dB Drop Δ	-0.003	Angle	69
UT Tip Signal Δ	0.338046		

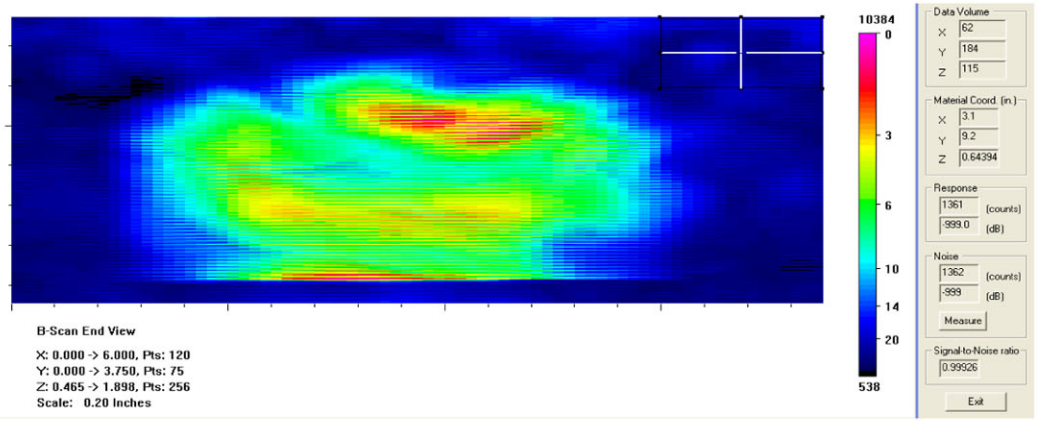

Noise Characterization

Peak Signal Response		10384	
Noise		S/N Ratio	dB
General Weld Root	N/A	N/A	N/A
Local Weld Root	N/A	N/A	N/A
Cursor Window	1362	7.6	17.6

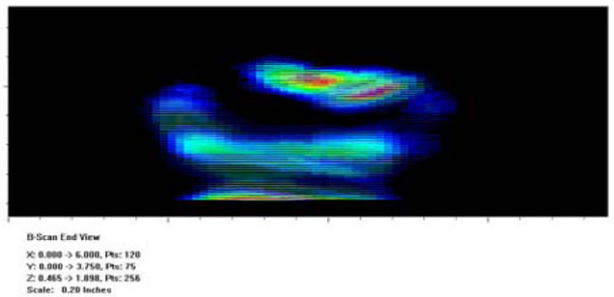

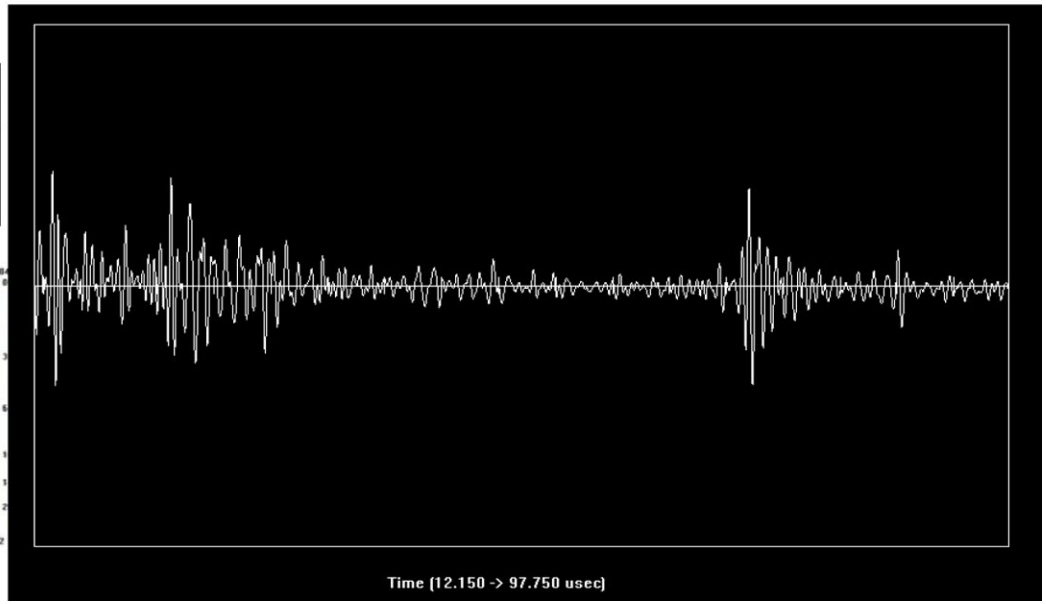

Section #1, Nearside, Saw Cut B, 28% Through Wall

2.25-MHz, 0.375-in.-diameter, 60° Shear

Length Sizing

Actual	2.565
6 dB Drop	1.95
Loss of Signal	2.3
6 dB Drop Δ	0.615
Loss of Signal Δ	0.265

Depth Sizing

Actual	0.403	Corner Tra	43.85
6 dB Drop	0.145	Tip Signal	40.25
UT Tip Signal	0.1125	Velocity	0.125
6 dB Drop Δ	0.258	Angle	60
UT Tip Signal Δ	0.2905		

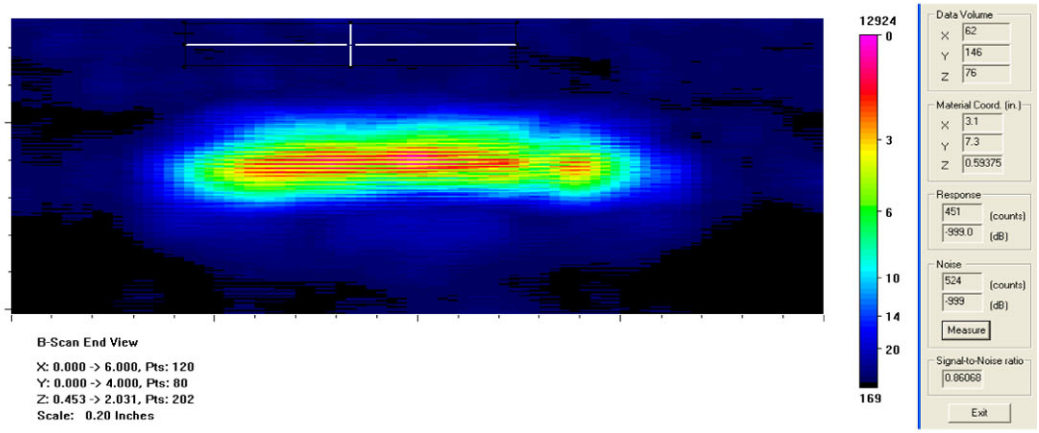

Noise Characterization

Peak Signal Response		12924	
Noise		S/N Ratio	dB
General Weld Root	N/A	N/A	N/A
Local Weld Root	N/A	N/A	N/A
Cursor Window	524	24.7	27.8

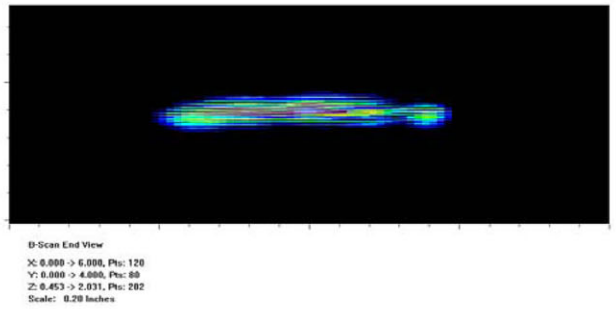

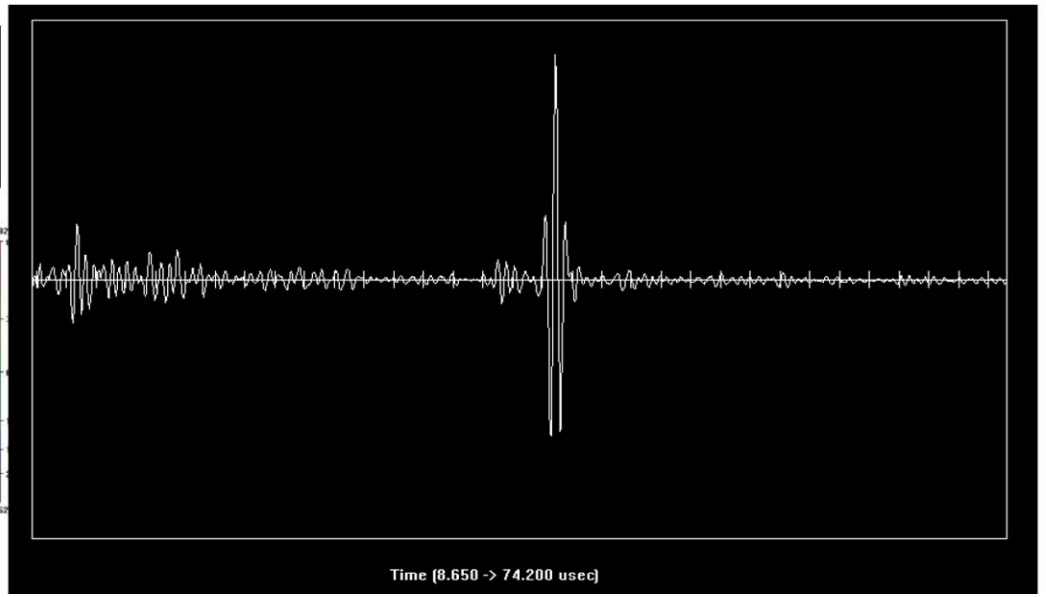

Section #1, Nearside, Saw Cut B, 28% Through Wall

2.25-MHz, 0.375-in.-diameter, 70° Shear

Length Sizing

Actual	2.565
6 dB Drop	2.05
Loss of Signal	2.6
6 dB Drop Δ	0.515
Loss of Signal Δ	-0.035

Depth Sizing

Actual	0.403	Corner Trap	
6 dB Drop	0.254	Tip Signal	None
UT Tip Signal	None	Velocity	0.125
6 dB Drop Δ	0.149	Angle	66
UT Tip Signal Δ	None		

Noise Characterization

Peak Signal Response		10120	
Noise		S/N Ratio	dB
General Weld Root	N/A	N/A	N/A
Local Weld Root	N/A	N/A	N/A
Cursor Window	1614	6.3	15.9

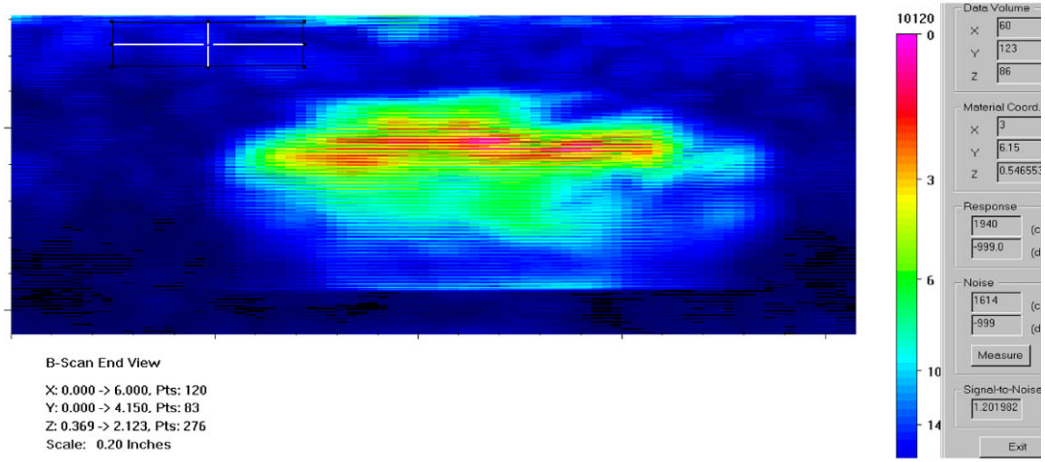

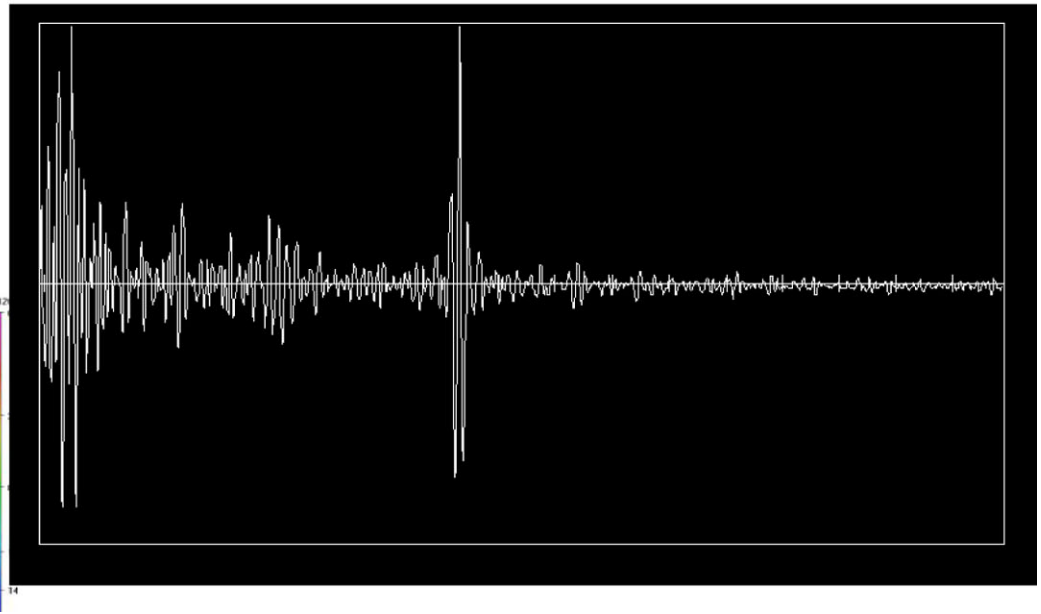

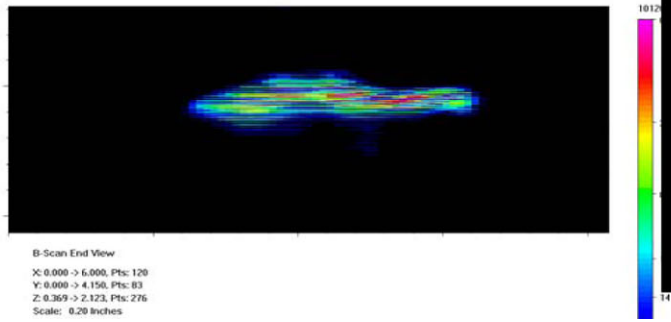

Section #1, Nearside, Flaw B, 43% Through Wall

1.5-MHz, 0.5-in.-diameter, 60° Shear

Length Sizing

Actual	1.2
6 dB Drop	1.25
Loss of Signal	1.65
6 dB Drop Δ	-0.05
Loss of Signal Δ	-0.45

Depth Sizing

Actual	0.585	Corner Tra	44.9
6 dB Drop	0.377	Tip Signal	36.6
UT Tip Signal	0.259375	Velocity	0.125
6 dB Drop Δ	0.208	Angle	60
UT Tip Signal Δ	0.325625		

Noise Characterization

Peak Signal Response		4558	
Noise		S/N Ratio	dB
General Weld Root	N/A	N/A	N/A
Local Weld Root	N/A	N/A	N/A
Cursor Window	778	5.9	15.4

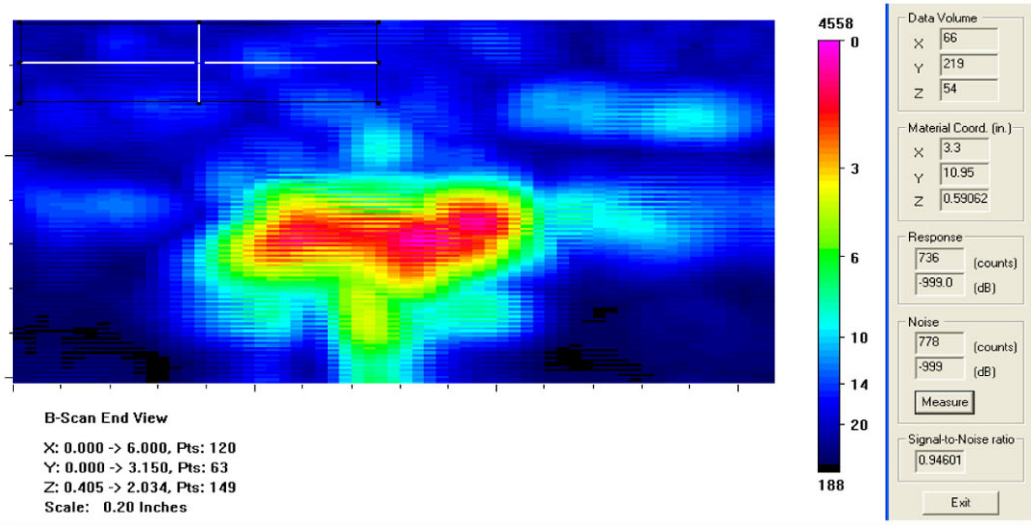

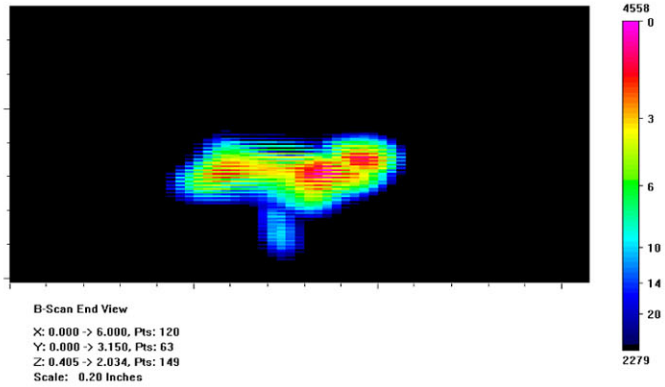

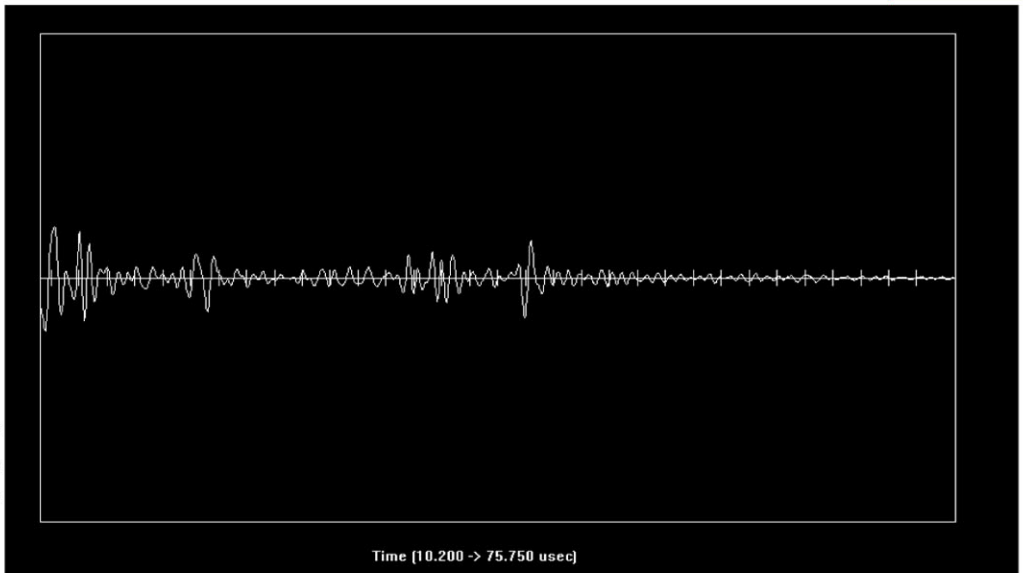

Section #1, Nearside, Flaw B, 43% Through Wall

1.5-MHz, 0.5-in.-diameter, 70° Shear

Length Sizing

Actual	1.2
6 dB Drop	1.1
Loss of Signal	1.45
6 dB Drop Δ	0.1
Loss of Signal Δ	-0.25

Depth Sizing

Actual	0.585	Corner Trap	
6 dB Drop	0.3	Tip Signal	None
UT Tip Signal	None	Velocity	0.125
6 dB Drop Δ	0.285	Angle	67.6
UT Tip Signal Δ	None		

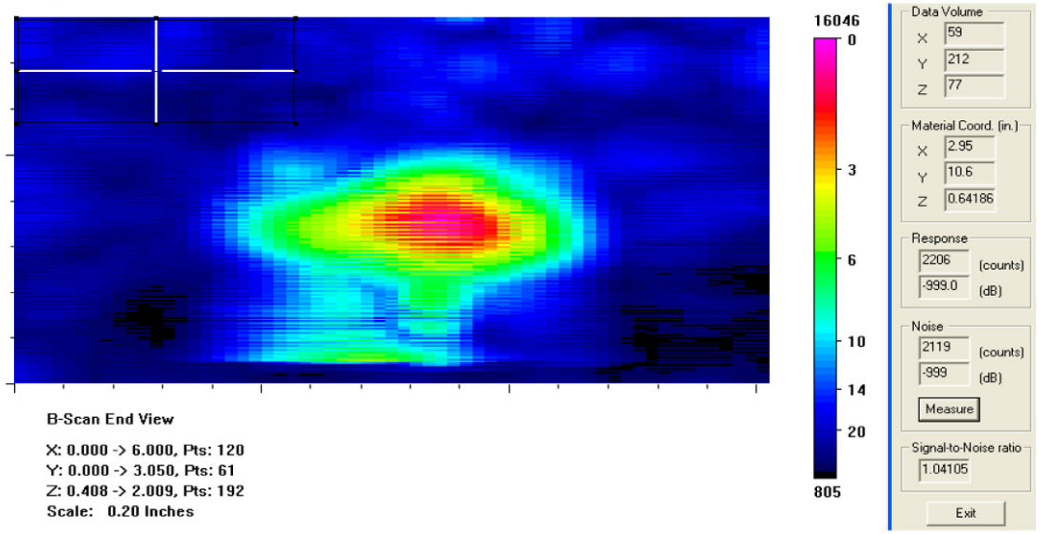

Noise Characterization

Peak Signal Response		16046	
Noise		S/N Ratio	dB
General Weld Root	N/A	N/A	N/A
Local Weld Root	N/A	N/A	N/A
Cursor Window	2119	7.6	17.6

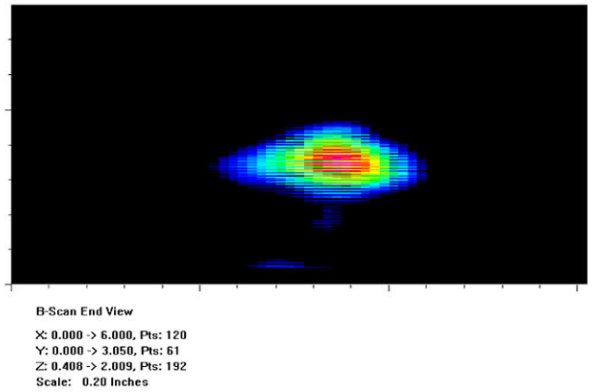

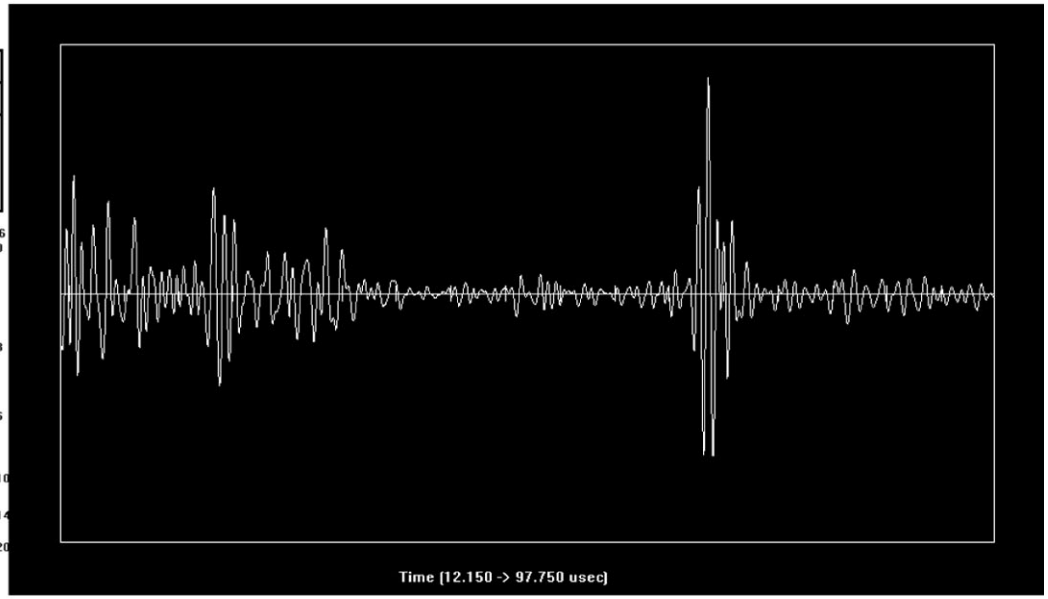

Section #1, Nearside, Flaw B, 43% Through Wall

1.5-MHz, 0.375-in.-diameter, 60° Shear

Length Sizing

Actual	1.2
6 dB Drop	1.3
Loss of Signal	1.3
6 dB Drop Δ	-0.1
Loss of Signal Δ	-0.1

Call due to position of flaw in relation to noise

Depth Sizing

Actual	0.585	Corner Trap	
6 dB Drop	0.389	Tip Signal	None
UT Tip Signal	None	Velocity	0.125
6 dB Drop Δ	0.196	Angle	59
UT Tip Signal Δ	None		

Noise Characterization

Peak Signal Response		1608	
Noise		S/N Ratio	dB
General Weld Root	N/A	N/A	N/A
Local Weld Root	2656	0.6	-4.4
Cursor Window	1286	1.3	1.9

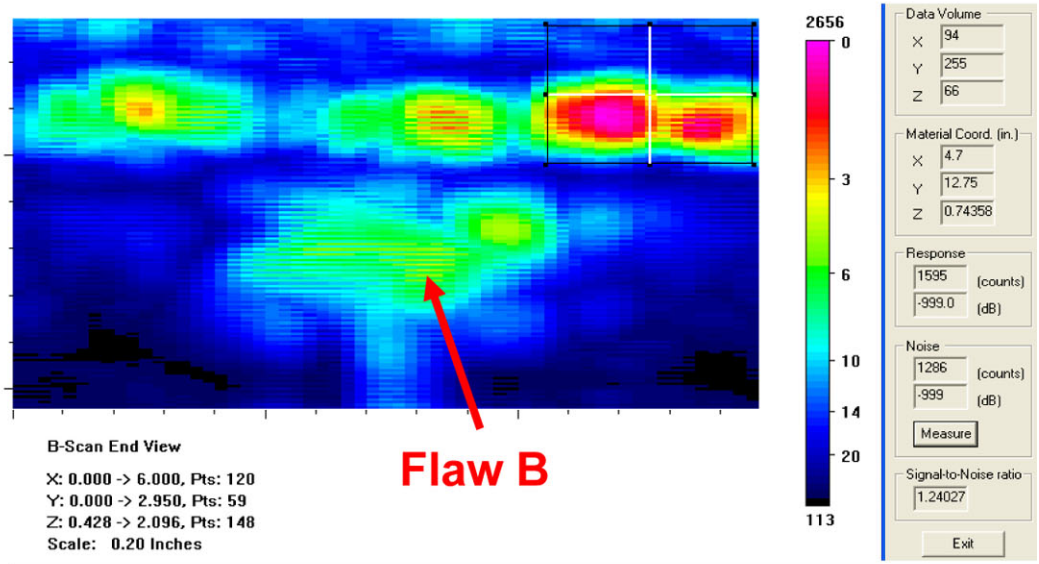

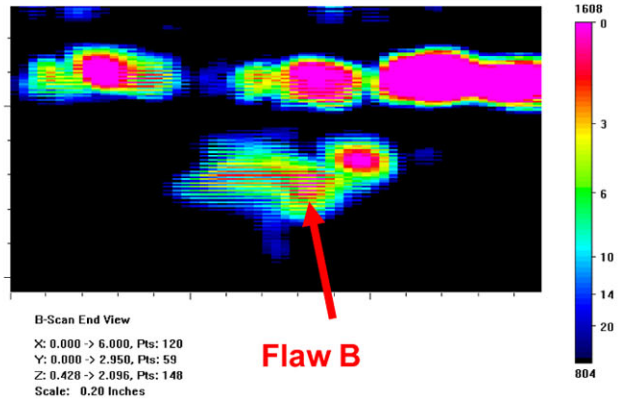

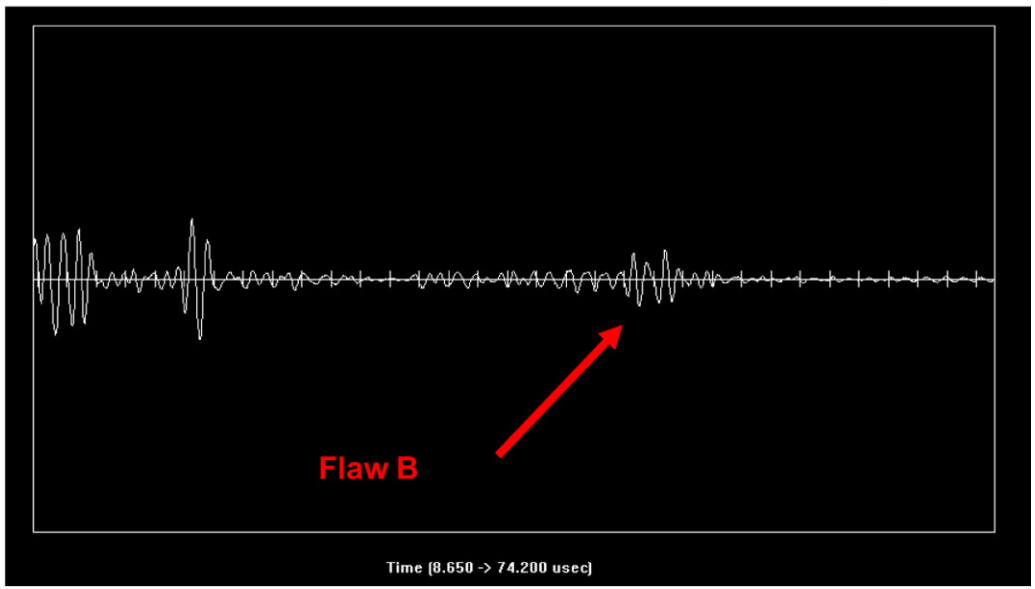

Section #1, Nearside, Flaw B, 43% Through Wall

1.5-MHz, 0.375-in.-diameter, 70° Shear

Length Sizing

Actual	1.2
6 dB Drop	1.15
Loss of Signal	1.45
6 dB Drop Δ	0.05
Loss of Signal Δ	-0.25

Depth Sizing

Actual	0.585	Corner Trap	
6 dB Drop	0.379	Tip Signal	None
UT Tip Signal	None	Velocity	0.125
6 dB Drop Δ	0.206	Angle	64
UT Tip Signal Δ	None		

Noise Characterization

Peak Signal Response		16326	
Noise		S/N Ratio	dB
General Weld Root	N/A	N/A	N/A
Local Weld Root	N/A	N/A	N/A
Cursor Window	2823	5.8	15.2

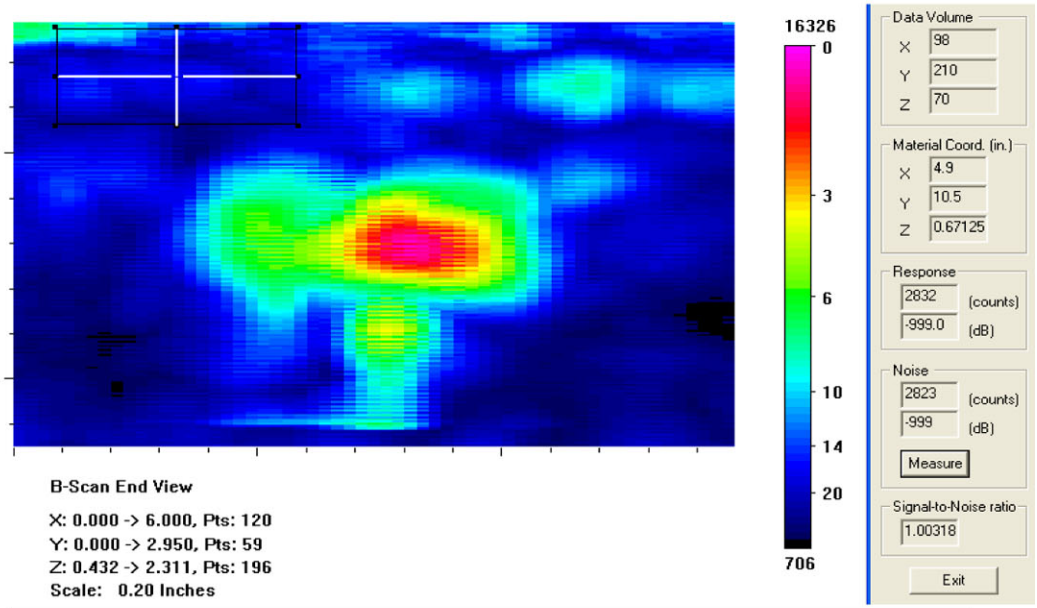

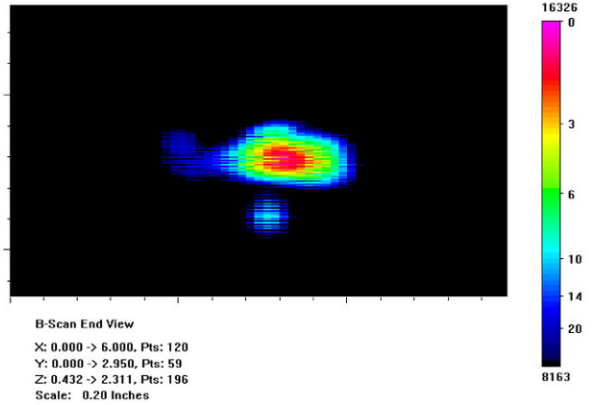

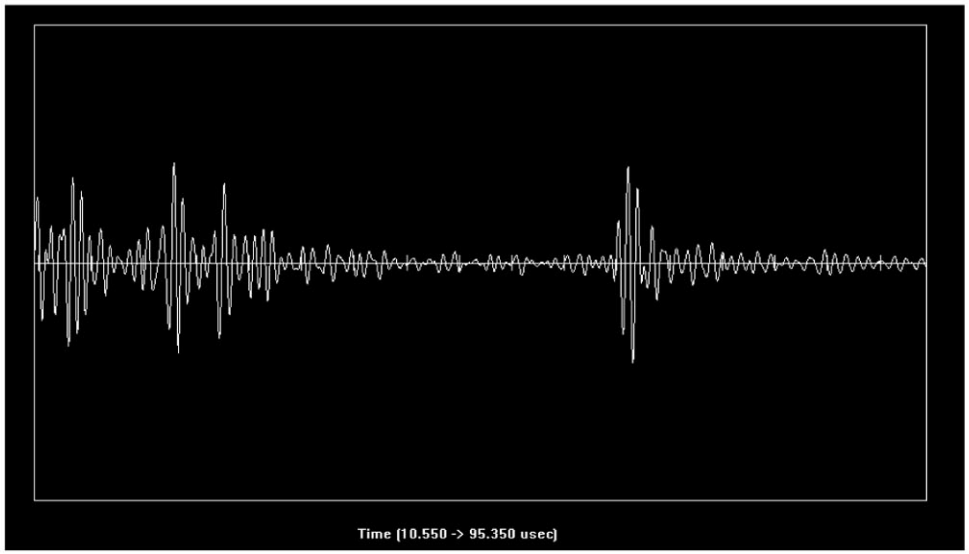

Section #1, Nearside, Flaw B, 43% Through Wall

2.25-MHz, 0.5-in.-diameter, 60° Shear

Length Sizing

Actual	1.2
6 dB Drop	1.25
Loss of Signal	1.5
6 dB Drop Δ	-0.05
Loss of Signal Δ	-0.3

Depth Sizing

Actual	0.585	Corner Tra	50.6
6 dB Drop	0.363	Tip Signal	42.85
UT Tip Signal	0.242188	Velocity	0.125
6 dB Drop Δ	0.222	Angle	60
UT Tip Signal Δ	0.342813		

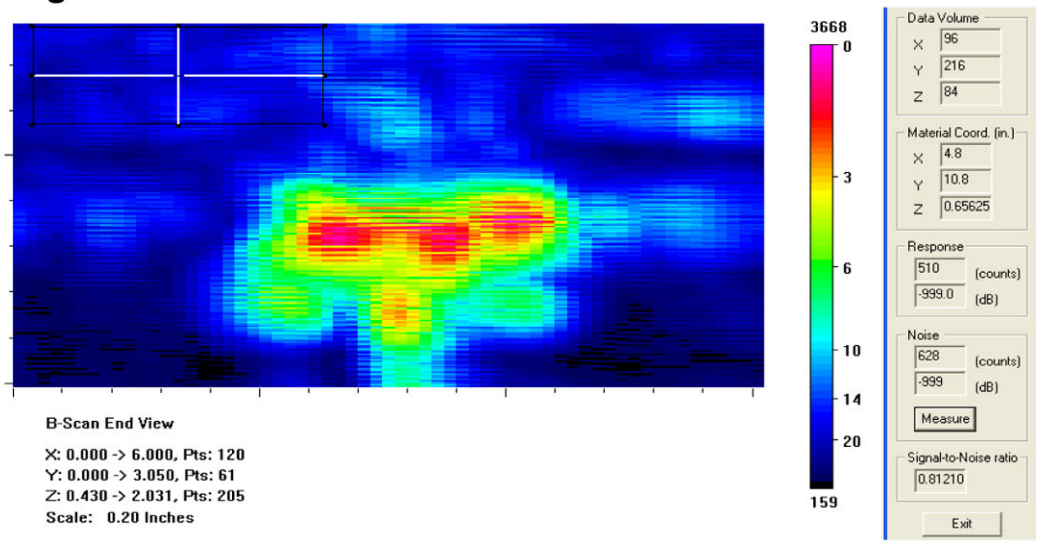

Noise Characterization

Peak Signal Response		3668	
Noise		S/N Ratio	dB
General Weld Root	N/A	N/A	N/A
Local Weld Root	N/A	N/A	N/A
Cursor Window	628	5.8	15.3

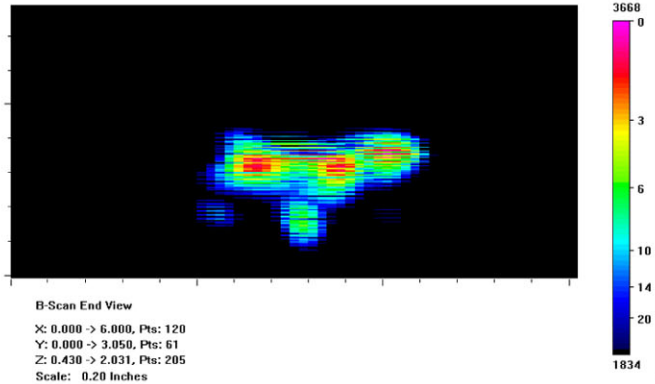

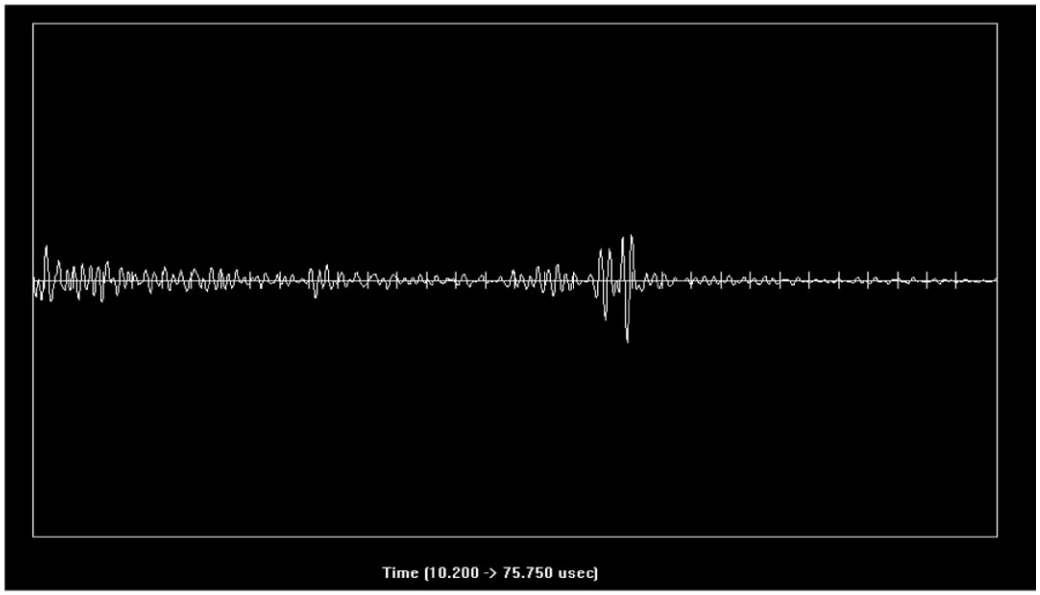

Section #1, Nearside, Flaw B, 43% Through Wall

2.25-MHz, 0.5-in.-diameter, 70° Shear

Length Sizing

Actual	1.2
6 dB Drop	1.15
Loss of Signal	1.4
6 dB Drop Δ	0.05
Loss of Signal Δ	-0.2

Depth Sizing

Actual	0.585	Corner Tra	67.45
6 dB Drop	0.227	Tip Signal	54.55
UT Tip Signal	0.288934	Velocity	0.125
6 dB Drop Δ	0.358	Angle	69
UT Tip Signal Δ	0.296066		

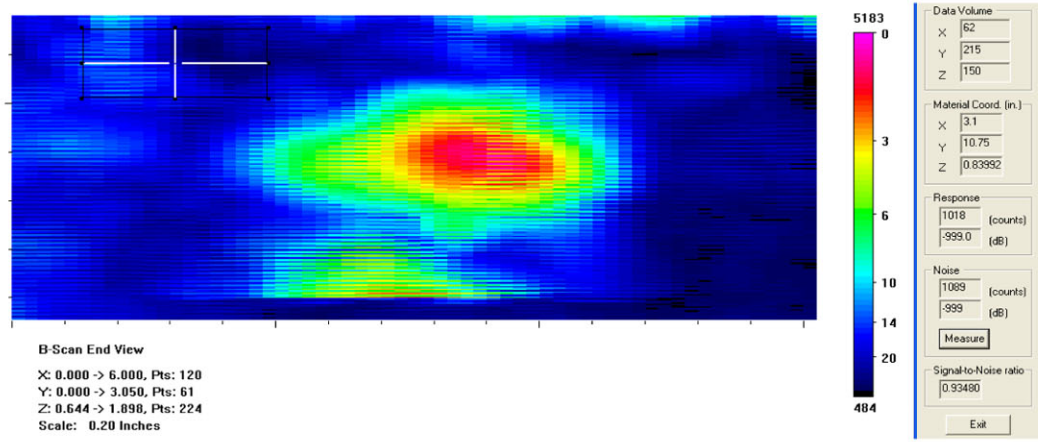

Noise Characterization

Peak Signal Response		5183	
Noise		S/N Ratio	dB
General Weld Root	N/A	N/A	N/A
Local Weld Root	N/A	N/A	N/A
Cursor Window	1089	4.8	13.6

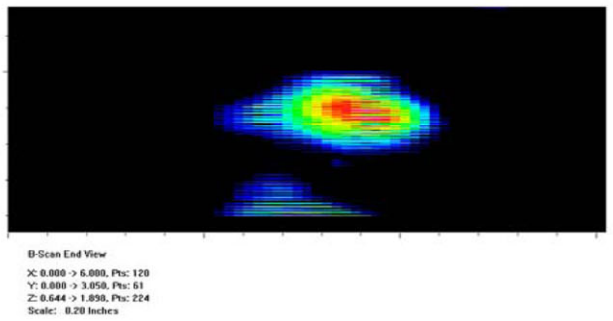

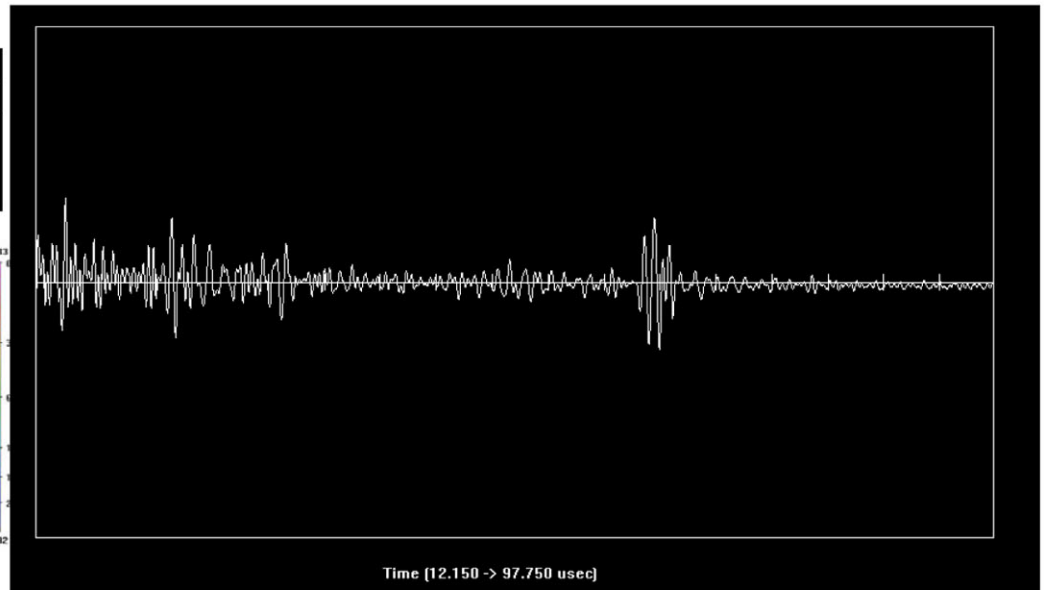

Section #1, Nearside, Flaw B, 43% Through Wall

2.25-MHz, 0.375-in.-diameter, 60° Shear

Length Sizing

Actual	1.2
6 dB Drop	1.2
Loss of Signal	1.4
6 dB Drop Δ	0
Loss of Signal Δ	-0.2

Depth Sizing

Actual	0.585	Corner Tra	46.25
6 dB Drop	0.336	Tip Signal	40.05
UT Tip Signal	0.19375	Velocity	0.125
6 dB Drop Δ	0.249	Angle	60
UT Tip Signal Δ	0.39125		

Noise Characterization

Peak Signal Response		3762	
Noise		S/N Ratio	dB
General Weld Root	N/A	N/A	N/A
Local Weld Root	N/A	N/A	N/A
Cursor Window	714	5.3	14.4

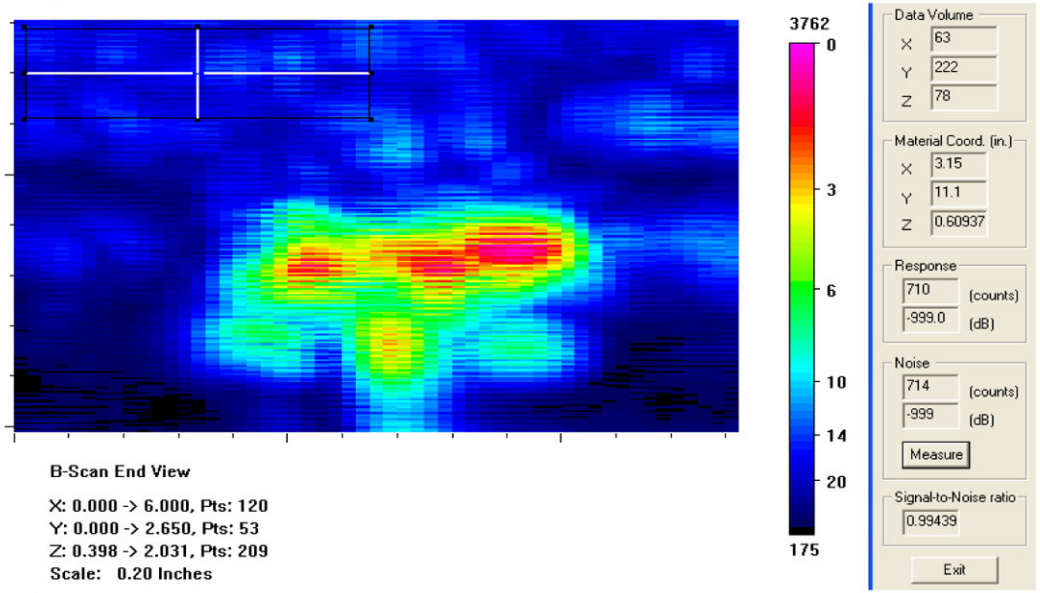

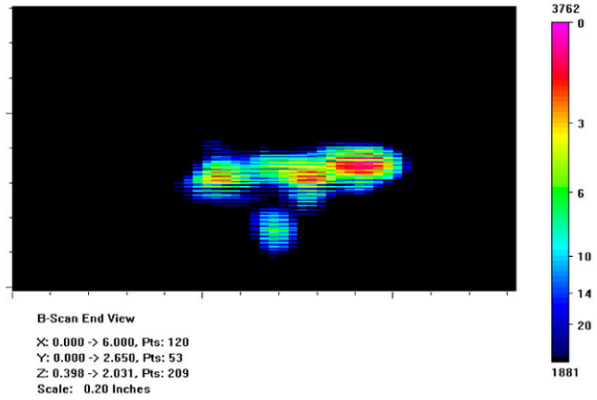

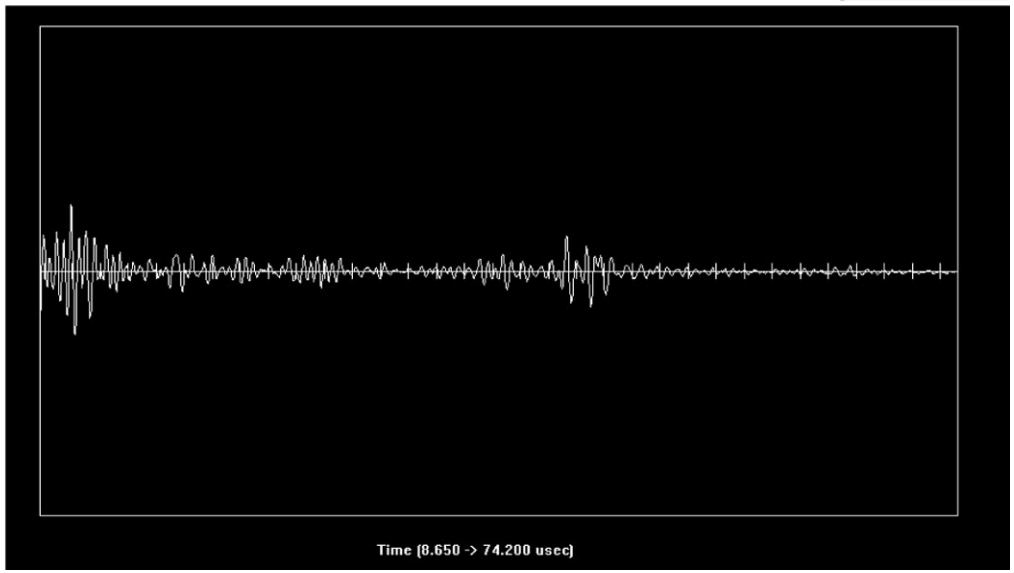

Section #1, Nearside, Flaw B, 43% Through Wall

2.25-MHz, 0.375-in.-diameter, 70° Shear

Length Sizing

Actual	1.2
6 dB Drop	1.3
Loss of Signal	1.55
6 dB Drop Δ	-0.1
Loss of Signal Δ	-0.35

Depth Sizing

Actual	0.585	Corner Trap	
6 dB Drop	0.432	Tip Signal	None
UT Tip Signal	None	Velocity	0.125
6 dB Drop Δ	0.153	Angle	66
UT Tip Signal Δ	None		

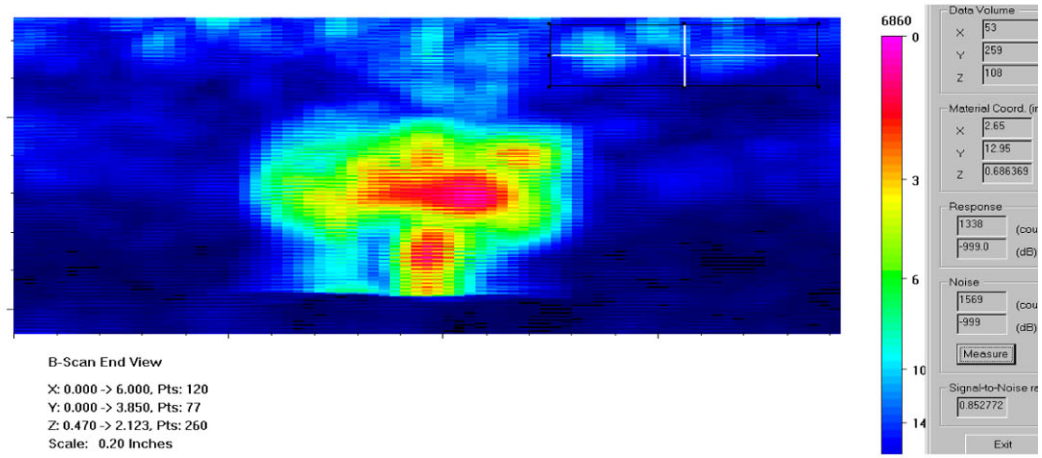

Noise Characterization

Peak Signal Response		6860	
Noise		S/N Ratio	dB
General Weld Root	N/A	N/A	N/A
Local Weld Root	N/A	N/A	N/A
Cursor Window	1569	4.4	12.8

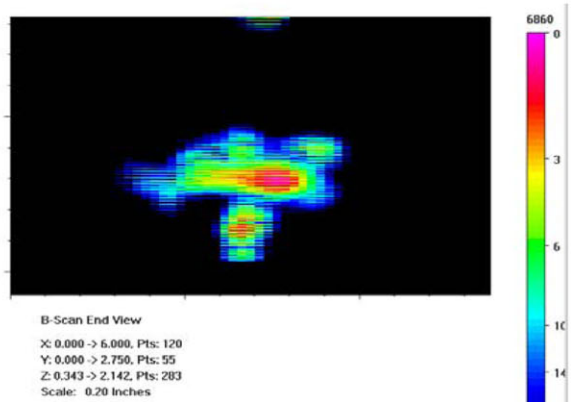

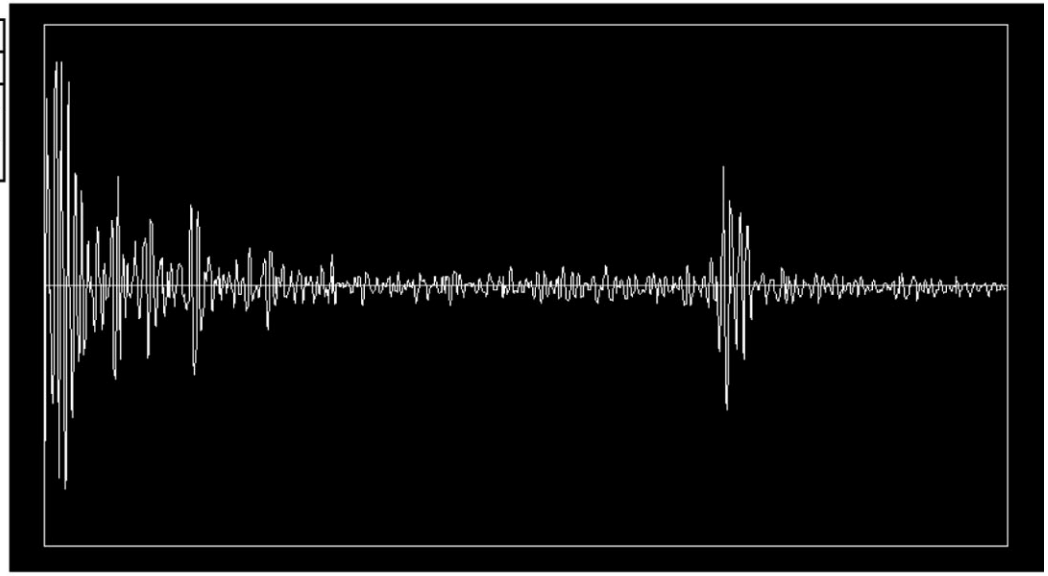

Section #1, Nearside, Saw Cut C, 7% Through Wall Angle

1.5-MHz, 0.5-in.-diameter, 60° Shear

Length Sizing

Actual	1.472
6 dB Drop	0.6
Loss of Signal	0.75
6 dB Drop Δ	0.872
Loss of Signal Δ	0.722

Depth Sizing

Actual	0.1	Corner Tra	50.55
6 dB Drop	0.17	Tip Signal	48.2
UT Tip Signal	0.073437	Velocity	0.125
6 dB Drop Δ	-0.07	Angle	60
UT Tip Signal Δ	0.026563		

Noise Characterization

Peak Signal Response		3669	
Noise		S/N Ratio	dB
General Weld Root	N/A	N/A	N/A
Local Weld Root	N/A	N/A	N/A
Cursor Window	655	5.6	15.0

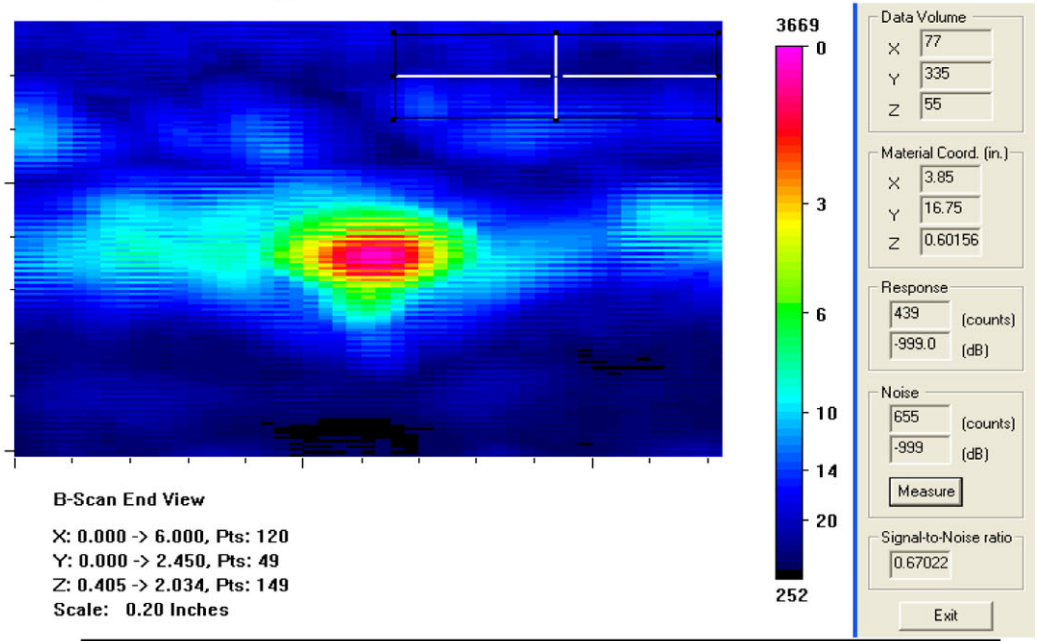

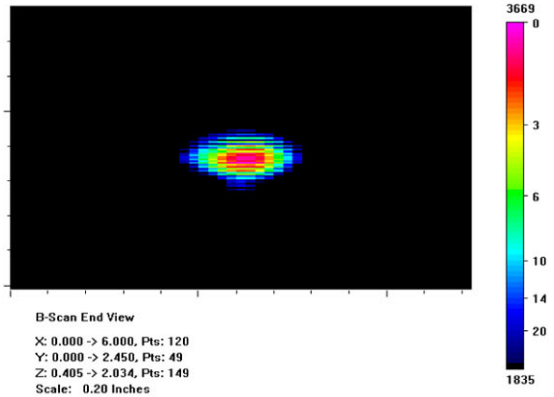

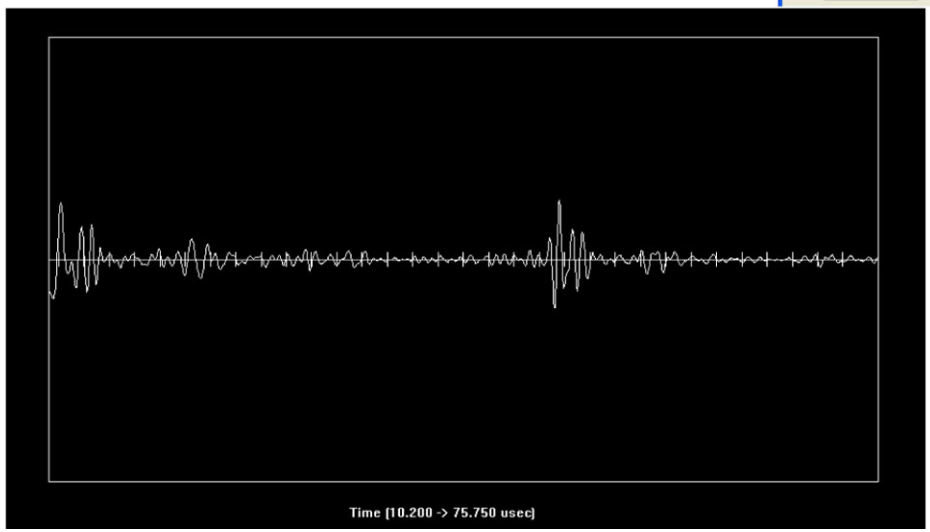

Section #1, Nearside, Saw Cut C, 7% Through Wall Angle

1.5-MHz, 0.5-in.-diameter, 70° Shear

Length Sizing

Actual	1.472
6 dB Drop	1.85
Loss of Signal	1.85
6 dB Drop Δ	-0.378
Loss of Signal Δ	-0.378

No Call due to low signal to noise ratio and high amplitude noise peaks

Depth Sizing

Actual	0.1	Corner Trap	
6 dB Drop	0.338	Tip Signal	None
UT Tip Signal	None	Velocity	0.125
6 dB Drop Δ	-0.238	Angle	67.6
UT Tip Signal Δ	None		

Noise Characterization

Peak Signal Response		4589	
Noise		S/N Ratio	dB
General Weld Root	N/A	N/A	N/A
Local Weld Root	N/A	N/A	N/A
Cursor Window	2507	1.8	5.3

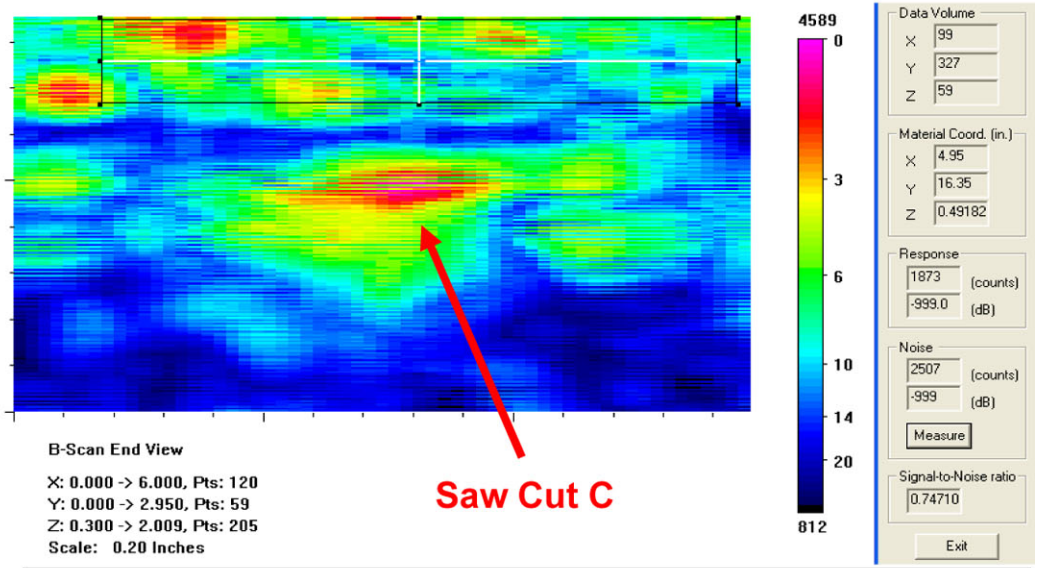

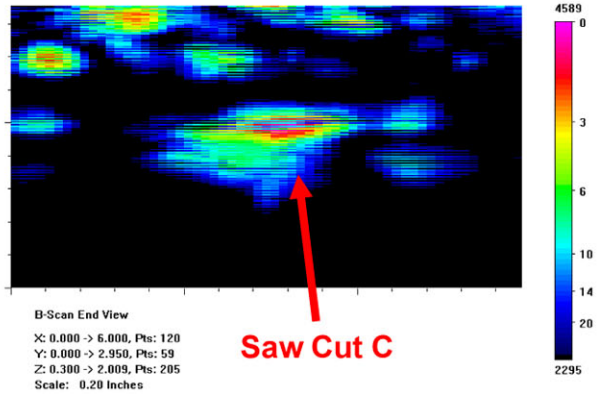

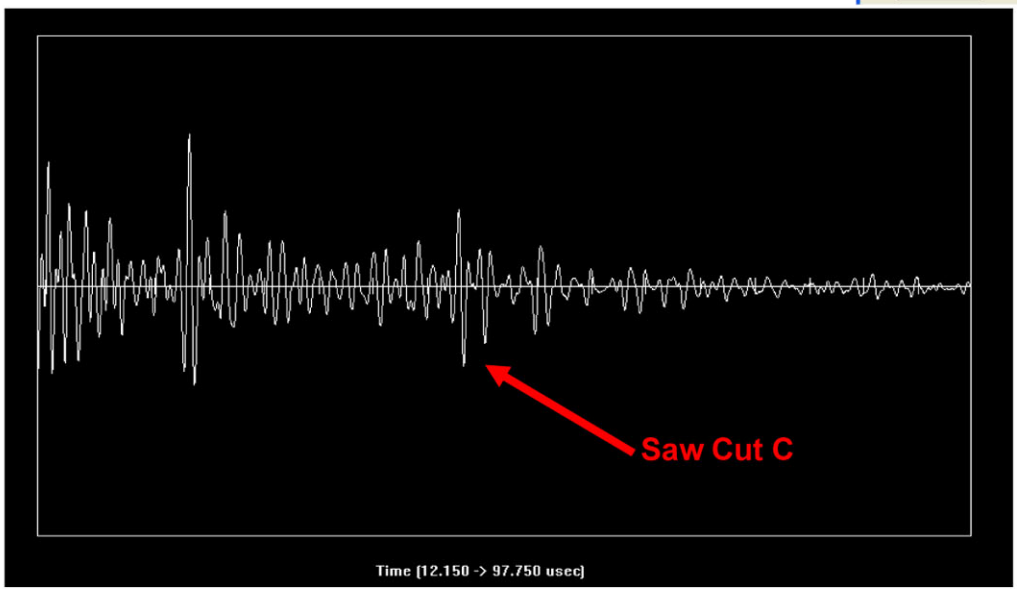

Section #1, Nearside, Saw Cut C, 7% Through Wall Angle

1.5-MHz, 0.375-in.-diameter, 60° Shear

Length Sizing

Actual	1.472
6 dB Drop	0.65
Loss of Signal	0.5
6 dB Drop Δ	0.822
Loss of Signal Δ	0.972

Call due to position of flaw in relation to noise

Depth Sizing

Actual	0.1	Corner Trap	
6 dB Drop	0.197	Tip Signal	None
UT Tip Signal	None	Velocity	0.125
6 dB Drop Δ	-0.097	Angle	59
UT Tip Signal Δ	None		

Noise Characterization

Peak Signal Response		998	
Noise		S/N Ratio	dB
General Weld Root	N/A	N/A	N/A
Local Weld Root	2367	0.4	-7.5
Cursor Window	796	1.3	2.0

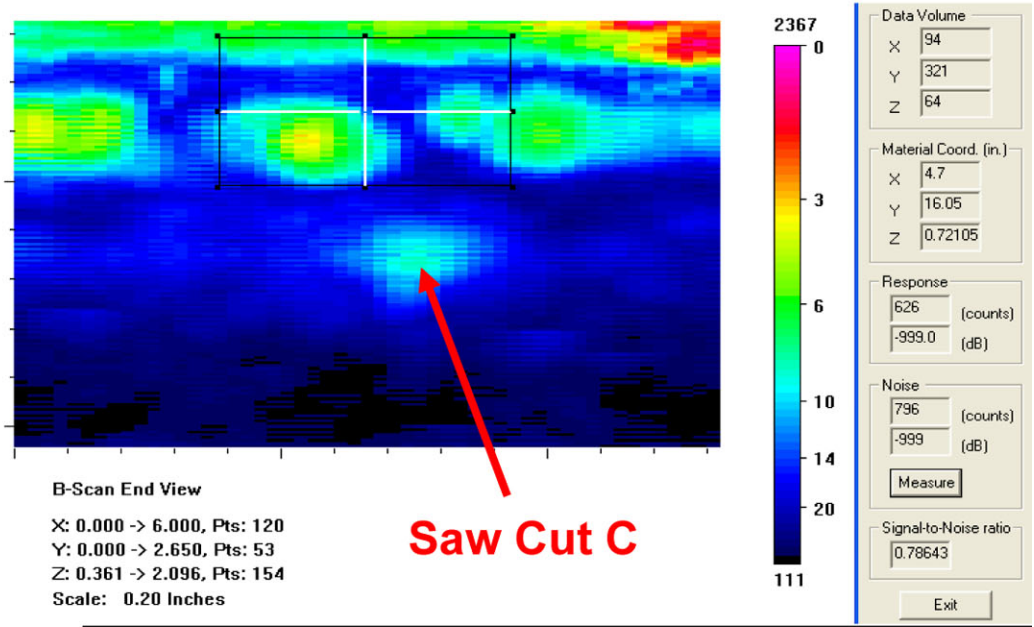

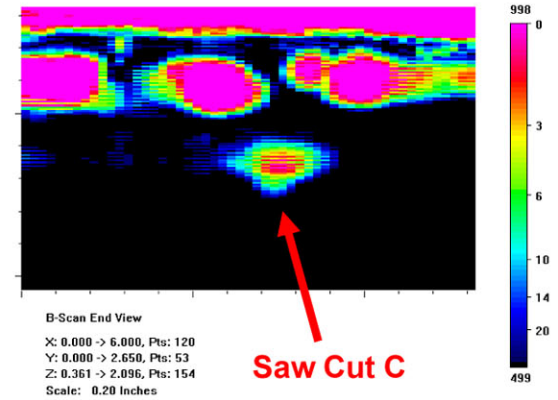

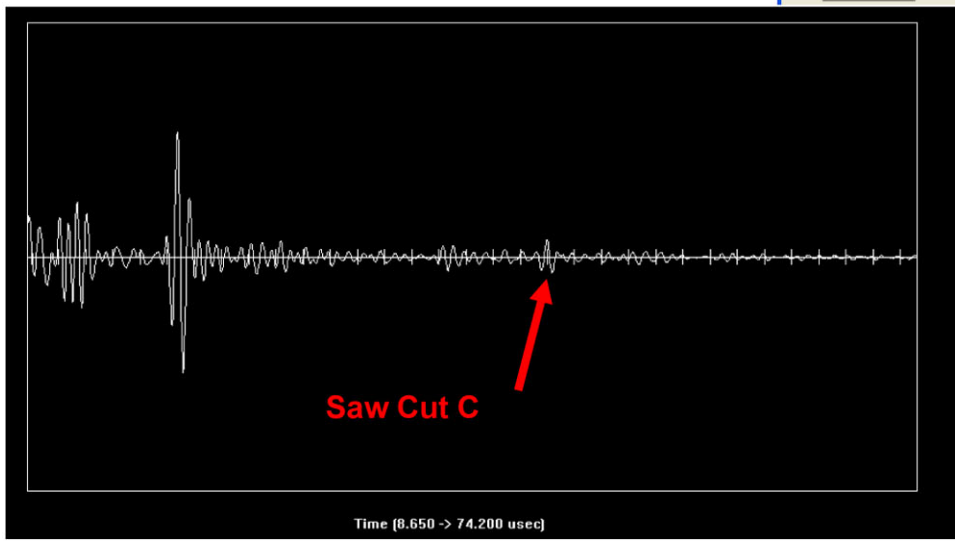

Section #1, Nearside, Saw Cut C, 7% Through Wall Angle

1.5-MHz, 0.375-in.-diameter, 70° Shear

Length Sizing

Actual	1.472
6 dB Drop	
Loss of Signal	
6 dB Drop Δ	1.472
Loss of Signal Δ	1.472

not detected

Depth Sizing

Actual	0.1	Corner Trap	
6 dB Drop		Tip Signal	
UT Tip Signal	0	Velocity	0.125
6 dB Drop Δ	0.1	Angle	64
UT Tip Signal Δ	0.1		

Noise Characterization

Peak Signal Response			
Noise		S/N Ratio	dB
General Weld Root	N/A	N/A	N/A
Local Weld Root	N/A	N/A	N/A
Cursor Window		N/A	N/A

Section #1, Nearside, Saw Cut C, 7% Through Wall Angle

2.25-MHz, 0.5-in.-diameter, 60° Shear

Length Sizing

Actual	1.472
6 dB Drop	0.45
Loss of Signal	0.65
6 dB Drop Δ	1.022
Loss of Signal Δ	0.822

Depth Sizing

Actual	0.1	Corner Tra	50.65
6 dB Drop	0.16	Tip Signal	48.35
UT Tip Signal	0.071875	Velocity	0.125
6 dB Drop Δ	-0.06	Angle	60
UT Tip Signal Δ	0.028125		

Noise Characterization

Peak Signal Response		3245	
Noise		S/N Ratio	dB
General Weld Root	N/A	N/A	N/A
Local Weld Root	N/A	N/A	N/A
Cursor Window	580	5.6	15.0

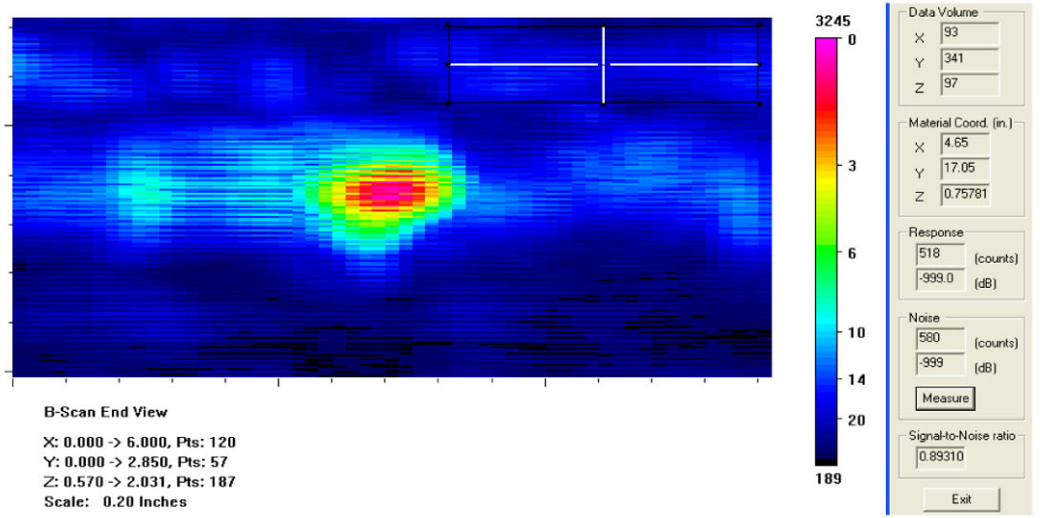

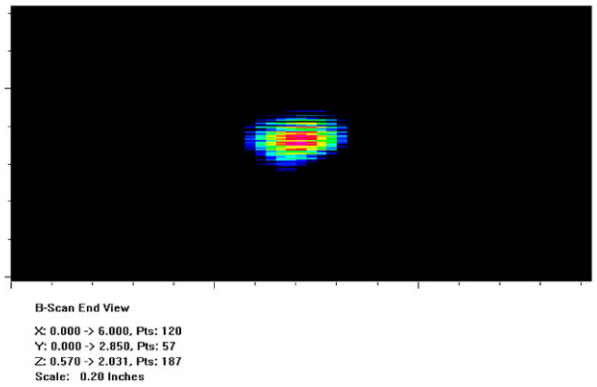

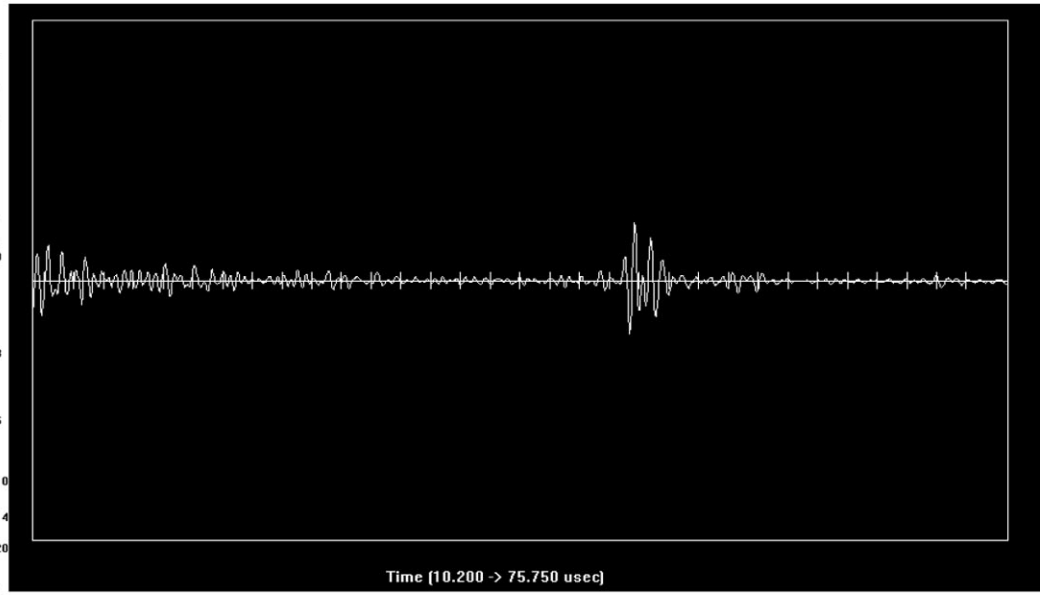

Section #1, Nearside, Saw Cut C, 7% Through Wall Angle

2.25-MHz, 0.5-in.-diameter, 70° Shear

Length Sizing

Actual	1.472
6 dB Drop	1
Loss of Signal	0.85
6 dB Drop Δ	0.472
Loss of Signal Δ	0.622

No Call due to low signal to noise ratio

Depth Sizing

Actual	0.1	Corner Trap	
6 dB Drop	0.28	Tip Signal	None
UT Tip Signal	None	Velocity	0.125
6 dB Drop Δ	-0.18	Angle	69
UT Tip Signal Δ	None		

Noise Characterization

Peak Signal Response		1270	
Noise		S/N Ratio	dB
General Weld Root	N/A	N/A	N/A
Local Weld Root	N/A	N/A	N/A
Cursor Window	551	2.3	7.3

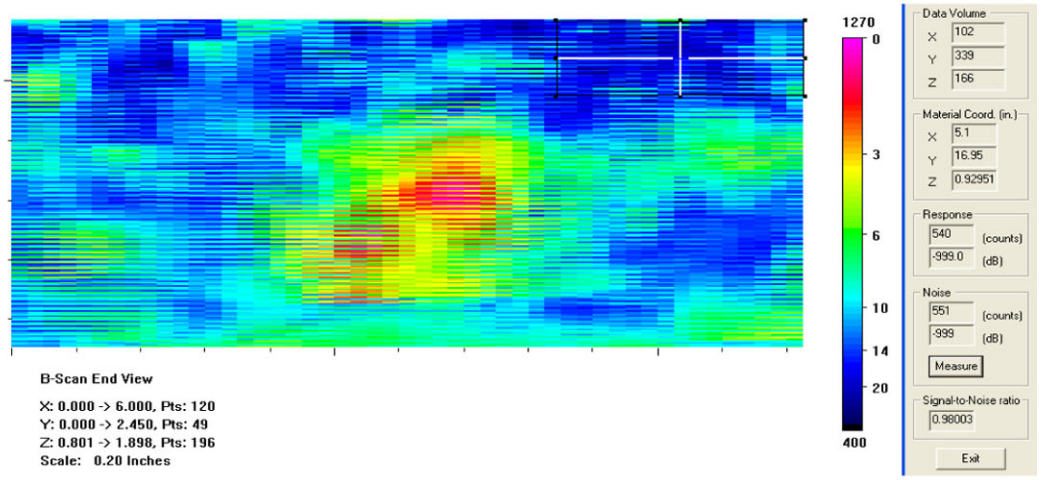

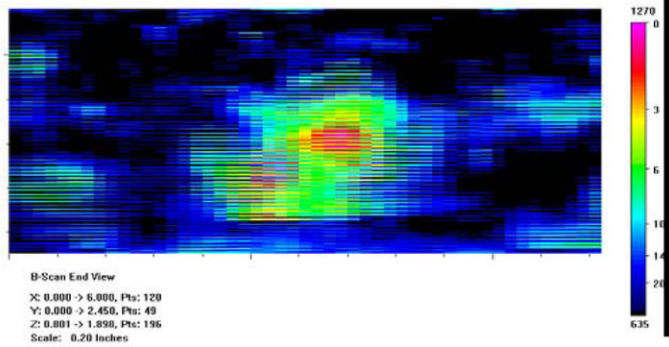

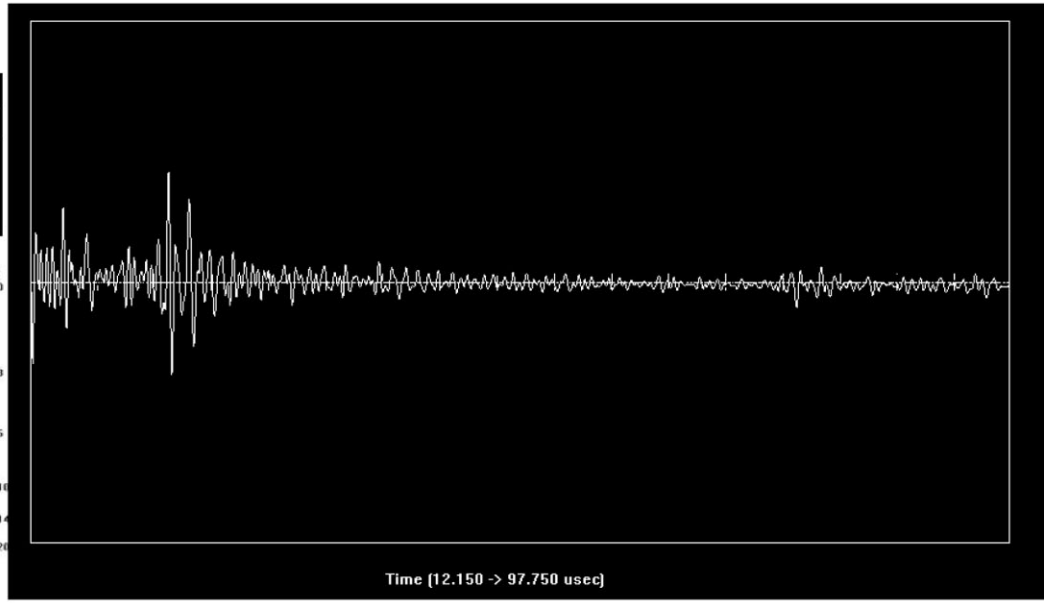

Section #1, Nearside, Saw Cut C, 7% Through Wall Angle

2.25-MHz, 0.375-in.-diameter, 60° Shear

Length Sizing

Actual	1.472
6 dB Drop	0.5
Loss of Signal	0.65
6 dB Drop Δ	0.972
Loss of Signal Δ	0.822

Depth Sizing

Actual	0.1	Corner Tra	43.2
6 dB Drop	0.133	Tip Signal	41.25
UT Tip Signal	0.060938	Velocity	0.125
6 dB Drop Δ	-0.033	Angle	60
UT Tip Signal Δ	0.039062		

Noise Characterization

Peak Signal Response		3318	
Noise		S/N Ratio	dB
General Weld Root	N/A	N/A	N/A
Local Weld Root	N/A	N/A	N/A
Cursor Window	561	5.9	15.4

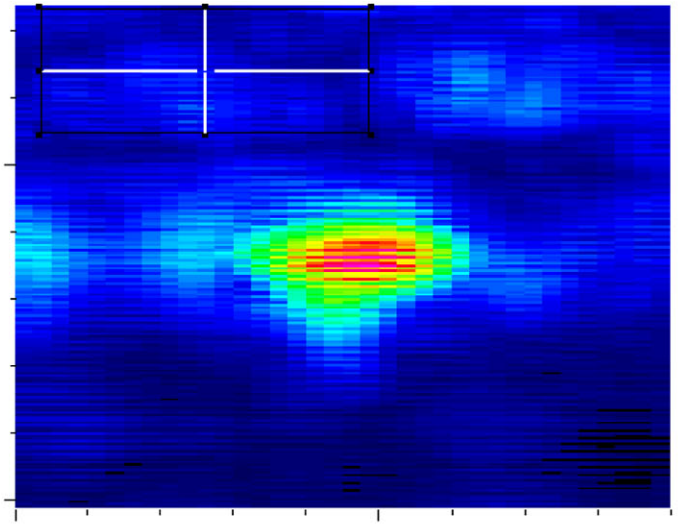

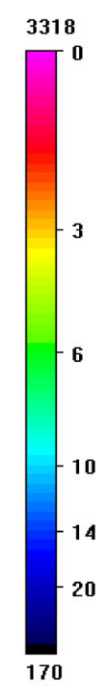

B-Scan End View

X: 0.000 -> 6.000, Pts: 120
Y: 0.000 -> 1.800, Pts: 36
Z: 0.531 -> 2.031, Pts: 192
Scale: 0.20 Inches

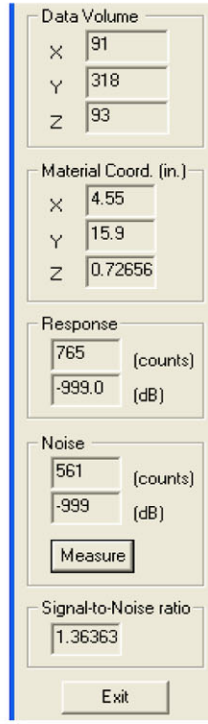

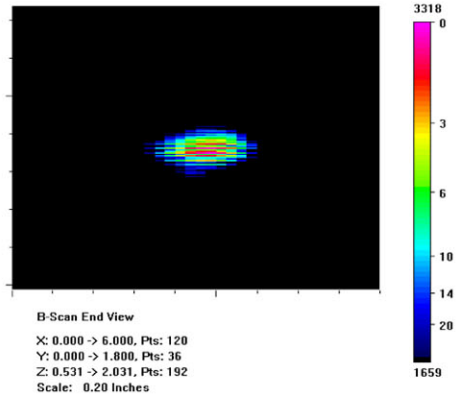

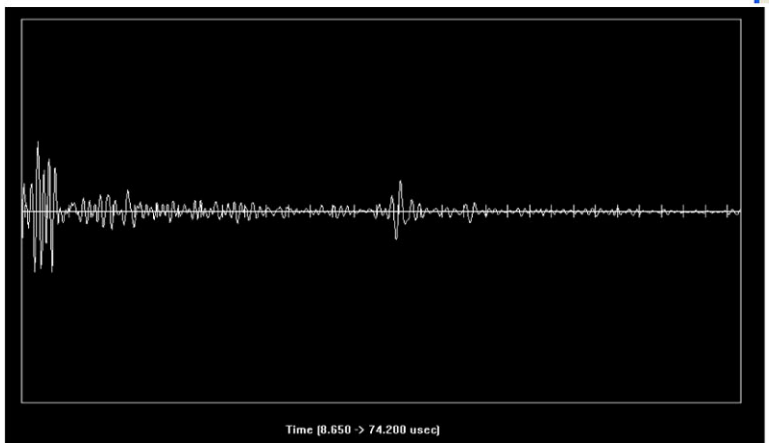

Section #1, Nearside, Saw Cut C, 7% Through Wall Angle

2.25-MHz, 0.375-in.-diameter, 70° Shear

Length Sizing

Actual	1.472
6 dB Drop	0.6
Loss of Signal	0.8
6 dB Drop Δ	0.872
Loss of Signal Δ	0.672

Depth Sizing

Actual	0.1	Corner Trap	
6 dB Drop	0.334	Tip Signal	None
UT Tip Signal	None	Velocity	0.125
6 dB Drop Δ	-0.234	Angle	66
UT Tip Signal Δ	None		

Noise Characterization

Peak Signal Response		2670	
Noise		S/N Ratio	dB
General Weld Root	N/A	N/A	N/A
Local Weld Root	N/A	N/A	N/A
Cursor Window	931	2.9	9.2

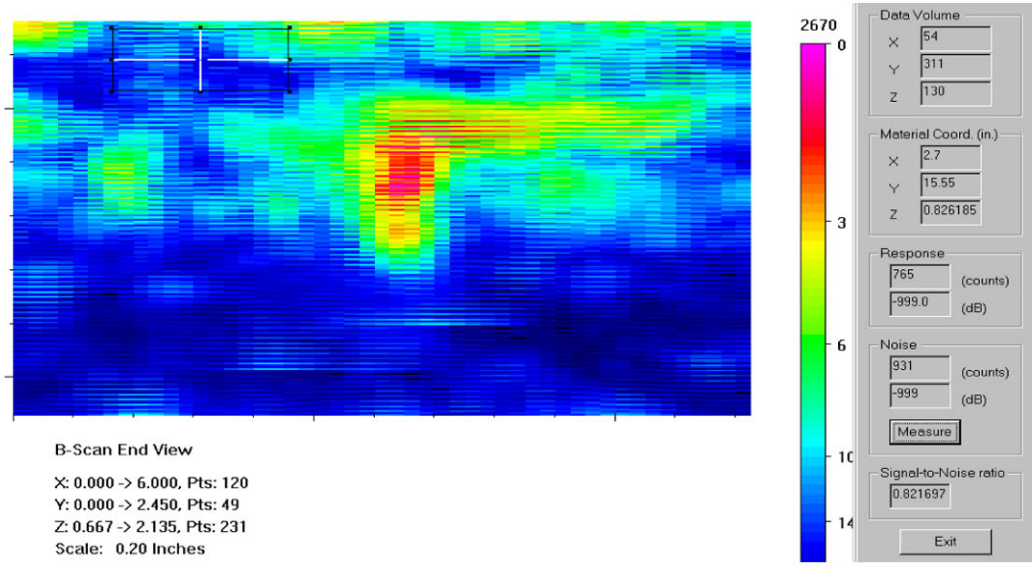

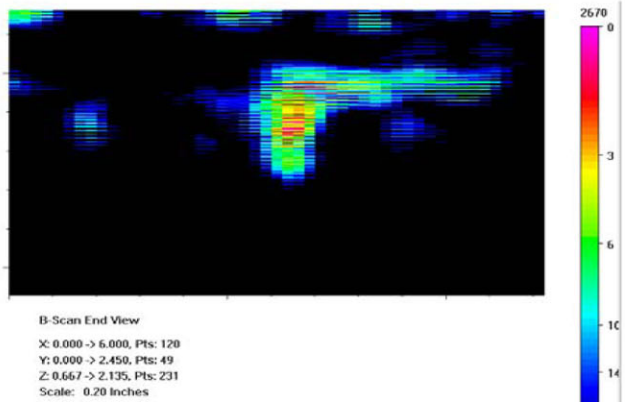

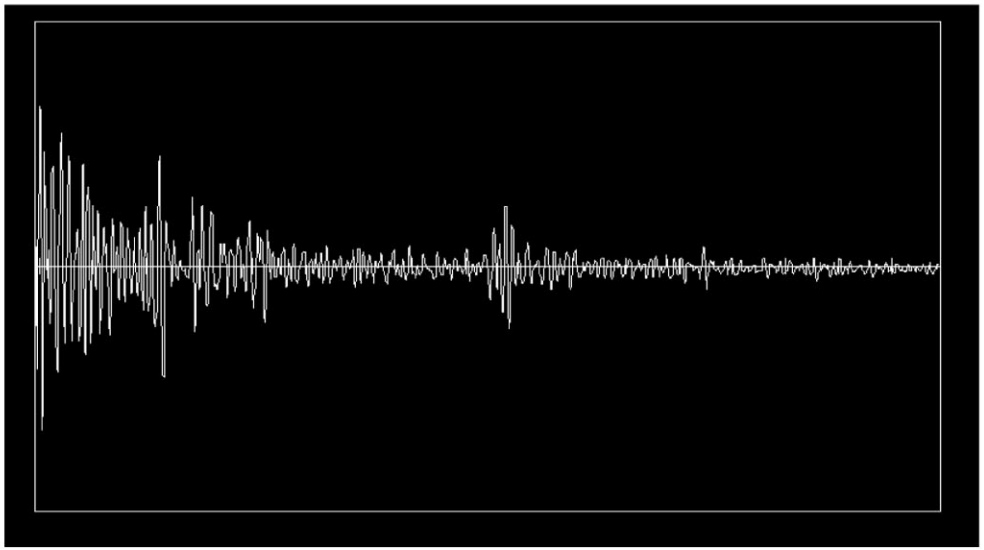

Section #1, Farside, Saw Cut A, 8% Through Wall

1.5-MHz, 0.5-in.-diameter, 60° Shear

Length Sizing

Actual	1.292
6 dB Drop	1.15
Loss of Signal	1.35
6 dB Drop Δ	0.142
Loss of Signal Δ	-0.058

Depth Sizing

Actual	0.106	Corner Tra	51.05
6 dB Drop	0.191	Tip Signal	38.9
UT Tip Signal	0.379688	Velocity	0.125
6 dB Drop Δ	-0.085	Angle	60
UT Tip Signal Δ	-0.27369		

Noise Characterization

Peak Signal Response		11729	
Noise		S/N Ratio	dB
General Weld Root	3786	3.1	9.8
Local Weld Root	7715	1.5	3.6
Cursor Window	2413	4.9	13.7

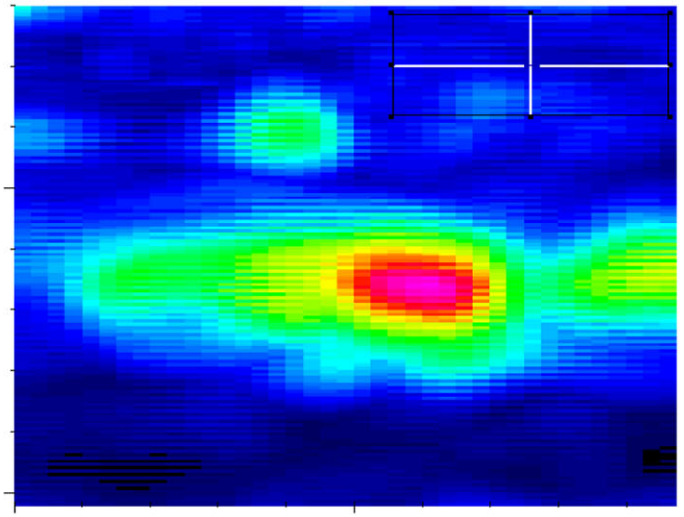

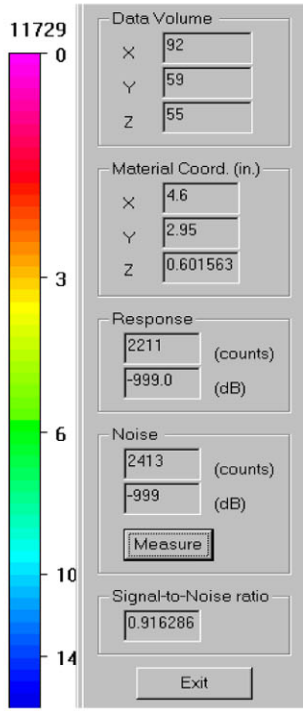

B-Scan End View

X: 0.000 -> 6.000, Pts: 120
Y: 0.000 -> 1.950, Pts: 39
Z: 0.394 -> 2.034, Pts: 150
Scale: 0.20 Inches

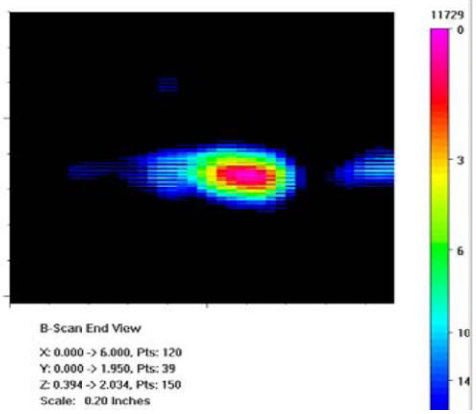

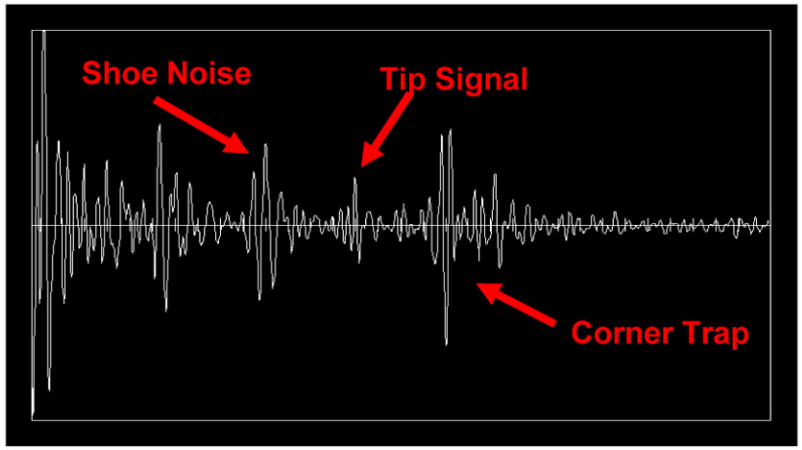

Section #1, Farside, Saw Cut A, 8% Through Wall

1.5-MHz, 0.5-in.-diameter, 70° Shear

Length Sizing

Actual	1.292
6 dB Drop	1.15
Loss of Signal	1.2
6 dB Drop Δ	0.142
Loss of Signal Δ	0.092

Depth Sizing

Actual	0.106	Corner Trap	
6 dB Drop	0.258	Tip Signal	None
UT Tip Signal	None	Velocity	0.125
6 dB Drop Δ	-0.152	Angle	67.6
UT Tip Signal Δ	None		

Noise Characterization

Peak Signal Response		8294	
Noise		S/N Ratio	dB
General Weld Root	2186	3.8	11.6
Local Weld Root	3172	2.6	8.3
Cursor Window	1888	4.4	12.9

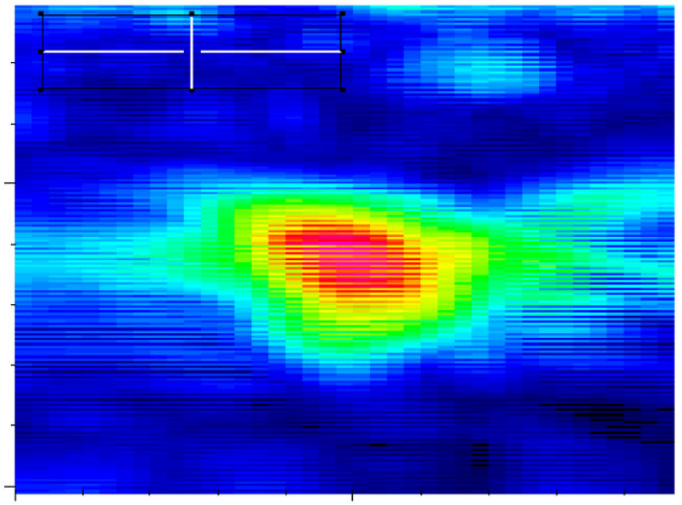

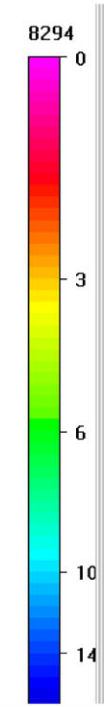

B-Scan End View

X: 0.000 -> 6.000, Pts: 120
Y: 0.000 -> 1.950, Pts: 39
Z: 0.400 -> 2.017, Pts: 194
Scale: 0.20 Inches

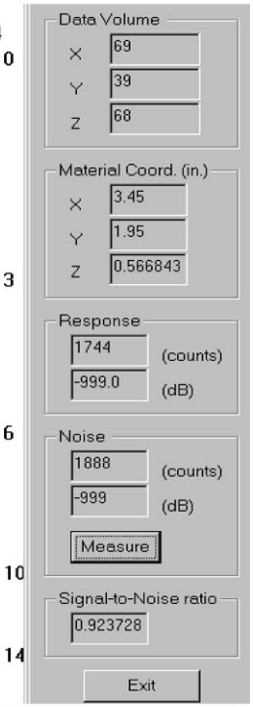

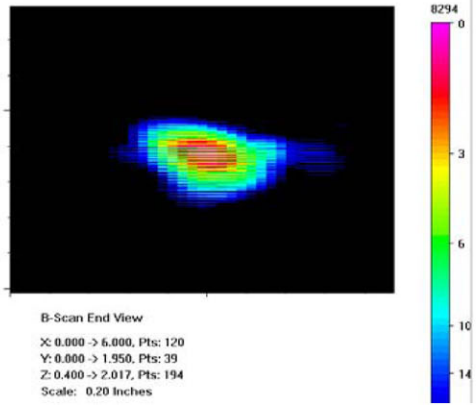

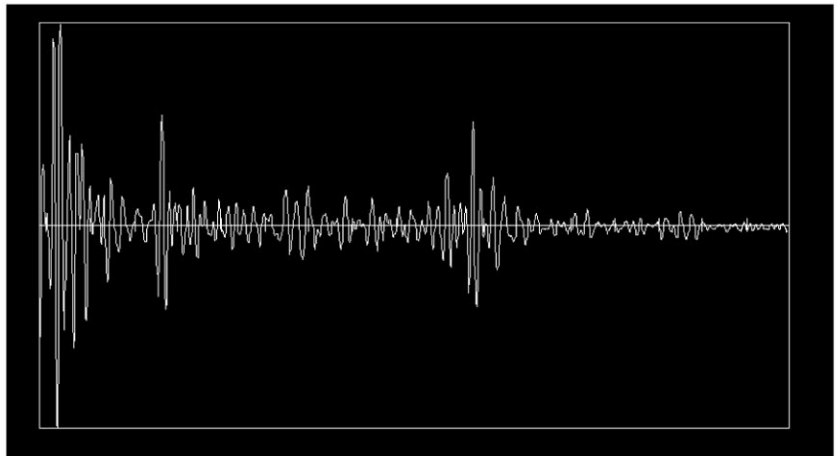

Section #1, Farside, Saw Cut A, 8% Through Wall

1.5-MHz, 0.375-in.-diameter, 60° Shear

Length Sizing

Actual	1.292
6 dB Drop	1.25
Loss of Signal	1.4
6 dB Drop Δ	0.042
Loss of Signal Δ	-0.108

Depth Sizing

Actual	0.106	Corner Tra	46.4
6 dB Drop	0.231	Tip Signal	32.6
UT Tip Signal	0.44422	Velocity	0.125
6 dB Drop Δ	-0.125	Angle	59
UT Tip Signal Δ	-0.33822		

Noise Characterization

Peak Signal Response		12541	
Noise		S/N Ratio	dB
General Weld Root	4208	3.0	9.5
Local Weld Root	6484	1.9	5.7
Cursor Window	3306	3.8	11.6

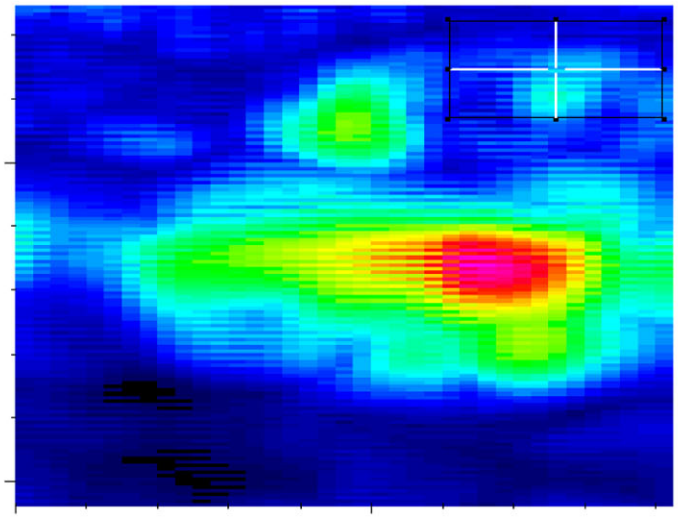

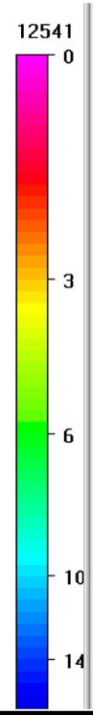

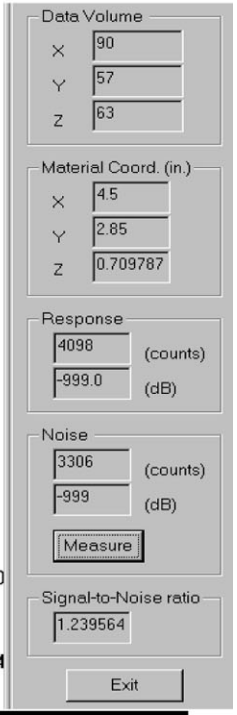

B-Scan End View

X: 0.000 -> 6.000, Pts: 120
Y: 0.000 -> 1.850, Pts: 37
Z: 0.496 -> 2.073, Pts: 140
Scale: 0.20 Inches

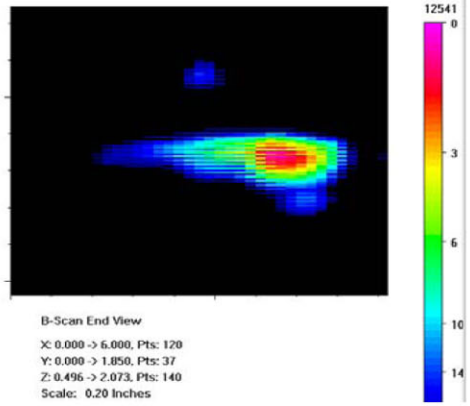

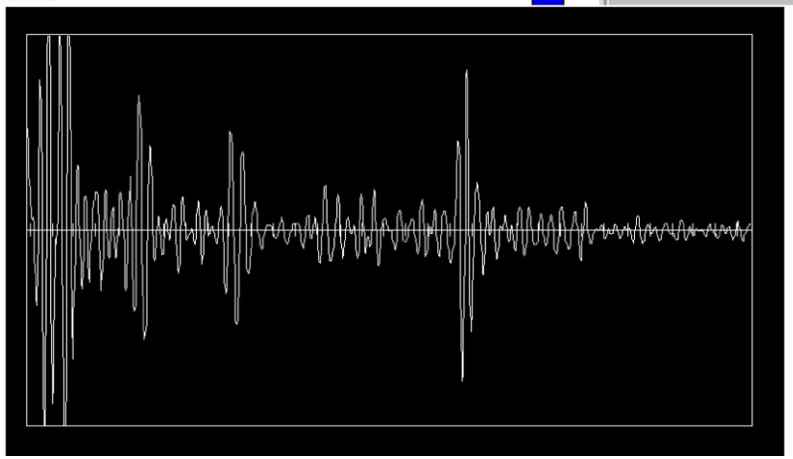

Section #1, Farside, Saw Cut A, 8% Through Wall

1.5-MHz, 0.375-in.-diameter, 70° Shear

Length Sizing

Actual	1.292
6 dB Drop	1.5
Loss of Signal	1.6
6 dB Drop Δ	-0.208
Loss of Signal Δ	-0.308

Depth Sizing

Actual	0.106	Corner Trap	
6 dB Drop	0.221	Tip Signal	None
UT Tip Signal	None	Velocity	0.125
6 dB Drop Δ	-0.115	Angle	64
UT Tip Signal Δ	None		

Noise Characterization

Peak Signal Response		11239	
Noise		S/N Ratio	dB
General Weld Root	3732	3.0	9.6
Local Weld Root	7384	1.5	3.6
Cursor Window	3133	3.6	11.1

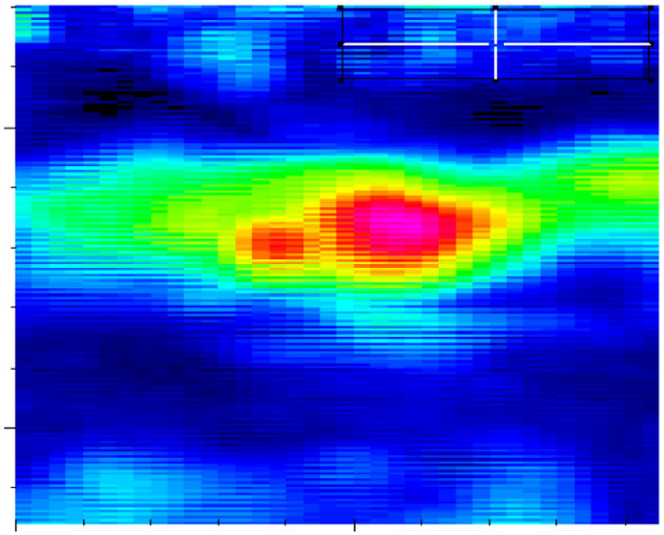

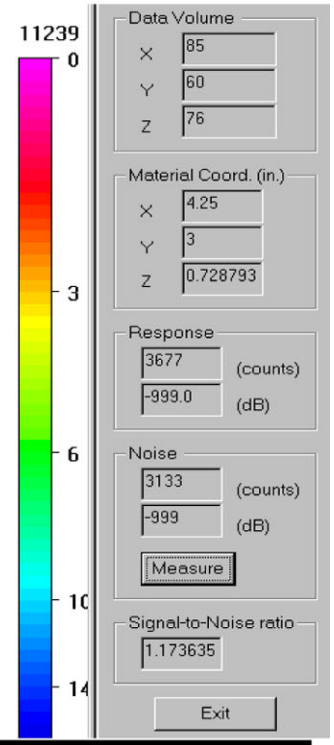

B-Scan End View

X: 0.000 -> 6.000, Pts: 120
Y: 0.000 -> 1.900, Pts: 38
Z: 0.585 -> 2.311, Pts: 180
Scale: 0.20 Inches

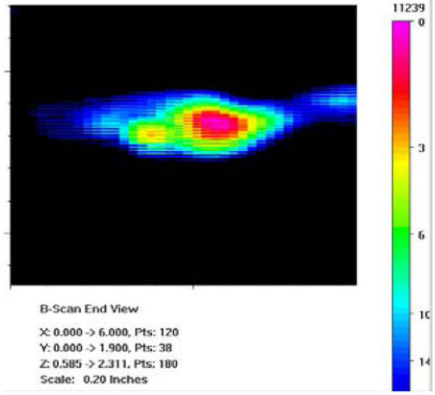

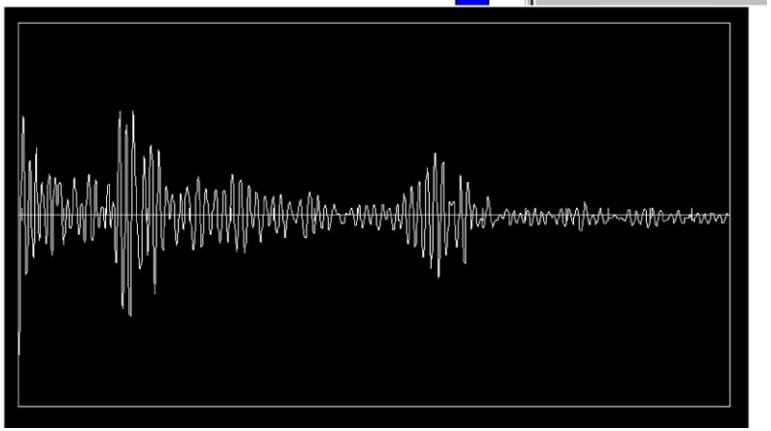

Section #1, Farside, Saw Cut A, 8% Through Wall

2.25-MHz, 0.5-in.-diameter, 60° Shear

Length Sizing

Actual	1.292
6 dB Drop	0.9
Loss of Signal	1.4
6 dB Drop Δ	0.392
Loss of Signal Δ	-0.108

Depth Sizing

Actual	0.106	Corner Tra	51.45
6 dB Drop	0.164	Tip Signal	38.65
UT Tip Signal	0.4	Velocity	0.125
6 dB Drop Δ	-0.058	Angle	60
UT Tip Signal Δ	-0.294		

Noise Characterization

Peak Signal Response		16012	
Noise		S/N Ratio	dB
General Weld Root	5151	3.1	9.9
Local Weld Root	10873	1.5	3.4
Cursor Window	2922	5.5	14.8

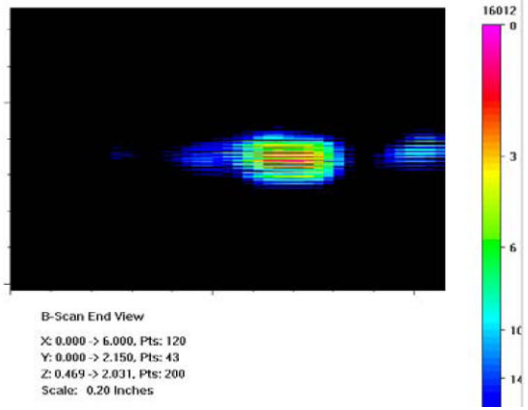

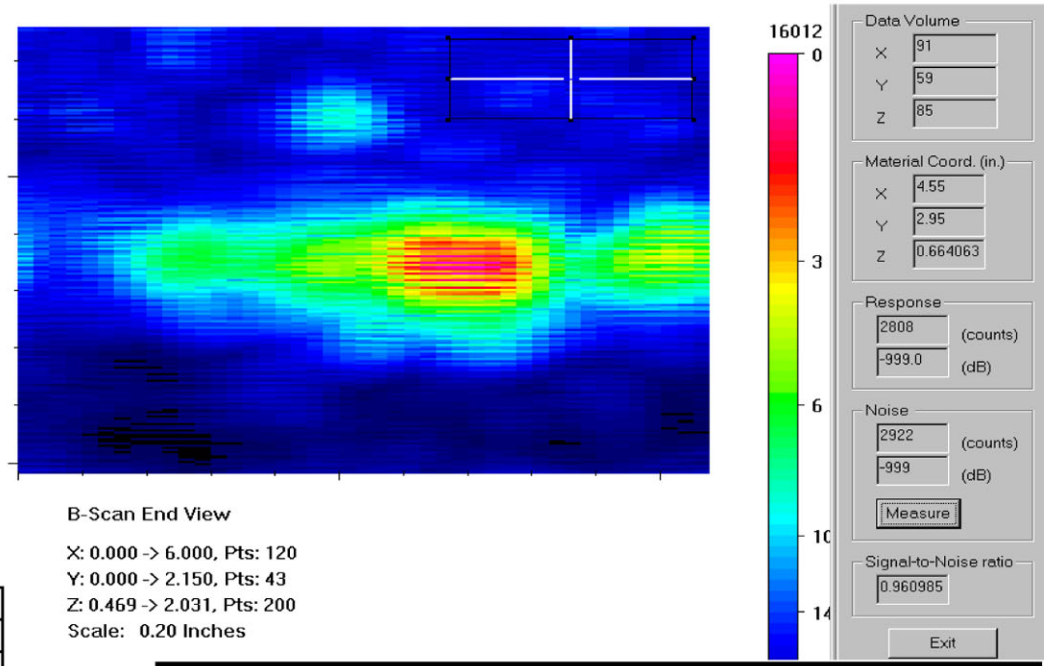

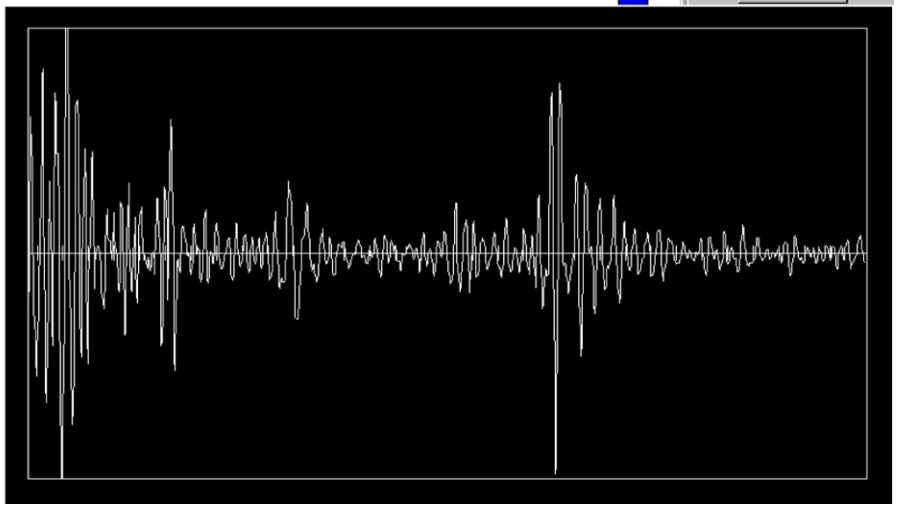

Section #1, Farside, Saw Cut A, 8% Through Wall

2.25-MHz, 0.5-in.-diameter, 70° Shear

Length Sizing

Actual	1.292
6 dB Drop	0.85
Loss of Signal	1.35
6 dB Drop Δ	0.442
Loss of Signal Δ	-0.058

Depth Sizing

Actual	0.106	Corner Tra	62.85
6 dB Drop	0.23	Tip Signal	49.1
UT Tip Signal	0.307972	Velocity	0.125
6 dB Drop Δ	-0.124	Angle	69
UT Tip Signal Δ	-0.20197		

Noise Characterization

Peak Signal Response		9668	
Noise		S/N Ratio	dB
General Weld Root	2244	4.3	12.7
Local Weld Root	3390	2.9	9.1
Cursor Window	2119	4.6	13.2

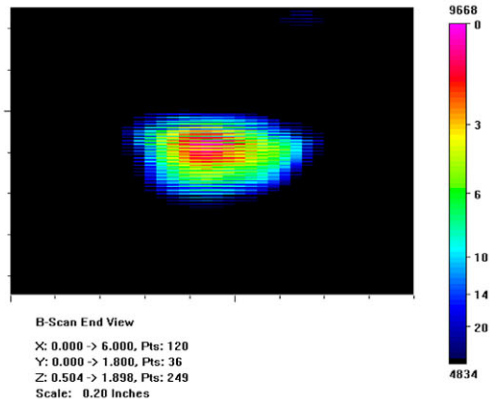

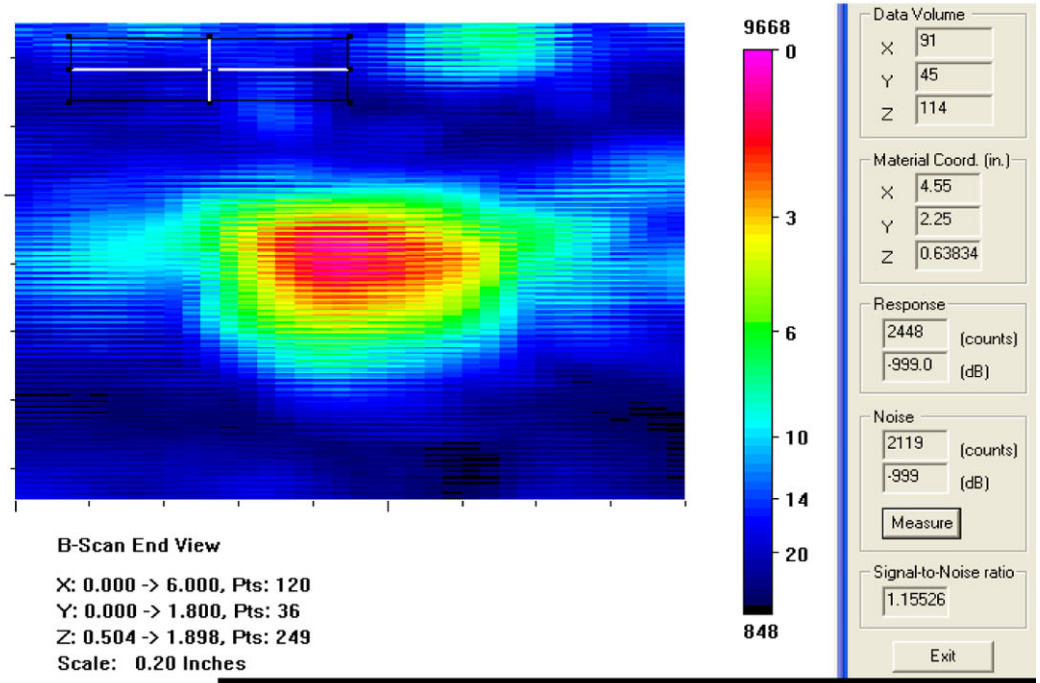

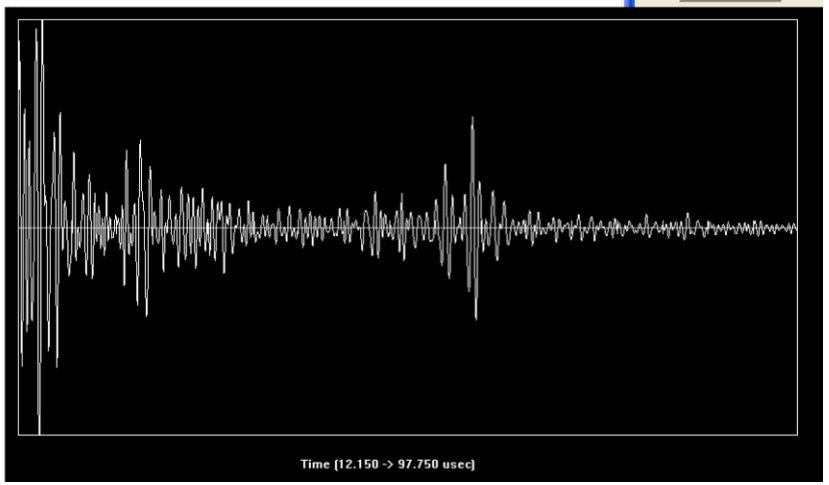

Section #1, Farside, Saw Cut A, 8% Through Wall

2.25-MHz, 0.375-in.-diameter, 60° Shear

Length Sizing

Actual	1.292
6 dB Drop	1.25
Loss of Signal	1.45
6 dB Drop Δ	0.042
Loss of Signal Δ	-0.158

Depth Sizing

Actual	0.106	Corner Tra	48.55
6 dB Drop	0.223	Tip Signal	38.2
UT Tip Signal	0.323438	Velocity	0.125
6 dB Drop Δ	-0.117	Angle	60
UT Tip Signal Δ	-0.21744		

Noise Characterization

Peak Signal Response		13020	
Noise		S/N Ratio	dB
General Weld Root	4347	3.0	9.5
Local Weld Root	8385	1.6	3.8
Cursor Window	2701	4.8	13.7

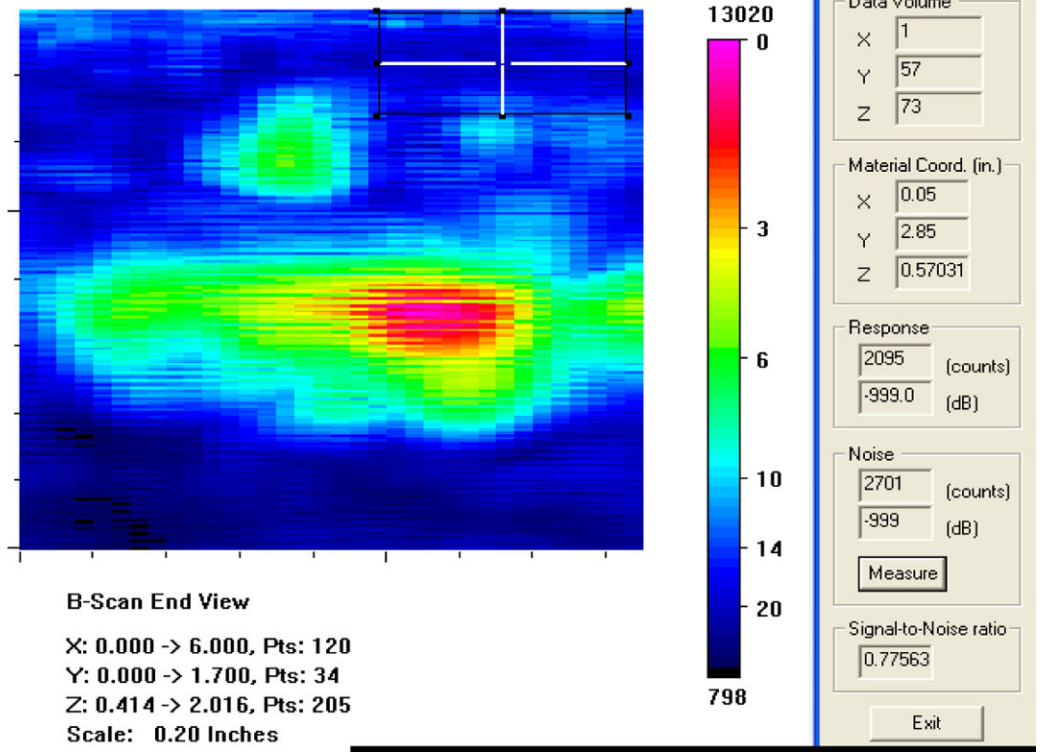

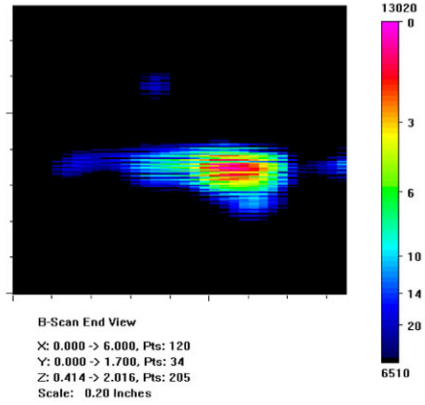

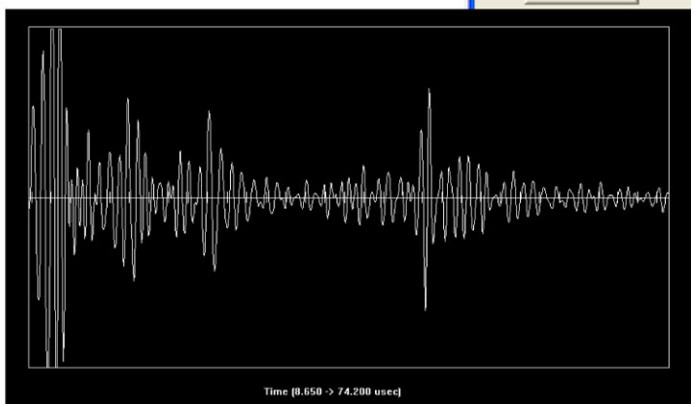

Section #1, Farside, Saw Cut A, 8% Through Wall

2.25-MHz, 0.375-in.-diameter, 70° Shear

Length Sizing

Actual	1.292
6 dB Drop	1.2
Loss of Signal	1.2
6 dB Drop Δ	0.092
Loss of Signal Δ	0.092

Depth Sizing

Actual	0.106	Corner Tra	58.3
6 dB Drop	0.264	Tip Signal	45.3
UT Tip Signal	0.330474	Velocity	0.125
6 dB Drop Δ	-0.158	Angle	66
UT Tip Signal Δ	-0.22447		

Noise Characterization

Peak Signal Response		6939	
Noise		S/N Ratio	dB
General Weld Root	2024	3.4	10.7
Local Weld Root	4253	1.6	4.3
Cursor Window	2362	2.9	9.4

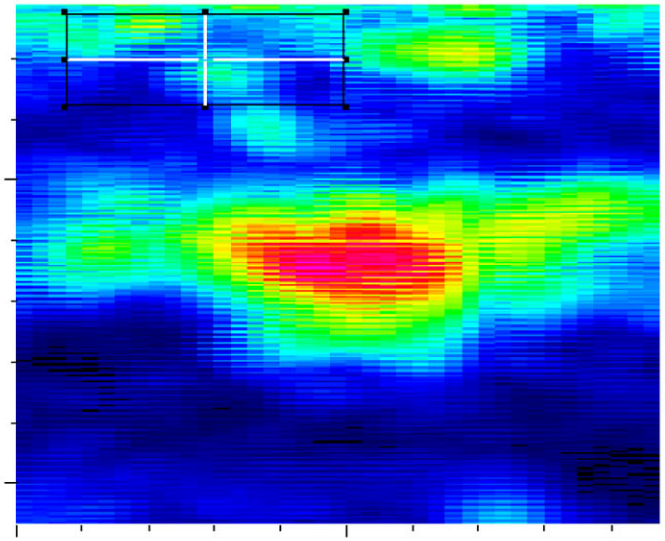

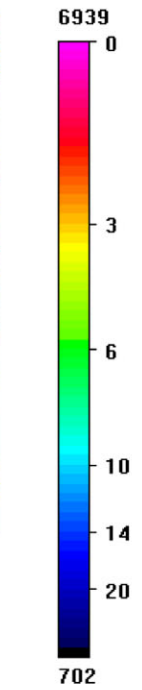

B-Scan End View

X: 0.000 -> 6.000, Pts: 120
Y: 0.000 -> 1.950, Pts: 39
Z: 0.432 -> 2.142, Pts: 269
Scale: 0.20 Inches

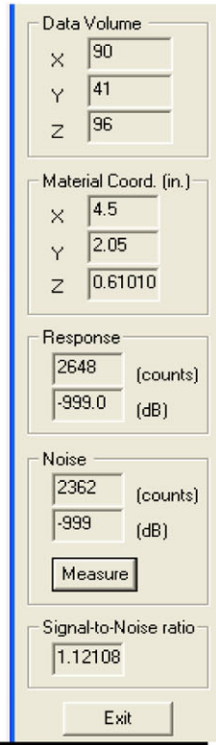

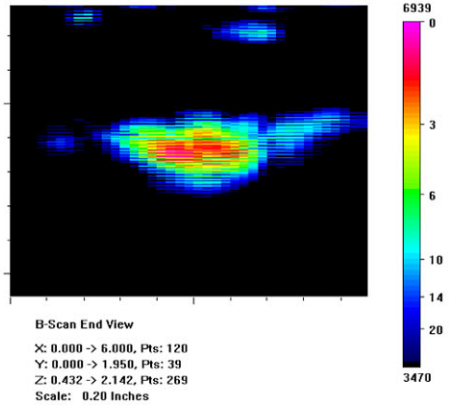

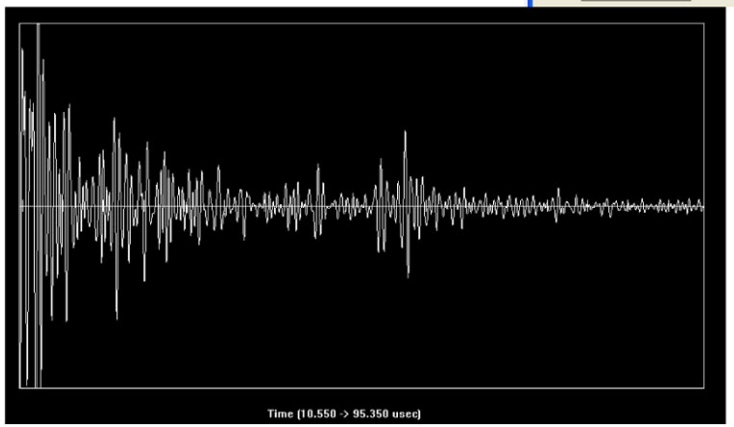

Section #1, Farside, Flaw A, 15% Through Wall

1.5-MHz, 0.5-in.-diameter, 60° Shear

Length Sizing

Actual	0.42
6 dB Drop	0.45
Loss of Signal	0.5
6 dB Drop Δ	-0.03
Loss of Signal Δ	-0.08

No Call due to low signal response compared to the weld root response

Depth Sizing

Actual	0.195	Corner Tra	58.65
6 dB Drop	0.213	Tip Signal	46.05
UT Tip Signal	0.39375	Velocity	0.125
6 dB Drop Δ	-0.018	Angle	60
UT Tip Signal Δ	-0.19875		

Noise Characterization

Peak Signal Response		6807	
Noise		S/N Ratio	dB
General Weld Root	3786	1.8	5.1
Local Weld Root	8274	0.8	-1.7
Cursor Window	1873	3.6	11.2

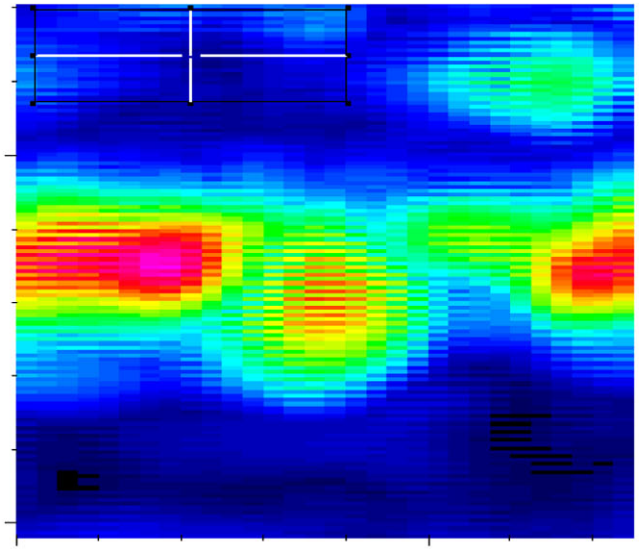

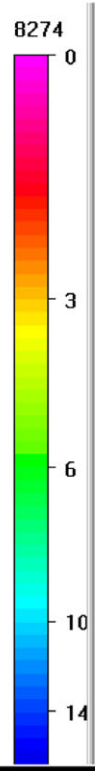

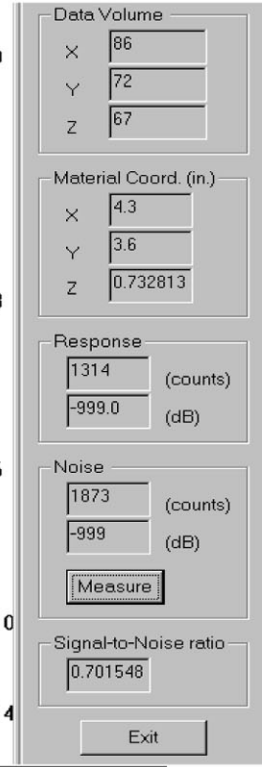

B-Scan End View

X: 0.000 -> 6.000, Pts: 120
Y: 0.000 -> 1.500, Pts: 30
Z: 0.580 -> 2.034, Pts: 133
Scale: 0.20 Inches

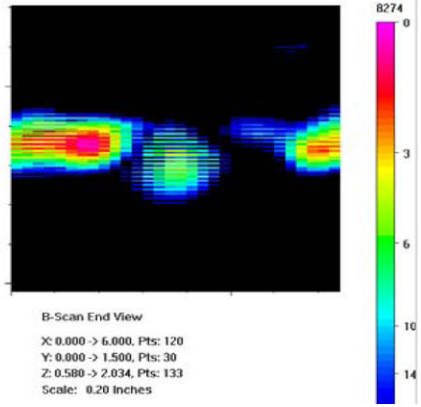

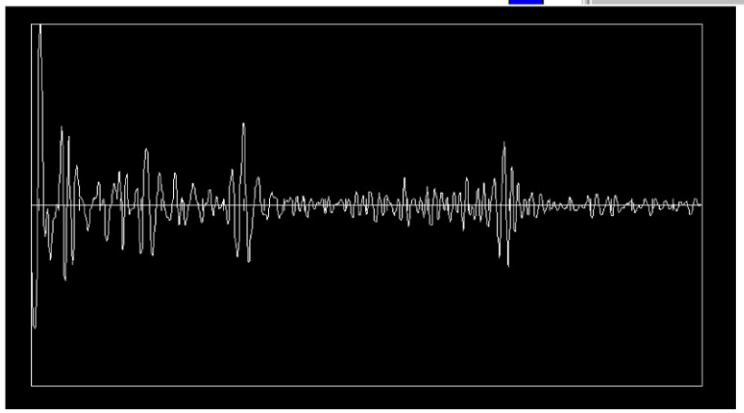

Section #1, Farside, Flaw A, 15% Through Wall

1.5-MHz, 0.5-in.-diameter, 70° Shear

Length Sizing

Actual	0.42
6 dB Drop	0.5
Loss of Signal	0.6
6 dB Drop Δ	-0.08
Loss of Signal Δ	-0.18

Depth Sizing

Actual	0.195	Corner Trap	
6 dB Drop	0.275	Tip Signal	None
UT Tip Signal	None	Velocity	0.125
6 dB Drop Δ	-0.08	Angle	67.6
UT Tip Signal Δ	None		

Noise Characterization

Peak Signal Response		8109	
Noise		S/N Ratio	dB
General Weld Root	2186	3.7	11.4
Local Weld Root	3187	2.5	8.1
Cursor Window	1600	5.1	14.1

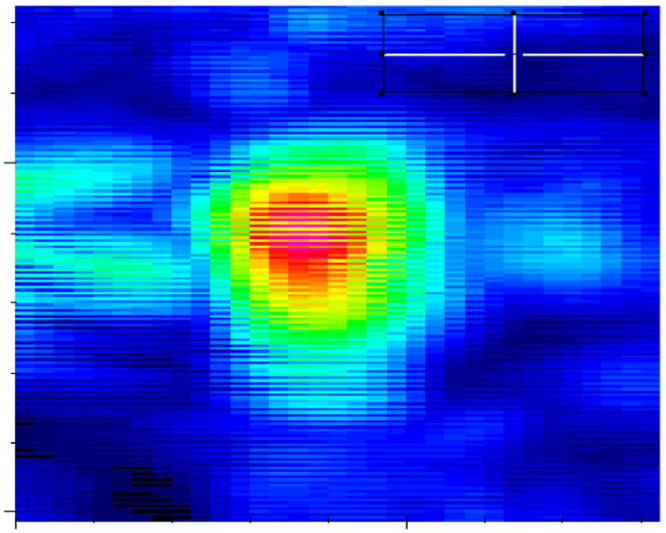

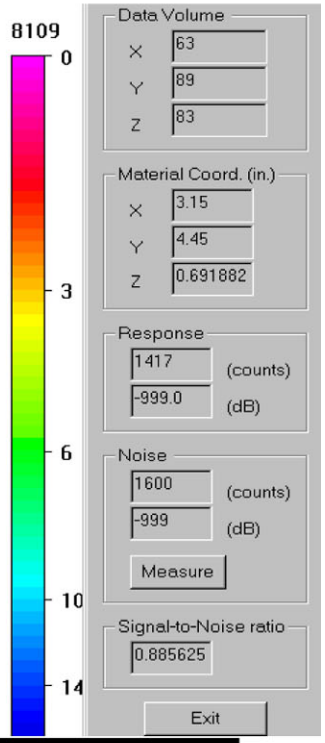

B-Scan End View

X: 0.000 -> 6.000, Pts: 120
Y: 0.000 -> 1.650, Pts: 33
Z: 0.542 -> 2.017, Pts: 177
Scale: 0.20 Inches

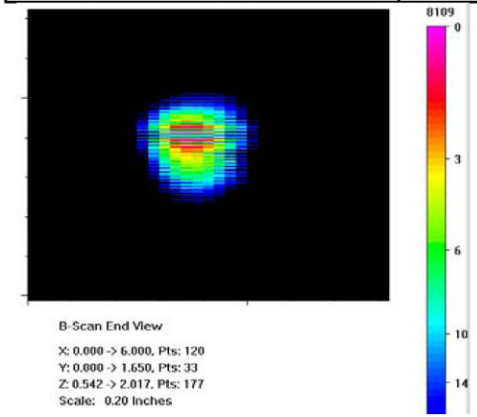

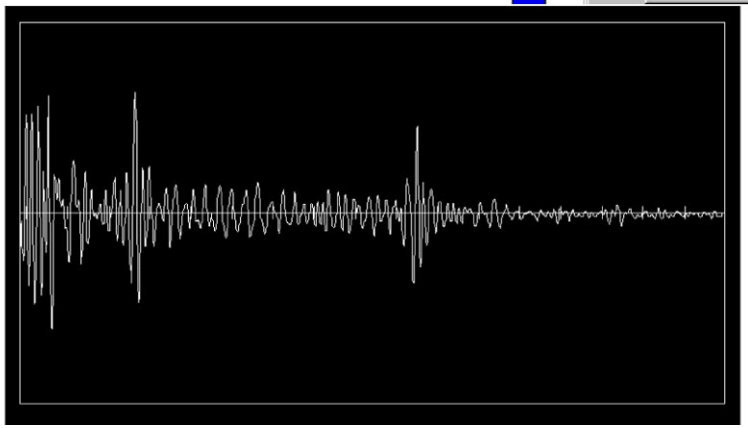

Section #1, Farside, Flaw A, 15% Through Wall

1.5-MHz, 0.375-in.-diameter, 60° Shear

Length Sizing

Actual	0.42
6 dB Drop	0.45
Loss of Signal	0.45
6 dB Drop Δ	-0.03
Loss of Signal Δ	-0.03

No Call due to low signal response compared to the weld root response

Depth Sizing

Actual	0.195	Corner Trap	
6 dB Drop	0.203	Tip Signal	None
UT Tip Signal	None	Velocity	0.125
6 dB Drop Δ	-0.008	Angle	59
UT Tip Signal Δ	None		

Noise Characterization

Peak Signal Response		6910	
Noise		S/N Ratio	dB
General Weld Root	4208	1.6	4.3
Local Weld Root	10083	0.7	-3.3
Cursor Window	3005	2.3	7.2

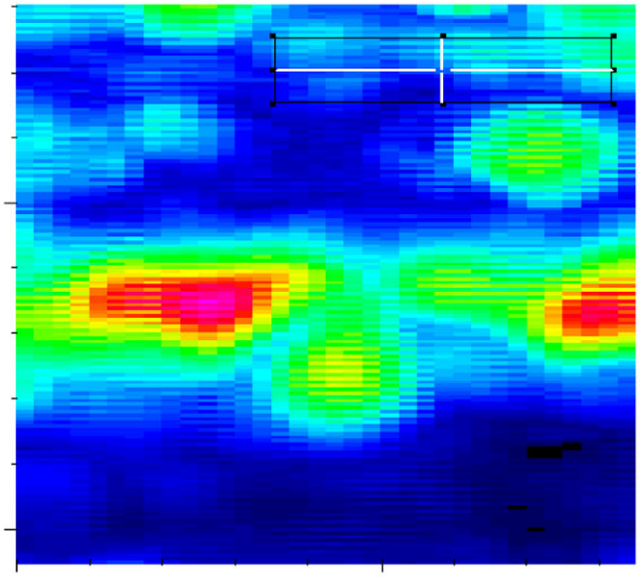

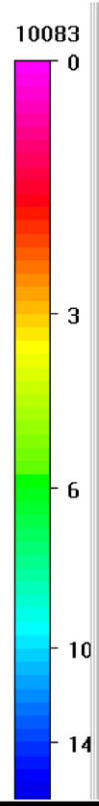

B-Scan End View

X: 0.000 -> 6.000, Pts: 120
Y: 0.000 -> 1.700, Pts: 34
Z: 0.383 -> 2.096, Pts: 152
Scale: 0.20 Inches

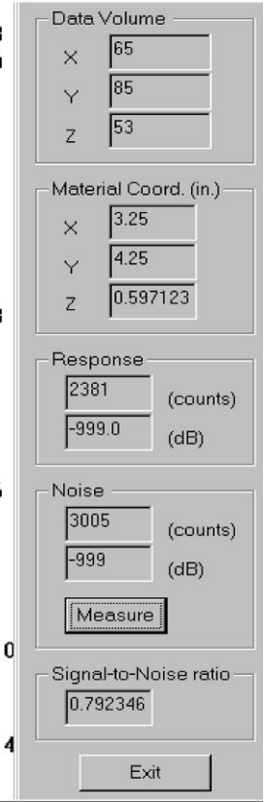

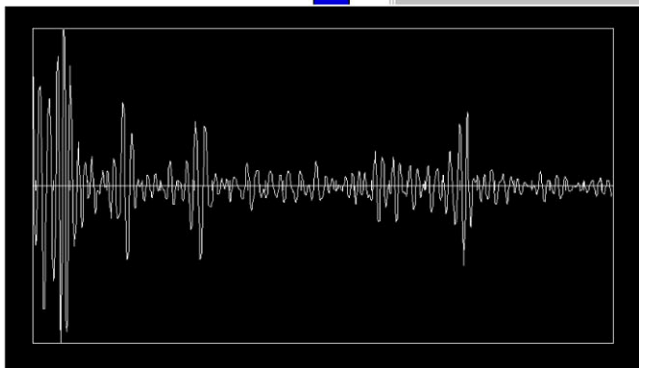

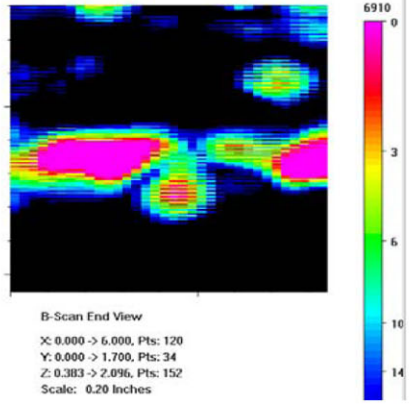

Section #1, Farside, Flaw A, 15% Through Wall

1.5-MHz, 0.375-in.-diameter, 70° Shear

Length Sizing

Actual	0.42
6 dB Drop	0.5
Loss of Signal	0.6
6 dB Drop Δ	-0.08
Loss of Signal Δ	-0.18

Depth Sizing

Actual	0.195	Corner Trap	
6 dB Drop	0.206	Tip Signal	None
UT Tip Signal	None	Velocity	0.125
6 dB Drop Δ	-0.011	Angle	64
UT Tip Signal Δ	None		

Noise Characterization

Peak Signal Response		9839	
Noise		S/N Ratio	dB
General Weld Root	3732	2.6	8.4
Local Weld Root	7573	1.3	2.3
Cursor Window	2849	3.5	10.8

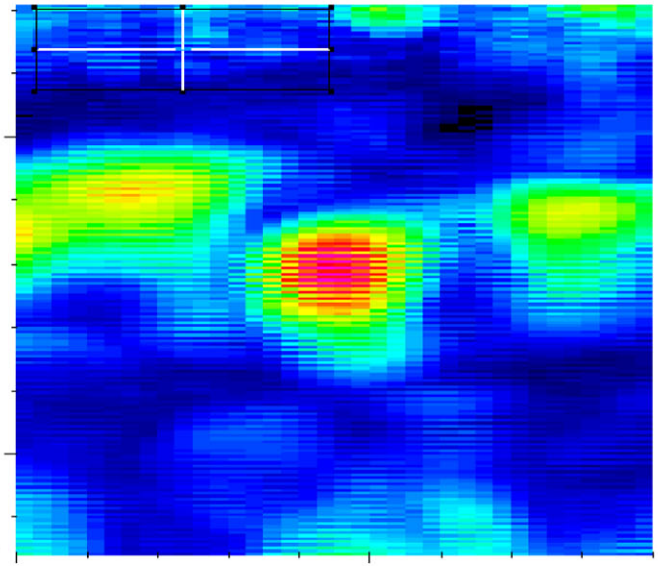

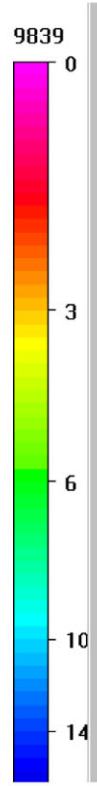

B-Scan End View

X: 0.000 -> 6.000, Pts: 120
Y: 0.000 -> 1.800, Pts: 36
Z: 0.575 -> 2.311, Pts: 181
Scale: 0.20 Inches

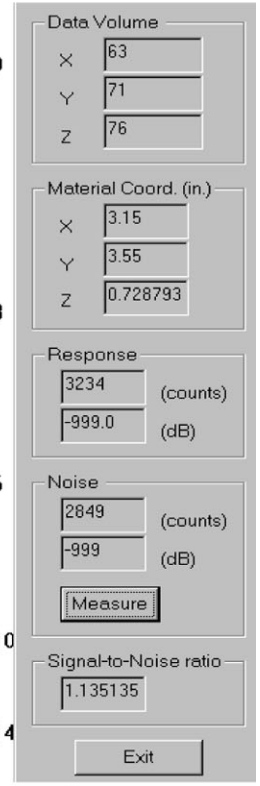

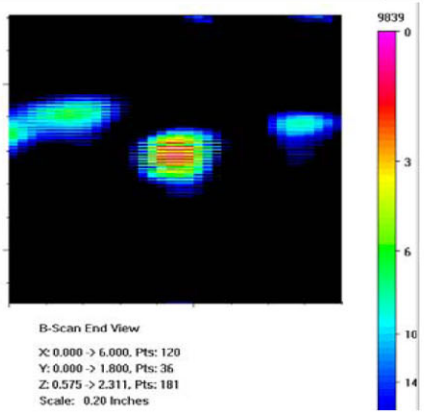

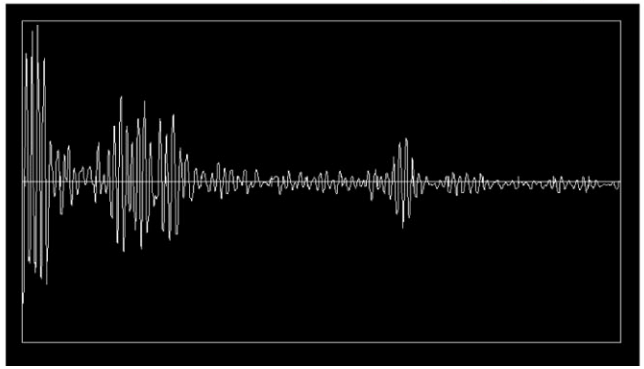

Section #1, Farside, Flaw A, 15% Through Wall

2.25-MHz, 0.5-in.-diameter, 60° Shear

Length Sizing

Actual	0.42
6 dB Drop	0.5
Loss of Signal	0.5
6 dB Drop Δ	-0.08
Loss of Signal Δ	-0.08

Depth Sizing

Actual	0.195	Corner Tra	47.35
6 dB Drop	0.227	Tip Signal	41.7
UT Tip Signal	0.176563	Velocity	0.125
6 dB Drop Δ	-0.032	Angle	60
UT Tip Signal Δ	0.018438		

Noise Characterization

Peak Signal Response		8359	
Noise		S/N Ratio	dB
General Weld Root	5151	1.6	4.2
Local Weld Root	11209	0.7	-2.5
Cursor Window	2738	3.1	9.7

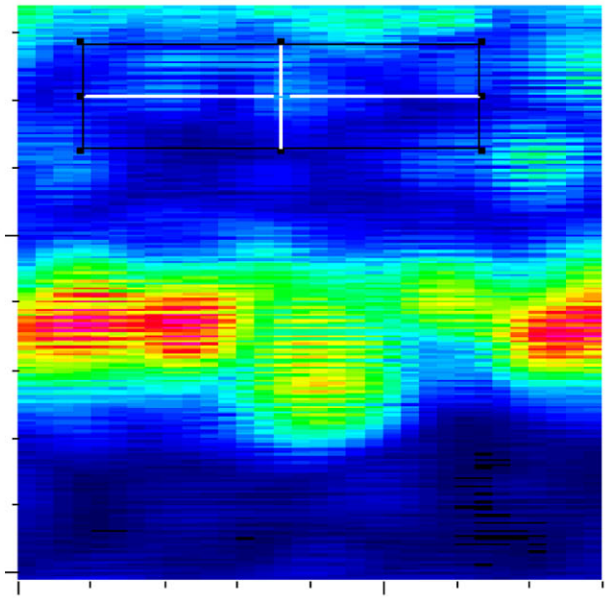

B-Scan End View

X: 0.000 -> 6.000, Pts: 120
Y: 0.000 -> 1.600, Pts: 32
Z: 0.328 -> 2.031, Pts: 218
Scale: 0.20 Inches

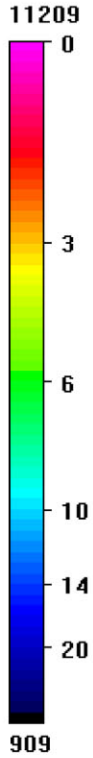

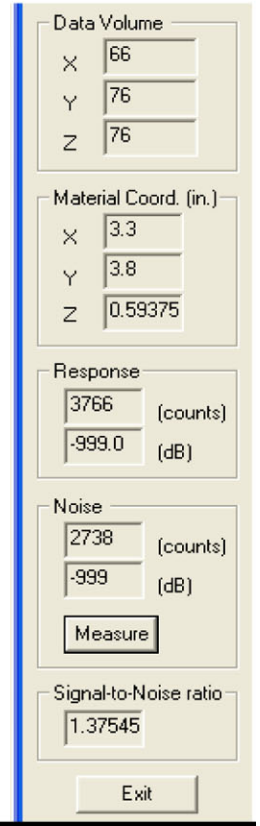

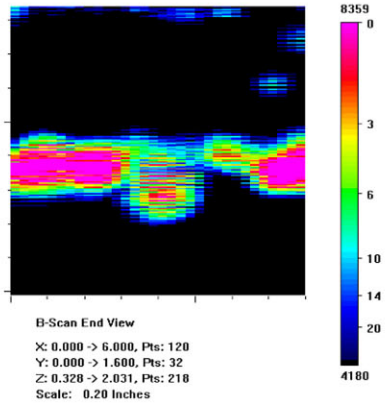

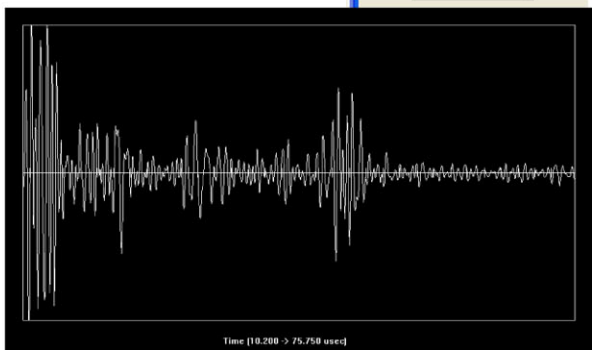

Section #1, Farside, Flaw A, 15% Through Wall

2.25-MHz, 0.5-in.-diameter, 70° Shear

Length Sizing

Actual	0.42
6 dB Drop	0.5
Loss of Signal	0.7
6 dB Drop Δ	-0.08
Loss of Signal Δ	-0.28

Depth Sizing

Actual	0.195	Corner Tra	62.2
6 dB Drop	0.263	Tip Signal	49.35
UT Tip Signal	0.287814	Velocity	0.125
6 dB Drop Δ	-0.068	Angle	69
UT Tip Signal Δ	-0.09281		

Noise Characterization

Peak Signal Response		8987	
Noise		S/N Ratio	dB
General Weld Root	2244	4.0	12.1
Local Weld Root	3431	2.6	8.4
Cursor Window	2486	3.6	11.2

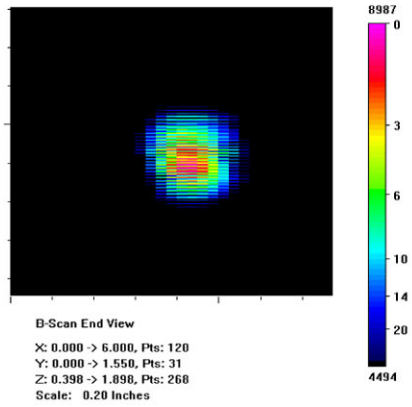

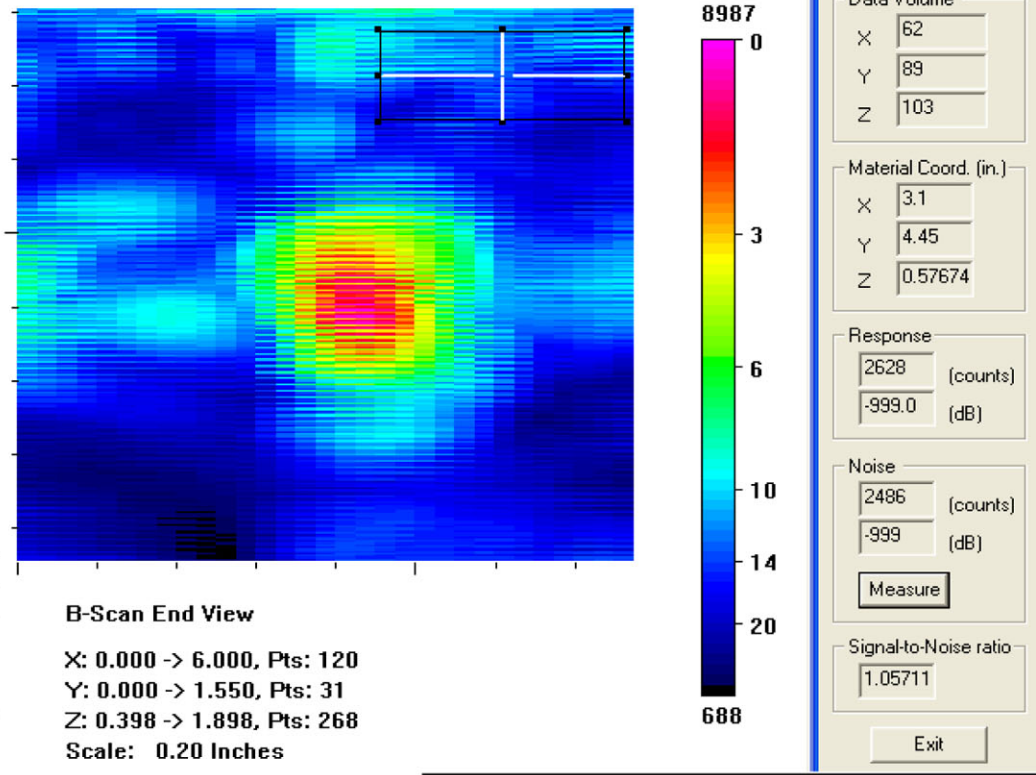

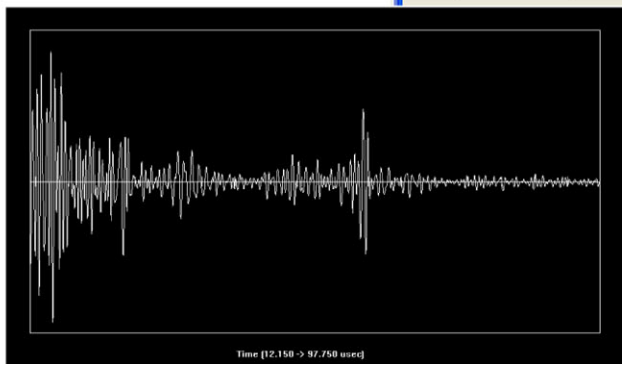

Section #1, Farside, Flaw A, 15% Through Wall

2.25-MHz, 0.375-in.-diameter, 60° Shear

Length Sizing

Actual	0.42
6 dB Drop	0.5
Loss of Signal	0.55
6 dB Drop Δ	-0.08
Loss of Signal Δ	-0.13

No Call due to low signal response compared to the weld root response

Depth Sizing

Actual	0.195	Corner Tra	57.85
6 dB Drop	0.238	Tip Signal	49.95
UT Tip Signal	0.246875	Velocity	0.125
6 dB Drop Δ	-0.043	Angle	60
UT Tip Signal Δ	-0.05188		

Noise Characterization

Peak Signal Response		7724	
Noise		S/N Ratio	dB
General Weld Root	4347	1.8	5.0
Local Weld Root	10599	0.7	-2.7
Cursor Window	3044	2.5	8.1

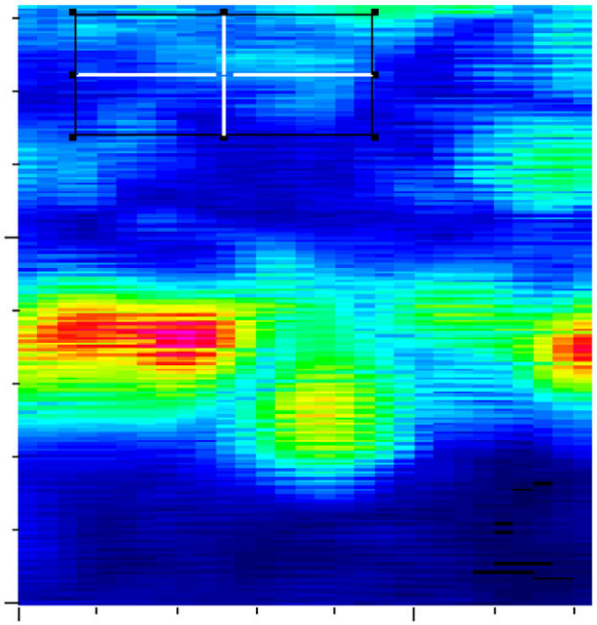

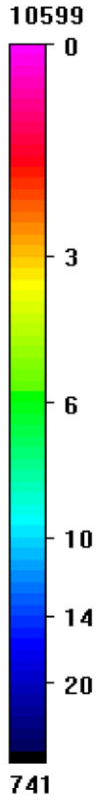

B-Scan End View

X: 0.000 -> 6.000, Pts: 120
Y: 0.000 -> 1.450, Pts: 29
Z: 0.375 -> 2.016, Pts: 210
Scale: 0.20 Inches

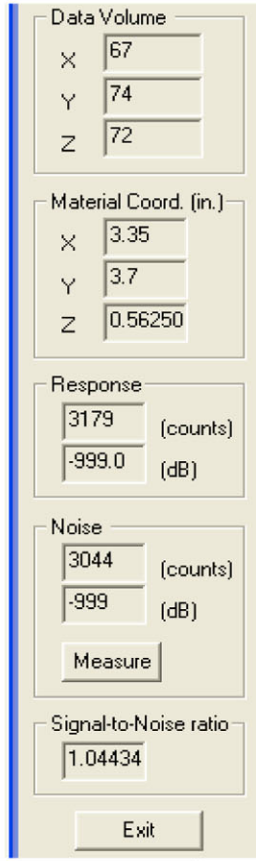

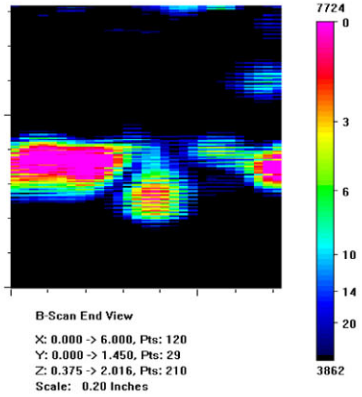

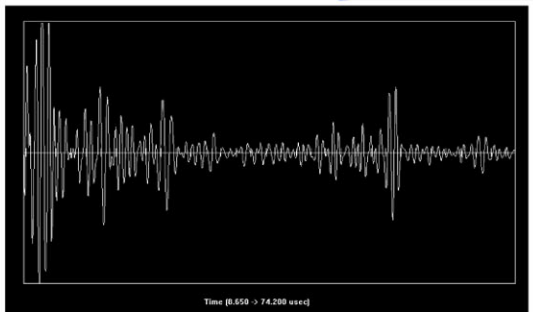

Section #1, Farside, Flaw A, 15% Through Wall

2.25-MHz, 0.375-in.-diameter, 70° Shear

Length Sizing

Actual	0.42
6 dB Drop	0.4
Loss of Signal	0.55
6 dB Drop Δ	0.02
Loss of Signal Δ	-0.13

Depth Sizing

Actual	0.195	Corner Tra	60.3
6 dB Drop	0.257	Tip Signal	44.65
UT Tip Signal	0.397839	Velocity	0.125
6 dB Drop Δ	-0.062	Angle	66
UT Tip Signal Δ	-0.20284		

Noise Characterization

Peak Signal Response		7600	
Noise		S/N Ratio	dB
General Weld Root	2024	3.8	11.5
Local Weld Root	4602	1.7	4.4
Cursor Window	2231	3.4	10.6

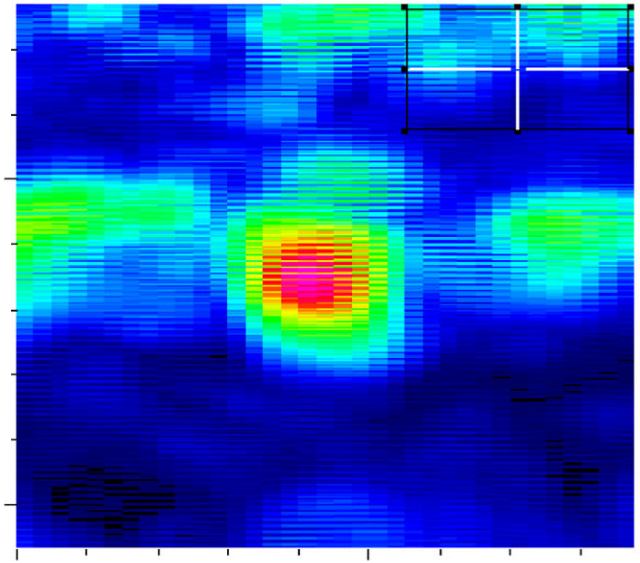

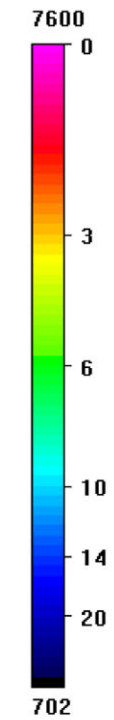

B-Scan End View

X: 0.000 -> 6.000, Pts: 120
Y: 0.000 -> 1.750, Pts: 35
Z: 0.470 -> 2.142, Pts: 263
Scale: 0.20 Inches

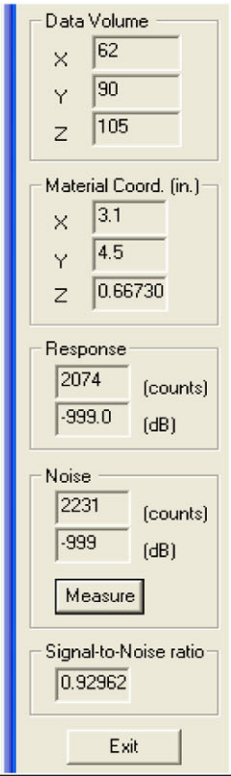

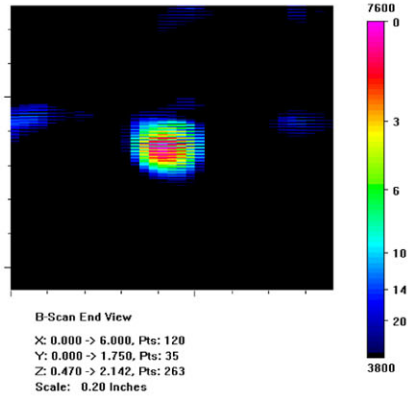

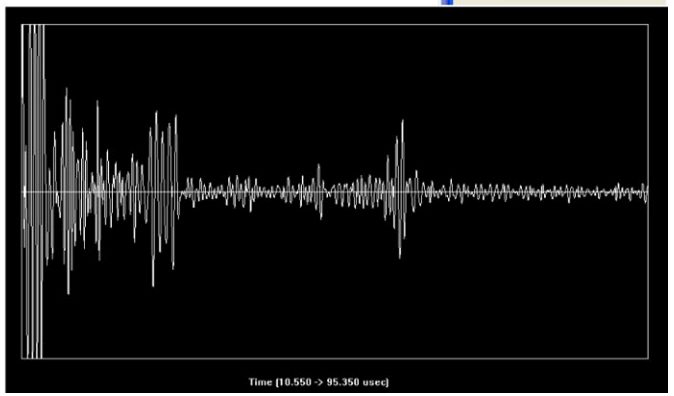

Section #1, Farside, Saw Cut B, 28% Through Wall

1.5-MHz, 0.5-in.-diameter, 60° Shear

Length Sizing

Actual	2.565
6 dB Drop	1.8
Loss of Signal	2.2
6 dB Drop Δ	0.765
Loss of Signal Δ	0.365

Depth Sizing

Actual	0.403	Corner Tra	53.8
6 dB Drop	0.186	Tip Signal	44.4
UT Tip Signal	0.29375	Velocity	0.125
6 dB Drop Δ	0.217	Angle	60
UT Tip Signal Δ	0.10925		

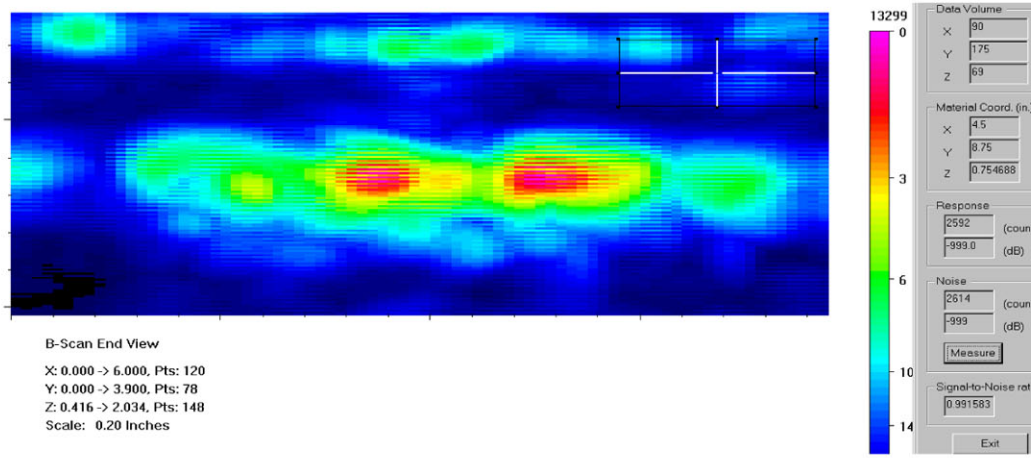

Noise Characterization

Peak Signal Response		13299	
Noise		S/N Ratio	dB
General Weld Root	3786	3.5	10.9
Local Weld Root	7105	1.9	5.4
Cursor Window	2592	5.1	14.2

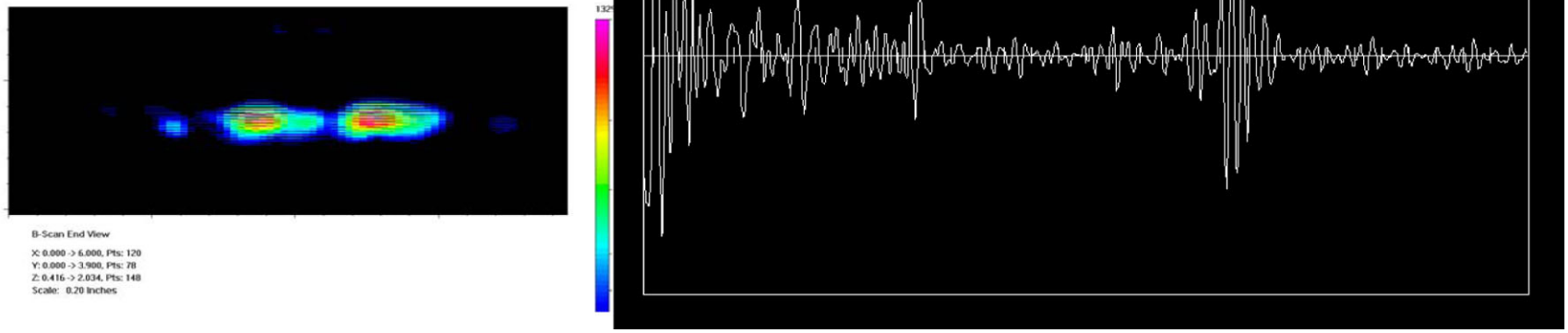

Section #1, Farside, Saw Cut B, 28% Through Wall

1.5-MHz, 0.5-in.-diameter, 70° Shear

Length Sizing

Actual	2.565
6 dB Drop	1.9
Loss of Signal	2.25
6 dB Drop Δ	0.665
Loss of Signal Δ	0.315

Depth Sizing

Actual	0.403	Corner Trap	
6 dB Drop	0.329	Tip Signal	None
UT Tip Signal	None	Velocity	0.125
6 dB Drop Δ	0.074	Angle	67.6
UT Tip Signal Δ	None		

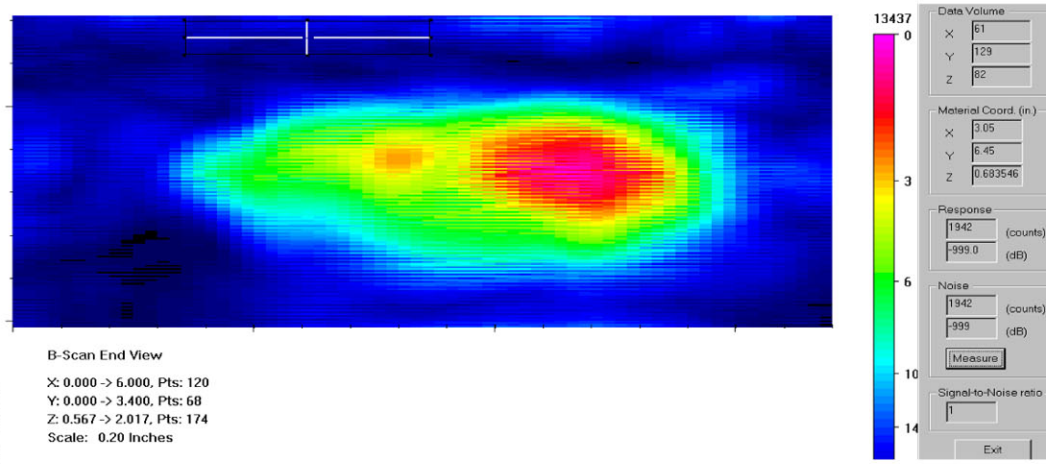

Noise Characterization

Peak Signal Response		13437	
Noise		S/N Ratio	dB
General Weld Root	2186	6.1	15.8
Local Weld Root	1942	6.9	16.8
Cursor Window	1942	6.9	16.8

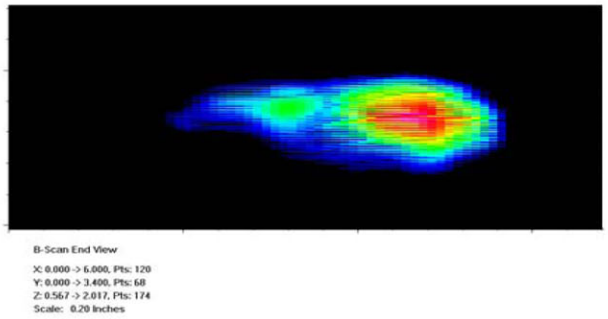

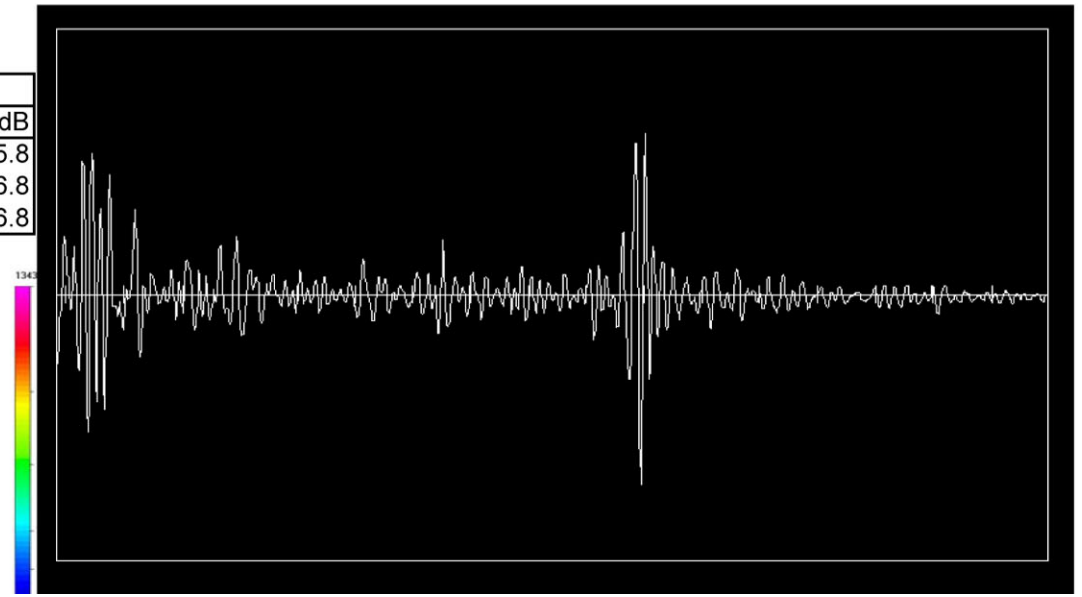

Section #1, Farside, Saw Cut B, 28% Through Wall

1.5-MHz, 0.375-in.-diameter, 60° Shear

Length Sizing

Actual	2.565
6 dB Drop	2.15
Loss of Signal	2.55
6 dB Drop Δ	0.415
Loss of Signal Δ	0.015

Depth Sizing

Actual	0.403	Corner Trap	
6 dB Drop	0.18	Tip Signal	None
UT Tip Signal	None	Velocity	0.125
6 dB Drop Δ	0.223	Angle	59
UT Tip Signal Δ	None		

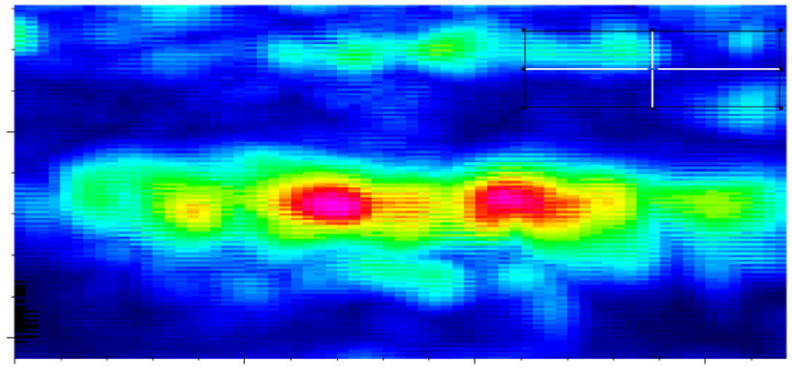

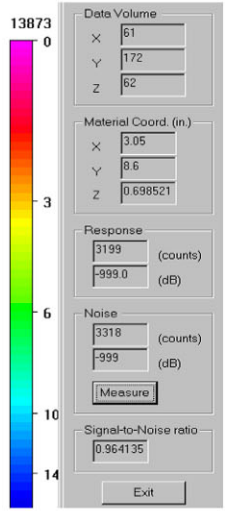

Noise Characterization

Peak Signal Response		13873	
Noise		S/N Ratio	dB
General Weld Root	4208	3.3	10.4
Local Weld Root	8348	1.7	4.4
Cursor Window	3318	4.2	12.4

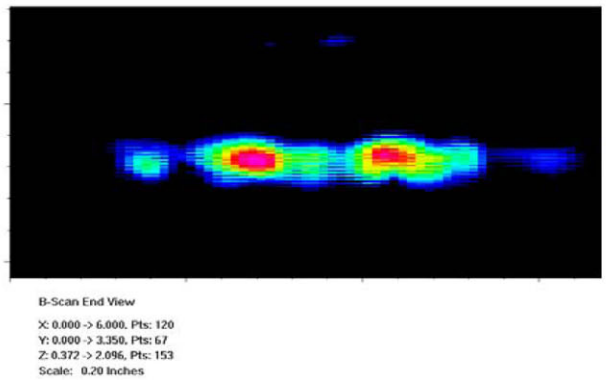

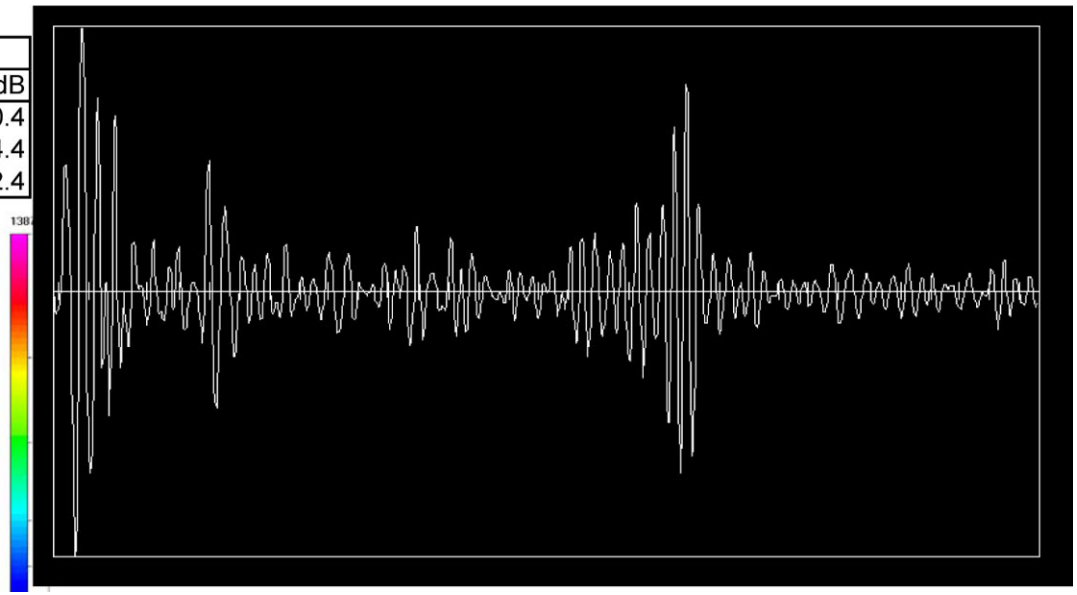

Section #1, Farside, Saw Cut B, 28% Through Wall

1.5-MHz, 0.375-in.-diameter, 70° Shear

Length Sizing

Actual	2.565
6 dB Drop	1.95
Loss of Signal	2.35
6 dB Drop Δ	0.615
Loss of Signal Δ	0.215

Depth Sizing

Actual	0.403	Corner Trap	
6 dB Drop	0.364	Tip Signal	None
UT Tip Signal	None	Velocity	0.125
6 dB Drop Δ	0.039	Angle	64
UT Tip Signal Δ	None		

Noise Characterization

Peak Signal Response		16157	
Noise		S/N Ratio	dB
General Weld Root	3732	4.3	12.7
Local Weld Root	6714	2.4	7.6
Cursor Window	4038	4.0	12.0

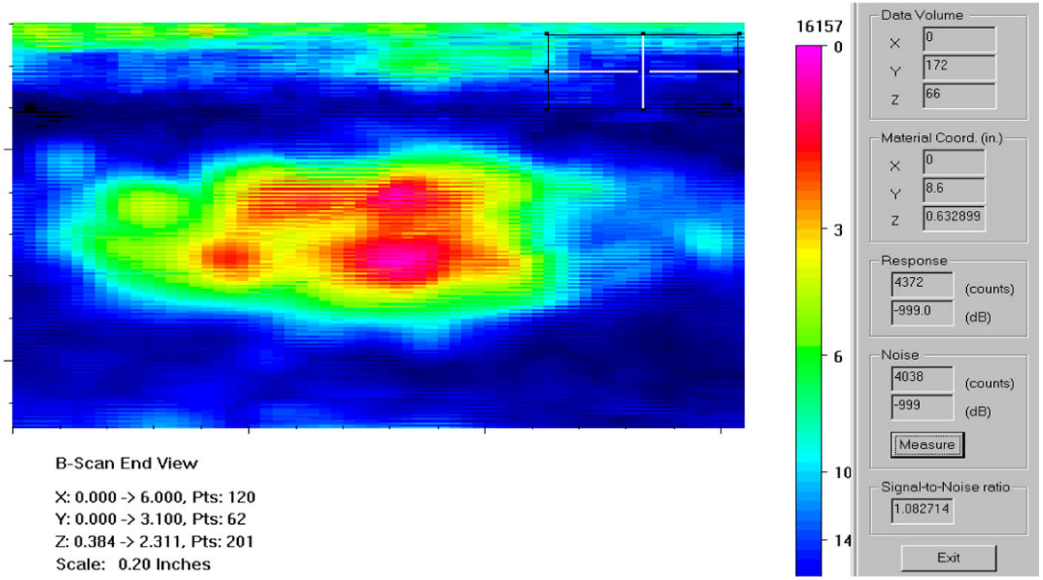

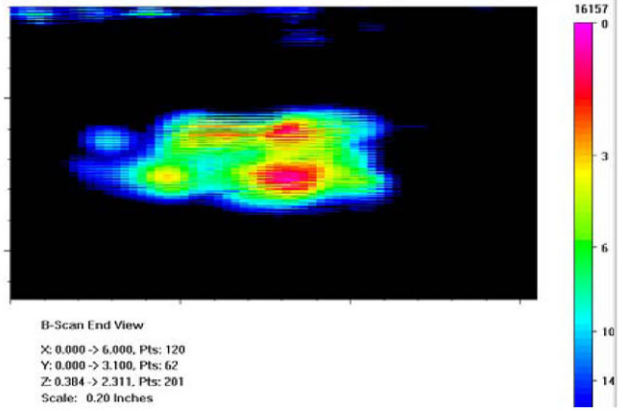

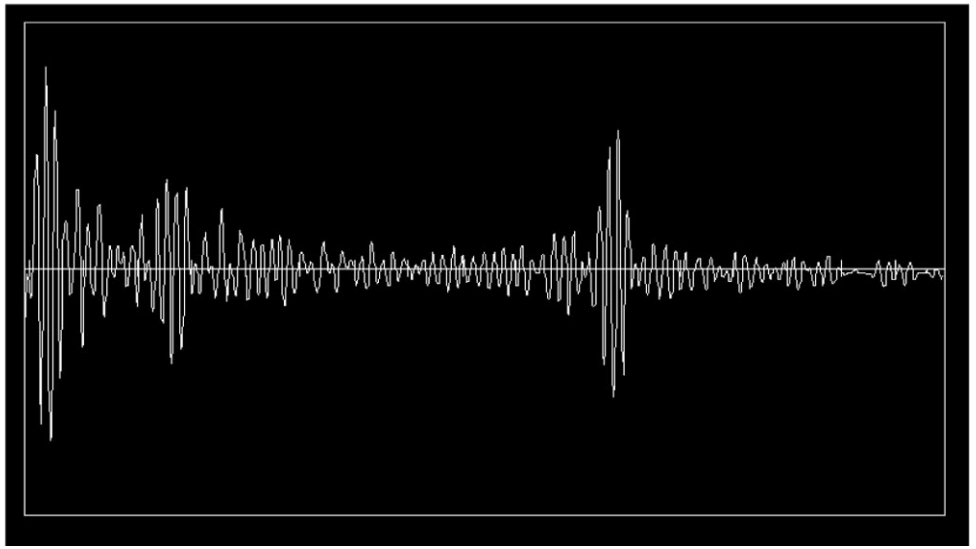

Section #1, Farside, Saw Cut B, 28% Through Wall

2.25-MHz, 0.5-in.-diameter, 60° Shear

Length Sizing

Actual	2.565
6 dB Drop	2.7
Loss of Signal	3.3
6 dB Drop Δ	-0.135
Loss of Signal Δ	-0.735

Depth Sizing

Actual	0.403	Corner Tra	52.8
6 dB Drop	0.242	Tip Signal	35.5
UT Tip Signal	0.540625	Velocity	0.125
6 dB Drop Δ	0.161	Angle	60
UT Tip Signal Δ	-0.13763		

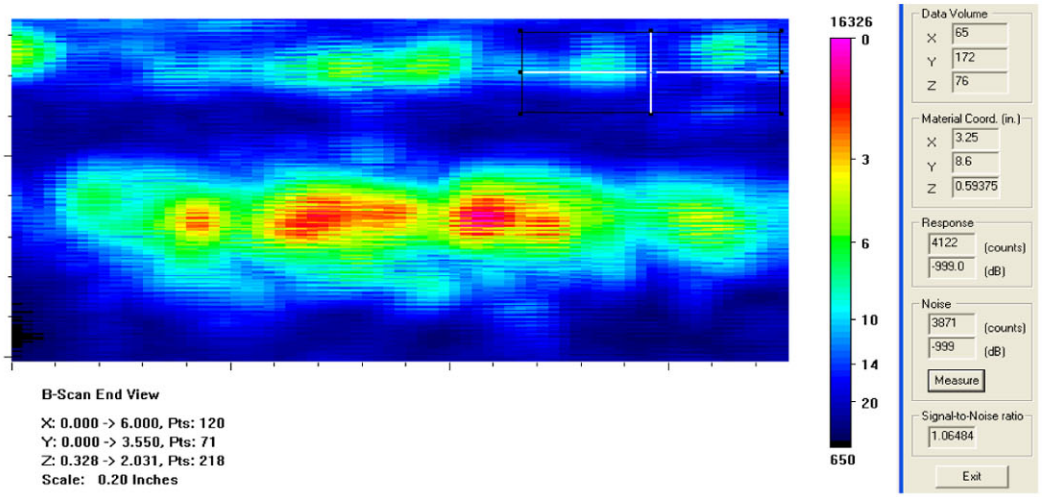

Noise Characterization

Peak Signal Response		16326	
Noise		S/N Ratio	dB
General Weld Root	5151	3.2	10.0
Local Weld Root	3800	4.3	12.7
Cursor Window	3871	4.2	12.5

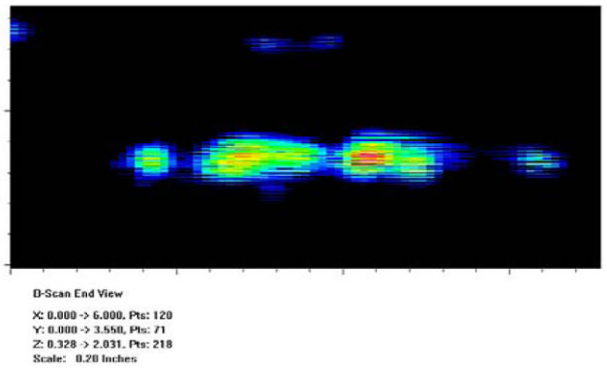

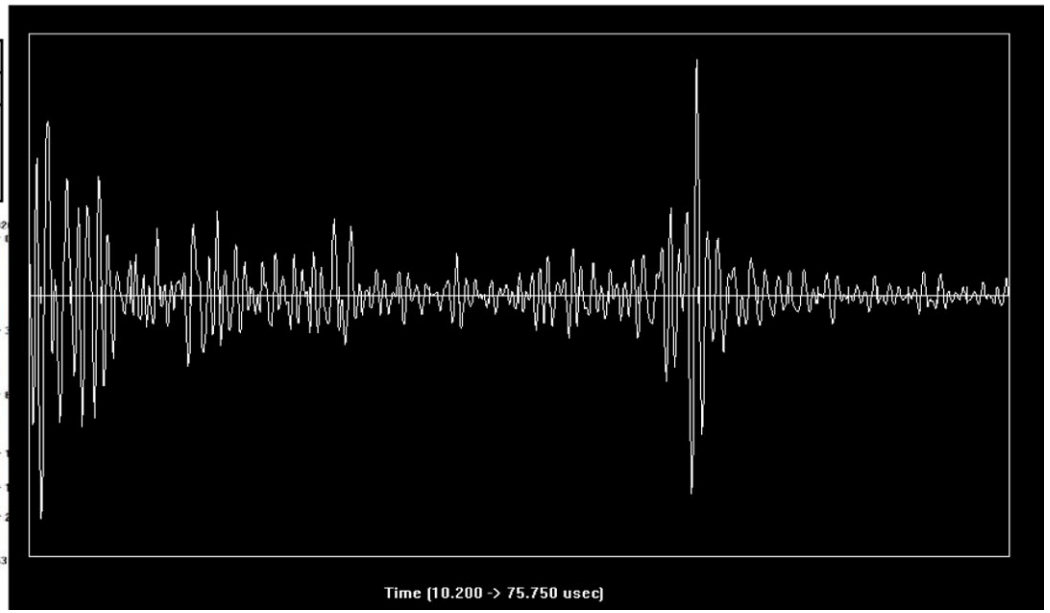

Section #1, Farside, Saw Cut B, 28% Through Wall

2.25-MHz, 0.5-in.-diameter, 70° Shear

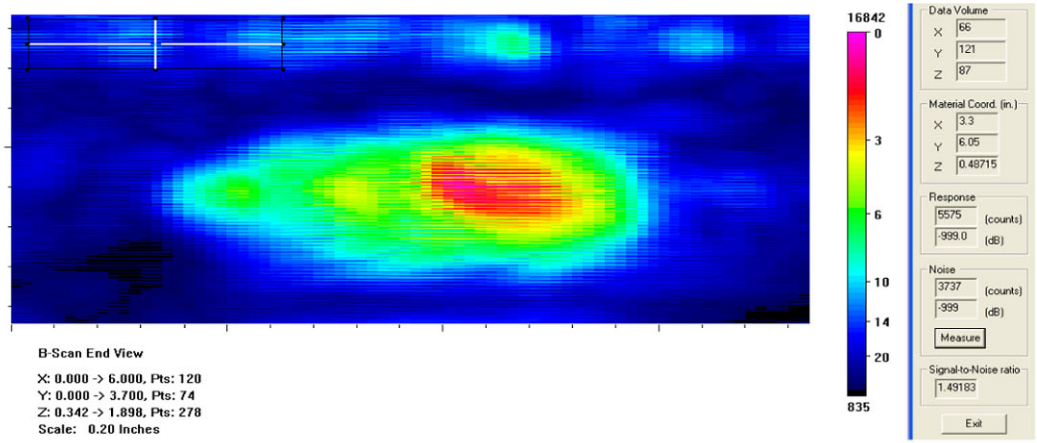

Length Sizing

Actual	2.565
6 dB Drop	1.85
Loss of Signal	2.35
6 dB Drop Δ	0.715
Loss of Signal Δ	0.215

Depth Sizing

Actual	0.403	Corner Tra	65.8
6 dB Drop	0.297	Tip Signal	47.1
UT Tip Signal	0.418843	Velocity	0.125
6 dB Drop Δ	0.106	Angle	69
UT Tip Signal Δ	-0.01584		

Noise Characterization

Peak Signal Response		16842	
Noise		S/N Ratio	dB
General Weld Root	2244	7.5	17.5
Local Weld Root	2727	6.2	15.8
Cursor Window	3737	4.5	13.1

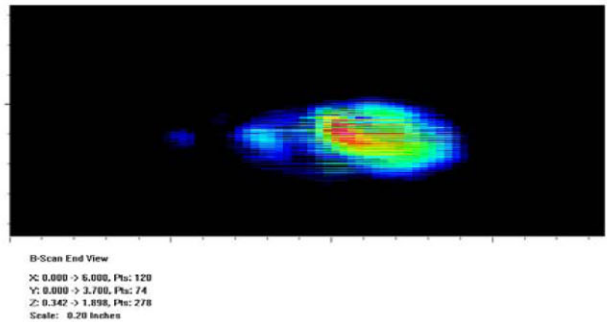

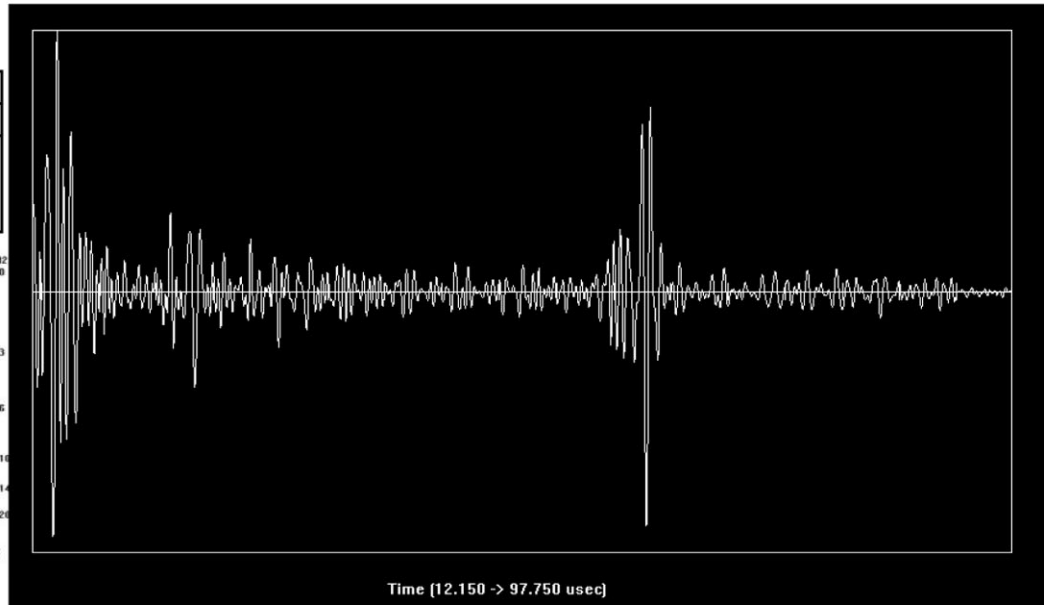

Section #1, Farside, Saw Cut B, 28% Through Wall

2.25-MHz, 0.375-in.-diameter, 60° Shear

Length Sizing

Actual	2.565
6 dB Drop	2.55
Loss of Signal	3.15
6 dB Drop Δ	0.015
Loss of Signal Δ	-0.585

Depth Sizing

Actual	0.403	Corner Tra	51.8
6 dB Drop	0.188	Tip Signal	39.8
UT Tip Signal	0.375	Velocity	0.125
6 dB Drop Δ	0.215	Angle	60
UT Tip Signal Δ	0.028		

Noise Characterization

Peak Signal Response		14912	
Noise		S/N Ratio	dB
General Weld Root	4347	3.4	10.7
Local Weld Root	6889	2.2	6.7
Cursor Window	3250	4.6	13.2

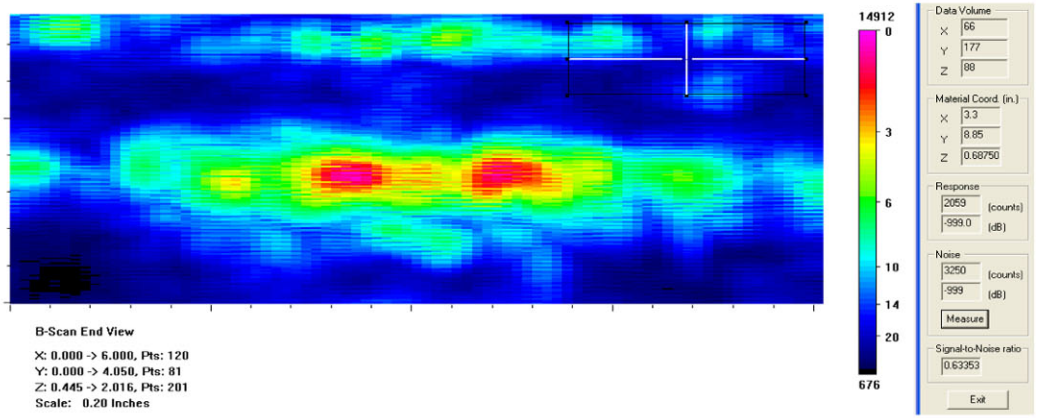

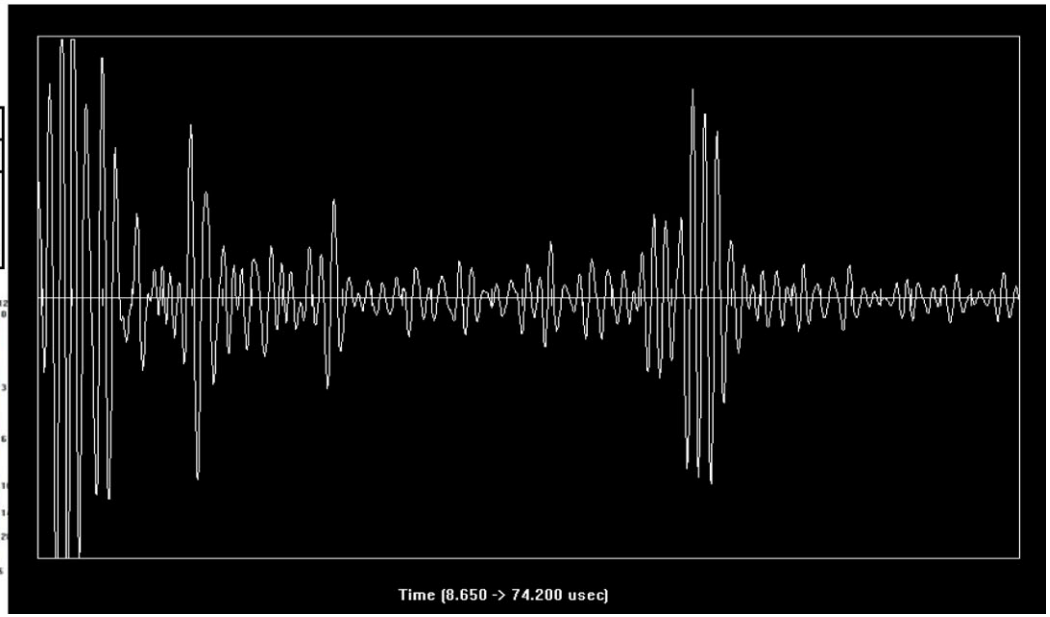

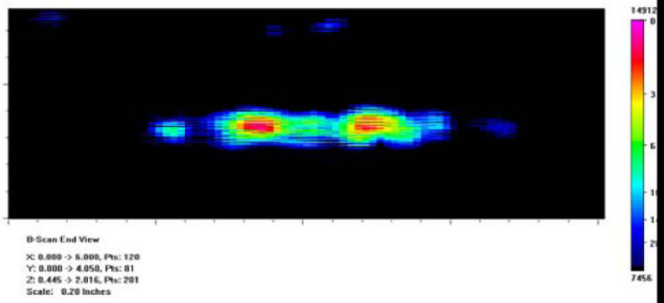

Section #1, Farside, Saw Cut B, 28% Through Wall

2.25-MHz, 0.375-in.-diameter, 70° Shear

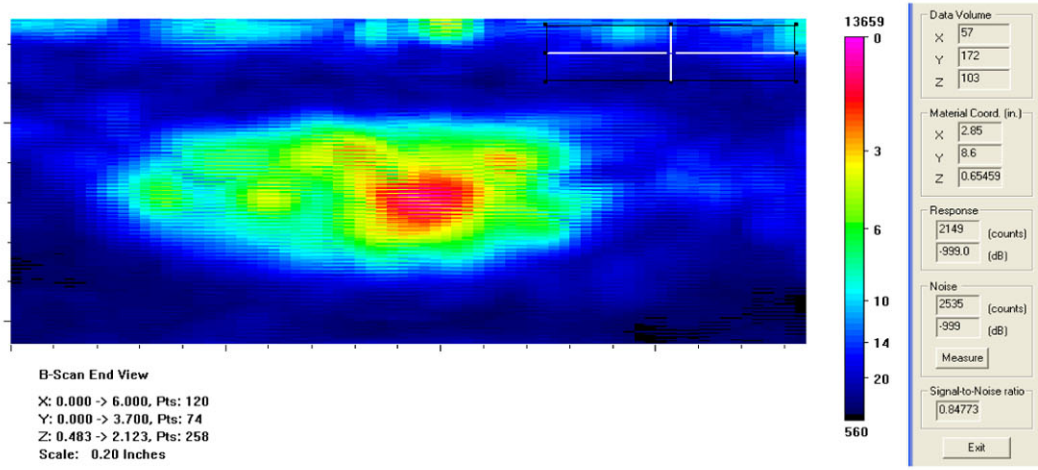

Length Sizing

Actual	2.565
6 dB Drop	1.85
Loss of Signal	2.45
6 dB Drop Δ	0.715
Loss of Signal Δ	0.115

Depth Sizing

Actual	0.403	Corner Tra	67.65
6 dB Drop	0.302	Tip Signal	46.7
UT Tip Signal	0.532571	Velocity	0.125
6 dB Drop Δ	0.101	Angle	66
UT Tip Signal Δ	-0.12957		

Noise Characterization

Peak Signal Response		13659	
Noise		S/N Ratio	dB
General Weld Root	2024	6.7	16.6
Local Weld Root	3321	4.1	12.3
Cursor Window	2535	5.4	14.6

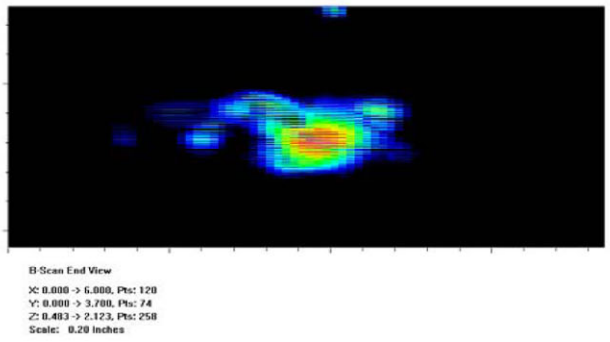

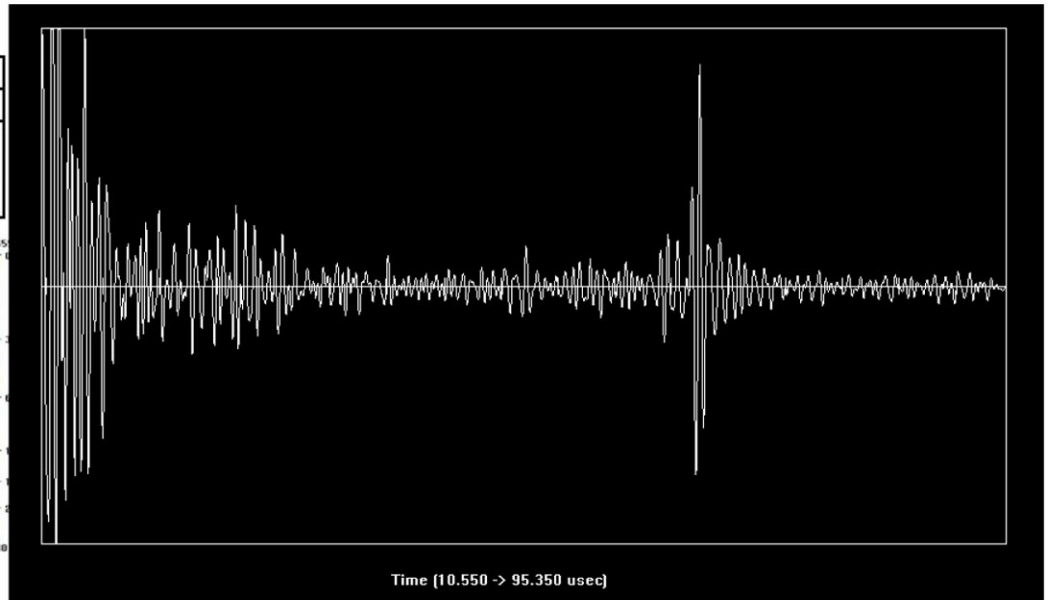

Section #1, Farside, Flaw B, 43% Through Wall

1.5-MHz, 0.5-in.-diameter, 60° Shear

Length Sizing

Actual	1.2
6 dB Drop	1.05
Loss of Signal	1.2
6 dB Drop Δ	0.15
Loss of Signal Δ	0

Depth Sizing

Actual	0.585	Corner Tra	49.55
6 dB Drop	0.219	Tip Signal	25.5
UT Tip Signal	0.751563	Velocity	0.125
6 dB Drop Δ	0.366	Angle	60
UT Tip Signal Δ	-0.16656		

Noise Characterization

Peak Signal Response		12531	
Noise		S/N Ratio	dB
General Weld Root	3786	3.3	10.4
Local Weld Root	11739	1.1	0.6
Cursor Window	1735	7.2	17.2

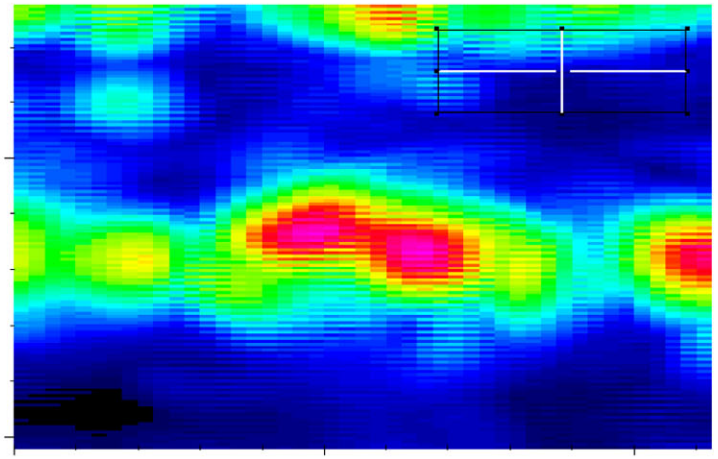

B-Scan End View

X: 0.000 -> 6.000, Pts: 120
Y: 0.000 -> 2.250, Pts: 45
Z: 0.438 -> 2.034, Pts: 146
Scale: 0.20 Inches

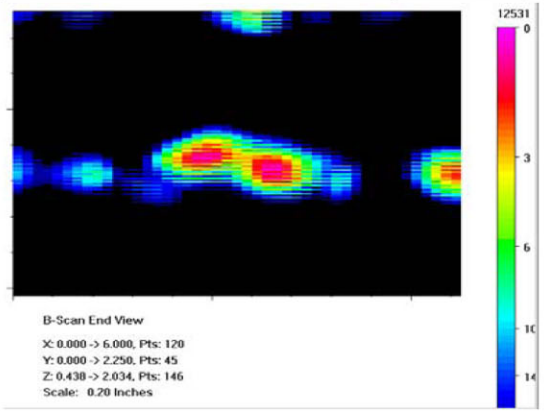

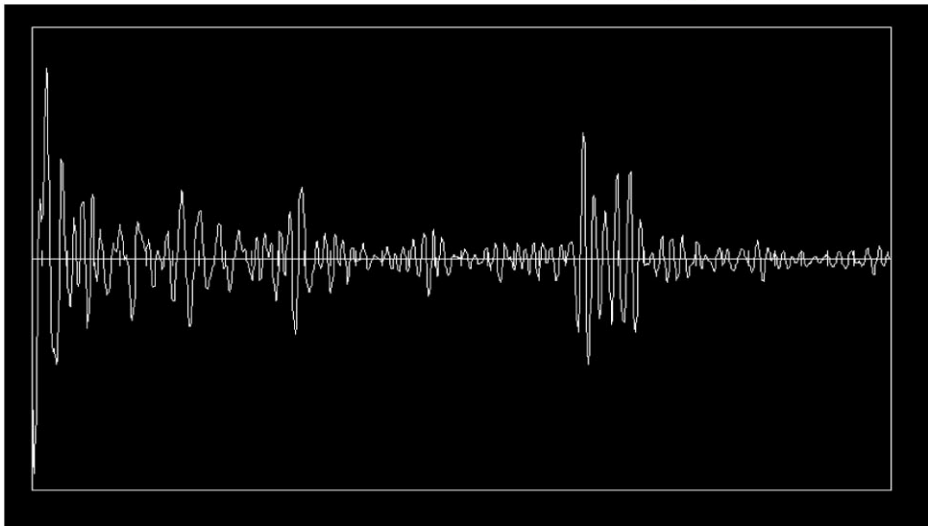

Section #1, Farside, Flaw B, 43% Through Wall

1.5-MHz, 0.5-in.-diameter, 70° Shear

Length Sizing

Actual	1.2
6 dB Drop	1.3
Loss of Signal	1.55
6 dB Drop Δ	-0.1
Loss of Signal Δ	-0.35

Depth Sizing

Actual	0.585	Corner Trap	
6 dB Drop	0.238	Tip Signal	None
UT Tip Signal	N/A	Velocity	0.125
6 dB Drop Δ	0.347	Angle	67.6
UT Tip Signal Δ	N/A		

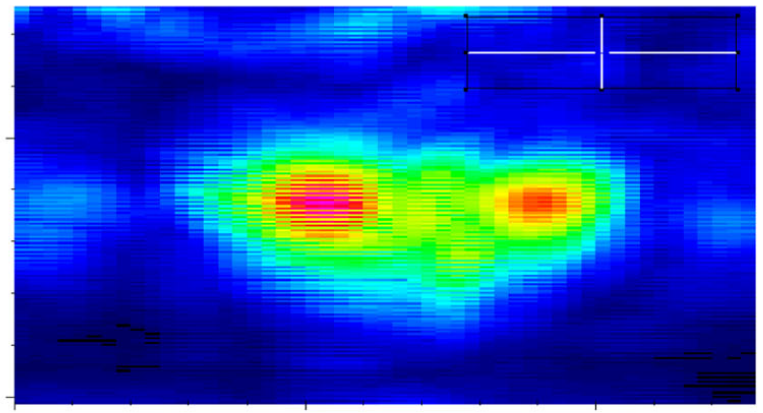

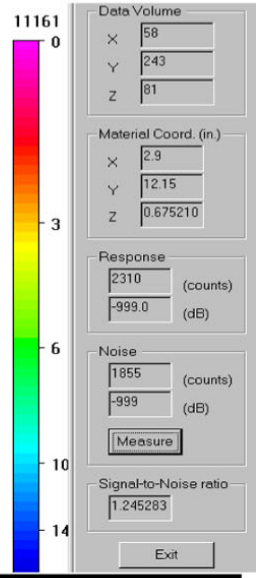

Noise Characterization

Peak Signal Response		11161	
Noise		S/N Ratio	dB
General Weld Root	2186	5.1	14.2
Local Weld Root	3599	3.1	9.8
Cursor Window	2310	4.8	13.7

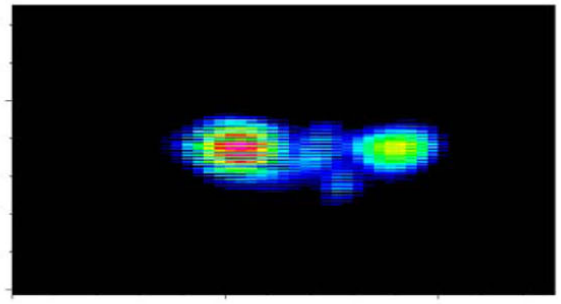

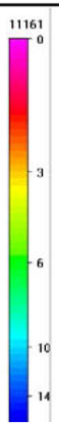

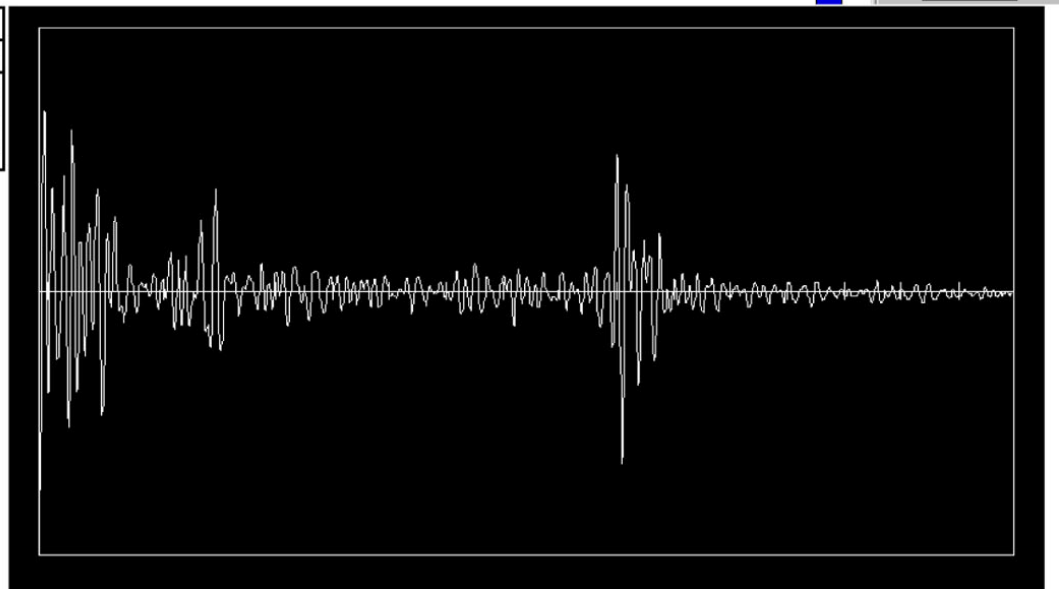

Section #1, Farside, Flaw B, 43% Through Wall

1.5-MHz, 0.375-in.-diameter, 60° Shear

Length Sizing

Actual	1.2
6 dB Drop	1
Loss of Signal	1.15
6 dB Drop Δ	0.2
Loss of Signal Δ	0.05

Depth Sizing

Actual	0.585	Corner Trap	
6 dB Drop	0.203	Tip Signal	None
UT Tip Signal	N/A	Velocity	0.125
6 dB Drop Δ	0.382	Angle	59
UT Tip Signal Δ	N/A		

Noise Characterization

Peak Signal Response		14812	
Noise		S/N Ratio	dB
General Weld Root	4208	3.5	10.9
Local Weld Root	10509	1.4	3.0
Cursor Window	2409	6.1	15.8

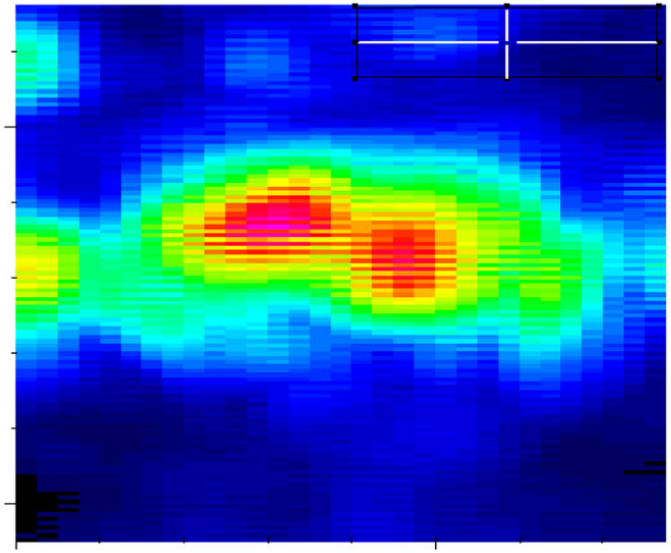

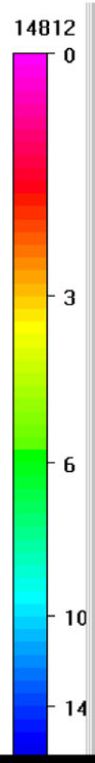

B-Scan End View

X: 0.000 -> 6.000, Pts: 120
Y: 0.000 -> 1.550, Pts: 31
Z: 0.665 -> 2.096, Pts: 127
Scale: 0.20 Inches

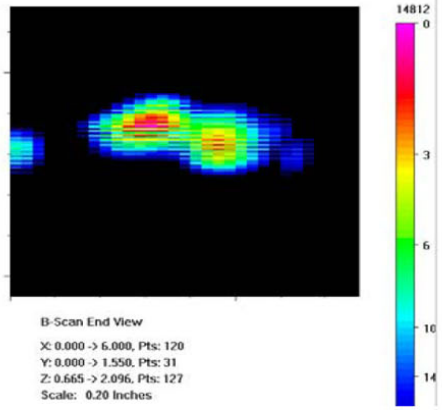

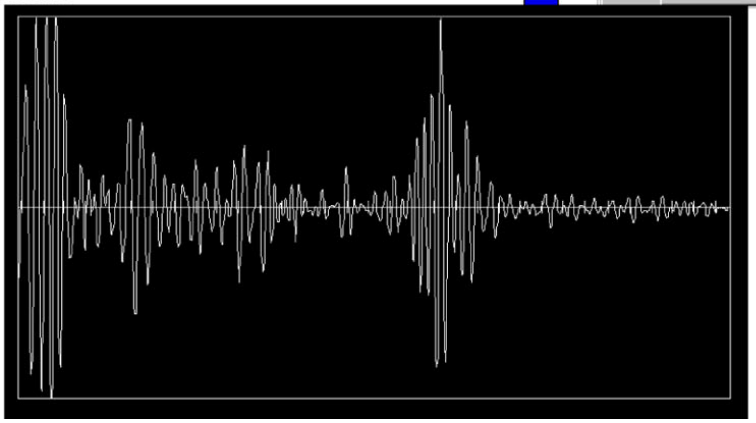

Section #1, Farside, Flaw B, 43% Through Wall

1.5-MHz, 0.375-in.-diameter, 70° Shear

Length Sizing

Actual	1.2
6 dB Drop	1.55
Loss of Signal	1.75
6 dB Drop Δ	-0.35
Loss of Signal Δ	-0.55

Depth Sizing

Actual	0.585	Corner Trap	
6 dB Drop	0.369	Tip Signal	None
UT Tip Signal	None	Velocity	0.125
6 dB Drop Δ	0.216	Angle	64
UT Tip Signal Δ	None		

Noise Characterization

Peak Signal Response		10892	
Noise		S/N Ratio	dB
General Weld Root	3732	2.9	9.3
Local Weld Root	8217	1.3	2.4
Cursor Window	2815	3.9	11.8

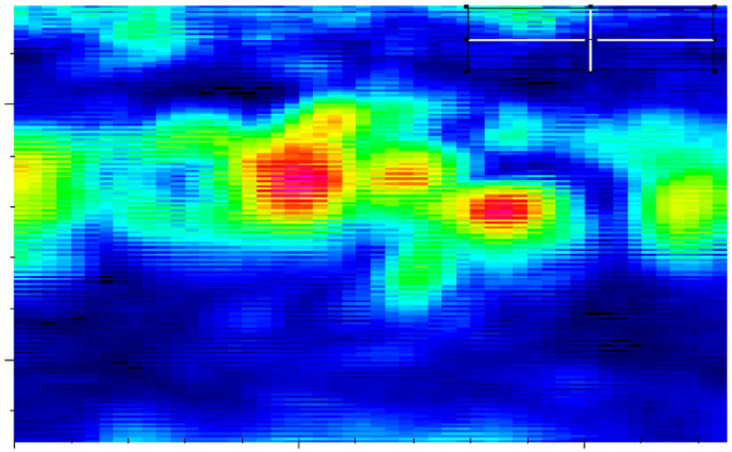

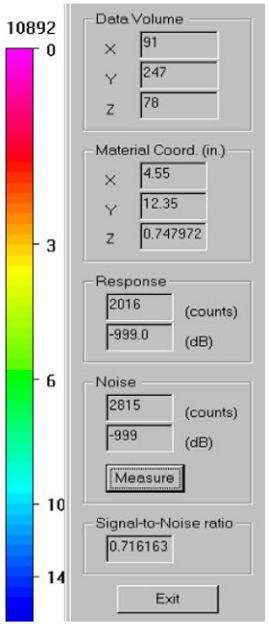

B-Scan End View

X: 0.000 -> 6.000, Pts: 120
Y: 0.000 -> 2.500, Pts: 50
Z: 0.604 -> 2.311, Pts: 178
Scale: 0.20 Inches

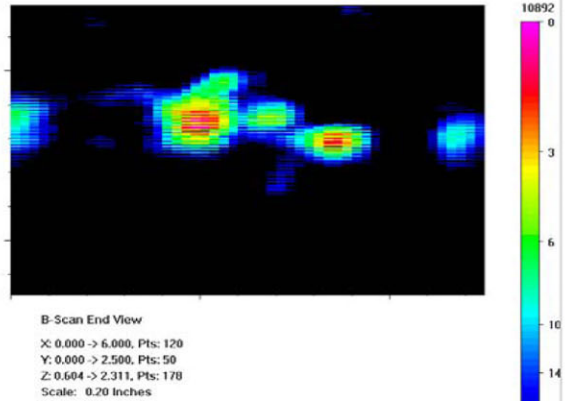

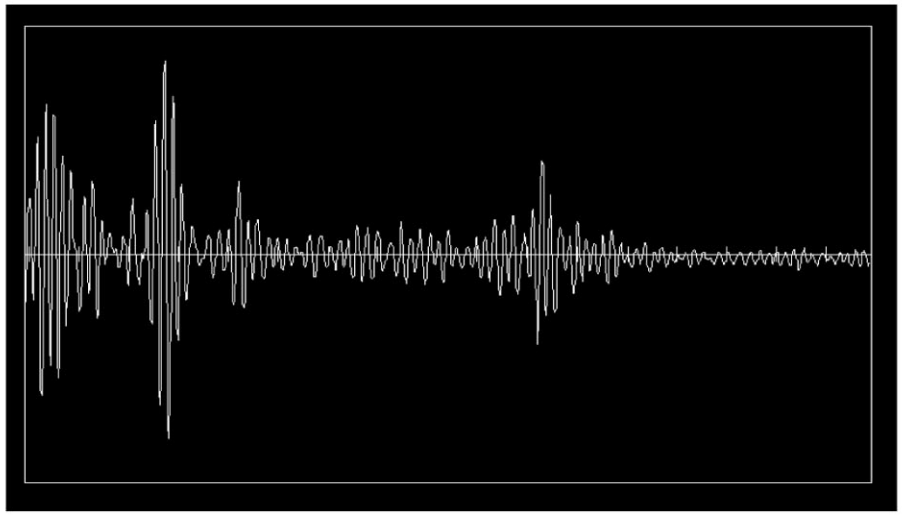

Section #1, Farside, Flaw B, 43% Through Wall

2.25-MHz, 0.5-in.-diameter, 60° Shear

Length Sizing

Actual	1.2
6 dB Drop	1.55
Loss of Signal	1.65
6 dB Drop Δ	-0.35
Loss of Signal Δ	-0.45

Depth Sizing

Actual	0.585	Corner Tra	51.05
6 dB Drop	0.219	Tip Signal	36.55
UT Tip Signal	0.453125	Velocity	0.125
6 dB Drop Δ	0.366	Angle	60
UT Tip Signal Δ	0.131875		

Noise Characterization

Peak Signal Response		15248	
Noise		S/N Ratio	dB
General Weld Root	5151	3.0	9.4
Local Weld Root	14000	1.1	0.7
Cursor Window	3346	4.6	13.2

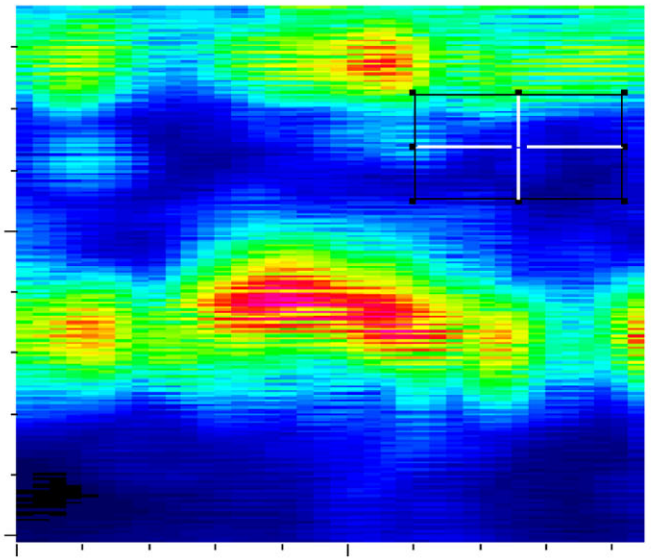

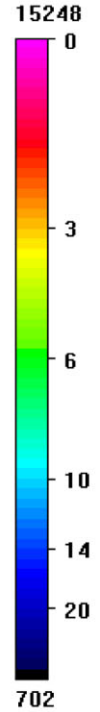

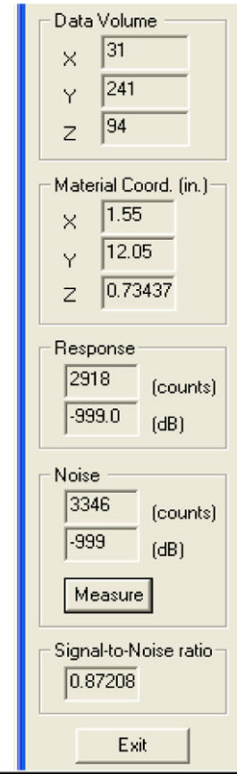

B-Scan End View

X: 0.000 -> 6.000, Pts: 120
Y: 0.000 -> 1.900, Pts: 38
Z: 0.273 -> 2.031, Pts: 225
Scale: 0.20 Inches

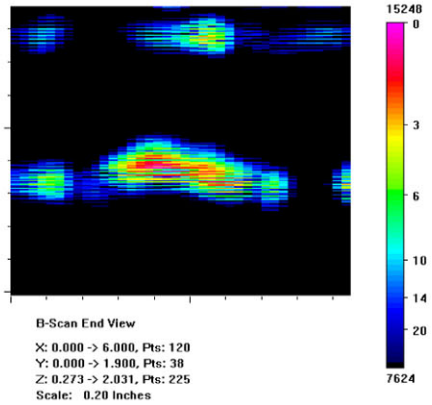

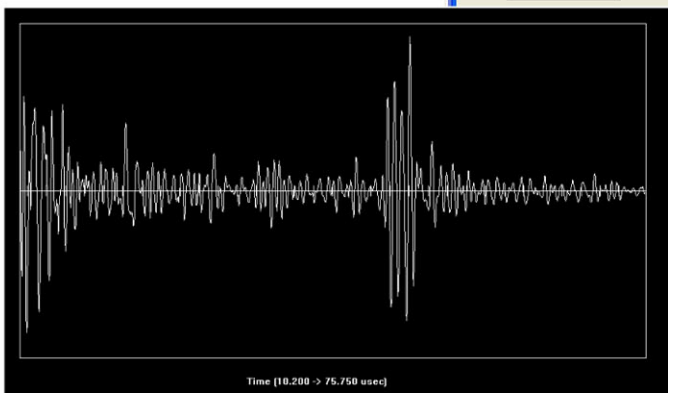

Section #1, Farside, Flaw B, 43% Through Wall

2.25-MHz, 0.5-in.-diameter, 70° Shear

Length Sizing

Actual	1.2
6 dB Drop	1.25
Loss of Signal	1.65
6 dB Drop Δ	-0.05
Loss of Signal Δ	-0.45

Depth Sizing

Actual	0.585	Corner Tra	62.3
6 dB Drop	0.241	Tip Signal	42.65
UT Tip Signal	0.440121	Velocity	0.125
6 dB Drop Δ	0.344	Angle	69
UT Tip Signal Δ	0.144879		

Noise Characterization

Peak Signal Response		11633	
Noise		S/N Ratio	dB
General Weld Root	2244	5.2	14.3
Local Weld Root	4673	2.5	7.9
Cursor Window	2979	3.9	11.8

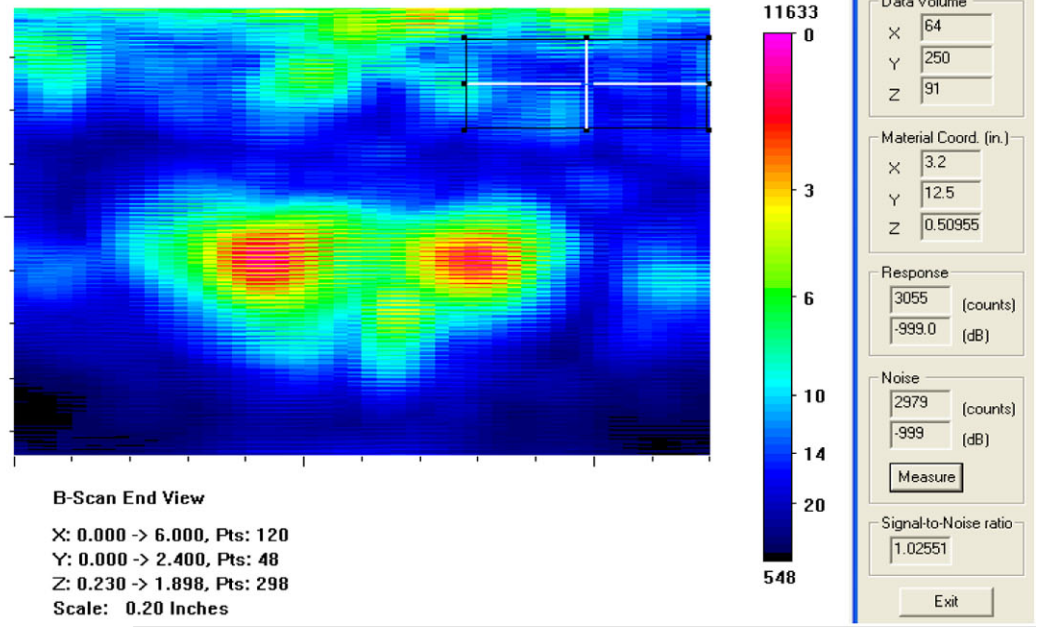

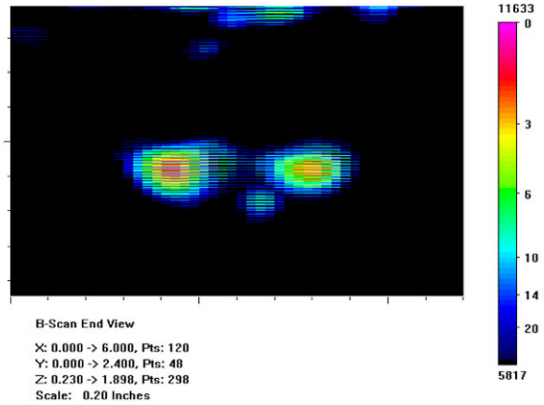

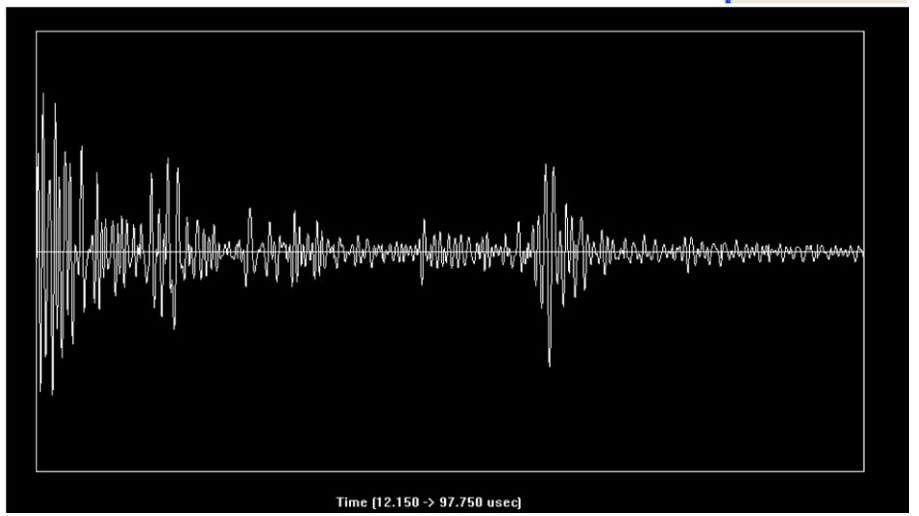

Section #1, Farside, Flaw B, 43% Through Wall

2.25-MHz, 0.375-in.-diameter, 60° Shear

Length Sizing

Actual	1.2
6 dB Drop	1.05
Loss of Signal	1.25
6 dB Drop Δ	0.15
Loss of Signal Δ	-0.05

Depth Sizing

Actual	0.585	Corner Trap	
6 dB Drop	0.203	Tip Signal	None
UT Tip Signal	None	Velocity	0.125
6 dB Drop Δ	0.382	Angle	60
UT Tip Signal Δ	None		

Noise Characterization

Peak Signal Response		15136	
Noise		S/N Ratio	dB
General Weld Root	4347	3.5	10.8
Local Weld Root	14244	1.1	0.5
Cursor Window	5037	3.0	9.6

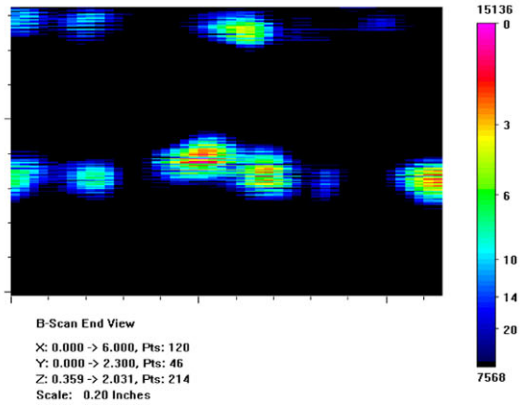

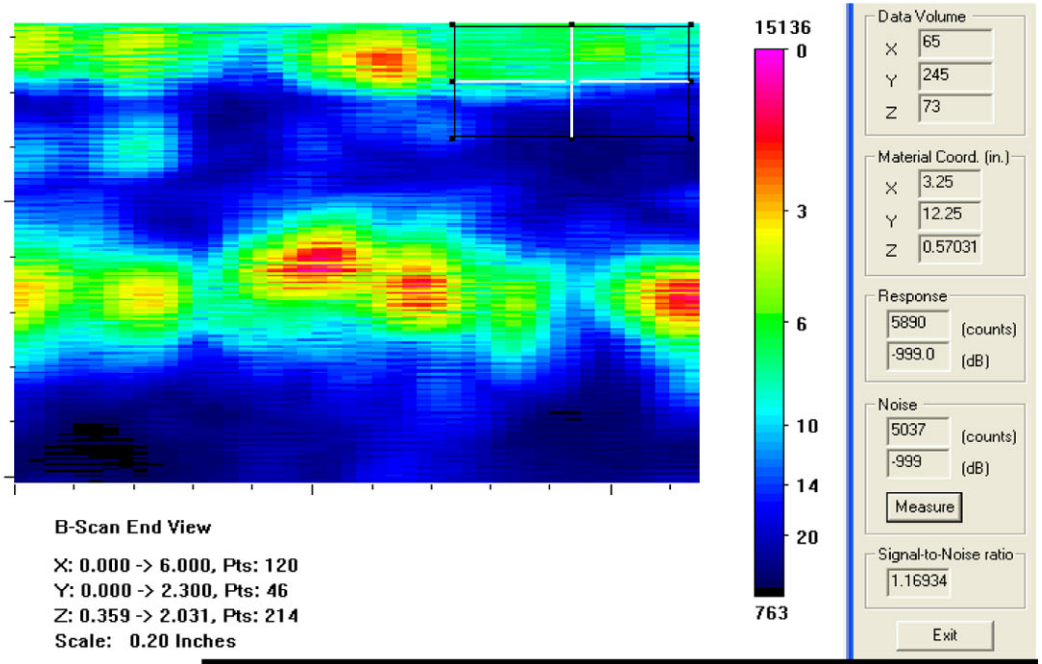

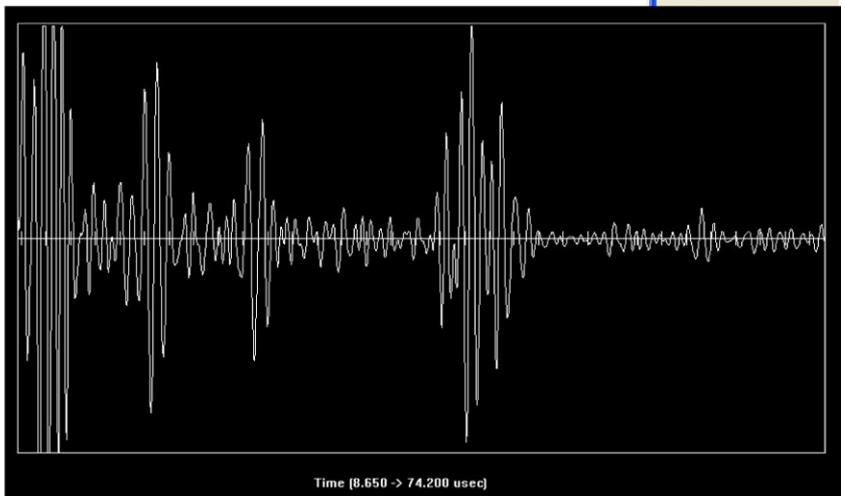

Section #1, Farside, Flaw B, 43% Through Wall

2.25-MHz, 0.375-in.-diameter, 70° Shear

Length Sizing

Actual	1.2
6 dB Drop	1.2
Loss of Signal	1.45
6 dB Drop Δ	0
Loss of Signal Δ	-0.25

Depth Sizing

Actual	0.585	Corner Tra	60.8
6 dB Drop	0.242	Tip Signal	43.25
UT Tip Signal	0.446139	Velocity	0.125
6 dB Drop Δ	0.343	Angle	66
UT Tip Signal Δ	0.138861		

Noise Characterization

Peak Signal Response		8443	
Noise		S/N Ratio	dB
General Weld Root	2024	4.2	12.4
Local Weld Root	5948	1.4	3.0
Cursor Window	2187	3.9	11.7

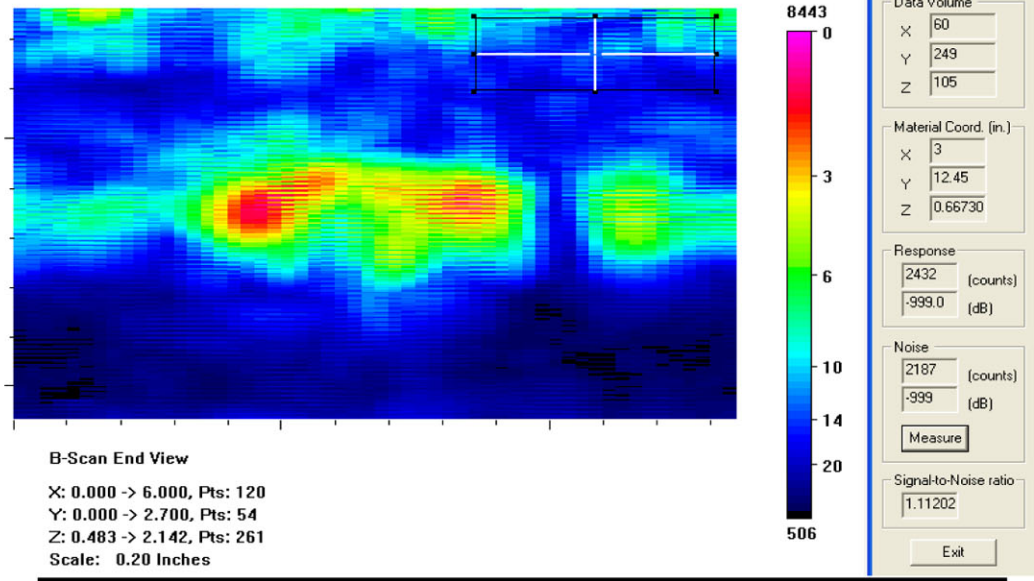

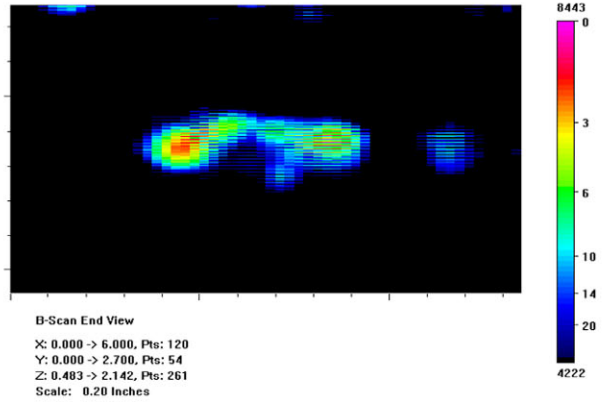

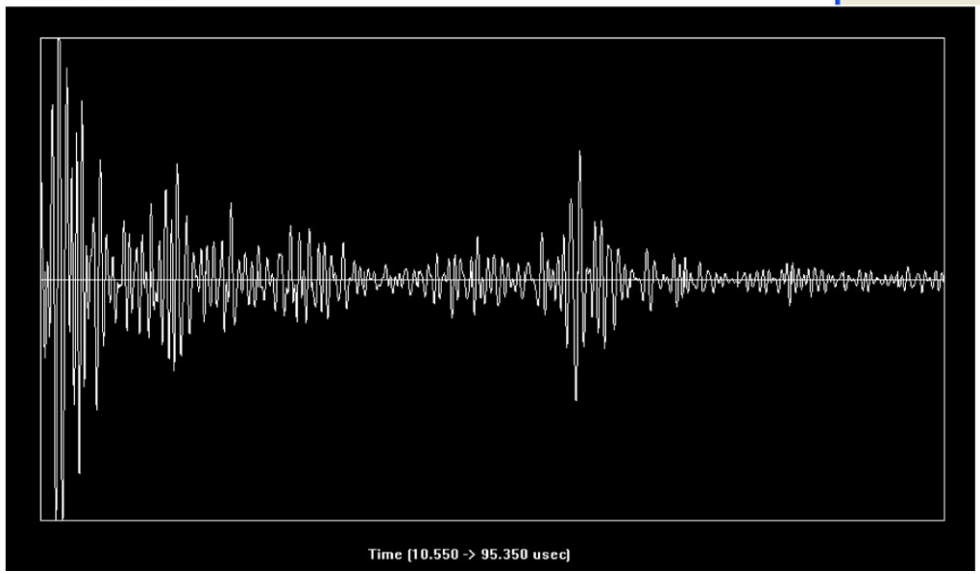

Section #1, Farside, Saw Cut C, 7% Through Wall Angle

1.5-MHz, 0.5-in.-diameter, 60° Shear

Length Sizing

Actual	1.427
6 dB Drop	0.35
Loss of Signal	0.35
6 dB Drop Δ	1.077
Loss of Signal Δ	1.077

No Call due to low signal response compared to the weld root response

Depth Sizing

Actual	0.1	Corner Tra	51.25
6 dB Drop	0.164	Tip Signal	44.5
UT Tip Signal	0.210938	Velocity	0.125
6 dB Drop Δ	-0.064	Angle	60
UT Tip Signal Δ	-0.11094		

Noise Characterization

Peak Signal Response		7161	
Noise		S/N Ratio	dB
General Weld Root	3786	1.9	5.5
Local Weld Root	9114	0.8	-2.1
Cursor Window	2543	2.8	9.0

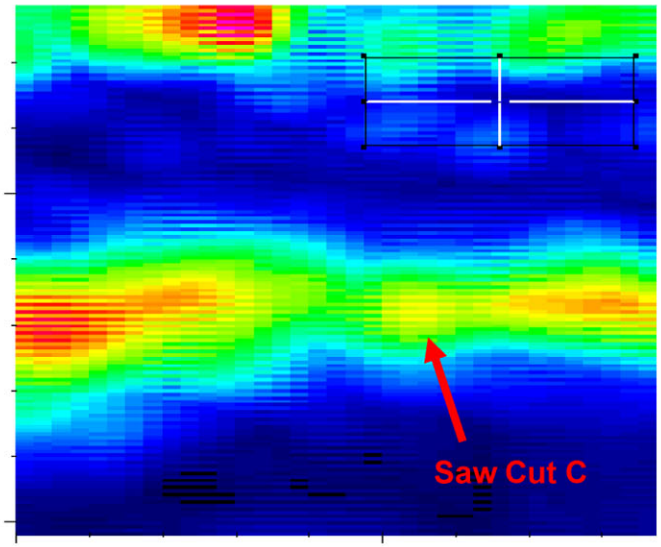

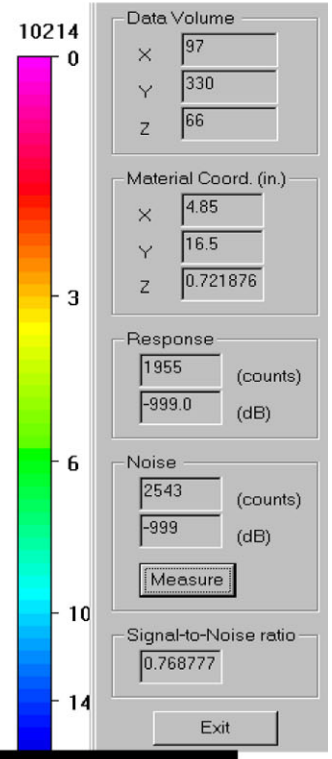

B-Scan End View

X: 0.000 -> 6.000, Pts: 120
Y: 0.000 -> 1.750, Pts: 35
Z: 0.416 -> 2.034, Pts: 148
Scale: 0.20 Inches

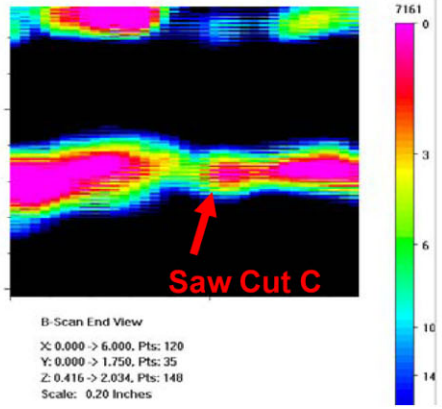

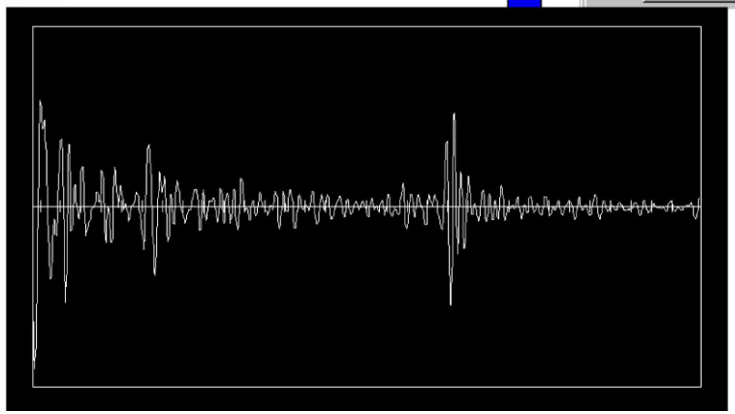

Section #1, Farside, Saw Cut C, 7% Through Wall Angle

1.5-MHz, 0.5-in.-diameter, 70° Shear

Length Sizing

Actual	1.427
6 dB Drop	
Loss of Signal	
6 dB Drop Δ	1.427
Loss of Signal Δ	1.427

Depth Sizing

Actual	0.1	Corner Trap	
6 dB Drop		Tip Signal	
UT Tip Signal	0	Velocity	0.125
6 dB Drop Δ	0.1	Angle	67.6
UT Tip Signal Δ	0.1		

Noise Characterization

Peak Signal Response			
Noise		S/N Ratio	dB
General Weld Root	2186	N/A	N/A
Local Weld Root	N/A	N/A	N/A
Cursor Window		N/A	N/A

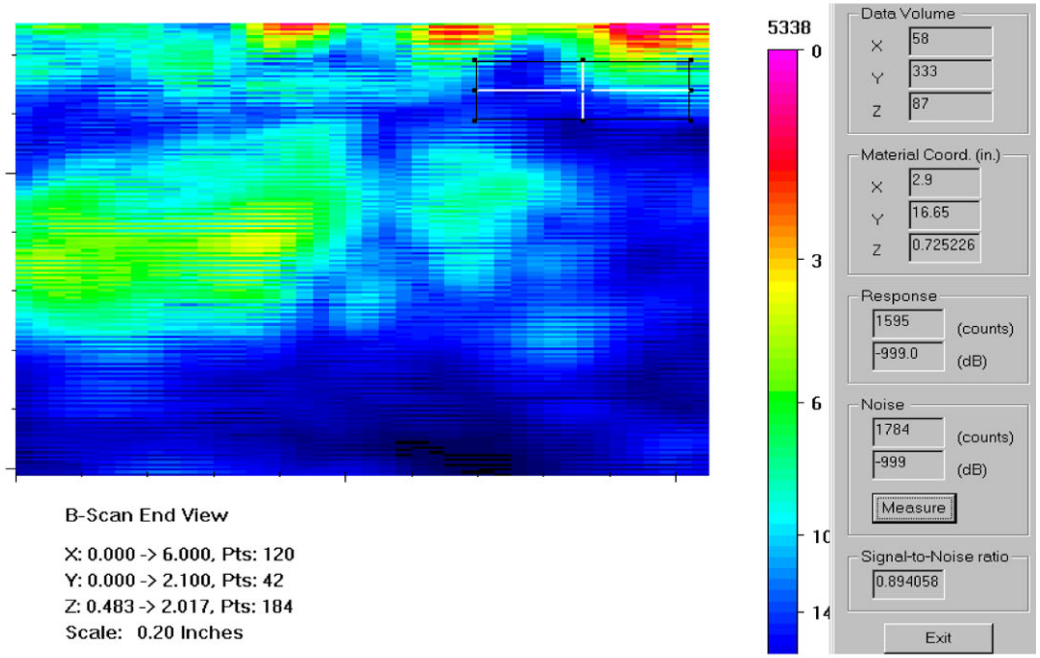

B-Scan End View

X: 0.000 -> 6.000, Pts: 120
Y: 0.000 -> 2.100, Pts: 42
Z: 0.483 -> 2.017, Pts: 184
Scale: 0.20 Inches

not detected

Section #1, Farside, Saw Cut C, 7% Through Wall Angle

1.5-MHz, 0.375-in.-diameter, 60° Shear

Length Sizing

Actual	1.427
6 dB Drop	
Loss of Signal	
6 dB Drop Δ	1.427
Loss of Signal Δ	1.427

Depth Sizing

Actual	0.1	Corner Trap	
6 dB Drop		Tip Signal	
UT Tip Signal	0	Velocity	0.125
6 dB Drop Δ	0.1	Angle	59
UT Tip Signal Δ	0.1		

Noise Characterization

Peak Signal Response			
Noise		S/N Ratio	dB
General Weld Root	4208	N/A	N/A
Local Weld Root	N/A	N/A	N/A
Cursor Window		N/A	N/A

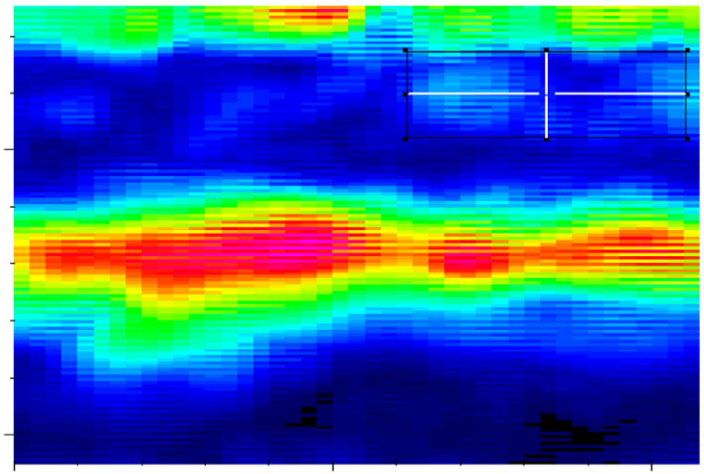

B-Scan End View

X: 0.000 -> 6.000, Pts: 120
Y: 0.000 -> 2.150, Pts: 43
Z: 0.484 -> 2.096, Pts: 143
Scale: 0.20 Inches

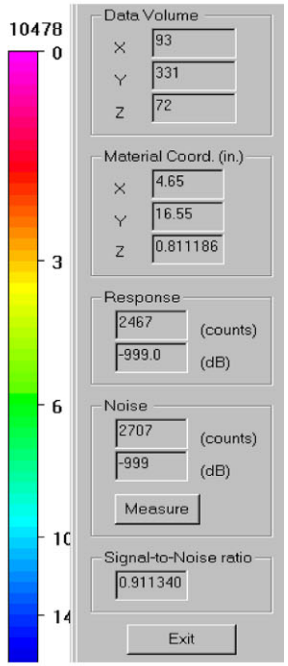

not detected

Section #1, Farside, Saw Cut C, 7% Through Wall Angle

1.5-MHz, 0.375-in.-diameter, 70° Shear

Length Sizing

Actual	1.427
6 dB Drop	
Loss of Signal	
6 dB Drop Δ	1.427
Loss of Signal Δ	1.427

Depth Sizing

Actual	0.1	Corner Trap	
6 dB Drop		Tip Signal	
UT Tip Signal	0	Velocity	0.125
6 dB Drop Δ	0.1	Angle	64
UT Tip Signal Δ	0.1		

Noise Characterization

Peak Signal Response			
Noise		S/N Ratio	dB
General Weld Root	3732	N/A	N/A
Local Weld Root	N/A	N/A	N/A
Cursor Window		N/A	N/A

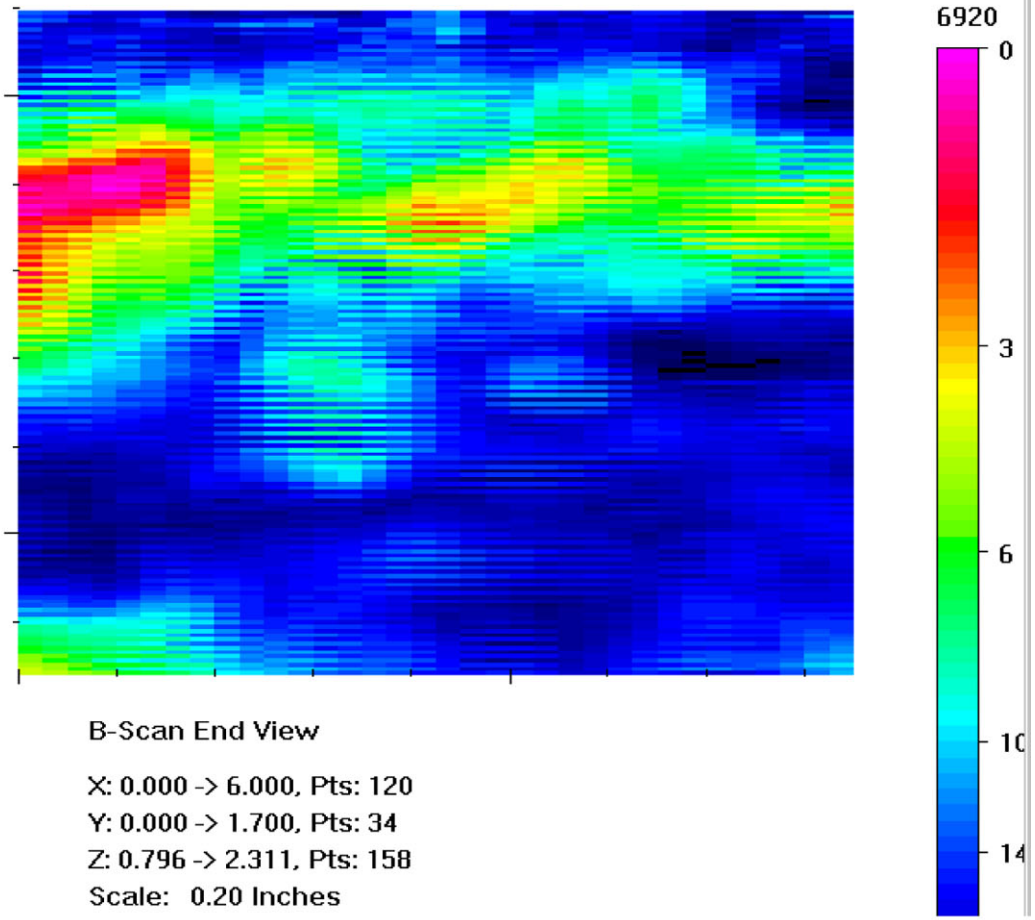

B-Scan End View

X: 0.000 -> 6.000, Pts: 120
Y: 0.000 -> 1.700, Pts: 34
Z: 0.796 -> 2.311, Pts: 158
Scale: 0.20 Inches

not detected

Section #1, Farside, Saw Cut C, 7% Through Wall Angle

2.25-MHz, 0.5-in.-diameter, 60° Shear

Length Sizing

Actual	1.427
6 dB Drop	
Loss of Signal	
6 dB Drop Δ	1.427
Loss of Signal Δ	1.427

Depth Sizing

Actual	0.1	Corner Trap	
6 dB Drop		Tip Signal	
UT Tip Signal	0	Velocity	0.125
6 dB Drop Δ	0.1	Angle	60
UT Tip Signal Δ	0.1		

Noise Characterization

Peak Signal Response			
Noise		S/N Ratio	dB
General Weld Root	5151	N/A	N/A
Local Weld Root	N/A	N/A	N/A
Cursor Window		N/A	N/A

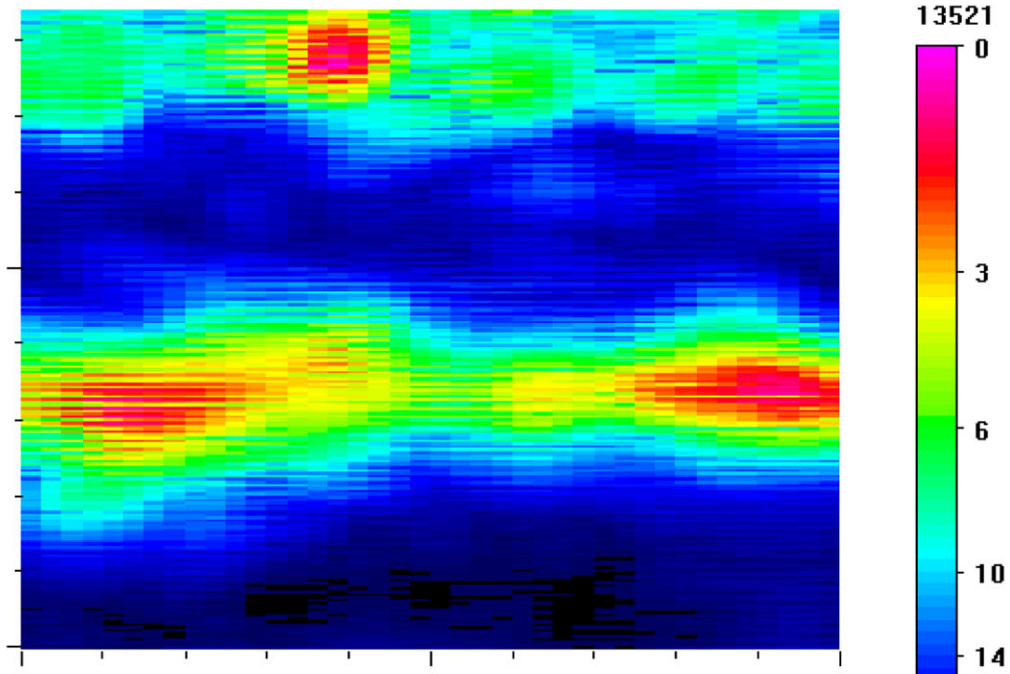

B-Scan End View

X: 0.000 -> 6.000, Pts: 120
Y: 0.000 -> 2.000, Pts: 40
Z: 0.328 -> 2.016, Pts: 216
Scale: 0.20 Inches

not detected

Section #1, Farside, Saw Cut C, 7% Through Wall Angle

2.25-MHz, 0.5-in.-diameter, 70° Shear

Length Sizing

Actual	1.427
6 dB Drop	
Loss of Signal	
6 dB Drop Δ	1.427
Loss of Signal Δ	1.427

Depth Sizing

Actual	0.1	Corner Trap	
6 dB Drop		Tip Signal	
UT Tip Signal	0	Velocity	0.125
6 dB Drop Δ	0.1	Angle	69
UT Tip Signal Δ	0.1		

Noise Characterization

Peak Signal Response			
Noise		S/N Ratio	dB
General Weld Root	2244	N/A	N/A
Local Weld Root	N/A	N/A	N/A
Cursor Window		N/A	N/A

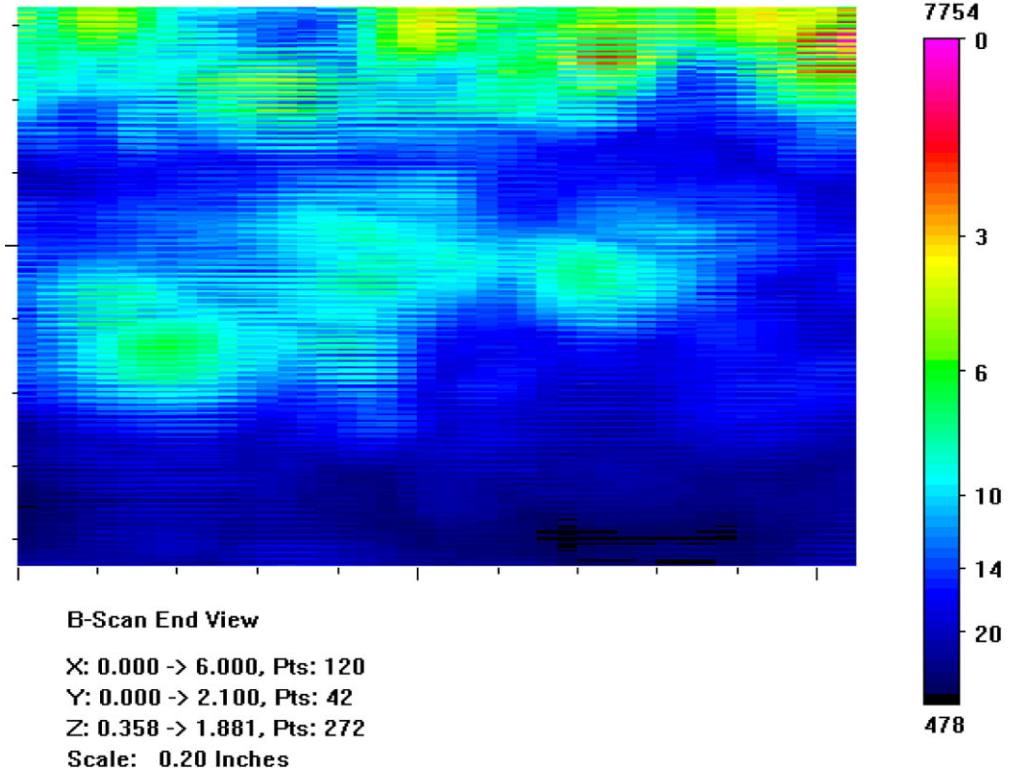

not detected

Section #1, Farside, Saw Cut C, 7% Through Wall Angle

2.25-MHz, 0.375-in.-diameter, 60° Shear

Length Sizing

Actual	1.427
6 dB Drop	0.4
Loss of Signal	0.4
6 dB Drop Δ	1.027
Loss of Signal Δ	1.027

No Call due to low signal response compared to the weld root response

Depth Sizing

Actual	0.1	Corner Tra	49.7
6 dB Drop	0.148	Tip Signal	42.8
UT Tip Signal	0.215625	Velocity	0.125
6 dB Drop Δ	-0.048	Angle	60
UT Tip Signal Δ	-0.11563		

Noise Characterization

Peak Signal Response		9792	
Noise		S/N Ratio	dB
General Weld Root	4347	2.3	7.1
Local Weld Root	12457	0.8	-2.1
Cursor Window	3629	2.7	8.6

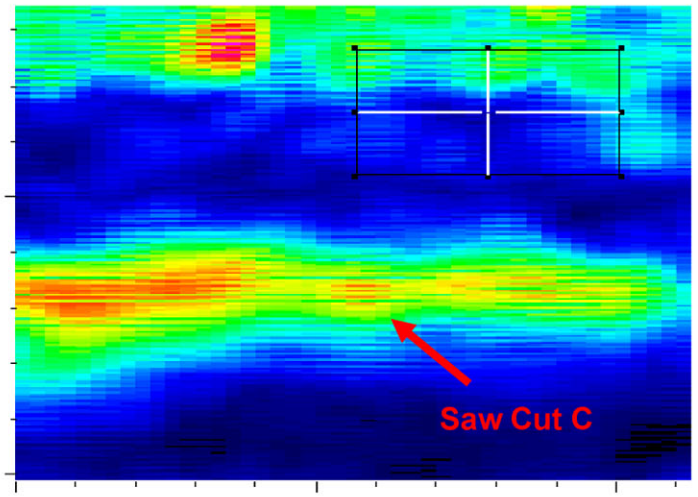

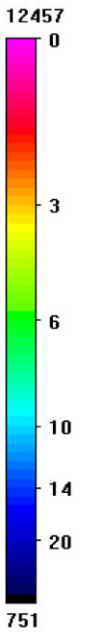

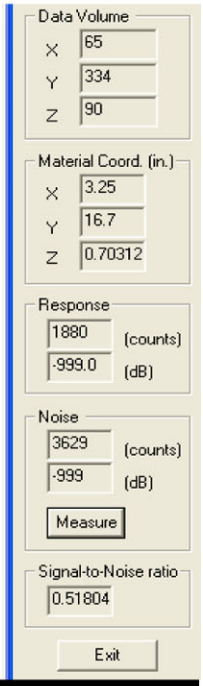

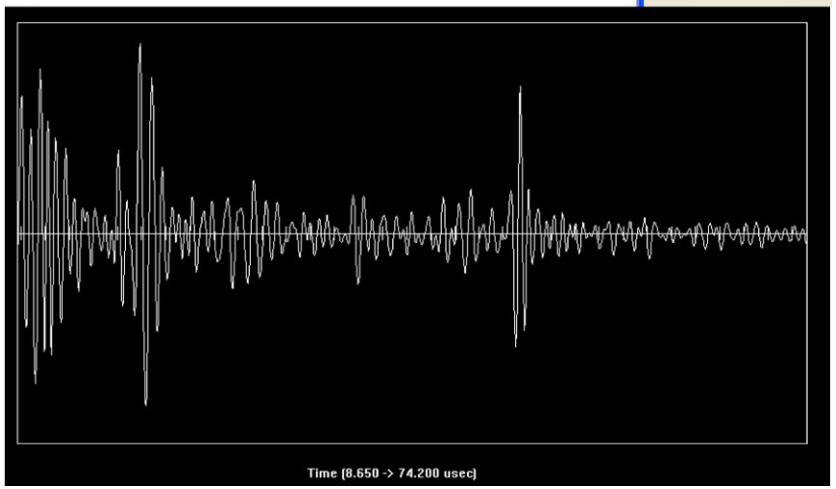

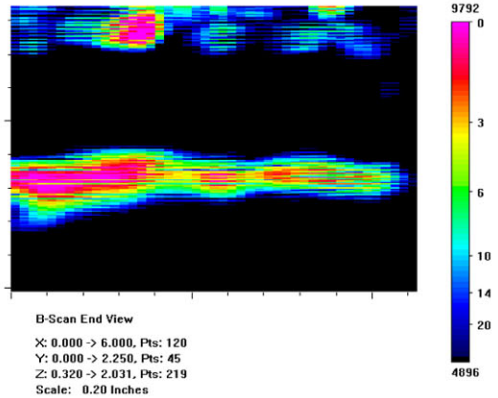

Section #1, Farside, Saw Cut C, 7% Through Wall Angle

2.25-MHz, 0.375-in.-diameter, 70° Shear

Length Sizing

Actual	1.427
6 dB Drop	
Loss of Signal	
6 dB Drop Δ	1.427
Loss of Signal Δ	1.427

Depth Sizing

Actual	0.1	Corner Trap	
6 dB Drop		Tip Signal	
UT Tip Signal	0	Velocity	0.125
6 dB Drop Δ	0.1	Angle	66
UT Tip Signal Δ	0.1		

Noise Characterization

Peak Signal Response			
Noise		S/N Ratio	dB
General Weld Root	2024	N/A	N/A
Local Weld Root	N/A	N/A	N/A
Cursor Window		N/A	N/A

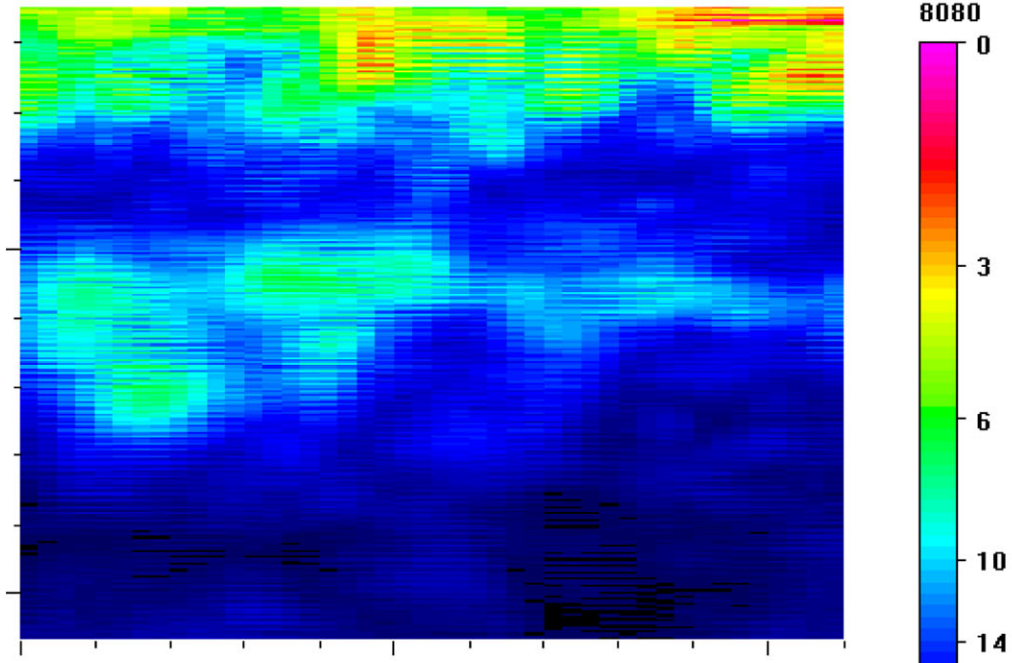

B-Scan End View

X: 0.000 -> 6.000, Pts: 120
Y: 0.000 -> 2.200, Pts: 44
Z: 0.305 -> 2.142, Pts: 289
Scale: 0.20 Inches

not detected

Section #2, Nearside, Saw Cut D, 19% Through Wall

1.5-MHz, 0.5-in.-diameter, 60° Shear

Length Sizing

Actual	2.131
6 dB Drop	1.45
Loss of Signal	2.05
6 dB Drop Δ	0.681
Loss of Signal Δ	0.081

Depth Sizing

Actual	0.267	Corner Trap	
6 dB Drop	0.153	Tip Signal	None
UT Tip Signal	None	Velocity	0.125
6 dB Drop Δ	0.114	Angle	60
UT Tip Signal Δ	None		

Noise Characterization

Peak Signal Response		16392	
Noise		S/N Ratio	dB
General Weld Root	N/A	N/A	N/A
Local Weld Root	N/A	N/A	N/A
Cursor Window	1142	14.4	23.1

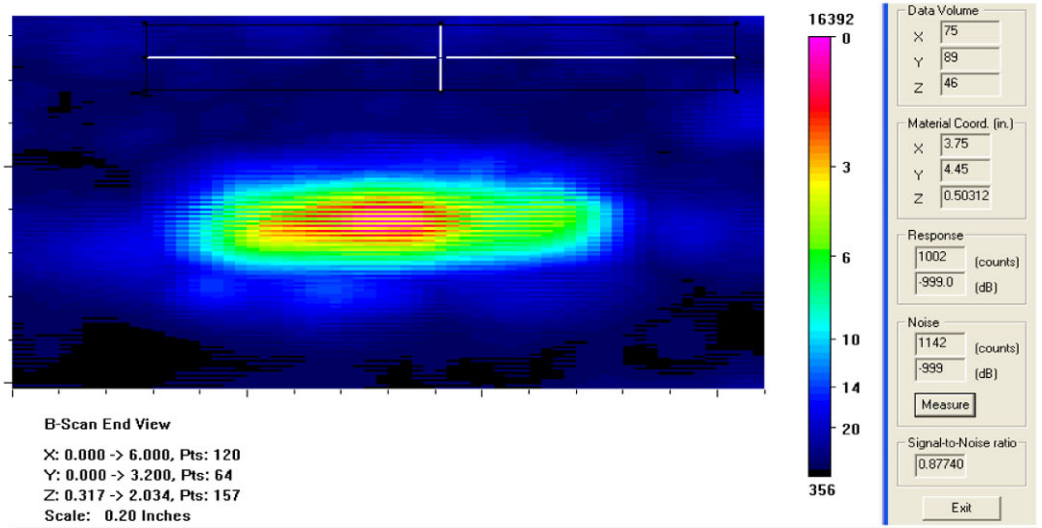

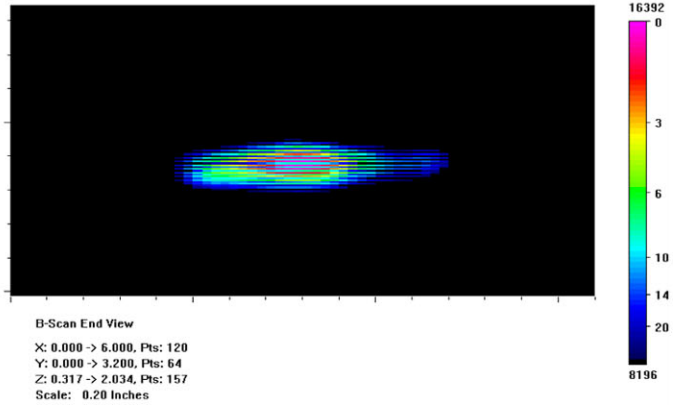

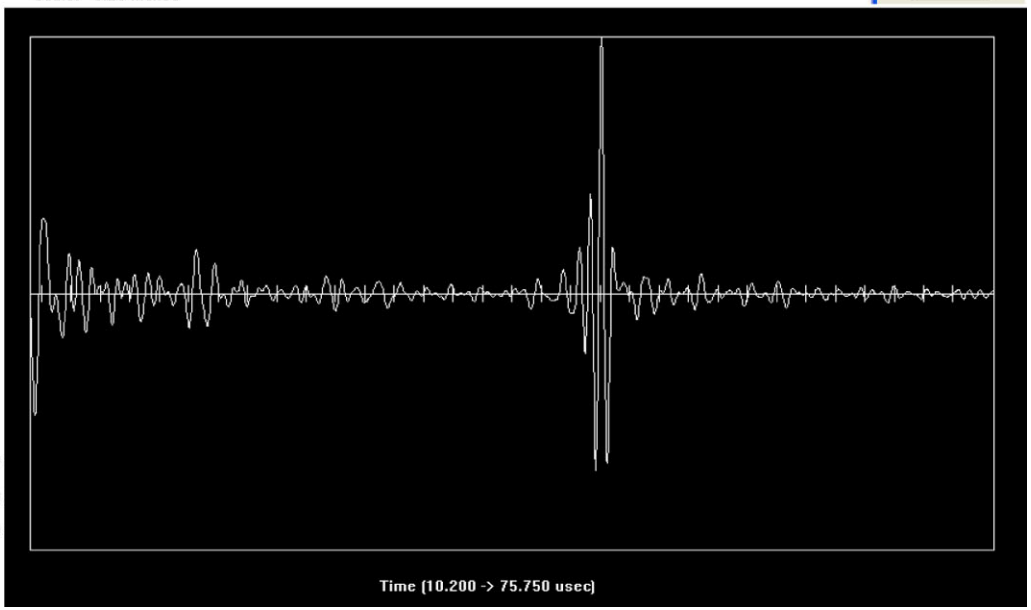

Section #2, Nearside, Saw Cut D, 19% Through Wall

1.5-MHz, 0.5-in.-diameter, 70° Shear

Length Sizing

Actual	2.131
6 dB Drop	1.65
Loss of Signal	1.95
6 dB Drop Δ	0.481
Loss of Signal Δ	0.181

Depth Sizing

Actual	0.267	Corner Tra	56.2
6 dB Drop	0.379	Tip Signal	46.15
UT Tip Signal	0.23936	Velocity	0.125
6 dB Drop Δ	-0.112	Angle	67.6
UT Tip Signal Δ	0.02764		

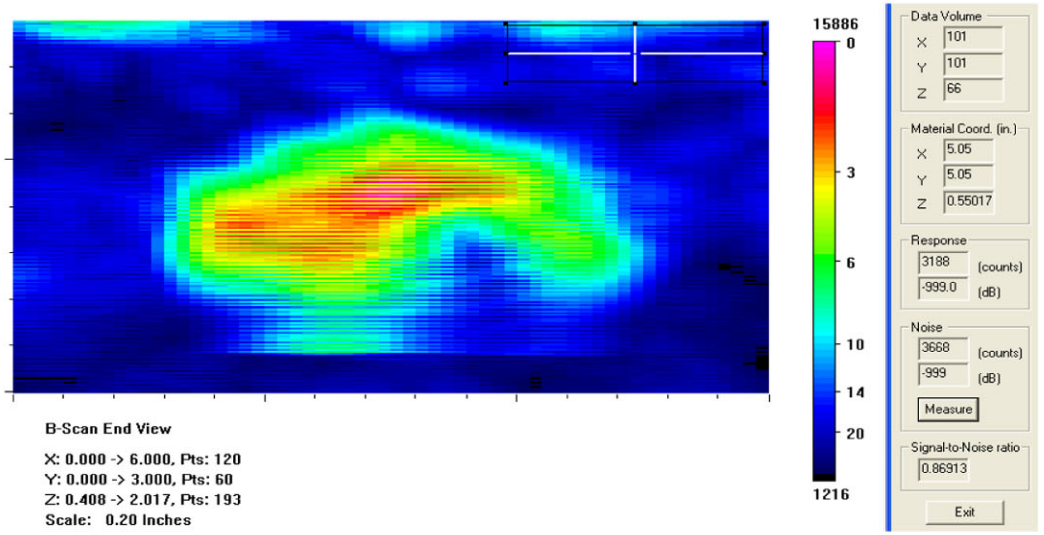

Noise Characterization

Peak Signal Response		15886	
Noise		S/N Ratio	dB
General Weld Root	N/A	N/A	N/A
Local Weld Root	N/A	N/A	N/A
Cursor Window	3668	4.3	12.7

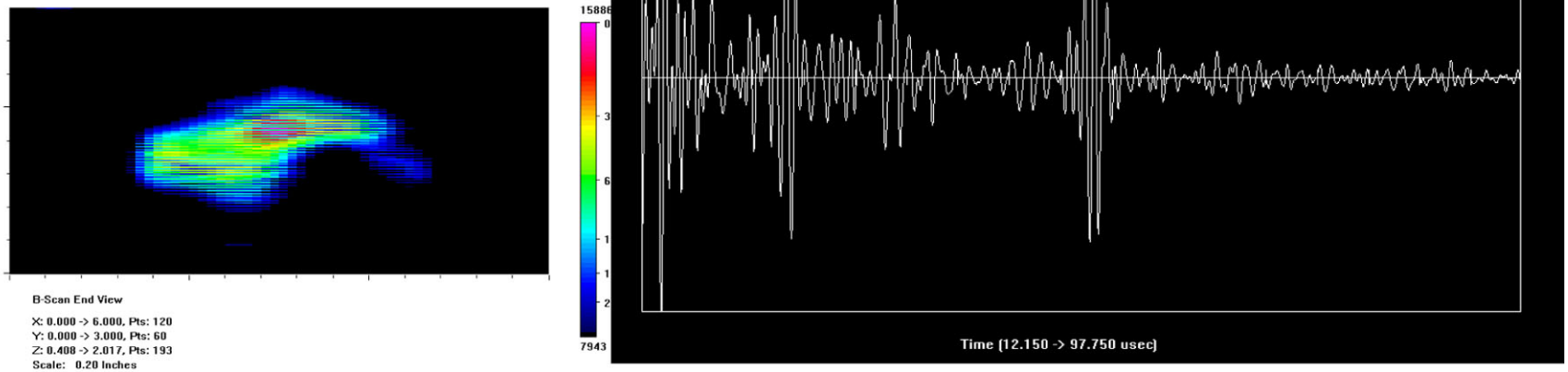

Section #2, Farside, Saw Cut D, 19% Through Wall

1.5-MHz, 0.5-in.-diameter, 60° Shear

Length Sizing

Actual	2.131
6 dB Drop	1.65
Loss of Signal	2.25
6 dB Drop Δ	0.481
Loss of Signal Δ	-0.119

Depth Sizing

Actual	0.267	Corner Tra	52.75
6 dB Drop	0.17	Tip Signal	37.35
UT Tip Signal	0.48125	Velocity	0.125
6 dB Drop Δ	0.097	Angle	60
UT Tip Signal Δ	-0.21425		

Noise Characterization

Peak Signal Response		12510	
Noise		S/N Ratio	dB
General Weld Root	2025	6.2	15.8
Local Weld Root	6678	1.9	5.5
Cursor Window	1781	7.0	16.9

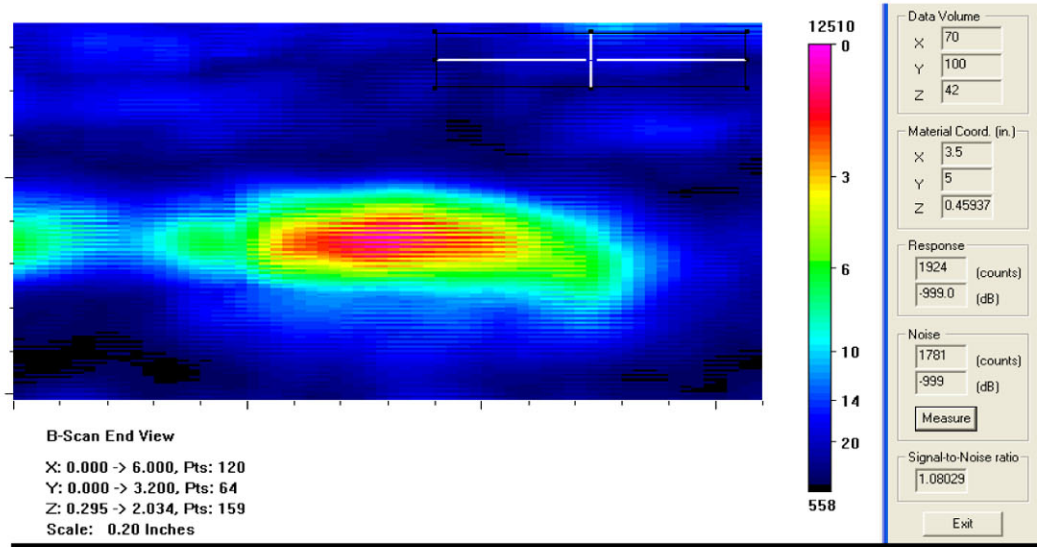

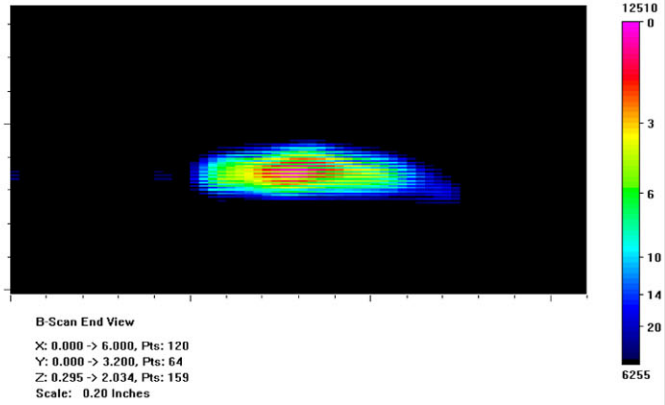

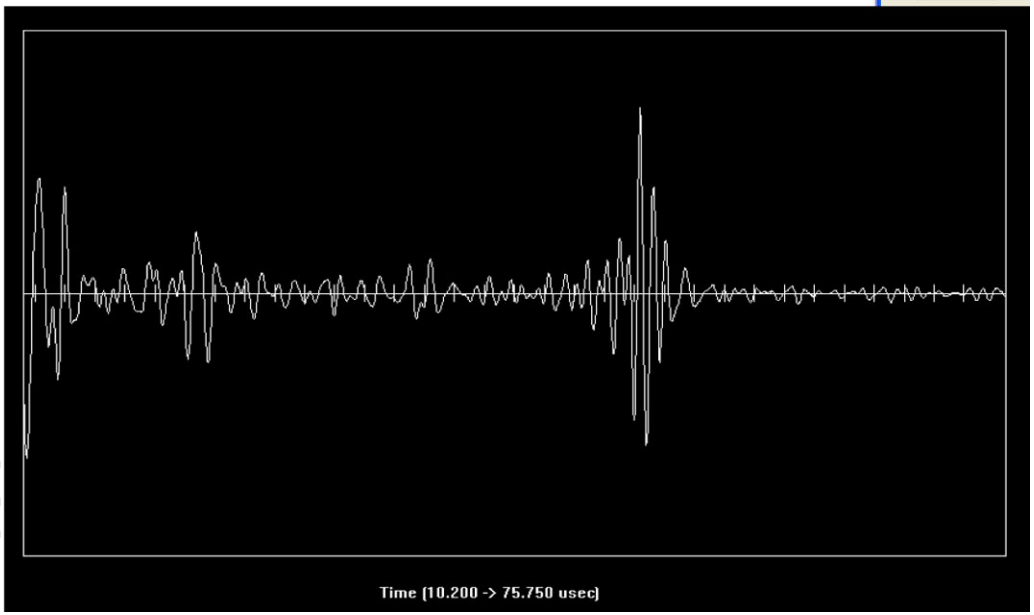

Section #2, Farside, Saw Cut D, 19% Through Wall

1.5-MHz, 0.5-in.-diameter, 70° Shear

Length Sizing

Actual	2.131
6 dB Drop	1.4
Loss of Signal	2.15
6 dB Drop Δ	0.731
Loss of Signal Δ	-0.019

Depth Sizing

Actual	0.267	Corner Tra	81.5
6 dB Drop	0.275	Tip Signal	70.9
UT Tip Signal	0.252459	Velocity	0.125
6 dB Drop Δ	-0.008	Angle	67.6
UT Tip Signal Δ	0.014541		

Noise Characterization

Peak Signal Response		17897	
Noise		S/N Ratio	dB
General Weld Root	3552	5.0	14.0
Local Weld Root	3593	5.0	13.9
Cursor Window	5154	3.5	10.8

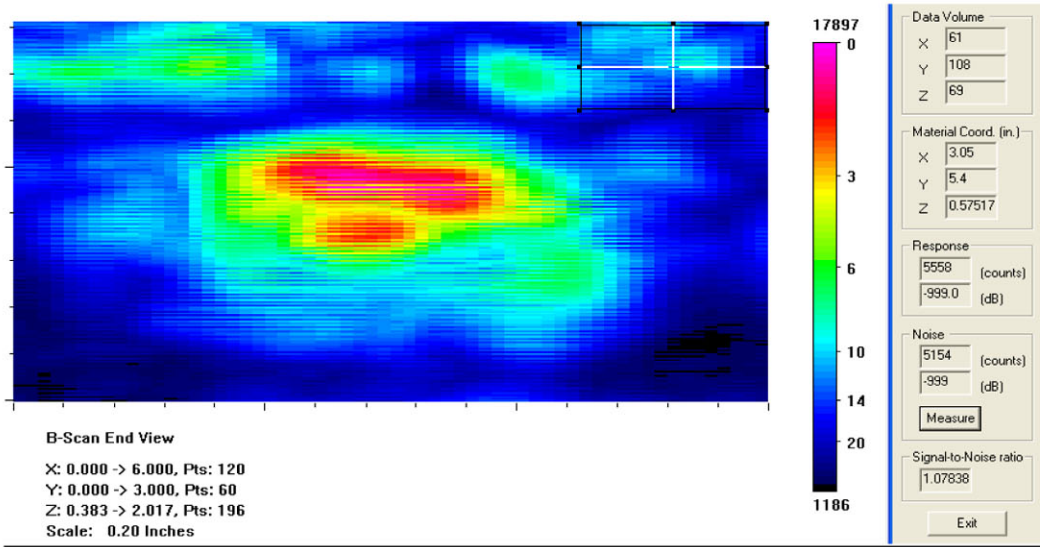

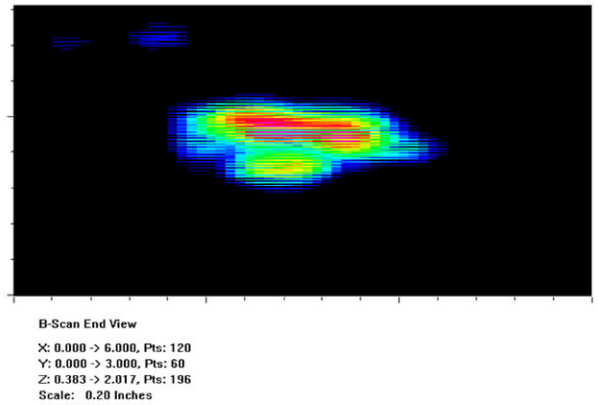

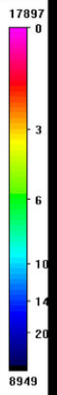

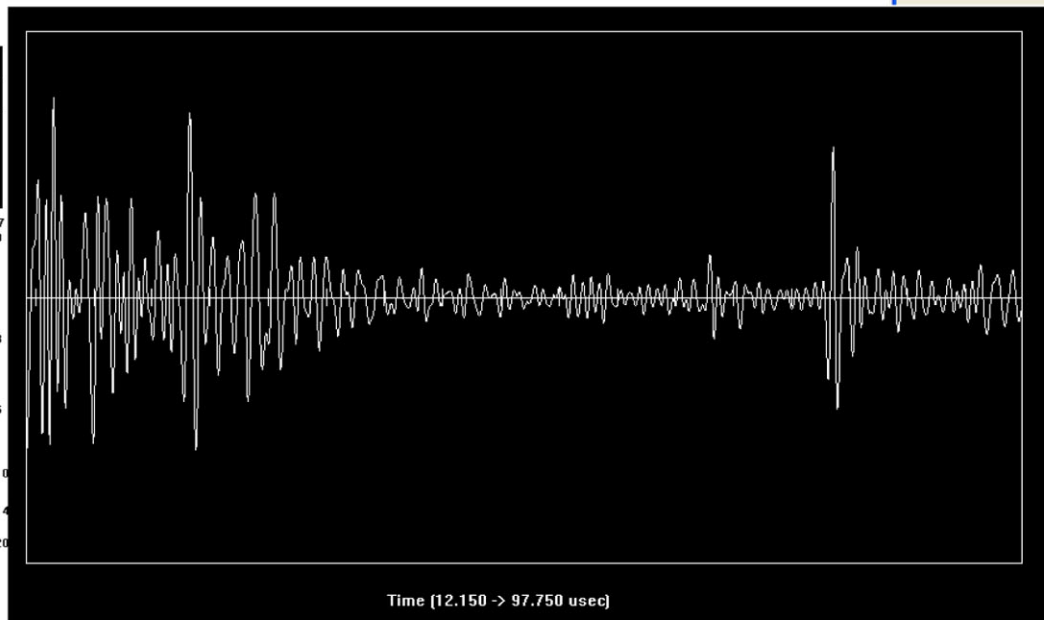

Section #2, Nearside, Flaw C, 64% Through Wall

1.5-MHz, 0.5-in.-diameter, 60° Shear

Length Sizing

Actual	1.715
6 dB Drop	1.55
Loss of Signal	2.15
6 dB Drop Δ	0.165
Loss of Signal Δ	-0.435

Depth Sizing

Actual	0.845	Corner Tra	54.2
6 dB Drop	0.755	Tip Signal	33.15
UT Tip Signal	0.657813	Velocity	0.125
6 dB Drop Δ	0.09	Angle	60
UT Tip Signal Δ	0.187188		

Noise Characterization

Peak Signal Response		8472	
Noise		S/N Ratio	dB
General Weld Root	N/A	N/A	N/A
Local Weld Root	N/A	N/A	N/A
Cursor Window	1096	7.7	17.8

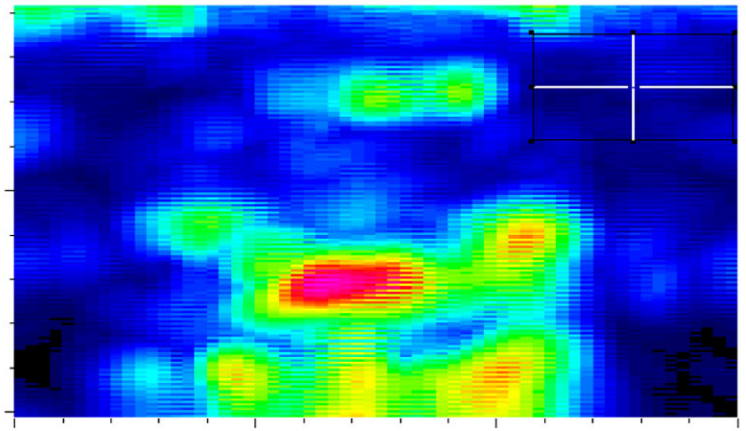

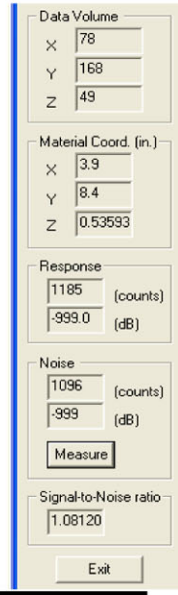

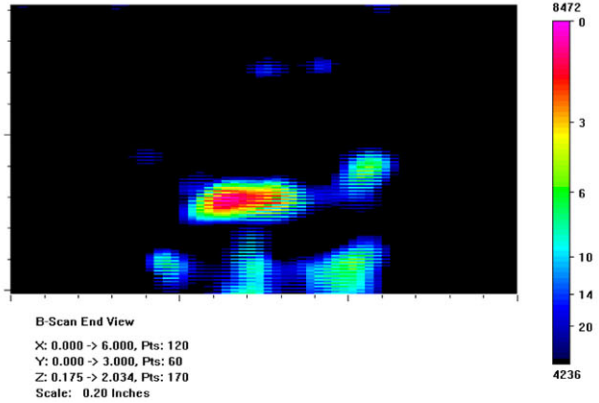

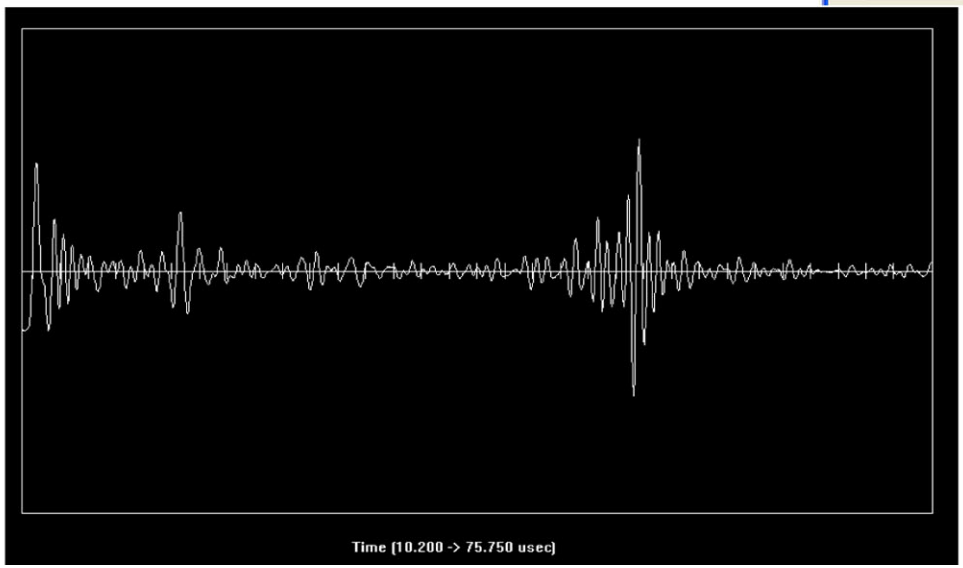

Section #2, Nearside, Flaw C, 64% Through Wall

1.5-MHz, 0.5-in.-diameter, 70° Shear

Length Sizing

Actual	1.715
6 dB Drop	1.65
Loss of Signal	2.2
6 dB Drop Δ	0.065
Loss of Signal Δ	-0.485

Depth Sizing

Actual	0.845	Corner Tra	93.05
6 dB Drop	0.475	Tip Signal	50.8
UT Tip Signal	1.006264	Velocity	0.125
6 dB Drop Δ	0.37	Angle	67.6
UT Tip Signal Δ	-0.16126		

Noise Characterization

Peak Signal Response		19657	
Noise		S/N Ratio	dB
General Weld Root	N/A	N/A	N/A
Local Weld Root	N/A	N/A	N/A
Cursor Window	3621	5.4	14.7

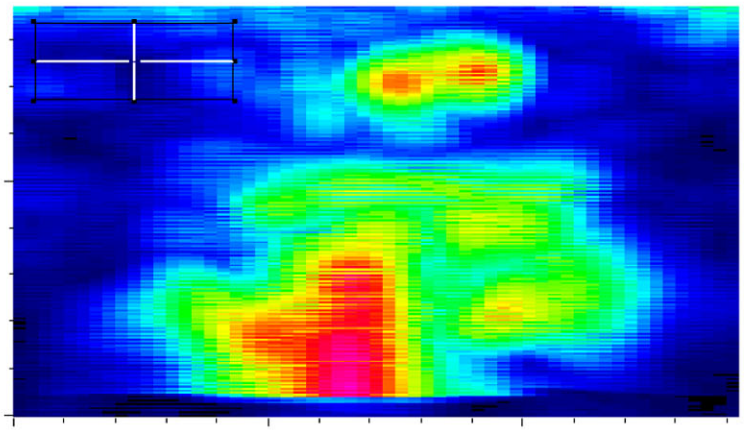

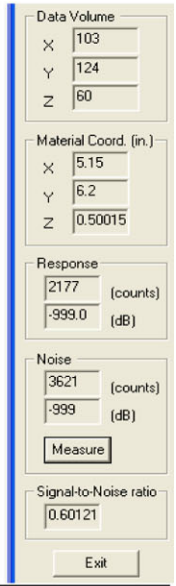

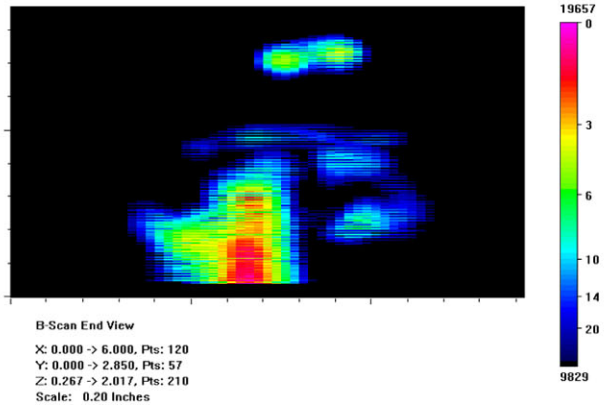

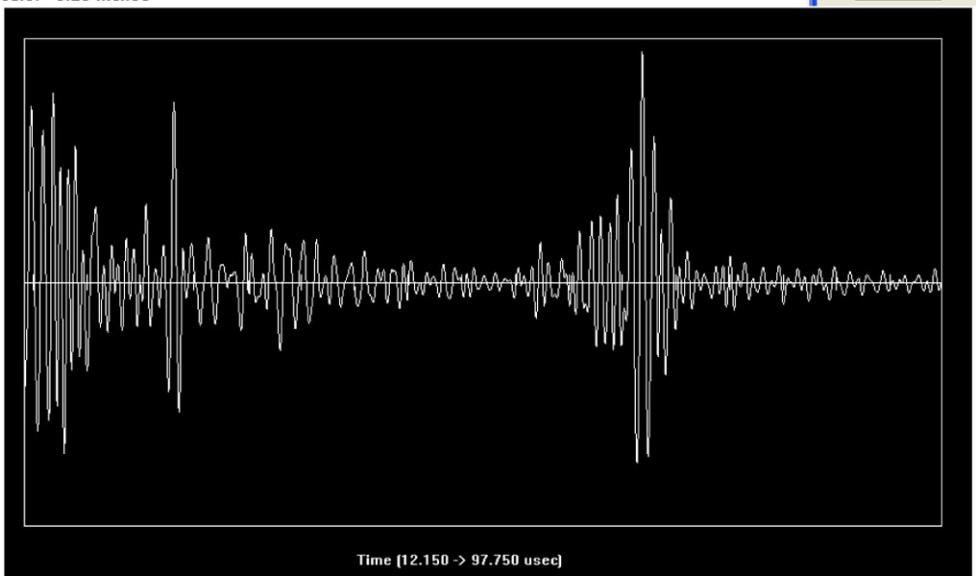

Section #2, Farside, Flaw C, 64% Through Wall

1.5-MHz, 0.5-in.-diameter, 60° Shear

Length Sizing

Actual	1.715
6 dB Drop	1.8
Loss of Signal	2.25
6 dB Drop Δ	-0.085
Loss of Signal Δ	-0.535

Depth Sizing

Actual	0.845	Corner Trap	
6 dB Drop	0.651	Tip Signal	None
UT Tip Signal	None	Velocity	0.125
6 dB Drop Δ	0.194	Angle	60
UT Tip Signal Δ	None		

Noise Characterization

Peak Signal Response		8766	
Noise		S/N Ratio	dB
General Weld Root	2025	4.3	12.7
Local Weld Root	2467	3.6	11.0
Cursor Window	1697	5.2	14.3

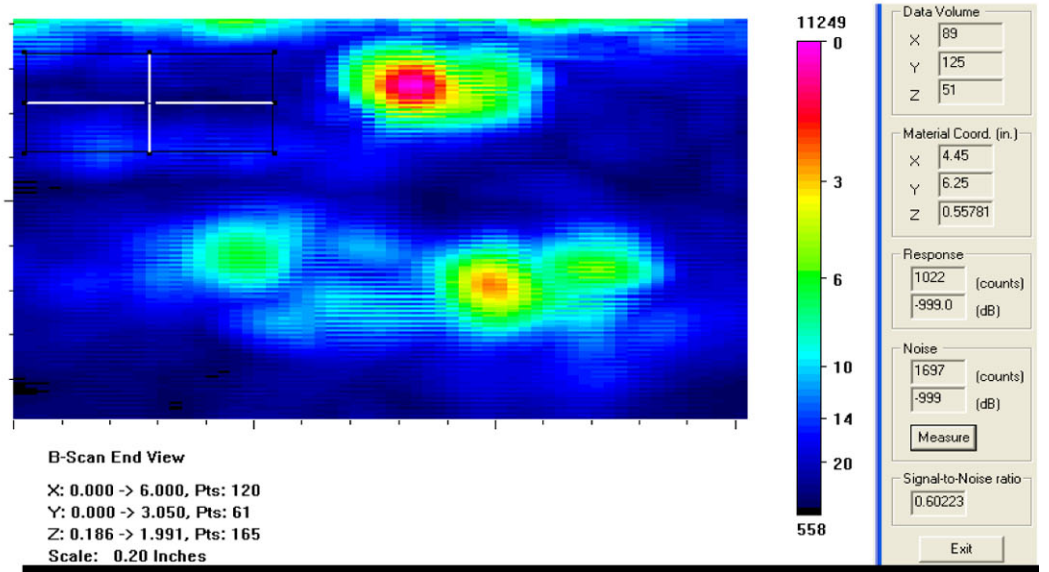

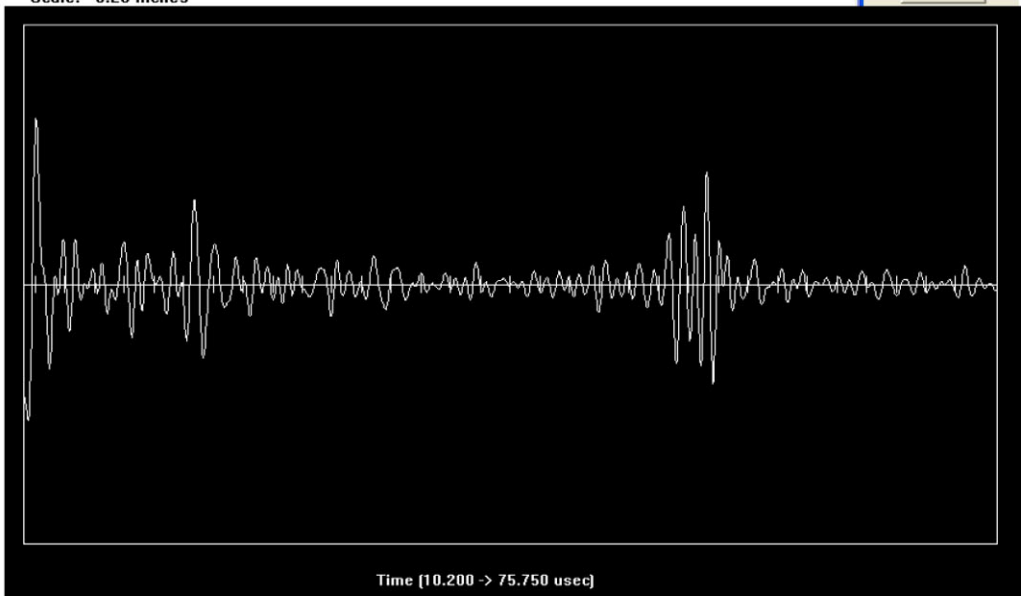

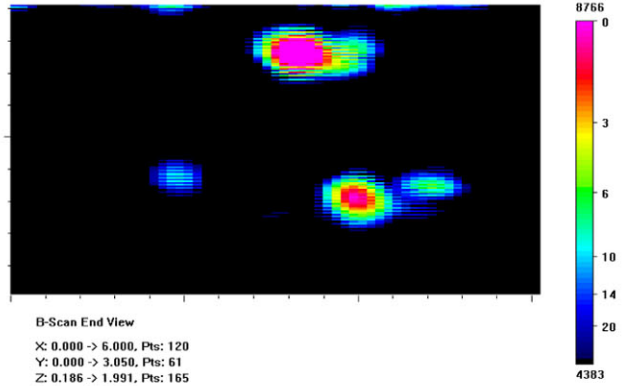

Section #2, Farside, Flaw C, 64% Through Wall

1.5-MHz, 0.5-in.-diameter, 70° Shear

Length Sizing

Actual	1.715
6 dB Drop	1.75
Loss of Signal	2.05
6 dB Drop Δ	-0.035
Loss of Signal Δ	-0.335

Depth Sizing

Actual	0.845	Corner Tra	64.3
6 dB Drop	0.563	Tip Signal	49.05
UT Tip Signal	0.363208	Velocity	0.125
6 dB Drop Δ	0.282	Angle	67.6
UT Tip Signal Δ	0.481792		

Noise Characterization

Peak Signal Response		18470	
Noise		S/N Ratio	dB
General Weld Root	3552	5.2	14.3
Local Weld Root	5021	3.7	11.3
Cursor Window	4969	3.7	11.4

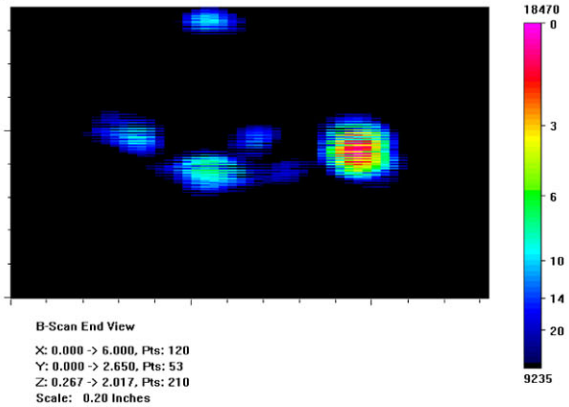

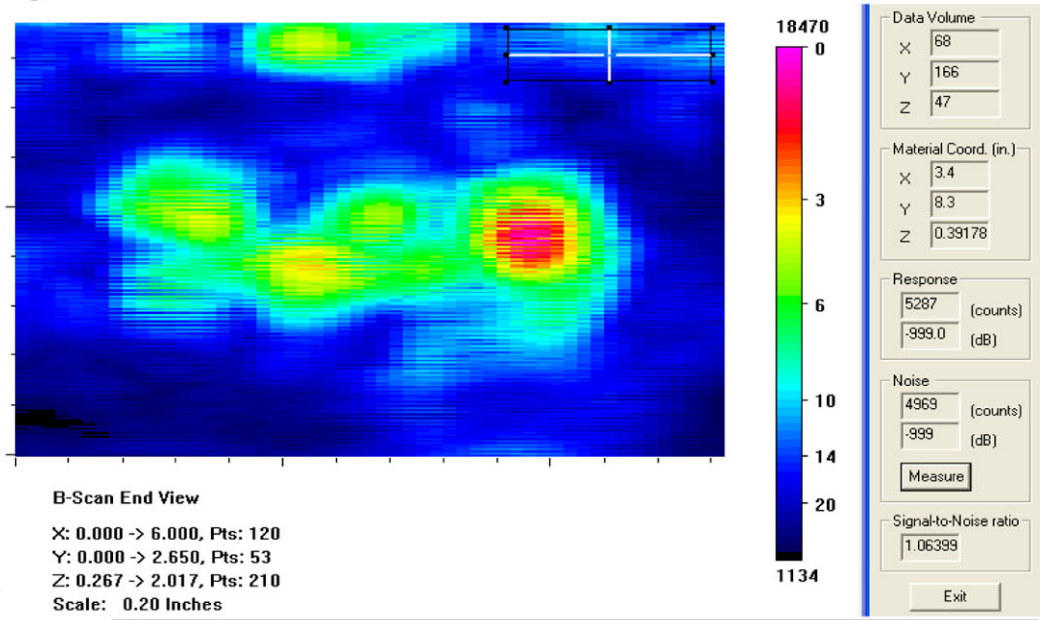

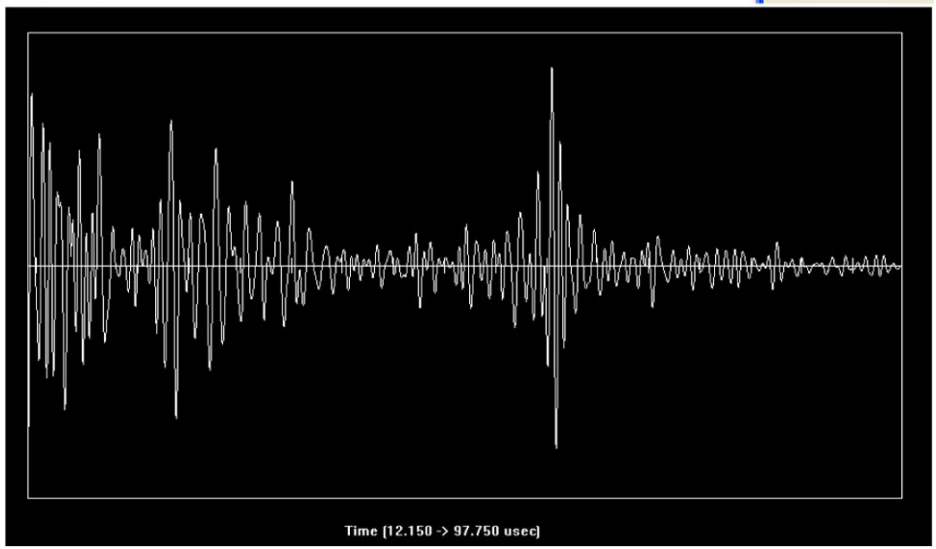

Section #2, Nearside, Saw Cut E, 12% Through Wall

1.5-MHz, 0.5-in.-diameter, 60° Shear

Length Sizing

Actual	1.72
6 dB Drop	1.25
Loss of Signal	1.65
6 dB Drop Δ	0.47
Loss of Signal Δ	0.07

Depth Sizing

Actual	0.169	Corner Trap	
6 dB Drop	0.164	Tip Signal	None
UT Tip Signal	None	Velocity	0.125
6 dB Drop Δ	0.005	Angle	60
UT Tip Signal Δ	None		

Noise Characterization

Peak Signal Response		9000	
Noise		S/N Ratio	dB
General Weld Root	N/A	N/A	N/A
Local Weld Root	N/A	N/A	N/A
Cursor Window	1201	7.5	17.5

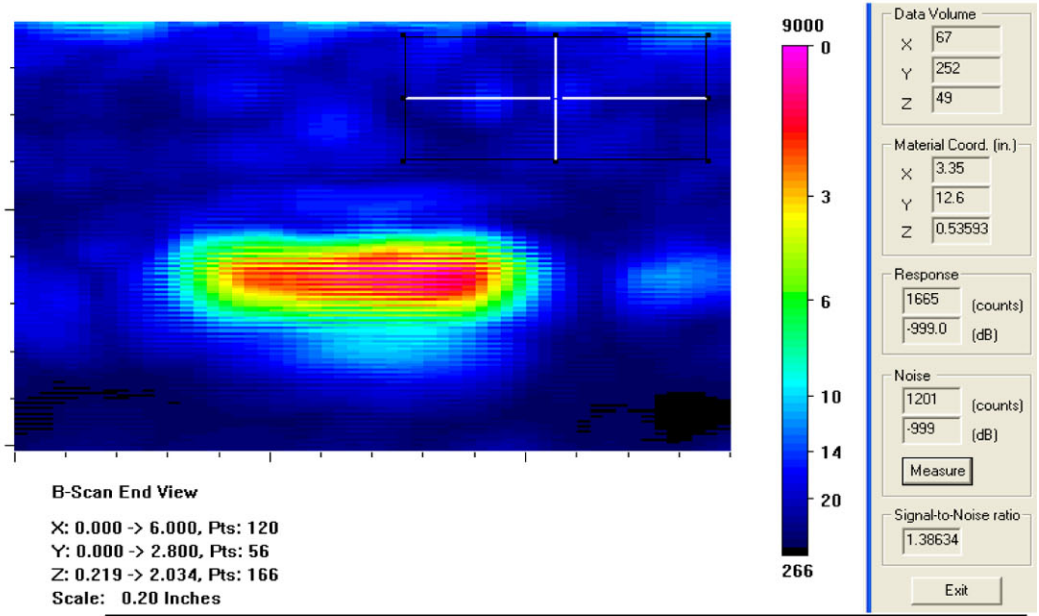

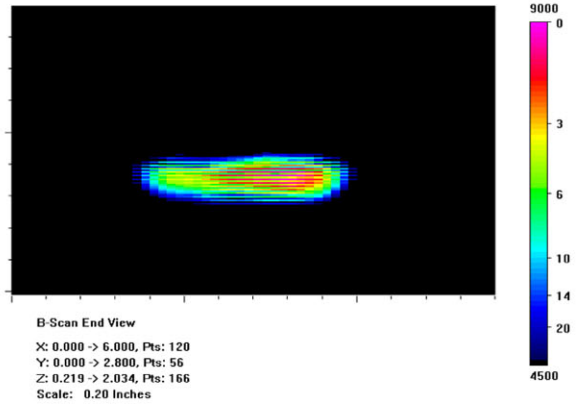

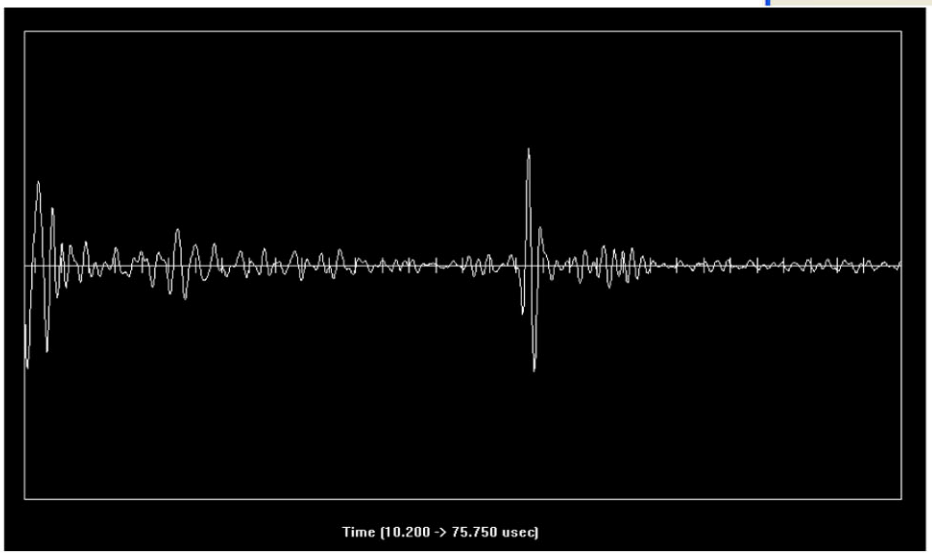

Section #2, Nearside, Saw Cut E, 12% Through Wall

1.5-MHz, 0.5-in.-diameter, 70° Shear

Length Sizing

Actual	1.72
6 dB Drop	1.15
Loss of Signal	1.55
6 dB Drop Δ	0.57
Loss of Signal Δ	0.17

Depth Sizing

Actual	0.169	Corner Tra	60.8
6 dB Drop	0.258	Tip Signal	53.95
UT Tip Signal	0.163146	Velocity	0.125
6 dB Drop Δ	-0.089	Angle	67.6
UT Tip Signal Δ	0.005854		

Noise Characterization

Peak Signal Response		13878	
Noise		S/N Ratio	dB
General Weld Root	N/A	N/A	N/A
Local Weld Root	N/A	N/A	N/A
Cursor Window	4043	3.4	10.7

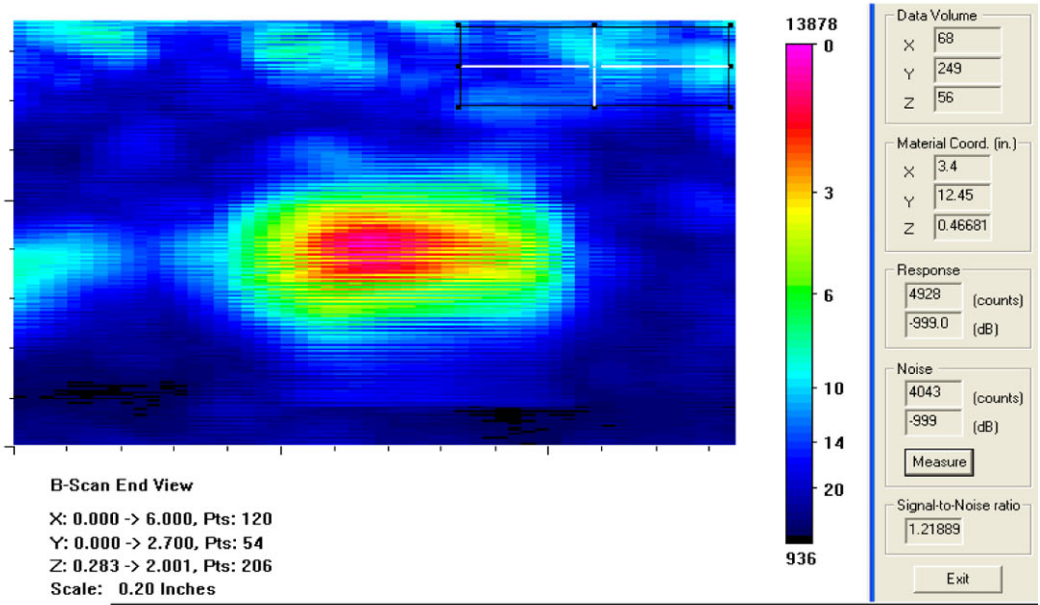

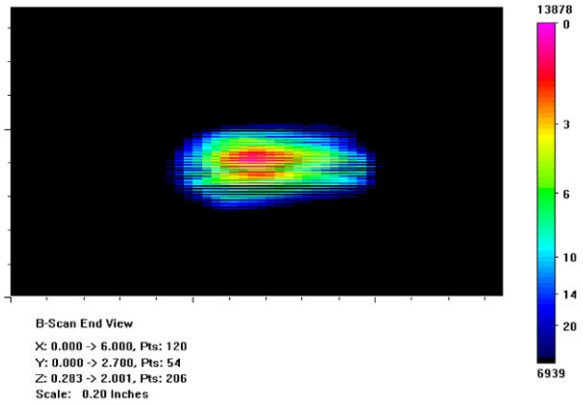

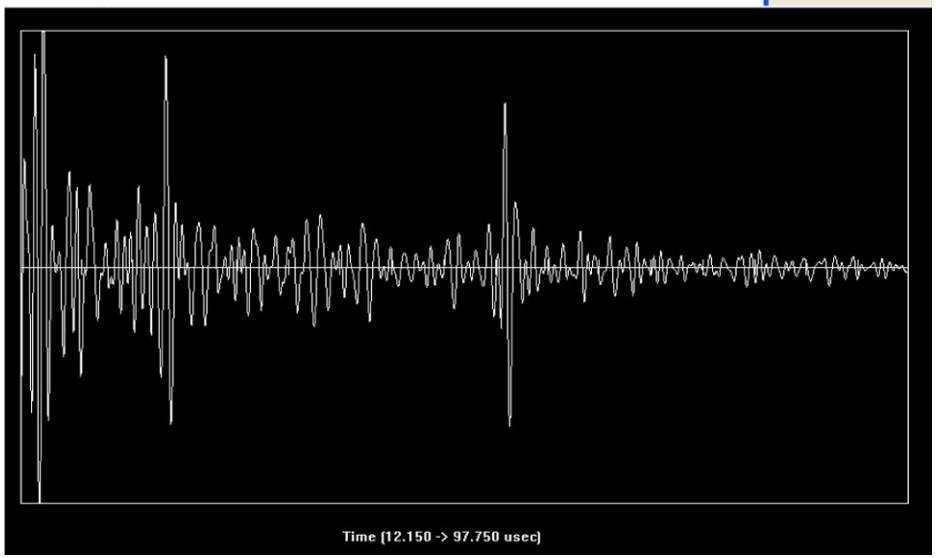

Section #2, Farside, Saw Cut E, 12% Through Wall

1.5-MHz, 0.5-in.-diameter, 60° Shear

Length Sizing

Actual	1.72
6 dB Drop	1.45
Loss of Signal	2.05
6 dB Drop Δ	0.27
Loss of Signal Δ	-0.33

Depth Sizing

Actual	0.169	Corner Tra	57.1
6 dB Drop	0.279	Tip Signal	48.55
UT Tip Signal	0.267188	Velocity	0.125
6 dB Drop Δ	-0.11	Angle	60
UT Tip Signal Δ	-0.09819		

Noise Characterization

Peak Signal Response		5263	
Noise		S/N Ratio	dB
General Weld Root	2025	2.6	8.3
Local Weld Root	3814	1.4	2.8
Cursor Window	1258	4.2	12.4

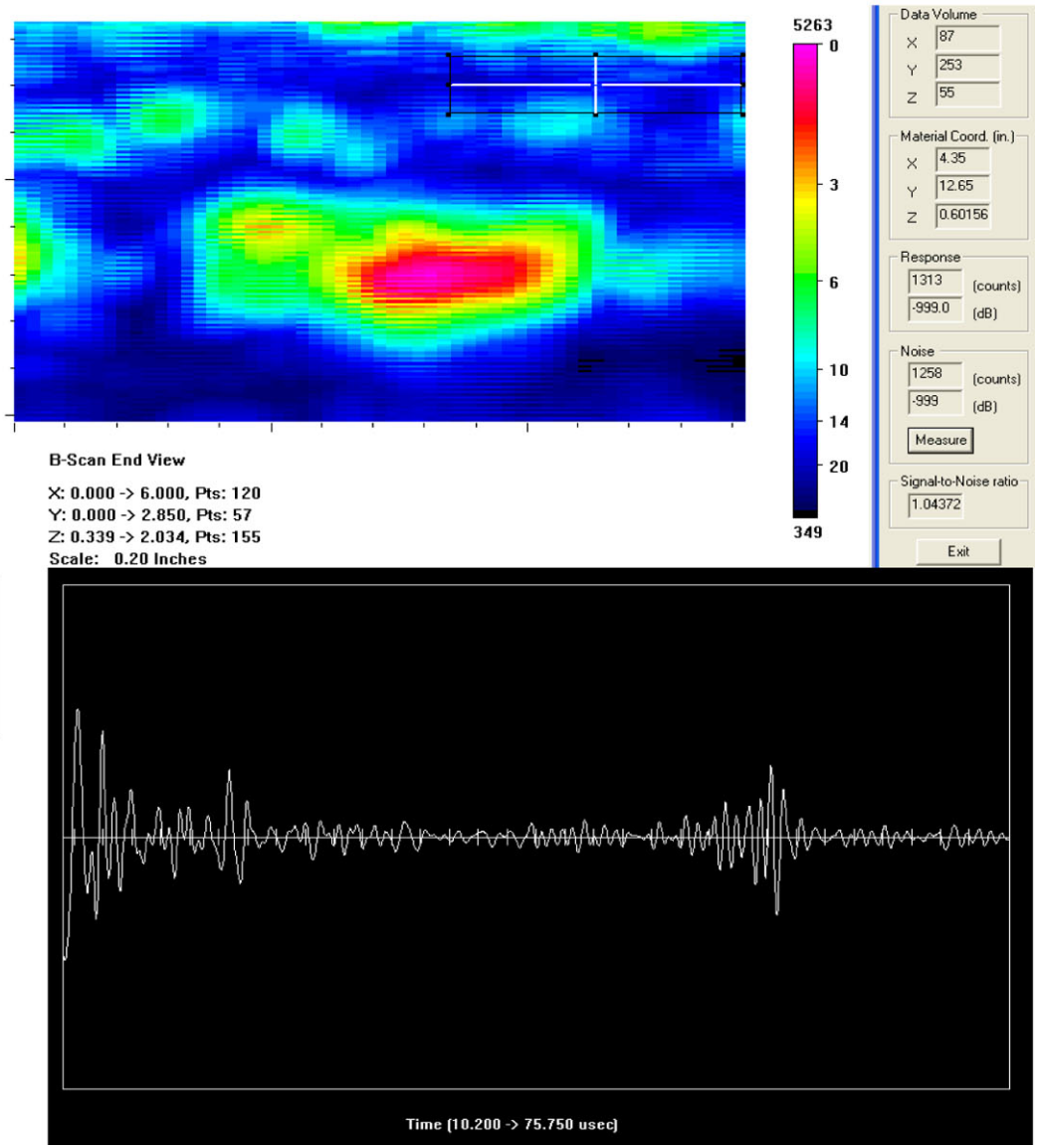

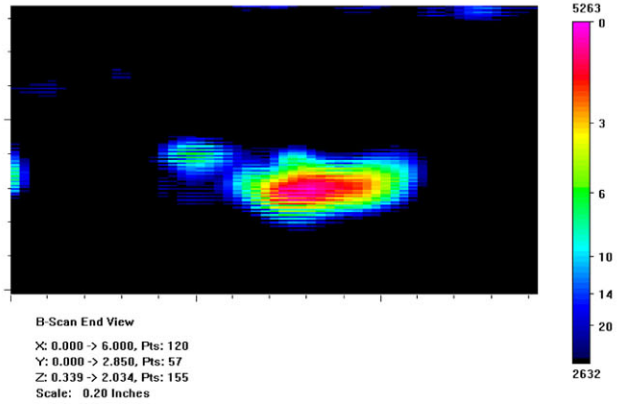

Section #2, Farside, Saw Cut E, 12% Through Wall

1.5-MHz, 0.5-in.-diameter, 70° Shear

Length Sizing

Actual	1.72
6 dB Drop	0.95
Loss of Signal	1.75
6 dB Drop Δ	0.77
Loss of Signal Δ	-0.03

Depth Sizing

Actual	0.169	Corner Trap	
6 dB Drop	0.283	Tip Signal	None
UT Tip Signal	None	Velocity	0.125
6 dB Drop Δ	-0.114	Angle	67.6
UT Tip Signal Δ	None		

Noise Characterization

Peak Signal Response		12682	
Noise		S/N Ratio	dB
General Weld Root	3552	3.6	11.1
Local Weld Root	5051	2.5	8.0
Cursor Window	3932	3.2	10.2

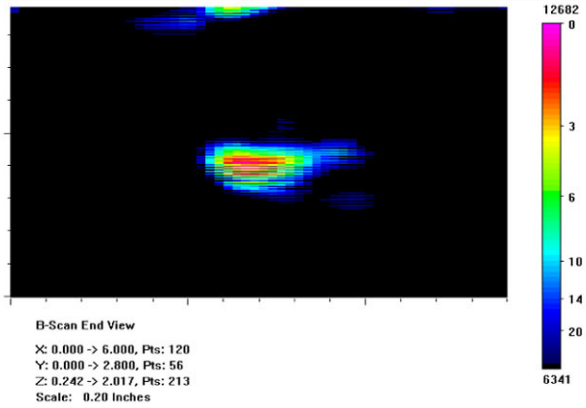

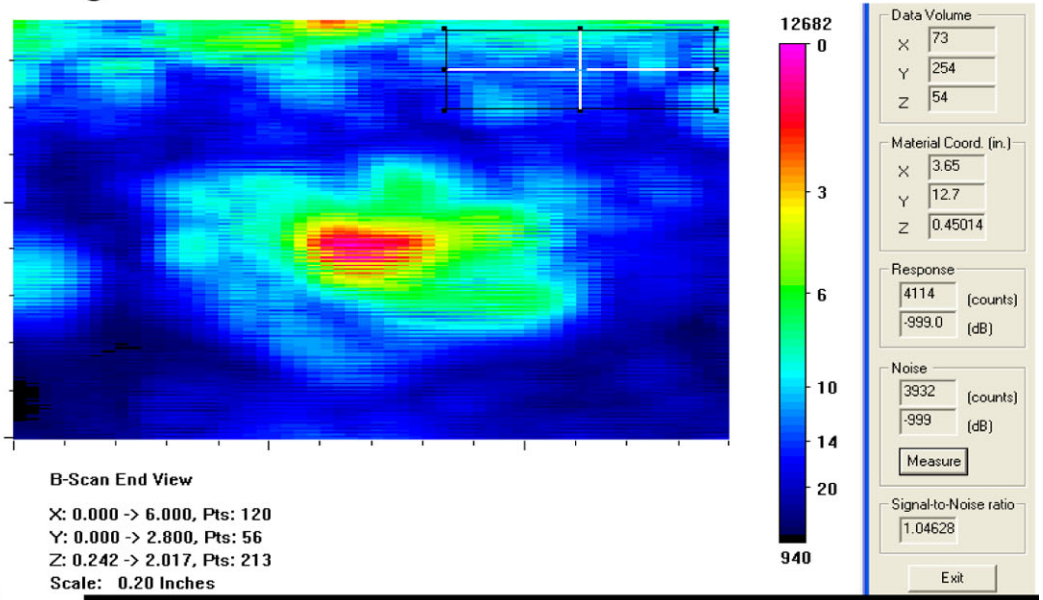

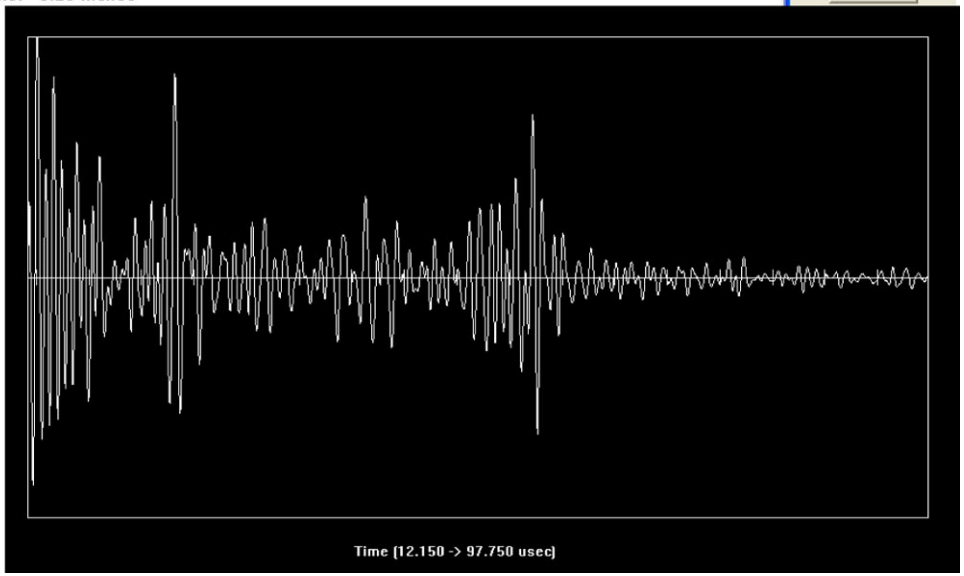

Section #2, Nearside, Saw Cut F, 19% Through Wall Angle

1.5-MHz, 0.5-in.-diameter, 60° Shear

Length Sizing

Actual	2.349
6 dB Drop	1.55
Loss of Signal	2
6 dB Drop Δ	0.799
Loss of Signal Δ	0.349

Depth Sizing

Actual	0.28	Corner Tra	53.6
6 dB Drop	0.284	Tip Signal	43.85
UT Tip Signal	0.304688	Velocity	0.125
6 dB Drop Δ	-0.004	Angle	60
UT Tip Signal Δ	-0.02469		

Noise Characterization

Peak Signal Response		8459	
Noise		S/N Ratio	dB
General Weld Root	N/A	N/A	N/A
Local Weld Root	N/A	N/A	N/A
Cursor Window	1189	7.1	17.0

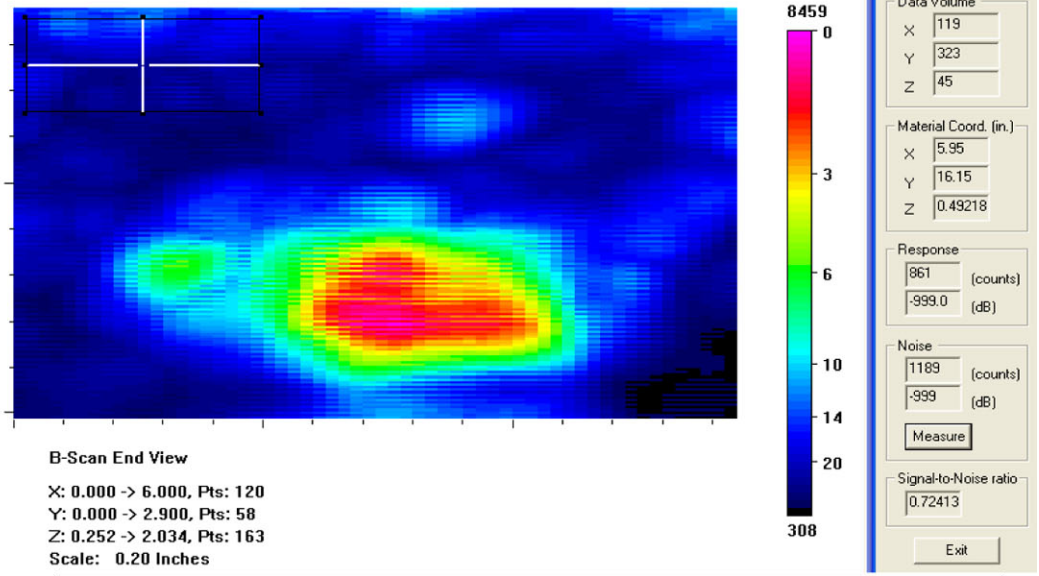

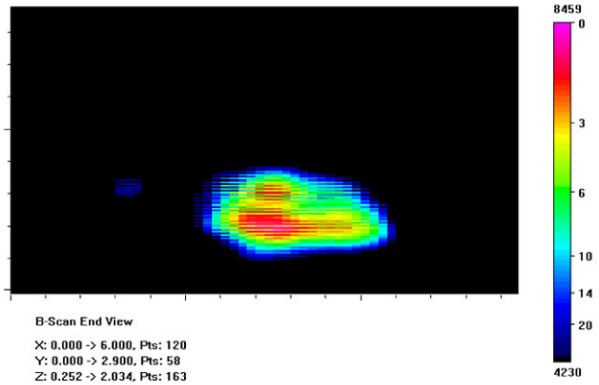

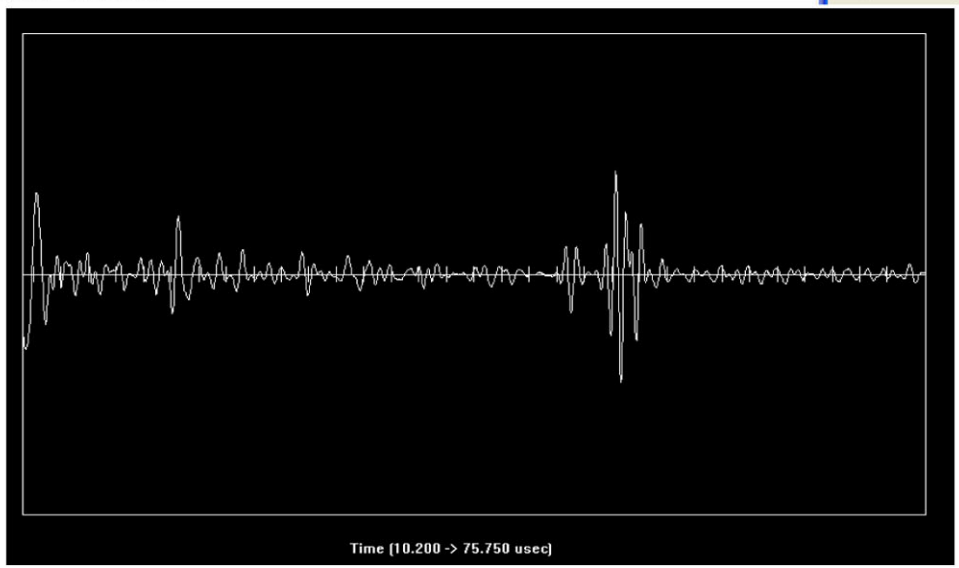

Section #2, Nearside, Saw Cut F, 19% Through Wall Angle

1.5-MHz, 0.5-in.-diameter, 70° Shear

Length Sizing

Actual	2.349
6 dB Drop	1.85
Loss of Signal	2.3
6 dB Drop Δ	0.499
Loss of Signal Δ	0.049

Depth Sizing

Actual	0.28	Corner Tra	74.5
6 dB Drop	0.271	Tip Signal	63.5
UT Tip Signal	0.261986	Velocity	0.125
6 dB Drop Δ	0.009	Angle	67.6
UT Tip Signal Δ	0.018014		

Noise Characterization

Peak Signal Response		19562	
Noise		S/N Ratio	dB
General Weld Root	N/A	N/A	N/A
Local Weld Root	N/A	N/A	N/A
Cursor Window	3350	5.8	15.3

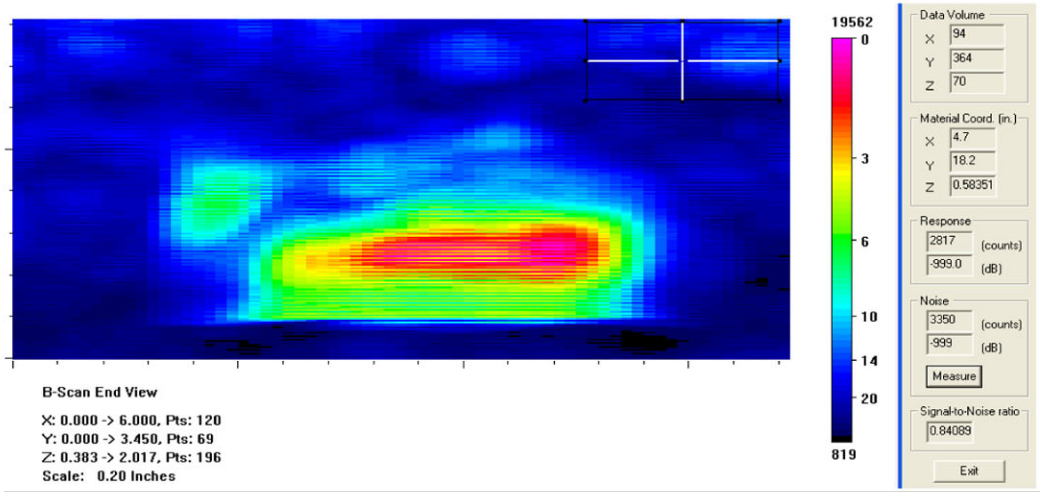

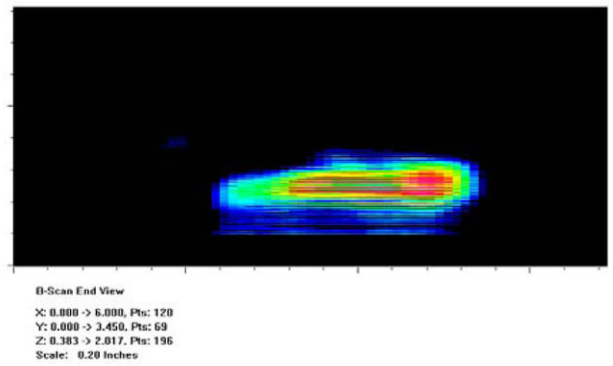

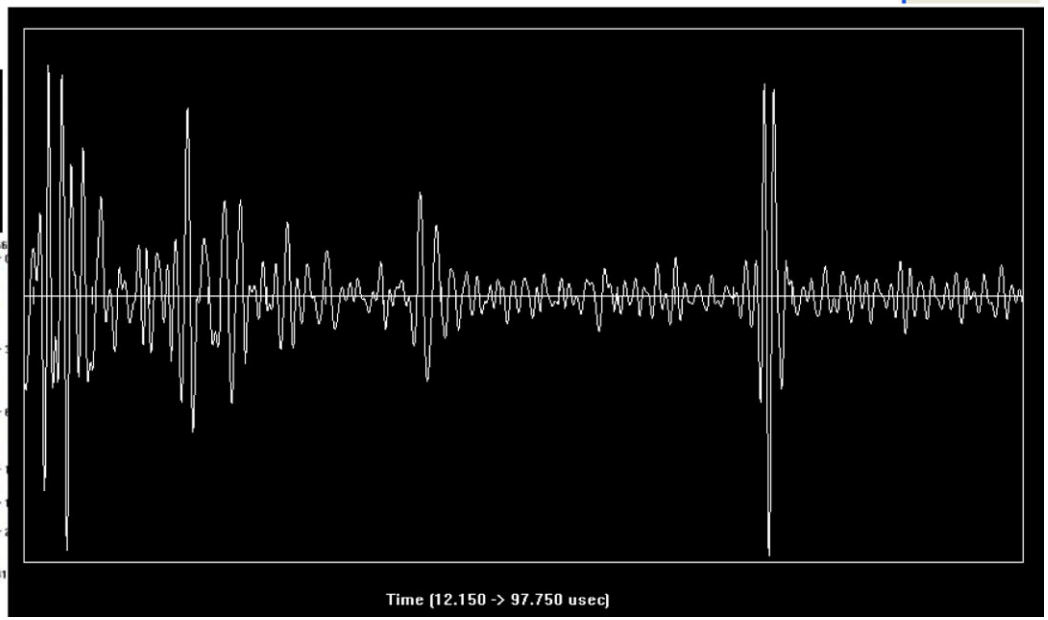

Section #2, Farside, Saw Cut F, 19% Through Wall Angle

1.5-MHz, 0.5-in.-diameter, 60° Shear

Length Sizing

Actual	2.349
6 dB Drop	1.9
Loss of Signal	2.35
6 dB Drop Δ	0.449
Loss of Signal Δ	-0.001

Depth Sizing

Actual	0.28	Corner Tra	55.55
6 dB Drop	0.202	Tip Signal	51.15
UT Tip Signal	0.1375	Velocity	0.125
6 dB Drop Δ	0.078	Angle	60
UT Tip Signal Δ	0.1425		

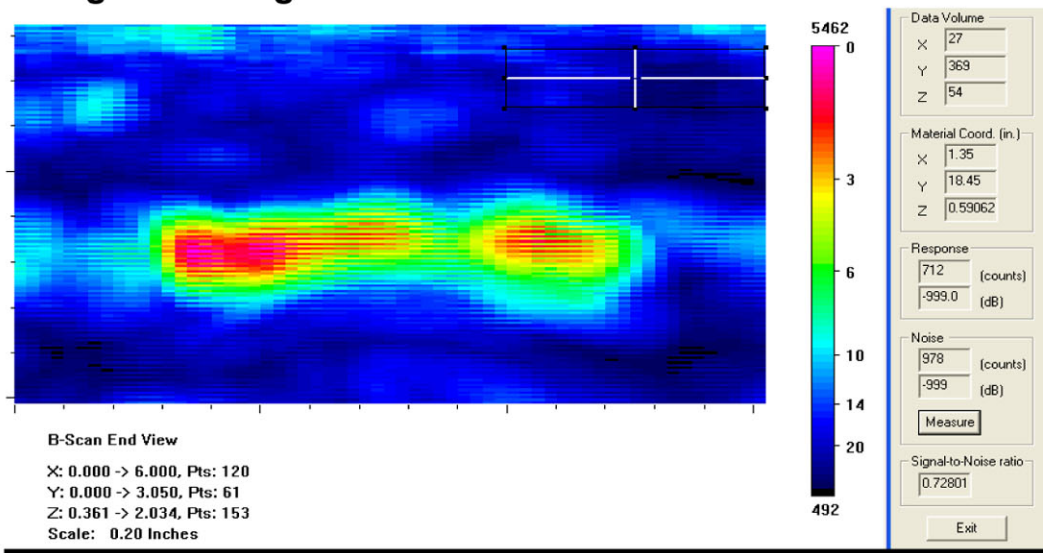

Noise Characterization

Peak Signal Response		5462	
Noise		S/N Ratio	dB
General Weld Root	2025	2.7	8.6
Local Weld Root	2138	2.6	8.1
Cursor Window	978	5.6	14.9

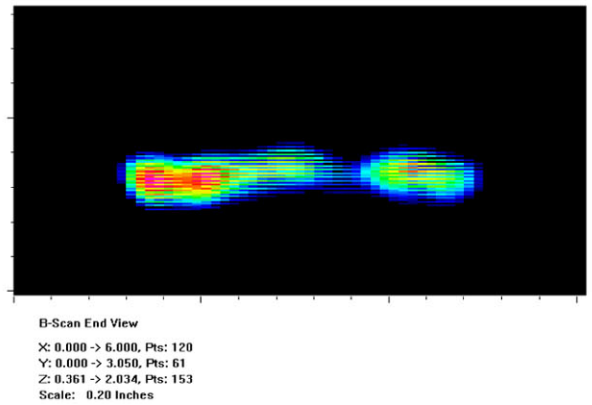

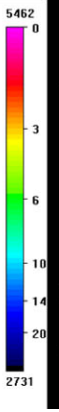

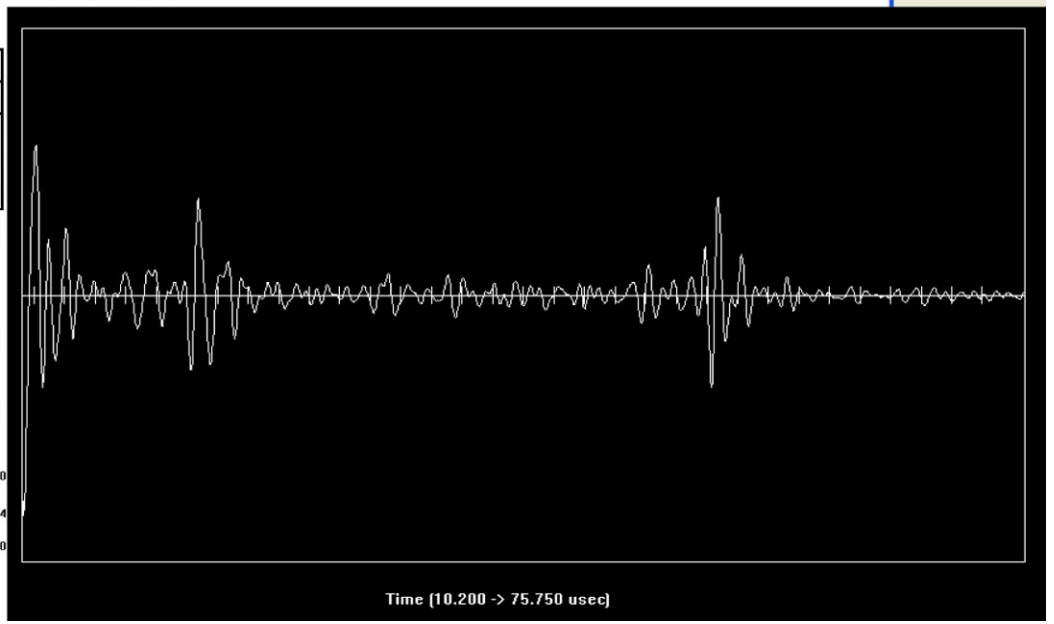

Section #2, Farside, Saw Cut F, 19% Through Wall Angle

1.5-MHz, 0.5-in.-diameter, 70° Shear

Length Sizing

Actual	2.349
6 dB Drop	1.85
Loss of Signal	2.2
6 dB Drop Δ	0.499
Loss of Signal Δ	0.149

Depth Sizing

Actual	0.28	Corner Tra	64
6 dB Drop	0.242	Tip Signal	57.5
UT Tip Signal	0.15481	Velocity	0.125
6 dB Drop Δ	0.038	Angle	67.6
UT Tip Signal Δ	0.12519		

Noise Characterization

Peak Signal Response		16779	
Noise		S/N Ratio	dB
General Weld Root	3552	4.7	13.5
Local Weld Root	3441	4.9	13.8
Cursor Window	4449	3.8	11.5

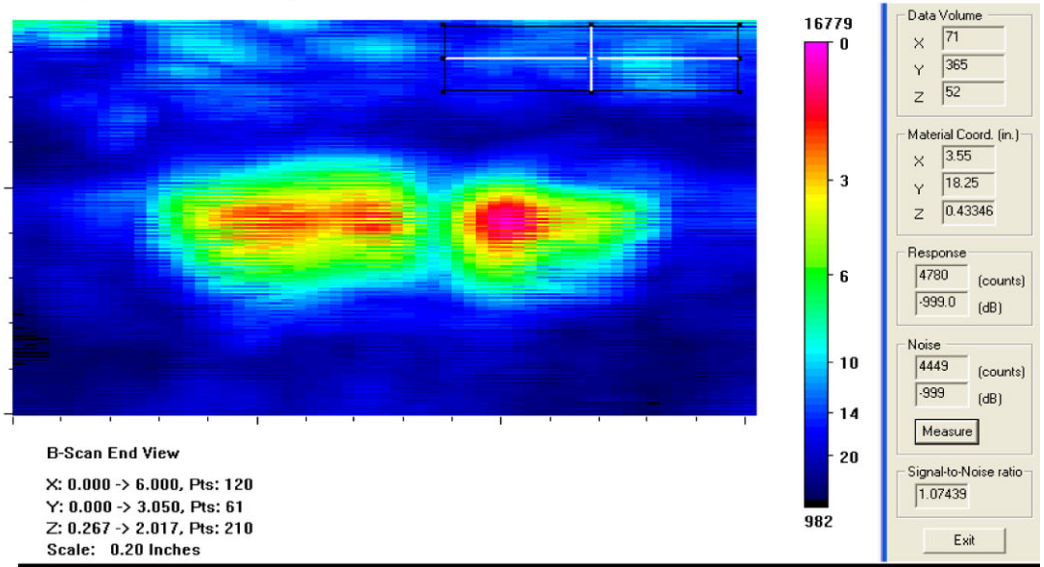

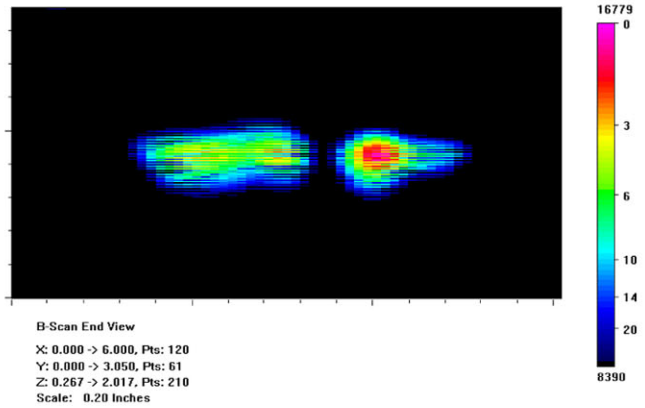

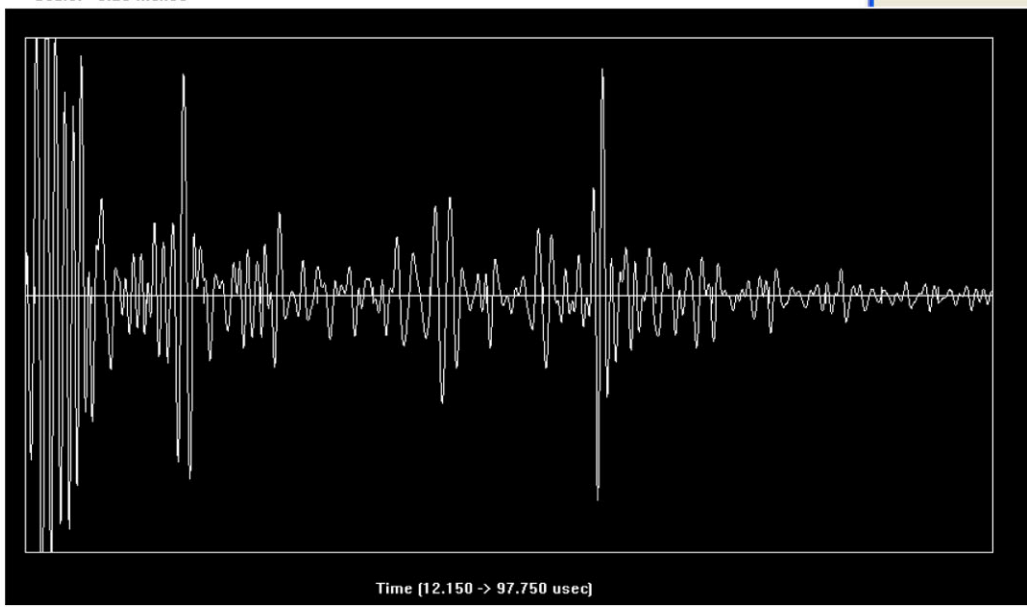

Section #3, Nearside, Saw Cut G, 18% Through Wall Angle

1.5-MHz, 0.5-in.-diameter, 60° Shear

Length Sizing

Actual	2.25
6 dB Drop	2.05
Loss of Signal	2.25
6 dB Drop Δ	0.2
Loss of Signal Δ	0

Depth Sizing

Actual	0.25	Corner Tra	51.65
6 dB Drop	0.317	Tip Signal	44.15
UT Tip Signal	0.234375	Velocity	0.125
6 dB Drop Δ	-0.067	Angle	60
UT Tip Signal Δ	0.015625		

Noise Characterization

Peak Signal Response		6662	
Noise		S/N Ratio	dB
General Weld Root	N/A	N/A	N/A
Local Weld Root	N/A	N/A	N/A
Cursor Window	2313	2.9	9.2

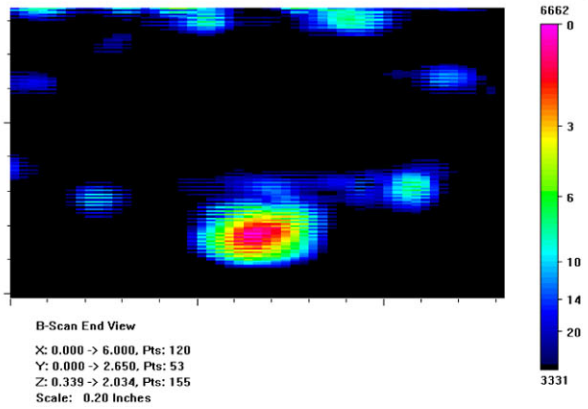

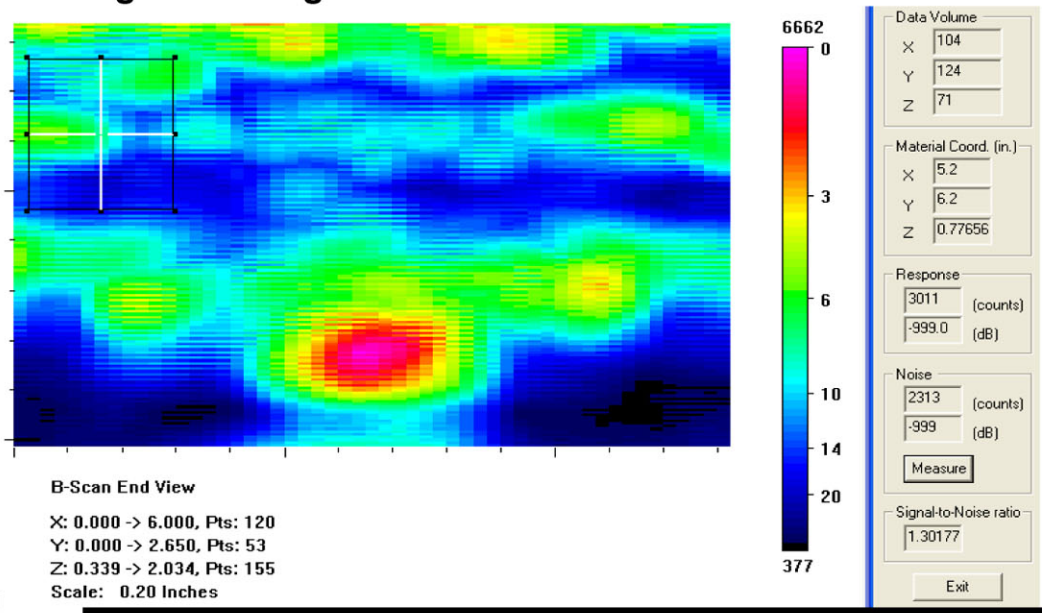

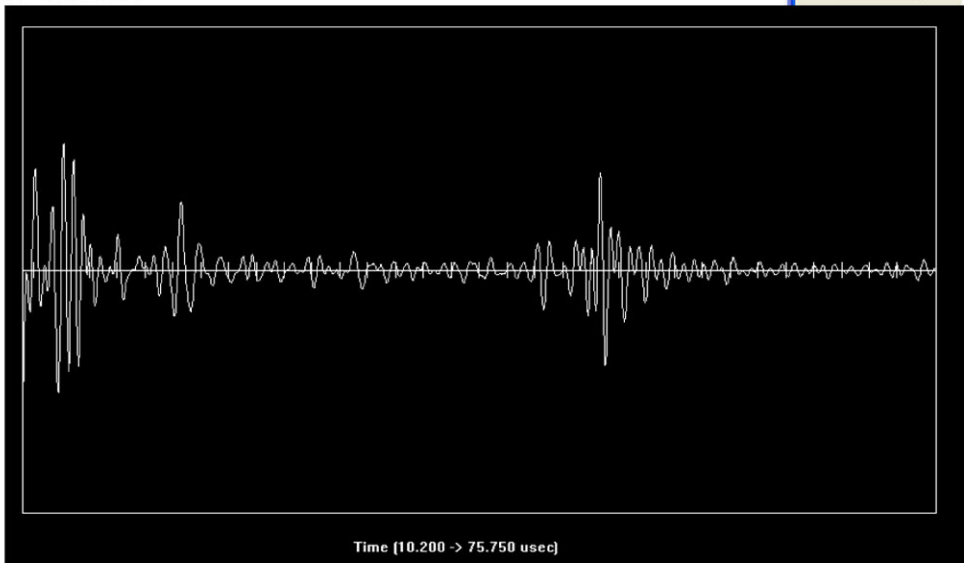

Section #3, Nearside, Saw Cut G, 18% Through Wall Angle

1.5-MHz, 0.5-in.-diameter, 70° Shear

Length Sizing

Actual	2.25
6 dB Drop	1.2
Loss of Signal	2
6 dB Drop Δ	1.05
Loss of Signal Δ	0.25

Depth Sizing

Actual	0.25	Corner Tra	70.6
6 dB Drop	0.292	Tip Signal	56.15
UT Tip Signal	0.344154	Velocity	0.125
6 dB Drop Δ	-0.042	Angle	67.6
UT Tip Signal Δ	-0.09415		

Noise Characterization

Peak Signal Response		14349	
Noise		S/N Ratio	dB
General Weld Root	N/A	N/A	N/A
Local Weld Root	N/A	N/A	N/A
Cursor Window	2516	5.7	15.1

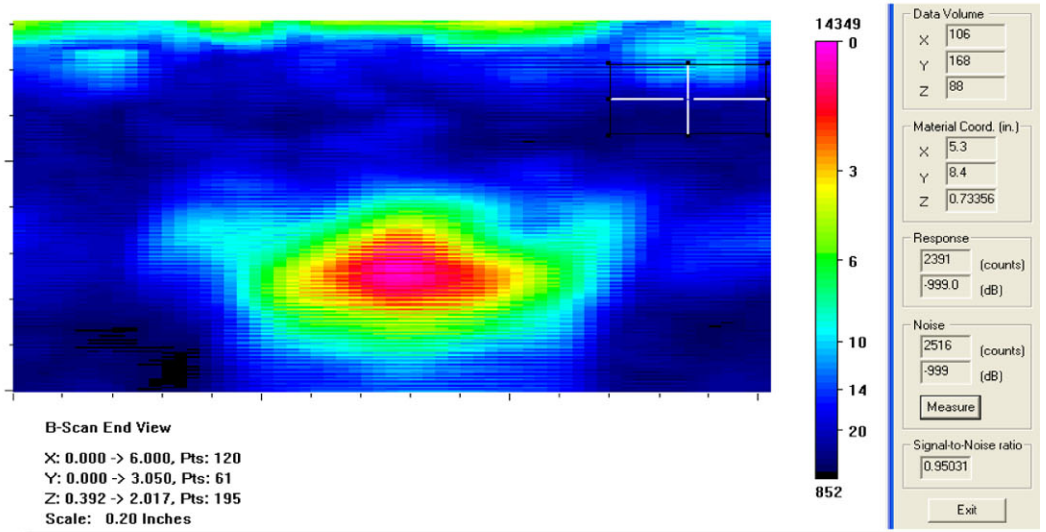

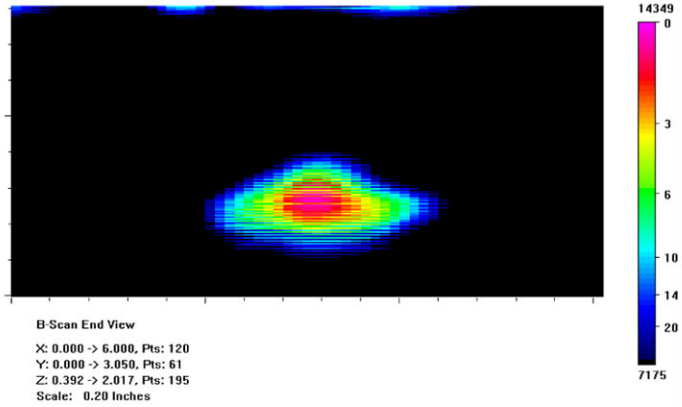

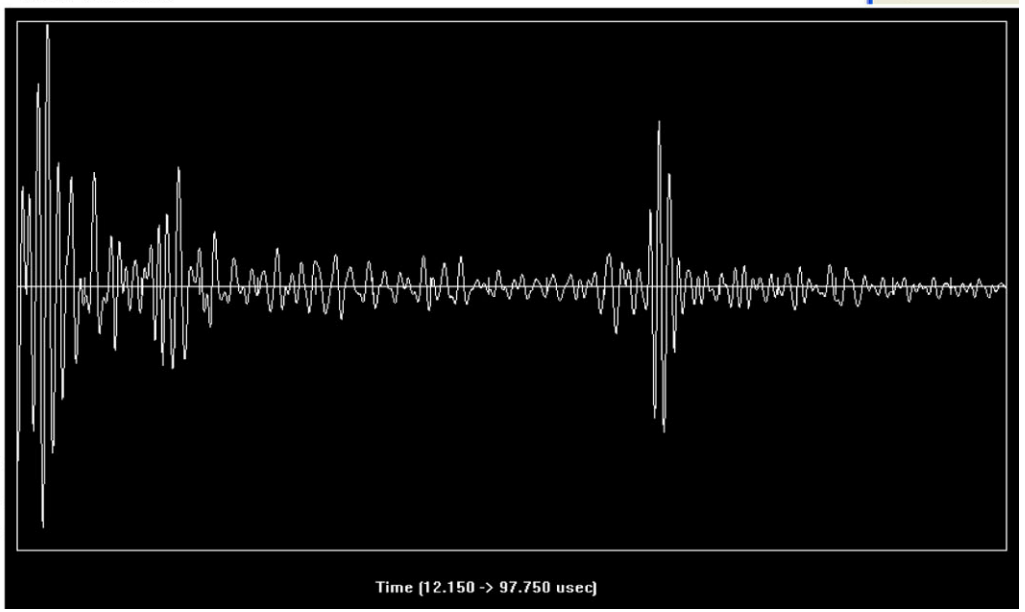

Section #3, Farside, Saw Cut G, 18% Through Wall Angle

1.5-MHz, 0.5-in.-diameter, 60° Shear

Length Sizing

Actual	2.25
6 dB Drop	1.7
Loss of Signal	2.15
6 dB Drop Δ	0.55
Loss of Signal Δ	0.1

Depth Sizing

Actual	0.25	Corner Tra	48.4
6 dB Drop	0.164	Tip Signal	42.85
UT Tip Signal	0.173438	Velocity	0.125
6 dB Drop Δ	0.086	Angle	60
UT Tip Signal Δ	0.076563		

Noise Characterization

Peak Signal Response		17645	
Noise		S/N Ratio	dB
General Weld Root	2025	8.7	18.8
Local Weld Root	7806	2.3	7.1
Cursor Window	3601	4.9	13.8

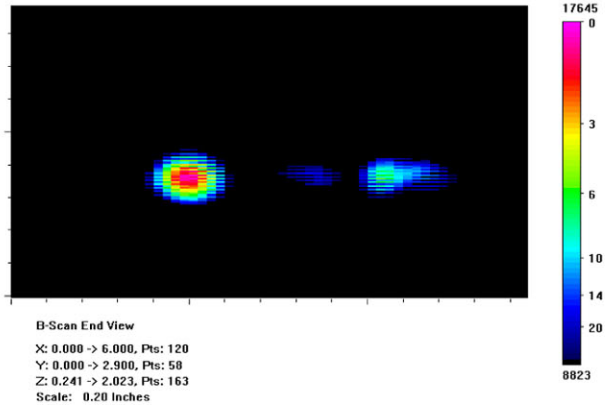

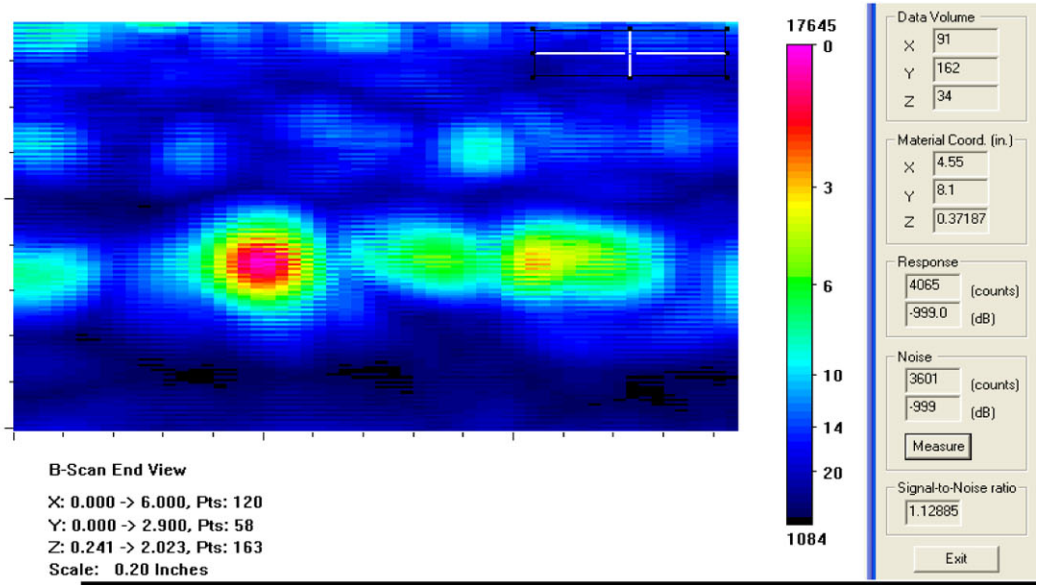

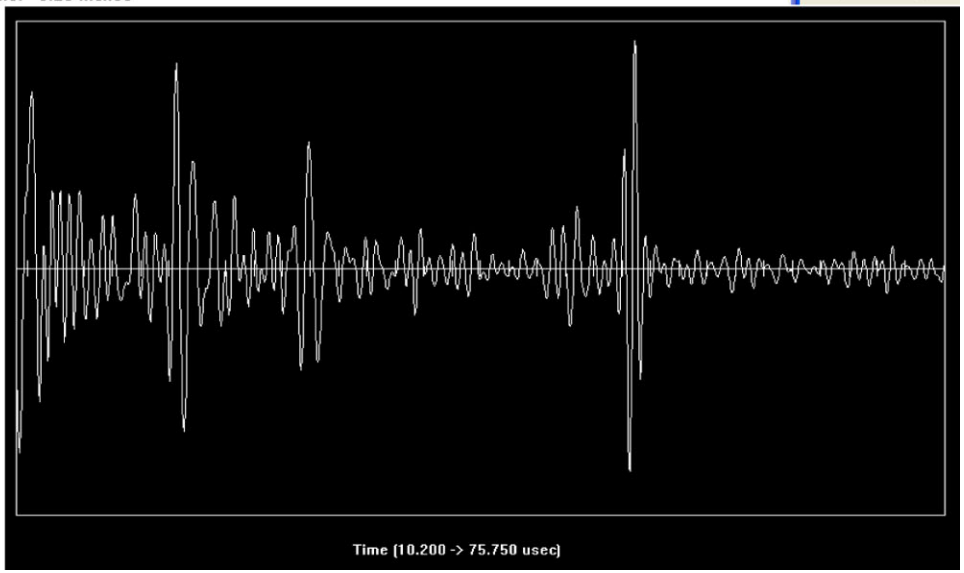

Section #3, Farside, Saw Cut G, 18% Through Wall Angle

1.5-MHz, 0.5-in.-diameter, 70° Shear

Length Sizing

Actual	2.25
6 dB Drop	1.4
Loss of Signal	2.3
6 dB Drop Δ	0.85
Loss of Signal Δ	-0.05

Depth Sizing

Actual	0.25	Corner Tra	72.9
6 dB Drop	0.182	Tip Signal	54.35
UT Tip Signal	0.441803	Velocity	0.125
6 dB Drop Δ	0.068	Angle	67.6
UT Tip Signal Δ	-0.1918		

Noise Characterization

Peak Signal Response		15757	
Noise		S/N Ratio	dB
General Weld Root	3552	4.4	12.9
Local Weld Root	5309	3.0	9.4
Cursor Window	5233	3.0	9.6

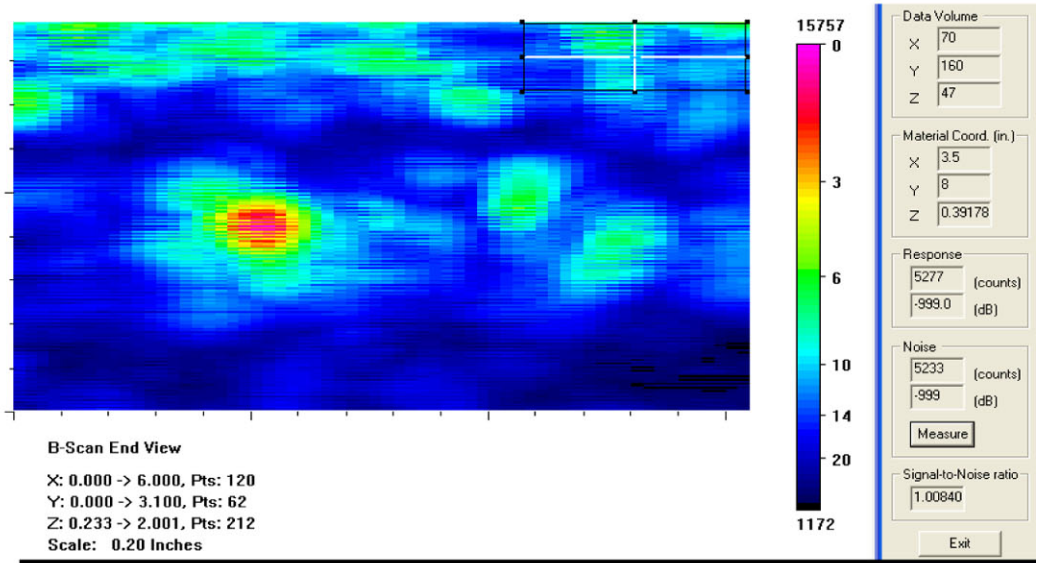

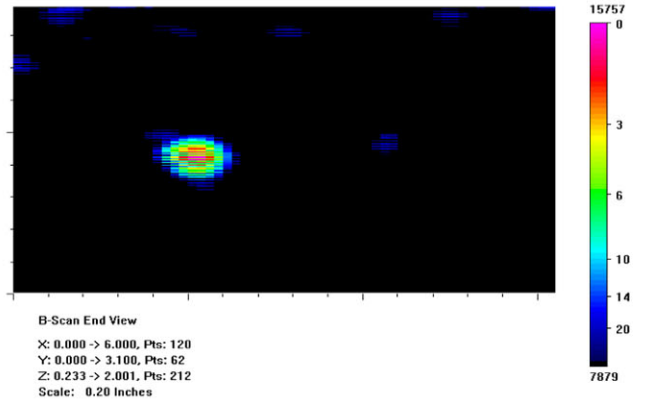

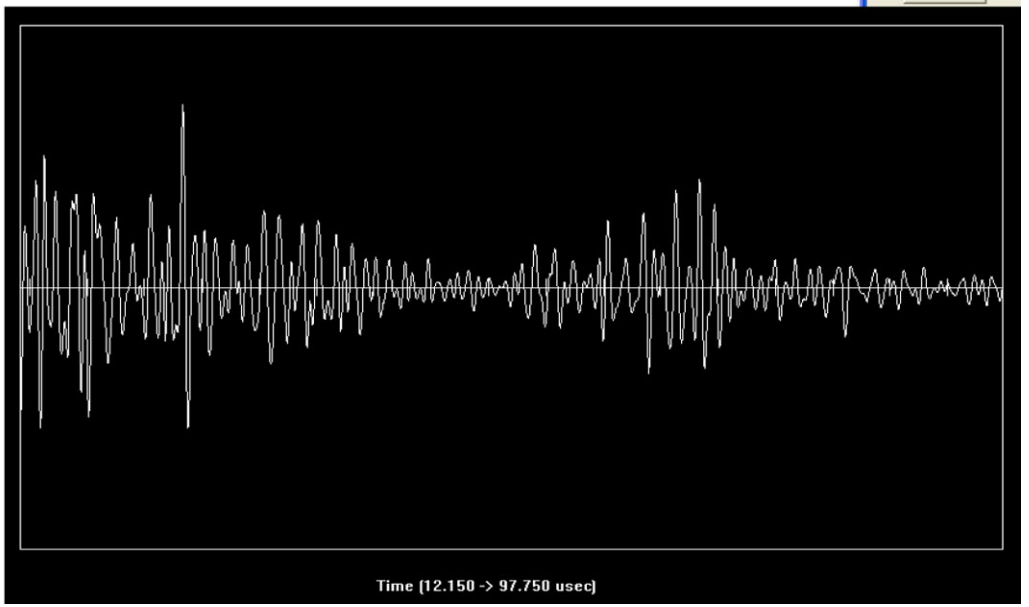

Section #3, Nearside, Saw Cut H, 26% Through Wall Angle

1.5-MHz, 0.5-in.-diameter, 60° Shear

Length Sizing

Actual	2.69
6 dB Drop	1.55
Loss of Signal	2.9
6 dB Drop Δ	1.14
Loss of Signal Δ	-0.21

Depth Sizing

Actual	0.37	Corner Tra	60.15
6 dB Drop	0.51407	Tip Signal	41.75
UT Tip Signal	0.575	Velocity	0.125
6 dB Drop Δ	-0.14407	Angle	60
UT Tip Signal Δ	-0.205		

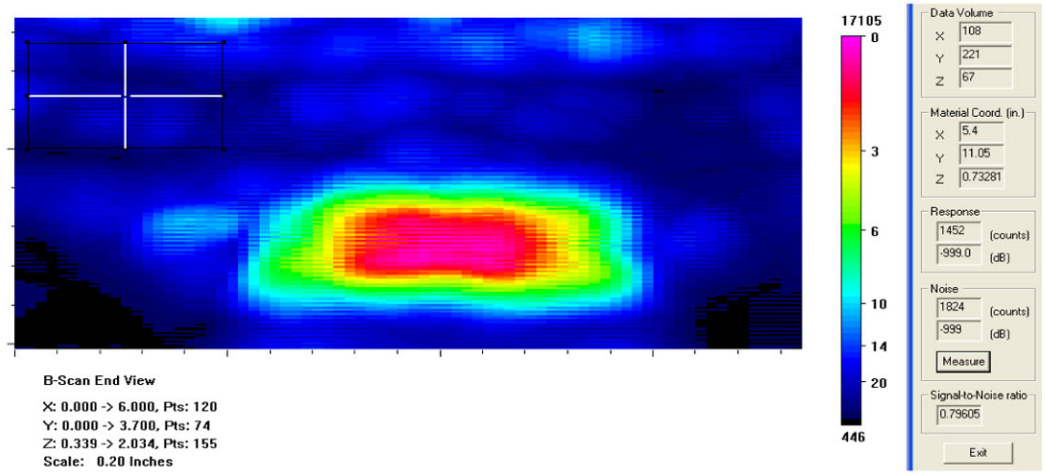

Noise Characterization

Peak Signal Response		17105	
Noise		S/N Ratio	dB
General Weld Root	N/A	N/A	N/A
Local Weld Root	N/A	N/A	N/A
Cursor Window	1824	9.4	19.4

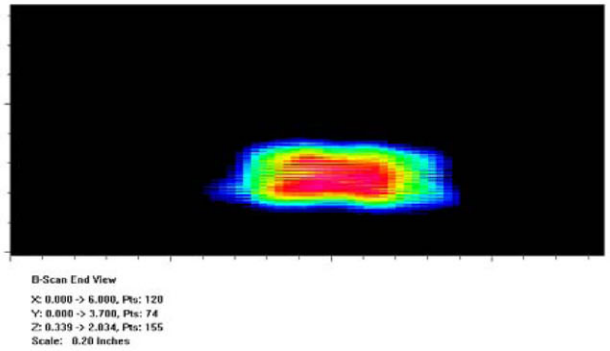

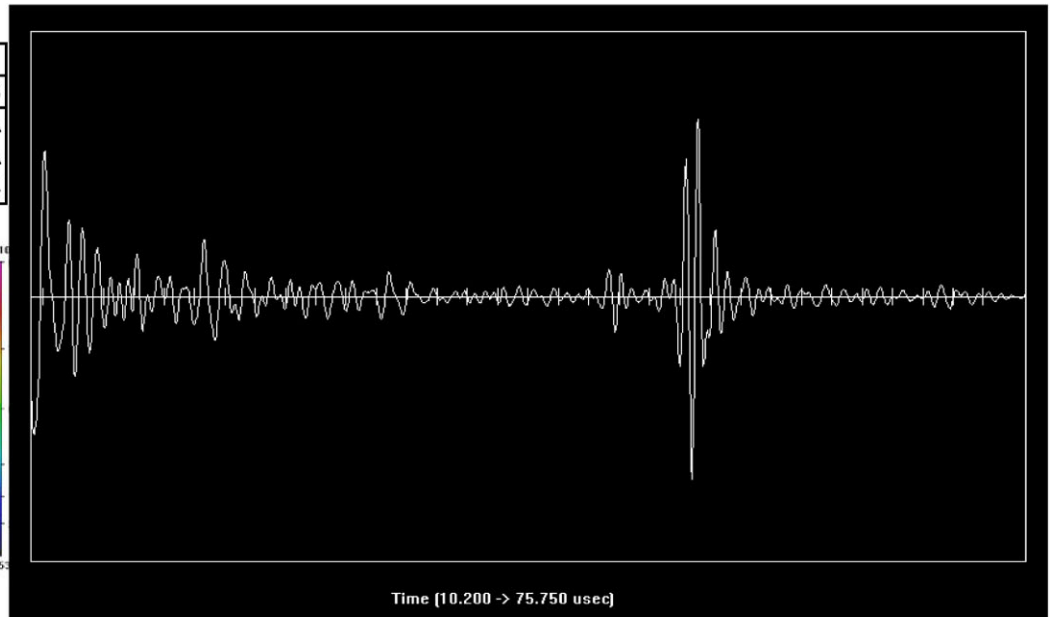

Section #3, Nearside, Saw Cut H, 26% Through Wall Angle

1.5-MHz, 0.5-in.-diameter, 70° Shear

Length Sizing

Actual	2.69
6 dB Drop	2.25
Loss of Signal	2.65
6 dB Drop Δ	0.44
Loss of Signal Δ	0.04

Depth Sizing

Actual	0.37	Corner Tra	60.75
6 dB Drop	0.35	Tip Signal	49.75
UT Tip Signal	0.261986	Velocity	0.125
6 dB Drop Δ	0.02	Angle	67.6
UT Tip Signal Δ	0.108014		

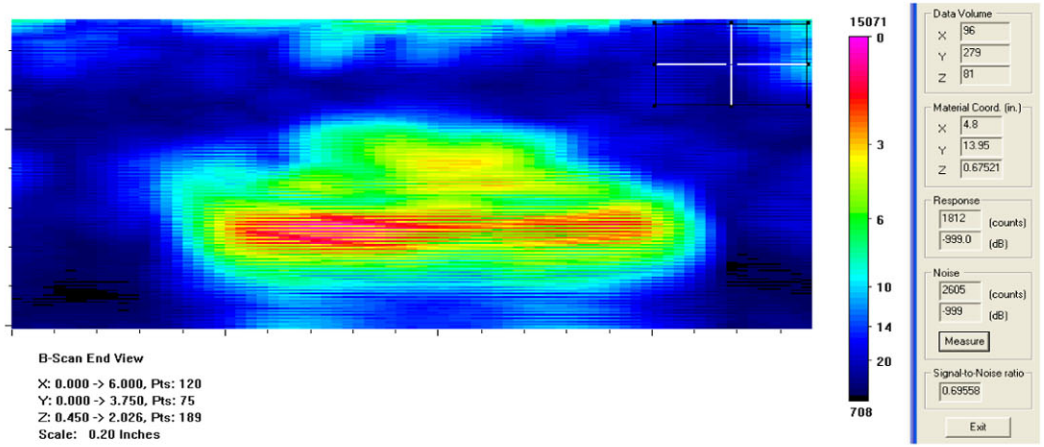

Noise Characterization

Peak Signal Response		15071	
Noise		S/N Ratio	dB
General Weld Root	N/A	N/A	N/A
Local Weld Root	N/A	N/A	N/A
Cursor Window	2605	5.8	15.2

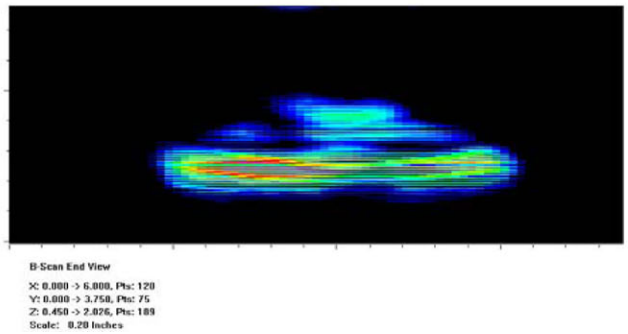

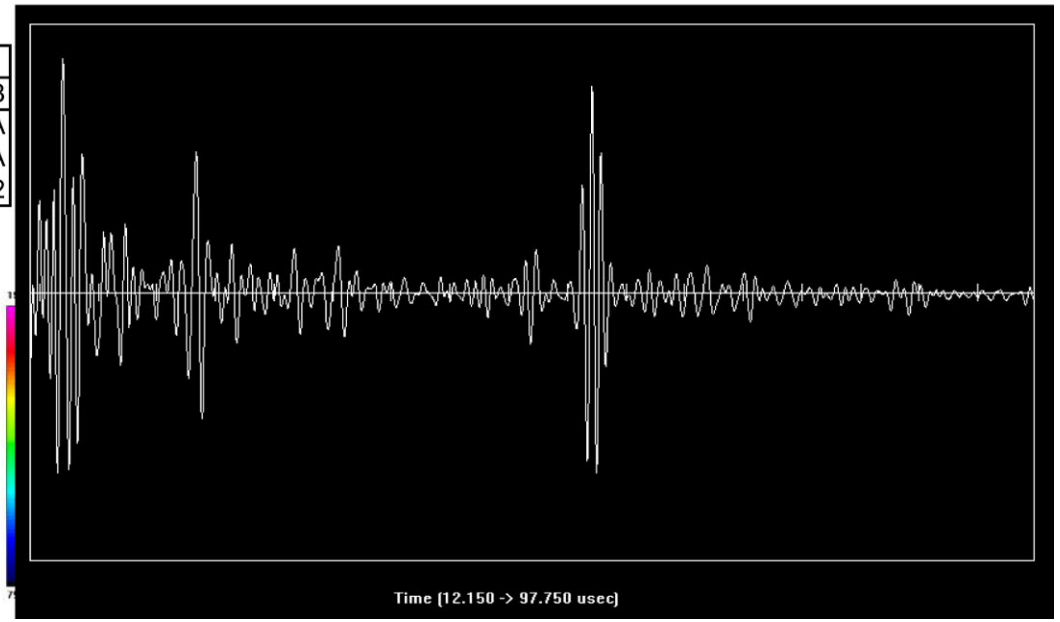

Section #3, Farside, Saw Cut H, 26% Through Wall Angle

1.5-MHz, 0.5-in.-diameter, 60° Shear

Length Sizing

Actual	2.69
6 dB Drop	2.05
Loss of Signal	2.9
6 dB Drop Δ	0.64
Loss of Signal Δ	-0.21

Depth Sizing

Actual	0.37	Corner Tra	50.7
6 dB Drop	0.186	Tip Signal	38.95
UT Tip Signal	0.367188	Velocity	0.125
6 dB Drop Δ	0.184	Angle	60
UT Tip Signal Δ	0.002812		

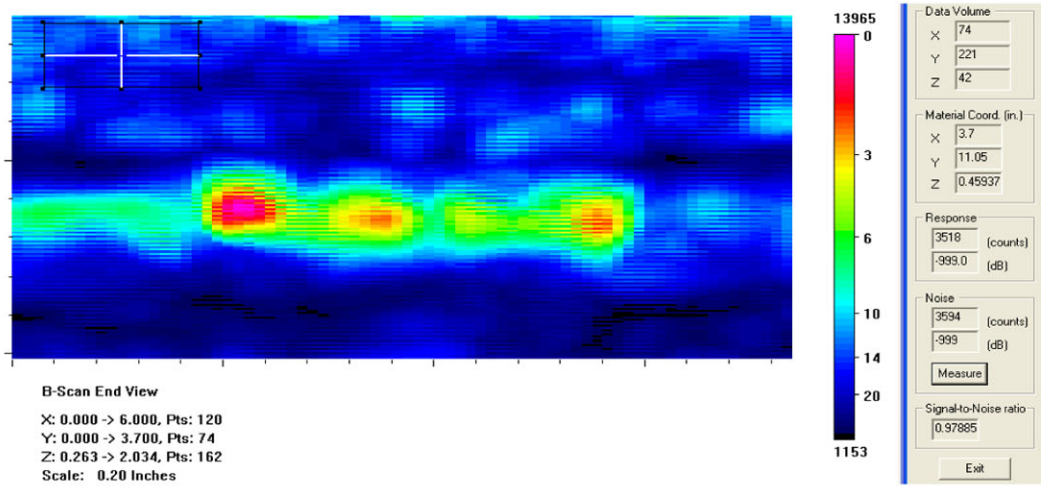

Noise Characterization

Peak Signal Response		13965	
Noise		S/N Ratio	dB
General Weld Root	2025	6.9	16.8
Local Weld Root	4598	3.0	9.6
Cursor Window	3594	3.9	11.8

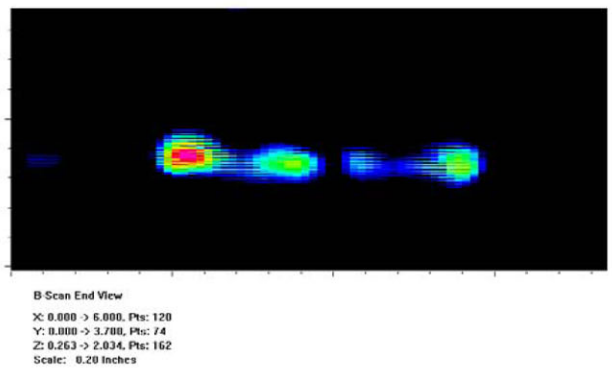

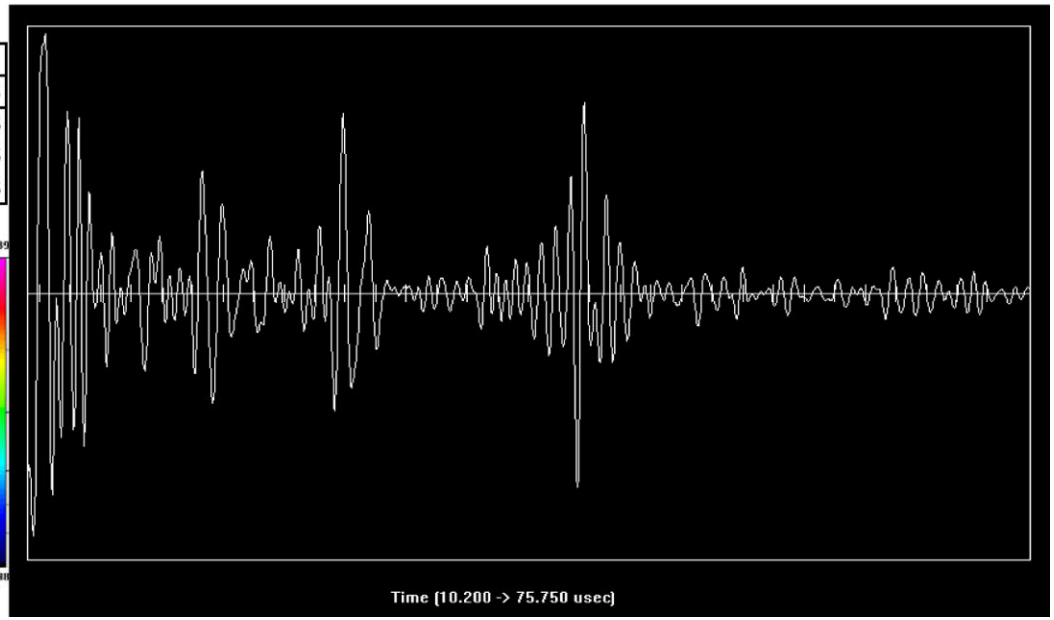

Section #3, Farside, Saw Cut H, 26% Through Wall Angle

1.5-MHz, 0.5-in.-diameter, 70° Shear

Length Sizing

Actual	2.69
6 dB Drop	2.45
Loss of Signal	2.75
6 dB Drop Δ	0.24
Loss of Signal Δ	-0.06

Depth Sizing

Actual	0.37	Corner Trap	
6 dB Drop	0.308	Tip Signal	None
UT Tip Signal	None	Velocity	0.125
6 dB Drop Δ	0.062	Angle	67.6
UT Tip Signal Δ	None		

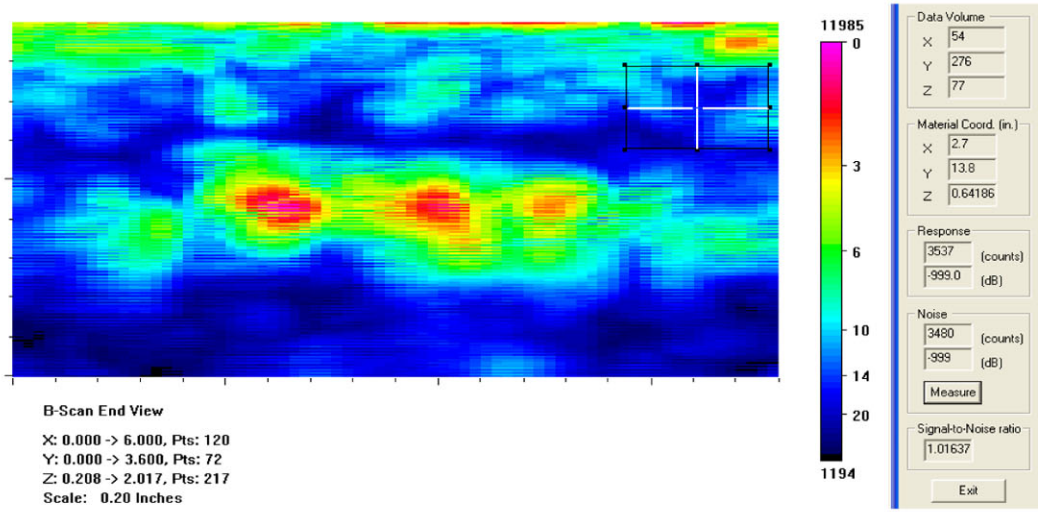

Noise Characterization

Peak Signal Response		11985	
Noise		S/N Ratio	dB
General Weld Root	3552	3.4	10.6
Local Weld Root	5258	2.3	7.2
Cursor Window	3480	3.4	10.7

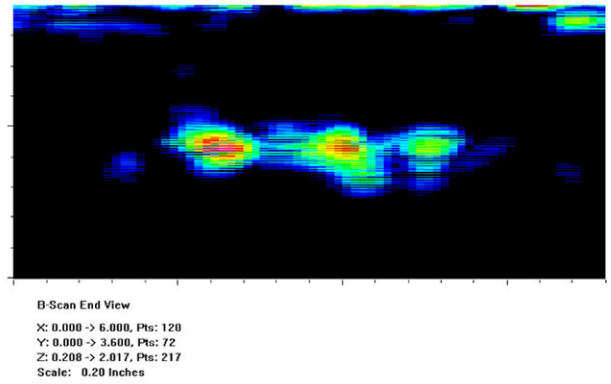

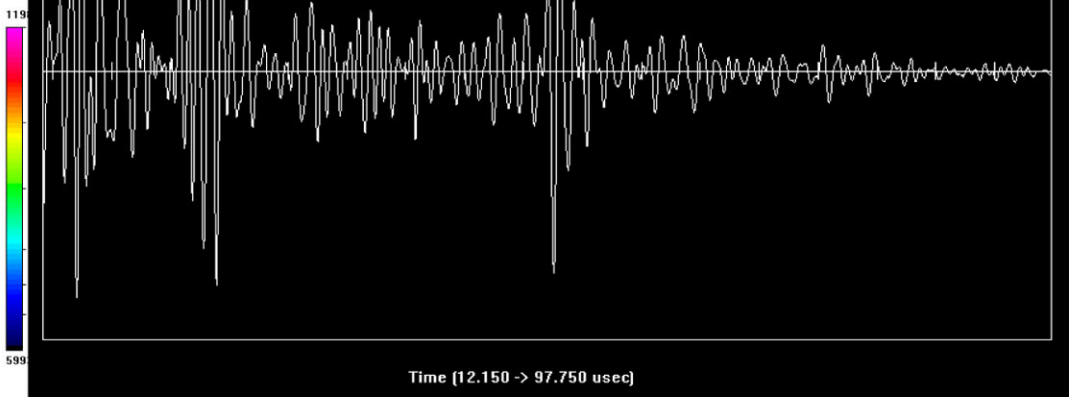

Section #3, Nearside, Flaw E, 48% Through Wall

1.5-MHz, 0.5-in.-diameter, 60° Shear

Length Sizing

Actual	1.33
6 dB Drop	1.2
Loss of Signal	2
6 dB Drop Δ	0.13
Loss of Signal Δ	-0.67

Depth Sizing

Actual	0.65	Corner Tra	53.2
6 dB Drop	0.443	Tip Signal	37.95
UT Tip Signal	0.476563	Velocity	0.125
6 dB Drop Δ	0.207	Angle	60
UT Tip Signal Δ	0.173438		

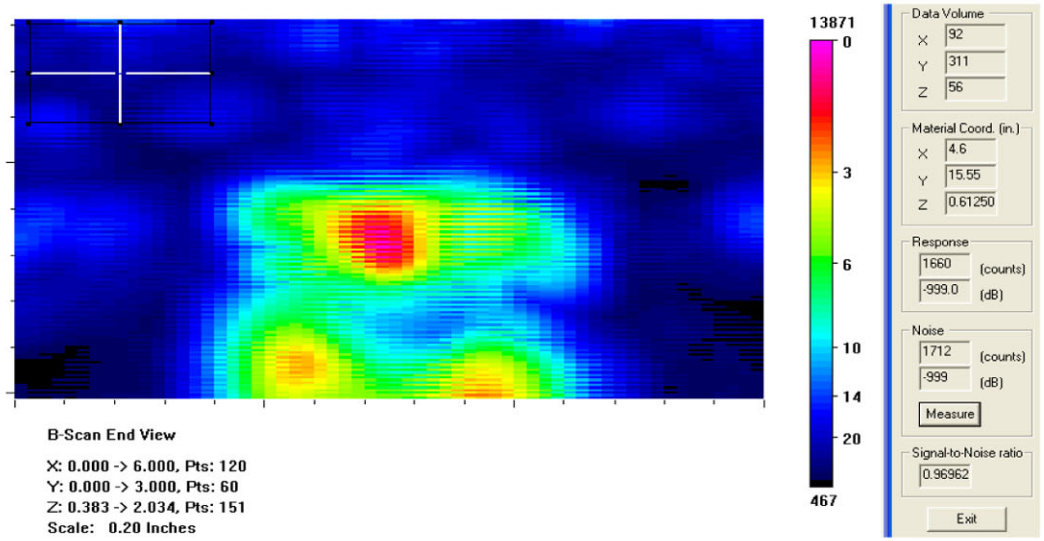

Noise Characterization

Peak Signal Response		13871	
Noise		S/N Ratio	dB
General Weld Root	N/A	N/A	N/A
Local Weld Root	N/A	N/A	N/A
Cursor Window	1712	8.1	18.2

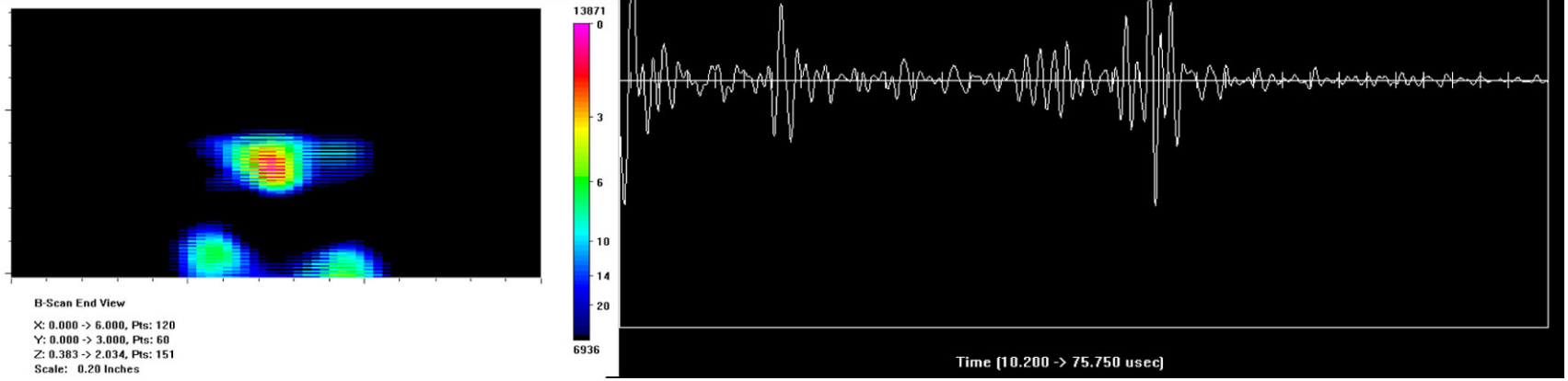

Section #3, Nearside, Flaw E, 48% Through Wall

1.5-MHz, 0.5-in.-diameter, 70° Shear

Length Sizing

Actual	1.33
6 dB Drop	1.3
Loss of Signal	1.85
6 dB Drop Δ	0.03
Loss of Signal Δ	-0.52

Depth Sizing

Actual	0.65	Corner Tra	85
6 dB Drop	0.471	Tip Signal	62.9
UT Tip Signal	0.526353	Velocity	0.125
6 dB Drop Δ	0.179	Angle	67.6
UT Tip Signal Δ	0.123647		

Noise Characterization

Peak Signal Response		20556	
Noise		S/N Ratio	dB
General Weld Root	N/A	N/A	N/A
Local Weld Root	N/A	N/A	N/A
Cursor Window	2711	7.6	17.6

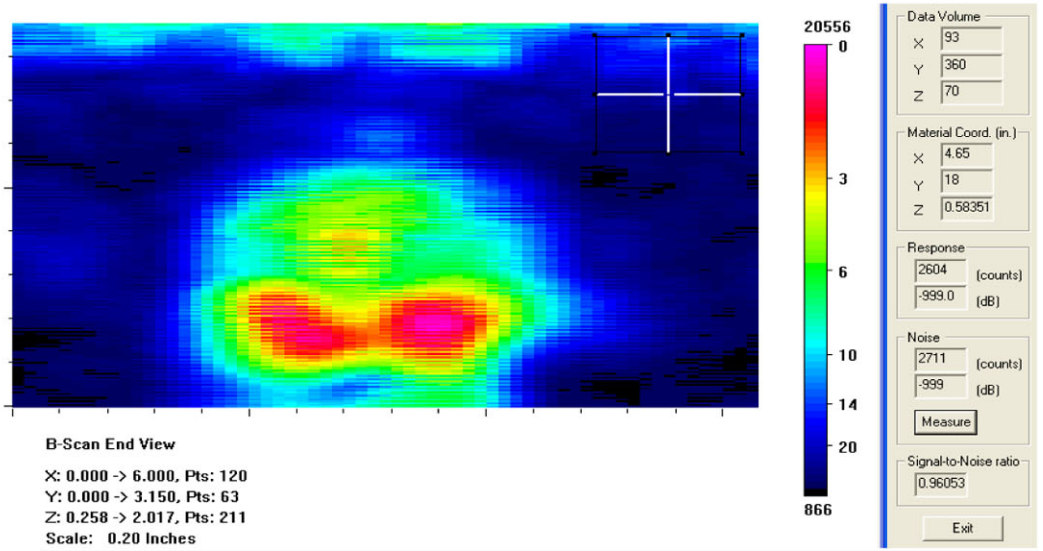

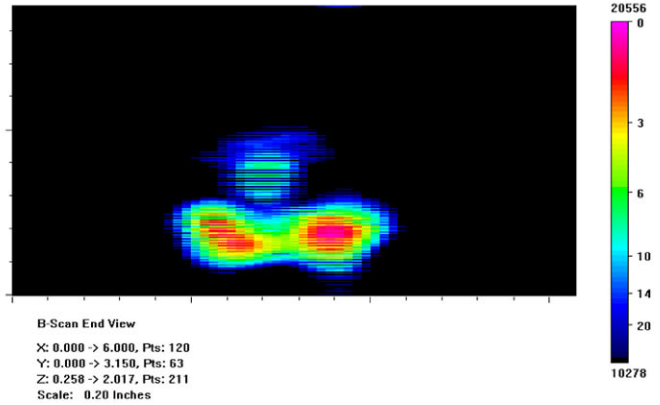

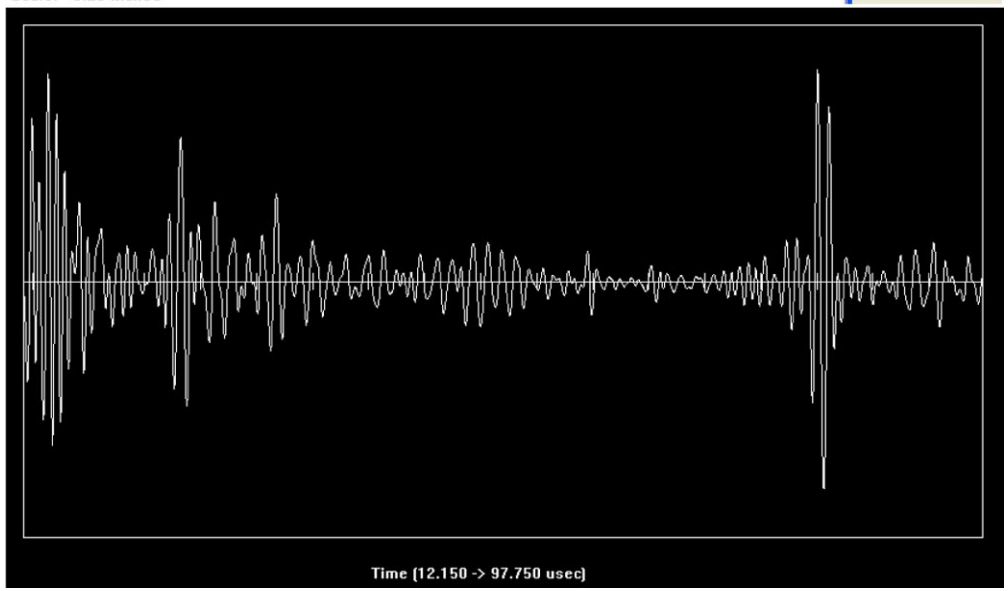

Section #3, Farside, Flaw E, 48% Through Wall

1.5-MHz, 0.5-in.-diameter, 60° Shear

Length Sizing

Actual	1.33
6 dB Drop	1.35
Loss of Signal	1.95
6 dB Drop Δ	-0.02
Loss of Signal Δ	-0.62

Depth Sizing

Actual	0.65	Corner Tra	55.55
6 dB Drop	0.273	Tip Signal	41.45
UT Tip Signal	0.440625	Velocity	0.125
6 dB Drop Δ	0.377	Angle	60
UT Tip Signal Δ	0.209375		

Noise Characterization

Peak Signal Response		16222	
Noise		S/N Ratio	dB
General Weld Root	2025	8.0	18.1
Local Weld Root	9522	1.7	4.6
Cursor Window	3847	4.2	12.5

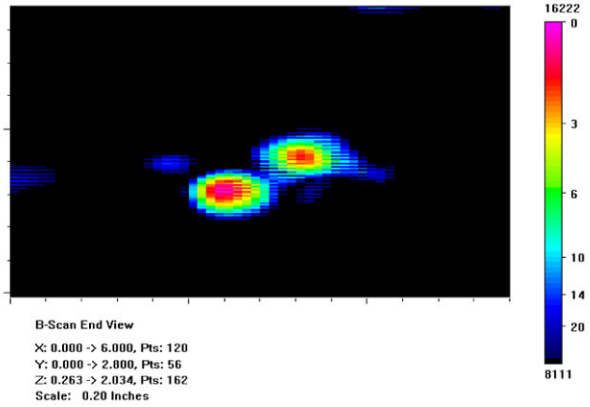

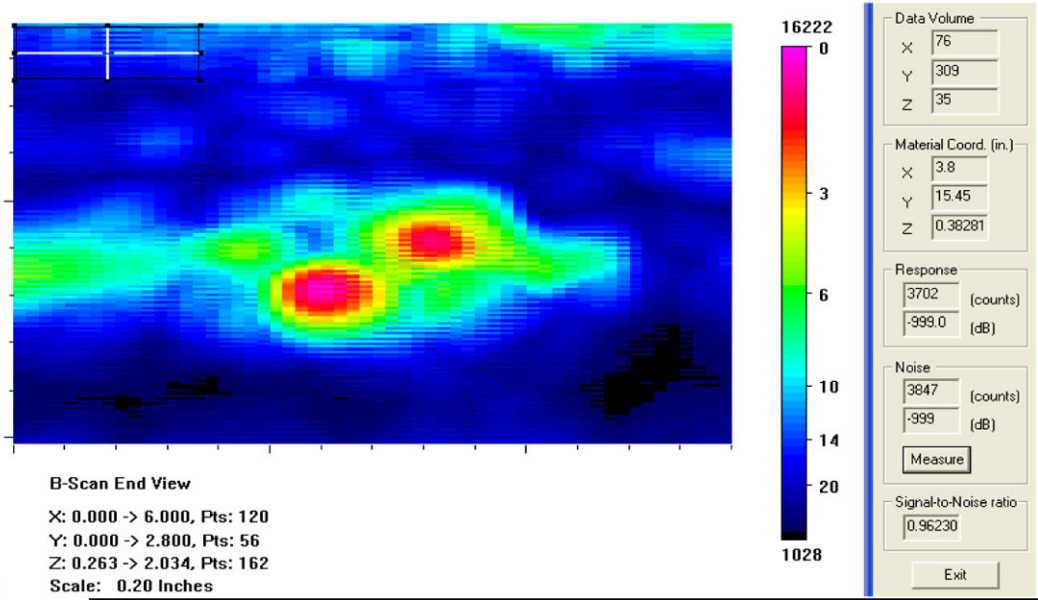

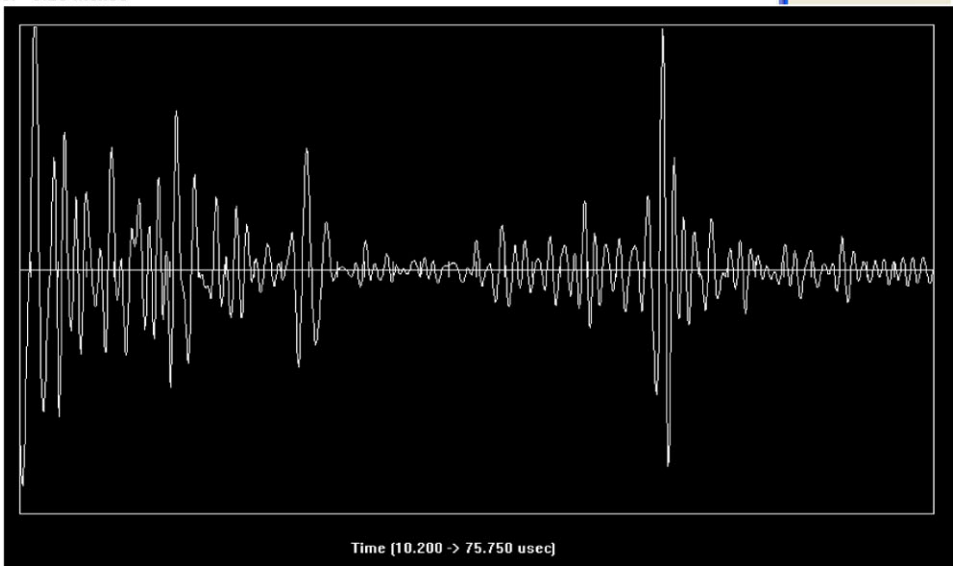

Section #3, Farside, Flaw E, 48% Through Wall

1.5-MHz, 0.5-in.-diameter, 70° Shear

Length Sizing

Actual	1.33
6 dB Drop	1.35
Loss of Signal	1.65
6 dB Drop Δ	-0.02
Loss of Signal Δ	-0.32

Depth Sizing

Actual	0.65	Corner Trap	
6 dB Drop	0.254	Tip Signal	None
UT Tip Signal	None	Velocity	0.125
6 dB Drop Δ	0.396	Angle	67.6
UT Tip Signal Δ	None		

Noise Characterization

Peak Signal Response		21975	
Noise		S/N Ratio	dB
General Weld Root	3552	6.2	15.8
Local Weld Root	6069	3.6	11.2
Cursor Window	4083	5.4	14.6